

## FLUIDS ENGINEERING DIVISION

Technical Editor  
**DEMETRI P. TELIONIS (1995)**  
Executive Secretary  
**PAT WHITE (1995)**  
Technical Editor's Office  
**SAAD A. RAGAB**  
Calendar Editor  
**M. F. ACKERSON**

## Associate Technical Editors

**R. K. AGARWAL (1994)**  
**O. BAYSAL (1995)**  
**MICHAEL L. BILLET (1992)**  
**DENNIS M. BUSHNELL (1993)**  
**N. A. CUMPSTY (1995)**  
**M. GHARIB (1995)**  
**A. F. GHONIEM (1995)**  
**CHIH-MING HO (1993)**  
**THOMAS T. HUANG (1993)**  
**J. A. C. HUMPHREY (1994)**  
**O. C. JONES (1995)**  
**G. KARNIADAKIS (1995)**  
**R. W. METCALFE (1995)**  
**L. NELIK (1995)**  
**R. L. PANTON (1995)**  
**ANDREA PROSPERETTI (1993)**  
**M. W. REEKS (1995)**

## BOARD ON COMMUNICATIONS

Chairman and Vice-President  
**R. D. ROCKE**

## Members-at-Large

**T. BARLOW, W. BEGELL, T. F. CONRY,**  
**T. DEAR, J. KITTO, R. MATES, W. MORGAN,**  
**E. M. PATTON, S. PATULSKI, R. E. REDER,**  
**A. VAN DER SLUYS, F. M. WHITE,**

President, **J. A. FALCON**

Exec. Dir.

**D. L. BELDEN**

Treasurer,

**ROBERT A. BENNETT**

## PUBLISHING STAFF

Mng. Dir., Publ.,

**CHARLES W. BEARDSLEY**

Managing Editor,

**CORNELIA MONAHAN**

Production Assistant, **MARISOL ANDINO**

Published Quarterly by The American Society of Mechanical Engineers

VOLUME 115 • NUMBER 1 • MARCH 1993

- 1 Editorial
- 2 Technical Forums
- 5 Perspective: Systematic Study of Reynolds Stress Closure Models in the Computations of Plane Channel Flows  
A. O. Demuren and S. Sarkar
- 13 Near-Wake Flow of a V-Gutter With Slit Bleed  
Jing-Tang Yang and Go-Long Tsai
- 21 On the Main Flow Pattern in Hydrocyclones  
C. C. Hwang, H. Q. Shen, G. Zhu, and M. M. Khonsari
- 26 Drag Reduction of a Cylinder/Endwall Junction Using the Iceformation Method  
R. S. LaFleur and L. S. Langston
- 33 Evaluation and Comparison of Bounding Techniques for Convection-Diffusion Problems  
M. A. R. Sharif and A. A. Busnaina
- 41 Hydraulic Characteristics of Mixed Convection in a Heated Vertical Pipe  
Jian-Chiu Han
- 48 Parametrical Investigation of the Interaction Between Turbulent Wall Shear Layers and Normal Shock Waves, Including Separation  
J. K. Kaldellis
- 56 Prediction of Turbulent Boundary Layers With a Second-Moment Closure: Part I—Effects of Periodic Pressure Gradient, Wall Transpiration, and Free-Stream Turbulence  
N. Shima
- 64 Prediction of Turbulent Boundary Layers With a Second-Moment Closure: Part II—Effects of Streamline Curvature and Spanwise Rotation  
N. Shima
- 70 Application of the  $k-\epsilon$  Turbulence Model to the Simulation of a Fully Pulsed Free Air Jet  
L. J. W. Graham and K. Bremhorst
- 75 Airfoil Shape Optimization Using Sensitivity Analysis on Viscous Flow Equations  
Mohamed E. Eleshaky and Oktay Baysal
- 85 The Flow Around Surface-Mounted, Prismatic Obstacles Placed in a Fully Developed Channel Flow  
R. Martinuzzi and C. Tropea
- 93 A Comparison of the Linear and Nonlinear  $k-\epsilon$  Turbulence Models in Combustors  
C. C. Hwang, Genxing Zhu, M. Massoudi, and J. M. Ekmann
- 103 Modeling and Computation of Flow in a Passage With 360-Degree Turning and Multiple Airfoils  
W. Shyy and T. C. Vu
- 109 LDV Measurements of Periodic Fully Developed Main and Secondary Flows in a Channel With Rib-Disturbed Walls  
T.-M. Liou, Y.-Y. Wu, and Y. Chang
- 115 Real Gas Effects for Compressible Nozzle Flows  
D. Drikakis and S. Tsangaris
- 121 An Inverse Inviscid Method for the Design of Quasi-Three-Dimensional Turbomachinery Cascades  
E. Bonataki, P. Chaviaropoulos, and K. D. Papailiou
- 128 An Investigation of Nucleating Flows of Steam in a Cascade of Turbine Blading  
F. Bakhtar, R. A. Webb, M. H. Shojaaee-Fard, and M. A. Siraj
- 135 A Theoretical Analysis of Rotating Cavitation in Inducers  
Y. Tsujimoto, K. Kamijo, and Y. Yoshida
- 142 The Accuracy of a Three-Component Laser Doppler Velocimeter System Using a Single-Lens Approach  
P-A. Chevrin, H. L. Petrie, and S. Deutsch
- 148 A Simple and Accurate Method of Calibrating X-Probes  
J. John and T. Schobeiri

(Contents continued on page 20)

**Contents (continued)**

- 153 **A New Approach to the Dynamic Parameter Estimation of a Viscoelastic System**  
S. Bennis
- Technical Briefs**
- 162 **A Relative Examination of  $C_D$ —Re Relationships Used in Particle Trajectory Calculations**  
D. D. Kladas and D. P. Georgiou
- 166 **A Unifying Method for Sizing Throttling Valves Under Laminar or Transitional Flow Conditions**  
H. D. Baumann
- 169 **Incompressible Fluid Flow Through Pipes Packed With Spheres at Low Dimension Ratios**  
R. M. Fand, M. Sundaram, and M. Varahasamy
- 172 **A Numerical Study on the Generation Mechanism of Turbulence-Driven Secondary Flow in a Square Duct**  
Hyon Kook Myong
- 175 **Flow Behavior in Thin-Gapped Diamond-Shaped Channels With Pins**  
N. Ashgriz, J. P. Seet, and J. D. Felske
- 178 **Fluids Engineering Calendar**
- 181 **List of Reviewers**
- 183 **Journal of Fluids Engineering Index**
- Announcements and Special Notices**
- 12 **Announcement—ICLASS '94**
- 69 **Call for Proposals from USNC/TAM**
- 74 **Twelfth U.S. National Congress of Applied Mechanics**
- 84 **17th Symposium of the IAHR**
- 92 **Call for Papers—Fifth International Symposium**
- 102 **Transactions Change of Address Form**
- 108 **AGU Chapman Conference**
- 147 **Call for Papers**
- 186 **Call for Papers—1994 ASME FED Summer Meeting**
- 189 **ASME Prior Publication Notice**
- 189 **Submission of Papers**
- 189 **Statement of Experimental Uncertainty**
- 189 **Access to the Journal Data Bank**



Each year we include in our March issue some standard information on the four issues of the previous volume, namely, the list of reviewers, and an index of papers of the previous year listed under certain technical categories. In the same issue, we also provide a report on the operation of the Journal. This is a report from the Editor to the readers and the contributing authors on the progress we made in our efforts to make the scientific material offered more accessible to fluids engineers, on reducing the reviewing time, etc.

In the past year we experienced a further increase in the number of submitted papers. This trend started about four years ago. In this period, the number of submitted papers more than doubled. In the same period, the number of submitted papers in the areas of fluid applications and systems and multi-phase flow have declined, which we attribute to the fact that relatively few symposia were organized in these areas by our Division. However, many members in our Division are very active in these areas and we anticipate this trend to be reversed very soon. It appears, therefore, that we could expect a further increase in the number of submitted papers.

An informal recent investigation indicated that rather few papers presented at the meetings of the Division are submitted to the Journal. To some extent, this may be due to the impression shared by some authors that papers included in symposium proceedings can not be submitted for Journal publication. In fact, ASME does not consider proceedings papers archival and such papers are accepted by all ASME Transactions for publication. We do not actively solicit conference papers but it appears that we would serve our readership better if the most significant papers from our meetings were eventually published in our Journal.

In the past few years, subscriptions to most ASME transactions have leveled off or experienced a mild decline. We have indications that in the coming year the national financial crunch will lead to further reductions of subscription levels. So far, our Journal has been spared this decline and in fact, in the past year it has seen a modest increase in the number of subscriptions.

With a surge in submitted papers, and even with rates of acceptance kept low (between 40 and 45 percent), the number of accepted papers has grown considerably and has created a serious backlog. Our next two issues (June and September) are full and we have been scheduling papers for our December issue. To remedy this situation, we pursued and were successful in obtaining modest increases in the allotted pages and we hope that this year too, we will be able to add about one hundred extra pages to our four issues. The growth of an archival publication in one way adds to the proliferation of papers, but the readers should keep in mind that our Journal is leaner than other ASME Transactions and publishes much less material than other peer journals like *Physics of Fluids*, *AIAA Journal*, and the *Journal of Fluid Mechanics*.

Our readers may have noticed that we are now devoting a few pages in each issue to a "Technical Forum." In this space we will be publishing information and opinions directly related to the goals of the Journal and the technical needs of its readers

and contributing authors. Space will also be available to contributors who would like to offer suggested directions to the research community and information on how to improve the technology transfer from research conducted in government laboratories and universities to development of products in industry. Related to these goals is a series of articles on U.S. Competitiveness which we started with our September issue. In our next issue we will add selected abstracts from a recent Forum sponsored by our Division on Research Needs in Fluid Mechanics.

The Editorial Board of the Journal has had many discussions over the past year on what this Journal could do to improve the process of technology transfer. For the time being, this Editor urges authors strongly and in specific terms to include in their papers information on their contribution, written in a way that could be easily understood and appreciated by practicing fluids engineers. This is an issue of current concern (see the article on U.S. Competitiveness in this issue) and we are eager to participate in the process of technology transfer after the Division defines the Journal's role.

Reducing the time from submission to publication is a permanent and often frustrating task. Last year we reported some gains. We were able to reduce the time from submission to acceptance to nine months in the average and the time to publication to twelve months. It is now embarrassing to have to report that these figures have somewhat increased this year. It is true that most delays are due to tardy reviewers but it is the duty of the editorial board to continuously urge the reviewers to return their comments in a timely manner. Unfortunately, it is impossible to guarantee turn around times. The most frustrating situation is when reviewers accept the responsibility to work on a paper and months later simply do not respond. An associate editor is then forced to turn to new reviewers and start the process all over again. The severe backlog we are now experiencing will further lengthen the period from first submission to final publication of a paper, but this is beyond the control of the Editorial Board.

Finally we should acknowledge the valuable contribution of two of our associate editors whose tenure has expired. They are (i) Dr. Franklin T. Dodge, in the area of fluid machinery and (ii) Dr. Efstathios E. Michaelides who served one extra year in the area of multi-phase flow. We sincerely appreciate their hard work, but here it is perhaps appropriate to acknowledge also the contributions of our reviewers. The names of the individuals who helped us out this year are listed in the last pages of this issue.

Individuals have been nominated to serve three-year terms as associate editors. These and the areas they will be working on are: Dr. Nicholas A. Cumpsty (Cambridge University), Dr. Lev Nelik (Goulds Pumps, Inc.)—fluid applications and systems; Professor Ralph W. Metcalfe (University of Houston), Professor George Em Karniadakis (Princeton University), Professor Ahmed F. Ghoniem (MIT)—fluid mechanics; and Professor Morteza Gharib (Cal Tech)—fluid measurements.

The Technical Editor

## QUESTIONS IN FLUID MECHANICS-III

by Lloyd M. Trefethen<sup>1</sup>

### Examining What We Do Not Know

An intriguing session at the Annual Meeting of the American Association for the Advancement of Science this February in Boston was called "Ignorance and Science: Emerging Perspectives." The session's speakers and discussers spent three hours talking about a change in people's attitudes towards ignorance, uncertainty, and unanswered questions. They even described a graduate "Ignorance Curriculum" given alongside the "Knowledge Curriculum" for medical students at the University of Arizona, focusing on awareness of what is not known. This is new to the medical profession, not conspicuous in other professions. Some organizers and speakers later dined together, pleased that they had pulled it off, that the august AAAS had actually sponsored a session on "Ignorance."

In a broad sense this is just what a society like the AAAS aims to do, to shake us up so that we will confront more effective ways of understanding ourselves and the world around us. But traditionally, natural science has suppressed awareness of ignorance. A counter influence has been the writings of Australian behavioral scientist Michael Smithson, one of the speakers, whose recent (1989) book *Ignorance and Uncertainty: Emerging Paradigms*, was a backdrop to the session. Focusing on ignorance is relatively new. This particular AAAS session will increase, to some degree, interest in deliberately examining what we don't know.

Which of course is exactly what these columns on Questions in Fluid Mechanics are all about. Most fluid dynamicists would unhesitatingly agree that there is far more about fluid dynamics that we don't know than what we do know.

This brings us to touch on biological fluid mechanics, which offers an array of engineering solutions far more subtle and far more vast than anything we have achieved. The following few questions about swimming animals large enough to use inertial propulsion are a minuscule tapping of biological clues to deeper understanding of fluid mechanics. A fuller set of such questions is referenced in the electronic Questions in Fluid Mechanics Newsletter II-1, available on request from [qbank@jade.tufts.edu](mailto:qbank@jade.tufts.edu).

Appreciation for suggestions is expressed to Niel Bose, Dennis Bushnell, Joseph A. C. Humphrey, John Lienhard, Jr., Ronald Panton, Michael Smithson, and Steven Vogel. The Journal welcomes submission of drafts for future questions columns.

<sup>1</sup>Mechanical Engineering Department, Tufts University, Medford, MA 02155. Fellow ASME.

### Questioning How Large Animals Swim

*How do fish stop?* Small fish stop and start easily, as does a rower by reversing oars. Large fish, not able to stop quickly, are like ships, avoiding collisions when they have enough room not by reversing engines but by steering. There has been some work on fish starting, but little if any research on the transient techniques for stopping.

*How do dolphin and ray fin cross-sections compare? Are they at all similar to the good NACA airfoil sections?* They both appear to have highly developed propulsive foils, thick, with heavy skin surfaces, but come from drastically different evolutionary histories. There has been little work on natural foil sections.

*Does the scalloped geometry of large-ocean-animal hydrofoils represent an evolved feature that increases propulsion efficiency?* The large variety of shapes of fins and tails of fish and swimming mammals has had some study, e.g., shark tails, but their functioning in swimming and maneuvering has only begun to be explored.

*Do the roughness elements of sharkskin reduce drag, as riblets do for man-made surfaces?* The success of the 3-M adhesive riblet tapes in reducing drag has led to curiosity, as yet unresolved, about whether there are comparable animal surfaces.

*In what ways, if any, can submerged swimming animals exploit a calm water surface?* A swimming fish close to the surface is followed by a set of surface waves unlike that associated with a moving body that pierces the surface. Is this wave packet necessarily an energy drag on the fish, or can there be an offsetting surface effect, caused, for example, by vortex images? Little attention has been paid to exploitation of the liquid surface by submerged animals.

*Do large whales take advantage of wave energy for propulsion, and did whaleboats tow whale carcasses head first to exploit a propulsive effect of waves on the flukes?* It is interesting that a dead whale in a moderate sea will propel itself at about one knot. The Whale Research Group at the University of Newfoundland is working on these questions, with both live and dead whales.

*How does the water strider propel itself?* Small enough to support itself by surface tension, but large enough to generate waves, the insect can move rapidly on fresh water. Just how is not well understood.



## U.S. Competitiveness: A Fluid Engineer's Viewpoint

Column 2—A Business/Industry Perspective on Closing the Technology Assimilation Gap

by Michael J. Werle<sup>1</sup>

### Background

The first two articles in this sequence have framed this topic and delineated the principal characteristics of the situation as follows; *technology assimilation toward products is being severely impeded due to attributes systemic in our political/social/economic systems today.*, i.e., we have a severe technology assimilation gap. The current article seeks to begin the process of turning attention away from what has been previously identified as wrong in our system toward what we might do about the situation, i.e., what should or could we collectively do to improve the assimilation rate and, thus, the productivity in the United States. Two more such articles in this series are scheduled, one each focusing on academic and government perspectives.

I begin by first admitting to a degree of uneasiness speaking for all of "business/industry," and even speaking as a representative of my own corporation. Thus, I prefer to take the position of an individual member of the fluids engineering profession, giving his views on the topic, guided by input from peers. However, I do have reason to feel somewhat uniquely positioned to give this perspective, and I will begin by sharing with you an interesting bit of data that I have gathered over the period of my career. I have been fortunate to spend a significant amount of time in each of the three constituent communities: academia, government and business/industry. *In each of these, I found that they were able to clinically prove that it is the other two that are the source of this problem.* I will now try to present what I think is a balanced approach to addressing the situation.

### Significance of the Issue: It is About Competitiveness

It is worth devoting some space to discussion of the significance of the issue as viewed from the business/industry position. Certainly, one of the most important dynamics playing out in our environment today is the shift away from defense-oriented activities. This has special significance to the fluids engineering community, since a very large part of its research and development activity is in support of defense-oriented technologies. Above and beyond that, though, is the clear issue that our very existence in the competitive marketplace on a worldwide basis is under extreme pressure, and, as such, demands that we find a way to more quickly move technology across the assimilation gap. This whole issue of intense, *albeit respectful competition*, is the new reality that must be dealt with within our society and business communities. It is unlikely to disappear, and if anything, is likely to get more intense in the near future. This, then, is not a topic that we can choose to ignore without concern.

My goal here is to suggest a possible path for action that might lead to improved technology assimilation in the United States. My conclusion, that I hope to support in the following paragraph, is that we must create a politically safe standing forum for interaction among the three principal communities, business/industry, academia and government, so that they can act collegially to address the issue. In this article, I will describe the first step for our group of three to take together across the assimilation gap.

<sup>1</sup>Director for International and External Programs, United Technologies Research Center, East Hartford, CT 06108.

### The Core Issue: Business Pull Versus Technology Push

My approach is to cause intense focus of our energies to make that one magic something happen to start the process of bridging the assimilation gap. The general starting position that I take, based on my experience in industry, is well depicted in Fig. 1 which delineates the technology gap between basic/applied research and those products and services that business/industry must deliver to its customers. This pictorial is meant to represent the process by which a multiplicity of research-generated ideas/concepts are first culled to a single opportunity which must then move through continuously increasing effort/cost phases and over staging hurdles to become a successful Product and/or Service. Movement to the right of this figure represents significant increases in both investment and risk which can only be justified in terms of anticipated return on such investments from the "business" end of the process. It is for this reason that the assimilation gap can only be crossed with a significant amount of business pull from the Products and Services end, and that technology push from the Research end, while a worthy attempt, has proven both frustrating and futile.

### Some Basic Definitions: Clarifying the Vocabulary

To proceed we now need to break the problem down into a few basic elements (as shown Table 1), the first of which is to delineate the difference between technology transfer and technology transport. Technology transfer is generally agreed to by those who write on the subject to be the process of maturation from the basic/applied level to the development of products. Note, however, that there are a significant number of people in the technical community who use the words "technology transfer" to describe the process of moving technology from one place (or unit) to another. This latter activity, I believe, must be defined as technology *transport*, a different arena with equally difficult problems. However, for the purposes of the current discussion, we want to make sure we stay clearly focused only on the *transfer of technology* across the gap (maturation cycle) from research to product.

Additionally, as indicated in Table 1, we have to understand that when we talk on this topic, there is a wide range of technology categories from which we need to choose our areas of focus. For current purposes, I submit that only two of these can be of interest to us here, those activities under *Basic* and *Emerging* technologies. The logic goes as follows. Technologies in the Key category are those that represent competitive differentiators for industry in the marketplace, and, as such, are not likely to present opportunities for synergy or open dialogue. Clearly, those technologies in the Obsolete category, again, are unlikely to be an area where people are willing to

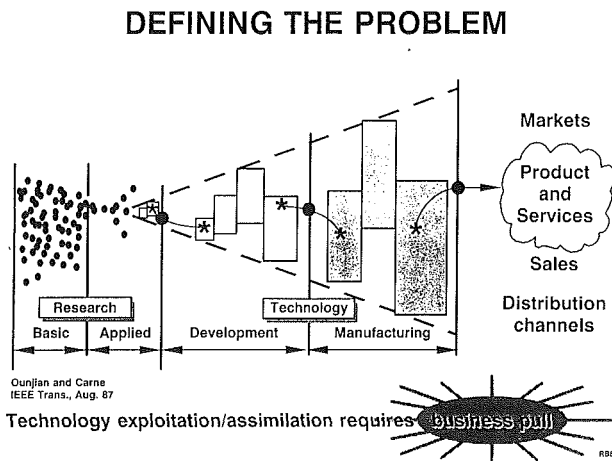


Fig. 1

Table 1 Terminology

<ul style="list-style-type: none"> <li>• <b>Technology Assimilation Dimensions</b> <ul style="list-style-type: none"> <li>– <i>Technology Transfer</i> : moving from R thru D</li> <li>– <i>Technology Transport</i> : moving from unit A to B</li> </ul> </li> <li>• <b>Technology Categories</b> <ul style="list-style-type: none"> <li>– <i>Basic</i> : required to be in the business</li> <li>– <i>Key</i> : provides competitive advantage</li> <li>– <i>Emerging</i> : new technologies, could become key</li> <li>– <i>Obsolete</i> : superseded technologies</li> <li>– <i>Incidental</i> : owned but not used in company's products</li> </ul> </li> </ul>
--

invest significant monies and/or energies. Incidental technologies fit into this same low-interest category but for obviously different reasons.

That then leaves, first, the area of Basic Technologies which are those necessary for virtually everyone in the “fluids” business, and for which improvements can be shared quite freely on a non-competitive basis. Similarly, Emerging Technologies offer an opportunity because they are in the pre-competitive phase of interest, and while causing certain anxieties about their eventual movement to the Key technology arena, present an area where value can be added and shared by the fluids community-at-large.

#### Focus For Action

For current interest then, we must stay focused on the area of the *transfer of technology* (as opposed to transport) across the assimilation gap from basic research to products and services with our attention directed at enhancing the process for *Basic* and *Emerging* technologies.

#### Roles of the Three Constituencies

We are now in a position to delineate a role for the three principal constituents within the tight framework sketched out.

I believe that it is industry’s role to delineate the level of business pull that exists for specific Basic and Emerging Technologies in fluids engineering. The result would be a published list of those *Basic* and *Emerging Technologies* for which industry saw specific need (i.e., for which business pull likely exists), and thus would be inclined to support in some fashion.

The academic research community then should guide its research into those identified arenas thereby contributing to a

more rapid movement across the assimilation gap and positioning themselves for contributing to industry’s needs in the more proprietary key technology categories. Additionally, I think that it would be worthy of the “teaching side” of the academic community to begin to capture the essence of this concept of relating technology development to business needs and bringing the student population, i.e., the next generation of engineers, up to speed on the concept.

As to the government’s role, it should be prepared to facilitate this process by providing funding support of the academic institutions in those specific areas so identified. Just as importantly, government agencies should establish policies and participation mechanisms for the government labs to be brought into this line of thinking.

#### The First Step

This, then, brings us to the point of proposing the first step of an action plan to help the process along. To this end, I believe the ASME (and perhaps its peer AIAA) to be uniquely positioned to be a prime facilitator of the process and to create a means by which we can take that important first step. In particular, I think it would be useful and appropriate to create a forum to spawn teams charged with the creation and publication of the Basic & Emerging Fluids Technology List. These teams, with membership from government, academia and industry would meet regularly to update and exercise custodial responsibility for the lists. The *Journal of Fluids Engineering* would publish yearly updates of the list and sponsor workshops to better inform the research community on each topic, most likely at the winter annual meeting or its like. With such lists in hand the sponsoring agencies could then solicit research packages in said areas knowing that the results would be more easily assimilated across the technology gap because of industry’s predisposition on such. Additionally, one would expect an improved tendency on industry’s part for cost sharing participation of the basic R&D efforts as well as follow-up support as the technology began its migration toward the product/services end of the gap.

Once this program was successfully installed and demonstrated, I believe a basis for building (or rebuilding) a level of trust and credibility among the three constituent communities will result—which, in turn, should lead to identification of further collective steps to be taken to further bridge the assimilation gap.

From here, the process is only limited by the imagination of the interested parties.

# Perspective: Systematic Study of Reynolds Stress Closure Models in the Computations of Plane Channel Flows

(Data Bank Contribution\*)

A. O. Demuren

Department of Mechanical  
Engineering and Mechanics,  
Old Dominion University,  
Norfolk, VA 23529  
Mem. ASME

S. Sarkar<sup>1</sup>

ICASE, NASA Langley Research Center,  
Hampton, VA 23665

*This paper investigates the roles of pressure-strain and turbulent diffusion models in the numerical calculation of turbulent plane channel flows with second-moment closure models. Only high Reynolds number models are considered. Three turbulent diffusion and five pressure-strain models are utilized in the computations. The main characteristics of the mean flow and the turbulent fields are compared against experimental data. All the features of the mean flow are correctly predicted by all but one of the Reynolds stress closure models. The Reynolds stress anisotropies in the log layer are predicted to varying degrees of accuracy (good to fair) by the models. It is found that, contrary to previous assertions, wall-reflection terms are not necessary to obtain the correct Reynolds stress anisotropy in the log-layer. The pressure-strain models determine the level of anisotropy in the log-layer, while the diffusion models strongly influence the rate of relaxation towards isotropy in the outer-layer. None of the models could predict correctly the extent of relaxation towards isotropy of the streamwise and lateral components of the Reynolds stresses in the wake region near the center of the channel. Results from direct numerical simulation are used to further clarify this behavior of the models.*

## 1 Introduction

Second-moment turbulence closure models first appeared about four decades ago with the proposal of a simple linear model for the pressure-strain correlation by Rotta (1951). Models with increasing complexity and sophistication have followed. The milestones are the works of Daly and Harlow (1970) (denoted DH), Hanjalic and Launder (1972) (denoted HL), Launder, Reece and Rodi (1975) (denoted LRR), Shih and Lumley (1985) (denoted SL), Fu, Launder and Tselepidakis (1987) (denoted FLT), and Speziale, Sarkar and Gatski (1991) (denoted by SGG). Speziale (1991) has recently reviewed this hierarchy of closure models. The earlier models (DH, HL, and LRR) propose approximations for the pressure-strain correlations which are linear in the Reynolds stresses, whereas the latter models (SL, FLT, and SGG) use nonlinear terms for these correlations. Although second-moment closure models have a sounder theoretical basis than eddy-viscosity based models such as the  $k$ - $\epsilon$  model, their superiority in predictive ability has not been demonstrated in a consistent and

systematic manner. Most of the models were derived with the use of homogeneous flow assumptions and the original applications have emphasized the prediction of homogeneous or nearly-homogeneous flows. There is a need for systematic studies in which the models are applied to flows with increasing complexity which are of practical importance, and the computed results compared to experimental data and results obtained with two-equation models, with the goal of establishing their capabilities and inadequacies. It is more usual to see a quantum leap in the application of the models to calculate highly complex two- and three-dimensional flows (Amano and Goel, 1987; Demuren, 1992). From the point-of-view of developing turbulence models, such as exercise is usually inconclusive since the performance of the models in the (inhomogeneous) elementary or component flows is not well known.

The present study is the first stage of an attempt to bridge this gap. The pressure-strain models tested here are: the quasi-isotropic model of LRR with and without wall-reflection terms, the models of SGG, SL, and FLT, all without any special wall-proximity treatment. Three formulations for the diffusion terms are also examined. These are proposals by DH, HL, and MH (Mellor and Herring, 1973). The first has been criticized for violating the symmetry of indices in  $\overline{u_i u_j u_k}$  (the triple velocity correlation) but is still widely used because of its simplicity. The last two preserve this symmetry in the indices of  $\overline{u_i u_j u_k}$ .

The test problem is the fully developed plane channel flow at high Reynolds number. Surprisingly, it was difficult to find

\* Data have been deposited to the JFE Data Bank. To access the file for this paper, see instructions on p. 189 of this issue.

<sup>1</sup> Currently at the Department of Applied Mechanics and Engineering Sciences, University of California at San Diego, La Jolla, CA 92093.

Contributed by the Fluids Engineering Division for publication in the JOURNAL OF FLUIDS ENGINEERING. Manuscript received by the Fluids Engineering Division May 7, 1992. Associate Technical Editor: T. T. Huang.



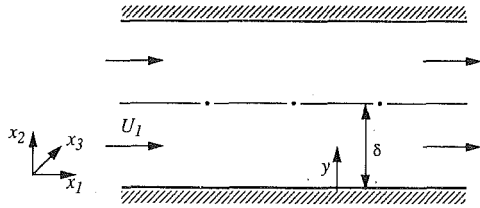


Fig. 1 Geometry and coordinate system for plane channel flow

complete sets of experimental data which fulfill the following requirements: high Reynolds number, high aspect ratio, long development length, and high accuracy and consistency. Comte-Bellot (1965) presented data at very high Reynolds numbers but these showed an inexplicable Reynolds number dependence. Channel flow data by Clark (1968) also showed an excessive dependence on Reynolds number, and values of the normalized turbulent kinetic energy  $k/U_1^2$  appeared to be too high in the near wall region. Laufer (1951) presented data for a 12:1 aspect ratio channel at Reynolds numbers (based on bulk mean velocity and half-width) in the range 10,300 to 52,000 taken at 86 half-widths from the inlet. Hussain and Reynolds (1975) suggested that this length would be insufficient for full development of the turbulence field. They presented measurements at 450 half-widths to support this, but their data set was incomplete since only the longitudinal normal stress component was given. A review of duct flow measurements by Klein (1981) supports their assertion. Nevertheless, Laufer's data represent then the best compromise, and hence was used to construct the anisotropy stress tensor components to which the present model computations are compared. It was supplemented with direct simulation results of Kim, Moin and Moser (1987) (denoted as KMM), and Kim (unpublished), in order to explore more detailed features of the turbulence fields in comparison to the turbulence models.

## 2 Mathematical Formulation

**2.1 Mean Flow Equations.** The Reynolds-averaged mean-flow equations for steady, incompressible turbulent flow can be written in Cartesian tensor notation as:

Continuity

$$\frac{\partial U_i}{\partial x_i} = 0 \quad (1)$$

Momentum

$$\frac{\partial}{\partial x_i} (U_i U_i) = -\frac{1}{\rho} \frac{\partial P}{\partial x_i} + \frac{\partial}{\partial x_i} \left[ -\overline{u_i u_i} + \frac{\mu}{\rho} \left( \frac{\partial U_i}{\partial x_i} + \frac{\partial U_i}{\partial x_i} \right) \right] \quad (2)$$

where  $x_i = (x_1, x_2, x_3)$  represent the Cartesian coordinates,  $U_i = (U_1, U_2, U_3)$  the Cartesian mean velocity components,  $P$  is the pressure,  $\mu$  the molecular viscosity, and  $\rho$  the density. Einstein's summation rule for repeated indices is utilized.  $\overline{u_i u_l}$  (with  $i = 1, 2, 3$ , and  $l = 1, 2, 3$ ) represents the six components of the Reynolds stress tensor  $R_{il}$  which must be determined by the turbulence model.

If, in the fully developed plane channel flow, the walls are in the (1-3) planes as shown in Fig. 1, then  $\partial/\partial x_1 = \partial/\partial x_3 = 0$  in Eqs. (1) and (2). Also, the Reynolds stress tensor  $R_{il}$  will have only 4 nonzero components; the three diagonal elements  $\overline{u_1^2}$ ,  $\overline{u_2^2}$  and  $\overline{u_3^2}$  which represent the normal stresses, and one off-diagonal element  $\overline{u_1 u_2}$  which represents the shear stress.

**2.2 Reynolds Stress Equations.** The transport equations for the Reynolds stress components can be written for high Reynolds number turbulent flow in Cartesian tensor notation as:

$$\frac{\partial}{\partial x_i} (U_i \overline{u_i u_j}) = D_{ij} + P_{ij} + \tau_{ij} - \epsilon_{ij} \quad (3)$$

where  $D_{ij}$  is the diffusion,  $P_{ij}$  is the production,  $\tau_{ij}$  is the pressure-strain correlation, and  $\epsilon_{ij}$  is the dissipation rate.

The production term is  $P_{ij} = -\overline{u_i u_l} (\partial U_l / \partial x_j) - \overline{u_j u_l} (\partial U_l / \partial x_i)$ ; and the dissipation is assumed to be locally isotropic so that  $\epsilon_{ij} = 2/3 \delta_{ij} \epsilon$ , where  $\epsilon$  is the dissipation rate of the turbulent kinetic energy  $k$ , to be determined from the solution of a transport equation (to be presented in a later section), and  $\delta_{ij}$  is the Kronecker delta. However, FLT attempts to account for anisotropy in the dissipation, as will be discussed in a later section.

The models for  $D_{ij}$  and  $\tau_{ij}$  are the subjects of the present study.

**2.3 Diffusion Models.** The three diffusion models examined are based on the proposals of DH, HL, and MH. They are written in tensor form as,

$$D_{ij} = (T_{ijk})_{,k} \quad (4)$$

where  $(\ )_{,k}$  represents the first derivative with respect to  $x_k$ , and  $T_{ijk}$  is given by:

$$\text{DH: } -T_{ijk} = c_{s1} \frac{k}{\epsilon} [\overline{u_k u_l} (\overline{u_i u_j})_{,l}] \quad (5)$$

$$\text{HL: } -T_{ijk} = c_{s2} \frac{k}{\epsilon} [\overline{u_i u_l} (\overline{u_j u_k})_{,l} + \overline{u_j u_l} (\overline{u_k u_i})_{,l} + \overline{u_k u_l} (\overline{u_i u_j})_{,l}] \quad (6)$$

$$\text{MH: } -T_{ijk} = c_{s3} \frac{k^2}{\epsilon} [(\overline{u_i u_j})_{,k} + (\overline{u_i u_k})_{,j} + (\overline{u_j u_k})_{,i}] \quad (7)$$

with  $c_{s1} = 0.22$ ,  $c_{s2} = 0.11$  and  $c_{s3} = 2/3 c_{s2}$ . These are essentially gradient diffusion models in which DH and HL have non-isotropic diffusion coefficients, but that for MH is isotropic. HL and MH diffusion models preserve symmetry in the indices but the DH model does not. In a general three-dimensional flow, the HL model requires the evaluation of 27 derivatives, whereas the DH and MH models each contain only 9 derivatives. For developed thin shear flow with  $(\ )_{,1} = (\ )_{,3} = 0$ , the diffusion terms are assembled in Table 1. These models result in expressions for the diffusion of  $k$  which are different from those usually given in two-equation models.

**2.4 Pressure-Strain Models.** Five models for the pressure-strain correlation are examined in this study. These are the quasi-isotropic version (model 1) of LRR, with and without wall-proximity treatment, the dynamical-systems based model of SSG, and the non-linear models of SL and FLT, both of which are derived from realizability constraints. The LRR model without wall treatment is denoted by LRRNW in this paper. In their model 1, LRR proposed to account for wall-proximity effects by making coefficients in the equations functions of the average distance from walls. In the simpler version (model 2) usually called by Gibson-Launder model, they are treated as wall-reflection terms. It should be noted that these wall-reflection terms are not near-wall corrections in the conventional sense, since they are applicable to the fully turbulent region beyond the viscous sublayer and the buffer zone, and they still have significant contributions at the center of the channel. However, there is uncertainty as to how rapidly the functions should decay with distance from walls, or how to estimate average distance from walls in complex geometries. Hence, it is now generally accepted that the need for wall-proximity treatment is an undesirable feature in a pressure-strain model. The comparison between LRR and LRRNW serves merely to show the dominant role wall reflection terms may play in determining the anisotropy levels.

The primary question that we address in this study is how do the sophisticated Reynolds stress models perform in a "building block" inhomogeneous shear flow such as channel flow. We are interested in evaluating the performance of these high Reynolds number models in a region ( $y^+ > 200$ ) away

**Table 1 Diffusion terms  $D_{ij}$  for developed thin shear flow**

	DH	HL	MH
$\overline{u_1^2}$	$c_{s1} \left[ \frac{k}{\epsilon} (\overline{u_2^2}) (\overline{u_1^2})_{,2} \right]_{,2}$	$c_{s1} \left[ \frac{k}{\epsilon} \{ 2(\overline{u_1 u_2}) (\overline{u_1 u_2})_{,2} + (\overline{u_2^2}) (\overline{u_1^2})_{,2} \} \right]_{,2}$	$c_{s3} \left[ \frac{k^2}{\epsilon} (\overline{u_1^2})_{,2} \right]_{,2}$
$\overline{u_2^2}$	$c_{s1} \left[ \frac{k}{\epsilon} (\overline{u_2^2}) (\overline{u_2^2})_{,2} \right]_{,2}$	$3c_{s2} \left[ \frac{k}{\epsilon} (\overline{u_2^2}) (\overline{u_2^2})_{,2} \right]_{,2}$	$3c_{s3} \left[ \frac{k^2}{\epsilon} (\overline{u_2^2})_{,2} \right]_{,2}$
$\overline{u_3^2}$	$c_{s1} \left[ \frac{k}{\epsilon} (\overline{u_2^2}) (\overline{u_3^2})_{,2} \right]_{,2}$	$c_{s2} \left[ \frac{k}{\epsilon} (\overline{u_2^2}) (\overline{u_3^2})_{,2} \right]_{,2}$	$c_{s3} \left[ \frac{k^2}{\epsilon} (\overline{u_3^2})_{,2} \right]_{,2}$
$\overline{u_1 u_2}$	$c_{s1} \left[ \frac{k}{\epsilon} (\overline{u_2^2}) (\overline{u_1 u_2})_{,2} \right]_{,2}$	$c_{s2} \left[ \frac{k}{\epsilon} \{ 2(\overline{u_1 u_2}) (\overline{u_2^2})_{,2} + (\overline{u_2^2}) (\overline{u_1 u_2})_{,2} \} \right]_{,2}$	$2c_{s3} \left[ \frac{k^2}{\epsilon} (\overline{u_1 u_2})_{,2} \right]_{,2}$
$k$	$c_{s1} \left[ \frac{k}{\epsilon} (\overline{u_2^2}) (k)_{,2} \right]_{,2}$	$c_{s2} \left[ \frac{k}{\epsilon} \{ (\overline{u_2^2}) (k)_{,2} + (\overline{u_2^2}) (\overline{u_2^2})_{,2} + (\overline{u_1 u_2}) (\overline{u_1 u_2})_{,2} \} \right]_{,2}$	$c_{s3} \left[ \frac{k^2}{\epsilon} \{ (k)_{,2} + (\overline{u_2^2})_{,2} \} \right]_{,2}$

**Table 2 Coefficients in Eq. (8) for various pressure-strain models**

	LRR	LRRNW	SSG	SL	FLT
$\alpha_0$	$-(3.0-f)$	-3.0	-3.4	$-\left(2 + Fe^{-\frac{11.65}{\sqrt{R_T}}}\right) \left\{ \frac{12}{\sqrt{R_T}} + 8.9 \ln[1 + 62.4(.5 \text{ II} + .77 \text{ III})] \right\}$	$-(60 \text{ II } F^{1/2})$
$\alpha_1$	0	0	4.2	0	$-72 \text{ II } F^{1/2}$
$\alpha_2$	0.8	0.8	$0.8-1.3 \text{ II}^{1/2}$	0.8	0.8
$\alpha_3$	0	0	-1.8	1.2	1.2
$\alpha_4$	1.745	1.745	1.25	$1.20 + 0.96 F^{1/2}$	1.20
$\alpha_5$	$1.309 - 0.24f$	1.309	0.40	$1.74 - 0.74 F^{1/2}$	1.73
$\alpha_6$	0	0	0	0.8	0.8
$\alpha_7$	0	0	0	0.8	0.8
$\alpha_8$	0	0	0	0	11.2

$$f = \left( \frac{L}{x_2} \right)^2, \text{ with } L = \left( \frac{c_\mu^{3/4}}{\kappa} \right) \left( \frac{k^{3/2}}{\epsilon} \right); R_T = \frac{k^2}{\nu \epsilon};$$

$$\text{II} = b_{mn} b_{nm}; \text{III} = b_{lm} b_{mn} b_{nl}; F = 1 - 4.5 \text{ II} + 9 \text{ III}$$

from the wall—an issue separate from near-wall turbulence modeling. Therefore, the same wall-function treatment is used to bridge the near-wall region in all the models considered here.

The pressure-strain models can be written in terms of the anisotropy tensor  $b_{ij} = (\overline{u_i u_j} / 2k - 1/3 \delta_{ij})$ , the rate of strain tensor,  $S_{ij} \equiv 1/2(\partial U_i / \partial x_j + \partial U_j / \partial x_i)$ , the rotation tensor  $W_{ij} \equiv 1/2(\partial U_i / \partial x_j - \partial U_j / \partial x_i)$ , and the rate of production of turbulent kinetic energy  $P_k$  in the general form:

$$\begin{aligned} \pi_{ij} = & \alpha_0 \epsilon b_{ij} + \alpha_1 \epsilon (b_{ik} b_{jk} - 1/3 \text{ II} \delta_{ij}) + \alpha_2 k S_{ij} + \alpha_3 P_k b_{ij} \\ & + k \{ \alpha_4 (b_{ik} S_{jk} + b_{jk} S_{ik} - 2/3 \delta_{ij} b_{kl} S_{kl}) + \alpha_5 (b_{ik} W_{jk} + b_{jk} W_{ik}) \} \\ & \text{linear terms} \\ & + \alpha_6 (b_{ik} b_{lk} S_{jl} + b_{jk} b_{lk} S_{il} - 2b_{kj} b_{li} S_{kl}) + \alpha_7 (b_{ik} b_{lk} W_{jl} + b_{jk} b_{lk} W_{il}) \\ & \text{quadratic terms} \\ & + \alpha_8 [b_{nl} b_{ln} (b_{ik} W_{jk} + b_{jk} W_{ik}) + 3b_{mi} b_{nj} (b_{mk} W_{nk} + b_{nk} W_{mk})] \\ & \text{(cubic terms)} \end{aligned} \quad (8)$$

The model coefficients  $\alpha_0 \dots \alpha_8$  may be, in general, functions of the invariants of the anisotropy tensor. The corresponding relations for the five pressure-strain models are presented in Table 2.

In the table,  $f$  is a wall-proximity function which takes a value of unity in the fully turbulent region near a wall and zero in a flow free from walls. LRR proposed a linear decay for  $f$ , but Demuren and Rodi (1984) found the wall effect too strong near the center of the channel, hence they prefer the

quadratic form used in this paper.  $\text{II} (= b_{ik} b_{kl})$  and  $\text{III} (= b_{ik} b_{km} b_{ml})$  are, respectively, the second and third invariants of the Reynolds stress anisotropy tensor and  $R_T$  is the turbulent Reynolds number. The constants  $c_\mu$  and  $\kappa$  take the standard values 0.09 and 0.42, respectively.

The first line in Eq. (8) contains a mixture of terms representing both “slow” and “rapid” contributions to the pressure-strain correlation. The first term is the usual Rotta term for the return to isotropy. All the models have this term, which has a constant coefficient in the LRRNW and SSG models, but is a function of the wall-proximity variable in the LRR model, and a function of the invariants in the SL and FLT models. In the latter, the particular forms are derived to ensure that the turbulence remains realizable in the two-component limit as the wall is approached. Such a condition is never approached in the present study since the integration is not performed all the way down to the wall. In the FLT model, unlike all the other models, this term does not contain the full return to isotropy term, since the value of the coefficient  $\alpha_0$  may become less than 2 when the second invariant  $\text{II}$  gets very small. The remaining contribution, which ensures the return to isotropy is contained in their approximation for  $\epsilon_{ij} (= 2/3 \delta_{ij} \epsilon + [2 - 2F^{1/2}] b_{ij} \epsilon)$ . The treatment corresponds more nearly to the usual practice if the second part of this expression is combined with the return to isotropy term. Only the SSG and FLT models have a non-linear contribution to the return to isotropy. The last two terms on the first line are contributions to the “rapid” part, the first of these is a linear term and the second is quadratic in  $b_{ij}$ , since  $P_k$  itself is linear in  $b_{ij}$ . The major

contributions to the “rapid” part of the pressure-strain correlation are those collection of terms in line 2 to 4 of Eq. (8). All models contain the linear terms. Only the SL and FLT terms contain the quadratic terms and only the FLT model has terms which are cubic in the anisotropy stress tensor.

**2.5 k- $\epsilon$  Model.** Calculations were also made with the standard high-Reynolds number form of the  $k$ - $\epsilon$  turbulence model. The equations for  $k$  and  $\epsilon$  can be expressed in tensor notation as:

$$\frac{\partial}{\partial x_i} (U_i k) = D_k + P_k - \epsilon \quad (9)$$

$$\frac{\partial}{\partial x_i} (U_i \epsilon) = D_\epsilon + c_{\epsilon 1} \frac{\epsilon}{k} P_k - c_{\epsilon 2} \frac{\epsilon^2}{k} \quad (10)$$

In the standard form of the model the terms  $D_k$  and  $D_\epsilon$  are approximated by gradient diffusion relations as:

$$D_k = \frac{c_\mu}{\sigma_k} \left( \frac{k^2}{\epsilon} k_{,i} \right)_{,i} \quad (11)$$

$$D_\epsilon = \frac{c_\mu}{\sigma_\epsilon} \left( \frac{k^2}{\epsilon} \epsilon_{,i} \right)_{,i} \quad (12)$$

These equations are routinely solved, even when the interest is only in the solution with the second-moment closure models. The equation for  $\epsilon$  is of course required for closure. The trace of the Reynolds stresses should be equal to  $2k$ , so that the solution of the  $k$ -equation is redundant. It serves, in this study, solely as an additional check for the convergence and the consistency of the solution. Thus, it was required that half the trace of the computed Reynolds stress distributions should agree with the computed distributions of  $k$  to within 0.2 percent, at every point in the flow. For consistency in this case,  $D_k$  must take the forms given in Table 1. The emphasis in the present study is on the models for the pressure-strain correlation and the turbulent diffusion, so the use of anisotropy diffusion coefficients in the  $\epsilon$ -equation, as proposed by HL may becloud the issue. The empirical constants in Eqs. (9)–(12) are:  $\sigma_k = 1.0$ ;  $\sigma_\epsilon = 1.3$ ;  $c_{\epsilon 1} = 1.44$ ;  $c_{\epsilon 2} = 1.92$ .

Note that some authors propose variations to the  $\epsilon$ -equation with different values for the model coefficients and different forms for the diffusion term  $D_\epsilon$ . The question arises as to whether such differences change the equilibrium Reynolds stress anisotropies in the log-layer. Consider the Reynolds stress equation in the fully developed, incompressible channel flow

$$D_{ij} + P_{ij} + \pi_{ij} - \frac{2}{3} \epsilon \delta_{ij} = 0 \quad (13)$$

In the log-layer, where diffusion can be neglected and (13) becomes

$$P_{ij} + \pi_{ij} - \frac{2}{3} \epsilon \delta_{ij} = 0$$

or

$$\frac{P_{ij}}{\epsilon} + \frac{\pi_{ij}}{\epsilon} - \frac{2}{3} \delta_{ij} = 0 \quad (14)$$

All the models for  $\pi_{ij}$  are of the form  $\pi_{ij}/\epsilon = f(b_{ij}, Sk/\epsilon)$  in a simple shear flow. Since  $P_k = \epsilon$  in the log-layer, we have  $Sk/\epsilon = -1/(2b_{12})$ , and thus  $\pi_{ij}/\epsilon = f(b_{ij})$ . Similarly,  $P_{ij}/\epsilon = g(b_{ij}, Sk/\epsilon) = g(b_{ij})$ . Thus, Eq. (14) becomes an algebraic equation for  $b_{ij}$  independent of  $\epsilon$ . Consequently, the anisotropy tensor  $b_{ij}$  in the log-layer is independent of the form and coefficients of the  $\epsilon$ -equation. Note that  $b_{ij}$  is determined completely by the form of the pressure-strain model and should be constant if there is no explicit  $y$  dependence in the model. This result is confirmed by computations with the SL pressure-strain model in which the form of the  $\epsilon$ -equation is taken from Shih et al.

(1991). In comparison to the present results, obtained with the standard  $\epsilon$ -equation,  $b_{ij}$  values in the log-layer are the same. Near the center of the channel, they differ by less than 2 percent. Mean streamwise velocity values and the wall shear stress also differ by less than 3 percent. The maximum change for any variable is found near the center of the channel where  $\epsilon$  increases by 25 percent, and  $k$  decreases correspondingly by 11 percent.

**2.6 Solution Procedure.** The problem, as formulated, is strictly one-dimensional, but a two-dimensional TEACH-type code which solves the full, time-averaged, Navier-Stokes equations is utilized, in order to ease extension to other flow cases in future studies. The redundant terms are simply set to zero in the present study. The standard hybrid (upwind/central) differencing for the convection terms and central differencing for the different terms, used in the original TEACH code, are accurate enough for the present work since the flow is parallel to one set of grid lines. Initial conditions for the mean flow and turbulence stresses are taken from the simulation data of Kim, Moin and Moser (1987), but these are scaled up to yield an effective Reynolds number (based on bulk mean velocity and half width) of  $5.2 \times 10^4$ , to coincide with the highest Reynolds number of Laufer’s experiments. The computed results (normalized with  $U_\tau$ ) are similar to those obtained (Demuren and Sarkar, 1992) at a higher Reynolds number ( $\sim 4 \times 10^5$ ). Computations are performed for half of the channel from the lower wall to the mid-plane. The calculations use 32 grid points in the transverse direction and sufficient lengths (over 400 half widths) in the longitudinal direction to ensure full flow development. Computations with twice as many points in each direction do not produce significantly different results, provided that the value of  $y^+$  at the node nearest to the wall is the same. For example, in computations with the SSG model on both grids, the mean flow velocity has exactly the same distribution. The levels of the Reynolds stress anisotropy differ by less than 0.5 percent, and the turbulence kinetic energy levels at the center of the channel differ by about 1.5 percent. The objective of this work is to compare the behavior of various pressure-strain and diffusion models, so the computations are for the high Reynolds number flow region only, in which the viscous sublayer is not resolved but is bridged using the standard wall-function method. Along the line of nodes nearest to the walls ( $y^+ \sim 30$ ) local equilibrium is assumed: The streamwise velocity component is specified based on the logarithmic velocity of the wall ( $U^+ = 1/\kappa \ln y^+ + 5.0$ );  $k = U_\tau^2/c_\mu^{1/2}$ ;  $\epsilon = U_\tau^3/(\kappa y)$ ;  $u_1^2 = 1.07 k$ ;  $u_2^2 = 0.41 k$ ;  $u_3^2 = 0.52 k$ ;  $\overline{u_1 u_2} = -0.30 k$ . These boundary conditions represent the correct near-wall properties in a channel flow. Low Reynolds number near-wall models such as those reviewed by So et al. (1991) will not contribute anything to the present study. Those models are really useful in calculations of wall-bounded flows with complicating effects such as transition, relaminarization, curvature, rotation, heat transfer, etc., where there is usually no universal log-law behavior. The specification of the second set of boundary conditions is that the first derivative of all dependent variables is set to zero normal to the symmetry plane.

### 3 Results and Discussion

The results of the computations to test the turbulent diffusion models are compared to results obtained with the  $k$ - $\epsilon$  model and experimental data in Figs. 2–4. For each of the computations with the second-moment closure the pressure-strain correlations are modelled with the SSG form, but the three diffusion models given by Eqs. (5)–(7) are used. Profiles of the streamwise velocity are presented in semi-logarithmic form in Fig. 2. All the profiles agree very well with the log-law ( $U^+ = 1/\kappa \ln y^+ + 5.0$ ) in the inner layer. The results with the  $k$ - $\epsilon$  model display a pronounced wake region, but the second-moment closures give only a small wake region. Since the



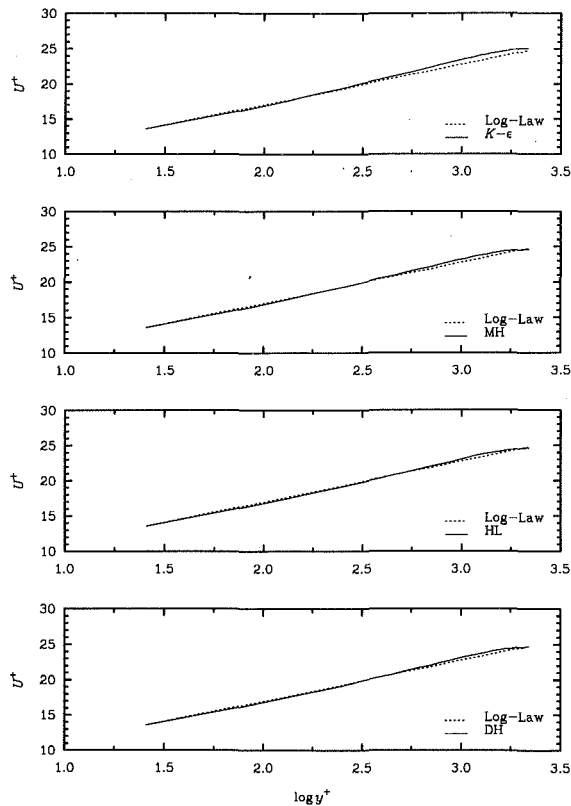


Fig. 2 Comparison of velocity profiles computed with the SSG pressure-strain model and various diffusion models to the log-law

channel flow has a favorable pressure gradient, the wake region is of course much smaller than that for a flat plate boundary layer. Measurements by Clark (1968), Laufer (1951), and Husain and Reynolds (1975) also show a very small wake region. Hence, the velocity profiles are well predicted by all the diffusion models. Another test of the diffusion models is in the prediction of the Reynolds stress anisotropy tensor in the relaxation region  $0.7 < y/\delta < 1.0$ . Figure 3 compares these results with the data of Laufer for the 4 nonzero components. As seen in the 11 and 22 components, the MH model produces the strongest rate of relaxation towards isotropy as the center of the channel is approached, and it gives the best agreement with experimental data. The DH model shows little change in the anisotropy level between the log-layer and the center of the channel. The results for the HL model lie somewhat between the other two. For the 33 component, the DH model shows slightly better agreement with the data. These results can be explained by considering order of magnitude estimates of the diffusion terms given in Table 1. DH and HL models have coefficients  $c_{s1}$  and  $c_{s2}$  which are, respectively, 3 and 1.5 times larger than that for the MH model. But they are modified by anisotropy coefficients, the most significant of which is  $\overline{u_2^2}/k$ , with a value 0.4 in the log-layer. Order of magnitude estimates then show that the diffusion terms for  $\overline{u_1^2}$  are roughly equal, but for  $\overline{u_2^2}$ , the MH model yields a diffusion term which is about 2.5 times greater than that for the DH model and 1.7 times greater than that for the HL model. The budgets of the Reynolds stresses from the present study (not shown) and from the DNS data of Kim (unpublished), show that the diffusion of the normal stresses are positive in the central part of the channel ( $y/\delta > 0.5$ ) while the diffusion of the shear stress is negative. Thus, an increase in the diffusion of  $\overline{u_2^2}$  would increase  $\overline{u_2^2}$  and move  $b_{22}$  closer to zero, thereby reducing the anisotropy, if  $\overline{u_1^2}$  and  $\overline{u_3^2}$  are not correspondingly increased. This is the case here, since the diffusion models yield magnitudes which are more nearly equal for  $\overline{u_1^2}$  and  $\overline{u_3^2}$ . Therefore, the MH model

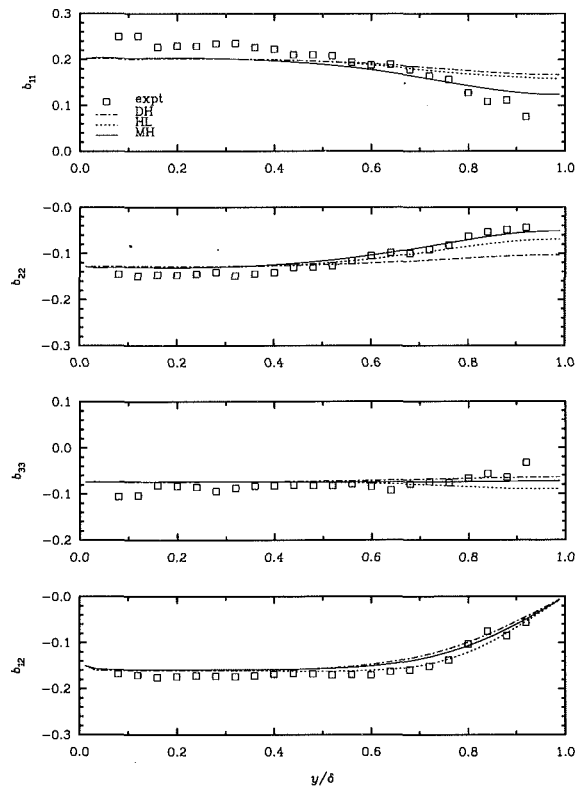


Fig. 3 Comparison of components of the Reynolds stress anisotropy tensor computed with the SSG pressure-strain model and three diffusion models to experimental data of Laufer (1951)

which has the largest diffusion term for  $\overline{u_2^2}$  produces the fastest rate of relaxation towards isotropy and the best agreement with experimental data. Similar order of magnitude estimates can be used to explain the results for  $b_{33}$  and  $b_{12}$ . Since the diffusion of  $\overline{u_1 u_2}$  is negative, a higher magnitude will produce a lower value of  $b_{12}$ . The comparisons of the predicted turbulent kinetic energy are presented in Fig. 4. The predictions are in reasonably good agreement with the data. The slight differences between the predicted results can also be explained by the aforementioned order of magnitude estimates.

The predictions with the five pressure-strain models are compared in Figs. 5–7. The MH model for the turbulent diffusion is used in each case. Figure 5 shows that all models except the SL model give reasonable prediction of the mean streamwise velocity profile in agreement with the universal logarithmic law of the wall. The explanation for this can be found in Fig. 6 and Table 3. The main requirement for the correct prediction of the mean velocity is that the model should yield an accurate distribution of the shear stress. The latter is related to the  $b_{12}$  component of the Reynolds stress anisotropy tensor. Table 3 shows that this component is reproduced fairly accurately by all but the SL model. In the inner core of the flow ( $y/\delta < 0.8$ ) the SL model underpredicts  $b_{12}$  by about 30 percent. Now, in the equilibrium layer for thin shear flows the ratio of production to dissipation is given by:

$$\frac{P_k}{\epsilon} = -2 b_{12} \left( \frac{Sk}{\epsilon} \right) \quad (15)$$

and since  $P_k/\epsilon$  is approximately unity the normalized shear rate ( $Sk/\epsilon$ ) is inversely proportional to  $b_{12}$ . Underprediction of  $b_{12}$  will produce excessive shear rate and hence a poor velocity profile. Experimental and DNS data suggest that  $Sk/\epsilon$  should be equal to about 3.3 in the inner layer. Most of the models predict values in the range 3.0–3.5, but the SL model predicts values of around 4.3. The latter is not surprising since

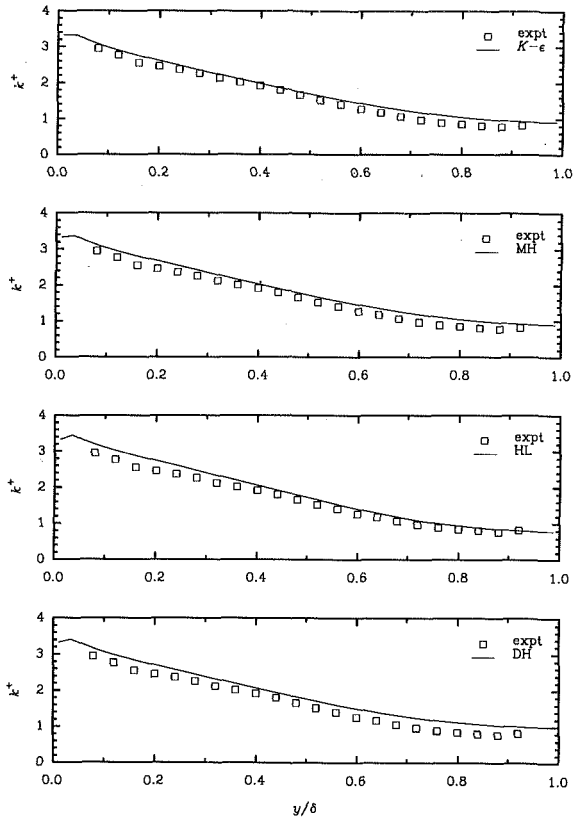


Fig. 4 Comparison of profiles of the turbulent energy computed with the SSG pressure-strain model and various diffusion models to experimental data of Laufer (1951)

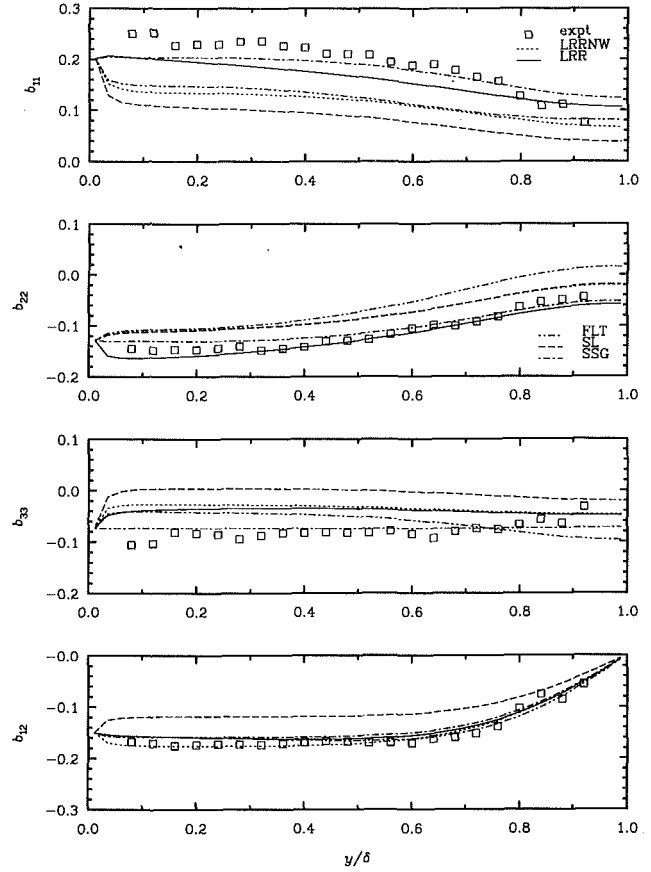


Fig. 6 Comparison of components of the Reynolds stress anisotropy tensor computed with the MH diffusion model and various pressure-strain models to experimental data of Laufer (1951)

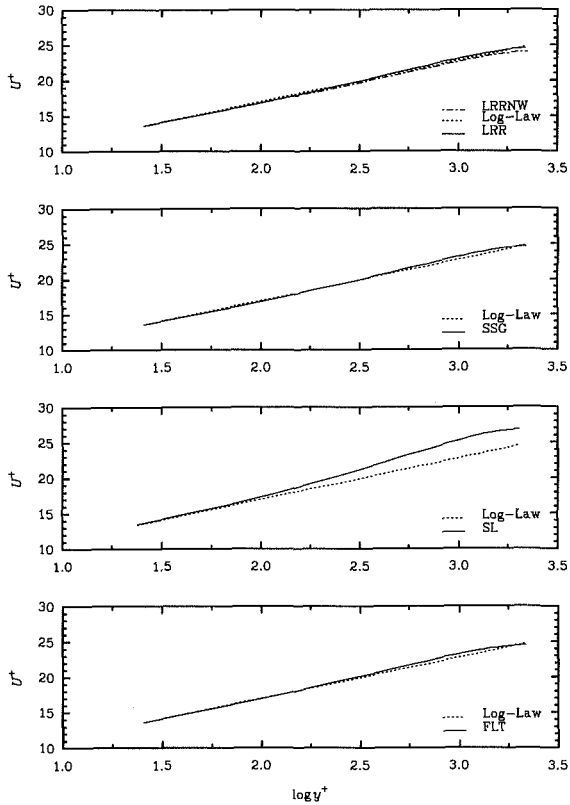


Fig. 5 Comparison of velocity profiles computed with the MH diffusion model and various pressure-strain models to the log-law

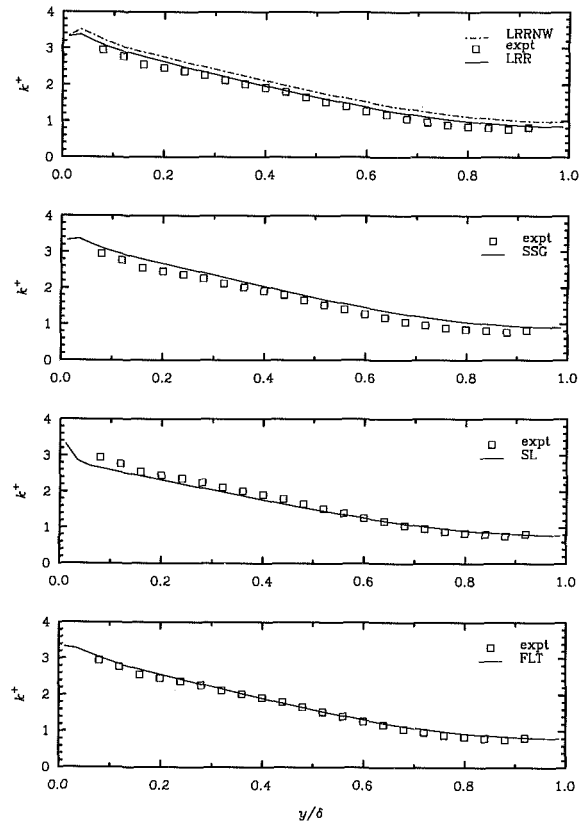


Fig. 7 Comparison of profiles of the turbulent energy computed with the MH diffusion model and various pressure-strain models to experimental data of Laufer (1951)

**Table 3 Comparison of predicted Reynolds stress anisotropies in the log-layer to experimental data of Laufer (1951)**

	LRR	LRRNW	SSG	SL	FLT	EXPT.
$b_{11}$	.16 to .21	.13	.20	.10	.14	.18 to .25
$b_{22}$	-.13 to -.17	-.10	-.13	-.10	-.10	-.15
$b_{33}$	-.04	-.03	-.07	.00	-.04	-.08
$b_{12}$	-.16	-.18	-.16	-.12	-.16	-.17

Speziale and Mac Giolla Mhuiris (1989) had reported that the SL model predicts equilibrium values, in homogeneous shear flow, of  $b_{12}$  and  $Sk/\epsilon$  of  $-0.12$  and  $6.93$ , which are, respectively, lower and higher in magnitudes than experimental values by about 20 percent. The channel flow is of course not a homogeneous shear flow but there are some similarities. For example  $b_{ij}$  and  $Sk/\epsilon$  have constant values in both the log-layer of the channel and the equilibrium homogeneous shear flow.

The comparisons of the normal components of the Reynolds stress anisotropy tensor in Fig. 6 are even more instructive. A comparison of results obtained with the LRR model to those with the LRRNW model shows the effects of the wall-reflection terms. They produce a significant increase in the anisotropy of 11 and 22 components, with little effect on the 33 component. Although the increase in anisotropy is strongest near the wall, it remains pronounced even at the center of the channel. This is contrary to expectation. The dilemma is how to devise a function for the wall reflection effects which decays at the right rate away from the wall that would also be general enough for application to more complex flows. Better still, the model should not require wall reflection terms.

If we consider the level of anisotropy in the inner layer, the SSG model (dash-dot curves in Fig. 6) gives the closest predictions of  $b_{11}$ ,  $b_{22}$ , and  $b_{33}$ . The LRR model gives reasonable predictions for  $b_{11}$  and  $b_{22}$ , but not for  $b_{33}$ . Both these models are relatively simple, without the quadratic and cubic terms in Eq. (8). Their good performance is probably due to their superior calibration for homogeneous flows. The SSG model was calibrated in a dynamical systems approach using data from the nearly-homogeneous shear flow experiments of Tavoularis and Corrsin (1981). The LRR model was calibrated with the earlier (and probably less reliable) experimental data for nearly-homogeneous shear flow of Champagne, Harris and Corrsin (1970) and the wall-reflection part of the model used a consensus of near-wall data. It is surprising that the FLT model which contains both the quadratic and cubic terms in Eq. (8) does not give predictions which are superior to the much simpler models. Furthermore,  $b_{33}$  shows an increase in anisotropy towards the center of the channel. Perhaps the calibration of the model is to blame. Numerical experiments indicate that the level of anisotropy in the 11 and 22 components can be increased by increasing the magnitude of the coefficient of the cubic terms,  $\alpha_3$  in Eq. (8). However, this produces little effect on the 33 component. Again the predictions by the SL model of  $b_{11}$  and  $b_{22}$  in the channel flow are much lower than in the experiments. Correspondingly,  $b_{33}$  is much too high. Such underprediction of  $b_{11}$  and  $b_{22}$  has also been observed in homogeneous shear flow (Speziale and Mac Giolla Mhuiris, 1989). The values of the Reynolds stress anisotropy tensor in the log-layer are summarized for all models and the experimental data in Table 3.

A notable feature of the predictions is that the models do not fully reproduce the rapid relaxation towards isotropy (especially in  $b_{11}$  and  $b_{33}$ ) in the outer-layer ( $y/\delta > 0.75$ ) in response to the relaxation in the shear rate. Figure 8 shows a comparison of the profiles of  $Sk/\epsilon$  obtained from the DNS results of Kim (unpublished), and predictions with the  $k-\epsilon$  model and the SSG Reynolds stress closure model. These all show that  $Sk/\epsilon$  is nearly constant in the inner layer and starts to decay rapidly beyond  $y/\delta = 0.7$ . All the models show only

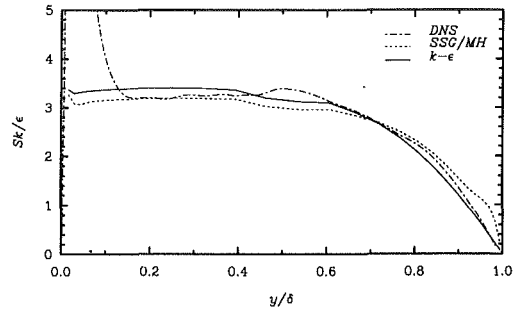


**Fig. 8 Comparison of computed shear rate ( $Sk/\epsilon$ ) in channel flow**

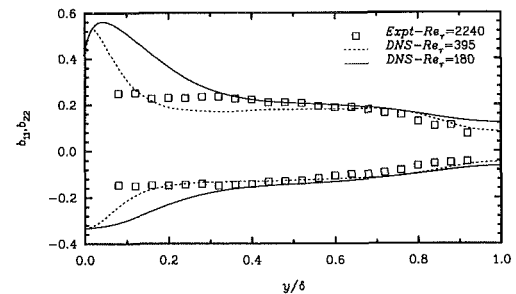


**Fig. 9 Comparison of Reynolds stress anisotropy tensor in channel flow from DNS of KMM (1987) and Kim (unpublished) and experiments of Laufer (1951)**

a mild decay in the anisotropy level of the 11 and 33 components in this region, but DNS and experimental data presented in Fig. 9 show strong relaxation towards isotropy in correspondence with the decay of the shear rate. The main effects of increasing the Reynolds number are seen to be the reduction of the anisotropy close to the wall and a faster rate of return to isotropy near the center of the channel. Figure 7 shows that all the pressure-strain models (in conjunction with the MH diffusion model) produce reasonably good prediction of the turbulent kinetic energy.

#### 4 Concluding Remarks

The  $k-\epsilon$  model and the second-moment closure models, apart from the SL model, produce similar predictions of the mean flow velocity, which agree well with the logarithmic law of the wall over most of the channel cross-section. In agreement with experimental observations in channel flows, there is only a small wake component. The SL model underpredicts the shear stress, and this leads to poor prediction of the mean flow velocity. All the other models predict the shear stress distribution correctly.

The different models for the turbulent diffusion have little effect on the normal components of the Reynolds stress tensor in the log-layer, but strongly influence the rate of relaxation towards isotropy in the outer layer near the center of the channel. The MH diffusion model gives the best agreement with experimental data.

LRR and SSG pressure-strain models give the best prediction of the streamwise and transverse components of the Reynolds stresses. The LRR model requires wall-reflection terms to achieve this but the SSG model does not. The wall reflection terms remain pronounced in the outer layer. Such an outer-layer influence is perhaps physically inappropriate. Only the SSG model could predict the lateral component of the Reynolds stress anisotropy correctly.

The models failed to predict correctly the rate of relaxation of the streamwise and lateral components of the Reynolds stresses towards isotropy when the shear rate decreases in the other layer  $y/\delta > 0.7$ .



The pressure strain models which performed well in the present study, such as the LRR and SSG models, are expected to give reasonable results in other equilibrium shear flows. But there is no indication as to their performance in other complex flows. That is a subject for future studies.

### JFE Data Bank Contributions

Data sets of the computational results obtained with the different models presented in this paper are being added to the *Journal of Fluids Engineering* Data Bank. The data sets include flow conditions, wall shear stress, and profiles of the mean velocity, the Reynolds stresses, the turbulent kinetic energy and its rate of dissipation. Budgets of the Reynolds stresses, the turbulent kinetic energy and the dissipation are also included. To access the file for this paper, see instructions on p. 189 of this issue.

### Acknowledgment

This work had its origin in the 1991 ICASE/LaRC Workshop on Turbulence and Transition. The computations were performed on the Cray YMP computer of the NAS program at NASA Ames Research Center, Moffet Field, California.

### References

- Amano, R. S., and Goel, P., 1987, "Investigation of Third-Order Closure Model for the Computation of Incompressible Flows in a Channel with a Backward-Facing Step," *ASME JOURNAL OF FLUIDS ENGINEERING*, Vol. 109, pp. 424-428.
- Champagne, F. H., Harris, V. G., and Corrsin, S., 1970, "Experiments in Nearly Homogeneous Turbulent Shear Flow," *Journal of Fluid Mechanics*, Vol. 41, pp. 81-139.
- Clark, J. A., 1968, "A Study of Incompressible Turbulent Boundary Layers in Channel Flow," *ASME Journal of Basic Engineering*, Vol. 90, pp. 455-467.
- Comte-Bellot, G., 1965, "Ecoulement Turbulent Entre Deux Parois Paralleles," *Publications Scientifiques et Techniques, du Ministere de L'air*, No. 419.
- Daly, B. J., and Harlow, F. H., 1970, "Transport Equations of Turbulence," *The Physics of Fluids*, Vol. B, pp. 2634-2649.
- Demuren, A. O., 1992, "Multigrid Acceleration and Turbulence Models for Computations of 3D Turbulent Jets in Crossflow," *International Journal of Heat and Mass Transfer*, Vol. 35, No. 11, pp. 2783-2794.
- Demuren, A. O., and Rodi, W., 1984, "Calculation of Turbulence-Driven Secondary Motion in Non-circular Ducts," *Journal of Fluid Mechanics*, Vol. 140, pp. 189-222.
- Demuren, A. O., and Sarkar, S., 1992, "Application of Second-Moment Closure Models to Complex Flows: Part 1—Wall Bounded Flows," *Proceedings ICASE/Langley Workshop on Instability, Transition and Turbulence*, Springer-Verlag, pp. 575-588.
- Fu, S., Launder, B. E., and Tselepidakis, D. P., 1987, "Accommodating the Effects of High Strain Rates in Modelling the Pressure-Strain Correlation," Report No. TFD/87/5, Department of Mechanical Engineering, University of Manchester Institute of Science and Technology, Manchester, UK.
- Hanjalic, K., and Launder, B. E., 1972, "A Reynolds Stress Model of Turbulence and Its Application to Thin Shear Flows," *Journal of Fluid Mechanics*, Vol. 52, pp. 609-638.
- Hussain, A. K. M. F., and Reynolds, W. C., 1975, "Measurements in Fully Developed Turbulent Channel Flow," *ASME JOURNAL OF FLUIDS ENGINEERING*, Vol. 97, pp. 568-578.
- Kim, J., Moin, P., and Moser, R., 1987, "Turbulence Statistics in Fully Developed Channel Flow at Low Reynolds Number," *Journal of Fluid Mechanics*, Vol. 177, pp. 133-166.
- Klein, A., 1981, "Review: Turbulent Developing Pipe Flow," *ASME JOURNAL OF FLUIDS ENGINEERING*, Vol. 103, pp. 423-429.
- Laufer, J., 1951, "Investigation of Turbulent Flow in a Two-Dimensional Channel," NACA Report No. 1053.
- Launder, B. E., Reece, G. J., and Rodi, W., 1975, "Progress in the Development of a Reynolds Stress Turbulence Closure," *Journal of Fluid Mechanics*, Vol. 68, pp. 537-566.
- Mellor, G. L., and Herring, H. J., 1973, "A Survey of Mean Turbulent Field Closure," *AIAA Journal*, Vol. 11, pp. 590-599.
- Rotta, J. C., 1951, "Statistische Theorie nichthomogener Turbulenz," *Zeitschrift für Physik*, Vol. 129, pp. 547-572.
- Shih, T.-H., Chen, J.-Y., and Lumley, J. L., 1991, "Second Order Modeling of Boundary-Free Turbulent Shear Flows," *AIAA 91-1779*.
- Shih, T.-H., and Lumley, J. L., 1985, "Modeling of Pressure Correlation Terms in Reynolds Stress and Scalar Flux Equations," Technical Report No. FDA-853, Cornell University.
- So, R. M. C., Lai, Y. G., Zhang, H. S., and Hwang, B. C., 1991, "Second-Order Near-Wall Turbulence Closures: A Review," *AIAA Journal*, Vol. 29, pp. 1819-1835.
- Speziale, C. G., 1991, "Analytical Methods for the Development of Reynolds-Stress Closures in Turbulence," *Annual Review of Fluid Mechanics*, Vol. 23, pp. 107-157.
- Speziale, C. G., and Mac Giolla Mhuiris, N., 1989, "On the Prediction of Equilibrium States in Homogeneous Turbulence," *Journal of Fluid Mechanics*, Vol. 209, pp. 591-615.
- Speziale, C. G., Sarkar, S., and Gatski, T. B., 1991, "Modelling the Pressure-Strain Correlation of Turbulence: An Invariant Dynamical Systems Approach," *Journal of Fluid Mechanics*, Vol. 227, pp. 245-272.
- Tavoularis, S., and Corrsin, S., 1981, "Experiments in Nearly Homogeneous Turbulent Shear Flows with a Uniform Mean Temperature Gradient," *Journal of Fluid Mechanics*, Vol. 104, pp. 311-347.

**Jing-Tang Yang**  
Professor.  
Mem. ASME

**Go-Long Tsai**  
Graduate Student.

Department of Power  
Mechanical Engineering,  
National Tsing Hua University,  
Hsinchu, Taiwan 30043

# Near-Wake Flow of a V-Gutter With Slit Bleed

(Data Bank Contribution\*)

*The cold-flow characteristics of a v-shape flame holder with flow bleed from a slit located at the leading edge have been investigated. According to experimental evidence, a nonsymmetric wake structure is developed behind the symmetric slit v-gutter. The flow through the slit induces greater reverse flow and greater back pressure in the near wake. It also provokes more extensive transport across the shear layers and reduces both the turbulent intensity and the Reynolds shear stress of the wake flow. These results indicate that the slit v-gutter can have a better flame holding ability and less pressure loss compared with the traditional v-gutter. In view of fluid dynamics features, the slit v-gutter is indeed a potentially useful design of flame holder.*

## 1 Introduction

Bluff body flame holders are widely used to make flames stable in industry, especially for combustors with high velocity flows. Research conducted during the past three decades indicates that the wake flow structure behind the bluff body is directly related to the flame-holding performance. In addition, the pressure distribution in the near wake region is closely correlated with the pressure loss of the flame holder. However, the wake flow contains the complexities of separation and recirculation, mass and momentum transport across the shear layers, and the vortex shedding; the study of the flow structure has not been thoroughly explored.

Earlier researchers (Bovina, 1958; Lefebvre, 1983; Zukoski, 1978) examined the effects of fuel, flow speed, ratio of fuel to air, blockage ratio, and the flame holder geometry on flame-holding in relation to the stability limits instead of fluid dynamics. They concluded that the higher blow-off velocity could be achieved by means of increasing inlet temperature, pressure, the size or the drag coefficient of the flame holder, or reducing the inlet turbulent intensity, the blockage ratio as the size constant, or setting the air/fuel equivalent ratio near 1.0. Gerard (1962) observed the vortex shedding process and its influence on both drag force and flow-induced vibration. Bearman (1967) explored the wake flow behind a wedge with mass bleed through a porous base; he reported that the increase of the base bleed results in an increase in the shedding velocity of the vortices. Moreover, the distance between vortices first increases and then decreases as the mass bleed is further increased. In addition to a comprehensive review, Taylor and Whitelaw (1984) used one-color laser Doppler anemometer (LDA) to explore the wake flow of a flat plate, a disk, and a cone, respectively, at a flow velocity 1 m/s; The results indicated that higher blockage ratio of disk owns longer recircu-

lation length, but narrower width relative to the diameter. The effect of the geometry of the traditional flame holder was also discussed in detail.

Sullerey et al. (1975) defined the characteristic length as the position of minimum pressure coefficient and found similar flow structures for different shapes of flame holders; they also concluded that the smaller the minimum pressure coefficient, the smaller is the size of the recirculation zone. Sirka et al. (1989) reported that the mechanism of heat transfer in the wake flow is significantly affected by the flow pattern.

Fujii and Eguchi (1981) used a hot-wire anemometer and one-color LDA to investigate the anisotropic structure of a wake flow for a wedge at low velocities and contrasted reacting flows and cold flows; they reported that the combustion process enlarged the recirculation zone and reduced the recirculation intensity and the turbulent intensity. Besides, they also showed that there are abnormal Reynolds shear stresses in the front part of the recirculation zone. It played a negative turbulent production term and transferred turbulent kinetic energy to the reverse mean flow. Rao and Lefebvre (1982) and Stwalley and Lefebvre (1988) further studied the effect of geometry on the ranges of stability; comparing the wake of a v-gutter having an irregular edge with that of a regular v-gutter and they found no significant difference.

As cold and hot flows are similar (Vortmeyer, 1962), the importance of the study of cold flow is thus clear. Bovina (1958) reported that the residence periods of cold wake flow and hot wake flow were interrelated. Kundu (1980) modified the previous theoretical analysis and confirmed the role of the intensity of recirculation on flame stabilization. He also found that the amount of recirculating mass in hot and cold flow tests was similar. In addition, the blow off velocity is proportional to the maximum intensity of recirculation but independent of the geometry of the flame holder.

In general, previous research indicates that engine performance depends on both the flame stabilization and the pressure loss caused by the flame holder; these two factors are contra-

\*Data have been deposited to the JFE Data Bank. To access the file for this paper, see instructions on p. 189 of this issue.

Contributed by the Fluids Engineering Division for publication in The JOURNAL OF FLUIDS ENGINEERING. Manuscript received by the Fluids Engineering Division February 6, 1992. Associate Technical Editor: Chih-Ming Ho.

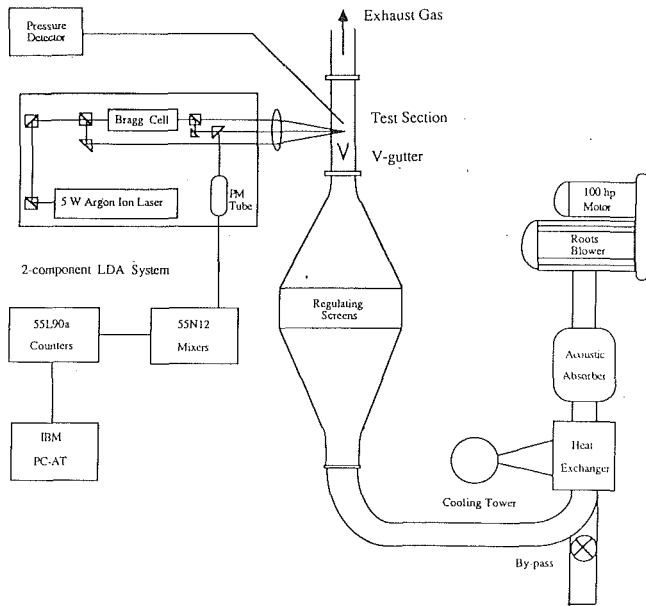


Fig. 1 Schematic diagram of the experimental apparatus

dictory for the performance of existing flame holders. Wong (1985) proposed that a small amount of base bleed through the rear of a bluff body might reduce both the drag and the induced vibration. Yang and Tsai (1991) further suggested that the open slit at the leading edge of the regular v-gutter generates a greater intensity of recirculation. Concurrently, both the pressure loss and vibration are significantly reduced. They indicated that the v-gutter with slit bleed may be a potentially practical device to hold a flame. We have investigated the effects of the width of the open slit on the recirculation zone and the drag in the near-wake region, and report here our results.

## 2 Experimental Techniques

**2.1 Test Rig.** The test rig is shown schematically in Fig. 1. The experiments were conducted in an open-circuit wind tunnel blown by a 75 kw Rootsblower, the speed of which was controlled by means of a frequency inverter. The blower provided a maximum flow rate  $50 \text{ m}^3/\text{min}$  with a maximum static pressure 70 kPa. The dimension of the test section was  $10 \times 10 \text{ cm}^2$ . The configurations and dimensions of v-gutters of the two types tested are shown in Fig. 2. The flow structures were investigated quantitatively through the measurements of velocities and pressures.

**2.2 Instrumentation.** We measured the velocities with a Dantec three-beam, 2-component backward-scattering LDA, connected to a computer-controlled traversing system for two-dimensional movement. The resolution of the traverse system was 0.03 mm. The instruments were mounted on an optical bench that was placed on a mill table for major movement.

The laser beam from a 5-watt argon-ion laser emitting mainly

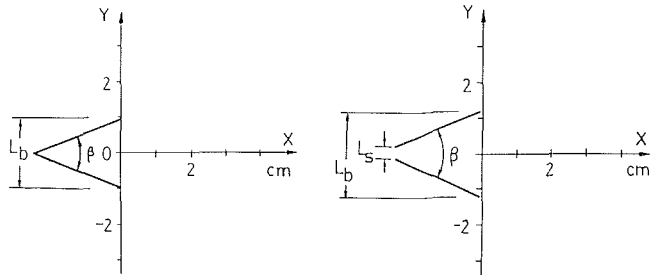
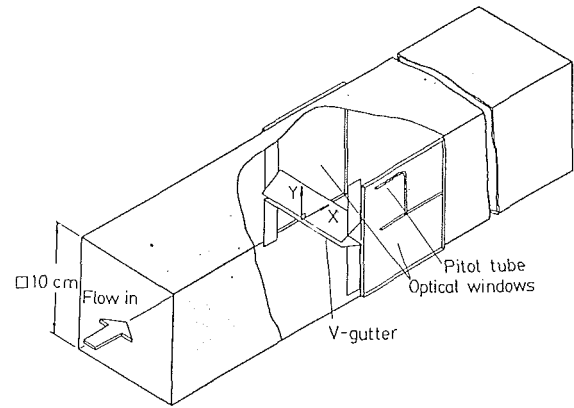


Fig. 2 Configurations and dimensions of the tested v-gutters

at wavelengths 514.5 and 488 nm was split into two beams. One beam passed a Bragg cell to produce a 40-MHz frequency shift and was then split again, through a color-selective beam splitter, into two beams of wavelengths 514.5 and 488 nm. The resulting two beams and the other original beam passed a beam translator, a beam expander and a convergent lens of focal length 310 mm, and were focused at the desired position. The two axes of the blue beam of the optical probe were 0.128 and 1.625 mm, whereas those of the green beam were 0.135 and 1.713 mm. The backward-scattering Doppler signals were detected by two photomultipliers and processed by a coincidence filter and two counter processors. A beam waist adjuster was used before the whole optical system in order to improve the signals. The seeding particles were generated from a seeding generator (Dantec) and heated and then introduced into the stream of flowing air at the divergent section of the wind tunnel. The particles, with a diameter of the order of 1  $\mu\text{m}$ , were made of 25 percent glycerin resolvent and a water solvent.

The measurements of pressure were made through a 1.5-mm-o.d. L-shaped tube with eight 0.1 mm holes drilled around the end of the tube. The validity of the similar measurement has been verified by Govinda Ram and Arakeri (1990). The detected data were then transmitted through a Kistler 7061 piezoelectric transducer, a charge amplifier, and a noise filter and finally analyzed by a Data Translation 6100 waveform analyzer. The mean pressures were measured by traversing a miniature pitot tube every 2 millimeters across the transverse direction and every 5 millimeters along the axial direction in the recirculation zone.

## Nomenclature

$C_p$  = pressure coefficient  
 $H$  = height of test section  
 $L_b$  = geometry blockage of v-gutter  
 $L_s$  = open-slit width of v-gutter  
 $\dot{m}_r$  = reverse volumetric flow rate  
 $\dot{m}_T$  = total volumetric flow rate  
 $P$  = pressure  
 $U, u$  = axial velocity

$V, v$  = vertical velocity  
 $W, w$  = spanwise velocity  
 $u'$  = axial velocity fluctuation  
 $v'$  = vertical velocity fluctuation  
 $w'$  = spanwise velocity fluctuation  
 $X$  = axial position  
 $Y$  = vertical position  
 $\rho$  = density

$\beta$  = span angle of v-gutter  
 $\nu$  = kinematic viscosity

### Subscripts

$\infty$  = upstream condition  
 $o$  = the condition of the maximum axial velocity outside the shear layer



**2.3 Experimental Conditions.** V-gutters of two types, regular and irregular, were tested. Those of irregular type had an open slit at the leading edge. Sketches of the configuration, coordinate system, and dimensions of the test section and the v-gutters are shown in Fig. 2. The span angle of the v-gutter was 45 degrees, corresponding to a blockage ratio 0.20. The range of the flow velocities was 1-20 m/s, corresponding to Reynolds numbers  $(U_\infty L_b/\nu)$   $1.2 \times 10^3 - 2.4 \times 10^4$ ;  $L_b$  is the width at the end of the v-gutters. In order to obtain better images, the tests of flow visualization were conducted at a flow velocity of 1 m/s. The turbulent intensity in front of the v-gutter was less than 0.85 percent. The widths of the open-slit ( $L_s$ ) of the irregular v-gutter were chosen to be 2-mm and 4-mm, respectively.

**2.4 Data Accuracy.** For statistical analysis, the mean values of 30,720 samples of velocity measurements near the rear-stagnation point (the variation of the mean velocity was less than 0.1 m/s at  $U_0 = 20$  m/s) were chosen as the "accurate" reference values. Since the measuring time for 30,720 data near the rear-stagnation point will consume 150 minutes, only 2048 measurements were typically made at each measuring point. The corresponding maximum uncertainties were 3.2 percent of the mean axial velocity, 4.9 percent of the mean transverse velocity, and 4.9 percent of the turbulent intensity at the 95 percent confidence level. In the mean time, the axial velocities were integrated along each cross section to obtain the mass flow rate. The results showed that the mass flow rates of all of the test sections normalized by the flow rate of upstream were between 0.95 and 1.05. The corresponding maximum uncertainty of the Reynolds shear stress was 13 percent.

The signal processing was conducted with two burst-period counters which used eight fringe crossings to determine the period of the signal. The counters then applied a 5/8 comparison and a three-level validation circuit to minimize erroneous period readings. The coincidence interval between the counters was of the order of nanoseconds to ensure the validity of the readings. The frequency offset of the Bragg cells was large compared with the frequency shift from the flow velocity. The cycle period of the data acquisition system was small compared with the lifetime of the signals of measurements in the recirculation zone. These efforts allow multiple readings on the same seeding particles, and the influence of the sampling bias is thus significantly reduced. Furthermore, a two-dimensional weighting model (Johnson, 1984) was applied to analysis of the raw data and showed fairly good agreement with our results.

The spanwise uniformity of the wake flow ( $U$ ,  $W$ ,  $u'$ ,  $w'$ ) was examined behind the 2-mm open slit v-gutter at  $X = 20$  mm and  $Y = 10$  mm. The location was near the center of the upper shear layer and the flow there was highly turbulent and likely to be three-dimensional. The results show that the distribution along the spanwise direction was almost constant and the three-dimensional effects were negligible in our experimental results.

More than 20,000 data were taken for each point of pressure measurement; the sampling period was 500  $\mu$ s. The uncertainty of the pressure measurement was calculated by systematically changing the revolution of instruments, recording 20 sets of data and then conducting a statistical analysis of deviations. The uncertainty of the pressure data was less than 5 percent.

### 3 Results and Discussion

**3.1 Velocity Measurement.** The flow pattern of the near wake of a regular v-gutter measured by means of the two-component LDA system is shown in Fig. 3. The distributions of velocity vector showed two recirculation zones enclosed by the upper and the lower shear layers and located symmetrically with respect to the center line along the duct. The axial positions

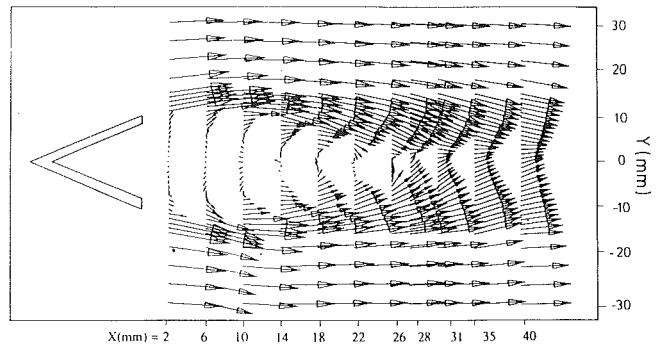


Fig. 3 Flow pattern behind a regular v-gutter with 45-degree span angle at  $U_\infty = 20$  m/s

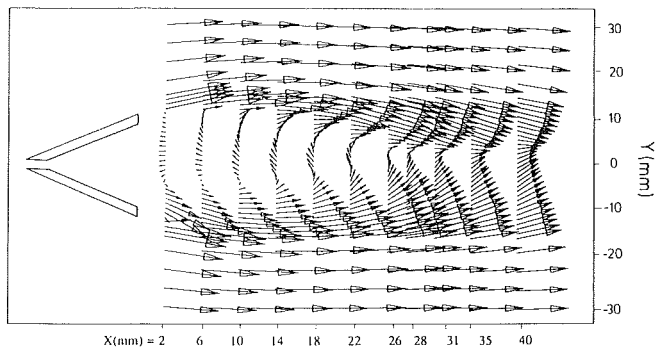


Fig. 4 The flow pattern behind a 2-mm open-slit v-gutter with 45-degree span angle at  $U_\infty = 20$  m/s

of the centers of the recirculation zone were both about  $X = 14$  mm ( $Y = 4$  and  $-4$  mm). As the fluid flowed downstream, the shear layers grew transversely and gradually penetrated to the center plane. The axial velocity of the center plane changed from negative to positive at  $X = 26$  mm, which indicates the end of recirculation.

The distribution of velocity vector of the wake flow behind the irregular v-gutter with slit width 2 mm ( $L_s/L_b = 0.1$ ) is shown in Fig. 4. The asymmetric features of the wake flow field are obvious. The fluid jet penetrating the leading open slit of the v-gutter turned toward either the upper or the lower wing and then stayed stable owing to the bi-stable status of the flow field. The jet fluid did not diffuse symmetrically in the near-wake region. This phenomenon is similar to the Coanda effect (McCloy and Martin, 1982) in hydrodynamic control. For convenience of discussion, all test results of the open-slit v-gutter are adopted as if the jet fluid turned downward to the lower wing.

There was a recirculation zone near the gutter, compared with Fig. 4, which was induced by the jet bending from the slit and recirculated between  $X = 6$  and 10 mm ( $Y = -5$  mm). The reverse velocity near the gutter was thus strengthened. Because the fluid around the center plane at  $X = 10$  mm was entrained in the reverse direction by the jet-induced recirculation, the momentum difference across the upper shear layer was enhanced and the shape of the upper recirculation zone was more slender than that of the regular v-gutter.

At the upper side the center of one recirculation zone, namely the vortex recirculation zone, was located near  $X = 14$  mm and  $Y = 5$  mm behind the upper wing and was analogous to that of the regular v-gutter. Because of the greater mixing effect between the deflected jet and the lower stream, the velocity gradient of the lower shear layer tended to be milder. For this reason, the initiation of the initial vortex extended farther downstream. Moreover, the velocity gradient of the lower shear

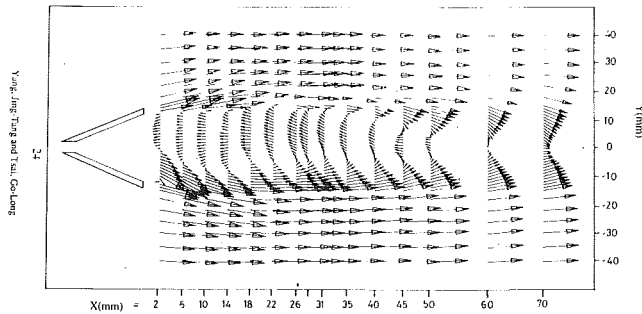


Fig. 5 Flow pattern behind a 4-mm open-slit v-gutter with 45-degree span angle at  $U_\infty = 20$  m/s

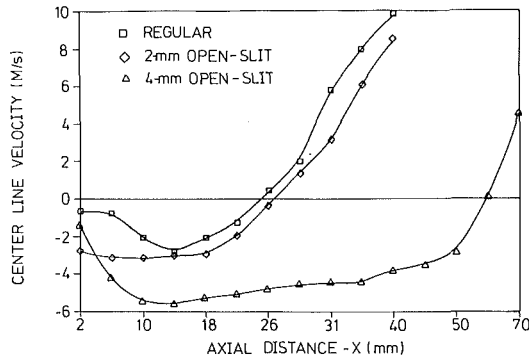


Fig. 6 Mean axial velocity distributions along the centerline for various v-gutters (uncertainty in mean axial velocity is less than  $\pm 3.2$  percent)

layer was smoother at about  $X = 10$  mm and the reverse velocity around center plane increased significantly.

The vector form of the velocity distribution behind an open-slit v-gutter with  $L_s = 4$  mm ( $L_s/L_b = 0.2$ ) is shown in Fig. 5; it exhibits the discontinuous structure of the velocity distribution in the upper shear layer. Therefore the transverse momentum transport of the upper shear layer was much delayed compared with that of the regular v-gutter. The velocity profiles were smooth up to  $X = 50$  mm. The center of the recirculation zone was located far downstream at  $X = 40$  mm and  $Y = 10$  mm; this tendency partially resulted from the increased back pressure as the mass bleed increased. The built-up large back pressure in turn retarded the formation of the initial vortex and momentum transport from the main stream, to the center plane.

The jet-induced recirculation zone was considerably enlarged and possessed greater strength compared with the narrower open-slit width. Its center was located at  $X = 18$  mm and  $Y = 5$  mm. The other recirculation zone at the lower side of the wake was scarcely detected. The measurements of axial reverse velocity showed that the recirculation length enlarged to 60 mm, which is more than twice that of the regular v-gutter.

**3.2 Reverse Flow.** Figure 6 shows the variation of the axial velocity along the centerline of the wake for v-gutters with various widths of the open slit. The reverse velocity of the regular v-gutter increased gradually along the centerline up to  $X = 6$  mm and then rapidly when the vortex rolled up occurs. The reverse velocity reached a maximum at  $X = 14$  mm, which corresponds to the center of the recirculation zones. Thereafter, the entrainment of mass into the wake region through vortex formation rapidly decreased the reverse velocity.

When the slit was open 2 mm, the reverse velocity was constant at 2.8 m/s in the region between  $X = 2$  and 18 mm. Because the strengths of both the jet-induced recirculation and

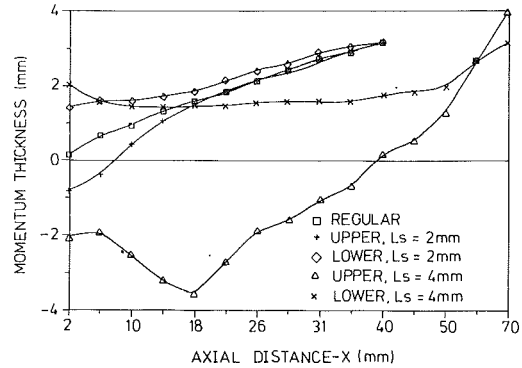


Fig. 7 Momentum thickness of various v-gutters along the axial distance (uncertainty in momentum thickness is less than  $\pm 9.7$  percent)

vortex recirculation zones were of the same order, the distribution of the reverse velocity between the two recirculation centers became smooth. The curves of both the regular and the 2-mm open-slit v-gutters were similar downstream from the recirculation zone. The reverse flow rate of the open-slit v-gutter increased mainly in the region before  $X = 10$  mm. The length of the recirculation zone was enlarged from 24 mm to 27 mm. The distance from the end of the recirculation zone to the rear end of the v-gutter was chosen as the length of the recirculation zone.

When the width of the slit was 4 mm, the recirculating effects were considerable. The reverse velocity reached a maximum at  $X = 14$  mm, which is near the axial position of the center of the jet induced recirculation zone. It decreased gradually towards the upper vortex-recirculation center at  $X = 40$  mm. The recirculating region extended to  $X = 60$  mm, which is more than 2.5 times the length of the regular v-gutter.

Figure 7 shows the variations of the momentum thicknesses,  $\theta$ , of three v-gutters along the axial positions. The momentum thickness is defined as

$$\theta = \int_0^{Y_{95}} \frac{u}{U_0} \left(1 - \frac{u}{U_0}\right) dY \quad (1)$$

in which  $U_0$  is the maximum axial velocity on the outside of the shear layer and  $Y_{95}$  denotes the position in which the axial velocity is 95 percent of  $U_0$ . The region of integration is from the centerline to either the upper or the lower side.

The momentum thickness of the regular v-gutter was almost linearly proportional to the axial distance. In the upper half plane of the 2-mm open-slit v-gutter,  $\theta$  was less than zero at  $X = 2$  mm due to the influence of the jet-induced recirculation. As the momentum difference across the upper shear layer was large, the slope of the curve increased rapidly until  $X = 18$  mm. The curve corresponding to the lower shear layer of the 2-mm open-slit v-gutter was positive and rose slowly because of the mixing of the jet with the lower shear layer before  $X = 18$  mm. Since the difference of the momentum thickness between the upper and lower half planes at  $X = 2$  mm is near 2 mm, this indicates that the fluid penetrating through the open slit essentially deflects toward the lower wing of the gutter.

The momentum thickness on the upper half plane of the 4-mm open-slit v-gutter was also negative at  $X = 2$  mm. However, it decreased after  $X = 6$  mm and reached a minimum at  $X = 18$  mm, which is the center of the jet-induced recirculation zone. For the same cause as in the upper wing, the momentum thickness along the lower half plane decreased progressively until  $X = 14$  mm. After  $X = 14$  mm it increased slowly as the deflective jet caused much smaller difference of momentum between the two sides of the shear layer.

The dimensionless reverse volumetric flow rate along the axial direction shown in Fig. 8 is defined as

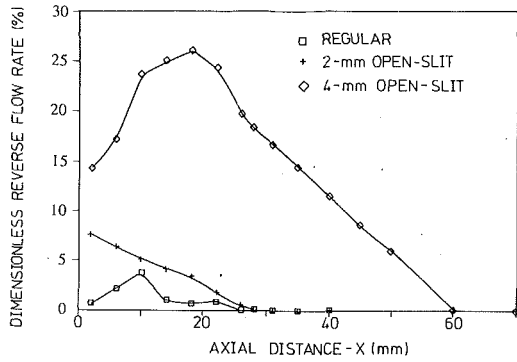


Fig. 8 Dimensionless reverse flow rate of the v-gutters along the axial distance (uncertainty in dimensionless reverse flow rate is less than  $\pm 3.2$  percent)

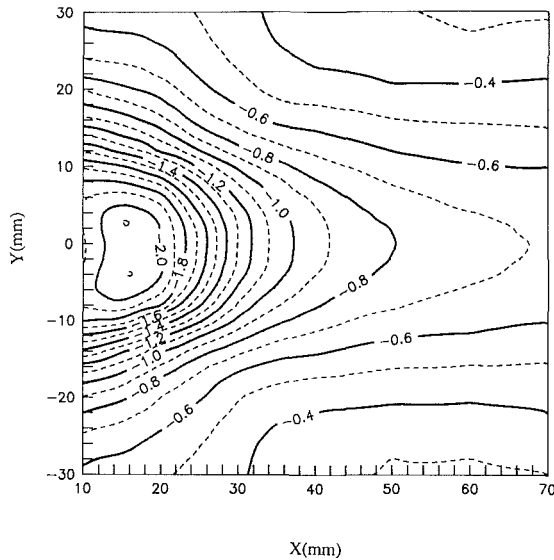


Fig. 9 Mean pressure distribution behind a regular v-gutter with 45-degree span angle in  $U_\infty = 20$  m/s (uncertainty in mean pressure is less than  $\pm 5$  percent)

$$\frac{\dot{m}_r}{\dot{m}_T} = \frac{\left| \int_{Y_1^*}^{Y_2^*} u \cdot dY \right|}{L_b \cdot U_\infty} \quad (2)$$

in which  $L_b$  is the blockage length of the test v-gutters,  $Y_1^*$  and  $Y_2^*$  are the boundaries enclosing the region of negative axial velocity and  $u=0$  on  $Y_1^*$  and  $Y_2^*$ . Figure 8 shows that the dimensionless reverse flow rate of the regular v-gutter attained its maximum, 0.75 percent, at  $X=10$  mm. The reverse flow rate of the 2-mm open-slit v-gutter decreased with increasing axial distance and was 1.5 percent at  $X=2$  mm. The corresponding maximum value for the 4-mm open-slit v-gutter was 5.3 percent at  $X=18$  mm, about 7 times that of the regular v-gutter. As the reverse flow rate is proportional to the flame stabilization limit as suggested by Kundu (1980), the open-slit v-gutter is expected to have a positive effect on the performance of the flame holders.

**3.3 Pressure Distribution and Drag Estimation.** The distributions of pressure coefficient of the wake flow behind the regular, the 2-mm and the 4-mm open-slit v-gutters are shown in Figs. 9–11, respectively. The reference pressure is chosen as the pressure measured at the center plane of  $X = -150$  mm. Those values are 155, 161, and 161 Pa relative to atmosphere

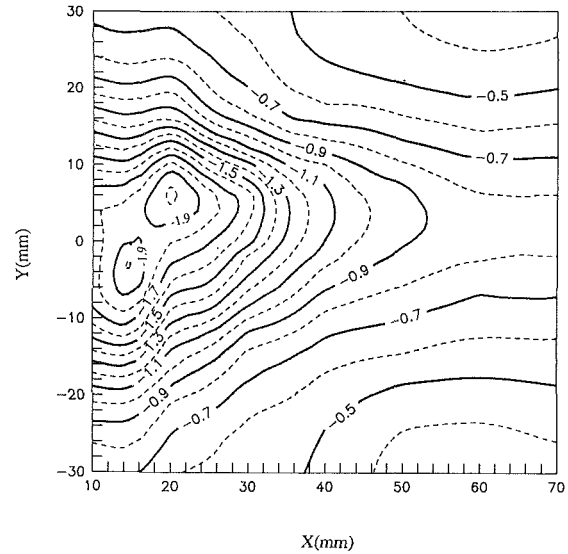


Fig. 10 Mean pressure distribution behind a 2-mm open-slit v-gutter with 45-degree span angle at  $U_\infty = 20$  m/s (uncertainty in mean pressure is less than  $\pm 5$  percent)

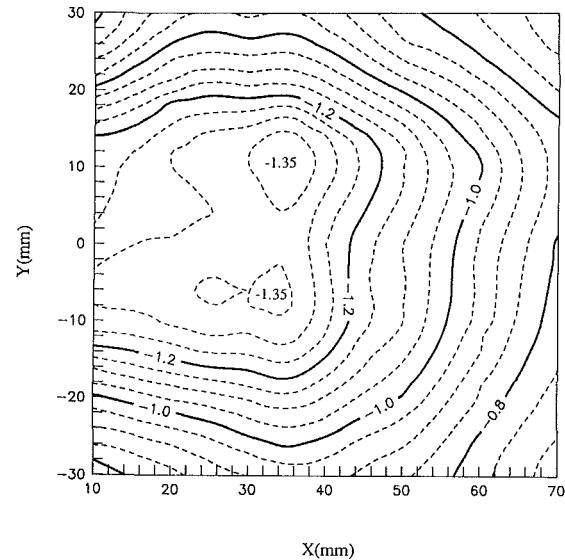


Fig. 11 Mean pressure distribution behind a 4-mm open-slit v-gutter with 45-degree span angle at  $U_\infty = 20$  m/s (uncertainty in mean pressure is less than  $\pm 5$  percent)

atmosphere pressure, respectively. Furthermore, the definition of the pressure coefficient  $C_p$ , is

$$C_p = \frac{P - P_{\text{ref}}}{\frac{1}{2} \rho U_\infty^2} \quad (3)$$

The smallest value of the pressure coefficient in the near wake of the regular v-gutter is  $-2.1$ , as shown in Fig. 9. The two locations of the lowest pressure are at  $X=15$  mm, which almost coincide with those of the recirculation centers discussed in Fig. 3. The distribution of the pressure coefficient of the 2-mm open-slit v-gutter is contrasted in Fig. 10. The nonsymmetric distribution is obvious. The smallest pressure coefficient for the upper and lower half planes occurred at  $X=20$  mm,  $Y=6$  mm and at  $X=15$  mm,  $Y=-4$  mm, respectively. Those points, which appeared after the upper vortex recirculation center and the lower jet-induced recirculation center were having  $C_p$  of the same value  $-1.95$ . When the slit was opened to 4 mm (Fig. 11), the smallest pressure coefficient increased

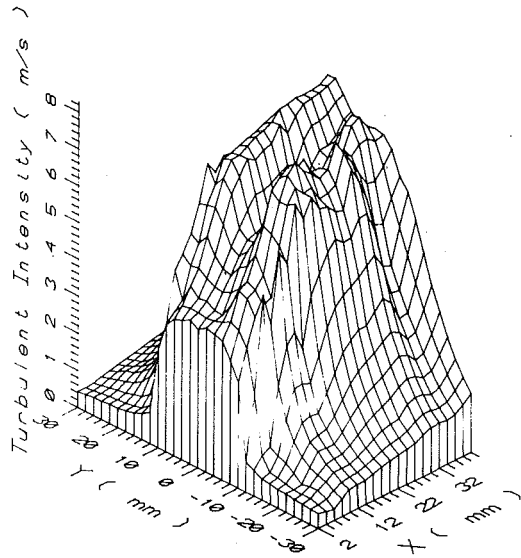


Fig. 12 Turbulent intensity distribution behind a regular v-gutter with 45-degree span angle at 20 m/s (uncertainty in turbulent intensity is less than  $\pm 4.9$  percent)

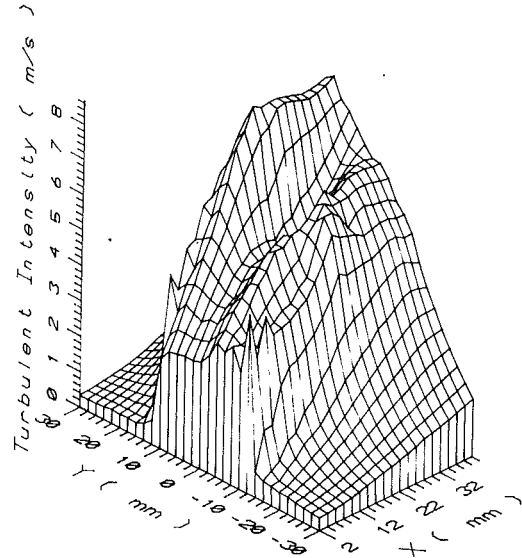


Fig. 13 Turbulent intensity distribution behind a 2-mm open-slit v-gutter with 45-degree span angle at 20 m/s (uncertainty in turbulent intensity is less than  $\pm 4.9$  percent)

considerably and developed far downstream. The smallest pressure in the upper half plane was located at  $X=35$  mm and  $Y=10$  mm, which was before the vortex recirculation center and has a value  $-1.35$ . The lowest coefficient of the lower half plane was obtained at  $X=26$  or  $34$  mm and  $Y=-6$  mm, which was after the jet-induced recirculation center, and at value of  $-1.35$ . The wider slit was open, the greater the smallest pressure coefficient increased. Furthermore, the order of the drag forces is judged according to the value of  $C_p$  for the constant pressure contour, which extended from the end of the two wings and enclosed the recirculation zone. Those corresponding  $C_p$  values are  $-1.7$ ,  $-1.6$ , and  $-0.9$ , corresponding to the regular, 2-mm, and 4-mm open-slit v-gutters, respectively. All the evidence indicates that the open slit is beneficial to reducing the drag force exerted on the v-gutter.

**3.4 Turbulent Intensity.** The definition of turbulent intensity is two dimensional and expressed as below:

$$\text{Turbulent intensity} = \left( \frac{u'^2 + v'^2}{2} \right)^{1/2} \quad (4)$$

Figures 12–14 depict distributions of turbulent intensity behind the regular, the 2-mm open-slit and 4-mm open-slit v-gutters, respectively. The transverse distribution of the turbulent intensity just downstream of the v-gutter was hat-shape, as shown in Fig. 12. The hat-shape gradually changes into “M” shape in the axial direction. The double peaks of the turbulent intensity are caused by the strong transport and mixing across the upper and lower shear layers. The turbulent intensities of the peaks increased slowly in the axial direction after  $X=18$  mm, whereas the value at the center line kept increasing. The vortices of both sides started to shed and to buffet intensely with each other at that position.

Figure 13 shows the distribution of the turbulent intensity of the wake flow behind a 2-mm open-slit v-gutter. The transverse distribution of the turbulent intensity at  $X=2$  mm had a spike near the trailing edge of the lower wing at  $Y=-10$  mm, whereas the distribution of the upper wing was almost the same as that of the regular v-gutter. The spike resulted from penetration of the fluid through the open slit first attaching on the inner face of the lower wing and then mixing with the lower shear layer. This effect caused large velocity fluctuations and thus led to the high turbulent intensity. Fur-

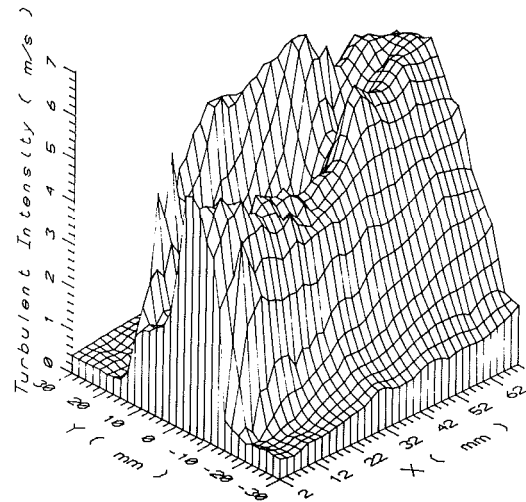


Fig. 14 Turbulent intensity distribution behind a 4-mm open-slit v-gutter with 45-degree span angle at 20 m/s (uncertainty in turbulent intensity is less than  $\pm 4.9$  percent)

thermore, the shear layer exhibited a less steep velocity gradient because of the mixing and mass addition effects. As a result, the instability of the lower shear layer decreased and the growth of vortices was retarded and weakened. The peak of the turbulent intensity after  $X=2$  mm increased more moderately than that of the regular v-gutter. As the vortices of the two shear layers interacted with each other only after  $X=22$  mm, the peaks of turbulent intensity of the upper shear layer increased sharply until  $X=22$  mm and then maintained a value about 8.5 m/s, which is 13.3 percent higher than that of the regular v-gutter.

The transverse distribution of the turbulent intensity at  $X=2$  mm for the 4-mm open-slit v-gutter is quite different from that of the regular v-gutter. This distribution had huge and wide peaks near the inner side of the trailing edge of the lower wing. The turbulent intensity of the upper shear layer kept increasing until  $X=46$  mm and, afterward, remained around the value of 6.3 m/s.

**3.5 Reynolds Shear Stress.** The distribution of Reynolds

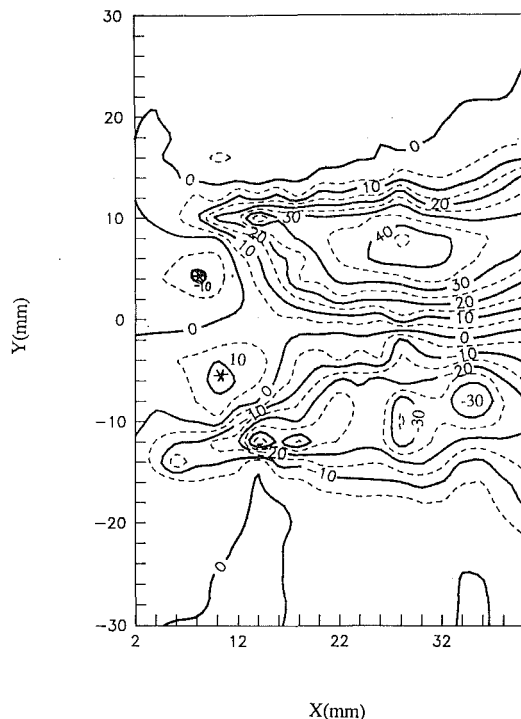


Fig. 15 Reynolds shear stress ( $400 \times (-u'v'/U_\infty^2)$ ) distribution behind a regular v-gutter with 45-degree span angle at 20 m/s (uncertainty in Reynolds shear stress is less than  $\pm 13$  percent)

stress of the wake flow behind the regular v-gutter is shown in Fig. 15. The maximum and minimum Reynolds stresses were  $45 \text{ N/m}^2$  and  $-35 \text{ N/m}^2$ , respectively, and occurred at  $X=28 \text{ mm}$ , which was 4 mm after the end of the recirculation zone. The distribution was asymmetric with respect to the centerline,  $Y=0 \text{ mm}$ . There were regions of negative Reynolds stress enclosed by the zero Reynolds stress contour before  $X=12 \text{ mm}$  above the centerline. At the same axial distance, there was also a position of positive peak Reynolds stress denoted by the "\*" symbol below the centerline. Both these abnormal Reynolds stresses were created as the separation recirculation obtained energy from the shear layer and then transferred it to the region of reverse flow at  $Y=0 \text{ mm}$ .

The Reynolds stress of the 4-mm open-slit v-gutter is shown in Fig. 16. The increase of the Reynolds stress along the upper shear layer began at  $X=12 \text{ mm}$ , at which the level of contour is 10. Then, it reached a value of 25 at  $X=25 \text{ mm}$  and remained nearly constant until  $X=62 \text{ mm}$ . The plateau along the upper shear layer was narrower and longer than those of the others. The reason for this phenomenon is that the shedding vortices on the upper shear layer failed to interact with the lower vortices, as shown in Fig. 5. Thus they moved downstream with nearly constant angular momentum. The development of the Reynolds stress of the lower shear layer was insignificant until  $X=34 \text{ mm}$ . The maximum absolute values of the upper peak and lower valley were respectively reduced to  $30 \text{ N/m}^2$  and  $25 \text{ N/m}^2$ , which are smaller than those of the regular v-gutter.

In general, the turbulent intensity and the Reynolds shear stress were both reduced for the open-slit v-gutters. However, because the size of the recirculation zone was increased up to twice, the extent of the overall transport between the recirculation zone and the main flow may still have been enhanced.

#### 4 Conclusions

We have produced cold-flow test data of v-shape flame holders with flow bleed from the slit on the leading edge. The

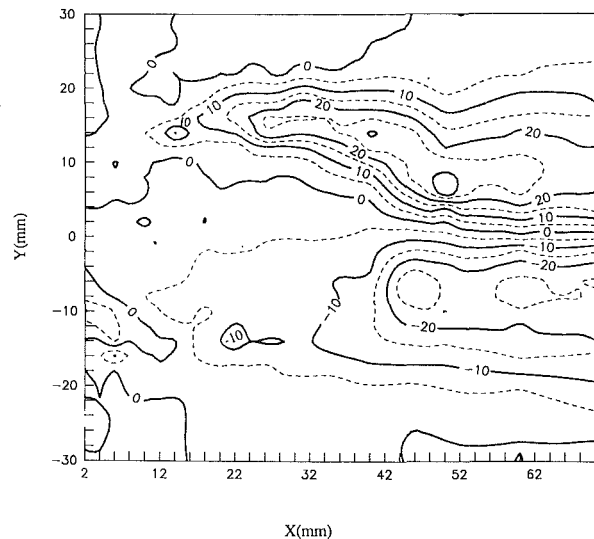


Fig. 16 Reynolds shear stress ( $400 \times (-u'v'/U_\infty^2)$ ) distribution behind a 4-mm open-slit v-gutter with 45 degree span angle at 20 m/s (uncertainty in Reynolds shear stress is less than  $\pm 13$  percent)

experimental results show that the fluid penetrating through the slit of the v-gutter diffuses nonuniformly, but acts like a jet which deflects toward either side of the two wings of the v-gutter. This effect results in a non-symmetric wake flow field. The diverted jet causes extensive mixing between the shear layer and the near-wake region and thus reduces the momentum difference across the shear layer. Consequently, the vortex originating from the unstable shear layer is observed farther downstream.

Both the size of the recirculation zone and the strength of the reverse flow reported were to be proportional to the flame stabilization limit. Our work shows that the slit v-gutter can increase considerably the strength of the reverse flow rate up to 7 times. The slit v-gutter also increases the length of the recirculation zone up to 2.5 times. Furthermore, the slit v-gutter not only generates a larger recirculation zone with stronger reverse flow, but also produces smaller pressure drop. The bleed mass adds more momentum within the near-wake and thus reduces both the turbulent intensity and the Reynolds shear stress. The extent of the reduction of the turbulent features is in proportion to the width of the slit. The region of the recirculation flow is also significantly enlarged as the width of the gutter is increased. Assuming that the rate of heat and mass transport in the mixing process is linearly proportional to the turbulent properties, and the total amount of transport increases with the size of the boundary between the main flow and the recirculation zone. The combination of these factors could be still in favor of the overall transport process.

This study indicates that the slit v-gutter can have a better flame holding ability and less pressure loss compared with the traditional v-gutter. In view of fluid dynamics features, the slit v-gutter is indeed a potentially useful design of flame holder.

#### 5 JFE Data Bank Contributions

The data presented in the figures of this paper have been edited and deposited in the JFE Data Bank for the use of any of the readers. The data include mean and r.m.s. fluctuation of horizontal velocity, mean and r.m.s. fluctuation of vertical velocity, mean and r.m.s. fluctuation of pressure, Reynolds shear stress, and turbulent velocity. The files also include instructions on the data format. To access the file of this paper, see instruction on p. 189 of this issue.



## References

- Bearman, P. W., 1967, "On Vortex Street Wakes," *Journal of Fluid Mechanics*, Vol. 28, pp. 625-641.
- Bovina, T. A., 1958, "Studies of Exchange between Recirculation Zone Behind the Flameholder and Outer Flow," *Seventh Symposium (Int.) on Combustion*, pp. 692-696.
- Fujii, S., and Eguchi, K., 1981, "A Comparison of Cold and Reacting Flows Around a Bluff Body Flame Stabilizer," *ASME JOURNAL OF FLUIDS ENGINEERING*, Vol. 103, 1981, pp. 328-334.
- Gerrad, J. H., 1962, "An Experimental Investigation of the Oscillating Lift and Drag of a Circular Cylinder Shedding Turbulent Vortices," *Journal of Fluid Mechanics*, Vol. 11, pp. 244-256.
- Govinda Ram, H. S., and Arkeri, V. H., 1990, "Studies on Unsteady Pressure Fields in the Region of Separating and Reattaching Flows," *ASME JOURNAL OF FLUIDS ENGINEERING*, Vol. 112, pp. 402-408.
- Johnson, D. A., Modares, D., and Owen, F. K., 1984, "An Experimental Verification of Laser-Velocimeter Sampling Bias and Its Correction," *ASME JOURNAL OF FLUIDS ENGINEERING*, Vol. 106, pp. 5-12.
- Kundu, K. M., Banerjee, D., and Bhaduri, D., 1980, "On Flame Stabilization by Bluff-Bodies," *Journal of Engineering for Gas Turbines and Power*, Vol. 102, pp. 209-214.
- Lefebvre, A. H., 1983, *Gas Turbine Combustion*, Hemisphere, New York, Chapter 6.
- McCloy, D., and Martin, H. R., 1980, *Control of Fluid Power*, Ellis Horwood, New York, Chapter 1.
- Rao, K. V. L., and Lefebvre, A. H., 1982, "Flame Blowoff Studies Using Large-Scale Flameholders," *ASME Journal of Engineering for Gas Turbines and Power*, Vol. 104, pp. 853-857.
- Sirka, V. P., Paujotas, P. M., and Zukauskas, A. A., 1989, "Characteristics of the Near Wake of a Cylinder in Crossflow," *Fluid Mechanics-Soviet Research*, Vol. 18, pp. 13-22.
- Stwalley, R. M., and Lefebvre, A. H., 1988, "Flame Stabilization Using Large Flameholders of Irregular Shape," *Journal of Propulsion and Power*, Vol. 4, pp. 4-13.
- Sullerey, R. K., Gupta, A. K., and Moorthy, C. S., 1975, "Similarity in the Turbulent Near Wake of Bluff Bodies," *AIAA Journal*, Vol. 13, pp. 1425-1429.
- Taylor, A.M.K.P., and Whitelaw, J. H., 1984, "Velocity Characteristic in the Turbulent Near Wake of Confined Axisymmetric Bluff Bodies," *Journal of Fluid Mechanics*, Vol. 139, pp. 391-410.
- Vortmeyer, D., 1962, "Examination of the Possibility of Predicting Reaction Rate-Controlled Flame Phenomena by use of Cold Model," *Tenth Symposium (Int.) on Combustion*, pp. 936-948.
- Wong, H. Y., 1985, "Wake Flow Stabilization by the Action of Base Bleed," *ASME JOURNAL OF FLUIDS ENGINEERING*, Vol. 107, pp. 378-384.
- Yang, J. T., and Tsai, G. L., 1991, "The Wake Flow Structure of an Open-Slit V-gutter," *Proceedings of The Second World Conference on Experimental Heat Transfer, Fluid Mechanics, and Thermodynamics*, pp. 193-201, Dubrovnik, Yugoslavia, June.
- Zukoski, E. E., 1978, "Afterburners," *The Aerothermodynamics of Aircraft Gas Turbine Engines*, G. C., Oates, ed., Chapter 21.

C. C. Hwang

H. Q. Shen

G. Zhu<sup>1</sup>

M. M. Khonsari

Department of Mechanical Engineering,  
University of Pittsburgh,  
Pittsburgh, PA 15261

# On the Main Flow Pattern in Hydrocyclones

*A theoretical model is developed for the prediction of the main flow pattern in hydrocyclones. The model regards the main body of the cyclone as inviscid and includes provisions for the fluid underflow in cyclones. The governing equations are solved analytically in closed form. To verify the results, a laboratory-scale conically-shaped hydrocyclone was designed, built, and tested. Experimental measurements for axial and tangential velocities are presented with a series of tests solely devoted to the effect of underflow. The theoretical and experimental results are shown to be in good agreement. It is concluded that such an inviscid model gives an adequate representation of the main flow field in a cyclone.*

## 1 Introduction

The cyclone is a funnel-shaped, industrial device for separating solid, liquid, and/or gaseous phases in a dispersed suspension. Its operation is chiefly based on the density difference and high rotational velocities that are imparted as the suspension is injected tangentially into the upper part of the cyclone (Bradley, 1965; Svarovsky, 1984; Dirgo and Leith, 1986). A particular type of cyclone known as the hydrocyclone is gaining increasing utility in a wide variety of practical applications such as food processing, mineral processing, and coal cleaning. Industrial hydrocyclones fall into several broad categories ranging from counter-current washing to liquid-liquid separation. While the basic design of the hydrocyclone dates as far back as its patent in 1891, each application has its particular requirements and calls for different design variables and operating conditions.

In a hydrocyclone, liquid enters through tangential inlets placed near the top cover. This incoming fluid takes on a swirling motion as it flows into the outer portion of the inverted cone. Some of the downward flow hereinafter referred to as the underflow, exits the hydrocyclone through the orifice in the apex of the cone while the rest reverses its vertical direction and swirls up and out of the vortex finder. Depending on the operating conditions, this swirling flow may create a region of low pressure in the center, forming a cylindrically shaped, rotating, free surface that runs the entire length of the cyclone.

Many existing hydrocyclones are largely designed based on field experience rather than detailed theoretical analyses. This is not surprising because the flow field in a cyclone is rather complex.

Despite the complexity of the problem, simple analytical solutions that can predict the flow pattern are also very desirable from the point-of-view of simplicity and effectiveness. Recently Bloor and Ingham (1987) reported a closed-form so-

lution for the axial and swirl velocity that, despite many simplifying assumptions, compared well with the experimental results of Kelsall (1952).

Of particular interest of the present paper is the examination of the underflow which was neglected by Bloor and Ingham (1987). We present experimental results in a laboratory scale, conically-shaped cyclone and report axial and tangential velocity measurements from a series of experiments that were solely devoted to the effect of underflow. As an extension of the work of Bloor and Ingham (1987), theoretical developments with a provision for the fluid underflow are also described.

## 2 Experimental Procedure and Results

The core section of the experimental apparatus included a laboratory-scale hydrocyclone, inlet and outlet flow regulators, and appropriate tubing. The cyclone had the conventional conical shape and was fabricated from a plexiglass block of square cross-section. The dimensions corresponded closely to those recommended by Rietema (1961) for optimal performance.

A steady flow of water regulated by three control valves placed at the inlet, overflow, and underflow positions made up a major part of the fluid supply loop to the cyclone. Two calibrated rotameters measured the rates of overflow and underflow and allowed the operator to set a flow split ratio of overflow to underflow to a desired value. The pressure level in the cyclone could be continuously monitored using a pressure gauge at the inlet. The connecting tubings were made of flexible Tygon and the model cyclone was mounted vertically on a transverse table so that it could be easily moved relative to other components of the loop. This repositioning is necessary since the velocity measuring device was set in a stationary position.

Velocity profile measurements were made using a laser doppler velocimeter (LDV) with a 15mW He-Ne laser in dual-beam mode with forward scattering to ensure good signal-to-noise ratio. To determine the direction of the velocity, a fre-

<sup>1</sup>Visiting Scholar, Chinese Academy of Sciences, Beijing, The People's Republic of China.

Contributed by the Fluids Engineering Division for publication in the JOURNAL OF FLUIDS ENGINEERING. Manuscript received by the Fluids Engineering Division October 3, 1991. Associate Technical Editor: J. Humphrey.

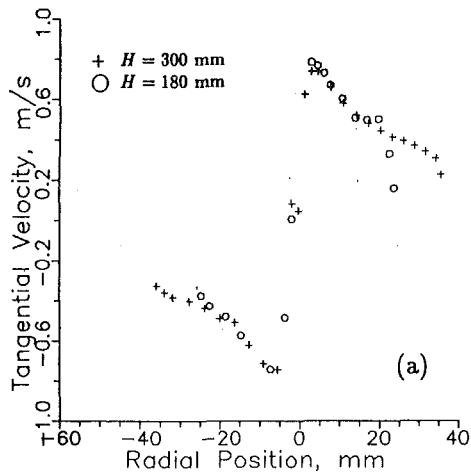


Fig. 1(a)

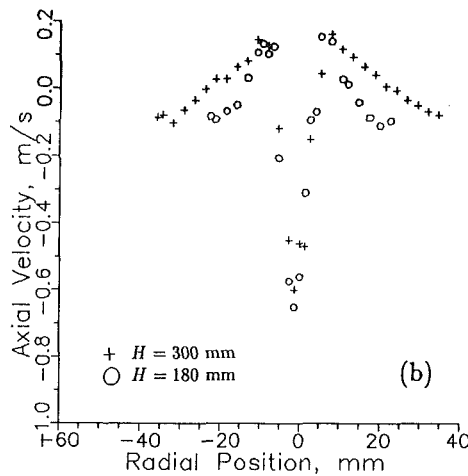


Fig. 1(b)

Fig. 1 Profiles of (a) tangential velocity and (b) axial velocity at two axial locations.  $H$  measured from the bottom of the cyclone. Flow rate 0.2 kg/s. Flow split ratio 1.0.

quency shift system (a Bragg cell type) was employed to shift the frequency of one of the laser beams.

By adjusting the flow rate and the cyclone pressure, it was possible to produce an air core in the form of bubbles several centimeters long in the axial direction. Lying along the true axis of the cyclone and perfectly stable, the air core serves as an alignment reference. After satisfactory alignment, the flow rates were readjusted and the cyclone was operated without an air core for the entire set of experiments described herein.

The experimental uncertainty of the data was as follows: the flow rate  $\pm 1.5$  percent, flow split ratio  $\pm 2$  percent, the mean velocity  $\pm 3$  percent; positioning in both radial and axial directions (including errors arising from difference in the refractive indices of materials)  $\pm 0.5$  mm.

Figure 1 depicts the axial and tangential velocity profiles at two axial locations. In general, the axial velocity profile shows a velocity defect (a dent) in the center core region of the cyclone. Similar type of velocity defect has been observed elsewhere (Escurdier, 1980). The tangential velocity component is zero at the center, increases sharply with the radius, to a maximum value, and then gradually decreases as it approaches the cyclone wall where it becomes zero. This central viscous region of the vortex is characterized by a linear variation of the tangential velocity (i.e.,  $v_\phi \sim r \sin\theta$ ).

In this paper we concentrate on the variation of the flow split ratio for it can have a profound effect on the shape of

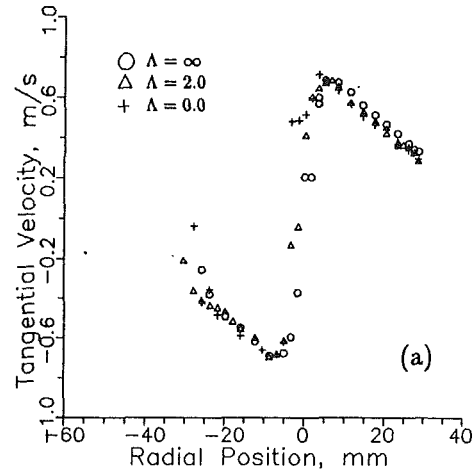


Fig. 2(a)

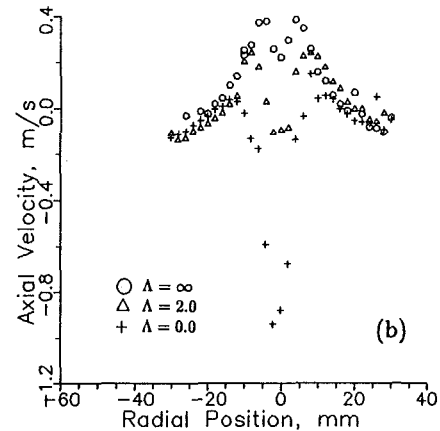


Fig. 2(b)

Fig. 2 Effect of flow split ratio,  $\Lambda$ , on (a) tangential velocity and (b) axial velocity.  $H = 240$  mm. Flow rate 0.2 kg/s.

the velocity components. Figure 2 shows the axial and tangential velocity profiles at the level  $H = 240$  mm in the cyclone with flow split ratios varying from 0 to  $\infty$ . As the flow split ratio is increased, the depth of the dent in the center of the axial velocity profile is reduced and the positive (upward) portion of the velocity profile is increased. Similar results have been reported by Dabir (1983). For the flow split ratios between 0 to 4, two cellular structures are observed; while for the flow split ratio of  $\infty$ , only a one-cell structure is seen.

As the results of these experiments are indicative of a pronounced influence of the flow split ratio on the velocity profiles, the theoretical analysis of Bloor and Ingham (1987) were extended to include the effect of underflow.

### 3 Theoretical Considerations

A hydrocyclone is generally operated at a large Reynolds number of the main flow, with viscous boundary layers forming on the walls. The viscous effect is also dominant in the central core region where a rigid rotation takes place. The mean flow in the main body of the cyclone, however, may be approximated by an inviscid flow. As observed experimentally, the flow in the region away from the entrance port is approximately axisymmetric. This permits the use of an axially symmetric flow in the theoretical development. The spherical polar coordinate system ( $r, \theta, \phi$ ) with the origin at the apex of the cone of the cyclone is shown in Fig. 3.

Similar to Bloor and Ingham (1987), it is assumed that the fluid enters perpendicularly to the cyclone lid and distributed

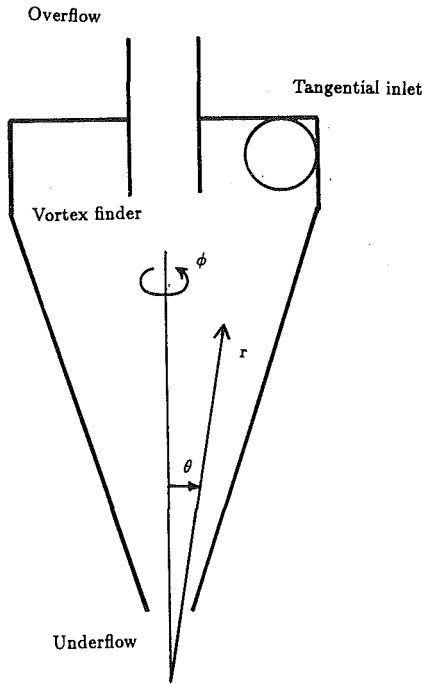


Fig. 3 A schematic of the cyclone showing the spherical polar coordinates systems

uniformly into the region where it becomes axially symmetric.

Let the fluid velocity in entrance region  $R_1 < r \sin \theta < R_0$  be denoted by  $W$ , where  $R_0$  is the radius of the cyclone and  $R_1$  is a radius yet to be determined. The streamfunction  $\psi$  and the volume flow rate  $Q$  at the entry are given by

$$\psi = \frac{1}{2} W (R_0^2 - r^2 \sin^2 \theta) \quad (1)$$

$$Q = \pi W (R_0^2 - R_1^2). \quad (2)$$

Referring to the work of Bloor and Ingham (1987), it can be shown that the dimensionless form of the streamfunction is given by

$$\frac{\partial^2 F}{\partial \eta^2} + \frac{\sin \theta}{\eta^2} \frac{\partial}{\partial \theta} \left( \frac{1}{\sin \theta} \frac{\partial F}{\partial \theta} \right) = -2\sigma, \quad (3)$$

where

$$F \equiv \frac{\psi}{Q/2\pi}, \quad \eta \equiv \frac{r}{R_0} \quad \text{and} \quad \sigma = -\frac{\pi R_0^2 V^2}{QW}.$$

To model the underflow, which is essential in the case of a small flow-split ratio, a sink is placed at the origin of the coordinate system. Let  $Q$  denote the total flow rate and  $\Lambda$  the flow split ratio. Then the fraction of the flow diverted to the underflow in a cyclone with a apex angle of  $2\alpha$  is  $Q/(1+\Lambda)$ . An appropriate stream function  $\psi_1$  for the sink that satisfies these conditions is

$$\psi_1 = \frac{Q(\cos \theta - \cos \alpha)}{2\pi(1+\Lambda)(1-\cos \alpha)}, \quad (4)$$

which gives  $\psi_1 = 0$  at the wall.

Putting the streamfunction  $\psi_1$  given by Eq. (4) in a dimensionless form yields:

$$F_1 = \frac{\cos \theta - \cos \alpha}{(1+\Lambda)(1-\cos \alpha)}. \quad (5)$$

Equation (3) has a solution of the form

$$F = F_1 + \eta^2 f(\theta), \quad (6)$$

which upon substitution into Eq. (3), yields

$$2f + \sin \theta \frac{d}{d\theta} \left( \frac{1}{\sin \theta} \frac{df}{d\theta} \right) = -2\sigma. \quad (7)$$

The solution for  $F$  is of the form

$$F(\eta, \theta) = \frac{\cos \theta - \cos \alpha}{(1+\Lambda)(1-\cos \alpha)} + \eta^2 \left\{ -\sigma + A \sin^2 \theta + B \left[ \sin^2 \theta \ln \left( \tan \frac{1}{2} \theta \right) - \cos \theta \right] \right\}, \quad (8)$$

where  $A$  and  $B$  are arbitrary constants.

The boundary conditions are:  $v_\theta = 0$  at  $\theta = 0$  and  $F = 0$  at  $\theta = \alpha$ . Since

$$v_\theta = -\frac{Q}{2\pi R_0^2} \frac{1}{\eta \sin \theta} \frac{\partial F}{\partial \eta},$$

the former boundary condition at  $\theta = 0$  is replaced by  $\partial F / \partial \eta = 0$ . Evaluating the constants and substituting in Eq. (8) yields the final solution for  $F$ :

$$F(\eta, \theta) = \frac{\cos \theta - \cos \alpha}{(1+\Lambda)(1-\cos \alpha)} + \eta^2 \sigma \left[ \frac{D(\alpha)}{\sin^2 \alpha} \sin^2 \theta - D(\theta) \right], \quad (9)$$

where

$$D(x) = 1 - \cos x + \sin^2 x \ln \left( \tan \frac{1}{2} x \right).$$

The value of  $\sigma$  can be determined by noting that the streamline  $F = 1$  just enters the vortex finder at  $r = r_f$ ,  $\theta = \theta_f$ . The radius of the vortex finder is  $r_f \sin \theta_f$ . With  $\eta_f = r_f / R_0$ ,  $\sigma$  is determined from Eq. (9) in the form

$$1 = \frac{\cos \theta_f - \cos \alpha}{(1+\Lambda)(1-\cos \alpha)} + \eta_f^2 \sigma \left[ \frac{D(\alpha)}{\sin^2 \alpha} \sin^2 \theta_f - D(\theta_f) \right]. \quad (10)$$

The tangential velocity  $v_\phi$  is

$$\frac{v_\phi}{V} = \frac{[1 + F\sigma Q^2 / (\pi R_0^2 V)^2]^{1/2}}{\eta \sin \theta}. \quad (11)$$

The other two velocity components are obtained from the continuity equation. The results are given below

$$v_r^* = \frac{v_r}{Q/2\pi R_0^2} = -\frac{(1+\Lambda)}{\eta^2} \frac{1}{1-\cos \alpha} + 2\sigma \left[ \frac{D(\alpha)}{\sin^2 \alpha} \cos \theta - 1 - \cos \theta \ln \left( \tan \left( \frac{1}{2} \theta \right) \right) \right], \quad (12)$$

and

$$v_\theta^* = \frac{v_\theta}{Q/2\pi R_0^2} = -2\sigma \left[ \frac{D(\alpha)}{\sin^2 \alpha} \sin \theta - \frac{D(\theta)}{\sin \theta} \right]. \quad (13)$$

To compare the theoretical results with those of experiments presented in Section 2, it is more convenient to use the radial and axial velocity components denoted by  $u$  and  $w$ , respectively. These components are related to  $v_r$  and  $v_\theta$  by the relationship shown below

$$u = v_r \sin \theta - v_\theta \cos \theta, \quad (14)$$

$$w = v_r \cos \theta + v_\theta \sin \theta. \quad (15)$$

## 4 Results and Discussion

Figure 4 depicts the nondimensional streamfunction  $F$ , rather than  $F/\sigma$  for easier identification of streamlines. Three values of  $\Lambda$  ( $\infty$ , 1.0, 0.0) were chosen as representative cases. For  $\Lambda = \infty$  (flow split ratio =  $\infty$ ), which corresponds to the case treated by Bloor and Ingham (1987) where the fluid exits through the overflow entirely as shown in Fig. 4(a). The streamline  $F = 1$  is the upper boundary of the flow which just enters the vortex finder. For  $\Lambda = 0.0$ , the fluid exits through the un-

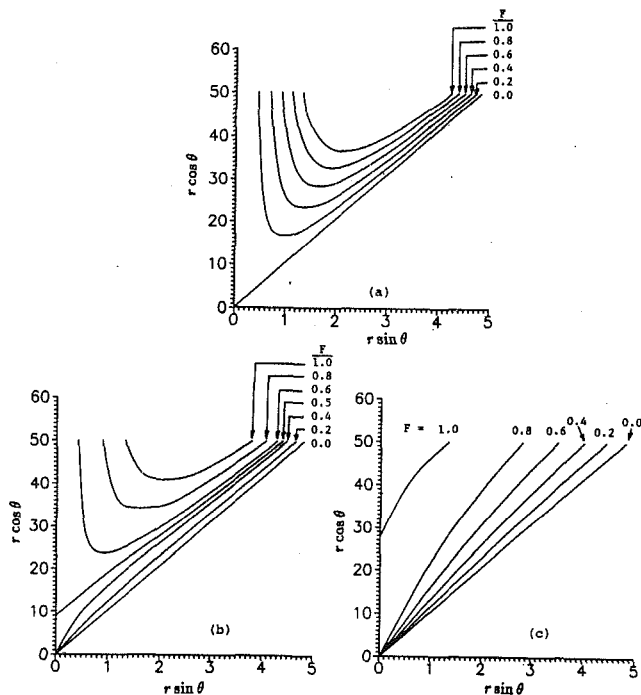


Fig. 4 Streamline pattern on the axial plane of the cyclone. (a)  $\Lambda = \infty$ , (b)  $\Lambda = 1.0$ , and (c)  $\Lambda = 0.0$ .

derflow. In this case, the streamline  $F=1$  intersects the center axis at some level in the cyclone (Fig. 4(c)). For  $\Lambda = 1.0$ , there are two regions of flow with a dividing streamline  $F=1/(1+\Lambda)=0.5$ . The dividing streamline meets the cyclone axis and branches into two lines, one running upward and the other, downward along the cyclone axis (Fig. 4(b)).

For  $\infty > \Lambda \geq 0.0$ , the streamline  $F=1$ , which defines the upper boundary of the flow, connects the cyclone inlet and the inlet to the vortex-finder. The fluid in the region enclosed by the streamlines  $F=1$  and  $F=1/(1+\Lambda)$  enters the cyclone downward, reverses its direction, and finally exits from the vortex finder. The locus of the points at which the streamlines reverse their directions provides the demarcation line for two regions where the axial velocity is pointed upward (central region) and that directed downward (annular region). The present model predicts one velocity reversal. The fluid in the region enclosed by the streamlines  $F=1/(1+\Lambda)$  and  $F=0.0$  enters the cyclone downward, continues to flow down, and exits from the underflow.

A series of experiments was designed to study the influence of the flow split ratio on the velocity profile. Results of a comparison study between experimental measurement and theoretical simulation for the axial and tangential velocity profiles are shown in Figs. 5 and 6. In these figures the split ratios of  $\infty$ , 2, and 0 are shown. The radial position at an axial location where  $v_\theta = 0$  is the center of the vortex. When the center of vortex does not coincide with the cyclone axis (2~3 mm eccentricity), the center of the vortex is taken as  $r=0$ . In performing the computations,  $\sigma$  is determined from Eq. (10) where  $Q$  and  $V$  were assumed, and  $W$  was calculated. Since the inviscid flow considered in the foregoing analysis occupies only a fraction of the flow cross-section, a numerical value of  $Q$  involved is smaller than the actual total flow rate. To compare with the experimental results of Knowles (1973), Bloor and Ingham (1987) performed their computations with a value  $Q$  which was 80 percent of the actual total flow rate. For  $\Lambda$  ranging from  $\infty$  to 0.0, where  $\Lambda = \infty$  corresponds to the analysis of Bloor and Ingham (1987), the percentage of the actual total flow rate to be used for  $Q$  in the analysis is not known a priori.

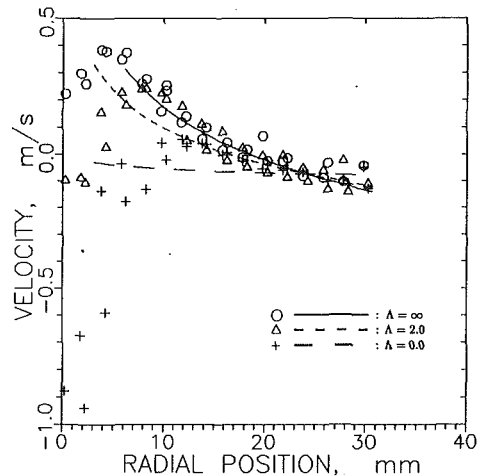


Fig. 5 Computed axial velocity profiles with three values of flow split ratios compared with the experimental results.  $H = 240$  mm; flow rate = 0.2 kg/s.

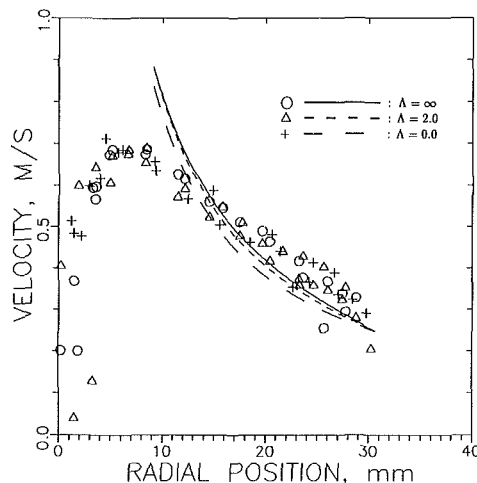


Fig. 6 Computed tangential velocity profiles with three values of flow split ratios compared with the experimental results.  $H = 240$  mm; flow rate = 0.2 kg/s.

Therefore, in this paper the actual total flow rate is used for  $Q$  and one-half of the mean velocity at the cyclone inlet is used for  $V$ . This set of values has been used in simulations shown in Figs. 5 and 6. Clearly in the main body of the flow, away from the axis and wall regions, the results of experiment and computations agree reasonably well. Nevertheless, as the flow split ratio decreases, the extent of the axial velocity defect at the central core region increases, thus causing the velocity maximum to shift outward. As a result, the agreement between the experiment and the computation becomes worse as the flow split ratio decreases.

## 5 Concluding Remarks

This paper presents an extension to the theoretical model of Bloor and Ingham which takes the effect of the underflow in a cyclone into consideration. To authenticate the results an experimental study was undertaken to measure the axial and tangential velocity profiles at flow split ratios ranging from  $\Lambda = 0$  to  $\infty$ . It is shown that prediction results and those obtained experimentally are in good general agreement for the main body of the cyclone and that the underflow plays an important role. The agreement between the experiment and the computation somewhat deteriorates as the split ratio is decreased.



## References

- Batchelor, G. K., 1967, *An Introduction to Fluid Dynamics*, Cambridge University Press, p. 543.
- Bloor, M. I. G., and Ingham, D. B., 1987, "The Flow in Industrial Cyclones," *Journal of Fluid Mechanics*, Vol. 178, p. 507.
- Boysan, F., Swithenbank, J., and Ayers, W. H., 1986, "Mathematical Model of Gas-Particle Flows in Cyclone Separators," in *Encyclopedia of Fluid Mechanics*, ed. N. P. Chermisinoff, Vol. 4, Chapter 42, Gulf Publishing Co., Houston.
- Bradley, D., 1965, *The Hydrocyclone*, 1st ed., Pergamon.
- Dabir, B., 1983, "Mean Velocity Measurements in a 3"-Hydrocyclone Using Laser Doppler Anemometry," Ph.D. thesis, Michigan State University.
- Dirgo, J., and Leith, D., 1986, "Design of Cyclone Separators," in *Encyclopedia of Fluid Mechanics*, ed., N. P. Chermisinoff, Vol. 4, Chapter 41, Gulf Publishing Co., Houston.
- Escudier, M. P., Bornstein, J., and Zehnder, N., 1980, "Observation and LDA Measurements of Confined Turbulent Vortex Flow," *Journal of Fluid Mechanics*, Vol. 98, p. 49.
- Kelsall, D. F., 1952, "A Study of the Motion of Solid Particles in a Hydraulic Cyclone," *Transactions Institution of Chemical Engineers*, Vol. 30, p. 87.
- Knowles, S. R., Woods, D. R., and Fuerstein, I. A., 1973, "The Velocity Distribution Within a Hydrocyclone Without an Air Core," *Canadian Journal of Chemical Engineers*, Vol. 51, p. 263.
- Pericleous, K. A., 1987, "Mathematical Simulation of Hydrocyclones," *Applied Mathematical Modeling*, Vol. 11, p. 242.
- Rietema, K., 1961, "Performance and Design and Hydrocyclones—I, II, III, IV," *Chemical Engineering Science*, Vol. 15, pp. 298, 303, 310, 320.

# Drag Reduction of a Cylinder/ Endwall Junction Using the Iceformation Method

**R. S. LaFleur**

Assistant Professor,  
Department of Mechanical and  
Aeronautical Engineering,  
Clarkson University,  
Potsdam, NY 13699

**L. S. Langston**

Professor,  
Mechanical Engineering Department,  
University of Connecticut,  
Storrs, CT 06268

*The iceformation design method was used to reduce the drag of a juncture between a cylinder and flat endwall. Ice was formed on a subfreezing flat endwall in a warmer laminar water flow. The ice shape was influenced by and altered the three-dimensional separated boundary layer and the cylinder wake. Preliminary experiments were used to indicate control parameter relationships. An adaptive selection theory was used to determine optimal control parameters. A sample optimal contour was generated and tested for juncture drag performance. High Reynolds number wind tunnel drag tests showed that the iceform contour had an average of 18 percent lower drag than a flat plate juncture given the same upstream boundary layer conditions. Flow visualizations showed that the iceform contour produced three larger diameter vortices compared to the laminar four vortex model of Baker (1979).*

## 1 Introduction

Forming ice on cooled objects or within containers from a flow of water produces new shapes that influence the flow field. In this paper, such a process will be called "the iceformation method." The goal of using such a process is to minimize the effects of flow separation and reduce the total drag around an immersed body or to reduce the pressure losses in internal flow.

Snow drifting, dangerous wing icing, and sedimentation are qualitatively similar to the ice formation mechanism because they are natural moving boundary mechanisms that are influenced by the flow field but also alter the flow field. The differences between mechanisms can be shown by examining the characteristic forces of growth and decay of the boundary as shown by LaFleur (1991a). In some cases, the mechanism is dynamically nonlinear and leads to surface/flow instabilities. To reduce drag, the natural mechanisms must be harnessed or controlled using optimization-type criteria. If the mechanism is unstable, it is difficult to control. For example, the force of growth in the wing icing problem is the fluid itself and in the natural case, no decay force is present. This is an unstable growth mechanism that drastically degrades the wing's performance. Alternatively, the ice formation mechanism proposed here is grown on a cooled substrate and decayed by the flow. The ice formation mechanism is stabilized by the opposite growth and decay forces and is controlled by the engineer to reduce energy dissipation or drag.

The theoretical and experimental aspects of the iceformation method have been dealt with extensively by LaFleur. The iceformation method is classified as a harnessed natural design tool (LaFleur, 1988a) and evolves shapes using natural variation and artificial selection (LaFleur, 1991a). LaFleur (1991b) explained the theoretical basis for optimal iceformation design.

An optimal control law was derived using variational theory by LaFleur (1990).

As a conceptual design method, the iceformation method may alleviate the expensive computational search for good geometries and put the designer in the "ballpark" of optimal shapes. Design theory has shown that the iceformation process generates geometries of minimum energy dissipation when certain values of flow and thermal parameters are selected (LaFleur, 1990, 1991b). Iceform geometries could be used as starting points for computational shape optimization to investigate performance of perturbed iceform shapes or features.

Past experimental work on iceformation design has shown that the method is feasible as a design tool. Bowley and Coogan (1967) used ice formation as a shaping mechanism in a smooth transition to the inlet of a square channel. A ninety degree elbow iceform (Lahey and Bowley, 1981) was generated using a dry ice cooled box with perpendicular inlet and exit. Carlson (1975) performed iceformations about a cylinder in crossflow and tested for drag reduction. Since the error bars were large, a conclusion of drag reduction could not be reached. However, the shapes that were generated had "ear" shapes that might delay separation. Cheng et al. (1981) found similar shape results.

In turbomachinery flows, LaFleur (1988a) first used the iceformation mechanism to generate monotonic diffusers and a new concept ring diffuser. The iceformation technique produced geometries of better pressure recovery than conical diffusers. Second, LaFleur (1988b) treated the practical, complex, three-dimensional separated flow of a turbine endwall. New concept turbine endwall iceforms were generated by forming ice on the flat plate "hub" between turbine blades.

In summary, past iceform studies showed that new geometry concepts can be generated for a variety of complex flow situations, performance improvements can be obtained for flows with a variety of pressure gradients, ice geometry features correspond to altered flow patterns, the ice geometry is con-

Contributed by the Fluids Engineering Division for publication in the JOURNAL OF FLUIDS ENGINEERING. Manuscript received by the Fluids Engineering Division August 2, 1991. Associate Technical Editor: D. M. Bushnell.

trolled by flow and thermal parameters, and steady state characterization is an alternative to transient modeling.

## 2 The Cylinder/Endwall Juncture Problem

A cylinder mounted on its end to a flat plate (called an endwall) was used to model the flow about body/lifting surface junctures (Fig. 1). This type of juncture occurs in many practical marine, aeronautical, turbomachinery and manufacturing situations where dissimilar geometries such as a wing and fuselage are attached.

Due to the cylinder pressure gradients, the boundary layer that develops on the endwall plate separates into a three-dimensional "horseshoe vortex." The laminar and turbulent horseshoe vortex formations are well documented for cylinder leading edge junctures with flat plates by Belik (1973), Baker (1979), Eckerle and Langston (1987), Pierce and Tree (1990), and Awad (1990). The major differences between these studies are the range of Reynolds numbers, inlet boundary form, and the number of vortices (instantaneous and time-averaged) observed on the leading edge plane of symmetry. For the turbulent inlet boundary layer, the number of vortices observed is a controversial issue while the laminar case has been established by Baker (1979).

The horseshoe vortices support high momentum and energy exchange between the free stream and the endwall near the juncture. Ireland and Jones (1986) and Goldstein et al. (1985) present mass/heat transfer contour data that indicate transport and stagnation of the free stream flow on the endwall surface. They also indicate relatively lower but more complex transport in the wake region. In this paper, shaping the endwall near the cylinder/endwall juncture is envisioned as a means to control the momentum transport of the horseshoe vortices and the unsteady wake and reduce the juncture drag power.

The cylinder body approximates the leading edge of wings or struts. A number of endwall shapes have been considered to improve the juncture flow between wing bodies and flat plates. Hoerner (1965) showed fillets reduced the interference drag of wing/strut junctures and fairings that reduced the drag of strut/strut junctures. More recently and in turbulent flow, Sung et al. (1988) stated that a leading edge fillet reduced the size and strength of the horseshoe vortex and reduced non-uniformities in the near-endwall wake velocity profiles. However, drag or drag reduction were not assessed. Devenport et al. (1990) reviewed leading edge fairings. These shapes were used by Sung et al. and Pierce et al. to reduce the leading edge separation and strength of the horseshoe vortex. Devenport et

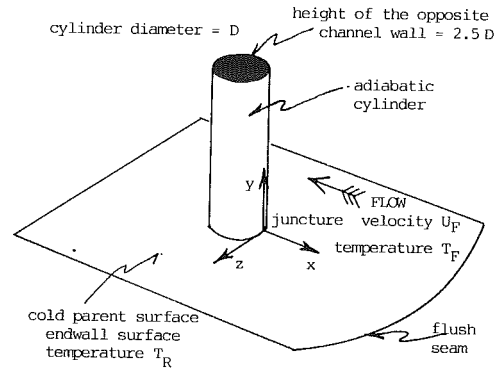


Fig. 1 Cylinder/endwall juncture model

al. evaluated the use of a fillet of radius 0.53 wing thickness around the entire perimeter of the juncture. Devenport et al. (1990) found that "...the fillet does not modify the wing-body juncture in a desirable way" and that "A flow-control device that eliminates leading-edge separation is likely to be more effective." Alternatively, this iceformation paper uses a method of contour design that alters the flow separation region, the horseshoe vortices and near-endwall wake flow with the goal of reducing drag.

## 3 Method Considerations

Use of the iceformation method requires careful consideration of procedures and constraints. Previous work on the method has established a design science basis (LaFleur, 1990, 1991a, 1991b). The relevant assumptions for this work are the following:

- 1 The inlet water boundary layer is of the laminar-Blasius type
  - 2 The interface geometry is a unique function of space, Reynolds number and the thermal parameter
  - 3 Free-stream velocity and temperature and the uniform endwall temperature are experimentally controlled
  - 4 The cold endwall contains the entire juncture flow region.
- These assumptions allow use of previous design theory and insure tractable design results.

**3.1 Iceformation Method Procedures.** The iceformation method uses three distinct procedures: preprocessing, processing and postprocessing (LaFleur, 1988b). Preprocessing is

## Nomenclature

### Geometric Variables

- $I$  = ice thickness  $y$  coordinate  
 $\zeta$  = normalized ice thickness  $I/\delta$   
 $y$  = flat plate normal coordinate  
 $l$  = wake structure  $x$  location relative to the cylinder's trailing edge  
 $\delta$  = water channel depth  
 $z$  = cross-stream coordinate  
 $x$  = axial coordinate  
 $D$  = cylinder diameter  
 $Z$  = geometric constraints

### Thermal Variables

- $T_W$  = water temperature  
 $T_I$  = ice temperature

- $T_0$  = phase change temperature  
 $\theta_T$  = thermal control

### Flow Variables

- $U_F$  = free-stream velocity  
 $Re$  = Reynolds number based on  $D$   
 $\nu$  = kinematic viscosity  
 $C_D$  = drag coefficient, based on frontal area  
 $W$  = drag power

### Subscript

- $S$  = steady-state condition  
 $M$  = optimal condition (minimum)  
 $i$  = vector counter  
 $j$  = vector counter

### Uncertainty of Measured Variables

- $Re$  = iceformation  $+/- 40$   
 $Re$  = drag test  $+/- 625$   
 $\theta_T$  = thermal control  $+/- 0.007$   
 $C_D$  = drag coefficient—Fig. 10  
 $\zeta_s$  = ice thicknesses normalized by the channel depth  $+/- 0.002$   
 $l/D$  = structure locations  $+/- 0.017$   
 Wake Fork Angle  $+/- 0.5$  degree  
 ice formation =  $\equiv$  phase change mechanism  
 iceformation =  $\equiv$  controlled design mechanism

**Table 1 Iceformation method procedures**

Procedure	Dependent variables	Independent variables	Relationships
Preprocessing	Re, $\theta_T$ and Z	$\zeta_S$ and W	$\theta_T(Re, Z, \zeta_S, W)$ or $Re(\theta_T, Z, \zeta_S, W)$ and $Z(Re, \theta_T, \zeta_S, W)$
Processing	$\zeta$	Z, Re, $\theta_T$ and t	$\zeta(Z, Re, \theta_T, t)$
Postprocessing	$\zeta_S$ and W	Z, Re and $\theta_T$	$W(Z, Re, \theta_T, \zeta_S)$ and $\zeta_S(Z, Re, \theta_T)$

**Table 2 Preliminary experiment parameter matrix**

Exp #	Re	$\theta_T$
1	1480	0.37
2	737	0.37
3	1843	0.37
4	1480	0.27
5	1480	0.44
6	737	0.28
7	1843	0.27
8	737	0.43
9	1843	0.45

Region A is bordered by experiments 1, 2, 5, and 8.

Region B is bordered by experiments 1, 2, 4, and 6.

Region C is bordered by experiments 1, 3, 4, and 7.

Region D is bordered by experiments 1, 3, 5, and 9.

used to inversely determine Z and thermal control parameters. Processing is shape design using either an experiment or numerical simulation of surface ice formation. Postprocessing interprets the geometric results, forms relationships, and determines drag performance. Postprocessing relationships can help solve the preprocess inverse problem and allow selection of beneficial geometric features. The procedures may be distinguished by which variables are dependent or independent as shown in Table 1. Information flow from one procedure to another forms "the iceformation method."

**3.2 Iceformation Control and Geometric Constraints.** The iceformation method has two control degrees of freedom; thus two conditions can be arbitrarily selected. To determine  $\theta_T$  and Re for optimization, two selections are permitted.

- 1 Optimization selection,  $\delta W = 0$
- 2 Geometric selection,  $\zeta_S$ , or Reynolds number selection, Re; or Temperature selection,  $\theta_T$ , where the control parameters are

$$\theta_T \equiv \frac{T_F - T_0}{T_0 - T_R} \text{ and } Re \equiv \frac{U_F D}{\nu} \quad (1)$$

The above selections are planes or loci on the function surface of drag versus geometry, flow and thermal control parameter coordinates.

In this work the geometric constraints were selected as zero initial ice thickness and cylinder diameter based on desired Reynolds number range. These selections insure that the geometries are applicable to an engineering system. Drag reduction can only be verified by comparing the "relevant" iceform shapes to other shapes that satisfy the same geometric constraints. "Artifacts" are those geometric features which are not relevant to the design problem but arise due to experimental design. Variation of the geometric constraints is performed to investigate whether a certain feature is an artifact or relevant geometry. Artifact geometries do not vary when geometric constraints are varied, i.e.,

$$\left( \frac{\partial \zeta_{S,i}}{\partial Z_j} \right)_{\theta_T, Re} = 0, \text{ then } \zeta_{S,i} \text{ is an artifact with respect to } Z_j. \quad (2)$$

Relevant geometries vary in response to geometric constraint variation.

**3.3 Experimental Error Effects in the Method.** Accounting of uncertainties is important because preliminary experimental data was used to control the design solution. Potential errors associated with the experiments are as follows:

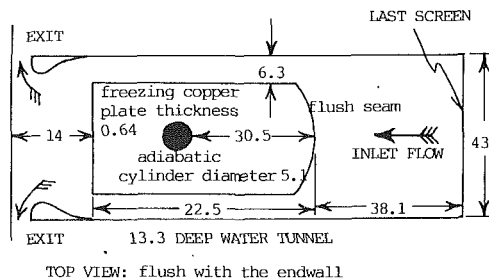


**Fig. 2 Axial flow water tunnel and cooled flat plate (all lengths in centimeters)**

- 1 geometrical measurements (maximum ice thickness)
- 2 thermal measurements (water, parent surface)
- 3 velocity measurements (free-stream velocity)
- 4 surface fitting of a finite number of points

The most probable magnitude of errors of 1, 2, and 3 are listed in the Nomenclature. Errors due to the surface fit are discussed later.

## 4 Preliminary Experiments

Preliminary iceformation experiments were used to explicitly relate steady state geometry and control parameters such that  $\zeta_S(\theta_T, Re)$  where  $\zeta_S$  is the nondimensional juncture geometry measured on the y axis (Fig. 1) normal to the flat plate parent surface.

**4.1 Experimental Apparatus and Preprocessing: Parameter Test Matrix.** The cylinder/endwall juncture contour was shaped by ice formation over a cooled flat plate in a water tunnel shown in Fig. 2. The laminar boundary layer flow of water starts upstream of the cooled plate after a series of flow straighteners. The adiabatic cylinder was placed on-end on the plate to create a juncture between two dissimilar shapes. The circular cylinder shape was chosen as an adiabatic geometric constraint for this study. Other shapes using cooled bodies such as cylinders, teardrops or wings are plausible for further work on the design of the body and its juncture such as the sail/hull problem being considered by LaFleur (1992).

The ice contours correspond to certain values of the flow and thermal control parameters,  $\theta_T$  and Re. The Reynolds number based on cylinder diameter range was relatively low ( $700 < Re < 2000$ ). The water and cold flat plate temperatures yield a thermal parameter range of  $0.25 < \theta_T < 0.5$ . A test matrix shown in Table 2 uses three values of each parameter. The  $3 \times 3$  test matrix created four control space regions.

**4.2 Processing: Generation of Ice Contours.** Experiments were run by selection of a  $\theta_T$  and Re pair, setting and verifying conditions, and then running the ice formation process. Free-stream velocity and boundary layer thickness were measured using a tracking laser and a hydrogen bubble technique outlined by Iritani et al. (1983). Hot film anemometer measurements verified that a Blasius velocity profile existed where the cylinder leading edge would be located. The conditions produced Baker's laminar four vortex flow regime (Baker, 1979) when the cylinder was placed in the flow.

Ice formation steady states were verified by laser-tracking the contour's maximum ice thickness point. The steady-state contours for the nine experiments were plaster cast for later study. The same test matrix, listed in Table 2, was used to generate nine contours *without* the cylinder to investigate the effect of the cylinder body constraint on flow separation and contouring. Without the cylinder, the boundary layer does not separate and a monotonic wedge shape was obtained. The *without* cylinder cases provide information about the wedge artifact.

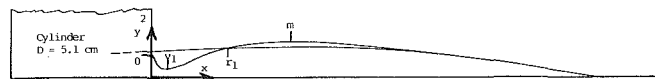


Fig. 3(a) Leading edge slice  $\theta_T = 0.37$ ,  $Re = 737$

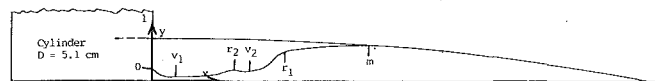


Fig. 3(b) Leading edge slice  $\theta_T = 0.37$ ,  $Re = 1480$

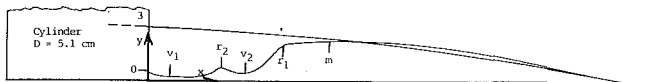


Fig. 3(c) Leading edge slice  $\theta_T = 0.37$ ,  $Re = 1843$

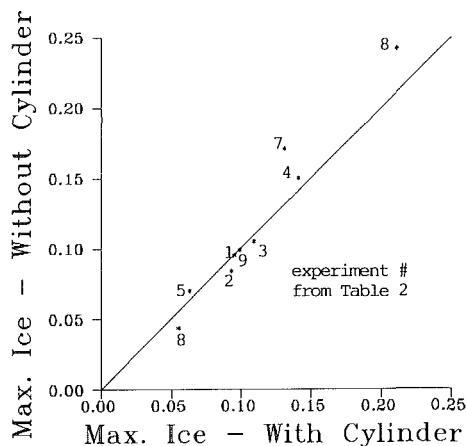


Fig. 4 Comparison of maximum ice thickness with and without cylinder to prove that the wedge is an artifact versus the cylinder

**4.3 Postprocessing: Horseshoe Vortex Iceform.** Figures 3(a), 3(b), and 3(c) show sample leading edge profiles of the iceform juncture geometries obtained using a carpenter's spline along the line of symmetry. The contour structures are valleys,  $v$ , ridges,  $r$ , and a maximum,  $m$ . In all cases the initial flow topology matched Baker's four vortex regime. As the ice formed on the flat plate, the flow topology bifurcated to result in two cases of one valley/one ridge (Fig. 3(a)), six cases of two valley/two ridge (Figs. 3(b) and 3(c)) and one borderline case where a ridge and valley coincide.

The effect of the cylinder on the flow is traditionally investigated (Baker, 1979 and Goldstein et al., 1985) by performing tests with and without the cylinder. Leading edge profiles for the "without cylinder" case are shown along with the "with cylinder" contours in Figs. 3(a), 3(b), and 3(c). A wedge shaped region does not vary appreciably when the cylinder is absent. Since the wedge feature is independent of the variation in the cylinder geometric constraint, the shape is hypothesized to be a "wedge artifact" and satisfies the artifact criterion of Eq. (2). Figure 4 shows a comparison of nondimensional ice thickness at the maximum ice point for the cases with and without the cylinder body. Therefore, the wedge is an artifact due to the artifact line.

**4.4 Postprocessing: Geometry Relationship to Control Parameters.** Characterization of the maximum ice point allows the point to be controlled. Figure 5 shows a plot of the maximum ice geometry versus the nine control parameter variations. Colder water yields thicker ice as indicated by lower  $\theta_T$  values. Intuition based on two-dimensional flat plate knowledge suggests that an increase in Reynolds number should increase the fluid Nusselt number and decrease ice thickness. This intuition is supported by the  $\theta_T = 0.27$  data. For  $\theta_T = 0.37$  and  $\theta_T = 0.44$  the relationship is reversed; increasing  $Re$ , increasing  $\zeta_S$ . Also cross-over points (Labelled I and II on Fig.

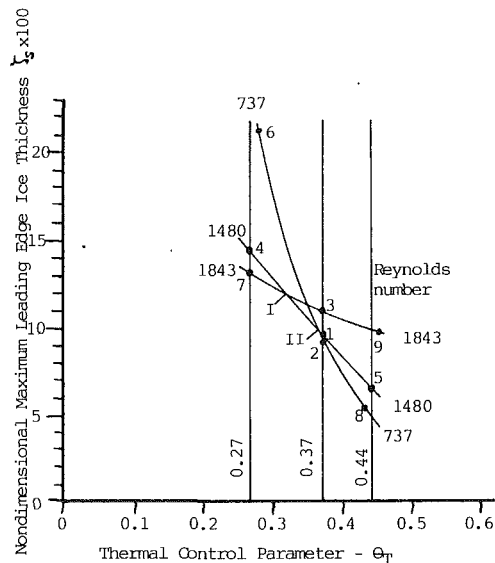


Fig. 5 Maximum leading edge ice thickness versus thermal and flow parameters

5) of the  $Re = \text{constant}$  curves indicate geometry independence of Reynolds number.

A second order surface fit of the nine-point maximum ice/parameter surface,  $\zeta_S(\theta_T, Re)$ , is used to characterize and control the maximum ice point by specifying the flow and thermal control parameters.

$$\zeta_S(\theta_T, Re) = (2.789 - 13.25\theta_T + 16.35\theta_T^2)$$

$$- \left( \frac{Re}{1000} \right) (3.02 - 15.76\theta_T + 21.03\theta_T^2) + \left( \frac{Re}{1000} \right)^2 (0.8892 - 4.813\theta_T + 6.751\theta_T^2) \quad (2)$$

The error associated with the fit is within  $-1$  to  $2$  percent. The value of the correlation could be improved by running further experiments. Overall the effect of experimental errors on optimal iceform design are small because the optimal criterion is robust due to the flat, near-optimal-neighborhood about the predicted optimal conditions.

**4.5 Postprocessing: Juncture Geometry Contour.** The three-dimensional separation and unsteady wake regimes cause great friction and heat transfer variation on the endwall surface. This results in a contoured endwall,  $\zeta_S(x, z)$ , which corresponds to altered flow phenomena, as shown by a sample contour in Fig. 6. The frontal contour roughly resembles the sedimentation shapes of Baker (1978).

The contour features suggest that separation zones have thick ice and form ridges while attachment regions remain thin and form valleys. The horseshoe vortex flow wraps around to the sides of the cylinder body creating a slight upward grade that is consistent with a decrease in Nusselt number in the downstream direction; a new boundary layer forms after separation of the inlet boundary layer. Figure 6 shows a juncture contour with two valleys and two ridges in the frontal separated region that is consistent with the slices of Figs. 3(b) and 3(c).

**4.6 Postprocessing: Unsteady Wake Iceformations.** The wake region contours depict steady iceformation geometries for unsteady flow. The results showed three dominant wake region structures. Nearest the cylinder is a teardrop shaped ridge which is referred to as a "fairing ridge" (Fig. 6). This resembles the wake region shown by Eibeck (1990) in the wake of a cylinder with a teardrop fairing. Eibeck's circular cylinder does not show this result.

The fairing ridge is followed, in the downstream direction, by a ridge which is coincident with the line of symmetry. This



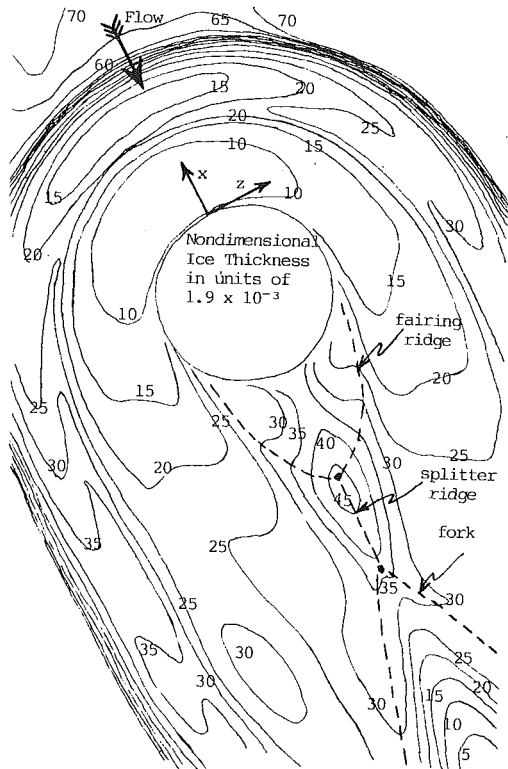


Fig. 6 Cylinder contour Map c7

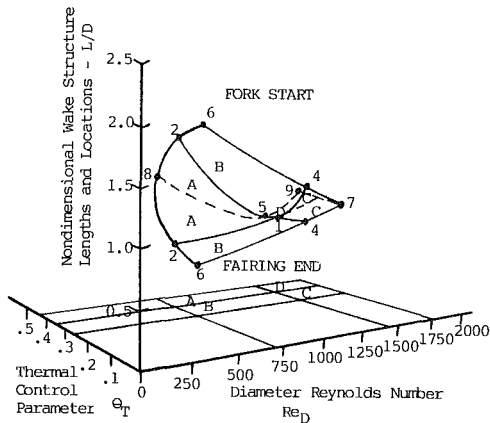


Fig. 7 Perspective of wake structure length and locations

ridge resembles a splitter plate (which is known to reduce drag) that is confined to the endwall region. The "splitter ridge" may promote streamwise velocities by resisting side velocities and oscillations.

Eventually the splitter topology changes to a double ridged fork shape between 1.0 and 2.0 cylinder diameters downstream of the cylinder. This seems to correspond with the beginning of wake separation lines shown by Eibeck (1990) and Ireland and Jones (1986). Figure 7 shows a relationship between the splitter extension (fork start) and the thermal and flow parameters. The half cycle length of the shed wake was calculated to be 2.5 diameters downstream based on a Strouhal number of 0.21. The splitter ridges end and the forks begin before this point. Upstream of the fork, the iceform structures may be influenced by early stages of the shedding vortices.

It is clear that the parameter surface on Fig. 7 bifurcates such that no splitter ridge exists for parameter region D. It is hypothesized that the region D geometries may have higher drag than other contours due to the absence of the beneficial splitter ridge.

The fork angle indicates the degree of spreading of the de-

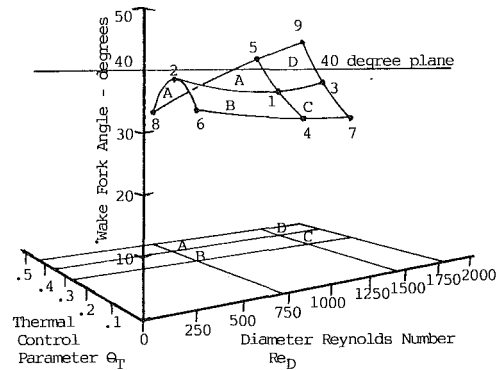


Fig. 8 Wake fork angle versus thermal and flow parameters

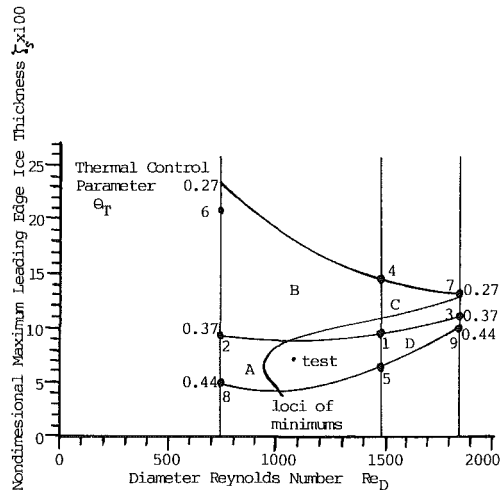


Fig. 9 Preprocess selection surface fit and loci of minimum maximum ice thickness versus thermal and flow control parameters

veloping wake and the drag coefficient of the body. Figure 8 shows the relationship between fork angle and the thermal and flow parameters. It is hypothesized that the larger fork angles on parameter region D geometries may result in higher drag than contours from other regions.

## 5 Juncture Drag Power Reduction

The leading edge and wake geometric features can be controlled by selection of  $\theta_T$  and  $Re$ . Consequently, the flow and thermal parameter selection influences the design process and potential drag reduction.

**5.1 Preprocessing: Optimal Parameter Selection.** The inverse problem of determining optimal flow and thermal parameters is solved using the preliminary experiment data with the adaptive control theory given by LaFleur (1991a). The optimum is stated in the parameter space, with the geometric constraints held fixed, as

$$\left( \frac{\partial \zeta_S}{\partial Re} \right)_{Z, \theta_T} = 0 \text{ at } Re = Re_M(\theta_T) \text{ for fixed } Z \quad (4)$$

Rather than seeking geometry that is optimum at one set of conditions, a geometry that performs well over a range of conditions is sought, i.e., a robust geometry.

Figure 9 shows a relationship between the maximum leading edge ice thickness and the flow and thermal parameters,  $\zeta_S(\theta_T, Re)$ . The crossing of  $Re = \text{constant}$  curves on Fig. 7 indicates points of Reynolds number independence which lie on a locus of minimums on the  $\zeta_S(\theta_T, Re)$  surface. The minimum is evident in the low slope area of  $\theta_T = \text{constant}$  curves in region A. This allows selection of minimum drag power by satisfying the necessary condition of the adaptive performance goal, Eq. (4).

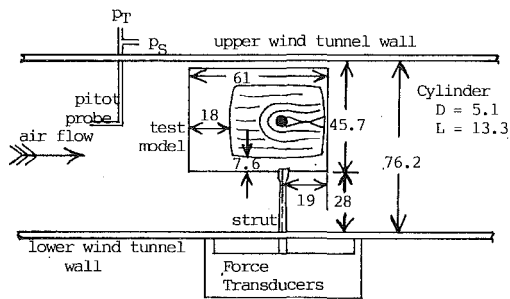


Fig. 10 Axial flow tunnel with cylinder endwall model (lengths in centimeters)

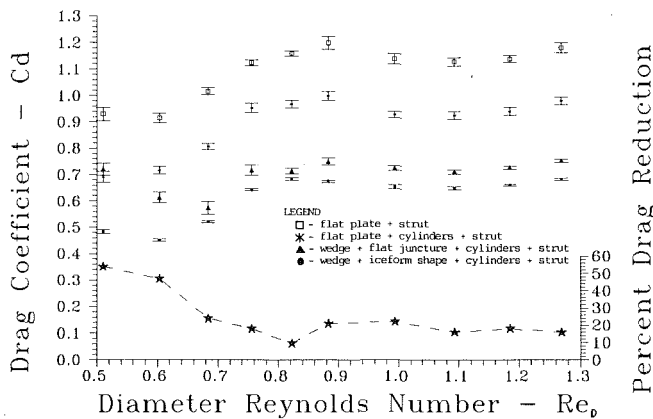


Fig. 11 Model drag coefficients and percent drag reduction versus diametrical Reynolds number

Based on Eq. (4), a derivative of the surface curve fit (Eq. (3)) yields an explicit formula for the minimum curve,  $Re_M(\theta_T)$  on the  $\zeta_S(\theta_T, Re)$  surface. The equation for the minimum curve is

$$Re_M(\theta_T) = 500 \frac{(3.02 - 15.76\theta_T + 21.03\theta_T^2)}{(0.8892 - 4.813\theta_T + 6.751\theta_T^2)} \quad (5)$$

Equation (5) can be inverted to obtain  $\theta_T(Re_M)$  for the range of Reynolds numbers from 700 to 2000. The loci of minimums is drawn on Fig. 9 by plotting  $Re_M(\theta_T)$  and  $\zeta_S(Re_M(\theta_T), \theta_T)$  with  $\theta_T$  as a curve parameter. The curve traverses region A, a corner of region B and through region C. Region D contains no part of the loci of minimums curve. Region D geometries were hypothesized to have higher drag; therefore it is prudent, both theoretically and experimentally, to use the loci of minimums for selecting drag reduction.

The control surface plots indicate the effect of thermal uncertainty on the attainment of the optimal condition and particular ice thicknesses (frontal area constraint). The lowest Reynolds number is the most sensitive to thermal errors as shown by Fig. 9. Moderate and high Reynolds number cases are less sensitive to thermal errors near the optimal criterion (see Fig. 9). The higher the Reynolds number, the less the effect of thermal errors on ice thickness selections.

**5.2 Processing: Test Case of Optimum Juncture Design.** A sample experiment was run to verify the preliminary experiment/optimal preprocess methodology. Experimental control parameters were chosen to lie near the loci of minimums on Fig. 9 in the low slope region A (test case) as  $Re = 1086$  and  $\theta_T = 0.396$ . These values were used in an iceformation experiment to generate a steady state juncture. The steady state contour was captured and cast twice, inverse and reverse (LaFleur, 1985), to produce a dental stone replica of the juncture iceform. Two copies were made to check casting accuracy and double measurement magnitude in the drag test.

## 6 High Reynolds Number Wind Tunnel Tests

The two cylinder/endwall juncture replicas were mounted on each side of a thin plate. The plate was mounted vertically on a drag strut aligned on the centerline of a wind tunnel as shown in Fig. 10. Drag force of the models was measured directly using a force transducer.

The junctures were tested for drag force over a range of Reynolds numbers,  $Re$ , from  $0.5 \times 10^6$  to  $1.3 \times 10^6$ . This range of Reynolds numbers is much higher than the range used in the iceformation experiments ( $Re = 700$  to  $2000$ ) because the water tunnel could not provide quality drag force data. Equation (4) indicates an adapted geometry that performs well over a range of conditions. Thus a geometry formed at a low Reynolds number may perform well at high Reynolds numbers.

The drag coefficient was calculated based on total frontal area including strut and plate mounting hardware. To examine the effects of the plate/strut mounting, the drag signature of a bare flat plate was measured. A cylinder/flat plate model was tested to show the effects of the wedge artifact. Due to the requirement of constant geometric constraints, the wedge/flat and wedge/contour models had the same frontal area and inlet boundary layer.

Figure 11 shows the model drag coefficients versus Reynolds number. The mean and scatter bar data correspond to the measured model drag forces including the strut mount. The flat plate + strut drag coefficient is the highest. This is because the frontal area is the lowest. The flat plate + cylinder + strut drag coefficient is next highest because the frontal area increase (by adding the cylinder to the flat plate) does not offset the increase in the drag due to the cylinder body, cylinder end, and juncture flows.

The drag of the wedge + cylinder models are comparable because the frontal area is the same. The iceform contour has the lowest drag coefficient over the tested Reynolds number range. The drag data for Reynolds numbers  $0.51 \times 10^6$  and  $0.6 \times 10^6$  may contain the influence of transition because of the two-dimensional cylinder transition between Reynolds number  $0.2 \times 10^6$  to  $0.5 \times 10^6$  (Schlichting, 1979). At Reynolds numbers above  $0.6 \times 10^6$ , the iceform juncture has a 10 percent lower total drag (including the strut) than the flat juncture.

Subtracting the wind tunnel strut, plate, cylinder and cylinder end-effect drag forces yields a greater percentage of juncture drag reduction; this is similar to interference drag used by Pierce and Nath (1990). This has practical appeal because interference drag can be added to the sum of the drag of the parts. However, the drag of this unsteady three-dimensional flow cannot be algebraically added to two-dimensional cylinder and plate flow because of nonlinear interactions.

In this paper, to calculate the percent drag reduction, the strut drag signature was subtracted from the wedge/flat and wedge/contour drag signatures to allow comparison of only the cylinder and endwall drag.

Percent Drag Reduction

$$= \frac{C_D(\text{wedge/flat}) - C_D(\text{wedge/contour})}{C_D(\text{wedge/flat})} \quad (6)$$

Figure 11 shows the percentage drag reduction of the wedge/flat contour versus Reynolds number based on Eq. (6). Above a Reynolds number of  $0.6 \times 10^6$ , the iceform juncture contour (wedge/contour) has an average of 18 percent lower drag than the flat (wedge/flat) juncture.

## 7 Low Speed Leading Edge Flow Visualization

Drag reduction corresponds to a difference in flow patterns over the different juncture geometries (flat versus contour). With the adaptive goal satisfied, drag may be reduced at low ( $1086$ ) and high ( $0.5 \times 10^6$  to  $1.2 \times 10^6$ ) Reynolds numbers. The juncture flow was visualized at the iceformation Reynolds

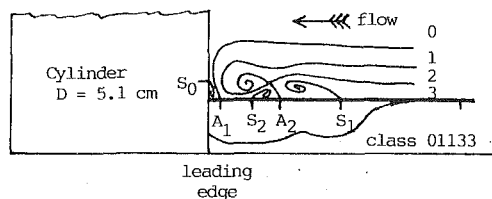


Fig. 12 Leading edge flow pattern for the flat endwall

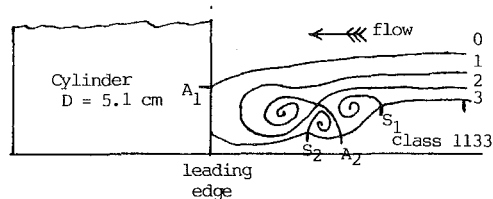


Fig. 13 Leading edge flow pattern for the contoured endwall

number ( $Re = 1086$ ) using a laser sheet aligned on the centerline upstream of the cylinder leading edge. Photographs were taken to examine the steady laminar vortex details.

The wedge/flat model produces a laminar flow which corresponds to Baker's (1979) four vortex regime as shown by Fig. 12. The iceform juncture geometry produces a flow that topologically has three vortices as shown in Fig. 13. This steady state flow matches the class 1133 topology suggested by LaFleur and Langston (1990).

Comparing the two flow visualizations indicates that ice shaping re-energizes the flow entering the corner vortex. Undoubtedly the complex pressure gradients and surface shear stresses are altered. The vortices for the wedge/flat model are smaller in diameter. Mapping the upstream boundary layer vorticity via pressure gradients into the vortices shown, one can assume that the total angular momentum in each vortex system is the same. By the principle of vortex filament stretching, it is fundamental that for the same angular momentum, a smaller vortex will lead to higher viscous dissipation. Therefore starting at the leading edge plane of symmetry flow, the iceform contour has the performance advantage. This advantage may accumulate in the downstream direction leading to the wake region.

The iceform contour may offer a pocket for the vortices. This results in less perturbed two-dimensional streamlines about a larger span of the cylinder body. The contour may reduce the drag by controlling the vortices and lowering the drag of the cylinder's span in the vicinity of the juncture.

## 8 Conclusions

A cylinder/endwall juncture was designed using the iceformation method. Postprocessing of preliminary experiments showed that iceform contour surface features in the horseshoe vortex and unsteady wake regions are related to control parameters. A test case of an optimal criterion was run to verify the methodology. An experimentally generated juncture iceform shape tested for drag performance had an average of 18 percent lower drag than a flat plate juncture. The juncture iceformation results indicate that the iceformation method is feasible for drag reduction of other unsteady three-dimensional flows.

## Acknowledgments

The authors dedicate this article to Professor W. W. Bowley who invented the iceformation design concept. Thanks go to Dr. O. Sharma, Dr. A. Carlson, Prof. F. Carlson, and Prof. A. Busnaina for their valuable advice. This work was com-

pleted at the University of Connecticut and Clarkson University with partial support from Clarkson University, the Pratt and Whitney Division of United Technologies, and ONR grant N00014-92-J-1290.

## References

- Awad, J. K., 1990, "Cooling of the Endwall Region Upstream of a Cylinder," Ph.D. thesis, Clarkson University.
- Baker, C. J., 1979, "The Laminar Horseshoe Vortex," *Journal of Fluid Mechanics*, Vol. 95; Part 2, pp. 347-367.
- Baker, C. J., 1978, "Vortex Flow around the Bases of Obstacles," Ph.D. thesis, University of Cambridge, Cambridge, England.
- Belik, L., 1973, "The Secondary Flow about Circular Cylinders Mounted Normal to a Flat Plate," *Aeronautical Quarterly*, No. 24, pp. 47-54.
- Bowley, W. W., and Coogan, C. H., 1967, "Two-Dimensional Melting in a Channel," ASME Paper No. 67-HT-75.
- Carlson, F. M., 1975, "An Investigation of the Solidification of a Flowing Liquid on a Circular Cylinder in Crossflow and Its Effect on the Drag Coefficient," Ph.D. thesis, University of Connecticut.
- Cheng, K. C., Inaba, H., and Gilpin, R. R., 1981, "An Experimental Investigation of Ice Formation around an Isothermally Cooled Cylinder in Cross-flow," *ASME Journal of Heat Transfer*, Vol. 103, pp. 733-738.
- Devenport, W. J., Agarwal, N. K., Dewitz, M. B., Simpson, R. L., and Poddar, K., 1990, "Effects of a Fillet on the Flow Past a Wing-Body Junction," *AIAA Journal*, Vol. 28, No. 12, pp. 2017-2024.
- Eckerle, W. A., and Langston, L. S., 1987, "Horseshoe Vortex Formation Around a Cylinder," *ASME Journal of Turbomachinery*, Vol. 109, pp. 278-285.
- Eibeck, P. A., 1990, "An Experimental Study of the Flow Downstream of a Circular and Tapered Cylinder," *ASME JOURNAL OF FLUIDS ENGINEERING*, Vol. 112, pp. 393-401.
- Goldstein, R. J., Chyu, M. K., and Hain, R. C., 1985, "Measurement of Local Mass Transfer on a Surface in the Region of the Base of a Protruding Cylinder with a Computer-Controlled Data Acquisition System," *International Journal of Heat Transfer*, Vol. 28, No. 5, pp. 977-985.
- Hoerner, S. F., 1965, *Fluid Dynamic Drag*, Hoerner Fluid Dynamics, Albuquerque, NM, pp. 8-10 to 8-13.
- Ireland, P. T., and Jones, T. V., 1986, "Detailed Measurements of Heat Transfer on and around a Pedestal in Fully Developed Passage Flow," 8th *International Heat Transfer Conference*, San Francisco, Aug. 1986.
- Iritani, Y., Kasagi, N., and Hirata, M., 1983, "Direct Velocity Measurement in Low-Speed Water Flows by Double-Wire Hydrogen-Bubble Technique," *Experiments in Fluids*, pp. 111-112.
- LaFleur, R. S., 1991a, "Evolutionary Design Theory using Dynamic Variation and Thermodynamic Selection," *Journal of Research in Engineering Design*, Vol. 3, pp. 39-55.
- LaFleur, R. S., 1988a, "Exploration of the Iceformation Method Applied to a Diffuser," *ASME JOURNAL OF FLUIDS ENGINEERING*, Vol. 110, pp. 244-250.
- LaFleur, R. S., 1988b, "Evolutionary Design of an Endwall Juncture," Ph.D. thesis, University of Connecticut, pp. 160-167, 245-290.
- LaFleur, R. S., 1991b, "Computational Evolution of Optimal Iceform Shapes over a Flat Plate," *Proceedings 1991 ASME International Computational Engineering Conference and Exposition*, Vol. I, Santa Clara, CA, August 1991, pp. 601-608.
- LaFleur, R. S., 1990, "A Basis for Iceformation Design," *Proceedings 1990 ASME International Computational Engineering Conference and Exposition*, Boston, MA, August 1990, pp. 393-401.
- LaFleur, R. S., and Langston, L. S., 1990, "Iceformation Design of a Cylinder/Hull Juncture with Horseshoe Vortices and Unsteady Wake," *Proceedings 2nd International Symposium on Performance Enhancement for Marine Applications*, Newport, RI, Oct., pp. 87-97.
- LaFleur, R. S., 1985, "Ice Formation as a Natural Design Tool," Master's thesis, University of Connecticut, pp. 91-103, 134-145.
- LaFleur, R. S., 1992, "First Quarter Report, Iceformation Design of a Sail/Hull Juncture," Technical Report to the Office of Naval Research, ONR N00014-92-1290, May 20, 1992.
- Lahey, F., and Bowley, W. W., 1981, Unpublished Iceformation Model of a 90 Degree Elbow, ME Dept., University of Hartford.
- Pierce, F. J., and Tree, I. K., 1990, "The Mean Flow Structure on the Symmetry Plane of a Turbulent Junction Vortex," *ASME JOURNAL OF FLUIDS ENGINEERING*, Vol. 112, pp. 16-22.
- Pierce, F. J., and Nath, S. K., 1990, "Interference Drag of a Turbulent Junction Vortex," *ASME JOURNAL OF FLUIDS ENGINEERING*, Vol. 112, pp. 441-446.
- Pierce, F. J., Frangistas, G. A., and Nelson, D. J., 1988, "Geometry-Modification Effects on a Junction-Vortex Flow," *Proceedings and Symposium on Hydromachinery Performance Enhancement for Marine Applications*, Newport, RI, Oct., pp. 37-44.
- Schlichting, H., 1979, *Boundary Layer Theory*, 7th Ed., McGraw-Hill, New York, pp. 739-743.
- Sung, C.-H., Yang, C.-I., and Kubendran, L. R., 1988, "Control of Horseshoe Vortex Juncture Flow using Fillet," *Proceedings and Symposium on Hydromachinery Performance Enhancement for Marine Applications*, Newport, RI, Oct., pp. 13-19.

# Evaluation and Comparison of Bounding Techniques for Convection-Diffusion Problems

**M. A. R. Sharif**

Assistant Professor,  
Department of Engineering Mechanics,  
University of Alabama, Tuscaloosa,  
AL 34587

**A. A. Busnaina**

Associate Professor,  
Department of Mechanical and Aeronautical  
Engineering,  
Clarkson University, Potsdam, NY 13676

*The effects of bounding the skew upwind and the second-order upwind discretization schemes for the convection terms in convection-diffusion transport equations have been studied. Earlier studies indicated that these two schemes produce less numerical diffusion but introduce unacceptable numerical dispersion or oscillations in the solution if not bounded. A simplified analytical treatment exploring the reason for this behavior is presented. Two bounding techniques, the flux-corrected transport and the filtering remedy and methodology were evaluated. Test problems used in the evaluation are (i) one-dimensional convection of a rectangular pulse, (ii) transport of a scalar step in a uniform velocity field at an angle to the grid lines, (iii) Smith and Hutton problem, (iv) two-dimensional convection of a square scalar pulse in a uniform velocity field at an angle to the grid lines, and (v) two interacting parallel streams moving at an angle to the grid lines. The results indicate that the flux-corrected transport eliminates the oscillations in the solution without introducing any additional numerical diffusion when used with both schemes. The filtering remedy and methodology also eliminates the oscillation when used with the skew upwind scheme. This technique, however, is not effective in reducing the over-shoots when used with the second-order upwind scheme.*

## 1 Introduction

Two of the main sources of errors in numerical modeling of convection-diffusion transport problems are numerical diffusion and numerical dispersion. The term "numerical diffusion" refers to numerically induced smearing of the predicted profile while, "numerical dispersion" refers to the nonphysical spatial oscillation or over-/under-shoots produced in the solution. These errors can be attributed to the differencing scheme used for discretizing the convective terms in the governing equations. Various differencing schemes for discretizing the advection terms in the convective-diffusive transport equations have been proposed and evaluated in the past. Among others, Leschziner (1980), Smith and Hutton (1982), Syed et al. (1985a), Syed and Chiappetta (1985), Shyy (1985), Huang et al. (1985), and Sharif and Busnaina (1988a, 1988b) evaluated several schemes including the skew upwind differencing (SUD) (Raithby, 1976) and the second-order upwind differencing (SOD) (Shyy, 1985). These studies indicated that, in general, lower-order schemes suffer from excessive numerical diffusion while higher-order schemes produce less numerical diffusion. But, higher-order schemes introduce unacceptable nonphysical spatial oscillations or numerical dispersion in the solution especially for high Peclet number<sup>1</sup> flows skewed at large angles to the grid lines. Although SUD is not formally a higher-order

scheme, finite differencing of the convection terms along the streamwise direction substantially reduces the cross-stream numerical diffusion (Leschziner, 1980). In the evaluation of SUD (Leschziner, 1980; Syed et al., 1985a; Syed and Chiappetta, 1985; Sharif and Busnaina, 1988a, 1988b) and of SOD (Shyy, 1985; Sharif and Busnaina, 1988a), it was shown that although the overall performance of these two schemes is better (than some other widely used schemes likely first-order upwind, weighted upwind, hybrid central/upwind, etc.) in the sense that numerical diffusion is significantly less, they suffer from numerical dispersion.

The oscillation errors produced by different schemes can be attributed to the dominance of the third (or other odd numbered) order derivatives in the modified equation derived from a model convection equation incorporating the particular scheme. This happens when the second-order derivative is eliminated from the modified equation in order to reduce numerical diffusion. Furthermore, if the scheme does not satisfy the boundedness principle (Syed et al., 1985b), over or under-shoots are expected in the solution. A scheme should be total variation diminishing (TVD) to produce oscillation free solution (Harten, 1983). The total variation of a discrete solution to a conservation law for a variable  $\phi$  is defined by  $TV(\phi) = \sum_i |\phi_{i+1} - \phi_i|$ . A numerical scheme is said to be TVD if  $TV(\phi^{n+1}) \leq TV(\phi^n)$  where the superscripts refer to the values at successive time steps. The TVD conditions can be imposed if the schemes are bounded by a suitable bounding or flux limiter algorithm. Several bounding or flux limiter TVD al-

<sup>1</sup>Pe = velocity  $\times$  cell width/diffusivity.

Contributed by the Fluids Engineering Division for publication in the JOURNAL OF FLUIDS ENGINEERING. Manuscript received by the Fluids Engineering Division March 19, 1991. Associate Technical Editor: D. G. Lilley.

gorithms have been proposed in the past. Boris and Book (1973) and Book et al. (1975) proposed the flux corrected transport (FCT) algorithm which was later improved by Zalesak (1979). In the method proposed by Zalesak, fluxes computed using a lower-order and a higher-order scheme, are blended to obtain monotonic solution. Chapman (1981) proposed the Filtering Remedy And Methodology (FRAM) which introduces a strong local nonlinear dissipation into each of the governing equations to dampen nonphysical noise due to the differencing scheme for the convection terms. Over the last several years Van Leer (1974) (Monotonic Upstream-centered Scheme for Conservation Laws, MUSCL), Roe (1981, 1985) (super-bee), Chakravarthy and Osher (1983), and Harten (1983) proposed TVD satisfying second-order flux limiter schemes to obtain oscillation free solution. Sweby (1984) reformulated these schemes on a general basis and compared their performances. These schemes are found to produce sharp profiles for one dimensional convection of discontinuities. Hirsch (1988, p. 528) provides an excellent review and analysis of these TVD schemes. Recently, Gaskell and Lau (1988) proposed a curvature compensated boundedness preserving transport algorithm (SMART) which ensures monotonic solution while maintaining a high degree of accuracy. Leonard (1988) proposed a Simple High-Accuracy Resolution Program (SHARP) which he used to eliminate the oscillation problems associated with his earlier proposed QUICK scheme (Leonard, 1979). Bell et al. (1988) developed an unsplit higher-order Godunov method for scalar conservation laws in two dimension. More recently, Bell et al. (1989) proposed a second-order projection method for incompressible Navier-Stokes equations.

The numerical diffusion of SUD or Soud is significantly less than that of the first-order schemes or comparable to some of the higher-order schemes. Therefore, it would be extremely useful if the oscillations produced by these schemes could be eliminated without introducing additional numerical diffusion. This is the motivation behind studying the bounding of these schemes for a variety of test cases. Extensive numerical evaluation of the bounded SUD and Soud schemes using diversified flow situations has not been performed yet. The present paper evaluates the effects of bounding the SUD and the Soud schemes to eliminate numerical dispersion or oscillations. A simplified analysis exploring the reason why these schemes may produce oscillations in the solution is presented. The FCT algorithm of Zalesak (1979) and the FRAM algorithm of Chapman (1981) are used for bounding the schemes. Although these algorithms are fundamentally TVD schemes, they are essentially a two-step procedure as opposed to the other TVD schemes which are single step procedure (Sweby, 1984). They can also be conveniently incorporated into any existing computer code based on a higher-order scheme prone to numerical oscillations, without any major modification. Relative comparisons of the effectiveness of these two bounding techniques are presented. The evaluation process is based on a few benchmark laminar flow test cases. Effects of blending the SUD or the Soud scheme with a lower-order scheme in a transient solution algorithm similar to the one used in this study, have not been examined before. Syed and Chiappetta (1985) studied the blending of SUD and quadratic upwind interpolation dif-

ferencing with full upwind differencing using steady-state TEACH-type algorithm and obtained oscillation free solutions.

## 2 Computational Procedure

**2.1 The Governing Equations.** The governing equations of the two-dimensional incompressible flow field are the continuity equation, the conservation of momentum in the  $x$  and  $y$  directions, and the scalar transport equation. These equations expressed in the conservative form in Cartesian coordinates are given respectively as

$$\frac{\partial u}{\partial x} + \frac{\partial v}{\partial y} = 0 \quad (1)$$

$$\frac{\partial u}{\partial t} + \frac{\partial uu}{\partial x} + \frac{\partial uv}{\partial y} = -\frac{\partial p}{\partial x} + \nu \left( \frac{\partial^2 u}{\partial x^2} + \frac{\partial^2 u}{\partial y^2} \right) \quad (2)$$

$$\frac{\partial v}{\partial t} + \frac{\partial uv}{\partial x} + \frac{\partial vv}{\partial y} = -\frac{\partial p}{\partial y} + \nu \left( \frac{\partial^2 v}{\partial x^2} + \frac{\partial^2 v}{\partial y^2} \right) \quad (3)$$

$$\frac{\partial \phi}{\partial t} + \frac{\partial u\phi}{\partial x} + \frac{\partial v\phi}{\partial y} = \Gamma_\phi \left( \frac{\partial^2 \phi}{\partial x^2} + \frac{\partial^2 \phi}{\partial y^2} \right) \quad (4)$$

**2.2 The Finite Difference Equations.** For the finite difference solution of the governing equations, a staggered mesh is used where the pressure and any scalar are placed at the center of the cell control volume while the velocity components  $u$  and  $v$  are placed at the cell faces. The numerical procedure followed here is based on the MAC method (Hirt et al., 1975). In the finite difference approximations, forward differencing is used for the time derivatives and central differencing is used for the pressure and the diffusion terms. The finite difference approximations for the convection terms (considering the scalar transport equation) are

$$\frac{\partial u\phi}{\partial x} \Big|_{i,j} \approx \frac{u_{R,\phi} \bar{\phi}_R - u_{L,\phi} \bar{\phi}_L}{\Delta x_i} \quad (5)$$

$$\frac{\partial v\phi}{\partial y} \Big|_{i,j} \approx \frac{v_{T,\phi} \bar{\phi}_T - v_{B,\phi} \bar{\phi}_B}{\Delta y_j} \quad (6)$$

where  $u_{L,\phi}$  and  $u_{R,\phi}$  are the  $x$ -component of velocity at the left and the right faces and  $v_{B,\phi}$  and  $v_{T,\phi}$  are the  $y$ -component of velocity at the bottom and top faces of the cell control volume, respectively. The quantities with  $\bar{\phantom{x}}$  on top are approximations to the convected quantities at the respective faces which are, in general, the interpolated (or extrapolated) values at some location. The interpolation method depends on the particular scheme employed. The explicit expression for  $\phi_{i,j}^{n+1}$  at time  $(n+1)\Delta t$  is given by

$$\phi_{i,j}^{n+1} = \phi_{i,j}^n + \Delta t(\dots)^n \quad (7)$$

Convection, diffusion, and source terms occur in the parentheses of the right-hand side in Eq. (7).

**2.2.1 Skew Upwind Differencing (SUD).** The advected values of  $u$ ,  $v$ , and  $\phi$  at the cell faces are approximated by considering the direction of the velocity vector at the cell face and interpolating between the nodal values for the particular

## Nomenclature

Co = Courant number  
 $h$  = width of the flow domain  
 $n$  = cross stream distance  
 $p$  = ratio of pressure and the constant density  $\rho$   
 Pe = Peclet number or cell Reynolds number  
 $s$  = streamwise distance  
 $t$  = time

$u$  = component of velocity in the  $x$  direction  
 $v$  = component of velocity in the  $y$  direction  
 $\bar{V}$  = resultant velocity  
 $x$  = coordinate direction  
 $y$  = coordinate direction  
 $\beta$  = adjustable parameter  
 $\Gamma_\phi$  = coefficient of diffusivity

$\Delta$  = cell width  
 $\Delta t$  = time increment  
 $\Delta x_i$  = width of the  $i$ th cell in the  $x$  direction  
 $\Delta y_j$  = width of the  $j$ th cell in the  $y$  direction  
 $\nu$  = kinematic viscosity  
 $\rho$  = density  
 $\phi$  = general scalar variable

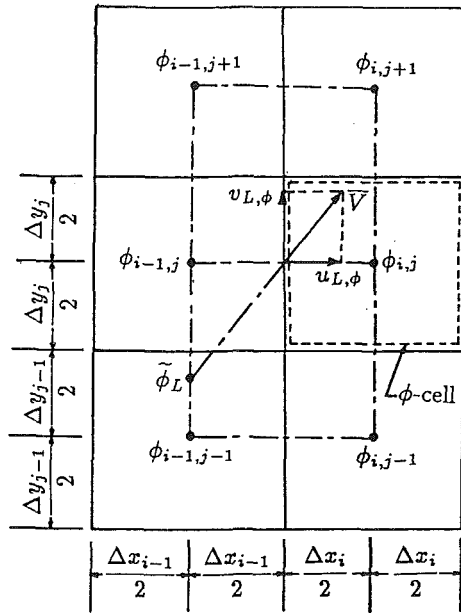


Fig. 1 (a)

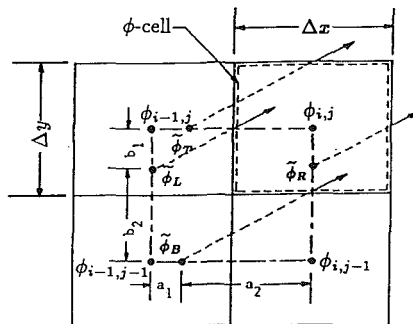


Fig. 1 (b)

Fig. 1 Illustration of the skew upwind differencing

variable at two appropriate nodes among the nodes surrounding the cell face. The two appropriate nodes are selected going upstream along the direction of the velocity vector at the cell face all the way back to the line joining the nodes as shown in Fig. 1(a).

**2.2.2 Second-Order Upwind Differencing (SOUD).** The advected quantities at cell faces are approximated by linear extrapolation to the cell face of two successive immediate upstream nodal quantities. For uniform grids this scheme yields second-order accuracy.

The formulations of the advected quantities at the cell faces for SUD and SOUD schemes are given elsewhere (Sharif and Busnaina, 1988a).

### 3 Bounding

**3.1 Boundedness of SUD and SOUD.** To analyze the boundedness of SUD and SOUD, consider two-dimensional convection of a scalar in a uniform flow field ( $u_{L,\phi} = u_{R,\phi} = u_\phi$  and  $v_{B,\phi} = v_{T,\phi} = v_\phi$ ). Also neglect diffusion and assume uniform square grids ( $\Delta x = \Delta y$ ) for simplicity. For a general scheme, the steady-state solution for  $\phi_{i,j}$  can be obtained as (Sharif and Busnaina, 1988b)

$$C_{i,j}\phi_{i,j} = C_{i-1,j-1}\phi_{i-1,j-1} + C_{i-1,j}\phi_{i-1,j} + C_{i-1,j+1}\phi_{i-1,j+1} + C_{i,j-1}\phi_{i,j-1} + C_{i,j+1}\phi_{i,j+1} + C_{i+1,j-1}\phi_{i+1,j-1} + C_{i+1,j}\phi_{i+1,j} + C_{i+1,j+1}\phi_{i+1,j+1} \quad (8)$$

where the coefficients  $C$ 's depend on the chosen scheme.

According to the boundedness or discrete maximum principle, in absence of any source, the solution of the transport equation should lie within the bounds of the values of  $\phi$  at the boundary of the flow domain (Syed et al., 1985b). The sufficient (but not necessary) conditions for the discrete solution to obey this boundedness principle are: (i) the coefficients in Eq. (8) must all be positive and (ii) the central coefficient must be the sum of its neighbors. These principles ensure that when there is no source,  $\phi_{i,j}$  is simply the weighted mean of the neighboring  $\phi$ 's such that no extraneous extreme can be produced (Syed et al., 1985b).

For SUD, with reference to the flow situation shown in Fig. 1(b), the steady-state solution for  $\phi$  can be obtained as (Sharif and Busnaina, 1988b)

$$(u_\phi b_2 + v_\phi a_1)\phi_{i,j} = (u_\phi b_1 + v_\phi a_2)\phi_{i-1,j-1} + (u_\phi b_2 - v_\phi a_2)\phi_{i-1,j} + (v_\phi a_1 - u_\phi b_1)\phi_{i,j-1} \quad (9)$$

Extended nine point computational molecule is used in SOUD for which the steady-state solution for  $\phi$  can be obtained as

$$1.5(u_\phi/\Delta x + v_\phi/\Delta y)\phi_{i,j} = (2u_\phi/\Delta x)\phi_{i-1,j} + (2v_\phi/\Delta y)\phi_{i,j-1} - (0.5u_\phi/\Delta x)\phi_{i-2,j} - (0.5v_\phi/\Delta y)\phi_{i,j-2} \quad (10)$$

Thus, for both SUD and SOUD, condition (ii) above is satisfied but the influence coefficients are not all positive implying that these schemes do not satisfy the boundedness principle and numerical oscillations in the solution are expected. For these reasons, there is a need to bound these schemes and to explore how different bounding techniques affect their predictions. This paper examines the effects of bounding these two schemes to eliminate the oscillations in the solution. The two selected bounding techniques for the study are (i) flux-corrected transport (Zalesak, 1979) and (ii) filtering remedy and methodology (Chapman, 1981).

**3.1.1 Flux Corrected Transport (FCT).** "In its simplest terms, FCT constructs the net transportive flux point by point (*non-linearly*) as a weighted average of a flux computed by a low order scheme and a flux computed by a high order scheme. The weighting is done in a manner which insures that the high order flux is used to the greatest extent possible without introducing ripples (overshoots and undershoots)" (Zalesak, 1979). The flux correction algorithm presented by Zalesak is adapted to suit the solution algorithm used in this study. SUD or SOUD is taken as the higher-order scheme and full donor cell upwind is taken as the lower-order scheme.

**3.1.2 Filtering Remedy and Methodology (FRAM).** In the FRAM algorithm, a provisional advanced time solution is calculated using a higher-order algorithm. Then local bounds on the advanced time solution are determined. Finally a strong local dissipation flux is introduced into the equations when the provisional solution is not within the local bounds. The local bounds are obtained from the maximum and minimum values of the surrounding nodal quantities. Consider a two-dimensional model convection equation

$$\frac{\partial \phi}{\partial t} + U \frac{\partial \phi}{\partial x} + V \frac{\partial \phi}{\partial y} = 0 \quad (11)$$

where  $U$  and  $V$  are positive constant velocity components in  $x$  and  $y$  directions. If full upwind differencing is used then the resulting modified equation is obtained as

$$\frac{\partial \phi}{\partial t} + U \frac{\partial \phi}{\partial x} + V \frac{\partial \phi}{\partial y} = \left( \frac{U\Delta x}{2} - \frac{U^2\Delta t}{2} \right) \frac{\partial^2 \phi}{\partial x^2} + \left( \frac{V\Delta y}{2} - \frac{V^2\Delta t}{2} \right) \frac{\partial^2 \phi}{\partial y^2} - UV\Delta t \frac{\partial^2 \phi}{\partial x \partial y} + \text{HOT} \quad (12)$$

The second-order derivatives in the right-hand side of Eq. (12) representing artificial diffusion are introduced into the higher-order equations when the solutions of those equations exceed local bounds.



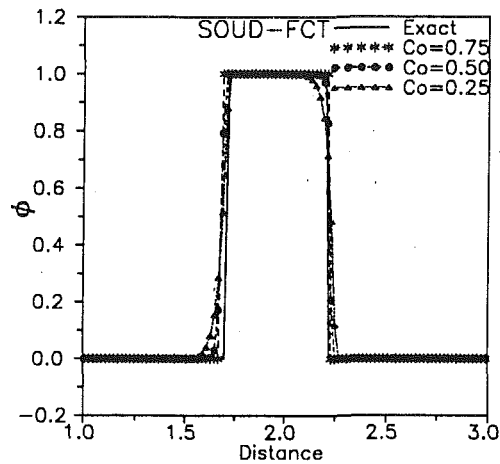


Fig. 2 Effect of Courant number  $Co$  on the SOUD-FCT prediction for the convection of a rectangular pulse

#### 4 Test Problems

The test cases chosen for comparison and evaluation of the selected bounding techniques are; (i) one-dimensional convection of a rectangular pulse, (ii) transport of a scalar step in a uniform velocity field at an angle to the grid lines, (iii) Smith and Hutton problem (Smith and Hutton, 1982), (iv) transport of a square scalar pulse in a uniform velocity field at an angle to the grid lines, and (v) interaction of two parallel streams.

The flow in all cases is laminar to avoid the question of the reliability of turbulence models. The differencing schemes are subjected to the same boundary and initial conditions, stability criteria, and solution procedure. Predictions are obtained for pure convection flows ( $Pe = \infty$ ) and convection-dominated flows where physical diffusion is present. Uniform square cells are used for all the test cases. In the following sections  $s$  represents the distance along the streamwise direction from the inlet,  $n$  represents the cross-stream distance,  $h$  represents the width of the flow domain, and  $\Delta$  represents the grid size.

##### 4.1 One-Dimensional Convection of a Rectangular Pulse.

Pure convection of a rectangular pulse is examined in this test problem. Fifty uniformly spaced grids ( $\Delta x = 1$ ) are used with a time step  $\Delta t = 0.2$ . The pulse is spread over  $10\Delta x$ . The constant convecting velocity  $U$  is specified equal to 1. This makes the Courant number  $Co = U\Delta t/\Delta x = 0.2$ . In the ideal case (if the scheme is error free), this pulse should be convected downstream with the initial profile.

For one-dimensional flow SUD reverts to full upwind differencing and introduces excessive numerical diffusion in the predicted profiles in this case. Bounding does not have any effect on the solution since oscillations are absent. On the other hand, SOUD produces over-shoots and oscillations which are totally eliminated by FCT without additional numerical diffusion and the pulse amplitude is also maintained (99.3 percent). FRAM, however, is not effective in eliminating the over-shoots and oscillations when used with SOUD.

The dependency of the predictions on the Courant number  $Co$  for this case is shown in Fig. 2. Results are shown for SOUD-FCT combination only. The figure indicates that the predictions are almost independent of the  $Co$ ; being slightly closer to the exact solution at larger  $Co$ . Since SUD predictions are largely diffusive for this case and SOUD-FRAM combination does not eliminate the oscillations, their predictions are not presented.

**4.2 Transport of a Scalar Step.** This test case examines the transport of a scalar step downstream in a uniform velocity field. A square flow domain of unit dimension is used. The left and bottom boundaries are taken as the inlet whereas the right and top boundaries are the outlet. A uniform flow velocity

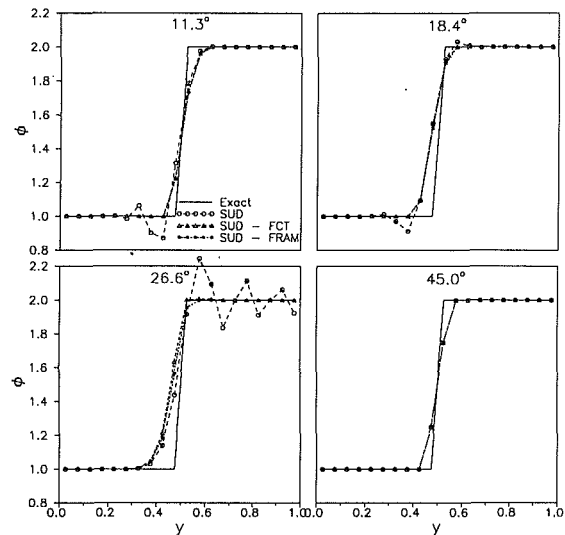


Fig. 3 Predicted steady-state profiles for different flow angles for the second test case

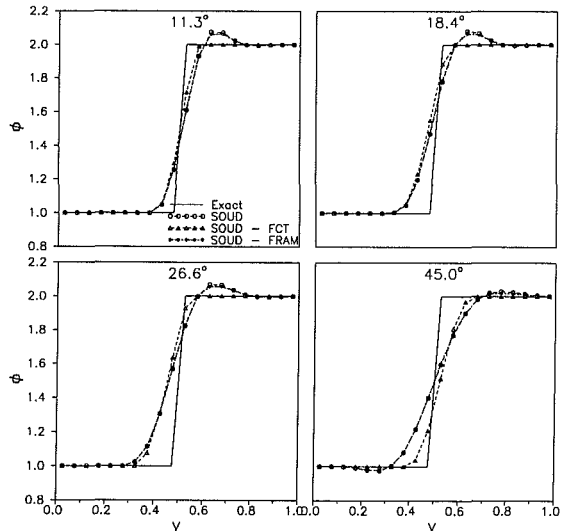


Fig. 4 Predicted steady-state profiles for different flow angles for the second test case

of unit magnitude at the particular angle of interest is specified. A scalar step profile (jump from 1 to 2) is specified at the inlet. Flow angles of 11.3, 18.4, 26.6, and 45 deg to the grid lines are considered. These angles correspond to diagonals across 1:5, 1:3, 1:2, and 1:1, respectively. A  $20 \times 20$  grid ( $\Delta x = \Delta y = 0.05$ ) is used with a time step of 0.02. The flow is assumed inviscid so that a step discontinuity should prevail across the dividing stream line and the exact profile at the vertical mid section ( $x = 0.5$ ) is a step at  $y = 0.5$ . The predicted profiles at the vertical mid section for different flow angles are shown in Figs. 3 and 4. These figures show that unbounded schemes produce over-shoots and oscillations of various magnitude at different flow angles. FCT eliminates the over-shoots and oscillations without introducing any additional numerical diffusion. SUD-FRAM combination also eliminates the oscillations. However, FRAM fails to eliminate the oscillations when used with SOUD. For 45 deg flow angle SUD has least numerical diffusion and does not produce any over-shoot. This is expected because at this flow angle with uniform square grid, SUD has zero numerical diffusion in the cross-stream direction (Leschziner, 1980). The estimates of the average errors of the predicted profiles at different flow angles are shown in Fig. 5. The average percent error is defined as

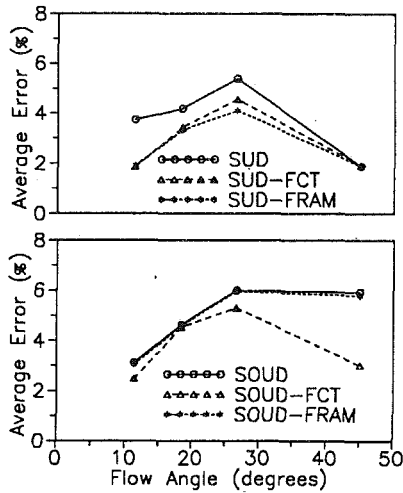


Fig. 5 Average errors at different flow angles ( $20 \times 20$  grid,  $|Pe| = \infty$ )

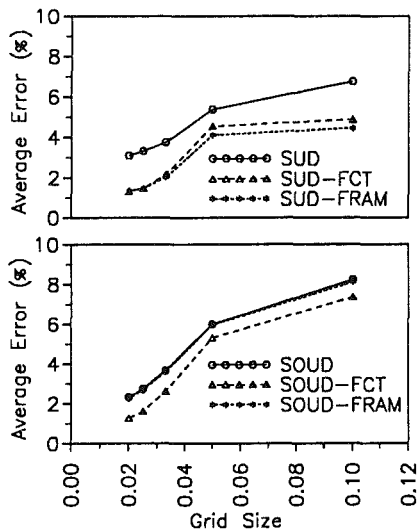


Fig. 6 Average errors for different grid sizes (flow angle 26.6 deg,  $|Pe| = \infty$ )

$$E = 100 \frac{1}{N} \sum_{n=1}^N \left( \frac{|\phi_e - \phi_c|}{\phi_e} \right) \quad (13)$$

where  $N$  is the total number of nodes along the mid section and  $\phi_e$  and  $\phi_c$  are the exact and computed solutions, respectively. As expected, errors for the bounded schemes are consistently and considerably less than that of unbounded schemes except for Soud-FRAM combination since FRAM is ineffective with Soud. It is also noted that the error is maximum around 26 deg flow angle.

In order to examine the effect of grid refinement, predictions for the preceding case are also done for different grid sizes and average errors are estimated for the profile at the mid-section. Grid sizes of 0.1 ( $10 \times 10$ ), 0.05 ( $20 \times 20$ ), 0.033 ( $30 \times 30$ ), 0.025 ( $40 \times 40$ ), and 0.02 ( $50 \times 50$ ) are used. The average errors are plotted against the grid size in Fig. 6. Since the velocity and time step are the same for all the grid sizes considered, the corresponding  $Co_x$ 's are 0.18, 0.36, 0.54, 0.72, and 0.90. The corresponding  $Co_y$ 's are half of these values since the velocity is half in the  $y$  direction. Thus the figure also represents average errors against Courant number. In this case also, the errors for the bounded schemes are consistently and considerably less than the errors for the unbounded schemes except for Soud-FRAM case. The errors decrease quickly as

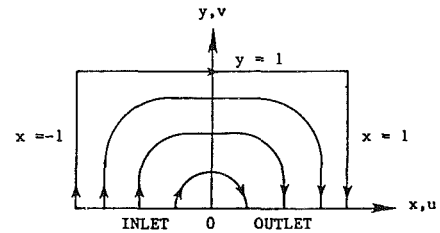


Fig. 7 Schematic of the third test case—Smith and Hutton problem

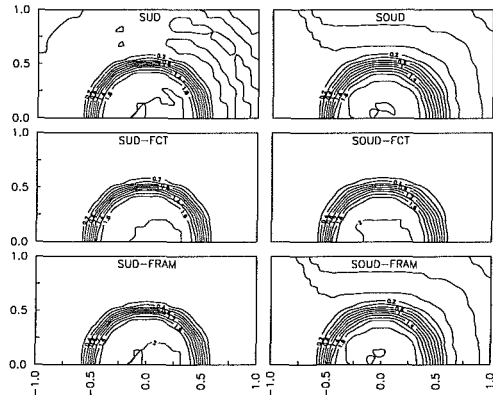


Fig. 8 Contour plots of the scalar  $\phi$  over the flow domain for the Smith and Hutton problem ( $Di = 10^6$ )

the grid is refined and the rate of decrease is slower for grid sizes less than 0.033. At a particular grid size or  $Co$ , the average error for SUD is less than that for Soud. This is because the cross-stream numerical diffusion for SUD is less than that for Soud. The same comments apply for bounded schemes also.

**4.3 Smith and Hutton Problem.** Smith and Hutton (1982) used this problem for comparative evaluation of several numerical schemes. Schematic illustration of the problem is shown in Fig. 7. The governing equation is given by

$$u \frac{\partial \phi}{\partial x} + v \frac{\partial \phi}{\partial y} = \frac{1}{Di} \left( \frac{\partial^2 \phi}{\partial x^2} + \frac{\partial^2 \phi}{\partial y^2} \right) \quad (14)$$

where all the quantities are assumed nondimensional and  $Di$  is a diffusion number. The velocity field is specified as

$$u = 2y(1-x^2), \quad v = -2x(1-y^2) \quad (15)$$

The boundary conditions are specified as

$$\phi = 1 + \tanh[10(2x+1)] \text{ for } y=0 \text{ and } -1 \leq x \leq 0 \text{ (inlet)} \quad (16)$$

$$\phi = 1 - \tanh(10) \begin{cases} x = -1 & 0 \leq y \leq 1 \\ y = 1 & -1 \leq x \leq 1 \\ x = 1 & 0 \leq y \leq 1 \end{cases} \quad (17)$$

This makes  $\phi$  essentially 0 on  $x = \pm 1$  and  $y = 1$  and nearly 2 at the origin. The rise of  $\phi$  from 0 to 2 occurs very sharply half way along the inlet. Zero normal gradient outflow conditions are imposed at the outlet portion of the boundary. This test case represents a complicated recirculating flow pattern where the convection variable changes rapidly over a small distance.

A  $40 \times 20$  uniform square mesh of size 0.05 with  $\Delta t = 0.005$  is used in the prediction for this test case. Predicted contour plots of the scalar for  $Di = 10^6$  over the flow domain is shown in Fig. 8. Predicted profiles at the outlet section are compared with a fine grid solution in Fig. 9. The fine grid solution was taken as a basis for comparison by Smith and Hutton (1982). From these figures, it is seen that the unbounded SUD produces little oscillations, and these are elim-

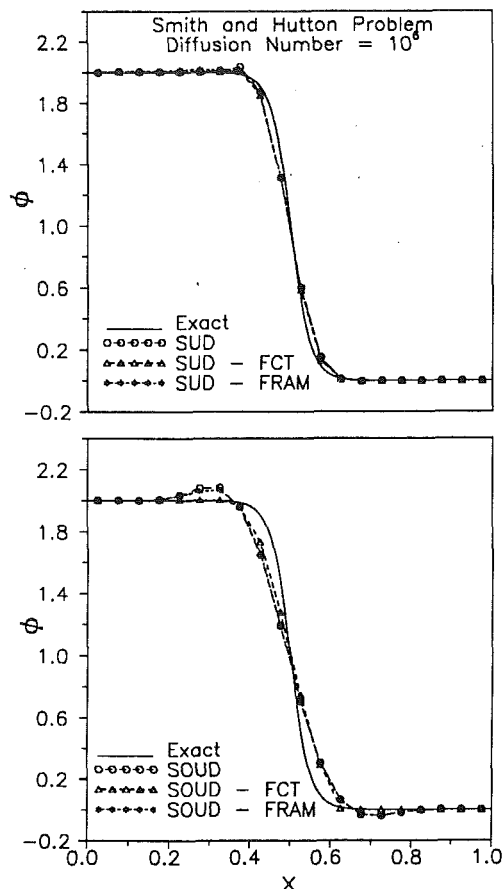


Fig. 9 Predicted steady-state profiles at outlet section for the Smith and Hutton problem ( $Di = 10^6$ )

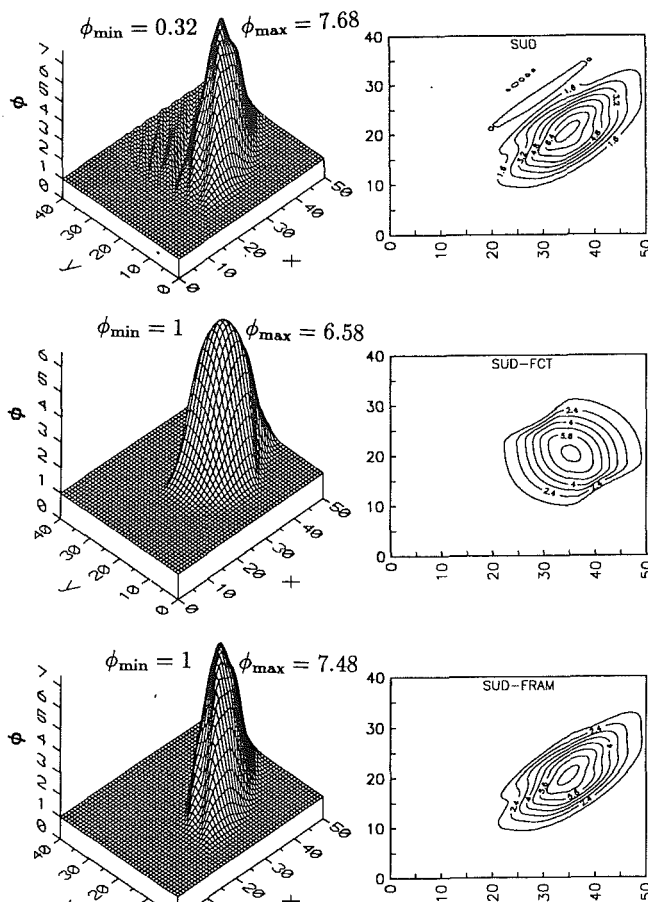


Fig. 11 Surface and contour plots of the predictions for the fourth test case by unbounded and bounded SUD

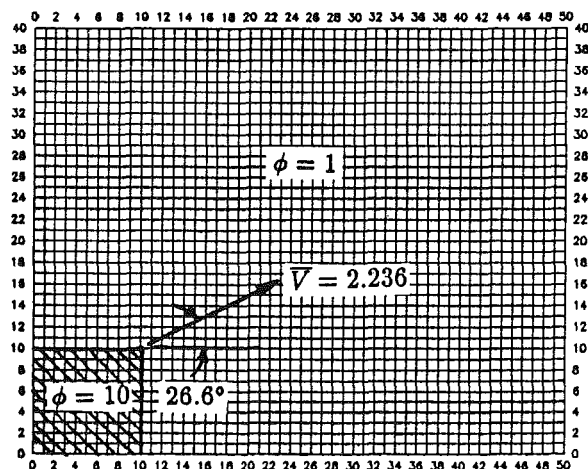


Fig. 10 Schematic of the fourth test case—convection of a square pulse in a uniform velocity field at an angle to the grid lines

inated by both FCT and FRAM technique. The unbounded SOUD produces small over- and under-shoots which are eliminated by FCT. The FRAM technique again is not effective when used with SOUD. The SUD-FCT and the SUD-FRAM predictions at the outlet section agree very well with the fine grid solution.

**4.4 Transport of a Square Pulse.** In this test problem, pure convection of a square pulse in a uniform velocity field inclined at an angle 26.6 deg to the grid line is considered. A uniform  $50 \times 40$  mesh with  $\Delta x = \Delta y = 1$  is used. The velocity field is specified as  $u = 2$  and  $v = 1$  throughout the domain.

The mesh and the initial conditions are shown in Fig. 10. A time step of  $\Delta t = 0.05$  ( $Co_x = 0.1$ ,  $Co_y = 0.05$ ) is used and the program is run for 100 time steps. As shown in Figs. 11 and 12 both SUD and SOUD schemes produce under and/or over-shoots. The streamwise diffusion by SUD is appreciable which is expected since SUD only reduces cross-stream diffusion (Leschziner, 1980). Bounded SUD is free from over and under-shoots. However, because of the streamwise diffusion the pulse is elongated in the streamwise direction. This indicates a deficiency of SUD for transient predictions. The SOUD-FCT scheme produces the best result (Fig. 12) since under-shoots and over-shoots produced by the unbounded SOUD is eliminated and the pulse amplitude is maintained ( $\phi_{max} = 9.92$ ) implying little numerical diffusion. The SOUD-FRAM scheme again is unable to eliminate the under and over-shoots.

The error estimates for these predictions are given in Table 1. The error is measured as

$$E = \Delta x \Delta y \frac{\sum_{ij} |\phi_e - \phi_c| / |\phi_e|}{N} \quad (18)$$

where  $\phi_e$  is the translated initial (undistorted) data,  $\phi_c$  is the predicted data, and  $N$  is the total number of grid points over which initial data is spread (100 for this test case). The errors do not vary considerably as the Courant number changes. A comparison of the SUD-FCT and the SOUD-FCT predictions for this test case at different  $Co_x$  is shown in Fig. 13. The figure shows that the SOUD-FCT predictions have less numerical diffusion and the pulse amplitude is maintained. The shape of the square pulse, however, becomes more and more distorted and the error increases as the Courant number increases. This is due to increasing cross-stream numerical dif-

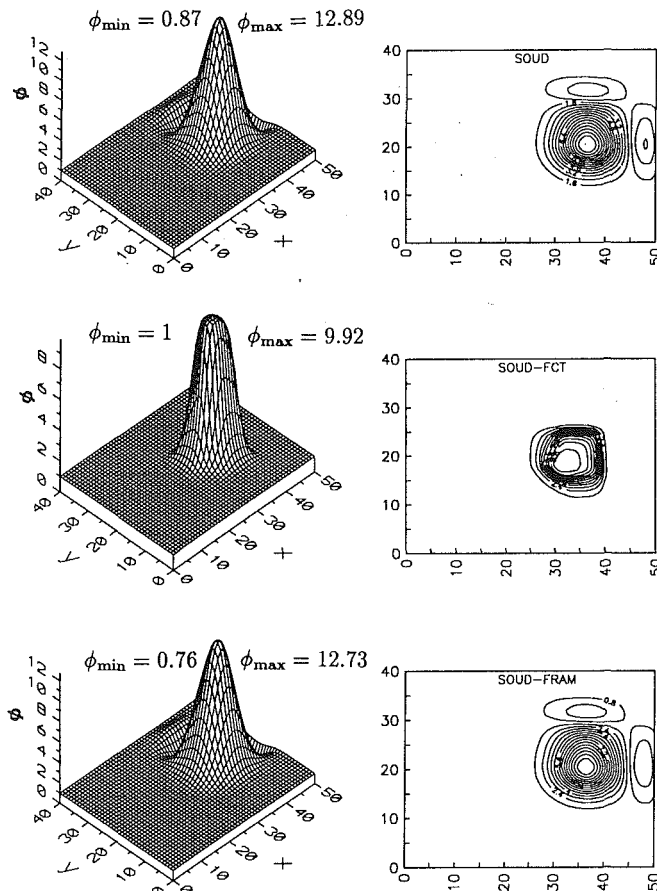


Fig. 12 Surface and contour plots of the predictions for the fourth test case by unbounded and bounded SUD

Table 1 Errors at different Courant number for the fourth test case

Scheme	Error at Co		
	0.1	0.2	0.4
SUD-FCT	4.45	4.31	3.99
SUD-FCT	1.94	2.27	2.87

fusion. The errors, however, are much less than the SUD-FCT errors. Figure 13 shows that the SUD-FCT predictions always suffer from streamwise numerical diffusion which reduces the pulse amplitude.

**4.5 Interaction of Two Parallel Streams.** The interaction of two parallel streams of different velocities moving at an angle of 26.6 deg to the grid lines is considered. In this case, since the advecting velocities are also functions of space and time, the momentum transport equations are nonlinear which makes it different from the first test case. The schematic for this test case is shown in Fig. 14. The velocity ratio between the two parallel streams is 2.0. The velocity of the faster stream is 2.236 ( $u = 2, v = 1$ ). A  $38 \times 43$  uniform square mesh of size 0.01 with  $\Delta t = 0.001$  is used in the computation. The predicted steady-state velocity profiles at a distance  $s/\Delta = 15$  from the inlet section are presented in Fig. 15 for inviscid as well as viscous flow. In the viscous case, the resultant Peclet number  $Pe = 20$  is based on the velocity of the faster stream. The corresponding kinematic viscosity is  $1.118 \times 10^{-3}$ . For nonzero viscosity, the analytical solution of the velocity distribution (similarity profile) by Schlichting (1968) is used for comparison. Similar to the second test case the oscillations or

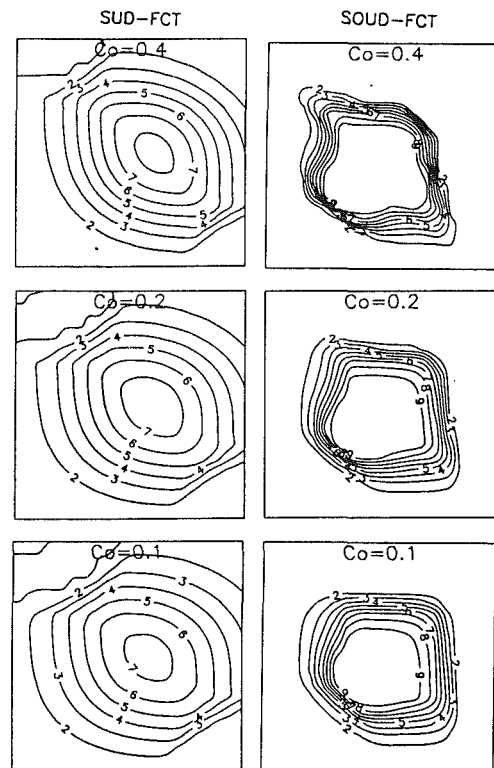


Fig. 13 Contour plots of the predictions for the fourth test case by the SUD-FCT and SUD-FCT schemes at different Courant numbers

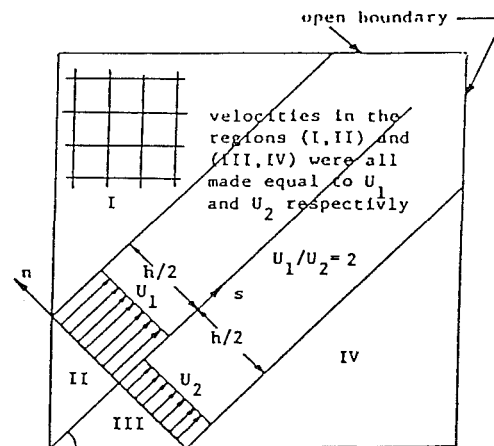


Fig. 14 Schematic of the fifth test case—interaction of two parallel streams moving with different velocities at an angle to the grid lines

over-shoots produced by unbounded SUD is totally removed without introducing any additional numerical diffusion when SUD is bounded with either FCT or FRAM technique. Figure 15 also displays a similar comparison for SUD. In this case, unbounded SUD produces little over-shoot for inviscid case which is eliminated when the scheme is bounded by FCT. For viscous flow, SUD did not produce any over-shoot and bounding produced identical profiles to that of unbounded scheme.

## 5 Conclusion

Using five test problems, the flux-corrected transport (FCT) and the filtering remedy and methodology (FRAM) algorithms have been evaluated to compare their effectiveness in eliminating the numerical dispersions or oscillations produced by the skew upwind differencing (SUD) and the second-order

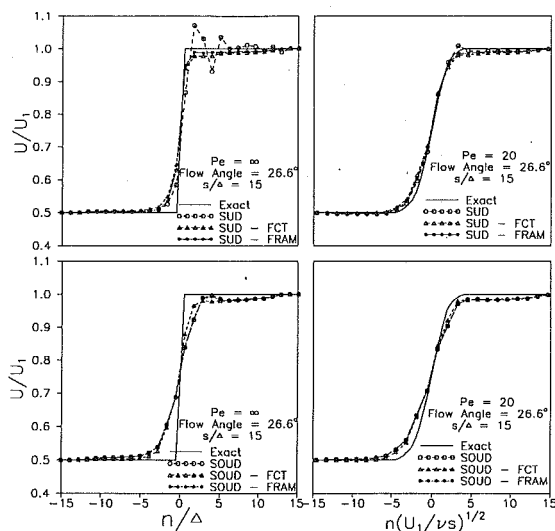


Fig. 15 Predicted steady-state profiles for the fifth test case

upwind differencing (SOUND) schemes. Based on the presented results, it can be concluded that the FCT algorithm effectively treats the dispersion problem for the SUD and SOUND schemes. The FRAM algorithm eliminates the dispersions when used with SUD but fails to eliminate the dispersions or over-shoots when used with SOUND. The results also show that neither of the bounding techniques add more numerical diffusion to the schemes than is already present.

Typically bounding increases the cpu time by a factor of about 2 to 3. Despite this fact, large improvement in accuracy makes bounding worthwhile. Furthermore, with today's computers, operation count is not as important as the ability of the scheme to be vectorized. The SUD or SOUND scheme with FCT or FRAM bounding technique is vectorizable for that matter. FCT uses about 1.3 times more cpu time than FRAM. This is because FCT applies bounding over the entire flow domain whereas FRAM applies it only where oscillations occur. However, failure of FRAM to eliminate oscillations when used with SOUND, makes it less attractive.

On the other hand, the streamwise numerical diffusion of unbounded or bounded SUD is appreciable as shown in the predictions for one and two dimensional convection of a pulse. This indicates that SUD is not suitable for transient predictions. However, if only the steady-state solution is desired then the SUD-FCT or the SUD-FRAM scheme can be used to obtain oscillation free solution. For transient solution SOUND-FCT is found to be better. Euler explicit time differencing, which is first-order accurate, is used here. When transient solutions are of interest, smaller time steps may be used since the first-order explicit scheme is very quick or higher-order time differencing may be incorporated. However, this study concentrates only on the errors associated with the discretization of the convection terms. For this reason, higher-order temporally accurate formulations have not been considered.

## References

Bell, J. B., Colella, P., and Glaz, H. M., 1989, "A Second-Order Projection

Method for the Incompressible Navier-Stokes Equations," *Journal of Computational Physics*, Vol. 85, pp. 257-283.

Bell, J. B., Dawson, C. N., and Shubin, G. R., 1988, "An Unsplit, Higher Order Godunov Method for Scalar Conservation Laws," *Journal of Computational Physics*, Vol. 74, pp. 1-24.

Book, D. L., Boris, J. P., and Hain, K., 1975, "Flux-Corrected Transport II: Generalizations of the Method," *Journal of Computational Physics*, Vol. 18, pp. 248-283.

Boris, J. P., and Book, D. L., 1973, "Flux-Corrected Transport. I. SHASTA, A Fluid Transport Algorithm that Works," *Journal of Computational Physics*, Vol. 11, pp. 38-69.

Chakravarthy, S., and Osher, S., 1983, "High Resolution Applications of the Osher Upwind Scheme for the Euler Equations," *Proceedings of the AIAA 6th Computational Fluid Dynamics Conference*, Paper No. AIAA-83-1943.

Chapman, M., 1981, "FRAM-Nonlinear Damping Algorithms for the Continuity Equation," *Journal of Computational Physics*, Vol. 44, pp. 84-103.

Gaskell, P. H., and Lau, K. C., 1988, "Curvature-Compensated Convective Transport: SMART, A New Boundedness Preserving Transport Algorithm," *International Journal of Numerical Methods in Fluids*, Vol. 8, pp. 617-641.

Harten, A., 1983, "High Resolution Schemes for Hyperbolic Conservation Laws," *Journal of Computational Physics*, Vol. 49, pp. 357-393.

Hirsch, C., 1988, *Numerical Computation of Internal and External Flows*, Vol. 2, John Wiley, New York.

Hirt, C. W., Nichols, B. D., and Romero, N. C., 1975, "SOLA—A Numerical Solution Algorithm for Transient Fluid Flow," Los Alamos Scientific Laboratory Report No. LA-5852.

Huang, P. G., Launder, B. E., and Leschziner, M. A., 1985, "Discretization of Non-linear Convection Processes: a Broad Range Comparison of Four Schemes," *Computer Methods in Applied Mechanics and Engineering*, Vol. 48, pp. 1-24.

Leonard, B. P., 1979, "A Stable and Accurate Convective Modelling Procedure Based on Quadratic Upstream Interpolation," *Computer Methods in Applied Mechanics and Engineering*, Vol. 19, pp. 59-98.

Leonard, B. P., 1988, "Simple High-Accuracy Resolution Program for Convective Modelling of Discontinuities," *International Journal of Numerical Methods in Fluids*, Vol. 8, pp. 1291-1318.

Leschziner, M. A., 1980, "Practical Evaluation of Three Finite Difference Schemes for the Computation of Steady-State Recirculating Flows," *Computer Methods in Applied Mechanics and Engineering*, Vol. 23, pp. 293-312.

Raithby, G. D., 1976, "Skew-Upstream Differencing Schemes for Problems Involving Fluids Flow," *Computer Methods in Applied Mechanics and Engineering*, Vol. 9, pp. 153-164.

Roe, P. L., 1981, "Numerical Algorithms for the Linear Wave Equation," Royal Aircraft Establishment Technical Report No. 81047.

Roe, P. L., 1985, "Some Contributions to the Modelling of Discontinuous Flows," *Proceedings of the AMS-SIAM Summer Seminar on Large Scale Computing, Lectures in Applied Mathematics*, Vol. 3, pp. 163-193.

Schlichting, H., 1968, *Boundary-Layer Theory*, Sixth Edition, McGraw-Hill, New York, pp. 174-175.

Sharif, M. A. R., and Busnaina, A. A., 1988a, "Assessment of Finite Difference Approximations for the Advection Terms in the Simulation of Practical Flow Problems," *Journal of Computational Physics*, Vol. 74, pp. 143-176.

Sharif, M. A. R., and Busnaina, A. A., 1988b, "An Investigation into the Numerical Dispersion Problem of the Skew Upwind Finite Difference Scheme," *Applied Mathematical Modelling*, Vol. 12, pp. 98-108.

Shyy, W., 1985, "A Study of Finite Difference Approximations to Steady State, Convection Dominated Flow Problems," *Journal of Computational Physics*, Vol. 57, pp. 415-438.

Smith, R. M., and Hutton, A. G., 1982, "The Numerical Treatment of Advection: a Performance Comparison of Current Methods," *Numerical Heat Transfer*, Vol. 5, pp. 439-461.

Sweby, P. K., 1984, "High Resolution Schemes Using Flux Limiters for Hyperbolic Conservation Laws," *SIAM Journal of Numerical Analysis*, Vol. 21, pp. 995-1011.

Syed, S., and Chiappetta, L., 1985, "Finite Difference Methods for Reducing Numerical Diffusion in TEACH-Type Calculations," AIAA 23rd Aerospace Sciences Meeting, Paper No. AIAA-85-0057.

Syed, S., Gosman, A., and Peric, M., 1985a, "Assessment of Discretization Schemes to Reduce Numerical Diffusion in the Calculation of Complex Flows," AIAA 23rd Aerospace Sciences Meeting, Paper No. AIAA-85-0441.

Syed, S., Chiappetta, L., and Gosman, A. D., 1985b, "Error Reduction Program," NASA Report No. 174776.

Van Leer, B., 1974, "Towards the Ultimate Conservative Difference Scheme," *Journal of Computational Physics*, Vol. 14, pp. 361-370.

Zalesak, S. T., 1979, "Fully Multidimensional Flux-Corrected Transport Algorithms for Fluids," *Journal of Computational Physics*, Vol. 31, pp. 335-362.

# Hydraulic Characteristics of Mixed Convection in a Heated Vertical Pipe

Jian-Chiu Han

Department of Mechanical Engineering,  
Massachusetts Institute of Technology,  
Cambridge, MA 02139

*By studying the integrated governing equations for mixed convection in a vertical pipe heated with constant wall heat flux, several concepts (or misconcepts) regarding convection mode and flow regimes are examined. A new alternative definition of convection mode reflecting the force balance in mixed convection is given. A new parameter,  $m$  ( $M$ ), is introduced to quantitatively characterize various regimes for mixed convection. Two specific cases for laminar and turbulent air flow with  $Re = 500$  and  $5000$  respectively are studied numerically in detail. Typical behavior of  $m$  ( $M$ ) for each case and other associated hydraulic characteristics of mixed convection are illustrated and discussed.*

## 1 Introduction

Mixed convection in a heated vertical pipe arises in many industrial situations, like in nuclear reactor cooling systems and boilers. An accurate understanding of mixed convection in a vertical tube not only has important industrial design implications but also imposes an academic challenge because of the complex nature of the problem due to the interplay of forced and natural convections. During the past two decades great progress has been made in this understanding, especially in the area of heat transfer characteristics of mixed convection. The review of Jackson et al. (1989) is the most updated and comprehensive account on this subject. Yet the paper mentioned nothing about hydraulic characteristics of mixed convection, namely, friction factor behavior of mixed convection. This reflected the fact that our understanding of mixed convection hydraulics is very much limited and the existing work is inconclusive.

Even some basic concepts about mixed convection are not precisely defined and sometimes confusions result. For instance, in the literature, no distinction is made between "upflow" and "aiding flow" for mixed convection in a heated pipe, and these terms are used as synonyms. However, as will be shown in this paper, "upflow" is an indication of flow direction as a result of interaction of different forces involved in mixed convection while "aiding flow" is an indication of the relation of external pressure and buoyancy; therefore they are really two different concepts and should not be confused with each other. Also, in low Reynolds number turbulent mixed convection, with respect to Nusselt number behavior, three flow regimes marked "forced", "mixed", and "natural" convection are introduced to denote the regions where the heat transfer is unaffected, impaired and enhanced compared with forced convection values. These terms do not precisely reveal

the nature of the flow conditions as they are intended to since forced, mixed and natural convection indicate only the relative magnitude of forced and natural components of pressures.

In this paper, several of these concepts about mixed convection in a heated vertical pipe will be examined by considering the integrated governing equations. A new parameter,  $M$  ( $m$ ), the ratio of external pressure (gradient) and its buoyancy counterpart, is introduced to characterize hydraulic behavior of mixed convection along the pipe. Classification of flow regimes is given in light of the values of the new parameter. Then examples of laminar air flow with  $Re = 500$  and turbulent air flow with  $Re = 5000$  are studied numerically. For the turbulent flow case, a low Reynolds number  $k-\epsilon$  turbulence model is used. Typical behavior of  $M$  ( $m$ ) and the implication of hydraulic characteristics of mixed convection is discussed.

## 2 Analysis

**2.1 Governing Equations.** In this work consideration is only given to situations where the Boussinesq approximation is valid. Also, in all cases, axial diffusion terms in all equations, radial pressure variation in momentum equation and viscous dissipation term in energy equation are neglected. Consistent with the uniform radial pressure assumption, radial momentum equation is neglected and radial velocity is solved from the continuity requirement. As indicated by Shah and London (1978), the effects of axial diffusion and radial pressure variation on developing flow are important only when  $Re < 400$  and their effects are confined within about 1 pipe diameter near the inlet. Therefore, the inclusion of axial diffusion and radial pressure variation is not expected to cause major modifications to the conclusions of this work. Taking a pipe heated with a constant wall heat flux, with the above assumptions, the normalized governing equations are:

$$\frac{\partial}{\partial x} (ru) + \frac{\partial}{\partial r} (rv) = 0 \quad (1)$$

Contributed by the Fluids Engineering Division for publication in the JOURNAL OF FLUIDS ENGINEERING. Manuscript received by the Fluids Engineering Division June 24, 1991. Associate Technical Editor: C. J. Freitas.

$$\frac{\partial}{\partial x} (ru^2) + \frac{\partial}{\partial r} (rvu) = -r \frac{dp}{dx} + \frac{1}{2} \frac{\partial}{\partial r} (-rf) + \frac{Gr}{4Re^2} r\theta \quad (2)$$

$$\frac{\partial}{\partial x} (ru\theta) + \frac{\partial}{\partial r} (rv\theta) = \frac{2}{RePr} \frac{\partial}{\partial r} (r\theta) \quad (3)$$

In these equations the lengths are normalized with pipe radius  $R_0$ , velocities with average velocity  $U_m$ , pressure with  $\rho U_m^2$  and  $\theta = (T - T_0)k/(q_w'' R_0)$ ,  $f$  and  $q$  are normalized shear stress and heat flux. A complete list of definitions of symbols is given in the Nomenclature. Integrating Eqs. (1)–(3) with respect to  $r$  from 0 to 1, we have,

$$\frac{d}{dx} (u_m) = 0 \quad (4)$$

$$\frac{dp_a}{dx} + ff = -\frac{dp}{dx} - \frac{dp_b}{dx} \quad (5)$$

$$\frac{d\theta_m}{dx} = \frac{4}{RePr} \quad (6)$$

where  $p_a = 2 \int_0^1 ru^2 dr$ , is acceleration;  $ff = 2\tau_w/\rho U_m^2$ , friction factor;  $dp_b/dx = -(Gr/4Re^2)\theta_a$ , buoyancy pressure gradient;  $\theta_a = (\int_0^1 r\theta dr)/(\int_0^1 r dr)$ , average temperature and  $\theta_m = (\int_0^1 ru\theta dr)/(\int_0^1 rudr)$ , is the bulk temperature.

Equation (4) states the simple fact that  $u_m$  is constant along the pipe. Equation (6) indicates that the bulk temperature linearly increases with  $x$ , a well known fact for constant wall heat flux condition. Equation (5) reveals the force balance between various components in mixed convection. The left hand side of Eq. (5) is the pressure loss due to acceleration and friction. The acceleration  $dp_a/dx$  can be either positive or negative in the entrance region depending on the inlet condition and it approaches zero away from the entrance region.  $ff$  is always positive. The right-hand side of Eq. (5) is the driving force: buoyancy and external pressure. The buoyancy term can be written explicitly as a function of  $x$  using Eq. (6):

$$-\frac{dp_b}{dx} = \frac{cGr}{Re^3 Pr} x \quad (7)$$

where  $c \equiv (\theta_a/\theta_m)$  is the temperature ratio and its value is around 1–1.1 depending upon the detailed velocity and temperature profiles concerned. Equation (7) indicates that buoyancy pressure gradient increases with the axial distance along the pipe. Now consider a fully developed flow. The LHS of Eq. (5) is a constant equals to  $ff$ . Since  $-dp_b/dx$  linearly increases along the pipe,  $-dp/dx$  must linearly decrease in order to keep the RHS constant as well. At certain point,  $-dp/dx$  will become negative if the pipe is long enough. So unlike in forced convection situation, in which the external pressure

gradient is a constant, in mixed convection the external pressure not only changes magnitude but also may change direction.

To make the above analysis quantitative and also to take account of the developing effect in general we introduce the following two parameters,  $m$  and  $n$  defined by:

$$dp/dx = m(dp_b/dx) \quad (8)$$

$$dp_a/dx = nff \quad (9)$$

With the above definitions, combining Eq. (7), Eq. (5) can be written in a rather compact form:

$$(1+m) \frac{cGr}{Re^3 Pr} x = (1+n)ff \quad (10)$$

This is one of the two equations we are going to use to analyze the hydraulic characteristics of mixed convection in the following sections. It reflects the local balance between various components of pressure gradient. The other one having the similar form reveals the global balance of various components of pressure drop along the pipe. It is obtained by integrating Eq. (5) with respect to  $x$  from 0 to  $x$ ,

$$\Delta p_a + FF = -\Delta p - \Delta p_b \quad (11)$$

where,  $FF = \int_0^x ff dx = ff_a x$  is the total friction and  $\Delta p_b = -(c_a Gr)/(2Re^3 Pr)x^2$ ;  $ff_a$  and  $c_a$  are averages of  $ff$  and  $c$  up to  $x$ . Similar to (8) and (9), define  $M$  and  $N$  such that:

$$\Delta p = M\Delta p_b \quad (12)$$

$$\Delta p_a = NFF \quad (13)$$

We finally have an equation describing the global hydraulic characteristics:

$$(1+M) \frac{c_a Gr}{2Re^3 Pr} x = (1+N)ff_a \quad (14)$$

**2.2 Flow Regimes and Meanings of  $m$  and  $M$ .** In mixed convection two driving forces are acting on the fluid simultaneously: one is the external pressure,  $-dp/dx$ , provided by mechanical means (pump, valve, etc.); and the other is buoyancy,  $dp_b/dx$ . If one force is absent, it is not a mixed convection; it is either a forced convection or a natural convection. So mixed convection is the result of the interaction of forced convection driven by  $-dp/dx$ , and natural convection driven by  $dp_b/dx$ . It can also be thought of as a superimposition of forced convection and natural convection in a complicated nonlinear fashion. Therefore the mode of a mixed convection flow should be determined by the relations between the two components and their driving forces.

However, in the literature, convection mode is classified according to the relation between the overall flow direction

## Nomenclature

$c$ = temperature ratio	$N$ = global acceleration ratio, Eq. (13)	$U, V$ = axial and radial velocities
$D$ = pipe diameter	$Nu$ = Nusselt number	$x$ = normalized axial coordinate, $X/R_0$
$f$ = normalized shear stress, $2\tau/\rho U_m^2$	$p$ = normalized pressure	$X$ = axial coordinate
$ff$ = friction factor, $2\tau_w/\rho U_m^2$	$Pr$ = Prandtl number	$\epsilon$ = viscous dissipation rate of turbulent kinetic energy
$FF$ = averaged friction factor	$q''$ = wall heat flux, $k(\partial T/\partial R) _w$	$\theta$ = normalized temperature, $k(T - T_0)/R_0 q_w''$
$Gr$ = Grashoff number, $\beta g q_w'' D^4/k\nu^2$	$q$ = normalized heat flux, $q''/q_w''$	$\tau$ = shear stress, $-\mu(\partial U/\partial R) _w$
$k$ = thermal conductivity;	$r$ = normalized radial coordinate, $R/R_0$	
turbulent kinetic energy	$R$ = radial coordinate	
$m$ = pressure gradient ratio, Eq. (8)	$R_0$ = pipe radius	<b>Subscripts</b>
$M$ = pressure drop ratio, Eq. (12)	$Re$ = Reynolds number, $U_m D/\nu$	$a$ = average, acceleration
$n$ = local acceleration ratio, Eq. (9)	$T$ = temperature	$b$ = buoyancy
	$T_0$ = inlet temperature	$m$ = bulk
	$u, v$ = normalized velocities, $U/U_m, V/U_m$	$t$ = turbulent
		$w$ = wall



and the natural convection direction. If the two directions are the same it is called an "aiding" flow; otherwise it is called an "opposing" flow. This definition does not reveal the relation between the two components that the flow is made of. It does not reflect the force balance relation as indicated by Eqs. (10) and (14). For instance, for heated vertical pipe, as long as the flow is upward it is considered an "aiding" flow, despite the fact that in some situations the external pressure and the buoyancy are acting in the opposite direction, therefore the forced convection and natural convection are not aiding each other.

To accurately indicate the relation between components of mixed convection, thus to better reflect the balance between force components, we propose an alternative definition of convection mode: In a mixed convection situation, if the external pressure and the buoyancy act in the same direction, the resulting flow is an aiding flow, otherwise it is an opposing flow. Recall the definition of  $m$  and  $M$  given by (9) and (12). It is clear that if  $m(M) > 0$ , it is an aiding flow; if  $m(M) < 0$ , an opposing flow results. The magnitude of  $m(M)$  represents the relative strength of the external pressure to that of the buoyancy. (The number  $m$  indicates the local convection mode, while the  $M$  reflects the global convection mode of a pipe of length  $x$ .) Depending upon the values of  $m(M)$  (both sign and magnitude), different flow situations will result. They are listed in Table 1.

In this classification, forced convection and natural convection are taken as special cases when one of the two convection components is completely dominant. Also notice that for mixed convection an upflow is not necessarily an aiding flow; and an opposing flow does not have to be a downflow. In other words, flow direction and convection mode are separate matters; they should not be confused with each other.

We now concentrate on upflow cases. From (10), we can get some ideas on the qualitative behavior of  $m$  along the pipe. As  $x$  changes from 0 to  $+\infty$ , to keep RHS of (10) positive and finite,  $m$  will change from  $+\infty$  to  $-1$ .  $m$  changes sign at

$$x_{m0} = \frac{\text{Re}^3 \text{Pr}}{\text{Gr}} \frac{1+n}{c} ff \quad (15)$$

When  $x < x_{m0}$ ,  $m > 0$ , it is an aiding flow; when  $x > x_{m0}$ , it is an opposing flow. Therefore  $x_{m0}$  is a critical point at which local convection mode changes from aiding to opposing flow. Similarly, one can easily see from (14) that the critical point for  $M$  to change sign, therefore change the global convection mode from aiding to opposing, is

$$x_{M0} = \frac{2\text{Re}^3 \text{Pr}}{\text{Gr}} \frac{1+N}{c_a} ff_a \quad (16)$$

In order to analyze the quantitative behavior of  $m(M)$  and accurately predict  $x_{m0}(x_{M0})$ , we need to know behaviors of  $c$ ,  $ff$ , and  $n$ . This can only be achieved by solving the governing equations numerically. In the next section, two cases representing laminar and turbulent mixed convection will be studied in detail numerically. For now, we close this section by pointing out that the statement in Table 1 is very general, regardless of laminar or turbulent flow, regardless of the type of fluid concerned. However, cautions should be exercised for high density fluid because in which case the elevation pressure gradient (static pressure), which is neglected in Eq. (2), might be important.

### 3 Case Study

**3.1 Solution Method.** The governing equations to be solved are (1)–(3), explicitly with

$$f = -\frac{4}{\text{Re}} \left( 1 + \frac{\nu_t}{\nu} \right) \frac{\partial u}{\partial r} \quad (17)$$

**Table 1 Different flow situations for different  $m(M)$**

$m(M)$	flow direction	convection mode
$= +\infty$	upflow	forced convection
$< +\infty, > 0$	upflow	mixed convection aiding flow
$= 0$	upflow	natural convection
$< 0, > -1$	upflow	mixed convection opposing flow
$= -1$	no flow	—
$> -\infty, < -1$	downflow	mixed convection opposing flow
$= -\infty$	downflow	forced convection

$$q = \left( 1 + \frac{\text{Pr} \nu_t}{\text{Pr}_t \nu} \right) \frac{\partial \theta}{\partial r} \quad (18)$$

where  $\nu_t$  is the effective turbulent viscosity and  $\text{Pr}_t = 1.1$  is the turbulent Prandtl number. For laminar flow,  $\nu_t$  is zero. For turbulent flow,  $\nu_t$  is calculated via a low-Reynolds number  $k-\epsilon$  model. Details about the model can be found in the Appendix.

Equations (1)–(3) (plus  $k-\epsilon$  model equations in case of turbulent flow) are solved using a marching procedure similarly to that reported by Patankar and Spalding (1972). The solver was well tested for laminar natural, mixed and forced convection. With this solver, the turbulent model was tested for both turbulent forced convection and turbulent mixed convection situations. For turbulent forced convection, the model's predictions were generally in agreement with the established correlations for friction factor and Nusselt number for various Reynolds number within 5 percent. Velocity profile also matched with the classic velocity profile. For mixed convection, cases drawn from literature were tested. Comparisons of Nusselt number for developing flow and fully developed flow, and velocity profile development along the pipe were made. Agreement between the model predictions and experimental results in the papers of Polyakov and Shindin (1988) and Steiner (1971) was generally good. This model almost exactly reproduced some of the results of Cotton and Jackson (1987) and Cotton and Nott (1989), which were obtained using a different low-Reynolds number  $k-\epsilon$  turbulence model. It is thus concluded that the solver is reliable for laminar flow, and as liable as to the extent that a  $k-\epsilon$  turbulence model can be in modelling real turbulent mixed convection. All the cases reported here were calculated with a mesh of 50 non-uniform grids in the radial direction and an axial step of 0.5 percent of pipe radius. Doubling grids in both radial and axial directions altered the friction factor and centerline velocity for fully developed flow by less than 0.13 and 0.12 percent respectively for laminar cases ( $\text{Re} = 500$ ,  $\text{Gr} = 10^5, 10^6$ ) and 1.2 and 0.97 percent, respectively, for turbulent cases ( $\text{Re} = 5000$ ,  $\text{Gr} = 10^7, 10^8$ ) tested. The code was implemented on a Sun-4 machine. The most demanding turbulent case took about 30 minutes cpu time. More details of the development of the numerical code and its complete validation can be found in Han et al. (1989) and Yesilyurt (1991).

### 3.2 Results and Discussion

**3.2.1 Laminar Flow.** Calculations were performed for air ( $\text{Pr} = 0.71$ ) flow of  $\text{Re} = 500$  and  $\text{Gr} = 10^4-10^6$ . In all cases, the fully developed forced convection velocity and uniform zero temperature profiles are imposed at the inlet. Pipe length is taken as 50D.

Figure 1 shows the development of friction factor along the pipe.  $ff$  is normalized with respective fully developed forced convection value. It is seen that the effect of buoyancy on  $ff$  becomes appreciable when  $\text{Gr} = 5 \times 10^4$ , and  $ff$  is increased compared with forced convection value. For high  $\text{Gr}$  cases ( $\text{Gr} = 10^6$ )  $ff$  oscillates near the entrance reflecting the initial over acceleration caused by buoyancy and subsequent deceleration.

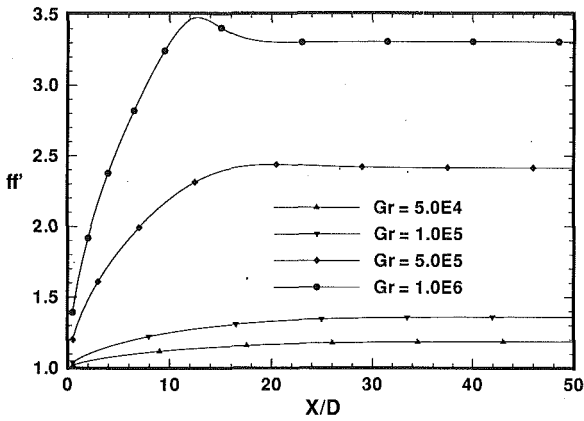


Fig. 1 Friction factor development along the pipe,  $Re = 500$ .  $ff' = ff/(16/Re)$

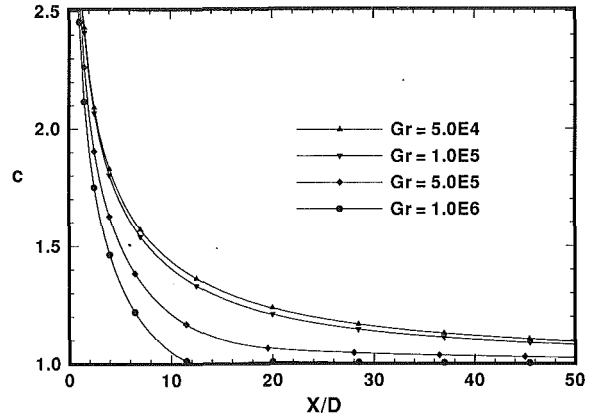


Fig. 3  $c$  value along the pipe,  $Re = 500$

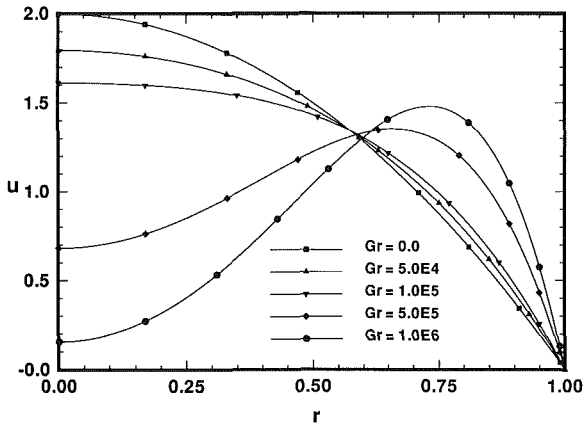


Fig. 2 Velocity profiles at  $X = 50D$ ,  $Re = 500$

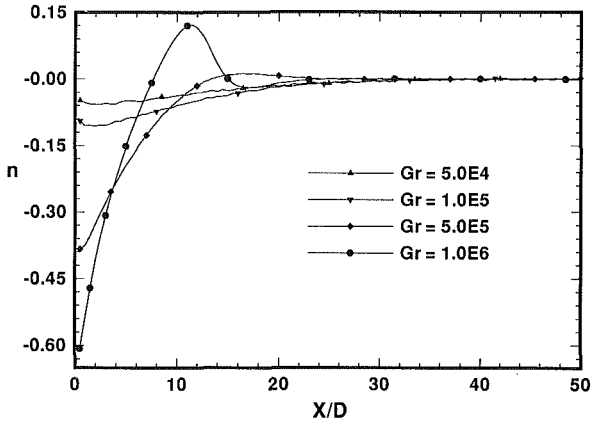


Fig. 4(a)

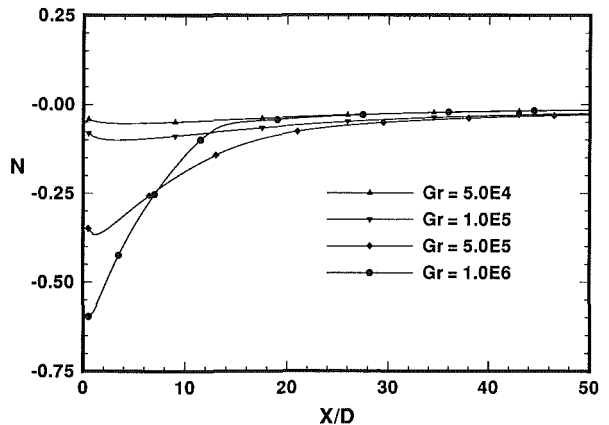


Fig. 4(b)

Fig. 4(a, b)  $n$  and  $N$  along the pipe,  $Re = 500$

In all cases, the flow is fully developed at  $X = 35D$ . In Fig. 2 the velocity profiles at the exit are plotted. It is seen that due to the buoyancy, the profiles are steeper near the wall, thus resulting in the mentioned increase in  $ff$ . Also noticeable is the shift of maximum velocity towards the wall and the continuous decrease of centerline velocity. (With even higher  $Gr$ , the centerline velocity may become negative and recirculating cells would appear. When this happens the parabolized solution method breaks down.)

Figure 3 illustrates the temperature ratio,  $c$ , along the pipe for different  $Gr$  values. Near the inlet thermal boundary layers develop. Since  $\theta_m$  is weighted with  $u$ , which is small in the wall region, where temperature is large,  $c$  picks up a big number near the entrance. At  $X = 1D$ ,  $c$  is about 2.5, and decreases monotonically downstream to an asymptotic value ranging from 1.004 ( $Gr = 10^6$ ) to 1.095 ( $Gr = 5 \times 10^4$ ). Figure 4 shows the  $n$  and  $N$  variations along the pipe. Near the entrance the deceleration due to the buoyancy is quite significant for high  $Gr$  cases, amounting to about 60 percent of the friction for  $Gr = 10^6$  (Fig. 4(a)). But it decreases rather rapidly. For all cases, at  $20D$ ,  $n$  is less than about 5 percent and at  $30D$ , where the flow is fully developed,  $n$  is practically zero. It is also seen from the figure that for high  $Gr$  case, there is an oscillation near the entrance, as also seen in Fig. 1 for  $ff$ , indicating an over-acceleration and subsequent deceleration. Figure 4(b) indicates  $N$  behaves more or less similar to  $n$  but dies out somewhat slower. At  $X = 50D$ ,  $N$  ranges from 1.6 to 2.9 percent. Also  $N$  is never greater than 0, indicating that there is no global over acceleration.

Figure 5 shows the behavior of the important parameters  $m$  and  $M$ . It is obvious that, except for  $Gr = 10^6$ ,  $m$  and  $M$

roughly behave as  $1/x$ , as implied by (10) and (14). It is also clear that  $x_{m0}$  and  $x_{M0}$  (where  $m$  and  $M$  cross 0) continues to decrease as  $Gr$  increases as predicted by (15) and (16). Finally Fig. 6 shows  $x_{m0}$  and  $x_{M0}$  for different  $Gr$ . On the figure also plotted are Eqs. (15) and (16) with  $c = c_a = 1.1$ ,  $n = 0$ , and  $ff = ff_a = 16/Re$ . It is seen that for low  $Gr$  value, the curves agree well with the calculated results since  $x_{m0}$  is large therefore  $n = 0$  and  $ff$  is not far from forced convection value. For large  $Gr$ , however, since  $c$ ,  $n$  and  $ff$  all have significant deviations from the fully developed forced convection values, Eqs. (15) and (16) are rather poor approximations.

3.2.2 Turbulent Flow. For turbulent flow cases, air flow

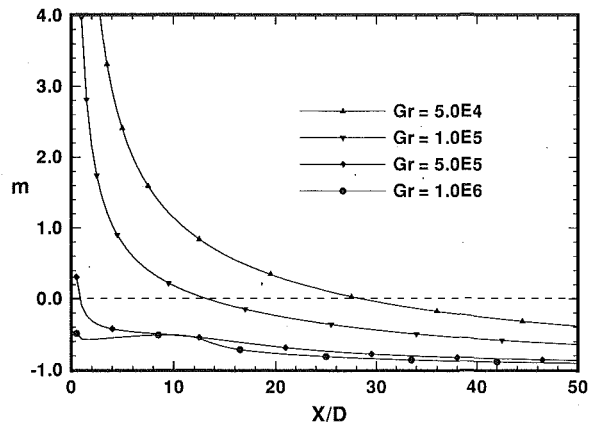


Fig. 5(a)

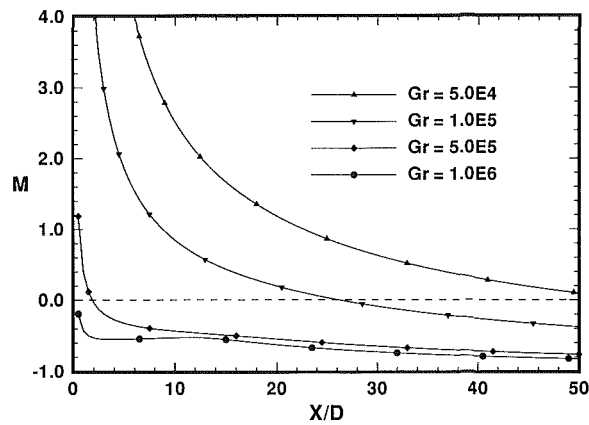


Fig. 5(b)

Fig. 5(a, b)  $m$  and  $M$  behavior along the pipe,  $R = 500$

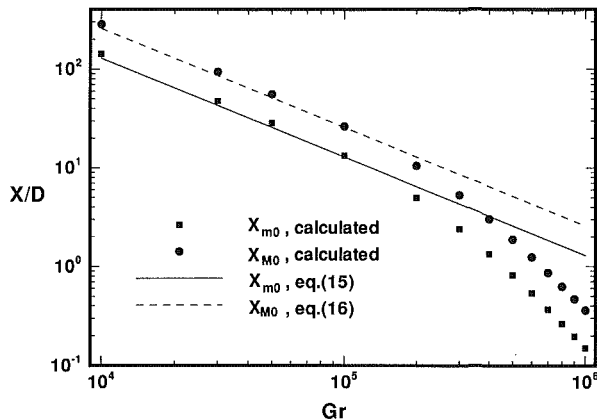


Fig. 6  $X_{m0}$  and  $X_{M0}$  for different Gr,  $Re = 500$

with  $Re = 5000$  and  $Gr = 3 \times 10^6 - 5 \times 10^8$  were calculated. In these calculations, fully developed forced convection velocity and turbulence quantities corresponding to  $Re = 5000$  were imposed at the inlet. The temperature is still uniform and zero. The pipe length is 100D.

Similar to what Fig. 1 does to laminar flow, Fig. 7 shows the development of the normalized  $ff$  along the pipe. Unlike in the laminar situation, fully developed values of  $ff$  for mixed convection are not always increased comparing with the forced convection ones. Specifically, for  $Gr = 5 \times 10^6$  and  $10^7$ ,  $ff$  is 2 percent and 11 percent lower than the forced convection value. The reason for this non-monotonic behavior of  $ff$  is due to the buoyancy force suppression of the turbulence pro-

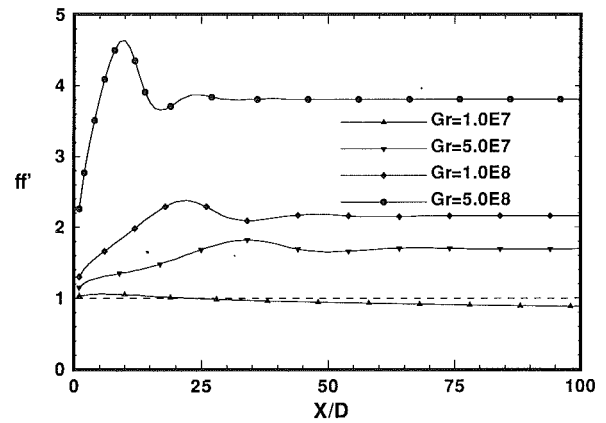


Fig. 7 Friction factor development along the pipe,  $Re = 5000$ .  $ff' = ff/0.00942$

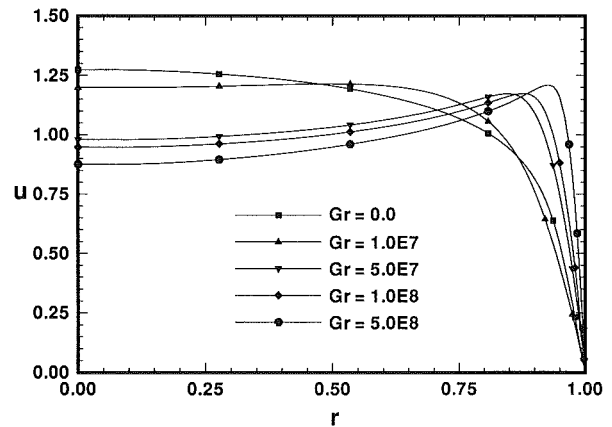


Fig. 8 Velocity profiles at  $X = 100D$ ,  $Re = 5000$

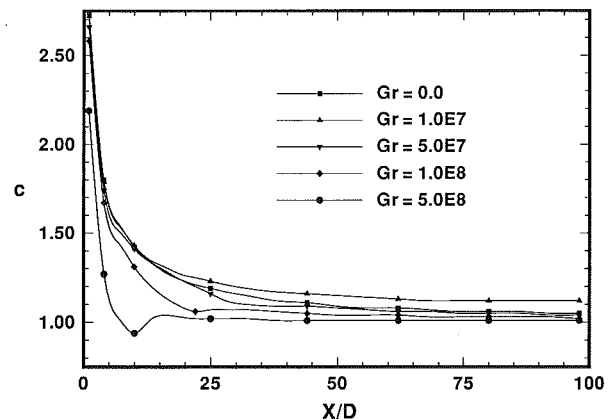


Fig. 9  $c$  value along the pipe,  $Re = 5000$

duction, as well explained in Jackson et al. (1989). Figure 8 shows the velocity profiles at the pipe exit. It can be seen from the figure that the slope of the profile at the wall is well in accordance with the observations about  $ff$  made from Fig. 7. Also, comparing with laminar profiles in Fig. 2, the turbulent velocity profiles are seen much flatter in the core region due to strong turbulent mixing, represented by a large  $\nu_t$  in this region.

Figure 9 illustrates the  $c$  behavior along the pipe. Again,  $c$  starts off a high value of about 3 at  $X = 1D$ , and decreases to somewhere between 1.005 ( $Gr = 5 \times 10^8$ ) and 1.115 ( $Gr = 10^7$ ) eventually. Figure 10 shows  $n$  and  $N$  along the pipe.

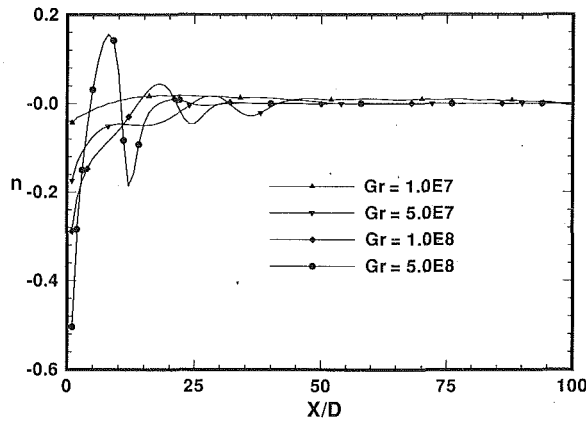


Fig. 10(a)

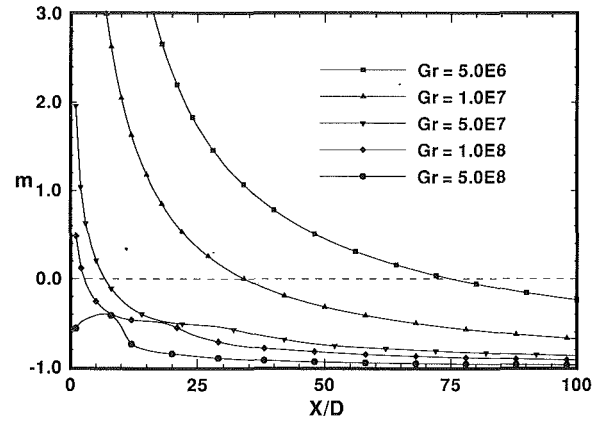


Fig. 11(a)

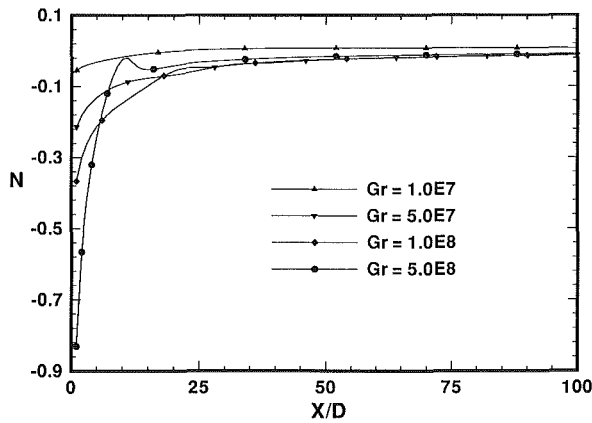


Fig. 10(b)

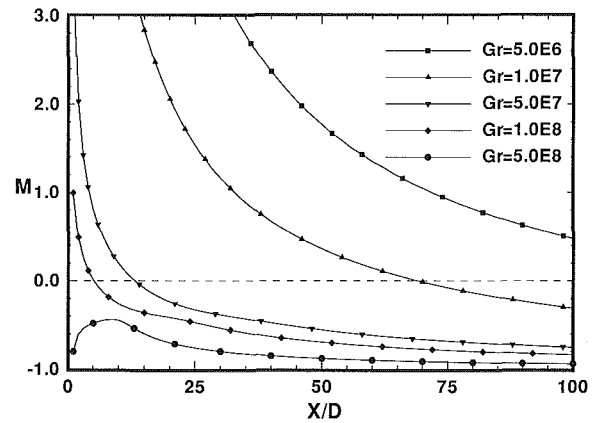


Fig. 11(b)

Fig. 10(a, b)  $n$  and  $N$  along the pipe,  $Re = 5000$

Fig. 11(a, b)  $m$  and  $M$  behavior along the pipe,  $R = 5000$

Again, the flow is decelerated near the entrance because the strong buoyancy near the wall tends to flatten the velocity profile. Similar to the laminar situation,  $n$  also oscillates near the entrance for high Gr number cases ( $Gr > 10^8$ ). In all cases,  $n(N)$  approaches zero as flow approaches fully developed downstream.

Figure 11 portrays  $m$  and  $M$  along the pipe for turbulent flow. For cases of  $Gr < 10^8$ , the general behaviors of  $m$  and  $M$  are quite similar as in laminating cases, i.e.,  $m(M) \sim 1/x$  and  $x_{m0}(x_{M0}) \sim 1/Gr$ . For the case of  $Gr = 5 \times 10^8$ ,  $m(M)$  is always negative, indicating an opposing flow right from the entrance. This means that high buoyancy resulted from high heating rate and the deceleration near the entrance region can not be balanced by shear force alone, therefore an adverse pressure is needed right from the start. In Fig. 12,  $x_{m0}$  and  $x_{M0}$  are plotted as functions of Gr together with curves representing Eqs. (15) and (16). Again forced convection  $ff = 0.00942$  and  $c = 1.1$ ,  $n = 0$  were used in (15) and (16) in plotting the curves. It can be concluded that the forced convection curves are fair approximations to  $x_{m0}$  and  $x_{M0}$  for  $Gr < 10^7$  and poor approximations for  $Gr > 10^7$ . Consistent with behavior of  $m$  and  $M$  in Fig. 11, we see that  $x_{m0}$  and  $x_{M0}$  approaches 0 at about  $Gr = 2 \times 10^8$ , meaning for  $Gr > 2 \times 10^8$   $m$  and  $M$  are always negative and the convection mode is always an opposing one.

**3.2.3 Practical Implications.** While  $m$  and  $x_{m0}$  indicate local convection mode and transition point,  $M$  and  $x_{M0}$  indicate the global convection mode and their values have implications in practical situations. For instance, one wants to conduct a mixed convection experiment with a pipe of length  $L$ . For certain  $Re$  and  $Gr$ ,  $x_{M0}$  has certain value. For cases with  $x_{M0}$

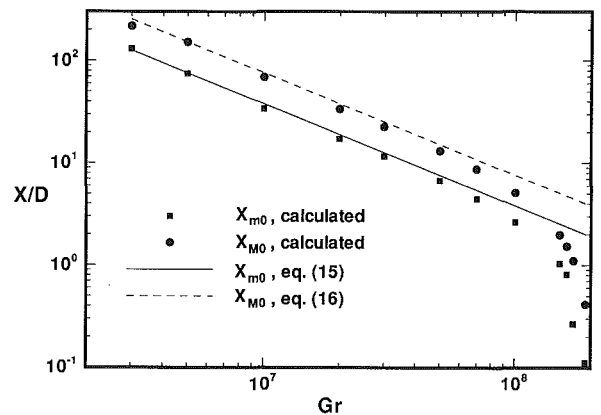


Fig. 12  $x_{m0}$  and  $x_{M0}$  for different Gr,  $Re = 5000$

$> L$ , one needs a pump to provide forced convection; for  $x_{M0} < L$ , one needs a valve to regulate flow. Specifically, take  $L = 30D$  (not very long if one wants to have a fully developed flow at the exit) and  $Re = 5000$ . In order to study the unaffected, impaired and enhanced heat transfer regimes, one has at least to vary Gr from  $10^6$  to  $5 \times 10^8$  (Jackson et al., 1989). From Fig. 12, we can see that when Gr is less than about  $2.5 \times 10^7$ , one will get an aiding flow, therefore a pump is needed; when  $Gr > 2.5 \times 10^7$ , one will get an opposing flow, therefore a flow restrictor has to be implemented. In an experiment where only a pump is used, in cases of high Gr, that pump may actually unknowingly function as a valve. Also for instance, in designing natural convection cooling system for advanced

nuclear reactors, risers (through which natural convection carry away the heat) can be modelled as vertical heated pipes operating under natural convection condition. Equation (16) describes a relation that the system must satisfy under such conditions. From Eq. (16) or Fig. 12, we know that corresponding to certain Gr (heating rate) and  $x_{M0}$  (geometry of the system) there is only one Re (flow rate). Once the Re is known, one can proceed to predict the thermohydraulic characteristics of the system.

#### 4 Concluding Remarks

The essence of mixed convection is the interaction of forced and natural convection components; therefore a classification of convection mode should be based on the relation between these two components. In this work, we suggested a classification of convection mode that reflects the nature of the force balance as indicated by the integrated governing equations and reveals the relation between the two components. A new parameter,  $m(M)$ , was introduced to quantize the relation between the two components. Flow regimes for mixed convection in a vertical heated pipe were given according to the value of the new parameter. Distinction between flow direction and convection mode was emphasized.

Laminar and turbulent air flow of  $Re = 500$  and  $5000$ , respectively, were studied in detail numerically. Typical behaviors of  $m(M)$  and other characteristics of mixed convection along the pipe were portrayed and discussed. It was indicated that in many mixed convection situations, the convection mode is actually an opposing flow, despite the seemingly upward flow direction. The implication of convection mode for practical situations was discussed.

#### Acknowledgment

The author wants to thank Professors N. E. Todreas and M. J. Driscoll for many stimulating discussions. This work was supported financially by the Bechtel National Inc. and Oak Ridge National Laboratory. These supports are gratefully acknowledged.

#### References

- Cotton, M. A., and Jackson, J. D., 1987, "Comparison Between Theory and Experiment for Turbulent Flow of Air in a Vertical Tube with Interaction Between Free and Forced Convection," in *Mixed Convection Heat Transfer—1987* eds. V. Prasad, I. Catton and P. Cheng, ASME Publication HTD-Vol. 84.
- Cotton, M. A., and Nott, I. D., 1989, "Computation of Developing Turbulent Mixed Convection Heat Transfer to Air in a Vertical Tube: Comparison of a Low-Reynolds-Number  $k-\epsilon$  Model with Recent Experiments," Paper presented at Anglo-Soviet Seminar on Turbulent Convection, Institute for High Temperature of the U.S.S.R. Academy of Science, Moscow, May.
- Han, J.-C., Driscoll, M. J., and Todreas, N. E., 1989, "Initial Report on Numerical Simulation of Turbulent Mixed Convection in RCCS Riser Using a  $k-\epsilon$  Model," MIT Nuclear Engineering Department Report, Apr.
- Henkes, R. A. W. M., and Hoogendoorn, C. J., 1989, "Comparison of Turbulence Models For the Natural Convection Boundary Layer along a Heated Vertical Plate," *International Journal of Transfer*, Vol. 32, pp. 157–169.
- Jackson, J. D., Cotton, M. A., and Axcell, B. P., 1989, "Studies of Mixed Convection in Vertical Tubes," *International Journal of Heat Fluid Flow*, Vol. 10, 1989, pp. 2–15.
- Lam, C. K. G., and Bremhorst, K., 1981, "A Modified Form of the  $k-\epsilon$  Model for Predicting Wall Turbulence," ASME JOURNAL OF FLUIDS ENGINEERING, Vol. 103, pp. 456–460.
- Patankar, S. V., and Spalding, D. B., 1972, "A Calculation Procedure for Heat, Mass and Momentum Transfer in Three-dimensional Parabolic Flows," *International Journal of Heat Mass Transfer*, Vol. 15, pp. 1787–1806.

Patel, V. C., Rodi, W., and Scheuerer, G., 1985, "Turbulence Model for Near-wall and Low-Reynolds Number Flows: a Review," *AIAA Journal*, Vol. 23, pp. 1308–1319.

Polyakov, A. F., and Shindin, S. A., 1988, "Development of Turbulent Heat Transfer over the Length of Vertical Tubes in the Presence of Mixed Air Convection," *International Journal of Heat Mass Transfer*, Vol. 31, pp. 987–992.

Shah, R. K., and London, A. L., 1978, "Laminar Flow Forced Convection in Ducts," Supplement 1 to *Advances in Heat Transfer*, Academic, New York.

Steiner, A., 1971, "On the Reverse Transition of a Turbulent Flow under the Action of Buoyancy Forces," *Journal of Fluid Mechanics*, Vol. 47, pp. 503–512.

Yesilyurt, S., 1991, "Numerical Calculation of Mixed Convection in a Duct under MHTGR Conditions," S.M. thesis, MIT.

## APPENDIX A

### Turbulence Model

The effective turbulent viscosity is calculated via:

$$\nu_t = C_\mu f_\mu \frac{k^2}{\epsilon} \quad (19)$$

Where  $C_\mu$  is an empirical constant of 0.09 and  $f_\mu$  is a damping function to account the turbulence damping effect of the wall;  $k$  and  $\epsilon$  are turbulent kinetic energy and viscous dissipation rate of kinetic energy, and they are modelled by the following transport equations:

$$\frac{\partial}{\partial X} (Uk) + \frac{1}{R} \frac{\partial}{\partial R} (RVk) = \frac{1}{R} \frac{\partial}{\partial R} \left[ R \left( \nu + \frac{\nu_t}{\sigma_k} \right) \frac{\partial k}{\partial R} \right] + \nu_t \left( \frac{\partial U}{\partial R} \right)^2 - \beta g \frac{\nu_t}{Pr_t} \frac{\partial T}{\partial X} - \epsilon \quad (20)$$

$$\frac{\partial}{\partial X} (U\epsilon) + \frac{1}{R} \frac{\partial}{\partial R} (RV\epsilon) = \frac{1}{R} \frac{\partial}{\partial R} \left[ R \left( \nu + \frac{\nu_t}{\sigma_\epsilon} \right) \frac{\partial \epsilon}{\partial R} \right] + C_{1f_1} \frac{\epsilon}{k} \left[ \nu_t \left( \frac{\partial U}{\partial R} \right)^2 - \beta g \frac{\nu_t}{Pr_t} \frac{\partial T}{\partial X} \right] - C_{2f_2} \frac{\epsilon}{k} \quad (21)$$

where  $C_1$ ,  $C_2$ ,  $f_1$ , and  $f_2$  are model constants and wall damping function.

There exist a few low-Reynolds number  $k-\epsilon$  turbulence model. Among them the model of Lam and Bremhorst (1981) is one of the best in predicting both forced and natural convection boundary layer flow (Patel et al., 1985; Henkes and Hoogendoorn, 1989). However, our direct application of this model failed in some cases in the form of appearance of negative  $k$ . This negative  $k$  problem was remedied by decoupling  $f_1$  and  $f_\mu$  and calculating  $f_1$  through a simpler form:

$$f_1 = 1 + A_1/Re_y \quad (22)$$

Functional form of  $f_2$  and  $f_\mu$  remained the same, with the constant involved being re-optimized as necessary.

$$f_2 = 1 - A_2 \exp(-Re_y^2) \quad (23)$$

$$f_\mu = [1 - \exp(-A_\mu Re_y^2)]^2 (1 + A_t/Re_y) \quad (24)$$

Values of the constants in the model are as following:

$$C_1: 1.44; C_2: 1.92; C_\mu: 0.09; A_1: 5.95; A_2: 1;$$

$$A_\mu: 0.01; A_t: 0; \sigma_k: 1; \sigma_\epsilon: 1.3; Pr_t: 1.1.$$

More details about the numerical method, turbulence model and its validation were reported in Han et al. (1989) and Yesilyurt (1991).

# Parametrical Investigation of the Interaction Between Turbulent Wall Shear Layers and Normal Shock Waves, Including Separation

J. K. Kaldellis<sup>1</sup>

The Institute for the Development  
and Management of Natural Resources,  
Athens, Greece

*The existence of strong shock waves plays a major role in the performance of modern aero-mechanical devices, since it is primarily responsible not only for the shock induced total pressure drop, but also for the increased shear layer losses due to flow separation. In this paper a fast energy-type integral method along with an approximate shock-turbulent shear layer interaction procedure are presented. This integral method, based on the two-zone model, is able to predict attached and fully detached shear flows. An extended turbulence model is also used in order to take the influence of the turbulence inside the interaction region better into account. The external flow pressure distribution results from an improved and extended form of an approximate small disturbance theory. A detailed investigation is carried out to estimate the influence of the inlet Mach number, the shear layer characteristics and the confinement of the geometry upon the static pressure field. The resulting method has been successfully applied to several test cases including ones where separation appears. Comparison between results of previous calculations, experimental data and results of the proposed method is also presented, along with the convergence history of the shear layer—shock wave interaction procedure. Finally, the method has been applied to one-stage high pressure supersonic flow compressor with normal shock appearance inside the rotor of the machine. The major conclusion drawn from the present work is that the shear layer characteristics (e.g., displacement thickness and form factor) have a dominant effect upon the flow field near the interaction region. Additionally, the proposed method requires no more than five overall iterations to reproduce the real flow field for all cases examined.*

## 1. Introduction

It is well known today that the existence of strong shock waves plays a major role in the performance of modern aero-mechanical devices, since it is primarily responsible not only for the shock induced total pressure drop, but also for the increased shear layer losses due to flow separation. There are only a few methods able to predict realistically the flow field pattern in the region of shock—shear layer interaction.

Generally speaking, there are two main approaches for the investigation of transonic-supersonic flow fields. The first is the solution of the compressible three dimensional Navier-Stokes equations (Dawes, 1988; Hah and Wennerstrom, 1990; etc.). The second approach is based on the viscous-inviscid interaction theory (Calvert, 1982; Edwards et al., 1986; Kaldellis et al., 1989; etc.).

In the recent years it has become possible to calculate fairly good the three-dimensional flow field using the first approach. However, due to their significant computational requirements,

these methods do not provide the necessary physical explanation for preliminary design purposes at present.

On the other hand, in the latest years it has been successfully demonstrated that a generalized interacting shear layer theory can be used to analyze even fully separated flows. Thus, taking into account that such methods are even more efficient for high Reynolds numbers, they can provide considerable insight into much of the relevant flow physics over a wide range of operating conditions. Additionally, the time and cost requirements are definitely lower than the ones needed to obtain similar information from a complete Navier Stokes approach.

In this paper a fast energy-type integral method along with an approximate shock-turbulent shear layer interaction procedure are presented. This integral method, based on the two-zone model, is able to predict attached and fully detached steady two-dimensional shear layers. An extended turbulence model takes better into account the influence of the turbulence terms inside the interaction region.

The shock-shear layer interaction procedure is used to realistically estimate the readjustment of the abrupt pressure rise occurring behind the shock wave, especially near the wall. This readjustment is directly related to the transfer of information

<sup>1</sup>Presently, Assistant Professor, Technological Education Institute of Piraeus; Permanent address: Pontou 58, 16777 Greece.

Contributed by the Fluids Engineering Division for publication in the JOURNAL OF FLUIDS ENGINEERING. Manuscript received by the Fluids Engineering Division July 11, 1991. Associate Technical Editor: R. K. Agarwal.

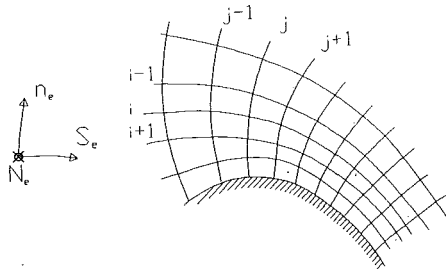


Fig. 1 External flow streamlines' system of coordinates ( $S_e$ ,  $N_e$ ,  $n_e$ )

not only downstream but also upstream through the subsonic part of the shear layer. For the majority of the test cases analyzed here, the incoming Mach number is between 1.25 and 1.40, and the corresponding normal shock waves are of sufficient strength to cause shear layer separation.

## 2. Governing Equations

**Turbulent Shear Layer.** The following equations describe the two-dimensional steady flow field of a viscous and compressible fluid. In these equations the gravity terms are neglected (gas flow) and the flow field is assumed to be adiabatic (zero heat exchange). The corresponding system of equations constitutes a higher approximation to the Navier-Stokes equations than the classical boundary layer approximation used before. This is because not only the dominant turbulent fluctuation terms are retained, but also the difference between the static pressure of the external and the viscous flow field is taken into account. The equations used are:

(a) The momentum conservation equations written in a orthogonal curvilinear coordinate system associated with the external flow streamlines (see Fig. 1). These equations are integrated along a normal  $-n_e$  from the solid wall to the end of the shear layer. In order to derive their final form (see also Katramatos and Kaldellis, 1991), terms containing transverse curvatures as well as derivatives of the viscous terms along the  $-S_e$  direction are neglected.

*Integral momentum equation in the marching direction  $-S_e$*

$$\frac{d(R \cdot \rho_e \cdot u_e^2 \cdot \delta_2)}{R \cdot \rho_e \cdot u_e^2 \cdot \delta_2} + t_3 \cdot H_{12} \cdot \frac{du_e}{u_e} = \frac{C_f \cdot t_3}{2 \cdot \delta_2} \cdot dS_e + t_3 \cdot H_{\rho 2} \cdot \frac{d(\omega_o^2 \cdot R^2)}{2 \cdot u_e^2} - d \ln t_3 + \frac{\delta \cdot d[\bar{K}_{S_e} \cdot \rho_e \cdot u_e^2 \cdot (\delta_1 + \delta_2)]}{\rho_e \cdot u_e^2 \cdot \delta_2} \quad (1)$$

## Nomenclature

$a$  = speed of sound  
 $C_d$  = dissipation factor  
 $C_f$  = skin friction coefficient  
 $h_t$  = total enthalpy  
 $H$  = passage height  
 $H_{12}$  = form shape factor ( $H_{12} = \delta_1 / \delta_2$ )  
 $H_{\rho 2}$  = density form factor ( $H_{\rho 2} = \delta_\rho / \delta_2$ )  
 $K_{S_e}, \bar{K}_{S_e}$  = curvature of  $-S_e$  lines, mean value  
 $M$  = Mach number  
 $p$  = static pressure  
 $R$  = radius  
 $(u, v, w)$  = components of the real velocity  
 $(S_e, N_e, n_e)$  = coordinates of an or-

thogonal curvilinear system based on the external flow streamlines  
 $(u', v', w')$  = components of velocity fluctuations with time  
 $\beta$  = flow angle  
 $\gamma$  = ratio of specific heats  
 $\delta$  = shear layer thickness  
 $\delta_1, \delta_2, \delta_3$  = displacement, momentum, energy thickness of the shear layer  
 $\rho$  = density  
 $\omega_o$  = angular velocity  
 $\langle \rangle$  = time mean averaged quantity

**Subscripts**  
 $e$  = external flow quantities  
 $k$  = kinematic shear layer quantities  
 $o$  = undisturbed external flow quantity in the shock-shear layer interaction region  
 $w, w'$  = value at the walls  
 $x, y$  = indicate the start and the end of the shock-shear layer interaction region  
 $*$  = theoretical shock position

with:

$$t_3 = 1 / (1 + A / \delta_2) \quad (2)$$

and

*Integral momentum equation in the normal direction  $-n_e$*

$$(p_e - p) = \rho \cdot \langle v'^2 \rangle + \int_0^{n_e} K_{S_e} \cdot (\rho_e \cdot u_e^2 - \rho \cdot u^2) \cdot dn_e' \quad (3)$$

(b) The total kinetic energy integral equation derived by considering the kinetic energy integral equation of the time-averaged flow field and the turbulent kinetic energy equation after neglecting the pressure fluctuation terms. The final equation is obtained when the production term in the kinetic energy integral equation is substituted by its equivalent expression from the turbulent kinetic energy equation. The resulting equation is integrated along a normal  $(-n_e)$  from the wall to the end of the shear layer.

*Integral total kinetic energy equation*

$$\frac{d(R \cdot \rho_e \cdot u_e^3 \cdot \delta_3)}{2 \cdot R \cdot \rho_e \cdot u_e^3 \cdot t_1} + \frac{du_e}{u_e} (\delta_1 - \delta_{1k}) = \frac{d(\omega_o^2 \cdot R^2)}{2 \cdot u_e^2} \cdot (\delta_1 - \delta_{1k}) + \frac{\delta_3 \cdot dt_1}{2 \cdot t_1^2} + C_d \cdot dS_e \quad (4)$$

with:

$$t_1 = 1 / (1 - B / \delta_3) \quad (5)$$

Parameters  $t_1$  and  $t_3$  describe the variation of the turbulent fluctuation terms, see also Katramatos and Kaldellis (1991). The corresponding terms "A" and "B" are defined as follows:

$$A = \int_0^\delta \frac{\rho \cdot (\langle u'^2 \rangle - \langle v'^2 \rangle)}{\rho_e \cdot u_e^2} \cdot dn_e \quad (6)$$

$$B = \int_0^\delta \frac{\rho \cdot u \cdot (3 \cdot \langle u'^2 \rangle - \langle v'^2 \rangle + \langle w'^2 \rangle)}{\rho_e \cdot u_e^3} \cdot dn_e \quad (7)$$

The above-mentioned equations are written after neglecting the time-averaged normal velocity component (axial configuration). Their complete form is given by Kaldellis (1988) and Katramatos and Kaldellis (1991). The importance of the turbulent terms for the successful prediction of the flow field has been proved, experimentally and computationally, especially in separated regions, which often appear inside the interaction area. In the following the turbulence model used to calculate the corresponding terms is briefly presented.



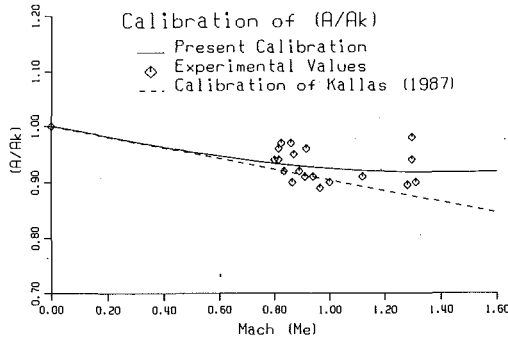


Fig. 2(a) Compressible correlation for the turbulent fluctuation term  $A$  Eq. (6)

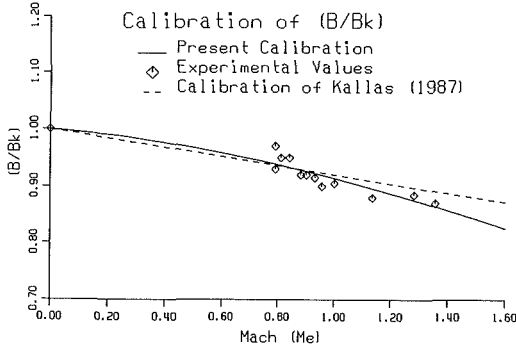


Fig. 2(b) Compressible correlation for the turbulent fluctuation term  $B$  Eq. (7)

**Turbulence Modeling.** For the description of the  $A$  and  $B$  integrals, which contain the turbulent terms (Eqs. (6), (7)), the available experimental data are used, see also Kaldellis (1988) and Katramatos and Kaldellis (1991). Thus, to realistically reconstruct the natural changes expressed by the experimental data and keeping in mind the scattering of the experimental points in case of a direct calibration of the incompressible form of the integrals  $A$  and  $B$  (Kallas et al., 1987; Kaldellis et al., 1991), the turbulent components  $\langle u'^2 \rangle$  and  $\langle v'^2 \rangle$  were calibrated instead. Then, the incompressible ( $\rho = \rho_e$ ) values of  $A$  and  $B$ ,  $A_k$  and  $B_k$ , respectively, are predicted by integrating numerically the distributions of  $\langle u'^2 \rangle$  and  $\langle v'^2 \rangle$ , see for details Kaldellis (1988).

Finally, the compressible form of the terms  $A$  and  $B$  are estimated using the following calibrations (see also Fig. 2(a) and 2(b)):

$$A = (1 + \epsilon_{11} \cdot M_e + \epsilon_{12} \cdot M_e^2) \cdot A_k \quad (8)$$

$$B = (1 + \epsilon_{21} \cdot M_e + \epsilon_{22} \cdot M_e^2) \cdot B_k \quad (9)$$

with  $\epsilon_{11} = -0.048$ ,  $\epsilon_{12} = -0.022$ ,  $\epsilon_{21} = -0.067$  and  $\epsilon_{22} = -0.0063$ . The above given relations are slightly different from the linear ones given by Kallas et al. (1987). However, they describe more successfully the experimental data in the area of interest (i.e.,  $0.8 \leq M_e \leq 1.5$ ).

### 3. Flow Field Calculation in the Shock-Shear Layer Interaction Region

For the calculation of the flow field inside the shock-shear layer interaction region, a modified small disturbances theory, similar to that of Inger and Mason (1976), Panaras (1981), Kallas et al. (1987), and Kaldellis et al. (1989) is used. Additional details concerning the development of this method may be found in the above mentioned references, while some more recent information concerning the extension of the method for the case of shock-secondary flow interaction is given by Kaldellis et al. (1991).

According to the small disturbances theory, which is supposed valid for Mach number inferior to 1.5, the flow field is decomposed into a basic flow field and a disturbance. The basic flow field is described by the external pressure field as calculated by an inviscid quasi-three dimensional code (e.g., Alkalai and Leboeuf, 1985) upstream of the shock wave and a fictitious continuation of it in the region downstream of the shock. The basic flow field is continuous. The disturbance consists of the shock wave induced pressure step, which, if added to the basic flow field downstream of the shock, restores the real flow field. The theoretical development is based on the Euler's equation (Kaldellis, 1988). Denoting the basic external flow quantities with the subscript zero and disturbances with  $\delta(\cdot)$ , we may write:

$$u_e = u_o + \delta(u) \quad (10)$$

$$v_e = \delta(v) \quad (11)$$

$$p_e = p_o + \delta(p) \quad (12)$$

$$h_{t_e} = h_{t_o} + \delta(h_t) \quad (13)$$

$$\rho_e = \rho_o + \delta(\rho) \quad (14)$$

In order to compute the flow field inside the interaction region, the external flow angle (i.e., the flow angle outside the shear layers) is considered unchanged through the shock wave, which is assumed normal to the flow direction. Introducing the above expressions (10) to (14) into Euler's equations, after several manipulations and rearrangements (see Kaldellis, 1988; Kaldellis et al., 1991), the following equation is derived:

$$\begin{aligned} \frac{\partial^2(\delta p)}{\partial n_e^2} + \left( \frac{1}{R} - \frac{2}{M_o} \cdot \frac{\partial M_o}{\partial n_e} \right) \cdot \frac{\partial(\delta p)}{\partial n_e} + (1 - M_o^2) \cdot \frac{\partial^2(\delta p)}{\partial S_e^2} \cdot \cos^2 \beta_o \\ - \frac{\partial p_o}{\partial n_e} \left[ - \frac{1}{\rho_o} \frac{\partial(\delta p)}{\partial n_e} - \frac{1}{\rho_o \cdot a^2} \frac{\partial(\delta p)}{\partial n_e} \right. \\ \left. + \left( \frac{2}{M_o} \cdot \frac{\partial M_o}{\partial n_e} + \frac{1}{\rho_o} \frac{\partial \rho_o}{\partial n_e} \right) \cdot \frac{(\delta p)}{\rho_o \cdot a^2} + \frac{2 \cdot \delta p}{\rho_o \cdot a^3} \cdot \left( \frac{\partial a}{\partial S_e} \cdot \cos \beta_o + \frac{\partial a}{\partial n_e} \right) \right. \\ \left. - \frac{\delta p}{\rho_o \cdot a^2 \cdot R} - \frac{1}{\rho_o \cdot a^2} \cdot \frac{\partial(\delta p)}{\partial S_e} \cdot \cos \beta_o \right] = 0 \quad (15) \end{aligned}$$

The equation describes the disturbance of the static pressure field and is written in the external streamline coordinates system relative to the wall.

For numerical analysis purposes, the above equation can be written (Kaldellis et al. (1989)) as:

$$\frac{\partial^2(\delta p)}{\partial n_e^2} + A \cdot \frac{\partial(\delta p)}{\partial n_e} + B \cdot \frac{\partial^2(\delta p)}{\partial S_e^2} + \Gamma = 0 \quad (16)$$

A first set of boundary conditions, which is considered valid inside the interaction region, is imposed (Inger and Mason (1976)) by demanding the equality of the pressure disturbance field at the edge of the shear layer. The continuity of the streamline slope across the edge of the shear layer is used as an additional boundary condition.

The numerical solution of Eq. (16) is obtained either through a Fourier transform or by a pure finite difference scheme. In the present work, the pressure disturbance field  $\delta p(S_e, n_e)$  is calculated at any distance from the wall using the first way.

It is important to mention, that the real static pressure jump across the shock wave is needed as a boundary condition too. In order to obtain this value, a modified Rankine-Hugoniot condition is applied, taking into account the area variation across the shock wave, resulting from the shear layer presence. Then, the real static pressure jump  $\delta p_r$  can be expressed, in relation to the theoretical one  $\delta p_{in}$  given by the Rankine-Hugoniot conditions, through the following equation:

$$\frac{\delta p_r}{\delta p_{in}} = 1 - \gamma \cdot \frac{\frac{p_{ox}}{p_{oy}}}{\frac{p_{ox}}{p_{oy}} - 1} \left[ \frac{\frac{(\delta_{1w} + \delta_{1w}') \cdot M_{oy}^2}{H}}{1 - \left[ 1 + \frac{(\delta_{1w} + \delta_{1w}') \cdot M_{oy}^2}{H} \right]} \right] \quad (17)$$

This expression is introduced in the shock-shear layer calculation procedure described below and gives a good approximation of the pressure distribution under which the shear layer will develop. However, as the displacement thicknesses are not known beforehand with accuracy, an iterative procedure is necessary.

**Shock-Shear Layer Interaction Algorithm.** The two methods described above, for the calculation of compressible attached or detached turbulent shear layers and for the prediction of the static pressure field across the shock wave, are combined to set up the complete procedure for the calculation of the real flow field through the interaction region.

Before describing the calculation steps, some additional comments must be made. For confined configurations an additional viscous-inviscid interaction procedure based on the mass conservation equation must also be used (see for details Kaldellis (1988) and Kaldellis et al. (1989)), in order to protect the shear layers from excessive positive pressure gradients.

Therefore the shock-shear layer interaction calculation algorithm "INTER" consists of the following steps, see also Kaldellis (1988):

**STEP 0:** The basic external flow field quantities are supposed known, along with the inviscid static pressure jump related with the upstream Mach number.

**STEP 1:** Assume a distribution of the shear layer parameters (e.g.,  $\delta_1$ ,  $H_{12}$ , or  $\delta$ ,  $u_r$ ) for the interaction region. The choice of the initial distribution of these parameters may be sometimes crucial for the complete interaction procedure, leading to failure if the expected increase of the shear layer in the interaction zone is not at all taken into account. In this way oversimplifications, like  $\delta_1 = \text{const.}$  through out the interaction region, are not recommended. Additionally, a realistic description for the evolution of the shear layer parameters always minimizes the total number of iterations. For this reason various polynomial distributions have been numerically tested (among them the linear one used by Kallas et al. (1987)). Based on its simplicity and its minimal computational requirements a parabolic distribution is adopted here.

Thus for the displacement thickness is assumed that:

$$\delta_1 - \delta_{1x} = b \cdot (S_e - S_{ex})^2 + (S_e - S_{ex}) \quad (18)$$

where the coefficients  $b$  and  $c$  are computed using the slope of  $\delta_1$  at the beginning ( $x$ ) of the interaction zone and the value of the  $\delta_1$  at the end ( $y$ ) of it. For this purpose an empirical formulae may be used:

$$\delta_{1y} = \omega(M_e) \cdot \delta_{1x} \quad (19)$$

where  $\omega(M_e)$  is a relaxation factor, depending on the Mach number, taking values between 1.0 and 3.0. Some interesting numerical results concerning the influence of  $\omega$  will be given in the next section.

**STEP 2:** Calculate the real pressure jump across the shock wave, making use of the Eq. (17) and the displacement thickness distribution. Then calculate the static pressure field  $\delta p$  throughout the interaction region. Using the previously calculated static pressure field, calculate the rest pertinent parameters of the external flow field (e.g., velocity, density, total enthalpy, etc.). For more details see Kaldellis (1988) and Kaldellis et al. (1989).

**STEP 3:** Calculate the shear layer evolution using the equations given in Section (2). The computational algorithm by Kaldellis and Ktenidis (1990) is used.

Wall Static Pressure Distribution: Gadd's Experiment

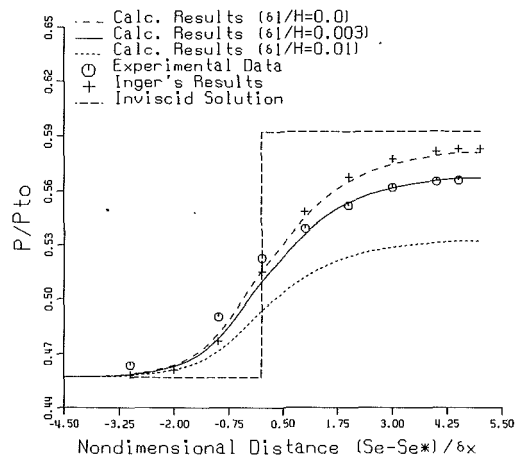


Fig. 3 The influence of the  $(\delta_1/H)$  on the wall static pressure

Wall Static Pressure Distribution ( $\mu_e = 1.32$ )

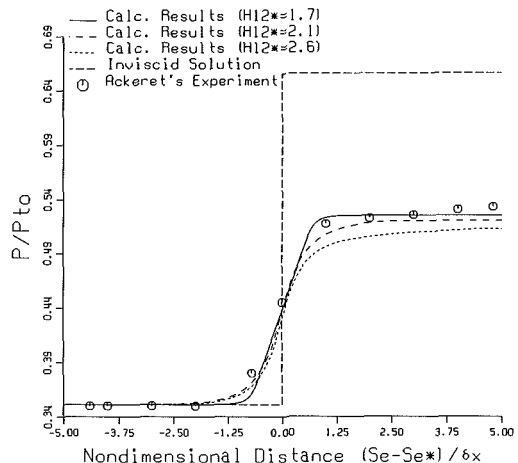


Fig. 4 The influence of the  $H_{12}^*$  on the wall static pressure

**STEP 4:** Compare the new values of the shear layer parameters with those of the previous iteration (step one). If convergence is not achieved, repeat steps two to four. Otherwise, proceed to the calculation of the shear layer downstream of the interaction region.

The above described algorithm is quite stable and presents an overlinear convergence rate. As it will be shown later, no more than five iterations are needed for complete convergence, depending of course on the comments given in step one. For a typical test case, each iteration requires approximately 50 sec CPU time on a 25 Mhz 386 machine.

#### 4. Parametrical Investigation of the Method-Convergence History

In order to investigate the influence of the shock induced shear layer blockage (i.e., ratio of  $\delta_1/H$ ) upon the static pressure field the experiment of Gadd (1961) is considered. Figure 3 shows a comparison between the wall pressure predicted by the proposed method for various  $(\delta_1/H)$  values (e.g., 0., 0.003, 0.01) and the experimental data given by Gadd for an unseparated flow field at  $M_e = 1.12$ ,  $C_f = 0.0023$  and  $H_{12}^* = 1.9$ . Note that for the unconfined case (with  $(\delta_1/H) \rightarrow 0.$ ) the results of the proposed method almost coincide with the results given by Inger and Mason (1976). The inviscid pressure distribution is also presented. The modification of the real pressure jump across the shock wave is obvious, and the static pressure rise

**Table 1. Static pressure jump across the shock wave**

$M_e$	$\delta p/P_{0x}$ Inv.	$\delta p/P_{0x}$ Real
1.10	0.1148	0.0431
1.20	0.2117	0.1639
1.30	0.2905	0.2558
1.40	0.3519	0.3227

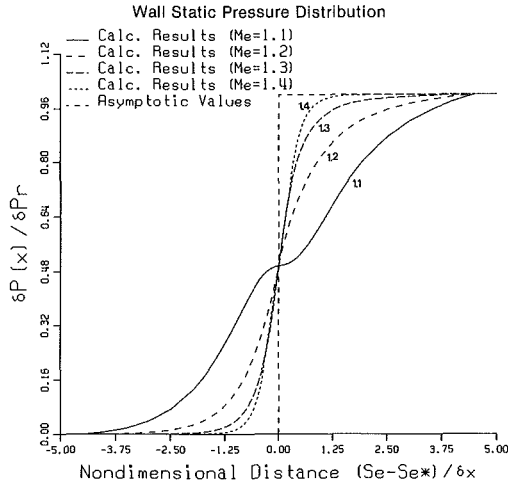


**Fig. 5 The influence of the  $M_e$  on the wall static pressure jump**

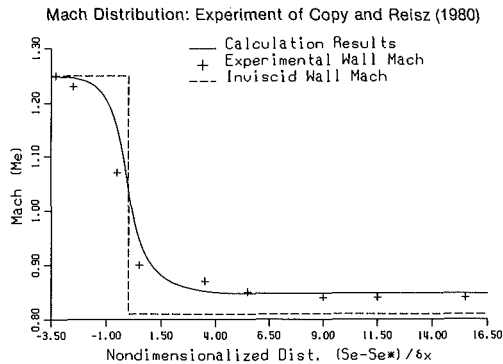


**Fig. 6 Mach distribution for the experiment of Copy and Reisz**

is reduced with the increase of the  $(\delta_1/H)$  ratio. Also note, that the results of the present method describe very well the experimental data for  $(\delta_1/H) = .003$ . Thus, while the results of Inger calculate 92 percent of the inviscid pressure rise, four boundary layer length downstream, the experiment has attained 80 percent of the inviscid pressure rise. This value is in accordance with the predicted results of the proposed method.

The influence of the momentum shape factor  $H_{12}^*$  upon the wall pressure distribution is presented in Fig. 4. A parametrical study is carried out for Ackeret's test case, with an incoming Mach of  $M_e = 1.32$ ,  $(\delta_1/H) = 0.008$  and  $\omega = 2.2$ . In this figure, besides the experimental data of Ackeret et al. (1947), the results of the present method for various typical values of  $H_{12}^*$  are given. The experimental data are satisfactorily described for  $H_{12}^* = 1.71$ . A similar  $H_{12}^*$  value ( $\approx 1.59$ ) has also been used by Panaras (1981). Additionally, according to the calculation results for lower values of  $H_{12}^*$ , the level of the downstream pressure achieves the asymptotic value almost immediately behind the shock position. On the other hand, for higher values of  $H_{12}^*$  the length of the interaction zone is greater. This behavior is justified since the subsonic part of

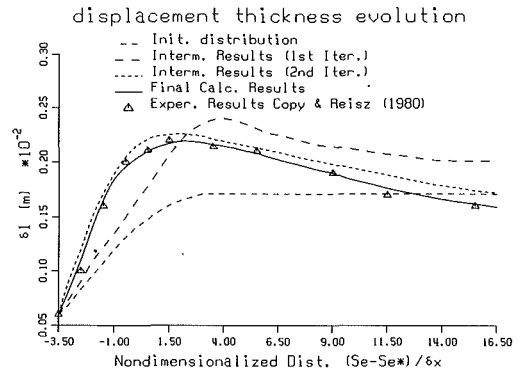


**Fig. 7 Convergence history of the algorithm "INTER". Experiment of Copy and Reisz**

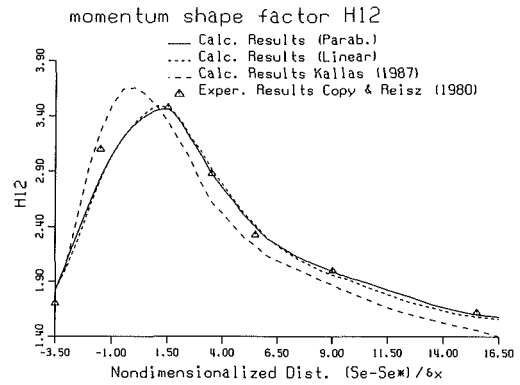


**Fig. 8 Momentum shape factor evolution for the experiment of Copy and Reisz**

the profile, which causes the diffusion of the shock pressure jump, is small.

Next the effect of incoming Mach number is presented in Fig. 5. In order to carry out a parametrical investigation a typical test case with  $\omega = \omega(M_e)$ ,  $H_{12}^* = 2.2$  and  $(\delta_1/H) = .005$  is considered. For this case, the real wall pressure jump distributions are given for a wide range of incoming Mach numbers (1.1 to 1.4), covering the area of interest. As  $M_e$  increases, the strength of the shock induced real pressure jump increases (Table 1), while the interaction region's length declines. The same trend is experimentally observed and is in agreement with Inger's comments. Note that in Fig. 5 the wall static pressure jump distributions are nondimensionalized with the corresponding asymptotic real pressure jump value for each case, given also in Table 1.

The experimental results of Copy and Reisz (1980) are used next to clarify the influence of the initial choice of the parameters of the shear layer upon the convergence rate and the quality of the results. The evolution of the Mach number inside the interaction region is presented in Fig. 6. Four iterations are only needed to describe accurately the experimental data when the parabolic initial distribution is used with  $\omega = 1.8$ . However, six iterations are needed for the linear distribution with the same  $\omega$  value, while convergence problems are encountered and more than eight iterations are needed for  $\omega = 1$  (constant  $\delta_1$  distribution), see also Eq. (19). More precisely, in Fig. 7 the convergence history of the  $\delta_1$  distribution is shown for the test case of Copy and Reisz, using the parabolic distribution with  $\omega = 1.8$  as an initial approach concerning the shear layer parameters inside the interaction region. The convergence rate is typical for all cases examined here.

Finally, the  $H_{12}$  distribution is given in Fig. 8, as it results from the proposed method, in comparison with the results given by Kallas et al. (1987) and the experimental points. The

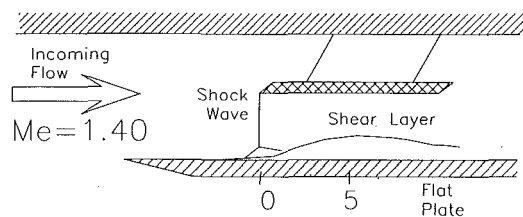


Fig. 9(a) Experiment of Kooi; experimental configuration

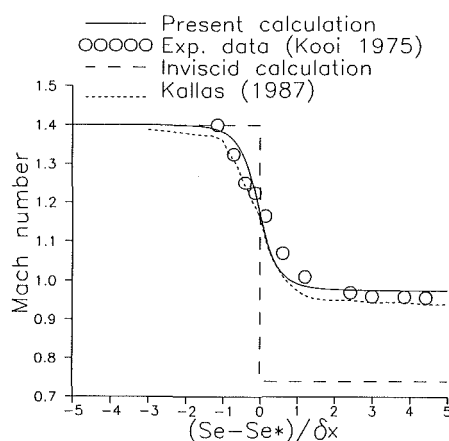


Fig. 9(b) Experiment of Kooi; Mach number distribution

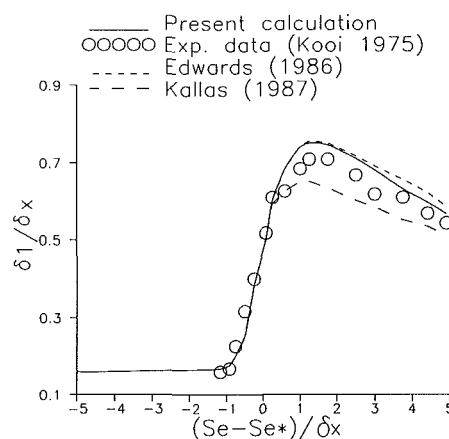


Fig. 9(c) Experiment of Kooi; displacement thickness distribution

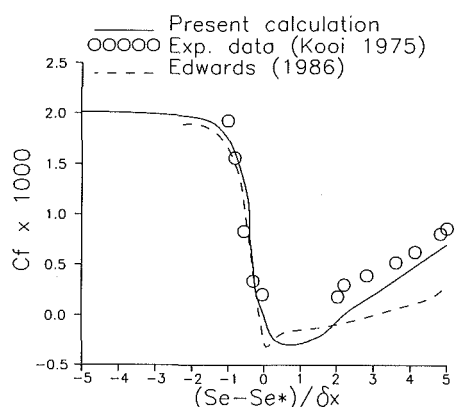


Fig. 9(d) Experiment of Kooi; friction coefficient distribution

choice of a linear or a parabolic type initial distribution, with the same  $\omega$  value, does not considerably affect the quality of the results. However, the parabolic distribution needs about 50 percent less computational time than the linear one.

## 5. Discussion of the Calculation Results

Having systematically analyzed the influence of the main flow parameters upon the pressure field, using some classical test cases, three more test cases which present flow separation or have industrial interest are investigated next.

**Kooi Separated Test Case ( $M_e = 1.40$ ).** The detailed experimental data of Kooi (1975) are used as the first test case (Fig. 9(a)) to be analyzed. For this case, the incoming Mach number is equal to 1.40 and the normal shock wave is of sufficient strength to separate the shear layer. In Fig. 9(b) the Mach number evolution is given in comparison with the experimental data and the results given by Kallas et al. (1987). The two theoretical methods predict with acceptable accuracy the real wall Mach distribution, which differs by more than 20 percent from the corresponding inviscid value. Note also that the real wall pressure attains only the 78 percent of the theoretical inviscid value downstream of the shock wave. This is mainly due to the flow acceleration imposed by the blockage effects related to the separation of the shear layer.

Subsequently, the predicted distributions of two main characteristics (i.e.,  $\delta_1$  and  $C_f$ ) of the shear layer are given in Figs. 9(c) and 9(d). In Fig. 9(c) not only the experimental data but also the results of Kallas et al. (1987) and Edwards et al. (1986) are also given for comparison. All three methods predict quite satisfactorily the experimental data. However this is not the case for the skin friction coefficient, given in Fig. 9(d). The results given by Edwards et al. (1986), for variable pressure along the shear layer and using a modified Cebeci-Smith turbulence model, underestimate the experimental skin friction and indicate a larger separated flow region than the experimental one.

**East-Wind Tunnel Test Case ( $M_e = 1.40$ ).** The test data examined here are from investigations of shock wave boundary layer interaction carried out in the 3 ft  $\times$  3 ft wind tunnel at R.A.E. In order to simulate the tests for prediction purposes the bottom half of the working section is modelled as a cascade of flat plates at 50° stagger angle and with pitch/chord ratio of 0.3, see also Fig. 10(a). More details concerning the experimental conditions are given by East (1976) and Calvert (1982).

The value of Mach number upstream of the shock is approximately 1.4 and  $Re\delta_1$  at the start of the interaction is 7000. In Figs. 10(b), 10(c) and 10(d) the predicted distributions of the wall Mach number, the displacement thickness and the boundary layer shape factor  $H_{12}$  on the suction surface are compared with the measured values along the floor of the experimental tunnel. In the same figures the results by Calvert (1982) are also given. The overall agreement between the predicted results and experimental data is good. Additionally, the values of  $\delta_1$  after the shock do not overestimate the experimental data, though the sidewall boundary layers are partially included in the present calculation using a simplified wall displacement approach. However, the results of the method concerning the  $\delta_1$  distribution almost coincide with the results of Calvert (1982) if the sidewall shear layers are not taken into account.

On the other hand, the  $H_{12}$  distribution is almost independent from the presence of the sidewall shear layers. The improvement of the results of the present calculation in comparison with the results given by Calvert (1982), is mainly related to the extended turbulence modeling (i.e., terms  $A$ , Eq. (7), and  $B$ , Eq. (8)) and the inverse way of solving the nonlinear system of equations (Kaldellis and Ktenidis, 1990).

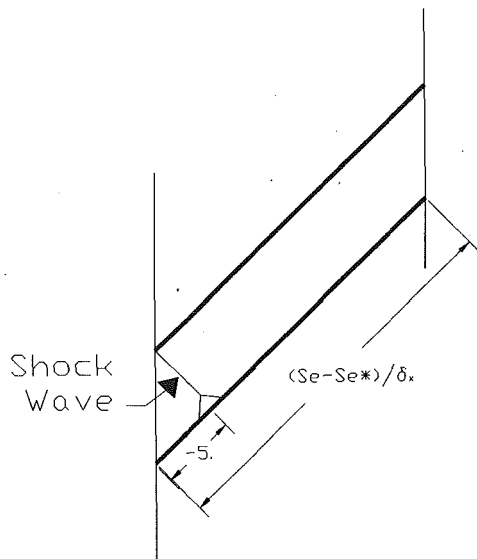


Fig. 10(a) Experiment of East; experimental configuration

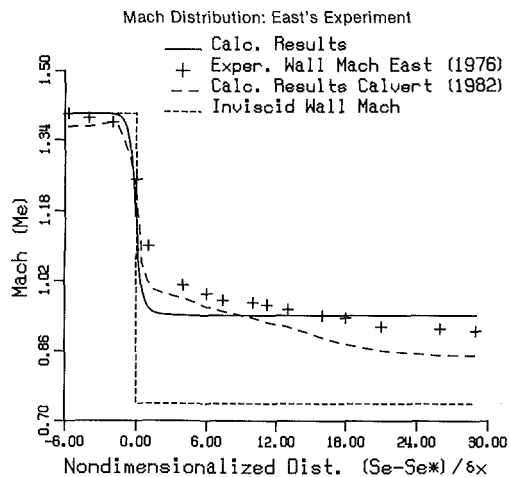


Fig. 10(b) Mach distribution for the experiment of East. Comparison between theory and experiment.

**ECL3 Supersonic Compressor-Rotating Blades ( $M_e = 1.31$ ).** In order to underline the applicability of the proposed pressure calculation method, the overall method has been used to analyze the flow field through the rotor of a supersonic axial compressor, Fig. 11(a), with a stage pressure ratio of  $\Pi_c = 1.84$ , specific mass flow rate  $m_s = 180 \text{ Kg/sec/m}^2$  and rotation speed  $n = 15965 \text{ rpm}$ . The integral equations used to analyze the flow field in the main flow direction are similar with those given in the present work (see also Kaldellis et al. (1989)). The secondary vorticity field, necessary to build the three dimensional flow field, is calculated using the secondary flow method developed by the authors (see Kaldellis, 1988; and Kaldellis and Ktenidis, 1990).

In the present analysis, the static pressure evolution along with the boundary layer thickness  $\delta$  and the wall friction velocity  $u_\tau$  are given for the tip of the rotor. The calculation results of the proposed method (Fig. 11(b, c, d)) are compared quite satisfactorily with the available experimental data at the inlet and the outlet of the rotor (see Goutines and Naviere, 1987). It is interesting to mention that for this test case the static pressure increases continuously, also far downstream of the interaction region, Fig. 11(b). Note, that the inviscid solution overpredicts by more than 15 percent the static pressure measured at the exit of the rotor.

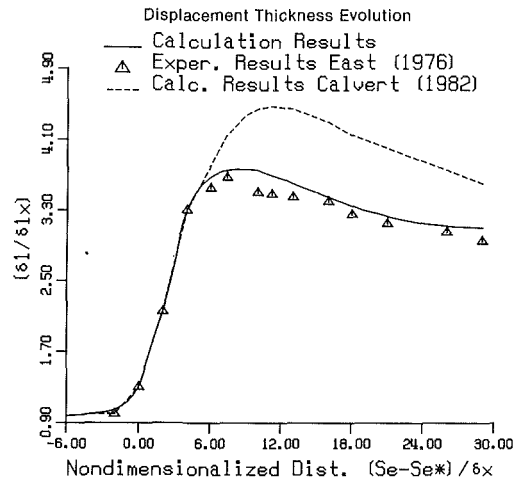


Fig. 10(c) Displacement thickness evolution. Experiment of East.

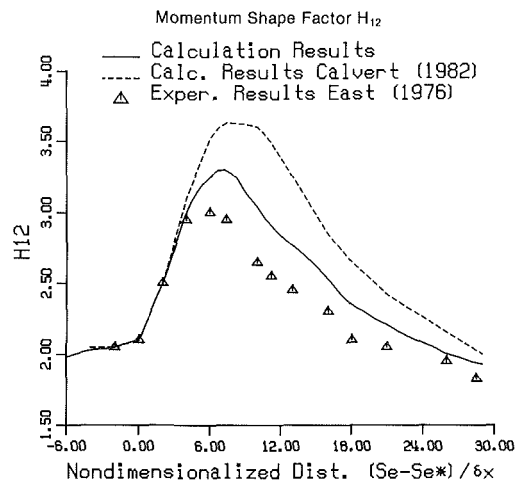


Fig. 10(d) Momentum shape factor evolution. Experiment of East.

Additionally, the tip shear layer increases very rapidly (Fig. 11(c)) after the shock wave. However, inside the rotor the shock-induced strong deceleration is balanced by the energy transfer from the rotating blades to the fluid. This fact explains why the friction velocity values (Fig. 11(d)) do not indicate flow separation, despite their strong decrease.

## 6. Conclusions

An extended shock-shear layer interaction method is developed in order to improve the understanding of the flow pattern inside the interaction region. For this purpose, the influence of the incoming Mach number and the shear layer characteristics on the complete flow field is examined in details.

Additionally, favorable comparisons are obtained between the calculation results and the corresponding experimental data for several test cases (including separation), proving the stability and the accuracy of the proposed method.

The method will be used in the near future as the main body for the investigation of the loss generation mechanisms in transonic-supersonic flow fields. It is important to mention that the losses of transonic and supersonic compressor bladings for example are mainly due to viscous effects and due to entropy rise in shock waves. Depending on the inlet Mach number, the inlet flow angle and the back pressure, the shock loss level reaches sometimes up to the 70 percent of the overall losses. Having the present work as a basis, a shock-shear layer loss model is under development. When completed, it should

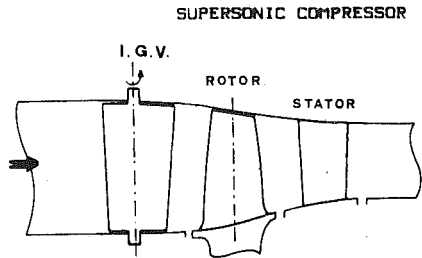


Fig. 11(a) Schematic representation of the ECL3 supersonic compressor; meridional view

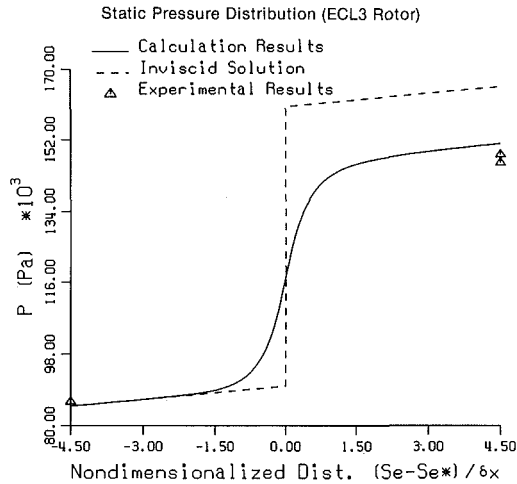


Fig. 11(b) Tip static pressure distribution for the rotor of the ECL3 supersonic compressor

lead to better blade design procedures and thus higher engine efficiencies.

## References

- 1 Ackeret, J., Feldman, F., and Rott, N., 1947, "Investigation of Compression Shocks and Boundary Layers in Gases Moving at High Speeds," NACA TM 1113.
- 2 Alkalai, K., and Leboeuf, F., 1985, "2D and 3D Potential Flows with Rotational Source Terms in Turbomachines," WAM, ASME, Miami.
- 3 Calvert, W. J., 1982, "An Inviscid-Viscous Interaction Treatment to Predict the Blade-to-Blade Performance of Axial Compressors with Leading Edge Normal Shock Waves," ASME Paper 82-GT-135.
- 4 Copy, C., and Reisz, J., 1980, "Analyse experimentale d'une interaction choc-couche limite turbulente a mach 1.3 (decollement naissant)," ONERA RT-42-7078 AY014.
- 5 Dawes, W. N., 1988, "Development of a 3D Navier-Stokes Solver for Application to All Types of Turbomachinery," ASME Paper 88-GT-70.
- 6 East, L. F., 1976, "The Application of Laser Anemometer to the Investigation of Shock-Wave Boundary-Layer Interactions," AGARD-CP-193, Applications of non-intrusive instrumentation in fluid flow research.
- 7 Edwards, D. E., Carter, J. E., and Hafez, M. M., 1986, "Viscous/Inviscid Analysis of Transonic Shock-Induced Separation Including Normal Pressure Gradients," *AIAA Journal*, Vol. 24, No. 5.
- 8 Gadd, G. E., 1961, "Interactions Between Normal Shock Waves and Turbulent Boundary Layers," ARC R&M, 3262.
- 9 Goutines, M., and Naviere, H., 1987, "Conception et Essais d' un Etage de Tete d' un Compresseur HP Avance," AGARD-CP-421, *Advanced Technology for Aero Gas Turbine Components*, Paris.
- 10 Hah, C., and Wennerstrom, A. J., 1990, "Three-Dimensional Flowfields Inside a Transonic Compressor with Swept Blades," ASME Paper GT-90-359.
- 11 Inger, G. R., and Mason, W. H., 1976, "Analytical Theory of Transonic Normal Shock-Boundary Layer Interaction," *AIAA Journal*, Vol. 14, pp. 1266-1272.
- 12 Kaldellis, J., 1988, "Computation of Shock/Secondary Flow Interaction," Doctorate thesis Thermal Turbomachines Lab., NTUA, Athens.

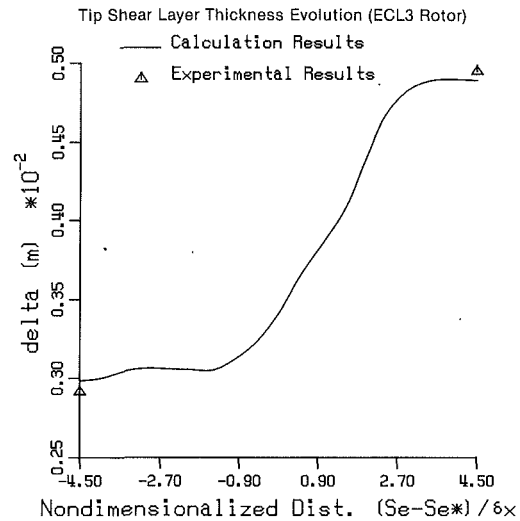


Fig. 11(c) Tip shear layer thickness evolution for the rotor of the ECL3 supersonic compressor

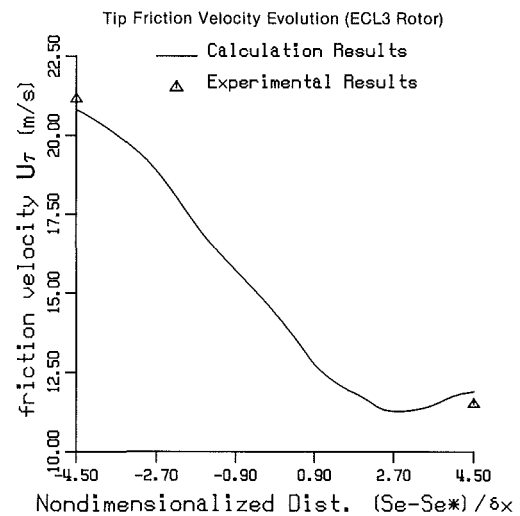


Fig. 11(d) Tip friction velocity evolution for the rotor of the ECL3 supersonic compressor

- 13 Kaldellis, J., Douvikas, D., Falchetti, F., and Papailiou, K., 1989, "A Secondary Flow Calculation Method for One Stage Axial Transonic Flow Compressors, Including Shock-Secondary Flow Interaction," ASME Paper 89-GT-210, also *ASME Journal of Turbomachinery*, Vol. 112, pp. 652-668.
- 14 Kaldellis, J., and Ktenidis, P., 1990, "High Turning Limit and Jet Like Profiles in Secondary Flow Field of Axial Turbines," ASME Paper 90-GT-327.
- 15 Kaldellis, J., Katramatos, D., and Ktenidis, P., 1991, "The Influence of Shock Waves on the Viscous Flow Field of Axial Compressors," ASME Paper 91-GT-173, Orlando, USA.
- 16 Kallas, J., and Papailiou, K., 1987, "A Method for the Calculation of the Interaction of a Turbulent Boundary Layer with a Shock Wave," 8th ISABE International Symposium, Cincinnati, Ohio, USA.
- 17 Katramatos, D., and Kaldellis, J., 1991, "3-D Loss Prediction Based on Secondary Flow and Blade Shear Layer Interaction," ASME Paper 91-GT-59, Orlando, USA.
- 18 Kooi, J. W., 1975, "Experiment on Transonic Shock-Wave Boundary Layer Interaction," AGARD-CP-168.
- 19 Panaras, A., 1981, "The Transonic Interaction of a Normal Shock with a Nonseparating Turbulent Boundary Layer," *Zeitschrift für Flugwiss, Weltraumforsch.* 5, Heft 6.

# Prediction of Turbulent Boundary Layers With a Second-Moment Closure: Part I—Effects of Periodic Pressure Gradient, Wall Transpiration, and Free-Stream Turbulence

**N. Shima**  
Professor,  
College of Engineering,  
Shizuoka University,  
Hamamatsu, 432 Japan

*The purpose of this two-part paper is to assess the performance of a second-moment closure applicable up to a wall. In the present part, the turbulence model is applied to the boundary layers with periodic pressure gradient, with wall transpiration and with free-stream turbulence. The predictions are shown to be in good agreement with experiments and a direct simulation. In particular, a tendency towards relaminarization and a subsequent retransition in the oscillating boundary layer are faithfully reproduced, and the effect of the length scale of free-stream turbulence is correctly captured.*

## 1 Introduction

Second-moment closures for turbulence generally seek a broad width of applicability. A model at this level should be tested with success in a wide range of turbulent flows before it claims to be definitely useful. The present paper reports the performance of such a turbulence model in a variety of turbulent boundary layers.

Although second-moment closures are very powerful in prediction of turbulent flows, their validity is usually limited to high-Reynolds-number regions. A representative closure of this type is the widely used model of Launder et al. (1975). Such closures, in computation of wall-bounded flows, rely on the "universal" law to specify the boundary conditions at the wall-adjacent nodes. Since, as is well-known, there are many flow situations where the "universal" law is not valid, several workers made attempts to extend the applicability right up to the wall. The turbulence model tested in the present study is such an extended closure of Launder and Shima (1989) (with some model functions recasted). Attempts at devising closures of this kind have also been made by Hanjalić and Launder (1976), by Vandromme et al. (1983), by Prud'homme and Elghobashi (1983), by Kebede et al. (1985), by So and Yoo (1986), by Shima (1988), by Launder and Tselepidakis (1988), by Shih and Mansour (1990), and by Lai and So (1990), among others.

When Launder and Shima (1989) proposed the model, they applied it to the boundary layers in zero, favorable, and adverse pressure gradients. The numerical solutions were generally in close agreement with experiments. In particular, the model

calculation reproduced a clear distinction between laminarizing flow and laminarizing flow for the sink flow boundary layer. Moreover, the model gave a reasonable level of shear stress for a strongly adverse pressure gradient case. These results clearly justify further testing of the turbulence model. In the present study, test flows are also limited to two-dimensional boundary layers. Even in this class of flows, however, there are a rich variety of effects to be considered.

The test flows in Part I of this two-part paper are as follows:

1. Oscillating boundary layer: the direct numerical simulation by Spalart and Baldwin (1989).
2. Boundary layer with wall transpiration: the experiments by Andersen et al. (1972) and Loyd et al. (1970).
3. Boundary layer with free-stream turbulence: the empirical skin-friction correlation of Hancock and Bradshaw (1983).

These flows introduce no additional terms into the governing equations for the reference case of flat-plate boundary layer (except the pressure-gradient term in the mean momentum equation). Flow cases with such additional terms are dealt with in Part II, where the effects of streamline curvature and spanwise rotation are considered.

## 2 Turbulence Model

The turbulence model employed in the present study is for incompressible flows. The stress transport model can be written as

$$\frac{D}{Dt} \overline{u_i u_j} = P_{ij} - \frac{2}{3} \delta_{ij} \epsilon + \phi_{(1)ij} + \phi_{(2)ij} + \phi_{(w1)ij} + \phi_{(w2)ij} - \frac{\partial}{\partial x_k} \left( J_{ijk} - \nu \frac{\partial}{\partial x_k} \overline{u_i u_j} \right) \quad (1)$$

Contributed by the Fluids Engineering Division for publication in the JOURNAL OF FLUIDS ENGINEERING. Manuscript received by the Fluids Engineering Division August 20, 1991. Associate Technical Editor: R. K. Agarwal.



where

$$P_{ij} = - \left( \overline{u_j u_k} \frac{\partial U_i}{\partial x_k} + \overline{u_i u_k} \frac{\partial U_j}{\partial x_k} \right) \quad (2)$$

$$\phi_{(1)ij} = - C_1 \frac{\epsilon}{k} \left( \overline{u_i u_j} - \frac{2}{3} \delta_{ij} k \right) \quad (3)$$

$$\phi_{(2)ij} = - C_2 \left( P_{ij} - \frac{2}{3} \delta_{ij} P \right) \quad (4)$$

$$\phi_{(w1)ij} = C_{w1} \frac{\epsilon}{k} \left( \overline{u_k u_m} n_k n_m \delta_{ij} - \frac{3}{2} \overline{u_k u_i} n_k n_j - \frac{3}{2} \overline{u_k u_j} n_k n_i \right) \frac{k^{3/2}}{C_f \epsilon d} \quad (5)$$

$$\phi_{(w2)ij} = C_{w2} \left( \phi_{(2)km} n_k n_m \delta_{ij} - \frac{3}{2} \phi_{(2)ik} n_k n_j - \frac{3}{2} \phi_{(2)jk} n_k n_i \right) \frac{k^{3/2}}{C_f \epsilon d} \quad (6)$$

$$J_{ijk} = - C_s \frac{k}{\epsilon} \overline{u_k u_l} \frac{\partial \overline{u_i u_j}}{\partial x_l} \quad (7)$$

$$P = - \overline{u_k u_l} \frac{\partial U_k}{\partial x_l} \quad (8)$$

with  $C_s = 0.22$  and  $C_l = 2.5$ .

The terms on the right-hand side of Eq. (1) are identified as production, dissipation, four redistributions, and diffusion. The model is an extension of the widely used high-Reynolds-number closure of Gibson and Launder (1978). While, in the parent model, the coefficients of the redistribution terms are taken to be constants, the present model makes them to depend on the two invariants of the stress anisotropy tensor  $A$ ,  $A_2$  and on the turbulence Reynolds number  $R_T$  as

$$C_1 = 1 + 2.58 A A_2^{1/4} [1 - \exp\{- (0.0067 R_T)^2\}] \quad (9)$$

$$C_2 = 0.75 A^{1/2} \quad (10)$$

$$C_{w1} = -2C_1/3 + 1.67 \quad (11)$$

$$C_{w2} = \max[2(C_2 - 1)/3 + 0.5, 0]/C_2 \quad (12)$$

where

$$A = 1 - 9A_2/8 + 9A_3/8 \quad (13)$$

$$A_2 = a_{ij} a_{ji} \quad (14)$$

$$A_3 = a_{ij} a_{jk} a_{ki} \quad (15)$$

$$a_{ij} = \overline{u_i u_j} / k - 2\delta_{ij}/3 \quad (16)$$

$$R_T = k^2/\nu\epsilon \quad (17)$$

Lumley (1978) has shown that the invariant  $A$  vanishes in the limit of two-dimensional turbulence. He has also argued that, in the limit, the coefficient of the Rotta term  $C_1$  should reduce to unity to satisfy the realizability condition if the high-Reynolds-number dissipation model,  $-2\delta_{ij}\epsilon/3$ , is retained. This constraint also emerges when one examines the behavior of the exact pressure-strain correlation and dissipation at a wall where turbulence becomes two-dimensional (Shima, 1988). The function  $C_1$  satisfies this requirement at the wall by employing the invariant  $A$ . The coefficient of the mean-strain part of redistribution  $C_2$  has been made to approach zero as the wall is approached so as to reduce the "isotropization-of-production" agency. The stress transport model thus incorporates the effect of high anisotropy of turbulent stresses as well as the effect of low Reynolds number in the immediate vicinity of the wall. The particular choices for the four model functions have been made principally by reference to relative levels of the Reynolds stresses in the flat-plate boundary layer.

The dissipation-rate transport model is given by

$$\frac{D\epsilon}{Dt} = (C_{e1} + \psi_1 + \psi_2) \frac{\epsilon}{k} P - C_{e2} \frac{\epsilon \tilde{\epsilon}}{k} + \frac{\partial}{\partial x_k} \left( C_\epsilon \frac{k}{\epsilon} \overline{u_k u_l} \frac{\partial \epsilon}{\partial x_l} + \nu \frac{\partial \epsilon}{\partial x_k} \right) \quad (18)$$

with  $C_{e1} = 1.45$ ,  $C_{e2} = 1.9$ , and  $C_\epsilon = 0.18$ , where

$$\tilde{\epsilon} = \epsilon - 2\nu \left( \frac{\partial k^{1/2}}{\partial x_l} \right)^2 \quad (19)$$

$$\psi_1 = 1.5A(P/\epsilon - 1) \quad (20)$$

$$\psi_2 = 0.35(1 - 0.3A_2) \exp[-(0.002R_T)^{1/2}] \quad (21)$$

If the two functions  $\psi_1$  and  $\psi_2$  appearing in the coefficient of the generation term are removed (and  $\tilde{\epsilon}$  is replaced by  $\epsilon$ ), this model again reduces to the parent model of Gibson and Launder (1978). These two functions have been introduced to produce proper length scales in the boundary layers in pressure gradients. The function  $\psi_1$  augments the wake component of boundary layers especially in adverse pressure gradients by reducing the turbulence length scale in the outer layer. The function  $\psi_2$  in contrast prevents too early laminarization in accelerated boundary layers.

The stress and  $\epsilon$  transport models given above are essentially those of Launder and Shima (1989); the difference lies just in values of the constants in the functions  $\psi_1$  and  $\psi_2$ . In the course of the present study, it has been found that the Launder and

## Nomenclature

$C_f$  = skin friction coefficient  
 $d$  = distance from wall  
 $D$  = channel width  
 $f$  = frequency  
 $k$  = turbulence energy  
 $n_i$  = unit vector normal to wall  
 $P$  = production rate of turbulence energy  
 $R$  = local radius of wall curvature  
 $R_T$  = turbulence Reynolds number =  $k^2/\nu\epsilon$   
 $t$  = time  
 $u, v, w$  = velocity fluctuations in  $x, y, z$  directions  
 $u', v', w'$  = rms velocity fluctuations

$u_i$  = velocity fluctuation vector  
 $U_i$  = mean velocity vector  
 $U, V$  = mean velocities in  $x, y$  directions  
 $U_m$  = bulk mean velocity through channel  
 $U_0$  = peak free-stream velocity  
 $U_p$  = potential flow velocity  
 $U_{pw}$  = potential flow velocity at wall  
 $U_r$  = friction velocity  
 $U^+$  =  $U/U_r$   
 $V_w$  = normal mean velocity at wall  
 $x$  = streamwise coordinate  
 $x_i$  = Cartesian coordinates  
 $y$  = coordinate normal to

wall (measured from wall)  
 $y^+$  =  $U_r y/\nu$   
 $z$  = spanwise coordinate  
 $\delta$  = boundary layer thickness  
 $\delta_l$  =  $(2\nu/f)^{1/2}$   
 $\epsilon$  = dissipation rate of turbulence energy  
 $\nu$  = kinematic viscosity  
 $\rho$  = density  
 $\tau$  = total shear stress  
 $\tau_w$  = wall shear stress  
 $\phi$  = phase angle =  $ft$   
 $\Omega$  = rotation rate  
 $\Omega_i$  = rotation rate vector

## Subscript

$e$  = free-stream

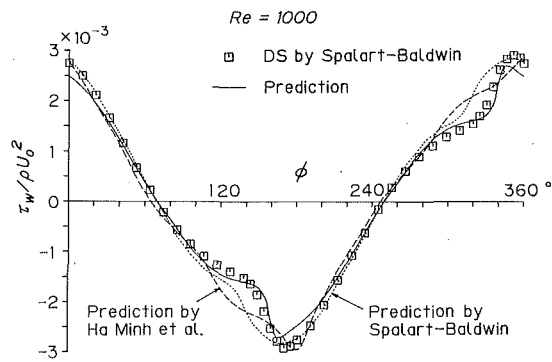


Fig. 1 Wall shear stress (oscillating boundary layer)

Shima's choice yields too low skin friction for fully developed channel flow. This is why the functions are recasted; the present choice gives good predictions for the fully-developed flow (as will be shown in Part II) and also for the boundary layer cases dealt with by Launder and Shima (1989).

The numerical solutions have been obtained with a solver developed by Launder and Shima (1989). It is based on the solver PASSABLE (Leschziner, 1982), a finite-volume parabolic code for computing two-dimensional boundary layers with turbulence models of high-Reynolds-number type. The wall function approach of the original version is discarded since the present model is applied right up to the wall itself. There the relation  $\epsilon = 2\nu(\partial k^{1/2}/\partial y)^2$ , which holds exactly, is applied as the boundary condition for the dissipation rate. Other variables (except the normal mean velocity in the case of wall transpiration) are, of course, set to zero at the wall. In the present code, the computational node for the shear stress is staggered to ensure the stability in computation. Except where otherwise indicated, the computations have been made with 71 nodes across the boundary layer, concentrated towards the wall. Launder and Shima (1989) made computations of four boundary layers with 71 and 121 nodes using the solver and found that the differences between the two sets of solutions were imperceptible. This indicates that computations with 71 nodes give grid-independent solutions if a substantial proportion of the nodes are located in the near-wall sublayer. In the present computations, it has been ensured that the number of the nodes located in the sublayer ( $y^+ < 50$ ) is, at least, comparable to that in the Launder and Shima's computations with 71 nodes.

### 3 Oscillating Boundary Layer

The boundary layer under a free-stream whose velocity varies in time as

$$U_e = U_0 \cos(ft) \quad (22)$$

is considered. Spalart and Baldwin (1989) have provided detailed data of direct simulations of the flow, which are employed to assess the performance of the present model. The flow is attractive because it has a rich variety of behaviors associated with the varying pressure gradient. Moreover, its configuration is very simple; the Reynolds-averaged quantities depend only on the phase angle and the distance from the wall. Due to these aspects, the flow may be considered as an advanced standard test case for turbulence models. In the flow, the law of the wall does not hold during at least part of the cycle. Therefore, a model applicable up to the wall itself, such as the present one, is needed to predict this flow. Our aim in this case is to see whether the present model, which was previously validated for the positive and negative pressure gradient cases separately, can faithfully reproduce the flow in which both gradients appear successively with time.

A care is needed in setting the phase angle step in the numerical computation because, as shown later, the flow shows

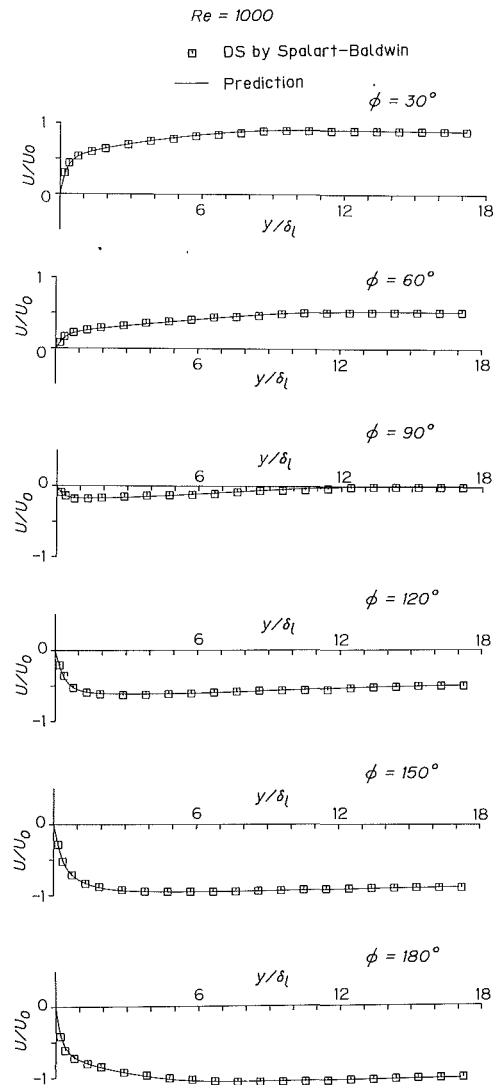
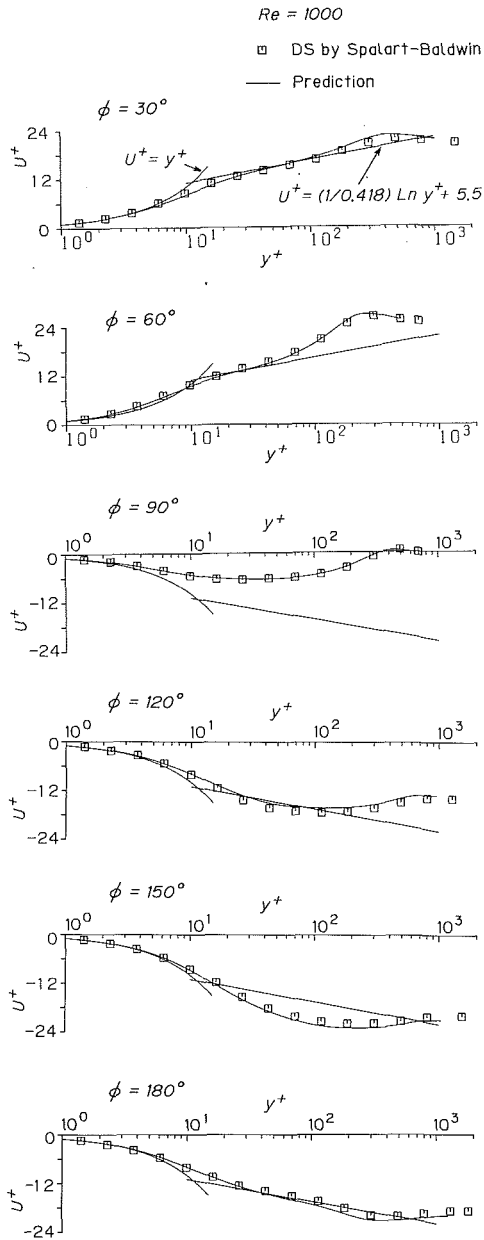


Fig. 2 Mean velocity profiles (oscillating boundary layer)

a sharp "retransition" that follows a tendency towards relaminarization during the acceleration phase. The computation was first carried out using the step 1 deg, but it did not reproduce the sharp retransition. In contrast, computations with 1/20 and 1/40 deg captured the behavior, and the difference between the two solutions was sufficiently small. The results shown below are those with the step 1/40 deg. Kebede et al. (1985) have reported a similar sensitivity to the step size in computation of a periodic pipe flow.

The nondimensional parameter governing the flow is the Reynolds number  $Re = U_0 \delta_l / \nu$ , where the characteristic thickness  $\delta_l = (2\nu/f)^{1/2}$ . The value has been set to 1000, for which Spalart and Baldwin (1989) have provided the most detailed data.

The variation of the wall shear stress with the phase angle is shown in Fig. 1, where the present prediction is compared with the direct simulation data. Also included are a one-equation model prediction by Spalart and Baldwin (1989) and a prediction with a (compressible) second-moment closure (Vandromme et al., 1983) by Ha Minh et al. (1989). The direct simulation shows a diminished gradient in the wall shear stress variation beginning at a phase angle of about 120 deg. According to Spalart and Baldwin, the behavior is attributed to a tendency towards relaminarization caused by the strong favorable pressure gradient. The tendency persists to a phase angle of about 150 deg, at which a sharp rising in the wall



**Fig. 3 Mean velocity profiles in wall coordinates (oscillating boundary layer)**

shear stress occurs associated with a “retransition” due to the declining acceleration. It is seen that these complex behaviors are faithfully reproduced by the present model. Overall agreement is also good, though discrepancies exist in the peak value and its location. The two other predictions give peak values better than the present one. The model of Spalart and Baldwin also produces the process of relaminarization and retransition, but the latter occurs too early. The process is less evident in the result of Ha Minh et al.

Figure 2 shows the mean velocity profiles. The agreement between the direct simulation and the prediction is almost perfect in this linear plot. Figure 3 shows the velocity profiles in wall coordinates. It is seen that the present model reproduces various features shown by the direct simulation, including the existence of the log-law region at  $\phi = 30$  deg, the large wake component at  $\phi = 60$  deg just before the separation, and the profile without the log-law region at  $\phi = 150$  deg that is characteristic of laminarizing boundary layers.

Figures 4 and 5 show the profiles of the Reynolds and total shear stresses and of the turbulence intensities, respectively.

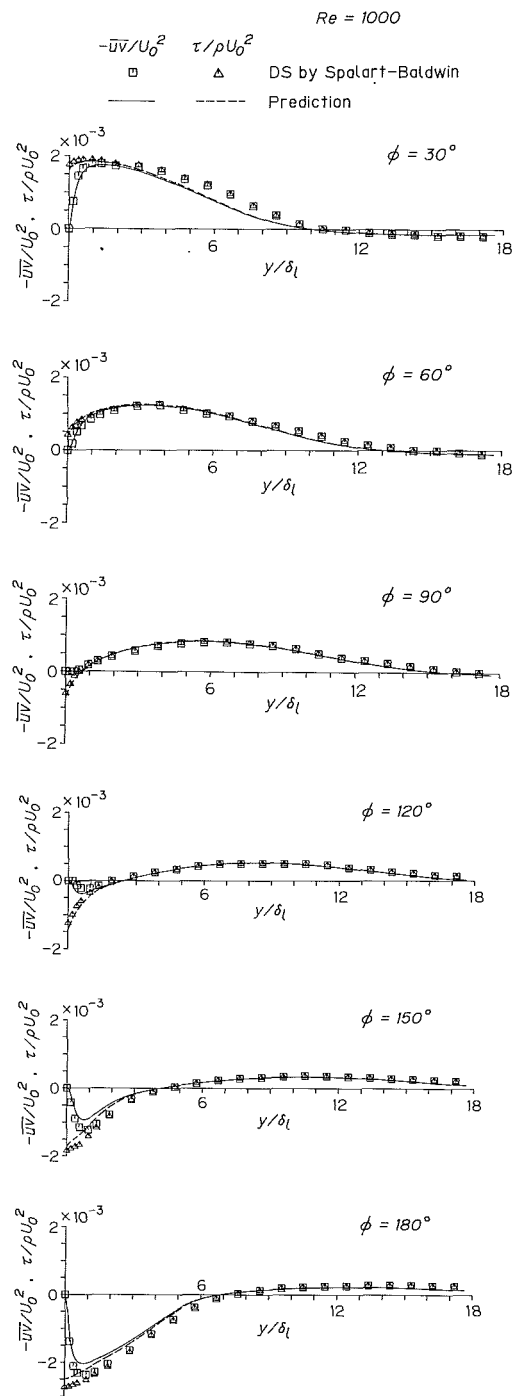


**Fig. 4 Shear stress profiles (oscillating boundary layer)**

The deceleration causes the decrease in the shear stress. Hence the production of  $u^2$  diminishes, and the Reynolds stresses become highly isotropic. The converse behavior appears during the acceleration phase; the stress redistribution process is not so rapid as to prevent the high anisotropy at  $\phi = 150$  deg. The present model faithfully reproduces these features. Quantitatively, the shear stresses near the wall at  $\phi = 150$  and  $180$  deg are somewhat too low.

As a whole the performance of the present model is excellent in this case. The present results further validate the model functions (9)–(12), (20), and (21). In particular, the function  $\psi_2$ , which was previously introduced to control a relaminarization process, works well in the situation where the laminarization is followed by a retransition.

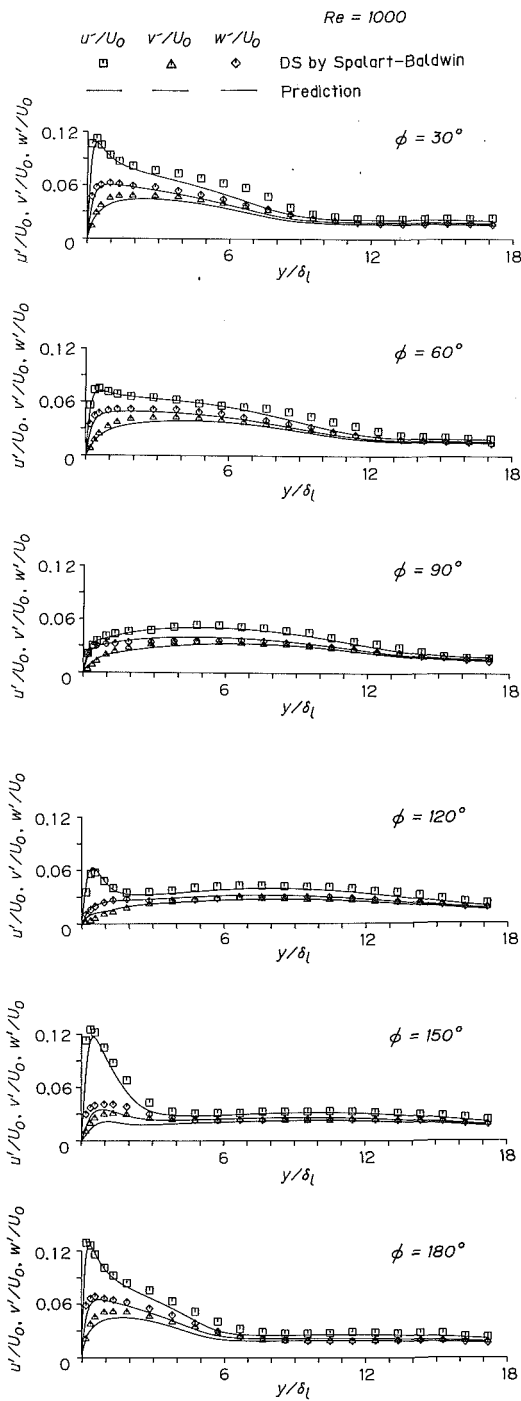


Fig. 5 Turbulence intensity profiles (oscillating boundary layer)

#### 4 Boundary Layer With Transpiration

The boundary layers with blowing or suction at the wall are of practical importance because they appear in the transpiration cooling and the boundary layer control. In the present study, the case of normal and continuous transpiration through a porous wall is considered. Since the present model is applicable right up to the wall, no special treatments are needed to deal with the transpiration except for the wall boundary condition for the normal mean velocity. Low-Reynolds-number  $k - \epsilon$  models neither need special treatments, but the prediction with such a model gives too large friction coefficients (Kline et al., 1981).

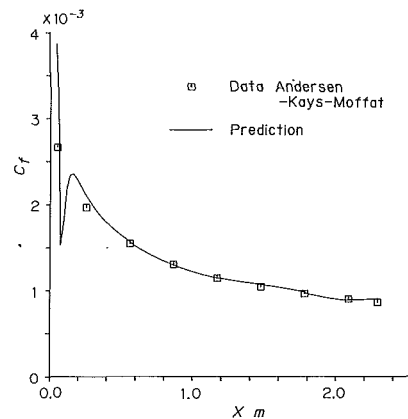


Fig. 6 Skin friction coefficient (transpiration, Case 1)

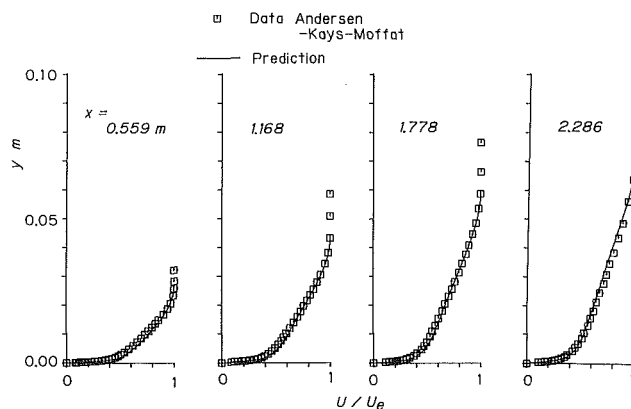


Fig. 7 Mean velocity profiles (transpiration, Case 1)

The test cases are as follows.

Case 1:  $U_e$  constant (zero pressure gradient),  $V_w/U_e = 0.00375$  (blowing); experiment by Andersen et al. (1972)

Case 2:  $U_e \propto x^{-0.15}$  (adverse pressure gradient),  $V_w/U_e = 0.004$  (blowing); experiment by Andersen et al. (1972)

Case 3:  $K \equiv \nu U_e^{-2} dU_e/dx = 2.6 \times 10^{-6}$  (favorable pressure gradient),  $V_w/U_e = 0.004$  (blowing); experiment by Loyd et al. (1970)

Case 4:  $U_e \propto x^{-0.15}$  (adverse pressure gradient),  $V_w/U_e = -0.004$  (suction); experiment by Andersen et al. (1972)

Of these cases, Cases 1 and 4 have been selected as test cases (Cases 0241 and 0242) at the 1980-81 Stanford Conference (Kline et al., 1981).

Figures 6 and 7 show the results of Case 1. In blown boundary layers, the total shear stress increases with the distance from the wall in the vicinity of the wall. In this respect, the effect of blowing is similar to the effect of adverse pressure gradient. In fact, in blown boundary layers, the friction coefficient becomes smaller and the velocity profile becomes less full than those in the flat-plate boundary layer. Such a development is seen to be closely predicted in Figs. 6 and 7.

Figures 8 and 9 show the friction coefficient and the mean velocity profiles of Case 2. In this case, the shear stress rising with the distance from the wall is enhanced by two agencies, i.e., the blowing and the adverse pressure gradient. Hence, the experiment shows a situation on the verge of separation. The agreement between the experiment and the prediction is less close than in Case 1; the calculated result in downstream region is even nearer to the separation than the experimental data. The prediction is thus not entirely satisfactory, but it should be noted that this is a difficult case both for prediction and for accurate measurement. Figure 10 shows the normal stress profiles at a location ( $x = 1.778$  m) in Case 2. The data show large maxima midway in the boundary layer corresponding to

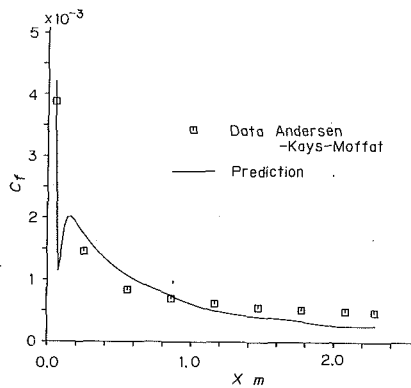


Fig. 8 Skin friction coefficient (transpiration, Case 2)

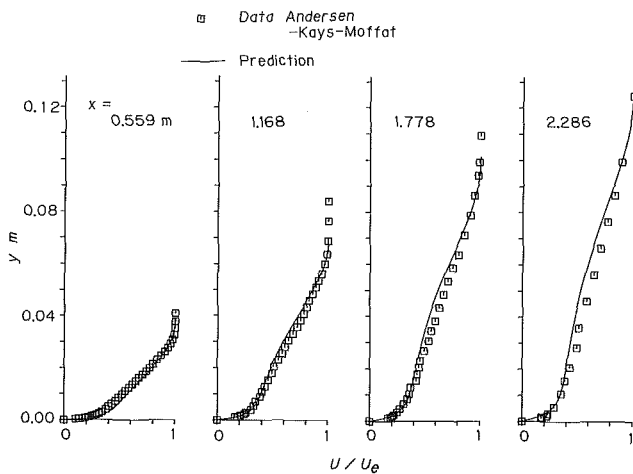


Fig. 9 Mean velocity profiles (transpiration, Case 2)

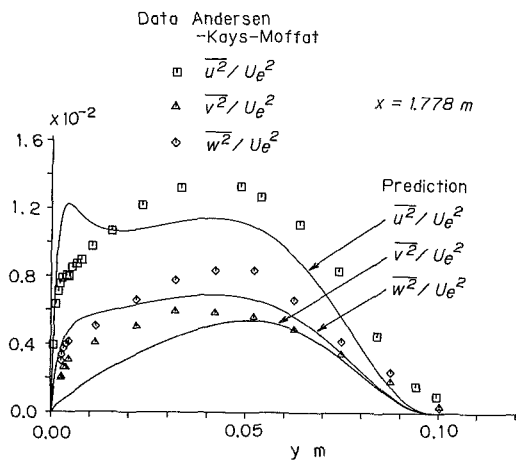


Fig. 10 Normal stress profiles (transpiration, Case 2)

the rising shear stress, and this feature is reproduced well by the calculation. In the vicinity of the wall, the calculated  $\overline{u^2}$  is too high, giving another distinct maximum, while the experimental data just bear a slight mark of the maximum. In the region the calculated  $\overline{v^2}$ , the most important normal stress for prediction of mean flow fields, is somewhat too low. These results suggest a weakness of the redistribution model.

In Case 3, the favorable pressure gradient acts to make the gradient of total shear stress negative at the wall, while the blowing acts to make it positive. In Case 4, the roles of the pressure gradient and the transpiration are interchanged. The results of these two cases are shown in Figs. 11-14. The mean velocity profiles of these cases are reproduced well by the

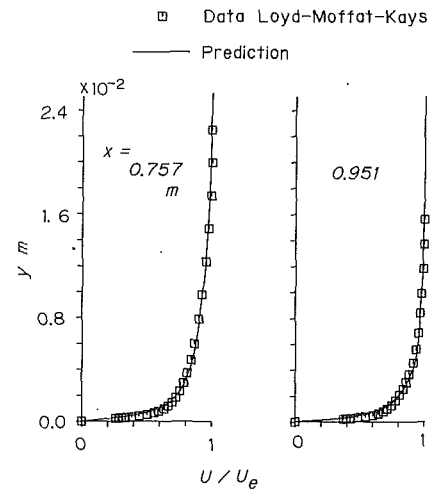


Fig. 11 Mean velocity profiles (transpiration, Case 3)

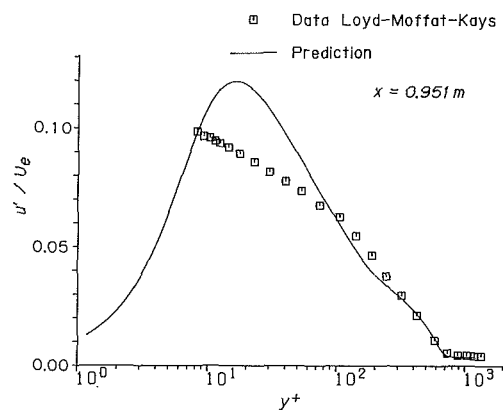


Fig. 12 Streamwise turbulence intensity profile (transpiration, Case 3)

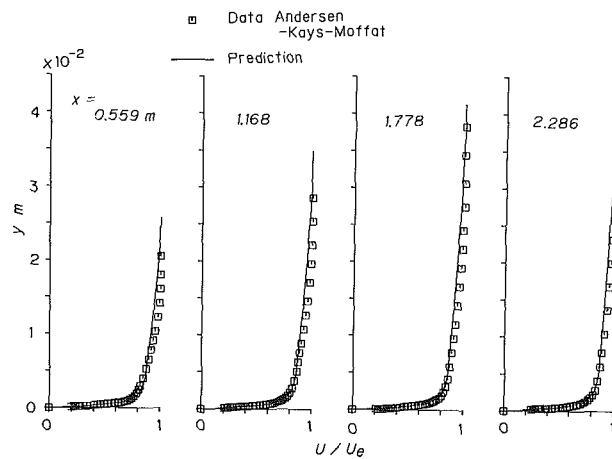


Fig. 13 Mean velocity profiles (transpiration, Case 4)

predictions, though in Case 4 the velocity defect in the outer layer is somewhat too large. In Case 3, the predicted peak value in the streamwise turbulence intensity is too high. Although the figure is not shown for brevity, the agreement at an upstream station ( $x = 0.757$  m) is better than in Fig. 12. In the experiment the intensity (normalized with  $U_e$ ) in the buffer region decreases in the downstream direction, while in the prediction it does not vary significantly.

## 5 Boundary Layer With Free-Stream Turbulence

It is well known that free-stream turbulence causes an increase in skin friction. The effect is of practical importance

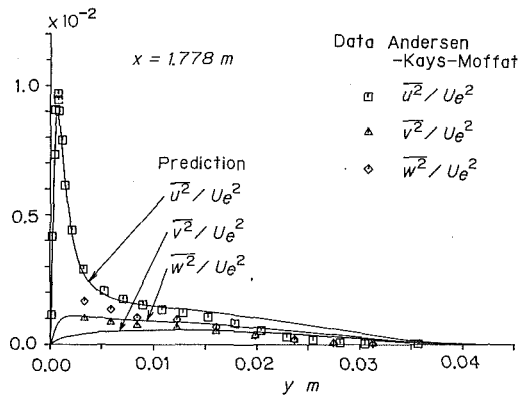


Fig. 14 Normal stress profiles (transpiration, Case 4)

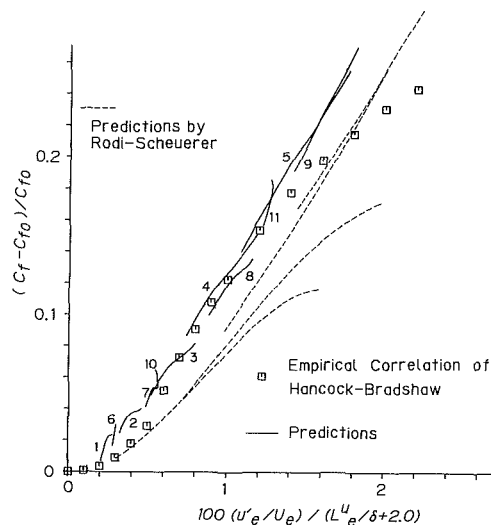


Fig. 15(a) Fractional change in skin friction coefficient as a function of free-stream turbulence intensity and length scale

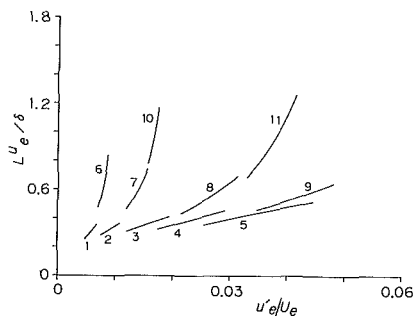


Fig. 15(b) Free-stream turbulence intensity and length scale in predictions (the numbers corresponding to those in Fig. 15(a))

because such a flow appears in various engineering applications; an example is the boundary layer on the blades of the later rows in a multistage axial turbomachine. Hancock and Bradshaw (1983) proposed an empirical correlation between the fractional increase in skin friction and a single parameter involving the intensity and length scale of free-stream turbulence. The correlation (with a slight modification) was selected as a test case (Case 0211) at the 1980-81 Stanford Conference (Kline et al., 1981), where  $k - \epsilon$  models were found to give considerably low increase in skin friction as compared to the empirical correlation. Rodi and Scheuerer (1985) obtained similar results from calculations using a  $k - \epsilon$  model and the second-moment closure of Gibson and Launder (1978). They pointed out that the models did not capture the effect of the length scale of free-stream turbulence.

Our aim in this section is to see whether the present model does or does not reproduce the empirical correlation. The calculation has been made with a minor change of a model constant: the value 0.0067 in Eq. (9) has been replaced by 0.0063, which gives slightly better values for the friction coefficient in the reference case of negligible free-stream turbulence. This minor change, however, will hardly affect the results presented below. (This is the only change in model constants throughout Parts I and II of the paper.)

Figure 15(a) compares the correlation of Hancock and Bradshaw with the results of 11 runs of the present calculation. Also included are the results of 4 runs of the second-moment closure prediction by Rodi and Scheuerer (1985) mentioned above. Here,  $C_f$  and  $C_{f0}$  ( $C_f$  for negligible free-stream turbulence) are determined at the same momentum-thickness Reynolds number, and the length scale of free-stream turbulence  $L_e^u$  is defined by

$$U_e \frac{du_e^2}{dx} = - \frac{u_e^{2.3/2}}{L_e^u} \quad (23)$$

Figure 15(b) shows the variations of the intensity and length scale of free-stream turbulence in the present predictions. The plot like Fig. 15(b) is not available in the Rodi and Scheuerer's paper. Their calculations started with  $u_e'/U_e = 0.1$  or  $0.15$  and  $L_e^u/\delta = 1$  or  $5$ , the four combinations corresponding to the four runs in Fig. 15(a). They obtained the solution independent of the starting conditions after approximately  $20\delta$  and plotted the subsequent region.

Some aspects of the present calculation should be noted. The fluctuating velocity component normal to the wall is attenuated by the presence of the wall. The turbulence model incorporates this real effect through the wall-reflection redistribution terms, Eqs. (5) and (6). Therefore, the calculation should employ a relatively large width normal to the wall to specify the free-stream turbulence sufficiently far away from the wall. When such calculations were made with a large number of nodes (141 points), it was found that the influence of initial distributions persisted for a long distance. Consequently, the solutions obtained, which are independent of initial distributions, cover a relatively narrow range of the intensity and length scale of free-stream turbulence, Fig. 15(b). Even with the wide computational width normal to the wall, the turbulence at the edge inevitably becomes anisotropic; the turbulence intensity normal to the wall is 9-15 percent smaller than the streamwise intensity. (The distance between the wall and the edge ranges from 1.0 to 4.2 times  $L_e^u$ .) However, the empirical correlation is also based on experiments with anisotropy; the intensities of the lateral components are smaller by 5-10 percent than the longitudinal component intensity (Hancock and Bradshaw, 1983; Kline et al., 1981). Therefore, it appears safe to make a comparison between the correlation and the prediction.

It is seen from Fig. 15(a) that, over an intermediate range of the free-stream parameter of Hancock and Bradshaw, the present predictions agree well with the correlation. For higher values of the parameter, however, a discrepancy is evident; the effect of free-stream turbulence tends to saturate in the empirical correlation, while the prediction still shows a steep increase in skin friction. For small values of the parameter, the prediction by Rodi and Scheuerer is better than the present prediction. As a whole, the present results are better than those in previous studies mentioned earlier including the Rodi and Scheuerer's prediction. In particular, the present model has captured the decrease of the free-stream turbulence effect with increasing length scale. It should be noted that values of the length scale parameter in the predictions [Fig. 15(b)] are smaller than those in experiments from which the correlation was deduced (Hancock and Bradshaw, 1983) ( $L_e^u/\delta$  ranges from 0.7 to 5 in the experiment by Hancock and Bradshaw and from 0.2 to 1.8 in the experimental data used by them.) However,

it is unlikely that the model will produce much different behaviors at higher length scales.

The reason why the present model produces the results distinct from previous studies is traced to the model function  $\psi_1$  in the dissipation-rate transport model. As described earlier, the function was previously introduced to reduce the length scale in the outer layer of boundary layers in adverse pressure gradients. In the present flow, in contrast to that case, the function perhaps acts to increase the length scale in the outer layer by reducing the generation of  $\epsilon$ . Consequently, the wake component decreases and the skin friction increases as compared to the case without the function. Once the model is fixed (and a proper level of  $\epsilon$  generation is ensured), the effect of free-stream turbulence decreases with increasing length scale, as already shown. This behavior is attributable to the attenuation of the fluctuation normal to the wall through the wall-reflection redistribution, as suggested by Hancock and Bradshaw (1983).

## 6 Concluding Remarks

Predictions have been made of the boundary layers with periodic pressure gradient, with wall transpiration and with free-stream turbulence. In general, the agreement with experiments and a direct simulation is quite good.

The present second-moment closure is applicable right up to a wall, and therefore can be used to predict the oscillating boundary layer. The model has successfully captured the tendency towards relaminarization in the boundary layer. The good predictions of the case of transpiration have been obtained by simply imposing the boundary condition for the normal mean velocity at the wall itself. Although the present model was devised as an extension of a widely used high-Reynolds-number closure, the extension is not restricted to the low-Reynolds-number effect. In the case of free-stream turbulence (which mainly affect the outer layer), a model function in the dissipation-rate transport model has led to predictions distinct from those of the parent model.

## References

Andersen, P. S., Kays, W. M., and Moffat, R. J., 1972, "The Turbulent Boundary Layer on a Porous Plate: An Experimental Study of the Fluid Mechanics for Adverse Free-Stream Pressure Gradients," Thermosciences Division, Department of Mechanical Engineering, Stanford University, Report No. HMT-15.

Gibson, M. M., and Launder, B. E., 1978, "Ground Effects on Pressure Fluctuations in the Atmospheric Boundary Layer," *Journal of Fluid Mechanics*, Vol. 86, pp. 491-511.

Ha Minh, H., Viegas, J. R., Rubesin, M. W., Vandromme, D. D., and Spalart, P., 1989, "Physical Analysis and Second-Order Modelling of an Unsteady Turbulent Flow: The Oscillating Boundary Layer on a Flat Plate," *Proceedings 7th Symposium on Turbulent Shear Flows*, Stanford University, pp. 11.5.1-11.5.6.

Hancock, P. E., and Bradshaw, P., 1983, "The Effect of Free-Stream Turbulence on Turbulent Boundary Layers," *ASME JOURNAL OF FLUIDS ENGINEERING*, Vol. 105, pp. 284-289.

Hanjalić, K., and Launder, B. E., 1976, "Contribution Towards a Reynolds-Stress Closure for Low-Reynolds-Number Turbulence," *Journal of Fluid Mechanics*, Vol. 74, pp. 593-610.

Kebede, W., Launder, B. E., and Younis, B. A., 1985, "Large-Amplitude Periodic Pipe Flow: A Second-Moment Closure Study," *Proceedings 5th Symposium on Turbulent Shear Flows*, Cornell University, New York, pp. 16.23-16.29.

Kline, S. J., Cantwell, B. J., and Lilley, G. M. (eds.), 1981, *Proceedings 1980-81 AFOSR-HTTM-Stanford Conference on Complex Turbulent Flows*, Department of Mechanical Engineering, Stanford University, Stanford.

Lai, Y. G., and So, R. M. C., 1990, "On Near-Wall Turbulent Flow Modelling," *Journal of Fluid Mechanics*, Vol. 221, pp. 641-673.

Launder, B. E., Reece, G. J., and Rodi, W., 1975, "Progress in the Development of a Reynolds-Stress Turbulence Closure," *Journal of Fluid Mechanics*, Vol. 68, pp. 537-566.

Launder, B. E., and Shima, N., 1989, "Second-Moment Closure for the Near-Wall Sublayer: Development and Application," *AIAA Journal*, Vol. 27, pp. 1319-1325.

Launder, B. E., and Tselepidakis, D. P., 1988, "Contribution to the Second-Moment Modelling of Sublayer Turbulent Transport," *Zarić Memorial Intl Seminar on Near-Wall Turbulence*, Dubrovnik, Yugoslavia.

Leschziner, M. A., 1982, "An Introduction and Guide to PASSABLE," Thermofluids Division, Department of Mechanical Engineering, UMIST.

Loyd, R. J., Moffat, R. J., and Kays, W. M., 1970, "The Turbulent Boundary Layer on a Porous Plate: An Experimental Study of the Fluid Dynamics with Strong Favorable Pressure Gradients and Blowing," Thermosciences Division, Department of Mechanical Engineering, Stanford University, Report No. HMT-13.

Lumley, J. L., 1978, "Computational Modeling of Turbulent Flows," *Advances in Applied Mechanics* 18, ed. C.-S. Yih, Academic, pp. 123-176.

Prud'homme, M., and Elghobashi, S., 1983, "Prediction of Wall-Bounded Turbulent Flows with an Improved Version of a Reynolds-Stress Model," *Proceedings 4th Symposium on Turbulent Shear Flows*, Karlsruhe, pp. 1.7-1.12.

Rodi, W., and Scheuerer, G., 1985, "Calculation of Turbulent Boundary Layers Under the Effect of Free Stream Turbulence," *Proceedings 5th Symposium on Turbulent Shear Flows*, Cornell University, New York, pp. 2.19-2.25.

Shih, T. H., and Mansour, N. N., 1990, "Modelling of Near-Wall Turbulence," *Engineering Turbulence Modelling and Experiments*, eds., W. Rodi and E. N. Ganić, Elsevier, pp. 13-22.

Shima, N., 1988, "A Reynolds-Stress Model for Near-Wall and Low-Reynolds-Number Regions," *ASME JOURNAL OF FLUIDS ENGINEERING*, Vol. 110, pp. 38-44.

So, R. M. C., and Yoo, G. J., 1986, "On the Modelling of Low-Reynolds-Number Turbulence," NASA, CR-3994.

Spalart, P. R., and Baldwin, B. S., 1989, "Direct Simulation of a Turbulent Oscillating Boundary Layer," *Turbulent Shear Flows 6*, eds. J.-C. André et al., Springer-Verlag, pp. 417-440.

Vandromme, D., Ha Minh, H., Viegas, J. R., Rubesin, M. W., and Kollmann, W., 1983, "Second Order Closure for the Calculation of Compressible Wall Bounded Flows With an Implicit Navier-Stokes Solver," *Proceedings 4th Symposium on Turbulent Shear Flows*, Karlsruhe, pp. 1.1-1.6.



# Prediction of Turbulent Boundary Layers With a Second-Moment Closure: Part II—Effects of Streamline Curvature and Spanwise Rotation

N. Shima

Professor,  
College of Engineering,  
Shizuoka University,  
Hamamatsu, 432 Japan

*Further testing of the second-moment closure employed in Part I is made. The present part considers the effects of streamline curvature and spanwise system rotation. As expected, the exact stress production terms broadly account for these effects. In addition, the present model, which is applied right up to a wall, successfully captures the laminarization in the rotating boundary layer. Attention is also given to the capability to reproduce the recovery process from curvature.*

## 1 Introduction<sup>1</sup>

The purpose of this two-part paper is to assess the performance of a second-moment closure of Launder and Shima (1989) (with some model functions recasted as described in Part I) in a variety of turbulent boundary layers. It has been shown in Part I that the turbulence model gives quite good predictions for the boundary layers with periodic pressure gradient, with wall transpiration and with free-stream turbulence. In Part II, further testing is made on the effects of streamline curvature and spanwise system rotation. Section 2 considers a boundary layer on a convex wall and a recovery flat wall, while Section 3 deals with a fully developed flow in a channel rotating about a spanwise axis (though the title of the paper indicates boundary layers only) and also with a boundary layer developing on the stable side of the channel.

In the present flows, in contrast to the flows considered in Part I, the additional agencies (curvature and rotation) directly influence the transport of turbulence quantities. Second-moment closures are expected to account for these effects through the exact stress generation terms, as emphasized by Launder (1989). The present predictions confirm this general benefit of second-moment closure. Attention is also given to some important aspects that remain unresolved, namely, the very slow recovery on a flat wall that follows a curved wall and the relaminarization at high rotation-rates.

## 2 Boundary Layer on a Convex Wall and a Recovery Flat Wall

The structure of turbulent boundary layers on a wall with streamwise curvature is very sensitive to the curvature (Brad-

shaw, 1973). When the wall is convex, the secondary mean-strain stabilizes the flow; the effect is by no means secondary but the shear stress and the wall friction are markedly reduced. Such flows appear on the turbomachine blades and airfoils. Second-moment closures, in contrast to  $k-\epsilon$  models, can capture the effect of the secondary strain without any curvature-specific modifications (e.g., Gibson et al., 1981).

In the present case, the stress and  $\epsilon$  transport models described in Part I together with the mean momentum equation are expressed in the coordinates with the  $x$  axis along the curved wall [i.e., the so-called  $s-n$  coordinates (Bradshaw, 1973) with different notations]. The equation set to be solved is then obtained by the boundary layer approximation with retaining the most dominant terms associated with streamline curvature. For brevity, only the shear stress transport equation is given here:

$$\begin{aligned} \frac{\partial}{\partial x} (U\overline{uv}) + \frac{\partial}{\partial y} (\alpha V\overline{uv}) - (\overline{u^2} - \overline{v^2}) \frac{U}{R} \\ = - \left( \alpha \overline{v^2} \frac{\partial U}{\partial y} - \overline{u^2} \frac{U}{R} \right) - C_1 \alpha \frac{\epsilon}{k} \overline{uv} + C_2 \left( \alpha \overline{v^2} \frac{\partial U}{\partial y} - \overline{u^2} \frac{U}{R} \right) \\ - \frac{3}{2} C_{w1} \alpha \frac{\epsilon}{k} \overline{uv} \frac{k^{3/2}}{C_1 \epsilon y} - \frac{3}{2} C_{w2} \left( \alpha \overline{v^2} \frac{\partial U}{\partial y} - \overline{u^2} \frac{U}{R} \right) \frac{k^{3/2}}{C_1 \epsilon y} \\ + \frac{\partial}{\partial y} \left[ \alpha \left( C_s \frac{k}{\epsilon} \overline{v^2} + \nu \right) \frac{\partial \overline{uv}}{\partial y} \right] \quad (1) \end{aligned}$$

where  $R$  denotes the local radius of wall curvature, and  $\alpha = 1 + y/R$ . [ $C_1$ ,  $C_2$ ,  $C_{w1}$ , and  $C_{w2}$  are model functions given by Eqs. (9)–(12) of Part I]. As is seen, there appears the curvature-related production  $(2\overline{u^2} - \overline{v^2})U/R$  (including the convection). This term, which has naturally appeared and acts to reduce the shear stress against the primary production, is mainly responsible for the stabilization by curvature.

The test case is taken from the experiment by Gillis and

<sup>1</sup>Nomenclature is listed in Part I of this two-part paper.

Contributed by the Fluids Engineering Division for publication in the JOURNAL OF FLUIDS ENGINEERING. Manuscript received by the Fluids Engineering Division August 20, 1992. Technical Editor: R. K. Agarwal.

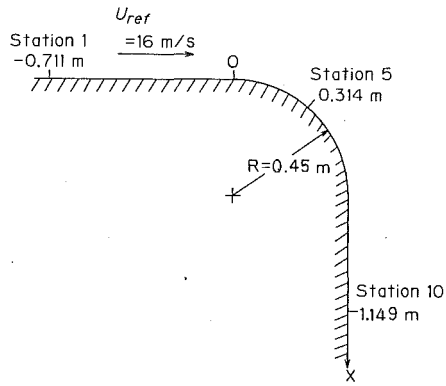


Fig. 1 Gillis and Johnston's flow

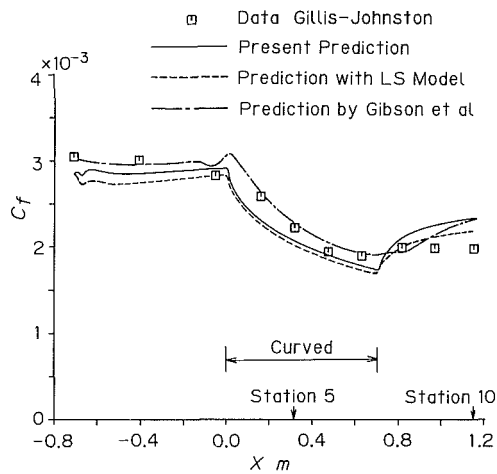


Fig. 2 Skin friction coefficient (boundary layer on a convex wall and a recovery flat wall)

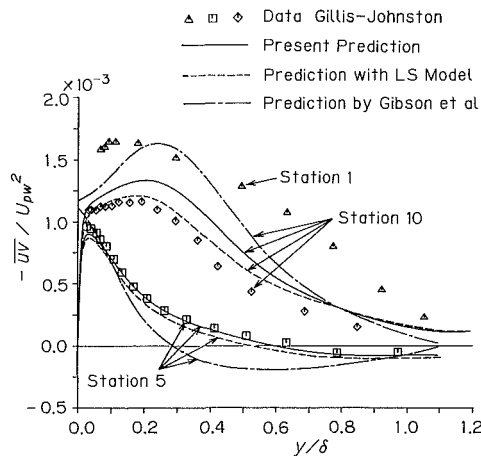


Fig. 3 Shear stress profiles (boundary layer on a convex wall and a recovery flat wall)

Johnston (1980), where a 90 degree bend with a circular arc wall is followed by a recovery flat wall, Fig. 1. This flow (in a slightly different experimental condition) was used as a test case (Case 0233) at the 1980-81 Stanford Conference (Kline et al., 1981). A paper of the experimenters (Gillis and Johnston, 1983) includes their computational work on this flow.

Figures 2 and 3 show the friction coefficient and the shear stress profiles. The prediction with a high-Reynolds-number second-moment closure by Gibson et al. (1981) is included for comparison. Also included is the prediction with the Launder and Shima's (1989) original version (denoted by LS model)

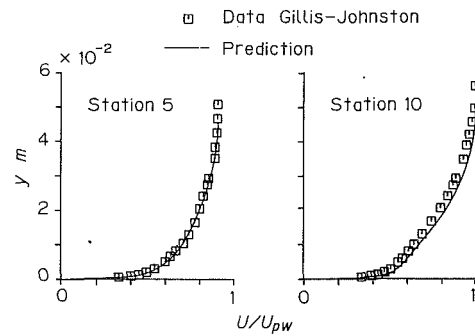


Fig. 4 Mean velocity profiles (boundary layer on a convex wall and a recovery flat wall)

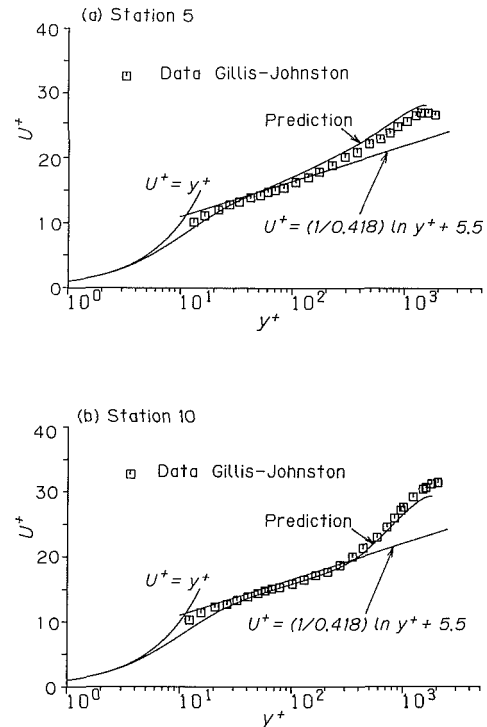


Fig. 5 Mean velocity profiles in wall coordinates (boundary layer on a convex wall and a recovery flat wall)

which, as remarked in Part I, differs from the present model in values of some model constants. For convenience, their difference is explicitly given here. For the generation term ( $C_{\epsilon 1} + \psi_1 + \psi_2$ ) $\epsilon P/k$  in the  $\epsilon$  transport equation [Eq. (18) of Part I], the present model adopts

$$\psi_1 = 1.5A(P/\epsilon - 1) \quad (2)$$

$$\psi_2 = 0.35(1 - 0.3A_2)\exp[-(0.002R_T)^{1/2}] \quad (3)$$

whereas the choices by LS are

$$\psi_1 = 2.5A(P/\epsilon - 1) \quad (4)$$

$$\psi_2 = 0.3(1 - 0.3A_2)\exp[-(0.002R_T)^2] \quad (5)$$

where  $A$  and  $A_2$  are the invariants of the stress anisotropy tensor, defined by Eqs. (13)–(16) of Part I.

It is seen from Fig. 2 that the three predictions capture the marked reduction in wall friction in the curved section, though the values with the present and LS models are somewhat too low. The performance clearly shows the general advantage of second-moment closure. Although the prediction by Gibson et al. gives better wall values of the shear stress in the curved section, the shear stress profile across the boundary layer is not very good; Fig. 3 indicates that their prediction gives too wide region of negative shear stress at Station 5. In contrast,

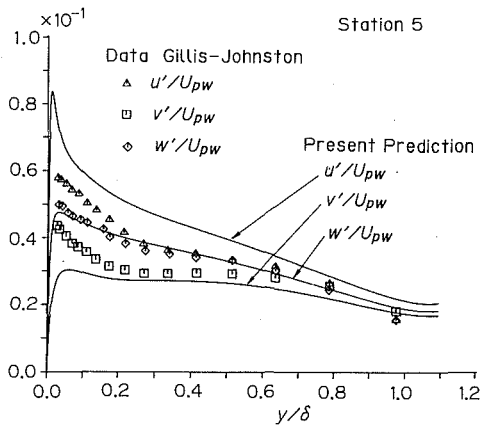


Fig. 6 Turbulence intensity profiles (boundary layer on a convex wall and a recovery flat wall)

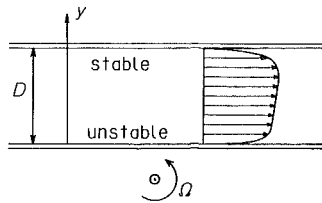


Fig. 7 Rotating channel flow

at the station the present model and the LS model reproduce the shear stress profile well.

The very slow recovery found in the experiment has not been captured by most of the previous predictions; see the very rapid recovery of the shear stress at Station 10 in the Gibson et al.'s prediction, Fig. 3. This behavior is best reproduced by the LS model among the three models. The prediction of the shear stress profile at Station 10 is quite good (Fig. 3), though the wall value is still larger than the experimental data (Fig. 2). The improvement by the LS model may be traced to the function  $\psi_1$  [Eq. (4)] in the  $\epsilon$  transport equation. When the flow enters the recovery section, the energy production rate  $P$  and the dissipation rate  $\epsilon$  tend to increase with removal of the extra strain. At the moment, most of the previous models perhaps give too sluggish increase in  $\epsilon$ , leading to the very rapid increase in the energy and shear stress, as suggested by Gibson et al. (1981). It is inferred that the function  $\psi_1$  augments the  $\epsilon$  generation at this stage (where  $P > \epsilon$ ), thus preventing the rapid increase in Reynolds stresses in the recovery flow. In the present model, the model constant in  $\psi_1$  has been changed as Eq. (2), which causes the faster recovery especially in the wall friction.

Figures 4 and 5 show the mean velocity profiles in linear and semilogarithmic coordinates, respectively. The large wake component in the recovery section, which corresponds to the very slow recovery discussed above, is reproduced well by the present model.

Finally the turbulence intensity profiles at a curved section are shown in Fig. 6. The experiment shows a marked isotropization even in the immediate vicinity of the wall. One might trace the behavior to the reduction in the primary production of  $u^2$ . (The curvature-related production in the  $u^2$  equation is just secondary in contrast to the case of the  $\overline{uv}$  equation.) However, the present model which of course retains the exact production terms does not reproduce the marked isotropization; the computed  $v'$  in the vicinity of the wall is just such that  $v'^2 \approx -\overline{uv}$ . Although the discrepancy should not be ignored, a major revision of the redistribution models to remove the defect is not justified at present.

### 3 Channel Flow With Spanwise Rotation

It is well known that the structure of turbulent flow in a rotating channel is strongly affected by the Coriolis force (Johnston et al., 1972). When the channel rotates about a spanwise axis, the Coriolis force stabilizes the suction-side flow and destabilizes the pressure-side flow, Fig. 7. Flows of this kind are of practical importance because they appear in the blade passages of turbomachinery. Two-equation models or models of lower level need to introduce special modifications related to the rotation to reproduce such flows. In contrast, second-moment closures can capture the flows without such modifications mainly due to an exact production term related to the Coriolis force in the stress transport equation. Launder et al. (1987) gave encouraging predictions using a high-Reynolds-number second-moment closure. As they noted, however, their calculation is inevitably limited to relatively low rotation-rates since, at higher rotation-rates, the stable-side flow is laminarized. Kristoffersen et al. (1990) calculated fully-developed channel flow at a rotation-rate with the LS model, and showed encouraging agreements with direct simulation data. This section gives predictions of fully developed and developing flows at wider range of rotation-rates using the present model which, as described in Part I, reproduces the non-rotating fully-developed flow more accurately than the LS version.

In this case the stress transport equation should include an exact production term related to the rotation:

$$G_{ij} = -2\Omega_i(\epsilon_{ijk}\overline{u_k u_j} + \epsilon_{jik}\overline{u_k u_i}) \quad (6)$$

where  $\Omega_i$  denotes the rotation rate vector. This term naturally appears when the stress transport equation is derived from the momentum equation including the Coriolis force. Note that, in this additional production, the shear factor is a constant  $\Omega$  (rotation rate) in contrast to the case of streamline curvature where the factor is  $U/R$  that decreases as a wall is approached. This implies that, in the case of rotation, the inner layer structure is relatively easily modified by the additional production.

Further, two redistribution terms:

$$\phi_{(3)ij} = -\frac{1}{2}C_2G_{ij} \quad (7)$$

$$\phi_{(w3)ij} = C_{w2} \left( \phi_{(3)km}n_k n_m \delta_{ij} - \frac{3}{2}\phi_{(3)ik}n_k n_j - \frac{3}{2}\phi_{(3)jk}n_k n_i \right) \frac{k^{3/2}}{C_\epsilon \epsilon d} \quad (8)$$

are added to the stress transport model. Rationale for inclusion of such terms has been given by several authors; see Launder et al. (1987). Briefly, the term  $\phi_{(3)ij}$  emerges consistently with the rapid term  $\phi_{(2)ij}$  [Eq. (4) of Part I] in modeling the pressure-strain correlation by reference to the Poisson equation for pressure fluctuation, while the term  $\phi_{(w3)ij}$  appears as the corresponding wall reflection.

Predictions are made for the fully developed channel flow and also for the boundary layer on the stable side of the channel. The solutions for both flows are obtained by calculating developing flows using 141 nodes across the channel. The distance from the wall appearing in the model equations is calculated by

$$\frac{1}{d} = \frac{1}{y} + \frac{1}{D-y} \quad (9)$$

according to Launder et al. (1975).

Attention is first given to the case of fully developed flow. The computed mean velocity profiles are compared with the experimental data of Johnston et al. (1972) in Fig. 8, where the Reynolds number and the rotation number are defined by  $Re = U_m D/\nu$  and  $Ro = \Omega D/U_m$ . The predictions for the rotating cases by Launder et al. (1987) are also included. The measured profiles at zero rotation are reproduced well by the present

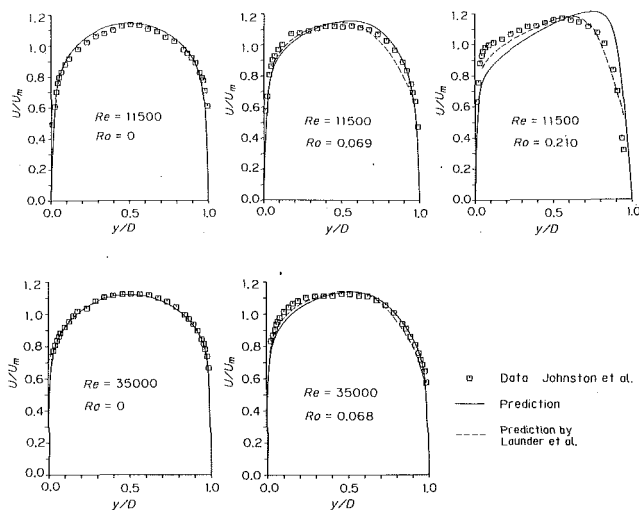


Fig. 8 Mean velocity profiles (fully developed rotating flow)

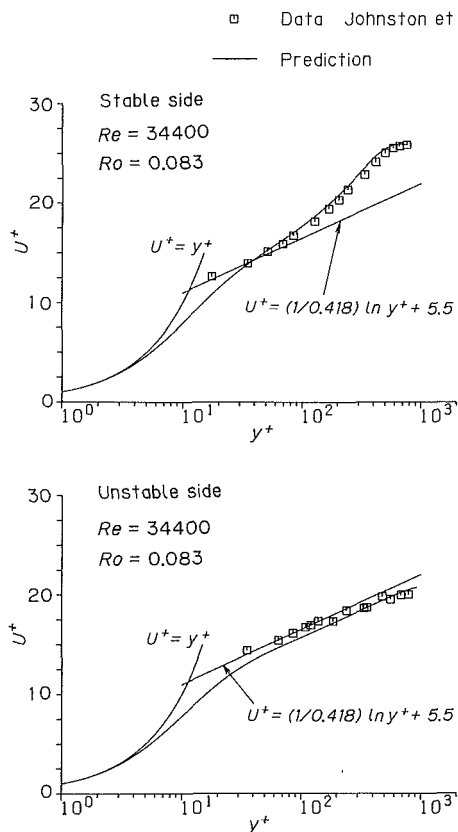


Fig. 9 Mean velocity profiles in wall coordinates (fully developed rotating flow)

model for two values of Reynolds number. The agreement for  $Ro = 0.07$  is somewhat worse. On the stable side (near  $y/D = 1$ ), the velocity profile becomes less full than the non-rotating case (in the region where  $U/U_m < 1$ ), indicating that the size of the log-law region becomes small due to the stabilizing effect. This behavior is well captured by the present computation. On the unstable side, however, a discrepancy is evident, particularly at the higher Reynolds number. As Johnston et al. (1972) suggest, the flow at  $Re = 35000$  may not be quite fully developed, thus giving the rather flatter measured profile. Moreover, there seems to be a discrepancy between the profile and the flow rate in the experimental data. For this rotation num-

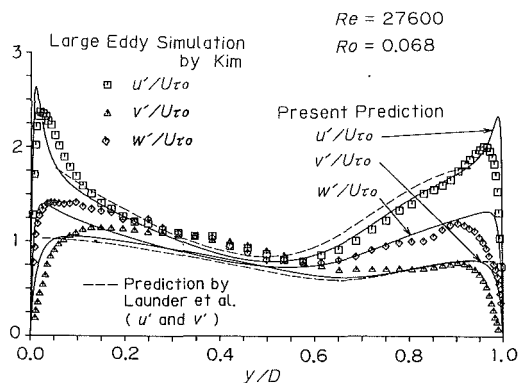


Fig. 10 Turbulence intensity profiles (fully developed rotating flow)

ber, 0.07, the results of Launder et al. are not much different from the present results, though the present predictions consistently give higher velocities on the stable side and lower velocities on the unstable side than their predictions. For the highest rotation number, 0.210, the computation by Launder et al. captures the experimental profile reasonably well while the present prediction does not; this point will be discussed shortly.

Figure 9 shows the semilogarithmic plots of velocity profiles both on the stable and unstable sides at  $Re \approx 35000$  and  $Ro \approx 0.08$ . It is seen that the wake component becomes very large on the stable side and vanishes on the unstable side. This feature is faithfully reproduced by the prediction. However, a discrepancy in the value of the additive constant in the log-law appears on the unstable side. The discrepancy may still be within an acceptable range for this rotation number, but it will become larger as the rotation number increases. This behavior corresponds to the rather poor profile at  $Ro = 0.210$  in the linear plot mentioned above.

According to Johnston et al. (1972), for  $Ro > 0.05 \sim 0.10$ , large-scale roll cells fully develop on the unstable side. Since the flow is actually three-dimensional due to the roll cells, it is somewhat questionable to discuss the model performance at high rotation numbers on the basis of the present two-dimensional calculation. A sound conclusion cannot be drawn concerning this point. As already shown, however, Launder et al. obtained a better velocity profile at  $Ro = 0.21$  with two-dimensional calculation by using the logarithmic law as the boundary conditions for both sides. Their practice cannot completely be justified because the flow on the stable side is laminarized at this rotation number. Nevertheless, the result appears to suggest that the three-dimensionality is weak enough to allow two-dimensional calculations and that the standard log-law nearly holds on the unstable side even at this rotation number. Therefore, the prediction at  $Ro = 0.210$  with the present model seems to indicate a real deficiency that the model does not reproduce the additive constant of the log-law in highly unstable wall regions. This is a typical difficulty in constructing closure models applicable up to a wall, though well-devised closures of this kind are clearly needed for predicting various flow situations.

Figure 10 compares the computed turbulence intensities with Kim's (1983) large eddy simulation data at  $Ro \approx 0.07$ . Also included is the computational result of Launder et al. (1987). Here,  $U_{\tau 0}$  denotes the friction velocity for nonrotating flow at the same Reynolds number. Overall, the departures of the profiles from symmetry are reasonably well captured by the present prediction. The asymmetries are readily traced to the stress production terms. On the unstable side, the rotation-induced production, Eq. (6), obviously augments  $v'$  and reduces  $u'$ , while on the stable side the production acts conversely. In the immediate vicinity of the walls, however, the change from the non-rotating case in the primary production,

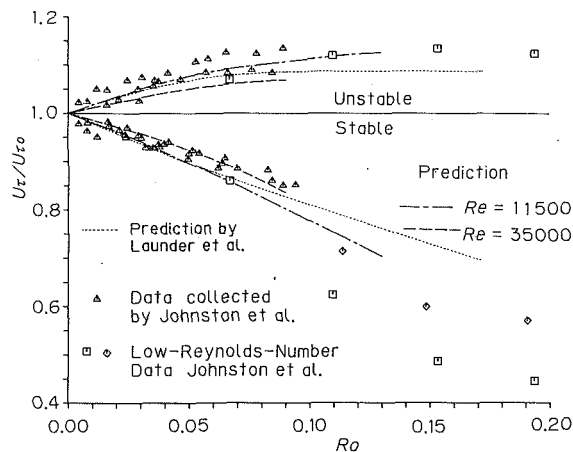


Fig. 11 Friction velocity (fully developed rotating flow)

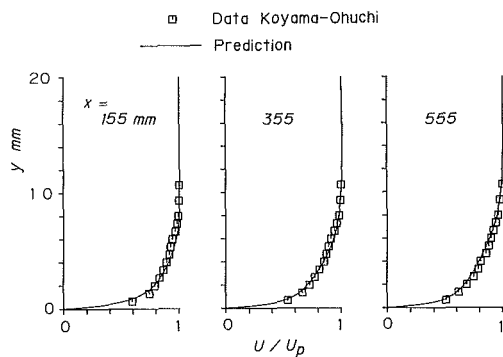


Fig. 12 Mean velocity profiles (rotating boundary layer:  $\Omega = 300$  rpm,  $U_m = 10$  m/s)

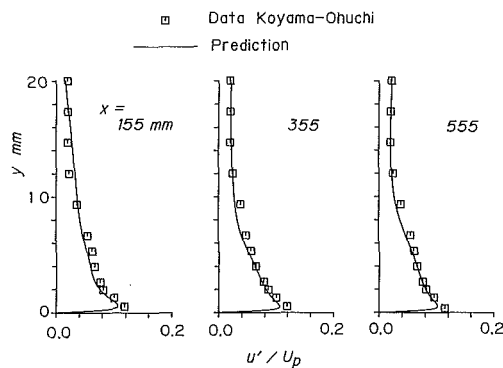


Fig. 13 Streamwise turbulence intensity profiles (rotating boundary layer:  $\Omega = 300$  rpm,  $U_m = 10$  m/s)

$-2\bar{u}v\partial U/\partial y$ , overwhelms the rotation-induced production, thus making  $u'$  on the unstable side higher than that on the stable side. The computed peak values in the  $u'$  distribution appear somewhat too high, but the Kim's simulation, even at zero rotation, gives rather small maximum as compared with the experimental value.

The variation with rotation number of the friction velocity on each of the walls is shown in Fig. 11. The computational results for two values of Reynolds number are compared with experimental data collected by Johnston et al. (1972) ( $Re \approx 25000 \sim 35000$ ) and their low-Reynolds-number data ( $Re \approx 10000$ ). This figure also includes the predictions at  $Re = 35000$  by Launder et al. (1987). The experimental data show that, on the unstable side, the increase in wall friction

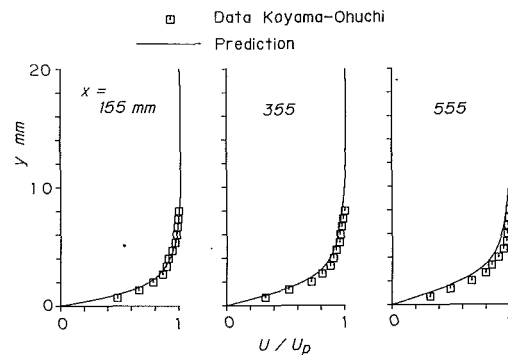


Fig. 14 Mean velocity profiles (rotating boundary layer:  $\Omega = 300$  rpm,  $U_m = 5$  m/s)

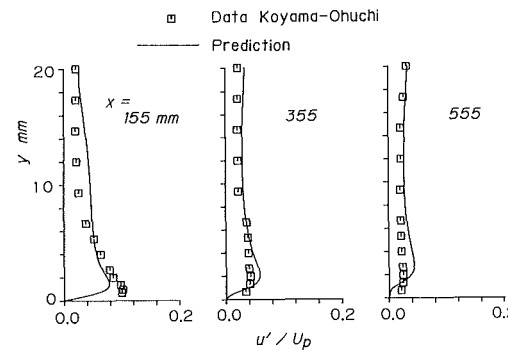


Fig. 15 Streamwise turbulence intensity profiles (rotating boundary layer:  $\Omega = 300$  rpm,  $U_m = 5$  m/s)

tends to saturate at  $Ro \approx 0.07$ . On the stable side, the low-Reynolds-number data for  $Ro > 0.1$  show a marked reduction in wall friction, indicating a laminarization of this side flow (Johnston et al., 1972). The present computational results are limited to relatively low rotation numbers because of a numerical instability for higher rotation numbers associated with the reverse transition on the stable side. (For much higher numbers, the solutions are easily obtained as already shown for  $Ro = 0.21$ .) The predictions show that the lower Reynolds-number flow is more strongly affected by the rotation than the higher Reynolds-number flow. Overall, the predictions for  $Ro < 0.1$  mimic the variations shown by the experimental data. It is seen that the Launder et al.'s prediction ( $Re = 35000$ ) gives higher magnitude both on the stable and unstable sides than the present prediction. (The Reynolds-number dependence was not given in their paper.)

Although the present model has captured the main features of the fully-developed rotating channel flow, the calculation has failed to reproduce the experiment at the highest rotation-rate ( $Ro = 0.21$ ) due to the difficulty in reproducing the log-law in the unstable-side flow. This obscures the capability of the present model to reproduce the relaminarization on the stable side since, in fully developed flow, one side flow largely affects the other side flow. Hence, the flow finally considered is a boundary layer developing on the stable side. The test cases are taken from an experiment by Koyama and Ohuchi (1985). Figures 12 and 13 show the mean velocity profiles and the streamwise turbulence intensity profiles for the case of relatively low rotation effect (the channel width being 40 mm). Figures 14 and 15 show those for the case of higher rotation effect. The experimental data show a clear distinction between the two cases especially in the turbulence intensity profiles. The computational results capture the distinction well, reproducing the laminarization in the case of higher rotation effect. The results indicate a clear advantage of the model applicable right up to a wall.

#### 4 Concluding Remarks

Testing of the full second-moment closure has been made on the effects of streamline curvature and spanwise system rotation. The exact production terms in the stress transport have broadly accounted for these effects, showing a decisive advantage of second-moment closure.

The present model is applied right up to a wall. Due to this feature, the model can be used to predict highly stabilized flows, and the laminarization in the rotating boundary layer has successfully been captured. Moreover, the model function  $\psi_1$  in the  $\epsilon$  transport model has shown its potentiality for reproducing the slow recovery from curvature. Remember that the present model also reproduces the laminarization caused by flow acceleration and that the function  $\psi_1$  also improves predictions of the boundary layers with adverse pressure gradient and with free-stream turbulence (Part I).

The results of this two-part paper show a fairly wide applicability of the turbulence model, though the test cases, at present, are limited to two-dimensional boundary layers and channel flows.

#### References

- Bradshaw, P., 1973, "Effects of Streamline Curvature on Turbulent Flow," AGARDograph No. 169.
- Gibson, M. M., Jones, W. P., and Younis, B. A., 1981, "Calculation of Turbulent Boundary Layers on Curved Surfaces," *Physics of Fluids*, Vol. 24, pp. 386-395.
- Gillis, J. C., and Johnston, J. P., 1980, "Experiments on the Turbulent Boundary Layer Over Convex Walls and Its Recovery to Flat-Wall Conditions," *Turbulent Shear Flows 2*, eds., L. J. S. Bradbury et al., Springer-Verlag, pp. 116-128.
- Gillis, J. C., and Johnston, J. P., 1983, "Turbulent Boundary-Layer Flow and Structure on a Convex Wall and Its Redevelopment on a Flat Wall," *Journal of Fluid Mechanics*, Vol. 135, pp. 123-153.
- Johnston, J. P., Halleen, R. M., and Lezius, D. K., 1972, "Effects of Spanwise Rotation on the Structure of Two-Dimensional Fully Developed Turbulent Channel Flow," *Journal of Fluid Mechanics*, Vol. 56, pp. 533-557.
- Kim, J., 1983, "The Effect of Rotation on Turbulence Structure," *Proceedings 4th Symposium on Turbulent Shear Flows*, Karlsruhe, pp. 6.14-6.19.
- Kline, S. J., Cantwell, B. J., and Lilley, G. M. (eds.), 1981, *Proceedings 1980-81 AFOSR-HTTM-Stanford Conference on Complex Turbulent Flows*, Department of Mechanical Engineering, Stanford University, Stanford.
- Koyama, H. S., and Ohuchi, M., 1985, "Effects of Coriolis Force on Boundary Layer Development," *Proceedings 5th Symposium on Turbulent Shear Flows*, Cornell University, New York, pp. 21.19-21.24.
- Kristoffersen, R., Nilsen, P. J., and Andersson, H. I., 1990, "Validation of Reynolds Stress Closures for Rotating Channel Flows by Means of Direct Numerical Simulations," *Engineering Turbulence Modelling and Experiments*, eds., W. Rodi and E. N. Ganić, Elsevier, pp. 55-64.
- Launder, B. E., 1989, "The Prediction of Force Field Effects on Turbulent Shear Flows via Second-Moment Closure," *Advances in Turbulence 2*, eds., H.-H. Fernholz and H. E. Fiedler, Springer-Verlag, pp. 338-358.
- Launder, B. E., Reece, G. J., and Rodi, W., 1975, "Progress in the Development of a Reynolds-Stress Turbulence Closure," *Journal of Fluid Mechanics*, Vol. 68, pp. 537-566.
- Launder, B. E., and Shima, N., 1989, "Second-Moment Closure for the Near-Wall Sublayer: Development and Application," *AIAA Journal*, Vol. 27, pp. 1319-1325.
- Launder, B. E., Tselepidakis, D. P., and Younis, B. A., 1987, "A Second-Moment Closure Study of Rotating Channel Flow," *Journal of Fluid Mechanics*, Vol. 183, pp. 63-75.

L. J. W. Graham  
CSIRO Postdoctoral Fellow.

K. Bremhorst  
Professor.

Department of Mechanical Engineering,  
The University of Queensland,  
Queensland 4072  
Australia

# Application of the $k - \epsilon$ Turbulence Model to the Simulation of a Fully Pulsed Free Air Jet

*The work describes application of the  $k - \epsilon$  turbulence model to a fully pulsed air jet. The standard model failed to predict the change in slope of the velocity decay where the jet changes from pulsed to steady jet behavior. A change in one of the constants of the  $k - \epsilon$  model based on the behavior of the periodic velocity component relative to the intrinsic component yielded satisfactory results. Features of the pulsed jet which were successfully simulated included the flow reversal near the edge of the jet, increased entrainment when compared to steady jets and large radial outflow near the leading edge of the pulse and large radial inflow near the outer edge of the jet for the remainder of the pulse.*

## 1 Introduction

The  $k - \epsilon$  model is still one of the more popular turbulence models used for prediction of turbulent flows. Its limitations are recognized, Bradshaw et al, (1991), and consequently it is essential to continue testing it against new experimental data. One type of free shear flow that has been examined in the past is the steady axisymmetric jet, Launder and Spalding (1974). Recently, extensive experimental data became available for a fully pulsed axisymmetric air jet, Bremhorst and Harch (1979) and Bremhorst and Hollis (1990). It would be of considerable interest to test the  $k - \epsilon$  model for this case as measurements showed a number of unusual features including a significant increase in entrainment when compared with a steady, axisymmetric jet, and a well defined change in slope of the inverse velocity decay curve where the jet changes from pulsed to steady jet like behavior.

The present paper reports simulation of a fully pulsed air jet using the  $k - \epsilon$  model of turbulence and the commercial package PHOENICS (Version 1.3.1 distributed by CHAM Ltd. of Wimbledon, London) for solution of the relevant partial differential equations. Most simulations were for a jet pulsed at 10 Hz issuing at  $36.6 \text{ ms}^{-1}$  from a 25.4 mm diameter exit to correspond to the detailed data of Bremhorst and Hollis (1990).

## 2 Theoretical Considerations

The flow considered in the present study, was assumed to be subsonic and incompressible. It was also assumed that the kinematic viscosity was constant. The Reynolds forms of the basic equations in Cartesian tensor notation are as follows;

$$\frac{\partial U_i}{\partial x_i} = 0 \quad (1)$$

$$\frac{\partial U_i}{\partial t} + U_j \frac{\partial U_i}{\partial x_j} = -\frac{1}{\rho} \frac{\partial P}{\partial x_i} + \frac{\partial}{\partial x_j} \left[ \nu \frac{\partial U_i}{\partial x_j} - \overline{u_i u_j} \right] \quad (2)$$

where the Einstein summation convention has been used. For the pulsed jet case  $U_i$  represents the periodic component of velocity while  $u_i$  and  $u_j$  represent the velocity fluctuations about the periodic components. These velocity fluctuations will be referred to as intrinsic velocity fluctuations associated with which are,  $\overline{u_i u_j}$ , the ensemble, phase averaged Reynolds stresses. For the steady jet case  $U_i$  becomes the mean velocity component as the time derivative term converges to zero after the jet has been turned on for a sufficient length of time. In the case of axisymmetric jets, the following simplified notation will be used -  $U_{i=1} = U_p$ ,  $U_{i=2} = V_p$ ,  $\overline{U}_{i=1} = U$ ,  $\overline{U}_{i=2} = V$ .  $P$  is the periodic static pressure which becomes the mean static pressure for a steady jet.

Closure of Eqs. (1) and (2) is by means of the  $k - \epsilon$  turbulence model for which the additional equations are,

$$\overline{u_i u_j} = -\nu_t \left( \frac{\partial U_i}{\partial x_j} + \frac{\partial U_j}{\partial x_i} \right) + \frac{2}{3} k \delta_{ij} \quad (3)$$

$$\nu_t = C_\mu \frac{k^2}{\epsilon} \quad (4)$$

$$\frac{\partial k}{\partial t} + U_j \frac{\partial k}{\partial x_j} = \left[ \nu_t \left( \frac{\partial U_i}{\partial x_j} + \frac{\partial U_j}{\partial x_i} \right) - \frac{2}{3} k \delta_{ij} \right] \frac{\partial U_i}{\partial x_j} + \frac{\partial}{\partial x_i} \left( \frac{\nu_t \partial k}{\sigma_k \partial x_i} \right) - \epsilon \quad (5)$$

$$\frac{\partial \epsilon}{\partial t} + U_j \frac{\partial \epsilon}{\partial x_j} = C_1 \nu_t \frac{\epsilon}{k} \left( \frac{\partial U_i}{\partial x_j} + \frac{\partial U_j}{\partial x_i} \right) \frac{\partial U_i}{\partial x_j} + \frac{\partial}{\partial x_i} \left( \frac{\nu_t \partial \epsilon}{\sigma_\epsilon \partial x_i} \right) - C_2 \frac{\epsilon^2}{k} \quad (6)$$

where  $k$  and  $\epsilon$  are ensemble, phase average turbulent kinetic energy and turbulent dissipation associated with the intrinsic velocity components of the pulsed jet whereas  $\bar{k}$  and  $\bar{\epsilon}$  denote their time averaged values over a complete cycle. For the steady jet case  $k = \bar{k}$  and  $\epsilon = \bar{\epsilon}$ . The standard set of constants are, Launder and Spalding (1974),

Contributed by the Fluids Engineering Division for publication in the JOURNAL OF FLUIDS ENGINEERING. Manuscript received by the Fluids Engineering Division October 9, 1991. Associate Technical Editor: R. K. Agarwal.

$$\begin{aligned}
C_\mu &= 0.09 \\
C_1 &= 1.44 \\
C_2 &= 1.92 \\
\sigma_k &= 1.0 \\
\sigma_\epsilon &= 1.3.
\end{aligned}
\tag{7}$$

although PHOENICS uses a value of 1.314 for  $\sigma_\epsilon$ .

Launder and Spalding (1974) also noted that for steady axisymmetric jets, two of the constants should be modified according to Eqs. (8) and (9) in order to avoid overestimation of the spreading rate.

$$C_\mu = 0.09 - 0.04f \tag{8}$$

$$C_2 = 1.92 - 0.0667f \tag{9}$$

where

$$f = \left| \frac{y}{2U_o} \left( \frac{\partial U_o}{\partial x} - \left| \frac{\partial U_o}{\partial x} \right| \right) \right|^{0.2}$$

for flow into still ambient fluid.  $y$  is the radial width of the mixing region and  $U_o$  is the centerline mean axial velocity. A simpler modification was suggested by Pope (1978) where the value of the constant  $C_1$  in Eq. (7) is changed from 1.44 to 1.6.

### 3 Details of Modeling

A rectilinear two-dimensional grid was used for calculations with fine grid spacings in the radial direction in order to obtain adequate spatial resolution especially near the exit region. The centerline of the jet was modeled using the default boundary condition of PHOENICS of a fluxless, frictionless wall. This condition was also used for the wall from which the jet issued. The other boundary conditions used an option available in PHOENICS which sets the boundary condition as if the domain extended to infinity.

**3.1 Steady Jet.** For the steady jet case the exit velocity was fixed at  $36.6 \text{ m s}^{-1}$  issuing from a 25.4 mm diameter nozzle with no radial flow. The exit turbulence energy is given by

$$k_{in} = 0.001 \bar{U}^2 \tag{10}$$

where  $\bar{U}$  is the bulk mean jet exit velocity, and the exit dissipation is given by

$$\epsilon_{in} = 0.1643(k_{in}^{1.5}/(0.035d)) \tag{11}$$

where  $d$  is the jet exit diameter.

Both the standard set of  $k$ - $\epsilon$  constants, Eq. (7), and a set with  $C_1$  changed to 1.6, Pope (1978), were used.

Solutions were obtained using the transient model until values of the various variables were independent of time. This procedure is recommended by the PHOENICS USERS MANUAL (CHAM LTD) and proved to be much better in terms of speed of convergence than a steady state solution. Results of the steady jet simulations are presented in Section 4.1.

**3.2 Pulsed Jet.** Exit mean velocity,  $\bar{U}$ , was again set at  $36.6 \text{ ms}^{-1}$  from a 25.4 mm diameter exit in order to coincide with available experimental data. Each 0.1 s cycle (equivalent to a 10 Hz frequency) of the pulsed jet was divided into 200 time steps. The latter were chosen to ensure that solutions are independent of the size of time steps. For the 80 Hz jet the cycle length was 0.0125 s. Exit velocity was modeled as a half sine curve during the valve on-time which was taken to be 0.03 seconds for the 10 Hz case in order to closely match experimental data near the exit. At each time step, continuity equation iterations were terminated when the sum of net inflows of mass into each cell became less than 1 percent of the average mass flow at the jet exit. For the momentum equations, iterations ceased when the sum of momentum equation imbalances became less than 1 percent of the average momentum convected into the system. Similar conditions were applied for  $k$  and  $\epsilon$ . Unless indicated otherwise, only the standard set of constants, Eq. (7), but with  $\sigma_\epsilon = 1.314$  was used.

The exit turbulence energy was set to

$$\frac{k_{in}}{U_p^2} = -\sin\left(\frac{t\pi}{t_{end}}\right) \times 0.1 + 0.11 \tag{12}$$

where  $t_{end}$  is the value of the time when the exit velocity reaches zero after the valve closes (set to 0.03 s for the present case). This equation was determined from the near exit experimental data of Hollis (1988). As for the steady jet, the exit dissipation

### Nomenclature

$C_1, C_2, C_\mu$ = constants in the $k$ - $\epsilon$ model	$u$ = velocity fluctuations about mean velocity of a steady jet or about $U_p$ for the pulsed jet	$y$ = lateral distance
$d$ = nozzle diameter	$u_p'$ = rms of $U_p$	$\overline{\quad}$ = denotes time or ensemble averaging
$f$ = function in $k$ - $\epsilon$ model used to modify $C_\mu$	$U$ = local mean streamwise velocity	<b>Subscripts</b>
$k$ = ensemble, phase averaged turbulent kinetic energy, also referred to as intrinsic turbulent kinetic energy	$U_p$ = local ensemble, phase averaged periodic streamwise velocity for pulsed jet	$i, j$ = coordinate directions 1, 2, or 3
$P$ = ensemble, phase averaged static pressure or periodic pressure	$\bar{U}$ = bulk mean velocity at jet exit	in = at jet exit
$Q$ = volume flow of jet at a given downstream position	$V$ = local mean radial velocity	0 = centerline value
$r$ = radial coordinate	$V_p$ = local ensemble, phase averaged periodic radial velocity for pulsed jet	<b>Greeks</b>
$r_{1/2,U}$ = half value radius, that is, radius at which the mean velocity is half that at the jet centerline	$x$ = coordinate in direction $i$ or $j$ also downstream distance from jet exit nozzle	$\delta_{ij}$ = Kronecker delta
$t$ = time	$x_{0c}$ = downstream distance at which jet changes from pulse domination to steady jet	$\epsilon$ = turbulent dissipation rate as defined in $k$ - $\epsilon$ model of turbulence
$t_{end}$ = time from valve opening to when mass flow at valve exit vanishes		$\nu$ = molecular kinematic viscosity
		$\nu_t$ = turbulent eddy viscosity
		$\pi$ = 3.1412...
		$\rho$ = density
		$\sigma_k, \sigma_\epsilon$ = effective Prandtl numbers or constants in the $k$ - $\epsilon$ model



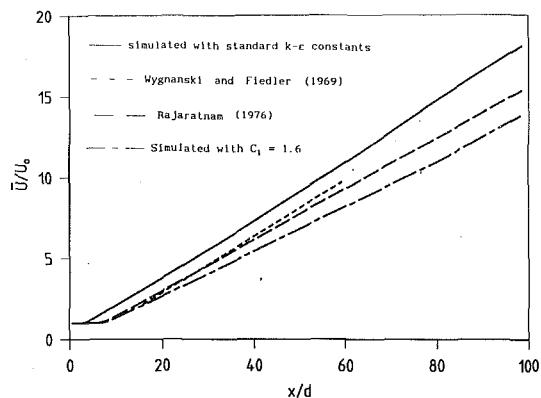


Fig. 1 Steady jet centerline axial velocity decay

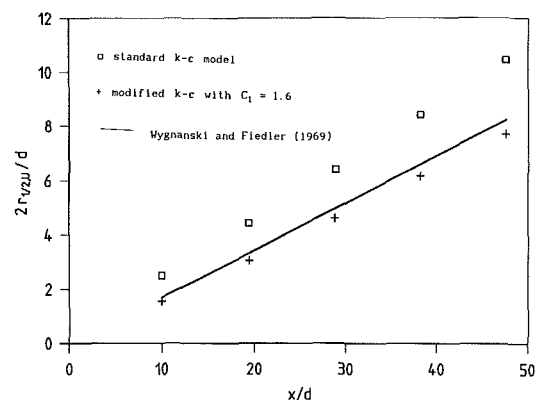


Fig. 2 Steady jet growth

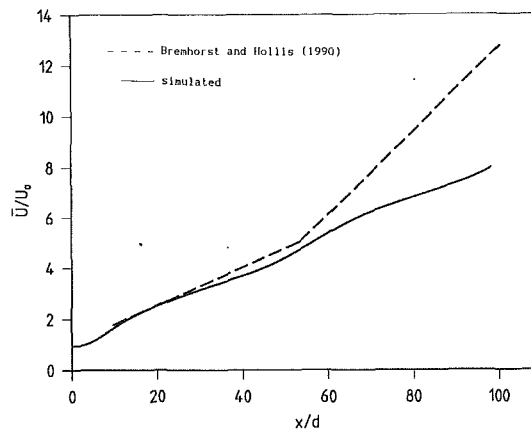


Fig. 3 Pulsed jet centerline axial velocity decay

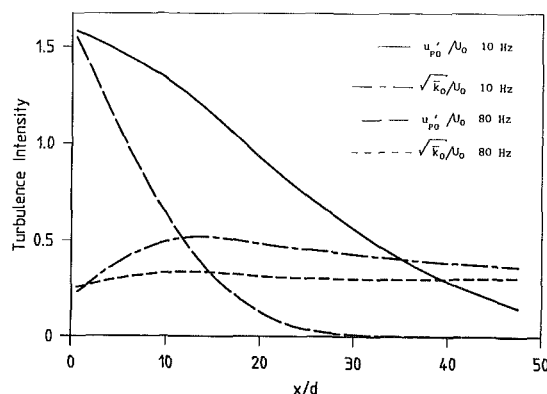


Fig. 4 Pulsed jet turbulence intensities at the jet centerline from standard  $k-\epsilon$  model

was set to that of Eq. (13) on the basis that the intrinsic turbulence velocity field is similar to the fluctuating velocity field of a steady jet.

$$\epsilon_{in} = 0.1643 \left( \frac{k_m^{1.5}}{0.035d} \right) \quad (13)$$

## 4 Results and Discussion

**4.1 Steady Jet.** Figure 1 shows the decay of centerline axial velocity for both the standard  $k-\epsilon$  constants and the modified set with  $C_1 = 1.6$ . It is readily seen that changing  $C_1$  has a significant effect on the slope of the curve. The slope of the standard  $k-\epsilon$  result is closer to that of the experimental data Wynanski and Fiedler (1969) while results with  $C_1 = 1.6$  agree well with the line given by Rajaratnam (1976).

Radial distributions of axial velocity, were found to follow Gaussian profiles closely. The half value radii—the radius at which the mean velocity is half that at the centerline—for both sets of  $k-\epsilon$  constants together with experimental data from Wynanski and Fiedler (1969) are given in Fig. 2. These results clearly show the overestimation of jet spreading by the standard  $k-\epsilon$  model. Changing  $C_1$  to 1.6 reduces jet growth near to the experimental value but as was seen in Fig. 1, decay of the centerline velocity is lower than experimental values. Hence, selection of the appropriate constants is a compromise based on whether  $U_o$  or  $r_{1/2,U}$  is to be predicted more correctly. In the present work the standard value of  $C_1 = 1.44$  is used throughout.

The effect of turbulence intensity at the jet exit was examined by running a number of simulations with different values of the exit turbulence energy. The effect is to shift the effective origin downstream a little as turbulence level increases but without changing the slope of the decay curve.

## 4.2 Unheated Pulsed Jet

**4.2.1 Centerline Results.** Figure 3 compares centerline axial velocity decay for the 10 Hz pulsed jet using the standard  $k-\epsilon$  model ( $C_1 = 1.44$ ) and the experimental results of Bremhorst and Hollis (1990). The simulated results do not show the characteristic change in slope where the jet switches from pulsed to steady jet behavior. Clearly, the standard  $k-\epsilon$  model cannot handle this type of transitional behavior.

Re-examination of the equations based on the physical significance of the various terms of the equations and trials with different values for the various constants suggested that better agreement with experimental results is possible. However, the only modification which led to satisfactory reproduction of the distinctive change in slope of the centerline velocity decay curve while also giving reasonable values for other jet properties involved a change in  $C_2$ . Best results were obtained with

$$\begin{aligned} C_2 &= 1.92 & x/d < x_{oc}/d \\ C_2 &= 2.32 & x/d > x_{oc}/d \end{aligned} \quad (14)$$

where  $x_{oc}/d$  is given by the axial position where the centerline normalized rms of the periodic velocity,  $\sqrt{U_{p0}^2}/U_o$ , equals the intrinsic turbulence level,  $\sqrt{k_0}/U_o$ , when using the standard  $k-\epsilon$  model. For the 10 Hz case this occurred at  $x/d = 36$  and the 80 Hz case at  $x/d = 17$  as shown in Fig. 4. The model was then rerun with the modified values of  $C_2$  of Eq. (14) to yield centerline axial velocity results in excellent agreement with experimental data for the 10 Hz pulsation frequency case of Bremhorst and Hollis (1990). The 80 Hz predicted results show transition to steady jet behavior occurring at a smaller value of  $x/d$  than for the 10 Hz case. This is consistent with similar results by Winter (1991) obtained with a smaller diameter jet.

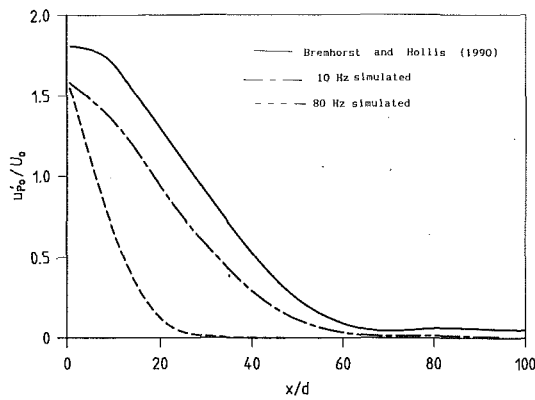


Fig. 5 Pulsed jet periodic turbulence

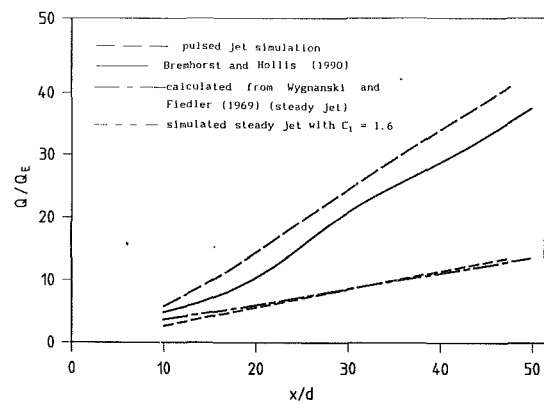


Fig. 8 Jet volume flows

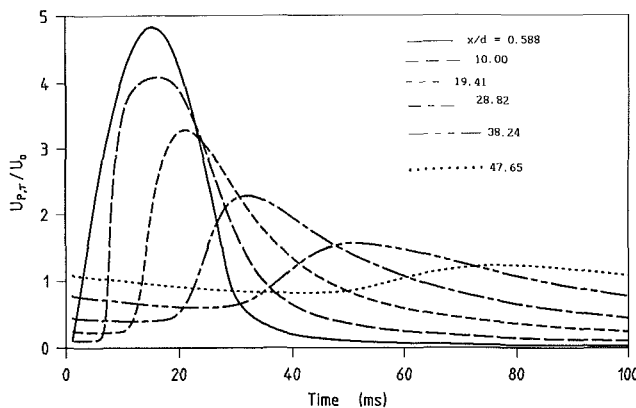


Fig. 6 Centerline profiles of axial periodic velocity through the pulse.

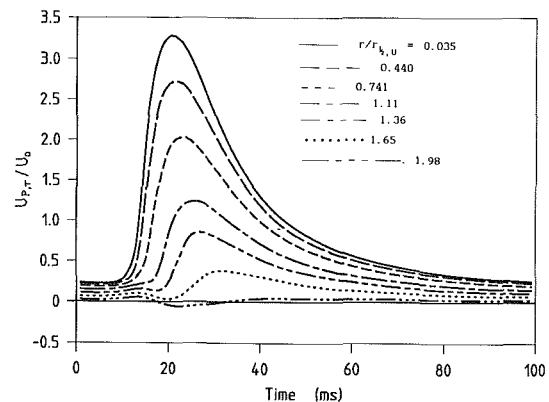


Fig. 9 Axial periodic velocity through the pulse.  $x/d = 19.41$ . Simulated results.

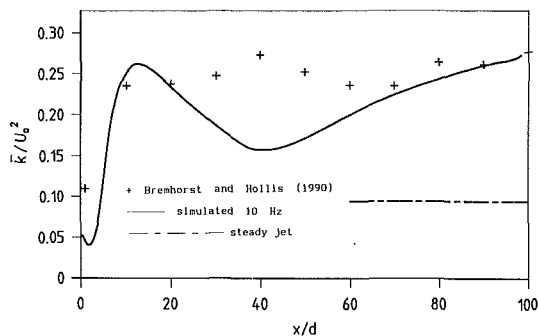


Fig. 7 Pulsed jet centerline intrinsic turbulence kinetic energy

At 10 Hz, results show that rms periodic velocity, Fig. 5, from the simulation gives a similar decrease to experimental values with the rms periodic velocity becoming negligible past  $x/d \sim 60$ . It is also seen that the 80 Hz results decrease more rapidly than the 10 Hz results which was also evident in the results of Winter (1991). Decay of the axial periodic velocity component, Fig. 6, as measured by the reduction in the size of the peaks is readily visible as the pulse moves downstream. Intrinsic turbulence kinetic energy for the 10 Hz jet, Fig. 7, is seen to be in reasonable agreement with experimental data but both results are significantly above the steady jet level.

**4.2.2 Pulsed Jet Radial Distributions of Velocities.** Radial profiles of the mean axial velocity,  $U$ , again follow quite closely a Gaussian curve which fitted the experimental data of Bremhorst and Hollis (1990) well. Growth of

the half-value radius is also in good agreement with the experimental results of Bremhorst and Hollis (1990).

If the axial mean velocity profiles are Gaussian, then the volume flow is given by

$$Q = \pi U_0 r_{1/2, U}^2 / \ln 2. \quad (15)$$

Volume flows for the steady and pulsed jet simulations, the pulsed jet data of Bremhorst and Hollis (1990) and the steady jet data of Wygnanski and Fiedler (1969) are compared in Fig. 8. Simulated pulsed jet results agree reasonably well with experimental values with both sets of pulsed jet data showing much larger volume flow than the steady jet as already observed earlier by Bremhorst and Harch (1979) and Bremhorst and Hollis (1990).

Predicted axial periodic velocities,  $U_p$ , through the pulse (1990), Fig. 9, clearly show the negative axial velocities at  $r/r_{1/2, U} > 1.5$  associated with the starting vortex. Corresponding results for the radial periodic velocity, Fig. 10, show the large radial outflow at the leading edge of the pulse together with the corresponding radial inflow after the peak of the pulse. For both axial and radial periodic velocities, the predicted peak values were lower than the experimental ones reported by Bremhorst and Hollis (1990) and spread too quickly axially thus suggesting that the use of a single diffusivity is inadequate. It should be noted that the largest value of the radial outflow occurs at  $r/r_{1/2, U} \sim 0.7$  at a position corresponding to the leading edge of the pulse while the largest radial inflow occurs at the edge of the jet but at a much later time in the pulse. This radial transport of fluid which corresponds to high and low axial velocities respectively, may be responsible for the increase in entrainment of fully pulsed jets.

## 5 Concluding Remarks

Most of the features of a fully pulsed air jet can be simulated

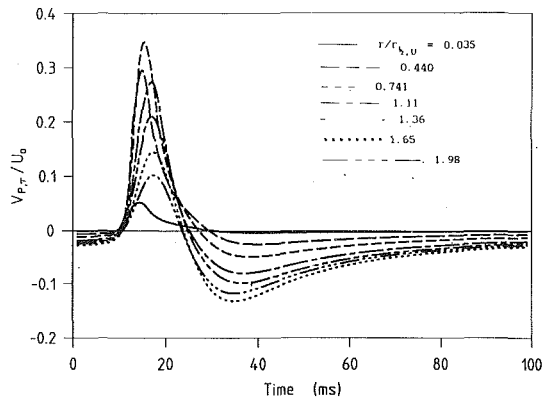


Fig. 10 Radial periodic velocity through the pulse.  $x/d=19.41$ . Simulated results.

using a modified  $k-\epsilon$  model where a change in one of the constants is based on the behavior of the periodic velocity component relative to the intrinsic component. This was successful for a 10 Hz jet and an 80 Hz jet. Features successfully simulated for the 10 Hz jet include flow reversal near the edge of the jet consistent with the starting vortex, increased entrainment when compared to steady jets, large radial outflow near the leading edge of the pulse and radial inflow near the edge of the jet later in the pulse. The results also showed that the pulsed component dominated up to  $x/d \sim 50$  for the 10 Hz pulsed jet with the change in slope of the centerline velocity decay curve simulated correctly when a modified value of  $C_2$  is used.

Changes of several constants in the  $k-\epsilon$  model lead to compensatory effects due to the coupled nature of the equations. However,  $C_2$  is an exception and by use of the modification of Eq. (14), permitted the most characteristic feature of a fully pulsed jet, namely, the change in slope of the mean velocity decay curve to be reproduced as well as maintaining realistic jet growth and turbulent kinematic energy.

It may seem that use of a nonstandard value for  $C_2$  as the jet returns to an essentially steady jet is physically unrealistic. However, the steady jet regime in question differs from that of a conventional steady jet significantly as the intrinsic turbulence level of the pulsed jet is considerably higher than for the steady jet. This undoubtedly leads to a different balance between turbulence energy and dissipation in that region. Such a changed balance can be expected to be reflected in  $C_2$ .

### Acknowledgments

The first author would like to acknowledge the support of a CSIRO Postdoctoral award. Support of the Australian Research Council and a University of Queensland computing grant are also acknowledged.

### References

- Bradshaw, P., Launder, B. E., and Lumley, J., 1991, "Collaborative Testing of Turbulence Models," *ASME JOURNAL OF FLUIDS ENGINEERING*, Vol. 113, pp. 3-4.
- Bremhorst, K., and Harch, W. H., 1979, "Near Field Velocity Measurements in a Fully Pulsed Subsonic Air Jet," *Turbulent Shear Flows I*, eds., F. Durst et al., Springer, pp. 37-54.
- Bremhorst, K., and Hollis, P. G., 1990, "Velocity Field of an Axisymmetric Pulsed, Subsonic Air Jet With a Significant No Flow Period Between Pulses," *AIAA Journal*, Vol. 28, pp. 2043-2049.
- CHAM TR/100, *Comprising Phoenix Beginner's Guide and User's Manual*, Cham Ltd. Wimbledon, London.
- Hollis, P. G., 1988, "Velocity Field Investigation of a Fully Pulsed Air Jet with a Laser Doppler Anemometer," Ph.D. thesis, Dept. Mechanical Engineering, The University of Queensland.
- Launder, B. E., and Spalding, D. B., 1974, "The Numerical Computation of Turbulent Flows," *Computer Methods in Applied Mechanics and Engineering*, Vol. 3, pp. 269-289.
- Pope, S. B., 1978, "An Explanation of the Turbulent Round-Jet/Plane-Jet Anomaly," *AIAA Journal*, Vol. 16, pp. 279-281.
- Rajaratnam, M., 1976, *Turbulent Jets*, Elsevier, Amsterdam.
- Winter, A. R., 1991, "A Laser-Doppler Anemometer Investigation Into Fully Pulsed Jet Flows with an Examination of Velocity Bias Errors," Ph.D. thesis, Dept. Mechanical Engineering, The University of Queensland.
- Wyganski, I., and Fiedler, H., 1969, "Some Measurements in the Self-Preserving Jet," *Journal of Fluid Mechanics*, Vol. 38, pp. 577-612.

# Airfoil Shape Optimization Using Sensitivity Analysis on Viscous Flow Equations

**Mohamed E. Eleashaky**

Research Associate.  
Assoc. Mem. ASME.

**Oktaý Baysal**

Professor.  
Mem. ASME.

Mechanical Engineering and  
Mechanics Department,  
Old Dominion University,  
Norfolk, VA 23529-0247

*An aerodynamic shape optimization method has previously been developed by the authors using the Euler equations and has been applied to supersonic-hypersonic nozzle designs. This method has also included a flowfield extrapolation (or flow prediction) method based on the Taylor series expansion of an existing CFD solution. The present paper reports on the extension of this method to the thin-layer Navier-Stokes equations in order to account for the viscous effects. Also, to test the method under highly nonlinear conditions, it has been applied to the transonic flows. Initially, the success of the flow prediction method is tested. Then, the overall method is demonstrated by optimizing the shapes of two supercritical transonic airfoils at zero angle of attack. The first one is shape optimized to achieve a minimum drag while obtaining a lift above a specified value. Whereas, the second one is shape optimized for a maximum lift while attaining a drag below a specified value. The results of these two cases indicate that the present method can produce successfully optimized aerodynamic shapes.*

## Introduction

Aerodynamic shape optimization has recently become a subject of considerable interest. This field of study involves the ability to determine the geometry of an aerodynamic configuration, that achieves certain objectives subject to specified constraints and satisfies the governing equations of its flowfield. For instance, in attaining the geometry of an optimum airfoil section two basic categories of design methods can be found in the literature, where several methods have been developed in each category.

The first category is the inverse design methods, in which one specifies the surface pressure distribution and the method calculates the corresponding airfoil geometry. Examples of this approach include the hodograph methods which solve the full potential equations in the hodograph plane (Bauer et al., 1977), and the method by Giles and Drela (1987) which treats the two-dimensional flow as a set of streamtubes coupled through the position of, and pressure at, the stream interfaces. The latter method solves the Euler equations and that guarantees a proper treatment of shocks. Some of these methods have recently included the viscous effects through a coupled integral boundary layer analysis.

The second category is the numerical optimization methods, which couple a flowfield analysis algorithm with an optimization algorithm. The aerodynamic quantities such as lift, drag,

pitching moment, pressure distribution are computed by the flowfield analysis algorithm for a certain configuration and are used in defining an objective function to be minimized or maximized. This objective function must relate changes in geometry to improvements in the aerodynamic quality of the design. The methods of Vanderplaats (1975, 1979), Hicks et al. (1974), and Pittman (1987) are examples of this category.

Some conclusions can be drawn from this brief literature survey. First of all, each of these categories has its advantages and its shortcomings, hence they have to be considered as complementary and not competitive. Secondly, each offers a different way of finding efficient aerodynamic shapes without resorting to an expensive cut-and-try wind tunnel testing. However, the general theme in all of them is that they require a significant level of experience and skill to define the geometrical aerodynamic shapes. This requirement is almost eliminated by the present method which automatically shapes the aerodynamic configuration to any arbitrary geometry during the optimization process. For the completion of the above survey, the readers should be referred to a survey paper by Dulikravich (1991), where other aerodynamic shape design concepts have been presented and classified according to their origin.

This paper presents an aerodynamic shape design method which falls into the second category. In concept, it couples a Computational Fluid Dynamics (CFD) analysis scheme with an optimization algorithm. But unlike other methods in its category, the gradients of the objective function and constraints (sensitivity coefficients) required for the optimizer are obtained via a sensitivity analysis algorithm based on a discretized form of the thin-layer Navier-Stokes equations used in the CFD analysis algorithm. In addition, the requirement

Contributed by the Fluids Engineering Division and presented at the Symposium on Multidisciplinary Applications of Computational Fluid Dynamics, Winter Annual Meeting, Atlanta, Ga., December 1-5, 1991 of THE AMERICAN SOCIETY OF MECHANICAL ENGINEERS. Manuscript received by the Fluids Engineering Division October 25, 1991. Associate Technical Editor: R. K. Agarwal.

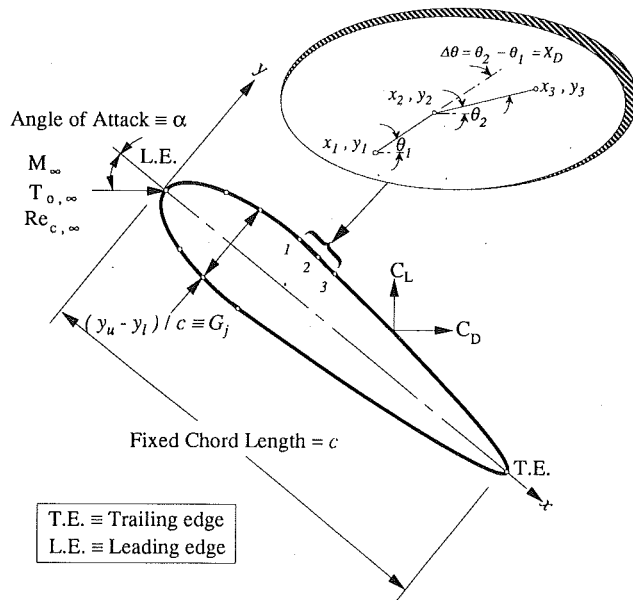


Fig. 1 Definition of the optimization problem

of repetitive CFD flow analyses inherent in other methods of its category, is alleviated by the use of a flow prediction technique developed previously by the authors (Baysal et al., 1990, 1991a, 1991b) and presently extended to the viscous flow equations. Hence, the current method is the natural extension of the aerodynamic shape design method developed by the authors (1991b). This method (Baysal et al., 1991b) treats the relative slope at each surface grid point as the design variable in the optimization problem and uses a sensitivity analysis algorithm based on a third-order discretized form of the Euler equations to get the gradient information as well as the predicted flowfield solution.

The present aerodynamic design optimization method is demonstrated by optimizing a low Reynolds number, laminar, transonic airfoil where the flow region is supercritical. However, the purpose of this study is not finding optimized airfoils of common interest; rather, they merely serve as examples to illustrate the behavior of the viscous sensitivity analysis algorithm in regions where highly nonlinear phenomena may occur in the flowfield. A survey of the different methods to determine the sensitivity coefficients as well as the flow prediction method are deemed unnecessary for the objectives of this paper. Such details, which are given by Baysal et al. (1990, 1991a, 1991b), are excluded from this paper for brevity.

### Optimization Problem

Two different design problems are addressed in this paper. The first problem is to optimize the upper surface of a NACA 0012 airfoil, which provides a reduced drag coefficient ( $C_D$ ) while keeping the lift coefficient ( $C_L$ ) greater than a specified value,  $C_{L_{\min}}$ . The second problem is to optimize the lower surface of NACA 0012 airfoil, which provides an increased  $C_L$  while keeping  $C_D$  less than a specified value,  $C_{D_{\max}}$ .

The contour of the airfoil to be optimized is defined by one of its coordinates ( $x$  or  $y$ ) and the relative slope at each surface grid point Fig. 1. This coordinate is kept fixed during the optimization process while the relative slope is perturbed to change the geometrical shape. Hence, the design variables,  $\bar{X}_D$ , of both optimization problems are the relative slopes at the surface grid points.

Any aerodynamic optimization problem, in general, is stated mathematically as follows:

Minimize

$$F(\bar{Q}(\bar{X}_D), \bar{X}_D) \quad (1)$$

subject to the following constraints:

(1) flow-type inequality constraints

$$G_j(\bar{Q}(\bar{X}_D), \bar{X}_D) \leq 0, \quad j = 1, NCON_f \quad (2)$$

(2) geometric-type inequality constraints

$$G_j(\bar{X}_D) \leq 0, \quad j = 1 + NCON_f, NCON \quad (3)$$

(3) side constraints

$$\bar{X}_{D_{\text{lower}}} \leq \bar{X}_D \leq \bar{X}_{D_{\text{upper}}} \quad (4)$$

where  $F$  denotes the objective function and  $\bar{Q}$  is the vector of the conserved variables of the fluid flow.  $NCON_f$  denotes the number of flow-type constraints and  $NCON$  is the total number of inequality constraints.  $\bar{X}_{D_{\text{lower}}}$  and  $\bar{X}_{D_{\text{upper}}}$  are the lower and the upper bounds of the design variables. A judicious choice of these bounds is necessary to maintain an acceptably smooth aerodynamic shape.

In the first problem, the objective function,  $C_D$ , is given by:

$$C_D = C_{D_{\text{inviscid}}} + C_{D_{\text{viscous}}} \quad (5)$$

and the lift constraint is written as:

$$G_1 = 1 - \frac{C_L}{C_{L_{\min}}} \leq 0 \quad (6)$$

where  $C_{L_{\min}}$  is a lower limit of  $C_L$ . The lift coefficient  $C_L$  is given by:

$$C_L = C_{L_{\text{inviscid}}} + C_{L_{\text{viscous}}} \quad (7)$$

In the second problem, the objective function is  $C_L$  and the drag constraint is written as:

$$G_1 = \frac{C_D}{C_{D_{\max}}} - 1 \leq 0 \quad (8)$$

where  $C_{D_{\max}}$  is an upper limit of  $C_D$ .

In addition to the flow-type constraints stated above for the two design problems, there are some geometric-type inequality constraints which are imposed on these optimization problems. These constraints involve the thickness-to-chord ratio, which must be positive and not to exceed a specified value, and the thickness at the trailing edge (T.E.), which must be zero for a closed airfoil;

$$0 \leq (y_u - y_l) / c \leq t_{\max} \quad (9)$$

where  $y_u$  and  $y_l$  are the coordinates of the upper and lower contours, respectively. ( $t_{\max}$ ) is the maximum thickness-to-chord ratio of the airfoil. To enforce the zero T.E. thickness, the initial airfoil is started with zero T.E. thickness and the T.E. grid point is simply excluded from the design variables. Instead, a geometric-type constraint is imposed on the relative slope at the surface grid point adjacent to the T.E. point.

Therefore, the total number of constraints  $NCON$  in each of these optimization problems is equal to  $(3 + 2 * NDV)$ , where  $NDV$  is the number of design variables and it is equal to the number of surface grid points.

This nonlinear, constrained optimization problem is solved using the feasible directions method implemented by Vanderplaats (1985). Given a set of initial values for the design variables, the method first drives all the design variables into a feasible design space, i.e., the space where none of the design constraints are violated. Then the optimum design is method-

ically searched for within this space. This search is controlled by search directions which are based on the objective function gradient and, therefore, efficiently guides the succeeding calculations towards incrementally improved designs. Since this optimization process requires many evaluations of the objective function and constraints before an optimum design is reached, the process can be very expensive if a CFD analysis were performed for each evaluation. In the present study, however, the higher fidelity viscous "flow prediction" method (approximate flow analysis) is performed during the one-dimensional searches of the optimization process. A complete CFD analysis was performed only when new gradients of the constraints and the objective function are needed, i.e., when the design changes substantially. The approximate flow analysis is based on a Taylor expansion around a given solution and its details can be found in the references by Baysal et al. (1990 1991a, 1991b) and Eleshaky (1992a).

### Sensitivity Coefficients

Because of the functional dependence of the objective function and the flow-type inequality constraints on the design variables and flowfield solution, their derivatives with respect to the design variables,  $\bar{X}_D$ , are given by:

$$\nabla F = \frac{\partial F}{\partial \bar{X}_D} = \left( \frac{\partial F}{\partial \bar{X}_D} \right)_Q + \left( \frac{\partial F}{\partial \bar{Q}} \right)^T \cdot \frac{\partial \bar{Q}}{\partial \bar{X}_D} \quad (10)$$

$$\nabla G_j = \frac{\partial G_j}{\partial \bar{X}_D} = \left( \frac{\partial G_j}{\partial \bar{X}_D} \right)_Q + \left( \frac{\partial G_j}{\partial \bar{Q}} \right)^T \cdot \frac{\partial \bar{Q}}{\partial \bar{X}_D} \quad j=1, NCON_f \quad (11)$$

These gradients include two parts; namely, an explicit part; e.g.  $(\partial F/\partial \bar{X}_D)_Q$  or  $(\partial G_j/\partial \bar{X}_D)_Q$ , plus an implicit part through the dependence on  $\bar{Q}$ . The explicit part is often easy to obtain compared to the implicit part. The implicit part of the derivatives is determined by the quasi-analytical or sensitivity analysis approach described by Baysal and Eleshaky (1990). In this approach, one of two methods can be used; either the direct method or the adjoint variable method. It is reported by the authors (1990) that if the number of design variables ( $NDV$ ) is greater than the number of adjoint vectors ( $1+NCON_f$ ), then the adjoint variable method is more efficient than the direct method. For instance, in the present study, there is only one flow-type constraint, hence, the number of adjoint vectors is only two. Since  $NDV$  is equal to the number of grid points on the airfoil surface under consideration, which are usually more than two, the adjoint variable method is selected to determine the sensitivity coefficients.

The flowfield of the present study is assumed to be governed by the two-dimensional, steady, compressible, thin-layer Navier-Stokes equations,

$$\frac{\partial \hat{g}}{\partial \eta} + \frac{\partial \hat{h}}{\partial \zeta} - \frac{\partial \hat{h}_v}{\partial \zeta} = 0 \quad (12)$$

and

$$\frac{\partial}{\partial \zeta} (\hat{h}_v) = Re^{-1} \left\{ \frac{\partial}{\partial \zeta} [V(\zeta_x r + \zeta_y s)] \right\} = 0 \quad (13)$$

where  $\hat{g}$  and  $\hat{h}$  are the inviscid fluxes in the generalized coordinates  $(\eta, \zeta)$ .  $Re$  is Reynolds number based on the speed of sound,  $(\rho_\infty \alpha_\infty c / u_\infty)$ .  $V$  is the inverse of the transformation Jacobian.  $(r)$  and  $(s)$  are the viscous fluxes in Cartesian coordinates. Details of Eqs. (12) and (13) are given by Baysal (1988).

The discrete residual form of Eq. (12) can be rewritten in terms of the design variables and conserved variables,  $\bar{Q}$ , as follows:

$$\bar{R}(\bar{Q}(\bar{X}_D), \bar{X}_D) = 0 \quad (14)$$

Consequently, the quasi-analytical approach (Baysal and Eleshaky, 1990) begins by differentiating Eq. (14) with respect to the design variables to yield the sensitivity equation,

$$\left[ \frac{\partial \bar{R}}{\partial \bar{Q}} \right] \left\{ \frac{\partial \bar{Q}}{\partial \bar{X}_D} \right\} = - \left[ \frac{\partial \bar{R}}{\partial \bar{X}_D} \right] \equiv \mathbf{R}_v \quad (15)$$

At this point, the adjoint variable method diverges from the direct method. First, Eq. (15) is substituted into Eqs. (10) and (11). Then, the vectors of adjoint variables  $(\bar{\lambda}_1, \bar{\lambda}_2)$  are defined to satisfy the following equations,

$$J^T \bar{\lambda}_1 = \frac{\partial F}{\partial \bar{Q}} \quad (16)$$

$$J^T \bar{\lambda}_{2j} = \frac{\partial G_j}{\partial \bar{Q}} \quad j=1, NCON_f \quad (17)$$

where  $J^T = [\partial \bar{R} / \partial \bar{Q}]^T$ . Equations (10) and (11) are rearranged using Eqs. (16) and (17) to form the following equations,

$$\frac{\partial F}{\partial \bar{X}_D} = \left( \frac{\partial F}{\partial \bar{X}_D} \right)_Q + \bar{\lambda}_1^T \mathbf{R}_v \quad (18)$$

$$\frac{\partial G_j}{\partial \bar{X}_D} = \left( \frac{\partial G_j}{\partial \bar{X}_D} \right)_Q + \bar{\lambda}_{2j}^T \mathbf{R}_v \quad j=1, NCON_f \quad (19)$$

The adjoint variable method requires the solution of Eq. (16) and Eq. (17) for the adjoint variable vectors, and substituting them into Eqs. (18) and (19), yields the derivatives of  $F$  and  $G_j$ 's. It should be noted that Eqs. (16) and (17) are independent of any differentiation with respect to  $\bar{X}_D$ ; hence, the vectors  $\bar{\lambda}_1$  and  $\bar{\lambda}_{2j}$  in Eqs. (16) and (17) remain the same for all elements of the vector  $\bar{X}_D$ .

Since the rest of the inequality constraints ( $NCON - NCON_f$ ) are of geometric-type, then they are functionally independent of the vector of conserved variables,  $\bar{Q}$ . Hence, the expressions for the gradient (11) of these constraints are given by:

$$\nabla G_j = \frac{\partial G_j}{\partial \bar{X}_D} \quad j = NCON_f + 1, NCON \quad (20)$$

### Sensitivity Solution Method

In order to analyze numerically the flowfield during the optimization process and to provide a baseline CFD solution for the flow prediction method, Eq. (12) is solved by an implicit, finite volume scheme (Rumsey et al., 1987), where the residual is driven to  $10^{-7}$  at each point of the computational domain. The inviscid terms in Eq. (12) are differenced by the upwind differences, according to the flux vector splitting method of van Leer, while the viscous terms are centrally differenced. Hence, the discretized form of Eq. (12) can be written for a nine-point stencil as follows:

$$\begin{aligned} \bar{R}_{j,k} = & \hat{g}^+ (\bar{Q}_{j+1/2,k}^-, M_{j+1/2,k}) - \hat{g}^+ (\bar{Q}_{j-1/2,k}^-, M_{j-1/2,k}) \\ & + \hat{g}^- (\bar{Q}_{j+1/2,k}^+, M_{j+1/2,k}) - \hat{g}^- (\bar{Q}_{j-1/2,k}^+, M_{j-1/2,k}) \\ & + \hat{h}^+ (\bar{Q}_{j,k+1/2}^-, M_{j,k+1/2}) - \hat{h}^+ (\bar{Q}_{j,k-1/2}^-, M_{j,k-1/2}) \\ & + \hat{h}^- (\bar{Q}_{j,k+1/2}^+, M_{j,k+1/2}) - \hat{h}^- (\bar{Q}_{j,k-1/2}^+, M_{j,k-1/2}) \\ & - \hat{h}_v (\bar{Q}_{j,k+1}, \bar{Q}_{j,k}, M_{j,k+1/2}) + \hat{h}_v (\bar{Q}_{j,k}, \bar{Q}_{j,k-1}, M_{j,k-1/2}) \end{aligned} \quad (21)$$

where  $\hat{g}^+$ ,  $\hat{g}^-$ ,  $\hat{h}^+$  and  $\hat{h}^-$  are the operator-split inviscid fluxes and

$$\hat{h}_v(\bar{Q}_{j,k+1}, \bar{Q}_{j,k}, M_{j,k+1/2}) = Re^{-1}(\mu_{k+1} + \mu_k)(V_{k+1} + V_k)^* \left\{ \begin{array}{l} 0 \\ |\nabla \xi|^2_{j,k+1/2} \cdot (u_{k+1} - u_k) \\ + \frac{1}{3} \xi_{x,j,k+1/2} (\nabla \bar{\xi}_{j,k+1/2} \cdot (\bar{V}_{k+1} - \bar{V}_k)) \\ |\nabla \xi|^2_{j,k+1/2} \cdot (v_{k+1} - v_k) \\ + \frac{1}{3} \xi_{y,j,k+1/2} (\nabla \bar{\xi}_{j,k+1/2} \cdot (\bar{V}_{k+1} - \bar{V}_k)) \\ |\nabla \xi|^2_{j,k+1/2} \cdot \left\{ \frac{1}{2} [(\bar{V} \cdot \bar{V})_{k+1} - (\bar{V} \cdot \bar{V})_k] \right. \\ \left. + \frac{1}{(\gamma-1)Pr} (a^2_{k+1} - a^2_k) \right. \\ \left. + \frac{W_{k+1/2}}{3} [|\nabla \xi|^2_{k+1/2} \cdot (\bar{V}_{k+1} - \bar{V}_k)] \right\} \end{array} \right\} \quad (22)$$

where  $\bar{V}$  is the velocity vector and  $(u, v)$  are the Cartesian velocity components. Pr is Prandtl number and  $W$  is the contravariant velocity in the  $\xi$ -direction.  $\mu$  is the molecular viscosity and  $V$  is the cell volume.

As it is seen from Eq. (21),  $\bar{R}_{j,k}$  is functionally dependent on the cell-face values of the conserved variables ( $\bar{Q}_{j\pm 1/2, k\pm 1/2}$ ), the cell values of the conserved variables ( $\bar{Q}_{j,k}$ ,  $\bar{Q}_{j,k\pm 1}$ ), and the geometric terms ( $M_{j\pm 1/2, k\pm 1/2}$ ). These geometric terms are involved in the transformation to the generalized coordinates and they are evaluated at the cell-interface locations. The conserved variables ( $\bar{Q}_{j\pm 1/2, k\pm 1/2}$ ) are functions of the conserved variables of the neighboring cells which are evaluated at the cell centers (Baysal and Eleshaky, 1991a). Hence, the linear vector form of the left-hand side of Eq. (15) for an interior cell  $(j,k)$  can be written as:

$$\begin{aligned} [\text{LHS of (15)}]_{j,k} = & \bar{D} \frac{\partial \bar{Q}_{j-2,k}}{\partial \bar{X}_D} + \bar{A} \frac{\partial \bar{Q}_{j-1,k}}{\partial \bar{X}_D} \\ & + \bar{B} \frac{\partial \bar{Q}_{j,k}}{\partial \bar{X}_D} + \bar{C} \frac{\partial \bar{Q}_{j+1,k}}{\partial \bar{X}_D} \\ & + \bar{E} \frac{\partial \bar{Q}_{j+2,k}}{\partial \bar{X}_D} + \bar{H} \frac{\partial \bar{Q}_{j,k-2}}{\partial \bar{X}_D} \\ & + \bar{F} \frac{\partial \bar{Q}_{j,k-1}}{\partial \bar{X}_D} + \bar{G} \frac{\partial \bar{Q}_{j,k+1}}{\partial \bar{X}_D} \\ & + \bar{I} \frac{\partial \bar{Q}_{j,k+2}}{\partial \bar{X}_D} \end{aligned} \quad (23)$$

The Jacobians of the viscous fluxes are included only in the coefficients  $\bar{B}$ ,  $\bar{F}$ , and  $\bar{G}$ , hence the viscous terms do not change the character of the left-hand side of Eq. (15). Details of the inviscid contribution in the coefficients  $\bar{A}$  through  $\bar{I}$  in Eq. (23) are described by Eleshaky (1992a). The coefficient matrices  $\bar{A}$  through  $\bar{I}$  are functions of the Jacobian matrices of the split fluxes  $\hat{g}^\pm$  and  $\hat{h}^\pm$  and the Jacobians of the viscous fluxes. Since the Jacobian matrices for interior cells are available from the flowfield solver, few computations are needed to assemble the coefficient matrix  $[\partial \bar{R} / \partial \bar{Q}]$  in Eq. (15). It should be emphasized that, if an implicit treatment of the boundary conditions were not used in the CFD algorithm, it is necessary to revise the residual expression (23) at the boundary points in order to include the boundary conditions. More details about the implicit treatment of the boundary conditions are given by Eleshaky (1992a).

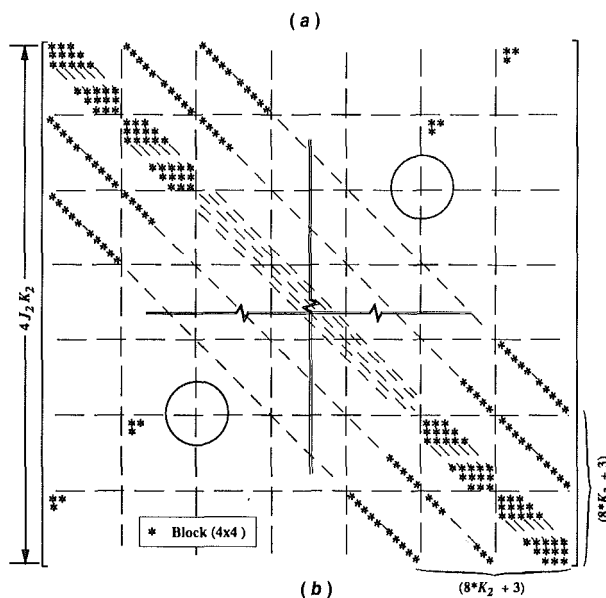
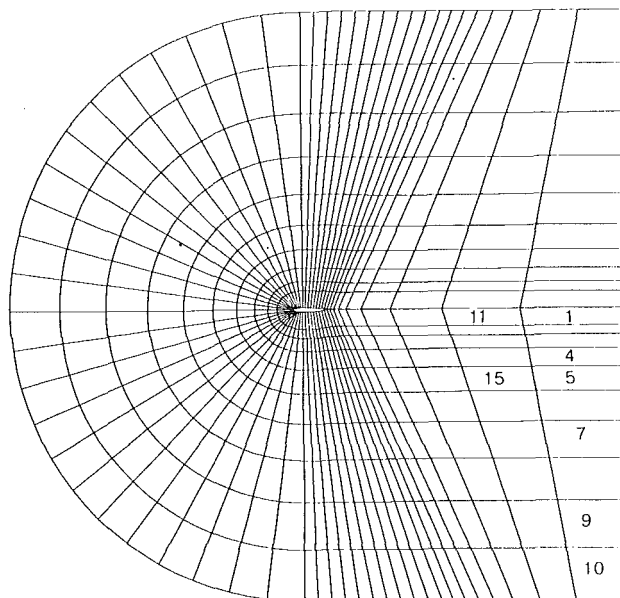
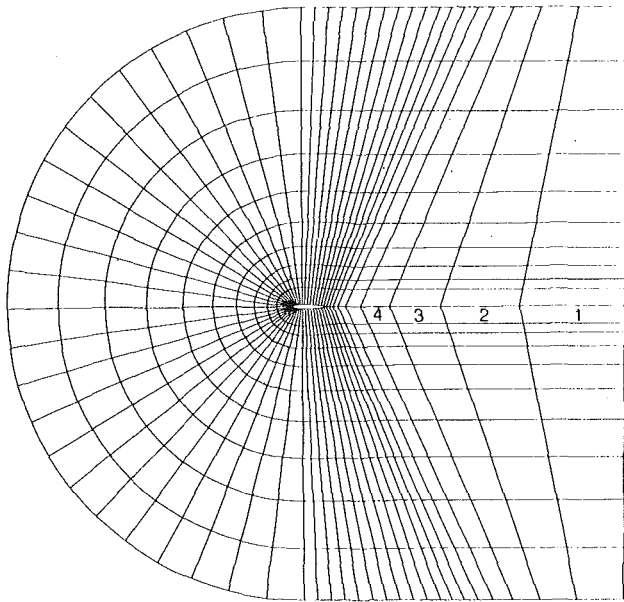


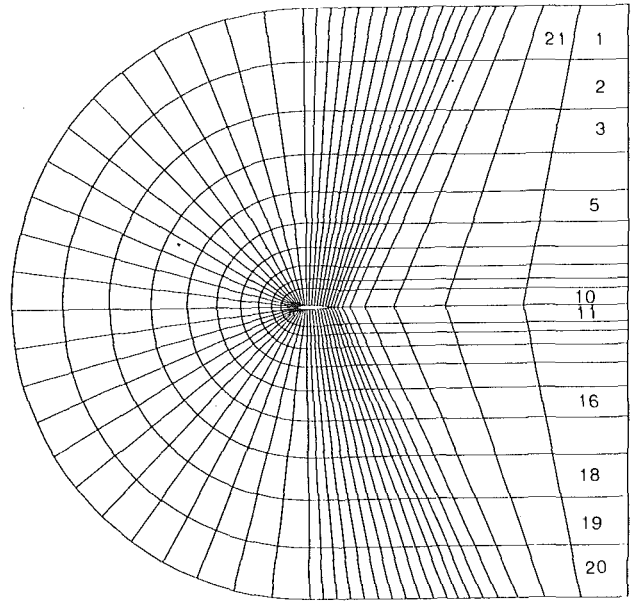
Fig. 2(a) A coarse C-grid representing Type A unknown ordering; (b) the structure of the coefficient matrix  $[\partial \bar{R} / \partial \bar{Q}]$  corresponding to Type A unknown ordering

The coefficient matrix  $[\partial \bar{R} / \partial \bar{Q}]$  is a square matrix with a block-banded structure, wherein all the nonzero elements are confined within a band formed by diagonals parallel to the main diagonal. It has a dimension  $(n \times n)$ . For a two-dimensional computational domain with  $J_2$  cells in the  $\eta$ -direction and  $K_2$  cells in the  $\xi$ -direction, the matrix dimension,  $n$ , is  $(4J_2 K_2)$ . This results in an enormous memory requirement of  $(16^*(J_2 K_2)^2)$ . However, the diagonal storage used by Baysal and Eleshaky (1990) reduces this memory requirement dramatically.

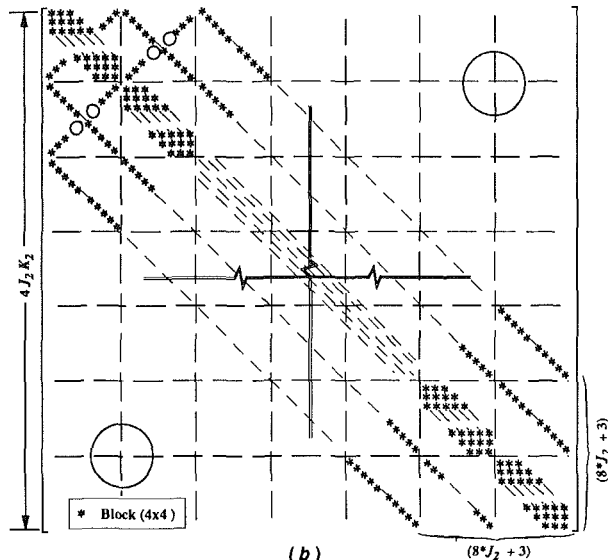
If a C-type grid is used, different strategies in the unknown ordering will have different influences on the memory requirement. For instance, shown in Fig. 2(a) is a coarse but representative C-grid around an airfoil. The cell nodes are ordered in one of various ways, which is called Order A herein (Venkatakrishnan, 1989). For the third-order upwind discretization of the governing equations, this ordering does not lead to a banded structure because of the coupling between cells on either side of the wake cut. Therefore, the coefficient matrix  $[\partial \bar{R} / \partial \bar{Q}]$  has a banded matrix with a half-bandwidth of



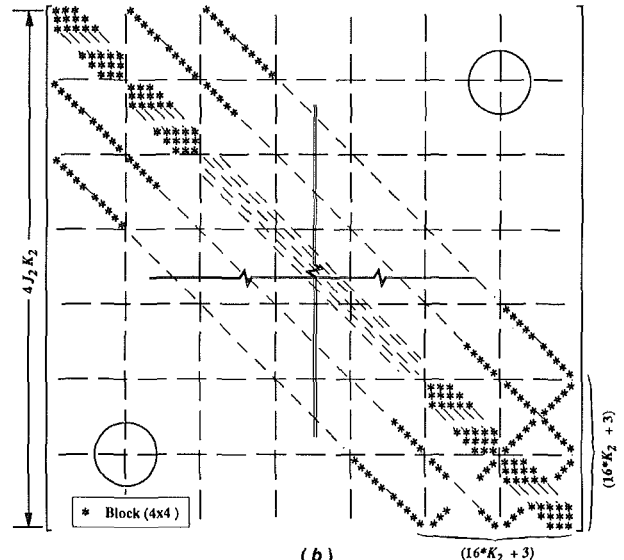
(a)



(a)



(b)



(b)

Fig. 3(a) A coarse C-grid representing Type B unknown ordering; (b) the structure of the coefficient matrix  $[\partial R/\partial Q]$  corresponding to Type B unknown ordering

Fig. 4(a) A coarse C-grid representing Type C unknown ordering; (b) the structure of the coefficient matrix  $[\partial R/\partial Q]$  corresponding to Type C unknown ordering

This results in requiring a sparse matrix solver, which is slower than the banded matrix solver (Baysal and Eleshaky, 1990), or a full matrix storage, which requires a prohibitively large memory. The second type of ordering is called Order B herein and is shown in Fig. 3(a). Although, for the third-order upwind discretization, Order B yields a fully banded matrix (Fig. 3(b)) with a half-bandwidth of  $(8*J_2 + 3)$ , it has the disadvantage of requiring relatively high memory since  $J_2$  is usually greater than  $K_2$ . Therefore, in the present study, a third type of ordering called Order C is used (Fig. 4(a)). For the third-order upwind discretization, this ordering leads to a fully banded matrix (Fig. 4(b)) with a half-bandwidth of  $(16*K_2 + 3)$ .

Because of the functional dependence of  $(\bar{R}_{j,k})$  on  $(M_{j+1/2, k+1/2})$ , the right hand side of Eq. (15) for an interior cell  $(j, k)$  can be written with the help of Eq. (21) as follows:

$$\frac{\partial \bar{R}_{j,k}}{\partial \bar{X}_D} = \left[ \frac{\partial \hat{g}^+ (\bar{Q}_{j+1/2,k}^-, M_{j+1/2,k})}{\partial (M_{j+1/2,k})} \right]$$

$$\begin{aligned} & + \frac{\partial \hat{g}^- (\bar{Q}_{j+1/2,k}^+, M_{j+1/2,k})}{\partial (M_{j+1/2,k})} \left] \frac{\partial (M_{j+1/2,k})}{\partial \bar{X}_D} \right. \\ & - \left[ \frac{\partial \hat{g}^+ (\bar{Q}_{j-1/2,k}^-, M_{j-1/2,k})}{\partial (M_{j-1/2,k})} \right. \\ & + \left. \frac{\partial \hat{g}^- (\bar{Q}_{j-1/2,k}^+, M_{j-1/2,k})}{\partial (M_{j-1/2,k})} \right] \frac{\partial (M_{j-1/2,k})}{\partial \bar{X}_D} \\ & + \left[ \frac{\partial \hat{h}^+ (\bar{Q}_{j,k+1/2}^-, M_{j,k+1/2})}{\partial (M_{j,k+1/2})} + \frac{\partial \hat{h}^- (\bar{Q}_{j,k+1/2}^+, M_{j,k+1/2})}{\partial (M_{j,k+1/2})} \right. \\ & \quad \left. - \frac{\partial \hat{h}_v (\bar{Q}_{j,k+1}, \bar{Q}_{j,k}, M_{j,k+1/2})}{\partial (M_{j,k+1/2})} \right] \frac{\partial (M_{j,k+1/2})}{\partial \bar{X}_D} \\ & - \left[ \frac{\partial \hat{h}^+ (\bar{Q}_{j,k-1/2}^-, M_{j,k-1/2})}{\partial (M_{j,k-1/2})} + \frac{\partial \hat{h}^- (\bar{Q}_{j,k-1/2}^+, M_{j,k-1/2})}{\partial (M_{j,k-1/2})} \right. \\ & \quad \left. - \frac{\partial \hat{h}_v (\bar{Q}_{j,k}, \bar{Q}_{j,k-1}, M_{j,k-1/2})}{\partial (M_{j,k-1/2})} \right] \frac{\partial (M_{j,k-1/2})}{\partial \bar{X}_D} \quad (24) \end{aligned}$$



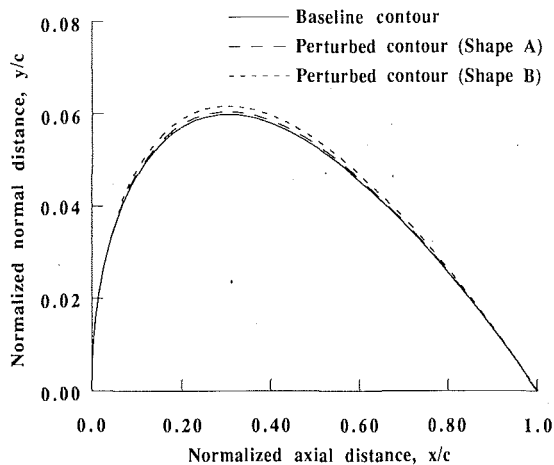


Fig. 5 Different perturbations of the upper surface of the NACA 0012 airfoil

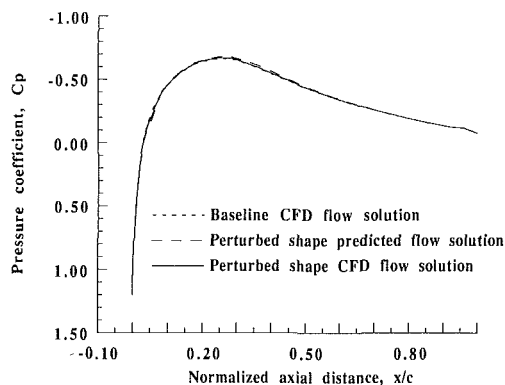


Fig. 6 Comparison of the pressure coefficient distributions along the upper airfoil surface of Shape A (Case 1a)

Determining the derivatives of the geometric terms ( $M_{j \pm 1/2, k \pm 1/2}$ ) with respect to the design variables,  $\bar{X}_D$ , depends on whether an analytical expression for  $M = M(\bar{X}_D)$  exists or not. If this exists, then this differentiation is straightforward. Otherwise, a finite-difference approximation for  $\partial(M_{j \pm 1/2, k \pm 1/2}) / \partial \bar{X}_D$  with a small step size  $\Delta \bar{X}_D$  can be used. In the present study, these derivatives are determined analytically. Details of Eq. (24) are given by Eleshaky (1992a).

Finally, the solution of the systems of adjoint variables (Eqs. (16) and (17)) is achieved by using a banded matrix solver (Martin et al., 1967). This solver stores only the elements within the bandwidth of the matrix to economize on the computer memory. Then, the matrix is inverted by the Gauss elimination method. In the flow prediction method, the solution of the system of linear algebraic equations (Eq. (15)) is also achieved by this matrix solver.

## Results and Discussion

The present computations are performed for flows past various airfoils at zero angle of attack. The free-stream Mach number is 0.8. The NACA 0012 airfoil is used as the baseline configuration for all the test cases. A C-grid with  $121 \times 33$  cells is used for the baseline airfoil (a much coarser but representative grid is shown in Fig. 2). The grid is regenerated for various airfoils that are formed during the optimization.

Before illustrating the capability of the present aerodynamic design method, it is essential to test the accuracy of the viscous flowfield prediction method, which is a key part in this design method. Therefore, a test case (Case 1a) of Fig. 5 is conducted, where all but the first two design variables of the upper airfoil

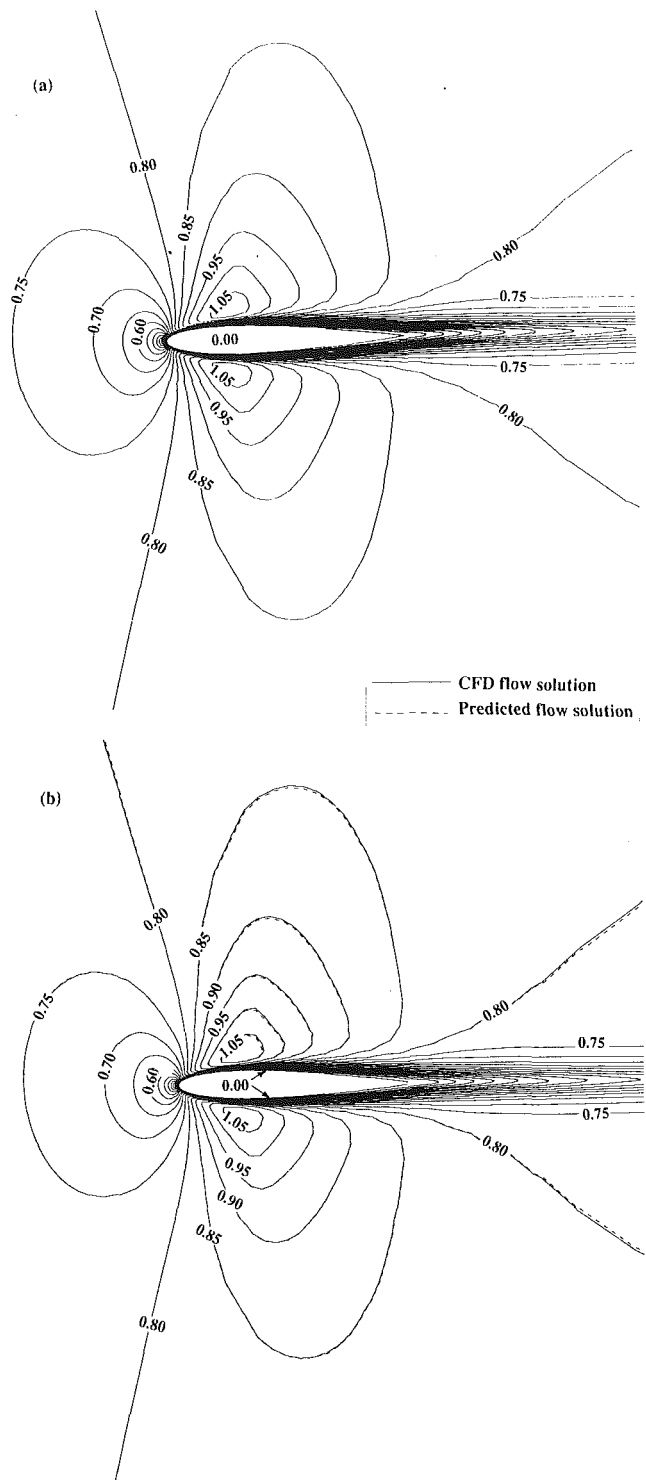


Fig. 7(a) Mach contours for flows over NACA 0012 airfoil (baseline) ( $M_\infty = 0.8$ ,  $Re = 5.0 \times 10^3$ ,  $\alpha = 0.0$ ); (b) comparison of computed and predicted Mach contours for the perturbed airfoil shape (Shape A)

surface are changed by 5 percent. The first two design variables are changed by 14 and by 35 percent to achieve the perturbed shapes (Shape A and Shape B, respectively) shown in this figure. The pressure coefficient ( $C_p$ ) distributions shown in Fig. 6 for Shape A are obtained from three different flowfield solutions, where the free-stream Reynolds number based on the chord length is given the value of 5000. The first and the second flowfield solutions are obtained by solving the viscous flow governing equations for the baseline configuration and the perturbed airfoil, respectively, where the residual error of

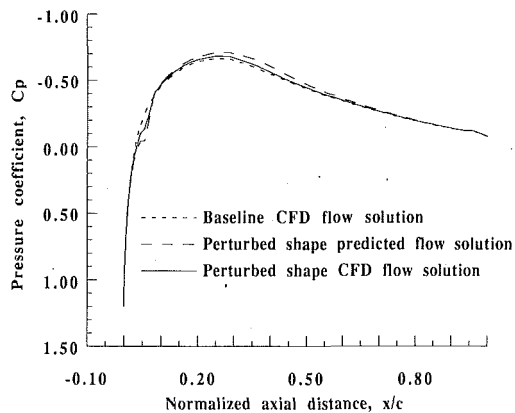


Fig. 8 Comparison of the pressure coefficient distributions along the upper airfoil surface of Shape B

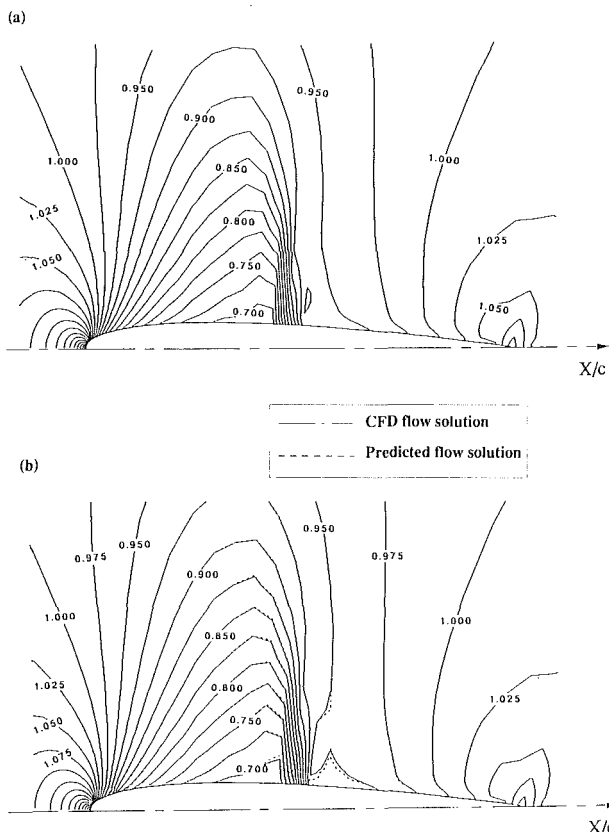


Fig. 9(a) Density contours for flows over NACA 0012 airfoil (baseline) ( $M_\infty = 0.8$ ,  $Re = 5.0 \times 10^5$ ,  $\alpha = 0.0$ ); (b) comparison of computed and predicted density contours for perturbed upper airfoil surface (Shape A)

these CFD solutions is driven to  $10^{-7}$ . Whereas, the third flowfield solution is obtained using the viscous flowfield prediction method. These flowfield solutions are shown via the Mach contours in Fig. 7. From Figs. 6 and 7, it can be seen that the analysis and the predicted results on the perturbed surface of the airfoil are almost indistinguishable except for slight discrepancies off surface. This may be attributed to the relatively large changes (14 percent) in the first two design variables. To investigate this reason of discrepancies further, the computations are repeated for larger changes in the design variables (Shape B). As seen from Fig. 8, the discrepancies increase as the changes in the design variables increase. This reconfirms the previous findings by the authors (1991b) which shows that the accuracy of the prediction result is strongly dependent on the magnitude of  $\Delta X_D$ .

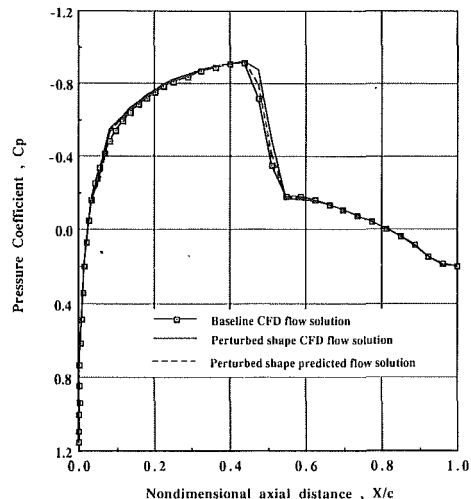


Fig. 10 Comparison of the pressure coefficient distribution along the upper surface of Shape A (Case 1b)

Furthermore, to test the accuracy of the viscous flowfield prediction method in the presence of shocks, a test case (Case 1b) is conducted, where the free-stream Reynolds number is increased to 0.5 million. The computation is performed using Shape A. Similar to Case 1a, three different flowfield solutions are obtained. The first and the second flowfield solutions are obtained by driving the residual error of the discretized flow governing equations to  $10^{-7}$  for the baseline configuration and the perturbed airfoil, respectively. The third flowfield solution is extrapolated from the baseline flowfield solution using the flow prediction method. These flowfield solutions are shown via the density contours in Fig. 9. The comparison between the pressure coefficient distributions along the upper surfaces is shown in Fig. 10. As seen from Figs. 9 and 10, the analysis and the predicted results on the perturbed surface of the airfoil are indistinguishable after and before the region where the shock and boundary layer interact. The slight discrepancies seen off surface may be due to the highly nonlinear phenomena associated with the shock-boundary layer interactions. Another contributor to these discrepancies is possibly the relatively large changes (14 percent) in the first two design variables. Therefore, during the optimization process the maximum  $\Delta X_D$  for each design variable per flow prediction step is conservatively restricted to 2 percent. This is important since an accurate prediction of the flow, particularly on the surface, is of great importance for a successful shape optimization.

Now, the aerodynamic shape optimization method is tested for two design problems in order to evaluate its efficiency and performance at transonic speeds. The free-stream Reynolds number in these design problems is given the value of 0.5 million and both design problems start by the NACA 0012 airfoil as the initial baseline airfoil. The Mach contours for the flow past this baseline airfoil are shown in Fig. 11. In both cases, only one surface of the airfoil is shape optimized and the immediate vicinity of the leading edge is excluded. Therefore, only 29 points on each surface, rather than all 89 points along the entire airfoil, become the design variables. The lower and upper bounds of the design variables are taken as  $-5$  and  $5$  degrees, respectively, to maintain an acceptably smooth aerodynamic shape. Also, the limit for the magnitude of the relative slope at the surface grid point adjacent to the T.E. point is given the value of 5 degrees.

The first design problem (Case 2) aims at reshaping the upper surface of the baseline airfoil in order to minimize the drag coefficient while keeping the lift coefficient greater than an arbitrarily assigned  $C_{L_{\min}}$  of 0.2. The final shape, as shown in Fig. 12(a), is appreciably different from the baseline. The pres-

sure distribution computed on the redesigned airfoil is also given in Fig. 12(a). The suction peak level on the upper surface is increased and the pressure gradient downstream of the shock is slightly increased. The new design results in an increased included angle at the trailing angle. This causes the increase in the pressure gradient, which in turn increases the viscous drag. On the other hand, the increased suction peak results in an increased wave drag, since the upper surface shock is located

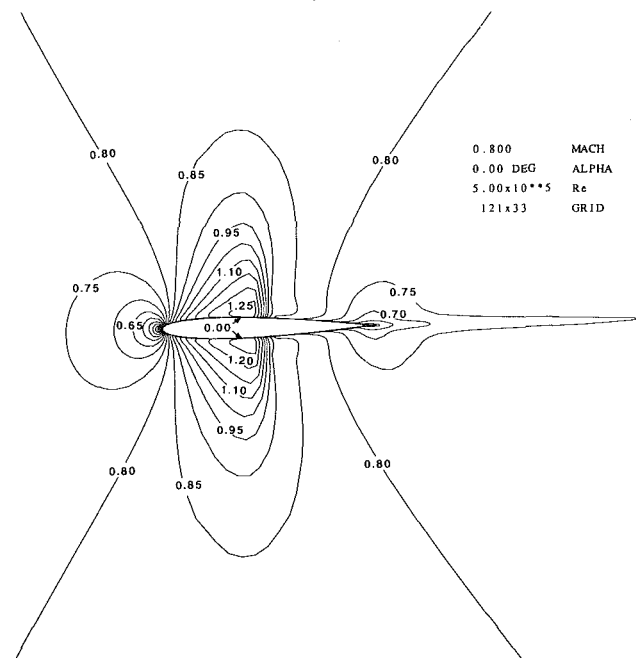


Fig. 11 Mach contours of flows over the NACA0012 airfoil (baseline airfoil)

further downstream compared to that of the baseline airfoil, as seen in Fig. 12(b). Although, the lower surface shock changes in just the opposite manner, this change is much less than that of the upper surface shock. Therefore, the total drag is increased, as it also is demonstrated by the optimization history (Fig. 12(c)). Certainly, the specified  $C_{L_{min}}$  would not have been accomplished otherwise. However, the optimum value of  $C_D$  (0.01713) is the minimum value for this specified  $C_{L_{min}}$ .

The airfoil shape of Case 2 was obtained after 13 optimization iterations, where 178 evaluations of the objective functions were needed. Only at the end of each iteration, there was a CFD analysis accompanied with the objective function evaluation for the new shape. This means that 13 CFD analyses were performed, whereas the flow prediction was performed 165 times. Comparing the computational time of a CFD analysis (~900 seconds) and a viscous flow prediction (~70 seconds), it can easily be realized that the aerodynamic optimization procedure becomes much more efficient by using the viscous flow prediction method. This design problem re-

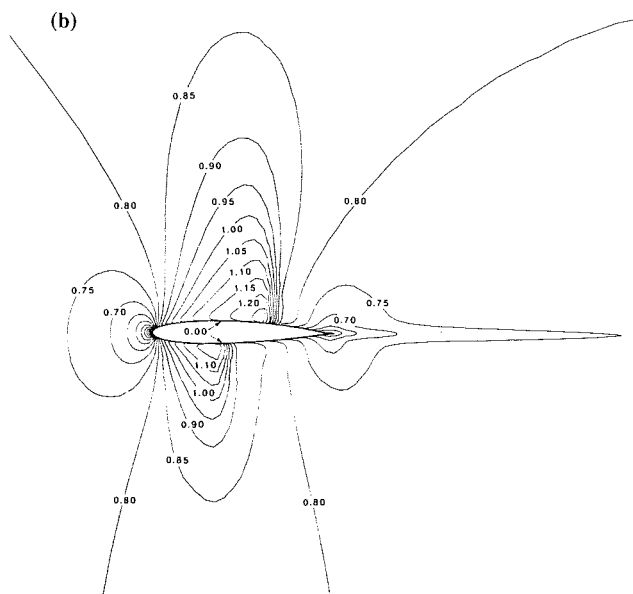


Fig. 12(b) Mach contours of flows over the optimized airfoil (Case 2)

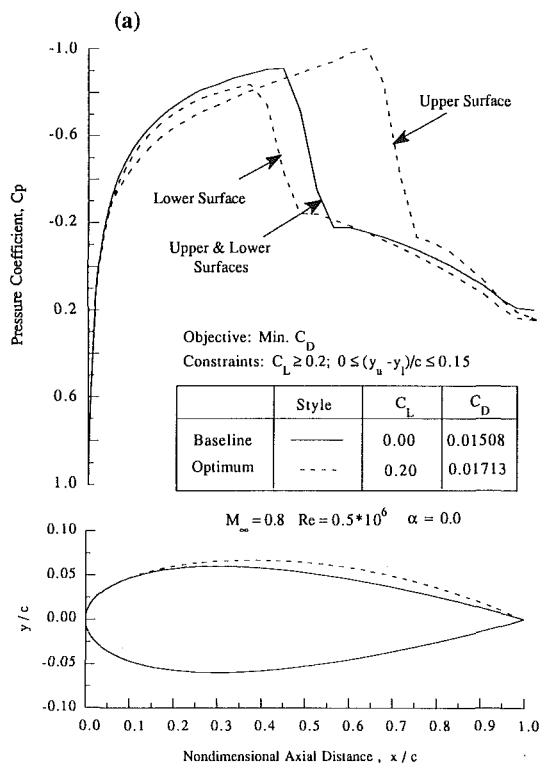


Fig. 12(a) Airfoil shape and distribution of surface pressure coefficient (Case 2)

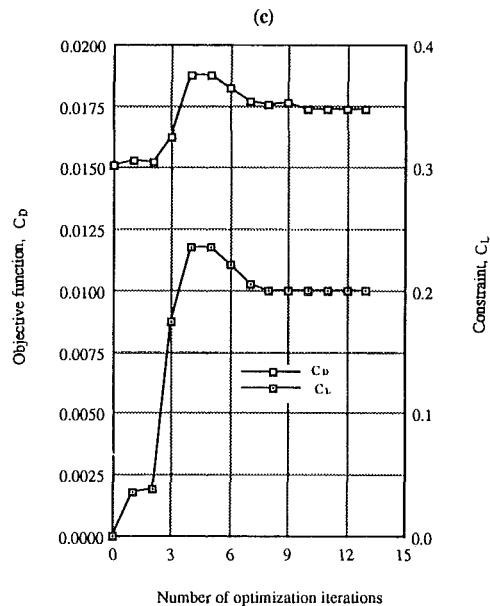


Fig. 12(c) Optimization history of Case 2 (drag minimization)

quired about eight hours on the CRAY-YMP computer located at Numerical Aerodynamic Simulation Center of NASA.

The second design problem (Case 3) is the reshaping of the lower surface of the baseline airfoil to maximize the lift coefficient while keeping the drag coefficient less than  $C_{D_{max}}$  of 0.02. The pressure distribution computed on the redesigned airfoil is shown in Fig. 13(a). Similar to Case 2, the total drag at the optimum design is increased, but the main reason in this case is the increased wave drag due to the location of the lower surface shock being further upstream. Also, unlike Case 2, the included trailing edge angle is decreased, hence, the pressure gradient downstream of the shock is decreased as seen from the final design shape in Fig. 13(a). Shown in Fig. 13(b) are the Mach contours for the optimized airfoil. By comparing Figs. 12(b) and 13(b), it is observed that the upper surface shock of Case 2 is located further downstream than that of Case 3.

The optimization history of Case 3 is plotted in Fig. 13(c). The optimum  $C_L$  value is 0.1751 which corresponds to  $C_D$  value of 0.01750. Unlike Case 2, the maximum of  $C_L$  does not correspond to the upper limit of  $C_D$ , instead it corresponds to the upper limit of the trailing edge geometric constraint, i.e., relative slope of 5 degrees. The airfoil shape of Case 3 was obtained after 9 optimization iterations, which is less than that required in Case 2. However, 190 objective function evaluations were needed in this case. Only nine CFD analyses were performed to compute the objective function, whereas the rest of the objective function evaluations were obtained by the flow prediction method. Case 3 required about seven hours on the CRAY-YMP computer.

## Conclusions

An aerodynamic shape optimization method based on the thin-layer Navier-Stokes equations is developed. This method includes a quasi-analytical determination of the objective function gradients and a flow prediction scheme based on the Taylor series expansion of an existing CFD solution. This flow prediction method requires at least an order of magnitude less computational time than a CFD analysis. Therefore, using the flow prediction method contributes significantly to the efficiency of the method. Furthermore, this shape optimization method does not require any prior knowledge of the optimized

shapes, which may be combined to produce the optimized shape. Unlike the inverse design methods, this method does not require prescribing any target flow feature, such as a pressure distribution.

The results from the prediction method are successfully compared with the CFD analysis results for a transonic flow past an airfoil, which includes a shock-boundary-layer interaction. The predictions, as expected, start deviating from the CFD analysis results, as the increment of the change in the design variables is increased.

The method is demonstrated by optimizing the shapes of supercritical transonic airfoils. Starting with the NACA-0012 airfoil at zero angle of attack as the baseline, first the upper surface is reshaped to achieve the minimum drag while obtaining a specified lift. The second optimization is started from the same baseline shape, but this time the lower surface is reshaped to achieve the maximum lift while retaining the drag below a specified value. The results of these cases indicate that the present method can produce successfully optimized aero-

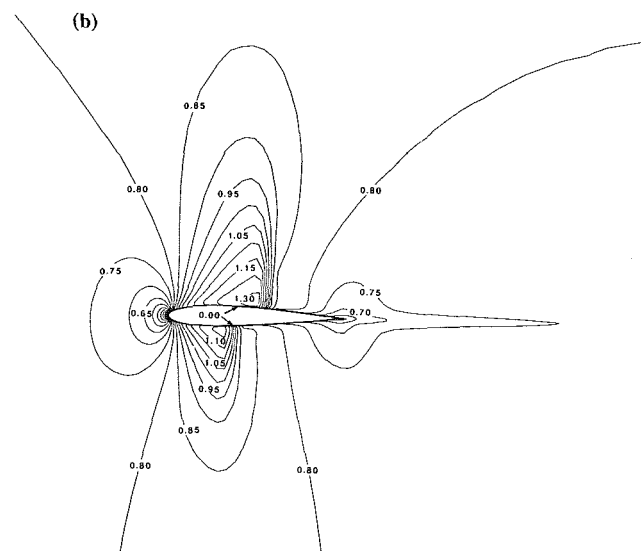


Fig. 13(b) Mach contours of flows over the optimized airfoil (Case 3)

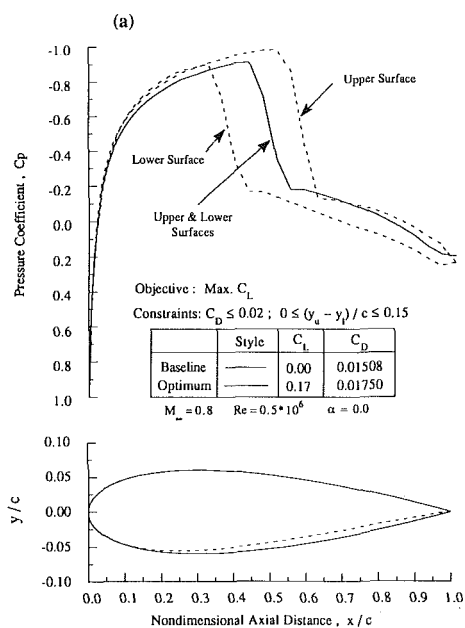


Fig. 13(a) Airfoil shape and distribution of surface pressure coefficient (Case 3)

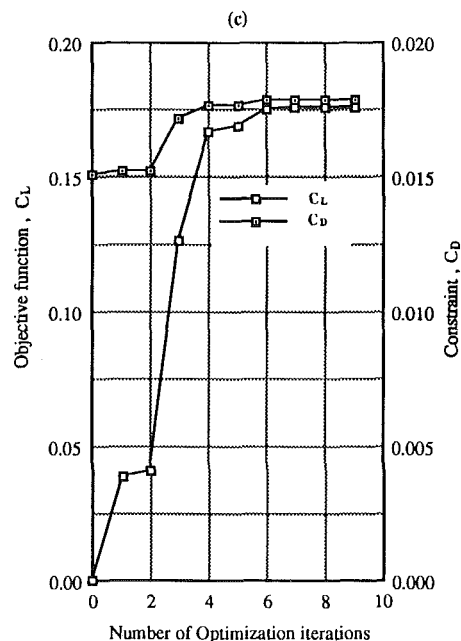


Fig. 13(c) Optimization history of Case 3 (lift maximization)

dynamic shapes. It should be mentioned here that the present computer code is not optimized for the CRAY-YMP computer system, and as a result, the CPU times quoted above are relatively high. With some improvements in the computer code as well as the overall optimization procedure, the CPU time has reduced by a factor of 10 (Burgreen et al., 1992). Furthermore, it is found that the memory requirements become prohibitively high for large 2-D problems and all 3-D problems. Therefore, a new aerodynamic sensitivity analysis scheme based on domain-decomposition principles has also been developed (Eleshaky, 1992a and Eleshaky and Baysal, 1992b) to handle these applications.

### Acknowledgment

This work is supported by NASA Langley Research Center under Grant No. NAG-1-1188. The technical monitor is David S. Miller. The authors would like to acknowledge G. W. Burgreen for his useful discussions.

### References

- Bauer, F., Garabedian, P., and Korn, D., 1977, "Supercritical Wing Sections III," *Lecture Notes in Economics and Mathematical Systems*, Springer-Verlag, New York.
- Baysal, O., 1988, "Supercomputing of Supersonic Flows Using Upwind Relaxation and MacCormack Schemes," *ASME JOURNAL OF FLUIDS ENGINEERING*, Vol. 110, No. 1, pp. 62-68.
- Baysal, O., and Eleshaky, M. E., 1990, "Aerodynamic Sensitivity Analysis Methods for the Compressible Euler Equations," *Recent Advances in Computational Fluid Dynamic*, ed., O. Baysal, ASME-FED Vol. 103, Winter Annual Meeting, November, pp. 191-202. Also, *ASME JOURNAL OF FLUIDS ENGINEERING*, Vol. 113, No. 4, pp. 681-688.
- Baysal, O., and Eleshaky, M. E., 1991a, "Aerodynamic Design Optimization Using Sensitivity Analysis and CFD," AIAA Paper No. 91-0471. Also, *AIAA Journal*, Vol. 30, No. 3, pp. 718-725.
- Baysal, O., Eleshaky, M. E., and Burgreen, G. W., 1991b, "Aerodynamic Shape Optimization Using Sensitivity Analysis on Third-Order Euler Equations," AIAA Paper No. 91-1577 CP, *Proceedings of the AIAA 10th Computational Fluid Dynamic Conference*, pp. 573-583. Also, to appear in *Journal of Aircraft*.
- Burgreen, G. W., Baysal, O., and Eleshaky, M. E., 1992, "Improving the Efficiency of Aerodynamic Shape Optimization Procedures," AIAA Paper No. 92-4697CP, *Proceedings of 4th AIAA/NASA/OAI Multidisciplinary Analysis and Optimization Conference*, Cleveland, Ohio, pp. 87-97. Also, to appear in *AIAA Journal*.
- Dulikravich, G. S., 1991, "Aerodynamic Shape Design and Optimization," AIAA Paper No. 91-0476.
- Eleshaky, M. E., 1992a, "A Computational Aerodynamic Design Optimization Method Using Sensitivity Analysis," Ph.D. Dissertation, Old Dominion University, Norfolk, VA.
- Eleshaky, M. E., and Baysal, O., 1992b, "Aerodynamic Shape Optimization via Sensitivity Analysis on Decomposed Computational Domains," AIAA Paper No. 92-4698 CP, *Proceedings of 4th AIAA/NASA/OAI Multidisciplinary Analysis and Optimization Conference*, Cleveland, Ohio, pp. 98-109.
- Giles, M. B., and Drela, M., 1987, "Two-Dimensional Transonic Aerodynamic Design Methods," *AIAA Journal*, Vol. 25, No. 9, pp. 1199-1206.
- Hicks, R. M., Murman, E. M., and Vanderplaats, G. N., 1974, "An Assessment of Airfoil Design by Numerical Optimization," NASA TM X-3092.
- Martin, R. S., and Wilkinson, J. H., 1976, "Solution of Symmetric and Unsymmetric Band Equations and the Calculations of Eigenvectors of Band Matrices," *Numerische Mathematik*, BD-9, pp. 279-301.
- Pittman, J. L., 1987, "Supersonic Airfoil Optimization," *AIAA Journal*, Vol. 24, No. 12, pp. 873-879.
- Rumsey, C. L., Taylor, S. L., Thomas, J. L., and Anderson, W. K., 1987, "Application of an Upwind Navier-Stokes Code to Two-Dimensional Transonic Airfoil Flow," AIAA Paper No. 87-0413.
- Vanderplaats, G. N., Hicks, R. M., and Murman, E. M., 1975, "Application of Numerical Optimization Techniques to Airfoils Design," *NASA Conference on Aerodynamic Analysis Requiring Advanced Computers*, NASA SP-347, Part II, pp. 749-768.
- Vanderplaats, G. N., 1979, "Approximation Concepts for Numerical Airfoil Optimization," NASA TN-1370.
- Vanderplaats, G. N., 1985, "ADS. A FORTRAN Program for Automated Design Synthesis," NASA CR-177985.
- Venkatakrishnan, V., 1989, "Newton Solution of Inviscid and Viscous Problems," *AIAA Journal*, Vol. 27, No. 7, pp. 885-891.

# The Flow Around Surface-Mounted, Prismatic Obstacles Placed in a Fully Developed Channel Flow

(Data Bank Contribution\*)

R. Martinuzzi

C. Tropea

Lehrstuhl für Strömungsmechanik,  
Universität Erlangen-Nürnberg,  
D-8520 Erlangen, Germany

*The flow field around surface-mounted, prismatic obstacles with different spanwise dimensions was investigated using the crystal violet, oil-film and laser-sheet visualization techniques as well as by static pressure measurements. The aim of this study is to highlight the fundamental differences between nominally two-dimensional and fully three-dimensional obstacle flows. All experiments were performed in a fully developed channel flow. The Reynolds number, based on the height of the channel, lay between  $8 \times 10^4$  and  $1.2 \times 10^5$ . Results show that the middle region of the wake is nominally two-dimensional for width-to-height ratios ( $W/H$ ) greater than 6. The separated region in front of wider obstacles is characterized by the appearance of a quasi-regular distribution of saddle and nodal points on the forward face of the obstacles. These three-dimensional effects are considered to be inherent to such separating flows with stagnation.*

## 1 Introduction

The study of the flow around surface-mounted, sharp-edged obstacles placed in a channel is fundamental to the understanding of the flow mechanisms for complex two- and three-dimensional geometries. There exists a considerable amount of published data for flows over two-dimensional geometries such as ribs and fences. However, there are markedly fewer studies in the literature concerned with the flow around three-dimensional obstacles. Of these, most are limited to the study of a single parameter, for example, the reattachment length. It is therefore the aim of this study to provide a general description of the flow around three-dimensional obstacles. Based on the flow visualization experiments performed for obstacles of different aspect ratio (width-to-height), the changes in the flow patterns as a function of aspect ratio are discussed qualitatively. Additionally, large-scale parameters such as the reattachment and separation lengths are discussed quantitatively.

The flow around single, surface-mounted, prismatic obstacles submerged in a boundary layer at high Reynolds numbers depends on a large number of parameters. Letting  $\Omega$  denote a general function describing this flow field, the functional relationship to these parameters expressed in terms of non-dimensional groups is:

$$\Omega = f_1 \left( \frac{\delta}{H}, \frac{u_\tau}{U_1}, \frac{l_w}{H}, \frac{W}{H}, \frac{L}{H}, \text{Re}_H, \Lambda, \alpha \right)$$

where  $\Lambda = l_w \sqrt{k_f} / U_1 H$  is the free-stream turbulence parameter.

\*Data have been deposited to the JFE Data Bank. To access the file for this paper, see instructions on p. 189 of this issue.

Contributed by the Fluids Engineering Division for publication in the JOURNAL OF FLUIDS ENGINEERING. Manuscript received by the Fluids Engineering Division February 28, 1992. Associate Technical Editor: R. L. Panton.

Assuming that the boundary layer develops over a smooth wall, it can be shown that  $l_w$ , the length scale of the wall turbulence, is a direct and simple function of  $u_\tau$ . Results of studies investigating these flows in terms of the parameters  $Hu_\tau/\nu$ ,  $H/\delta$  (Good and Joubert, 1968),  $HU_1/\nu$  (Castro, 1979),  $\delta/H$  (Castro and Robins, 1977) and of the free-stream turbulence parameter,  $\Lambda$  (Vincent, 1977, 1978) demonstrate that for a fixed obstacle geometry, these flows are mainly influenced by  $H$ ,  $\delta$ ,  $\Lambda$ , and  $u_\tau$ .

For the case of an obstacle placed in a fully developed channel flow, the number of parameters influencing the flow field is reduced. For this case, the boundary layer thickness is no longer relevant. The parameter  $\Lambda$  varies only to a small degree with the Reynolds number and the wall shear velocity ( $u_\tau$ ) changes slightly over a large range of Reynolds numbers ( $u_\tau/U_1$  varies about 20 percent between  $\text{Re} = 10^4$  and  $\text{Re} = 10^5$ ). Since the parameters defining the obstacle geometry are held constant, the flow can be considered to depend mainly on the parameters  $h/H$  and  $\text{Re}_H = U_B H/\nu$ .

There is little published data on the flow around surface-mounted obstacles placed in a channel. Hence, the following general description of the flow field around surface-mounted, prismatic obstacles relies on data from investigations performed in boundary layer flows. The shape and form of the separation region over and behind the obstacle depends on the relative boundary layer thickness,  $\delta/H$ . Whereas the form of the pressure distribution on the front face of a prismatic obstacle has been shown, for example, by Good and Joubert (1968) and Hunt (1982), to be insensitive to this parameter, the location of the separation point upstream of the obstacle is strongly dependent on  $\delta/H$ . The separation point moves

closer to the obstacle with decreasing relative boundary-layer thickness. The slope of the separation streamline changes, which in turn determines the shape of the recirculation "bubble" downstream of the leading edge.

Up to four vortices have been observed to form in the region upstream of the wall-obstacle junction. This structure is similar to that observed for vertical, wall-mounted cylinders (Baker, 1980, 1991). These vortices extend over the entire width of the obstacle and are deflected downstream at its ends thereby forming the well-known horseshoe vortex system.

The mean flow reattaches on top of the three-dimensional obstacles at streamwise lengths much shorter than those of two-dimensional obstacles (Schofield and Logan, 1990). Moreover, the streamwise length of the obstacle for which reattachment occurs has been shown by Castro and Dianat (1984) to be a function of  $\delta/H$ .

The recirculation region on top of the obstacle has been observed to consist of a multiple vortex system (see Castro and Robins, 1977; Woo et al., 1978) which gives rise to complicated surface shear stress patterns as shown by Dianat and Castro (1983) and Castro and Dianat (1984).

The flow around surface-mounted, three-dimensional obstacles is characterized by streamwise vortices generated within the shear layer. These vortices drastically affect the flow in the obstacle's vicinity, acting to reorganize the recirculation region and influence the downstream recovery region. As a result, the flow field for three-dimensional obstacle flows is intrinsically more complex than for the two-dimensional case.

Based on results obtained mainly from surface flow visualization techniques (Hunt et al., 1978; Perry and Hornung, 1984; and Fairlie, 1984), it has been shown that fluid is exchanged between the different separation regions formed around any three-dimensional obstacle. These regions are at the origin of line vortices which are shed into the downstream flow. It follows that the separation "bubble" formed around any surface-mounted, three-dimensional obstacle cannot be closed (Hunt et al., 1978).

Results from investigations performed by Logan and Lin (1982) and Fackrell and Pearce (1981) show that the separation length,  $x_R$ , and the recovery region downstream of the obstacle are much shorter for three-dimensional cases than for two-dimensional ones. This effect is probably due to the fact that the flow is mostly around, as opposed to over three-dimensional obstacles.

## 2 Experimental Apparatus and Techniques

The flows considered in this paper were investigated by means of static pressure measurements, laser light sheet, oil-film and crystal violet visualization techniques. The latter visualizations were performed in the water channel described by Ziegler (1987). A detailed description of this technique can be found in Dimaczek et al. (1988). The other experiments were performed in an open, blower-type air channel described in La-

rousse et al. (1991). The dimensions of the channel are 390 cm  $\times$  60 cm  $\times$  5 cm ( $1 \times w \times h$ ). The leading edge of the obstacles was placed 52 channel heights downstream of the inlet. The boundary-layer was tripped at the inlet in order to obtain fully-developed conditions at least 5 channel heights upstream of the front face of the obstacles.

Pressure taps of 1.0 mm diameters were provided on the channel walls and the faces of the obstacles in order to perform static pressure measurements. These measurements were conducted using commercially available membrane-type pressure transducers (HBM) with a measuring range of  $\pm 0.01$  bar. The analogue transducer signal was sampled at frequencies of 100 Hz to 400 Hz and averaged for periods extending from 2 to 20 seconds.

A mixture of kerosene, light transmission oil and carbon powder (toner) was used for the oil-film visualizations. The results were preserved on black and white film.

The crystal violet experiments were conducted using a gen-tian violet based indicator solution deposited on fixed photographic paper which also served as a permanent record of the results.

The tracer particles for the laser light sheet visualization experiments were obtained using smoke from a commercially available fog-generator. The experiments were recorded with a video camera.

## 3 Experimental Results

Tests were conducted for Reynolds numbers based on the channel height,  $Re_h$ , ranging from 80,000 to 115,000. Prismatic obstacles with square cross-sections of various widths were mounted on the surface of the channel floor. The on-coming channel flow was determined to be fully developed (see Larousse et al., 1991).

The effect of the aspect ratio ( $W/H$ ) on the flow patterns was investigated by performing visualization experiments. A cube and a rib spanning the entire width of the channel were chosen as representative cases for the fully three-dimensional and fully two-dimensional obstacle geometries respectively. Other obstacles with aspect ratios ranging between these were also investigated in order to study the transition between these two flow regimes. The geometric parameters for the different cases are summarized in Table 1. The geometry studied and the nomenclature used are summarized in Fig. 1.

The flow pattern for the two-dimensional rib obtained with the oil-film technique is shown in Fig. 2. With the exception of the corner effects due to the channel walls, the flow behind the obstacle is uniform. In this figure, line **A** corresponds to a clearly defined separation line upstream of the obstacle, while line **R** corresponds to the reattachment line.

On the front face of the obstacle, as can be seen from the crystal violet visualization results shown in Fig. 3, there is a series of alternating saddle and nodal points. This pattern can also be observed on the channel floor in the recirculation region

## Nomenclature

$B$ = blockage ratio (= $W \cdot H / w \cdot h$ )	$k_f$ = free-stream turbulence kinetic energy	$x, y, z$ = streamwise, vertical and cross-stream coordinates
$C_p$ = $(P - P_{atm}) / \frac{1}{2} \rho U_1^2$ , pressure coefficient	$Re_h$ = $U_B h / \nu$ , Reynolds number based on the channel height	$\alpha$ = angle of attack
$\Delta C_p$ = total pressure loss due to the obstacle	$Re_H$ = $U_1 H / \nu$ , Reynolds number based on the obstacle height	$\delta$ = boundary layer thickness
$h, w, l$ = channel height, width and length	$u, v, w$ = velocity components	$l_f$ = free-stream turbulent length scale
$H, L, W$ = obstacle height, stream-wise length, cross-stream width	$U_1$ = characteristic velocity	$l_w$ = length scale of the wall turbulence
$W/H$ = obstacle aspect ratio	$U_B$ = channel bulk velocity	$\Lambda$ = $l_f \sqrt{k_f} / U_1 H$ , free stream turbulence parameter
	$u_\tau$ = $\sqrt{\tau_w / \rho}$ , wall shear velocity	$\rho$ = fluid density
		$\nu$ = fluid kinematic viscosity

**Table 1 Summary of the obstacle geometries**

$H$ (cm)	$H/h$	$W$ (cm)	$W/H$	$H/W$	$H$ (cm)	$H/h$	$W$ (cm)	$W/H$	$H/W$
2.50	0.50	2.50	1.00	1.000	2.50	0.50	25.0	10.0	0.100
2.50	0.50	5.00	2.00	0.500	2.50	0.50	35.0	14.0	0.071
2.50	0.50	10.0	4.00	0.250	2.50	0.50	50.0	20.0	0.050
2.50	0.50	12.5	5.00	0.200	2.50	0.50	55.0	22.0	0.045
2.50	0.50	15.0	6.00	0.167	2.50	0.50	60.0	24.0	0.041
2.50	0.50	20.0	8.00	0.125					

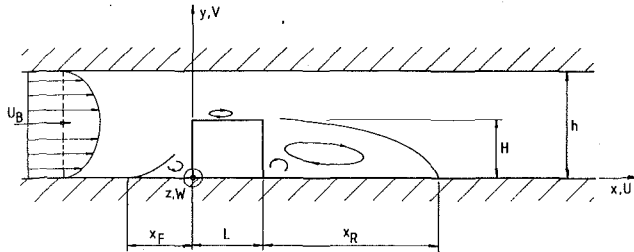


**Fig. 1 Sketch of the obstacle geometry in a channel flow**

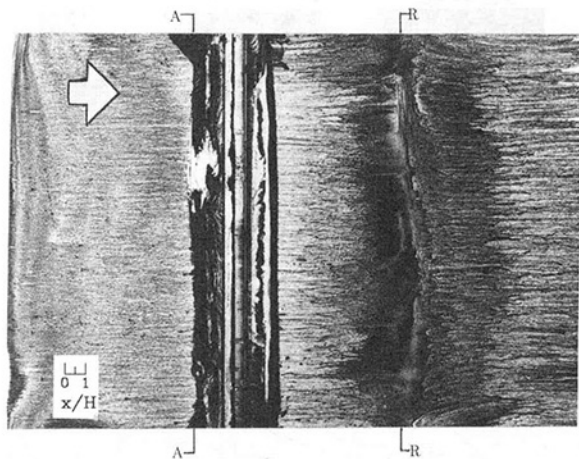


**Fig. 2 Oil-film visualization results for a two-dimensional rib ( $Re_h = 10^5$ )**

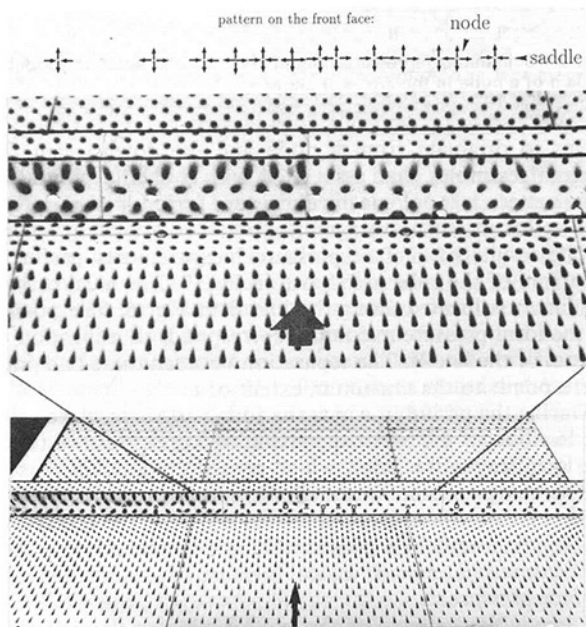


**Fig. 3 Crystal violet results for a two-dimensional rib showing saddle and nodal points ( $Re_h = 10^5$ )**

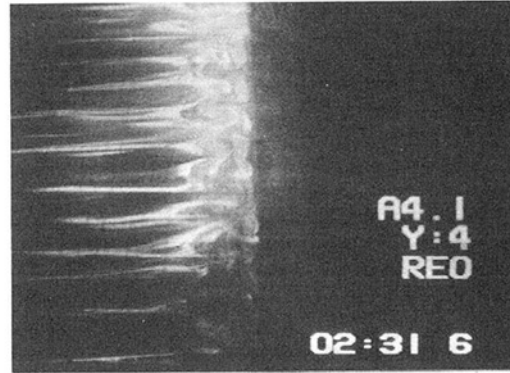


**Fig. 4 Laser-sheet visualization of the flow over a two-dimensional rib (plane  $y/H = 0.16$ )**

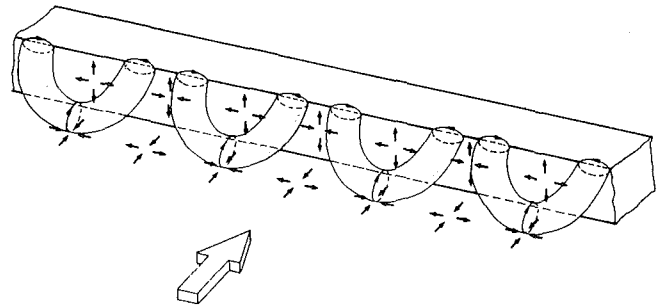


**Fig. 5 Model of the flow on the upwind face of an obstacle**

upstream of the obstacle. The location of these has been shown by Theisinger (1990) to be insensitive to small irregularities in the obstacle geometry. Further experiments performed using a laser light sheet technique show that the flow impinging on the front face of the obstacle does not preserve a two-dimensional character. Instead, the flow field develops a cellular structure, as can be seen in Fig. 4, which can still be recognized in the flow over the obstacle downstream of the leading edge. These three-dimensional structures suggest that the flow does not uniformly pass over the obstacle, but rather that this process occurs along preferred paths as is shown schematically in Fig. 5. Although highly idealized, this representation of the flow field is consistent with the observed surface patterns.

The results of the oil-film visualization for the flow around the cube are shown in Fig. 6(a) and Fig. 6(b). In these two figures, line **A** corresponds to the primary, upstream separation line and line **B** corresponds to the approximate time-averaged location of the center of the horseshoe vortex. Line **C** indicates a secondary recirculation at the front base of the cube.

As discussed by Larousse et al. (1991) and Devenport and Simpson (1990), the flow in the region between lines **A** and **B** is unstable and it is postulated that the fluid here is intermittently convected down to line **B**. The flow pattern seen adjacent to line **B** in Fig. 6(b) suggests however, a separation saddle point. This observation would only be topologically consistent





Fig. 6(a)

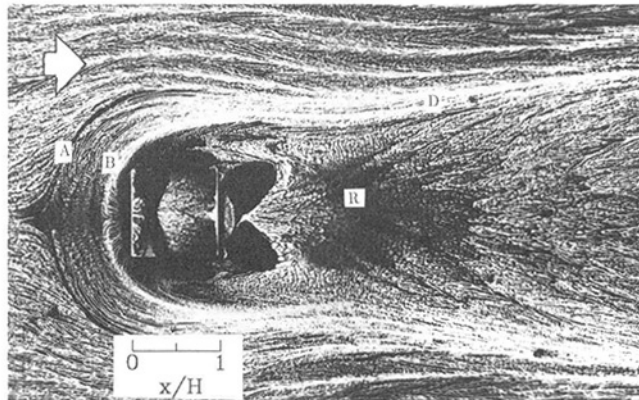


Fig. 6(b)

Fig. 6 Oil-film visualization results upstream of a surface-mounted cube

if there were an additional reattachment node between lines **A** and **B** along the axis of symmetry. Such a node could not be observed in these visualization results. However, this pattern may be explained in one of two ways. First, the separation between the suspected reattachment node and the saddle point is smaller than can be resolved by either visualization technique. Such a flow pattern corresponds to that suggested by Hunt et al. (1978) and Baker (1980). A second possibility is, as suggested by Devenport and Simpson (1990) who also observed a similar pattern, that this pattern is due to an abrupt change in the magnitude of the shear stress along line **B**. It therefore does not correspond to a saddle point and the reverse flow adjacent to the channel floor is convected back to line **A**. A similar conclusion has been drawn by Eckerle and Awad (1991) based on time-averaged velocity measurements of the flow around a surface-mounted cylinder. It should be noted, however, that this interpretation is topologically inconsistent, since it violates Euler's criterion (see Hunt et al., 1978).

Pictures of the flow patterns in this region obtained from laser light sheet visualization experiments show that: In one mode, a jet adjacent to the wall can be observed (see Fig. 7(a)) which rolls up to form a series of vortices as is seen in Fig. 7(b)). Hence, it is postulated that the vortex structure suggested by Baker (1980) represents one of the two possible modes in this region. It follows that the two 'separation' lines observed in the oil-film visualization experiments correspond to the extent of the separation zone of one of the two modes, respectively. This latter explanation prompted the flow pattern proposed here in Fig. 8.

The point marked  $D'$  designates the location of a doublet which can be interpreted as a system consisting of a free node, a reattachment and a separation half-saddle. The two half-saddle points are separated by a distance,  $\epsilon$ , which has a time-averaged value of zero. Hence, the flow upstream of this point

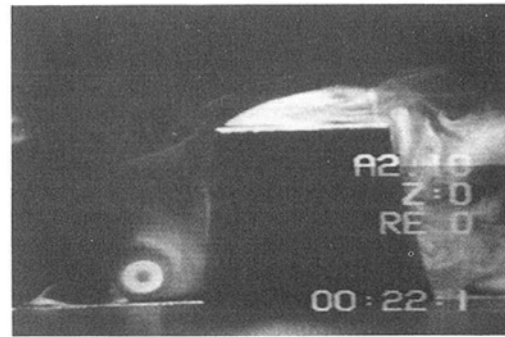


Fig. 7(a)

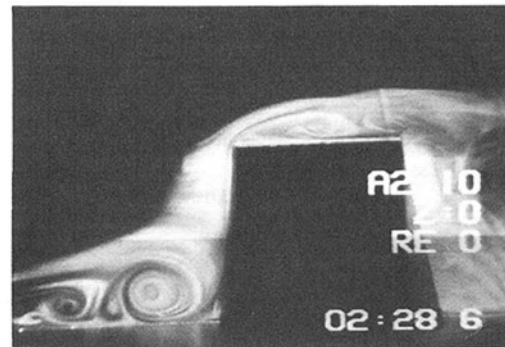


Fig. 7(b)

Fig. 7 Laser-sheet visualization of the flow in front of a cube (plane  $z/H = 0$ )

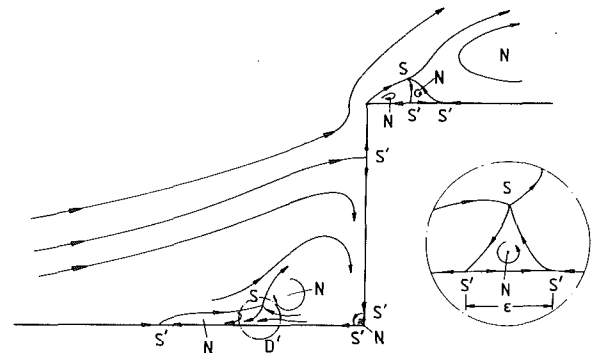


Fig. 8 Schematic representation of the mean-streamline model upstream of a cube in the  $z/H = 0$  plane

seems to originate from a node and the downstream flow pattern resembles that associated with a saddle point. This flow pattern is topologically consistent for both flow states as well as for the time-averaged flow.

The results of surface pressure measurements performed upstream of the cube are shown in Fig. 9. The local pressure minimum is located along the line **B** in Fig. 6. The position of the local pressure maximum corresponds to a location upstream of the line **B**. The separation between these two points corresponds to the maximum extent of  $\epsilon$ .

During the period in which the four-vortex structure exists, the location of the pressure maximum corresponds to that of the local stagnation point which causes the local increase of the surface pressure. Since the relaxation time of the pressure field is greater than that of the velocity field, the imprint left on the pressure field is preserved long enough such that it can be measured in terms of a local increase of the time-averaged surface pressure.

Directly downstream of the leading edge on the side of the cube there is a corner vortex located at the junction of the channel floor and cube in addition to the horseshoe vortex,

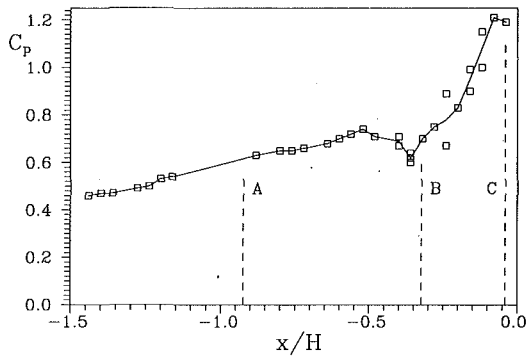


Fig. 9  $C_p$  versus  $x/H$  along  $z/H = 0$  in the region upstream of the cube ( $Re_h = 10^5$ ). Uncertainty estimate on positioning,  $\Delta x = \pm 0.5$  mm,  $\Delta x/H = \pm 0.02$  and on pressure coefficient,  $\Delta C_p = \pm 0.02$

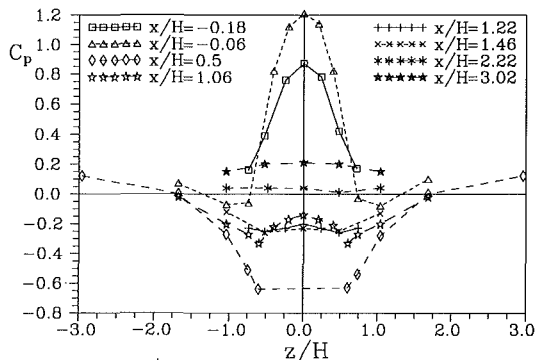


Fig. 10  $C_p$  versus  $z/H$  for the flow around a cube ( $Re_h = 10^5$ ). Uncertainty estimate on positioning,  $\Delta x = \pm 0.2$  mm,  $\Delta x/H = \pm 0.008$  and on pressure coefficient,  $\Delta C_p = \pm 0.02$ .

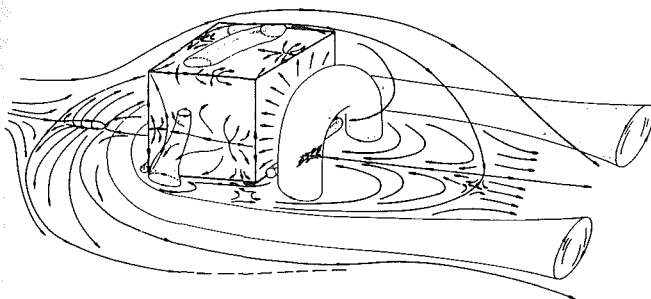


Fig. 11 Schematic representation of the flow around a surface-mounted cube

the imprint of which can be seen as local minima along the line for  $x/H = 0.5$  in Fig. 10. From the visualizations, it was possible to determine that this vortex extends up the side along the lateral face of the cube and that it is fed along the floor-body junction by the corner vortex situated aft of the obstacle.

In Fig. 6(a), two corner vortices can be clearly seen behind the cube. The flow patterns observed on the leeward face of the obstacles suggest that the extension of these vortices join at the symmetry plane ( $z/H = 0$ ) to form a closed arch behind the obstacle as suggested by Hunt et al. (1978).

The line **D** in Fig. 6(a) corresponds to the outer limits of the cube wake. The distance between the two ends of this line decreases up to approximately the reattachment point and then increases again. It is hereby postulated that directly behind the cube, the recirculation vortex entrains the surrounding fluid towards the axis of symmetry. After the reattachment point, the initially rapid expansion of the wake is due to the increase of the mass flux in the wake close to the channel floor as the shear layer reattaches and is subsequently entrained by the horseshoe vortex. Further downstream, the wake grows more

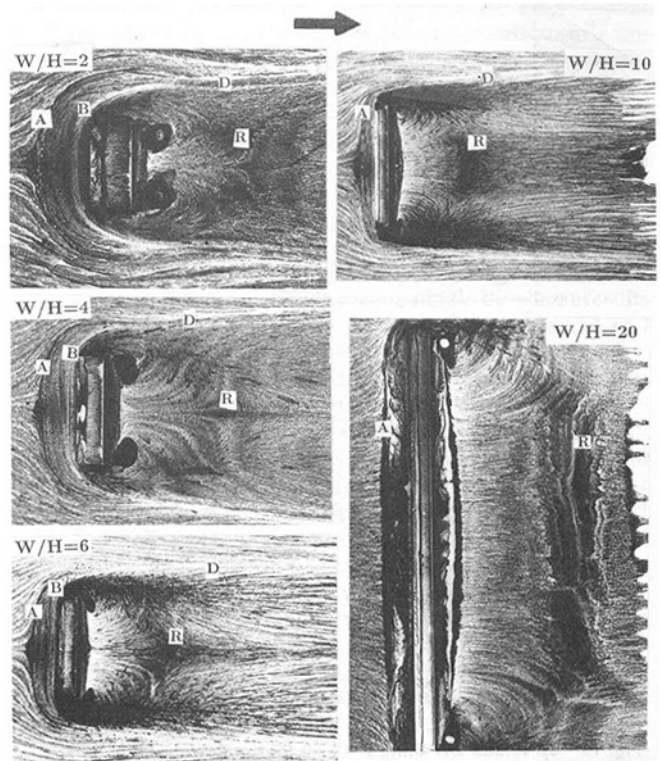


Fig. 12 An overview of oil-film visualization results for selected obstacles

slowly as fluid is gradually entrained from the surrounding flow. This flow pattern was observed for obstacles with aspect ratios of up to  $W/H = 4$ . The main features of the flow around small aspect ratio obstacles are summarized in schematic form in Fig. 11. This model was constructed with the aid of the results from the oil-film visualization experiments and those obtained from a detailed investigation of the velocity field around a cube (see Larousse et al., 1991).

An overview of the visualization results for selected geometries is shown in Fig. 12. Upstream of the obstacle, both the distance between lines **A** and **B** as well as the curvature of the separation line **A** decrease with increasing aspect ratio. For very large aspect ratios, only a single line of pigment accumulation can be recognized.

As reported by Devenport and Simpson (1990) and Larousse et al. (1991), the flow in the region between lines **A** and **B** is unsteady. Velocity measurements made by the latter authors and by Theisinger (1990) could not locate the characteristic velocity probability distribution associated with the bimodal-type instability for obstacles with aspect ratios greater than 10.

A clearly defined stagnation point can be seen on the front face of the obstacles with small aspect ratios. For aspect ratios greater than 10, an array of alternating saddle and node points similar to those for the two-dimensional rib (see Fig. 3) can be observed both on the front face and on the channel floor in the separated flow region.

The maximum and minimum pressures measured on the front and back of the obstacles, respectively, are lower for the three-dimensional cases than for the two-dimensional ones. The flow acceleration over the cube is weaker than over the rib which is consistent with this observation. Whereas the pressure recovery occurs rather quickly for small aspect ratios (see Fig. 13), the recovery region for the velocity field is significantly longer. Flow visualizations on the channel floor show significant mean cross-stream velocity components behind the cube for at least 20 heights downstream. The measured pressure coefficients shown in Fig. 10 clearly indicate the position of

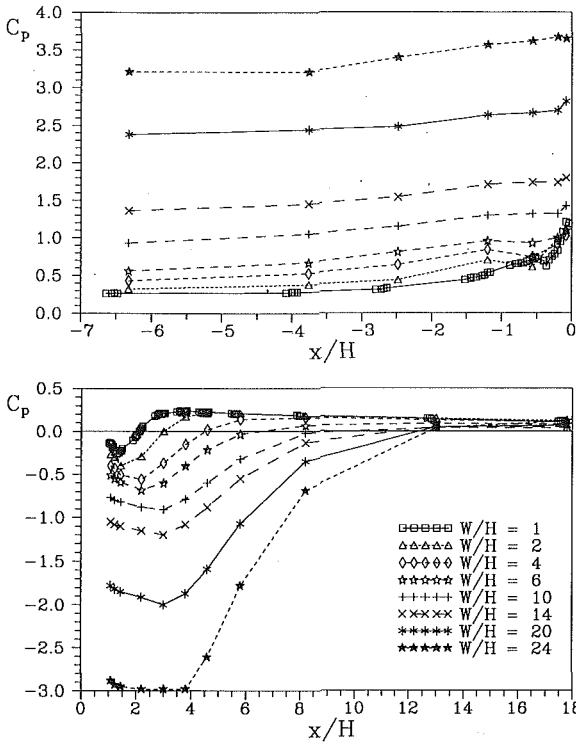


Fig. 13  $C_p$  versus  $x/H$  along  $z/H = 0$  for the flow around obstacles of varying  $W/H$  ( $Re_h = 10^5$ ). Uncertainty estimate on positioning,  $\Delta x = \pm 0.2$  mm,  $\Delta x/H = \pm 0.008$  and on pressure coefficient,  $\Delta C_p = \pm 0.02$ .

the horseshoe vortex on the side of the obstacle (local minima for the curve  $x/H = -0.06$ ) and the influence of the two corner vortices in the recirculating region (local minima for the curves  $x/H = 1.06$  and  $1.46$ ).

For small aspect ratios, the visualization experiments show that the cross-channel velocity component,  $w$ , is non-zero in the wake. Pressure measurements indicate that the cross-channel pressure gradients in the wake are not negligible (see Fig. 10). The strongly three-dimensional nature of the wake is attributed to the influence of the streamwise oriented vorticity of the two ends of the horseshoe vortex. The relative separation of the two ends of the horseshoe vortex increases with the aspect ratio and there is a region of negligible  $w$  velocity about the  $z/H = 0$  plane. The curvature of the reattachment line (marked **R** in Fig. 12) about the axis of symmetry is small for obstacles with aspect ratios greater than 6.

In the recirculation region, the orientation of the major axes and the location of the corner vortices change as a function of the aspect ratio. For small aspect ratios, the major axes of the elliptically shaped vortices are oriented away from the symmetry axis. For larger aspect ratios, these are oriented almost parallel to the obstacles. These changes are attributed to the effect of the pressure trough at the plane of symmetry which is stronger for longer obstacles.

The normalized leeward reattachment length ( $X_R/H$ ) and windward separation length ( $X_F/H$ ) are plotted as a function of the aspect ratio in Fig. 14. These show that on the back side of the obstacle, the reattachment length increases linearly with the obstacle width,  $W$ , up to about  $W/H \approx 4$  and asymptotically approaches an end value of about 7.2. The location of the forward separation points appears to increase with  $W$  until  $W/H \approx 6$  and then decreases slightly to a value of  $X_F/H \approx 1.3$ . However, because the effects of the blockage ratio,  $B$ , have not been explicitly investigated, it is difficult to draw further conclusions.

In all of the visualizations (see Figs. 2, 6, 12), except for the two-dimensional rib, the line **A** coincides with an accumulation of pigment associated with the presence of the separation zone

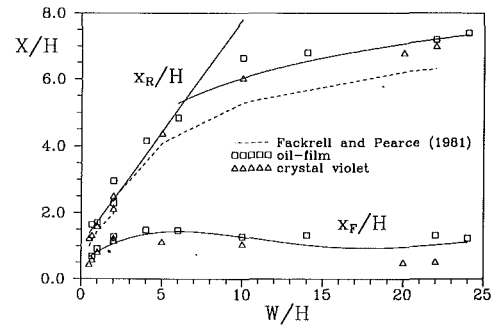


Fig. 14 Length of the upstream separation,  $X_F/H$ , and downstream reattachment,  $X_R/H$ , lengths as a function of  $W/H$  ( $Re_h = 10^5$ ). Uncertainty estimate on crystal violet,  $\Delta X_F = \pm 15$  percent ( $W/H \leq 10$ ) and on oil-film,  $\pm 5$  percent;  $\Delta X_F = \pm 60$  percent ( $W/H > 14$ ) and on oil-film  $\pm 7$  percent;  $\Delta X_R = \pm 3.5$  percent and on oil-film  $\pm 5$  percent

upstream of the obstacles. The pigment is transported to the sides by the deflected flow which extends this line around the forward corner of the obstacle.

Along the line **D**, which appears to be an extension of line **B**, there is a strong streamwise velocity component which rapidly transports pigment downstream leaving behind this white line. Line **D** effectively separates the wake from the flow to its sides. The flow in the wake is being convected away from the plane  $z = 0$ , while on the other side of this white line, the flow is predominantly in the streamwise direction. The change in the  $w$  velocity component occurs abruptly along this line.

#### 4 Discussion

On the back and top sides of the obstacles, the appearance of a nominally two-dimensional region about the plane of symmetry can be recognized as soon as  $W/H \approx 6$ . The flow aft of the obstacle with small aspect ratio is dominated by the interaction of the horseshoe vortex with the recirculation vortex and the reattaching shear layer. For larger aspect ratios, the effect of the horseshoe vortex is predominantly observed along the edges of the wake. The inner portion of the wake is characterized by a small  $w$  velocity component and can be considered two-dimensional.

On the front of the obstacles, the appearance of a nominally two-dimensional region is characterized by a weak cross-channel velocity component,  $w$ , as well as with the appearance of an alternating saddle-nodal point arrangement typically found for the "2-D" rib on the front face of the obstacle. A two-dimensional region upstream of the separation line can be observed for  $W/H$  greater than 10.

The fact that the saddle-node array on the front-side of the obstacle appears at roughly the same aspect ratio for which the region of unsteady flow (located between the lines **A** and **B** in Fig. 12) can no longer be identified suggests that these two events are related. The evolution of the forward separating length,  $X_F/H$ , is consistent with this premise. For obstacles with a small aspect ratio, the on-coming flow is mostly deflected to the sides. For these small obstacles, the relative amount of fluid deflected increases proportionally with  $W/H$ . The size of the separation region, must, therefore, also increase. However, for larger obstacles, fluid accumulates in the recirculation region faster than it can flow around the sides. Hence, the fluid is increasingly forced over the obstacle. This mechanism explains the initial increase of  $X_F/H$  for small  $W/H$  and its near constant value for larger aspect ratios.

The process by which fluid is removed from the front of the obstacles is not uniform. As discussed in Simpson and Devenport (1990) and Larousse et al. (1991), the flow in the region between lines **A** and **B** is unsteady and oscillates between two preferred states. In one state, the recirculating region upstream of the obstacle is larger than that in the other, implying

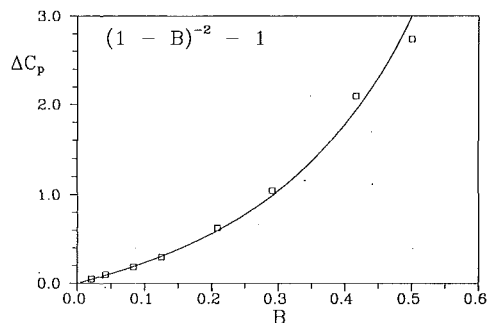


Fig. 15 Total pressure loss coefficient as a function of the blockage ratio,  $B = W \cdot H/w \cdot h$  ( $Re_h = 10^6$ ). Uncertainty estimate on pressure coefficient,  $\Delta C_p = \pm 5$  percent for  $W/H = 1$ , based on 25 point curve and  $\Delta C_p = \pm 9$  percent for  $W/H > 2$  based on 6 point curve.

that the mass flux to the sides of the obstacle is irregular. This mechanism is considered to be typical for three-dimensional flows around obstacles with small aspect ratios.

As the aspect ratio increases, proportionally less fluid is channeled along the sides of the obstacles and correspondingly more must flow over the top. As this occurs, a distinct, quasi-equidistant array of alternating node and saddle points becomes evident. These suggest that the flow over the obstacle follows preferred paths and that this feature is an inherent characteristic of separating flows with stagnation for large aspect ratios. It follows then that the flow is always locally three-dimensional even in the case of the two-dimensional rib.

In view of this interpretation, it is to be expected that the blockage ratio is an important parameter in determining the total pressure loss in the channel. As can be seen in Fig. 15, the total pressure loss due to the obstacle, expressed as a loss coefficient,  $\Delta C_p$ , is related to the blockage ratio,  $B$ , by the expression:

$$\Delta C_p = \frac{1}{(1 - B)^2} - 1$$

which is obtained by assuming that the entire gain in kinetic energy at the obstacle plane is dissipated downstream. The expression for the average gain in kinetic energy was derived from the Bernoulli and continuity equations. In order to experimentally determine  $\Delta C_p$ , the pressure difference between two locations, one far upstream and the other far downstream of the obstacle, was measured. The pressure difference between the same two locations was then measured for the same Reynolds number with the obstacle removed. The difference between these two values represents the loss due to the presence of the obstacle and, when normalized with  $\frac{1}{2}\rho U_B^2$ , yields  $\Delta C_p$ .

For three-dimensional flows, there is typically an additional thin separation region in front of the horseshoe vortex adjacent to the wall where strong, adverse pressure gradients dominate. The presence of a free-stream stagnation saddle point in this region, which can be seen in Fig. 8, indicates that this region is not a part of the horseshoe vortex and that no vortex is present in this region in this plane. This view subscribes to those offered by Eckerle and Awad (1991) as well as Devenport and Simpson (1990).

## 5 Conclusions

The flow around obstacles of different aspect ratios ( $W/H$ ) was investigated. It has been shown that a nominally two-dimensional region exists behind the obstacle for  $W/H > 6$  and upstream of the recirculation region in front of the obstacles for  $W/H > 10$ . Typically for such obstacles, the recirculation region on the upstream side is inherently three-dimensional. It is characterized by the appearance of a nearly equally spaced array of alternating saddle and node points on

the front face of the obstacles. This observation suggests that for large aspect ratios, the flow in the recirculation area upstream of the obstacle develops a cellular structure and passes over the obstacle along preferred paths.

For obstacles of small aspect ratio, the separation region upstream of the obstacles is characterized as alternating between two states. In one mode, high-inertia fluid is deflected on the front face of the obstacle back upstream in a jet adjacent to the wall. This fluid moves against the pressure gradient. As the fluid loses energy, it rolls up to form a system of up to four vortices. This structure characterizes the second mode. This mechanism helps reconcile the seemingly divergent results obtained by Baker (1980, 1991) with those by Eckerle and Awad (1991).

Pressure measurements and visualization results indicate that the recovery length behind a three dimensional obstacle is shorter than in the case of a two-dimensional flow. The interaction of the horseshoe vortex with the corner vortex behind the cube and with the impinging mixing-layer in the wake dominates the flow structure for obstacle with small aspect ratios ( $W/H < 4$ ). It has also been shown that the total pressure loss is a function of the blockage ratio.

As the aspect ratio increases, the two ends of the horseshoe vortex are farther apart and have a smaller influence on the middle region of the wake. For larger aspect ratios, the  $w$  velocity component and the pressure gradient in the cross-channel direction in the middle of the wake are negligible. This region can therefore be treated as nominally two-dimensional.

## JFE Data Bank Contributions

The experimental data obtained for the cube obstacle have been added to the *Journal of Fluids Engineering Data Bank*. These data include the three components of the mean velocity and all Reynolds stress components at numerous upstream and downstream positions. To access the file for this paper, see instructions on page 189 of this issue.

## Acknowledgment

This work was financially supported by the Deutsche Forschungsgemeinschaft under contract TR 194/3.

## References

- Baker, C. J., 1980, "The Turbulent Horseshoe Vortex," *Journal of Wind Engineering and Industrial Aerodynamics*, Vol. 6, pp. 9-23.
- Baker, C. J., 1991, "The Oscillation of Horseshoe Vortex System," *ASME JOURNAL OF FLUIDS ENGINEERING*, Vol. 113, pp. 489-495.
- de Brederode, V., and Bradshaw, P., 1972, "Three-Dimensional Flow in Nominally Two-Dimensional Separation Bubbles I: Flow Behind a Rearward-Facing Step," IC Aero Report, 72-19, Imperial College, London.
- Castro, I. P., and Robins, A. G., 1977, "The Flow Around a Surface-Mounted Cube in Uniform and Turbulent Streams," *Journal of Fluid Mechanics*, Vol. 79, part 2, pp. 307-335.
- Castro, I. P., 1979, "Relaxing Wakes Behind Surface-Mounted Obstacles in Rough Wall Boundary Layers," *Journal of Fluid Mechanics*, Vol. 93, part 4, pp. 631-659.
- Castro, I. P., and Dianat, M., 1984, "Surface Flow Patterns on Rectangular Bodies in Thick Boundary Layers," *Journal of Wind Engineering and Industrial Aerodynamics*, Vol. 11, pp. 107-119.
- Devenport, W. J., and Simpson, R. L., 1990, "Time-Dependent and Time-Averaged Turbulence Structure Near the Nose of a Wing-Body Junction," *Journal of Fluid Mechanics*, Vol. 210, pp. 23-55.
- Dianat, M., and Castro, I. P., 1983, "Fluctuating Surface Shear Stresses on Bluff Bodies," *Journal of Wind Engineering and Industrial Aerodynamics*, Vol. 17, pp. 133-146.
- Dimaczek, G., Eh, C., and Tropea, C., 1988, "Sichtbarmachung von Wasserströmungen mit Hilfe des Kristalviolettverfahrens," DLGR Workshop 2D-Meatechnik, Marktdorf, DLGR-Bericht 88-04.
- Dimaczek, G., Kessler, R., Martinuzzi, R., and Tropea, C., 1989, "The Flow Over Two-Dimensional, Surface-Mounted Obstacles at High Reynolds Numbers," *Proc. 7th Symposium on Turbulent Shear Flows*, Stanford, CA.
- Eckerle, W. A., and Awad, J. K., 1991, "Effect of Freestream Velocity on the Three-Dimensional Separated Flow Region in Front of a Cylinder," *ASME JOURNAL OF FLUIDS ENGINEERING*, Vol. 113, pp. 37-44.
- Fackrell, J. E., and Pearce, J. E., 1981, "Parameters Affecting Dispersion in the Near Wake of Buildings," CEBG Report No. RD/M/1179/N81.

Good, M. C., and Joubert, P. N., 1986, "The Form Drag of Two-Dimensional Bluff-Plates Immersed in Turbulent Boundary Layers," *Journal of Fluid Mechanics*, Vol. 31, pp. 547-582.

Hunt, J. C. R., Abell, C. J., Peterka, J. A., and Woo, H., 1978, "Kinematical Studies of the Flows Around Free or Surface-Mounted Obstacles, Applying Topology to Flow Visualization," *Journal of Fluid Mechanics*, Vol. 86, pp. 179-200.

Hunt, A., 1982, "Wind-Tunnel Measurements of Surface Pressure on Cube Building Models at Several Scales," *Journal of Wind Engineering and Industrial Aerodynamics*, Vol. 10, pp. 137-163.

Hussain, A. K. M. F., and Reynolds, W. C., 1975, "Measurements in Fully Developed Turbulent Channel Flow," *ASME JOURNAL OF FLUIDS ENGINEERING*, Dec. pp. 568-579.

Larousse, A., Martinuzzi, R., and Tropea, C., 1991, "Flow Around Surface-Mounted, Three-Dimensional Obstacles," *Proceedings 8th Symposium on Turbulent Shear Flows*, Munich, FRG.

Logan, E., and Lin, S. H., 1982, "Wakes from Arrays of Buildings," NASA Cr-170666.

Moore, J., and Forlini, T. J., 1984, "A Horseshoe Vortex in a Duct," *ASME Journal of Engineering for Gas Turbines and Power*, Vol. 106, pp. 668-675.

Schofield, W. H., and Logan, E., 1990, "Turbulent Shear Flow Over Surface-Mounted Obstacles," *ASME JOURNAL OF FLUIDS ENGINEERING*, Vol. 112, pp. 376-385.

Theisinger, J., 1990, "Untersuchung der Dreidimensionalität einer Rippenströmung im Flachkanal mittels LDA," Diplomarbeit, at the Lehrstuhl für Strömungsmechanik of the University Erlangen-Nuremberg.

Vincent, J. H., 1977, "Model Experiments on the Nature of Air Pollution Transport Near Buildings," *Atmospheric Environments*, Vol. 11, pp. 765-774.

Vincent, J. H., 1978, "Scalar Transport in the Near Aerodynamic Wakes of Surface-Mounted Cubes," *Atmospheric Environments*, Vol. 12, pp. 1319-1322.

Woo, H. G. C., Peterka, J., and Cermak, J. E. 1976, "Wind Tunnel Measurements in Wakes of Structures," Colorado State Univ. Rept. CER7575-76 HGWC-JAP-JEC40.

Ziegler, T., 1987, "Experimentelle Untersuchungen der Strömung über ein zweidimensionales Hindernis," Diplomarbeit at the Lehrstuhl für Strömungsmechanik of the University Erlangen-Nuremberg.

# A Comparison of the Linear and Nonlinear $k - \epsilon$ Turbulence Models in Combustors

C. C. Hwang

Genxing Zhu

Department of Mechanical Engineering,  
University of Pittsburgh,  
Pittsburgh, PA 15261

M. Massoudi

J. M. Ekmann

U.S. Department of Energy,  
Pittsburgh Energy Technology Center,  
Pittsburgh, PA 15236

*In swirling turbulent flows, the structure of turbulence is nonhomogeneous and anisotropic and it has been observed that the assumptions leading to the formulation of the  $k-\epsilon$  model, which is used very often in many engineering applications, are inadequate for highly swirling flows. Furthermore, even with the various modifications made to the  $k-\epsilon$  model, it is still not capable of describing secondary flows in noncircular ducts and it cannot predict non-zero normal-Reynolds-stress differences. Recently Speziale (1987) has developed a nonlinear  $k-\epsilon$  model, which extends the range of validity of the standard  $k-\epsilon$  model while maintaining most of the interesting features of the  $k-\epsilon$  model; for example, the ease of application in existing Computational Fluid Dynamics (CFD) codes. In this work, we will use the nonlinear  $k-\epsilon$  closure to model the turbulence in combustors. The particular combustor geometries selected for this study are (i) the flow in a round pipe entering an expansion into another coaxial round pipe, and (ii) the flow in two confined co-axial swirling jets. The results show that there are no significant differences in the performance of the two models. It is speculated that the inlet conditions for  $k$  and  $\epsilon$  may play as crucial a role in achieving predicted accuracy as turbulence modeling details. Also it is possible that weaknesses in the performance of the modeled equations for  $k$  and  $\epsilon$  may have masked differences in the two models.*

## 1 Introduction

Advanced combustion technologies are being developed with the intent of achieving higher overall system efficiencies and reduced environmental loading of air, water, and solid pollutants. Further developments may tend toward systems combining a pressurized, high-intensity combustor with some combination of gas and steam turbines to optimize the cycle efficiency and to minimize pollutant formation.

For these high-intensity combustors, swirl has been commonly used to improve the flame stability and to produce higher rates of entrainment of the ambient fluid and fast mixing. Traditionally, designers have relied heavily on experiments to produce empirical formulas and correlations. One obvious difficulty with this approach is that, in general, changing the experiment or some of the conditions, such as geometry, inlet conditions, etc., may change the outcome and hence produce different correlations. The traditional approach is now being supplemented with theoretical and computational modeling techniques, which provide the designer with the predictive capability and the freedom to change and choose many of the conditions leading to a better design of combustors with higher efficiency, optimum geometry, less pollution, etc.

Fluid dynamics plays an important role in all practical com-

bustion systems. The computation of turbulent flows has been a problem of major concern for nearly a century. In spite of all the recent advances in computer technology, turbulent flows cannot at present be calculated with an exact method. The exact equations describing the turbulent motion are believed to be the Navier-Stokes equations and numerical procedures are available to solve these equations. However, the storage capacity and the speed of modern computers are not yet sufficient to allow a solution for any practically relevant flow. An alternate approach is to use averaged equations over a time scale that describe the mean motion.

In swirling turbulent flows, the structure of turbulence is nonhomogeneous and anisotropic. It has been suggested that the assumptions leading to the formulation of the  $k-\epsilon$  model are inadequate for the modeling of turbulence in highly swirling flows (Sloan et al., 1986). An alternative approach is to reduce the partial differential equations for the Reynolds stresses into algebraic forms where the combined convection and diffusion terms of Reynolds stress transport equation are related to the kinetic energy of turbulence, rate of production, and dissipation (Rodi, 1976). Using this approach, i.e., the algebraic stress models (ASM), the solution procedure may be simplified, but accuracy of the solution is still questionable due to both the assumptions and lack of transport of the stresses.

In general, a shortcoming of the linear models is their inaccuracy for the types of turbulent flows where the normal Reynolds stress differences play an important role (e.g., sec-

Contributed by the Fluids Engineering Division for publication in the JOURNAL OF FLUIDS ENGINEERING. Manuscript received by the Fluids Engineering Division September 30, 1991. Associate Technical Editor: C. J. Freitas.

ondary flows in a non-circular duct or separated flows). However, one of the advantages of, say,  $k-\epsilon$  model is that it reduces to the mixing length theory for thin shear flows that can, in general, describe many turbulent boundary layer flows with no separation (Launder and Spalding, 1974).

Recently, Speziale (1987) has developed a nonlinear  $k-\epsilon$  model<sup>1</sup> that extends the range of validity of the standard  $k-\epsilon$  model (e.g., secondary flows or separated flows) while maintaining most of the interesting features of the  $k-\epsilon$  model (e.g., the mixture length theory for thin shear flows and the ease of application in existing CFD codes). Speziale and Ngo (1988) used this model to study the flow past a backward-facing step. Later Hur et al. (1990) studied the fully developed turbulent flow of a viscous fluid in curved ducts using the nonlinear  $k-\epsilon$  model. The effect of mesh refinement on the computed results in the case of flow past a backward-facing step using the nonlinear  $k-\epsilon$  model was studied by Thangan and Hur (1991). This nonlinear model will be used in this study to describe the flow field in two combustor geometries and comparisons will be made with the standard  $k-\epsilon$  model.

## 2 The Governing Equations and the Nonlinear $k-\epsilon$ Model

The governing equations for the flow of an incompressible Newtonian fluid are the Reynolds equation and the conservation of mass, which are of the general form

$$\rho \left( \frac{\partial \mathbf{v}}{\partial t} + (\text{grad } \mathbf{v})\mathbf{v} \right) = -\text{grad } p + \mu \nabla^2 \mathbf{v} + \text{div } \bar{T}, \quad (1)$$

$$\text{div } \mathbf{v} = 0, \quad (2)$$

where  $\mathbf{v}$  is the mean velocity field,  $p$  the mean pressure field,  $\rho$  the density of the fluid,  $\mu$  the dynamic viscosity of the fluid, and  $\bar{T}$  the Reynolds stress tensor whose components, in a cartesian coordinate system, are given by

$$T_{ij} = -\rho \bar{u}_i \bar{u}_j, \quad (3)$$

where  $\mathbf{u}$  is the fluctuating part of the velocity field. In many engineering problems, the closure is achieved via the  $k-\epsilon$  model of turbulence. Recently, Speziale (1987) has derived a nonlinear

<sup>1</sup>This model has the basic structure of the stress tensor of a Rivlin-Ericksen fluid of third grade. Actually, Rivlin (1957) suggested that the turbulent flow of a Newtonian fluid may, for certain purposes, be assumed as the flow of a non-Newtonian fluid.

model, based on principles of continuum mechanics,<sup>2</sup> in which the standard  $k-\epsilon$  model constitutes the linear portion of it. He showed that the Reynolds stress tensor  $\bar{T}$  is related to the mean field quantities via

$$\bar{T} = -\frac{2}{3} \rho k \bar{I} + 2\rho C_\mu \frac{k^2}{\epsilon} \bar{D} + 4C_D C_\mu^2 \frac{k^3}{\epsilon^2} \left[ \bar{D}^2 - \frac{1}{3} (\text{tr } \bar{D}^2) \bar{I} \right] + 4C_E C_\mu^2 \frac{k^3}{\epsilon^2} \left[ \dot{\bar{D}} - \frac{1}{3} (\text{tr } \dot{\bar{D}}) \bar{I} \right], \quad (4)$$

where

$$k = -\frac{1}{2\rho} (\text{tr } \bar{T}), \quad (5)$$

$$\bar{D} = \frac{1}{2} [(\text{grad } \mathbf{v}) + (\text{grad } \mathbf{v})^T], \quad (6)$$

and  $\dot{\bar{D}}$  is the frame-indifferent Oldroyd derivative of  $\bar{D}$ , given by

$$\dot{\bar{D}} = \frac{\partial \bar{D}}{\partial t} + (\text{grad } \bar{D})\mathbf{v} - \bar{D}(\text{grad } \mathbf{v})^T - (\text{grad } \mathbf{v})\bar{D}. \quad (7)$$

It should be noted that the first two terms in Eq. (4) correspond to the  $k-\epsilon$  model, and  $C_D$  and  $C_E$  are two new universal constants that would have to be determined. Speziale (1987) used the experimental data of Laufer (1951) to evaluate these two new constants, which are

$$C_D = C_E = 1.68. \quad (8)$$

Speziale and Ngo (1988) indicated that, as a result of the Oldroyd derivative term  $\dot{\bar{D}}$  and the quadratic terms in  $\bar{D}$ , "this nonlinear  $k-\epsilon$  model is able to describe turbulent memory effects and yields much more accurate predictions for the normal Reynolds stresses in turbulent channel flow."

For an axisymmetric two-dimensional cylindrical geometry the flow field is given by

$$\mathbf{v} = v(r, x)\mathbf{e}_r + w(r, x)\mathbf{e}_\theta + u(r, x)\mathbf{e}_x, \quad (9)$$

where the components of the velocities are denoted in this manner so as to make the comparison with existing published work easier. For the present problem,  $\bar{D}$  in the cylindrical system becomes

<sup>2</sup>In particular, Speziale (1987) used the following: (i) general coordinate and dimensional invariance, (ii) realizability, (iii) material frame-indifference.

## Nomenclature

$C_{\epsilon 1}, C_{\epsilon 2}, C_\mu, \sigma_\epsilon$  = turbulence model constants in the  $k-\epsilon$  model

$C_D, C_E$  = turbulence model constants in the nonlinear  $k-\epsilon$  model

$D$  = chamber diameter

$\bar{D}$  = rate of stretching tensor

$\dot{\bar{D}}$  = the Oldroyd derivative of  $\bar{D}$

$d$  = nozzle diameter

$E$  = constant

$\mathbf{e}_r, \mathbf{e}_\theta, \mathbf{e}_x$  = unit vector in  $r, \theta, x$  direction

$G$  = volumetric rate of generation of  $k$

$\bar{I}$  = idemfactor

$k$  = kinetic energy of turbulence

$R_i$  = radius of inner tube

$R_o$  = radius of outer tube

$S^\psi$  = source term

$\bar{T}$  = Reynolds stress tensor

$\hat{\bar{T}}$  = nonlinear portion of Reynolds stress tensor

$(U_i)_{av}$  = bulk average velocity of inner jet

$U_0$  = reference velocity

$u, v, w$  = time mean velocity (in  $x, r, \theta$  direction)

$V$  = total tangential velocity

$V^+$  = dimensionless total tangential velocity

$x, r, \theta$  = axial, radial, azimuthal cylindrical polar coordinates

$Y^+$  = dimensionless distance

$\alpha$  = side-wall angle

$\alpha_\lambda$  = length scale factor at the inlet

$\alpha_T$  = turbulence intensity factor at inlet

$\Gamma_\psi$  = exchange coefficients

$\epsilon$  = turbulence energy dissipation rate

$\kappa$  = constant

$l$  = turbulence length scale

$\mu$  = effective viscosity

$\rho$  = time-mean density

$\phi$  = swirl vane angle

$\psi$  = flow quantities,  $u, v, w, k, \epsilon$



$$(\bar{D}) = \begin{pmatrix} \frac{\partial v}{\partial r} & \frac{1}{2} \left( r \frac{\partial}{\partial r} \left( \frac{w}{r} \right) + \frac{1}{r} \frac{\partial v}{\partial \theta} \right) & \frac{1}{2} \left( \frac{\partial u}{\partial r} + \frac{\partial v}{\partial x} \right) \\ \frac{1}{2} \left( r \frac{\partial}{\partial r} \left( \frac{w}{r} \right) + \frac{1}{r} \frac{\partial v}{\partial \theta} \right) & \left( \frac{1}{r} \frac{\partial w}{\partial \theta} + \frac{v}{r} \right) & \frac{1}{2} \left( \frac{\partial w}{\partial x} + \frac{1}{r} \frac{\partial u}{\partial \theta} \right) \\ \frac{1}{2} \left( \frac{\partial u}{\partial r} + \frac{\partial v}{\partial x} \right) & \frac{1}{2} \left( \frac{\partial w}{\partial x} + \frac{1}{r} \frac{\partial u}{\partial \theta} \right) & \frac{\partial u}{\partial x} \end{pmatrix}. \quad (10)$$

If we set

$$\Lambda_1 \equiv 4C_D C_{\mu}^2 \frac{k^3}{\epsilon^2}, \quad (11)$$

$$\Lambda_2 \equiv 4C_E C_{\mu}^2 \frac{k^3}{\epsilon^2}, \quad (12)$$

then the nonlinear portion  $\hat{T}_{ij}$  of  $T_{ij}$  in Eq. (4) can be expressed in 3-D cylindrical polar coordinates

$$\hat{T}_{rr} = \frac{\Lambda_1}{3} (2D_{rr}^2 - D_{\theta\theta}^2 - D_{xx}^2 + D_{r\theta}^2 + D_{rx}^2 - 2D_{\theta x}^2) + \frac{\Lambda_2}{3} [2\bar{D}_{rr} - (\bar{D}_{\theta\theta} + \bar{D}_{xx})], \quad (13)$$

$$\hat{T}_{\theta\theta} = \frac{\Lambda_1}{3} (-D_{rr}^2 + 2D_{\theta\theta}^2 - D_{xx}^2 + D_{r\theta}^2 + D_{\theta x}^2 - 2D_{rx}^2) + \frac{\Lambda_2}{3} [2\bar{D}_{\theta\theta} - (\bar{D}_{rr} + \bar{D}_{xx})], \quad (14)$$

$$\hat{T}_{xx} = \frac{\Lambda_1}{3} (-D_{rr}^2 - D_{\theta\theta}^2 + 2D_{xx}^2 + D_{rx}^2 + D_{\theta x}^2 - 2D_{r\theta}^2) + \frac{\Lambda_2}{3} [2\bar{D}_{xx} - (\bar{D}_{rr} + \bar{D}_{\theta\theta})], \quad (15)$$

$$\hat{T}_{r\theta} = \Lambda_1 (D_{rr}D_{r\theta} + D_{r\theta}D_{\theta\theta} + D_{rx}D_{\theta x}) + \Lambda_2 \bar{D}_{r\theta}, \quad (16)$$

$$\hat{T}_{\theta x} = \Lambda_1 (D_{r\theta}D_{rx} + D_{\theta\theta}D_{\theta x} + D_{\theta x}D_{xx}) + \Lambda_2 \bar{D}_{\theta x}, \quad (17)$$

$$\hat{T}_{rx} = \Lambda_1 (D_{rx}D_{rr} + D_{\theta x}D_{r\theta} + D_{xx}D_{rx}) + \Lambda_2 \bar{D}_{rx}, \quad (18)$$

and the expressions for  $\bar{D}_{ij}$  are given by

$$\bar{D}_{rr} = \frac{\partial D_{rr}}{\partial t} + \left( v \frac{\partial}{\partial r} + \frac{w}{r} \frac{\partial}{\partial \theta} + u \frac{\partial}{\partial x} \right) D_{rr} - 2 \frac{w}{r} D_{r\theta} - 2 \left[ \frac{\partial v}{\partial r} D_{rr} + \left( \frac{1}{r} \frac{\partial v}{\partial \theta} - \frac{w}{r} \right) D_{r\theta} + \frac{\partial v}{\partial x} D_{rx} \right], \quad (19)$$

$$\bar{D}_{\theta\theta} = \frac{\partial D_{\theta\theta}}{\partial t} + \left( v \frac{\partial}{\partial r} + \frac{w}{r} \frac{\partial}{\partial \theta} + u \frac{\partial}{\partial x} \right) D_{\theta\theta} + 2 \frac{w}{r} D_{r\theta} - 2 \left[ \frac{\partial w}{\partial r} D_{r\theta} + \left( \frac{1}{r} \frac{\partial w}{\partial \theta} + \frac{v}{r} \right) D_{\theta\theta} + \frac{\partial w}{\partial x} D_{\theta x} \right], \quad (20)$$

$$\bar{D}_{xx} = \frac{\partial D_{xx}}{\partial t} + \left( v \frac{\partial}{\partial r} + \frac{w}{r} \frac{\partial}{\partial \theta} + u \frac{\partial}{\partial x} \right) D_{xx} - 2 \left( \frac{\partial u}{\partial r} D_{rx} + \frac{1}{r} \frac{\partial u}{\partial \theta} D_{\theta x} + \frac{\partial u}{\partial x} D_{xx} \right), \quad (21)$$

$$\bar{D}_{r\theta} = \frac{\partial D_{r\theta}}{\partial t} + \left( v \frac{\partial}{\partial r} + \frac{w}{r} \frac{\partial}{\partial \theta} + u \frac{\partial}{\partial x} \right) D_{r\theta} + \frac{w}{r} (D_{rr} - D_{\theta\theta}) - \left[ \frac{\partial v}{\partial r} D_{r\theta} + \left( \frac{1}{r} \frac{\partial v}{\partial \theta} - \frac{w}{r} \right) D_{\theta\theta} + \frac{\partial v}{\partial x} D_{\theta x} \right] - \left[ \frac{\partial w}{\partial r} D_{rr} + \left( \frac{1}{r} \frac{\partial w}{\partial \theta} + \frac{v}{r} \right) D_{\theta r} + \frac{\partial w}{\partial x} D_{rx} \right], \quad (22)$$

$$\bar{D}_{\theta x} = \frac{\partial D_{\theta x}}{\partial t} + \left( v \frac{\partial}{\partial r} + \frac{w}{r} \frac{\partial}{\partial \theta} + u \frac{\partial}{\partial x} \right) D_{\theta x} + \frac{w}{r} D_{rx} - \left[ \frac{\partial w}{\partial r} D_{rx} + \left( \frac{1}{r} \frac{\partial w}{\partial \theta} + \frac{v}{r} \right) D_{\theta x} + \frac{\partial w}{\partial x} D_{xx} \right] - \left[ \frac{\partial u}{\partial r} D_{r\theta} + \frac{1}{r} \frac{\partial u}{\partial \theta} D_{\theta\theta} + \frac{\partial u}{\partial x} D_{\theta x} \right], \quad (23)$$

$$\bar{D}_{rx} = \frac{\partial D_{rx}}{\partial t} + \left( v \frac{\partial}{\partial r} + \frac{w}{r} \frac{\partial}{\partial \theta} + u \frac{\partial}{\partial x} \right) D_{rx} - \frac{w}{r} D_{\theta x} - \left[ \frac{\partial u}{\partial r} D_{rr} + \frac{1}{r} \frac{\partial u}{\partial \theta} D_{r\theta} + \frac{\partial u}{\partial x} D_{rx} \right] - \left[ \frac{\partial v}{\partial r} D_{rx} + \left( \frac{1}{r} \frac{\partial v}{\partial \theta} - \frac{w}{r} \right) D_{\theta x} + \frac{\partial v}{\partial x} D_{xx} \right]. \quad (24)$$

The nonlinear parts of the stress tensors are considered as the source terms in the original code. Therefore, these terms are added at appropriate parts of the code.

The governing equations of motion, 1 and 2, using Eqs. (4) and (9) can be put in a general conservation law of the form

$$\frac{\partial}{\partial t} (\rho\psi) + \text{div}(\rho v\psi) = \text{div}(\Gamma_\psi \text{grad } \psi) + S^\psi, \quad (25)$$

where  $\psi$  represents any of the following quantities:  $u$ ,  $v$ ,  $w$ , turbulent kinetic energy  $k$ , and turbulent dissipation rate  $\epsilon$ ,  $\Gamma_\psi$  is the corresponding exchange coefficients, and  $S^\psi$  is the source term. The appropriate equations for these variables for a  $k$ - $\epsilon$  turbulence model are given in Lilley and Rhode (1982):

$$\frac{\partial}{\partial x} (\rho u) + \frac{1}{r} \frac{\partial}{\partial r} (\rho r) = 0, \quad (26)$$

$$\frac{1}{r} \left[ \frac{\partial}{\partial x} (\rho u^2 r) + \frac{\partial}{\partial r} (\rho v r u) - \frac{\partial}{\partial x} \left( r \mu \frac{\partial u}{\partial x} \right) - \frac{\partial}{\partial r} \left( r \mu \frac{\partial u}{\partial r} \right) \right] = - \frac{\partial p}{\partial x} + S^u, \quad (27)$$

$$\frac{1}{r} \left[ \frac{\partial}{\partial x} (\rho u r v) + \frac{\partial}{\partial r} (\rho v^2 r) - \frac{\partial}{\partial x} \left( r \mu \frac{\partial u}{\partial x} \right) - \frac{\partial}{\partial r} \left( r \mu \frac{\partial v}{\partial r} \right) \right] = - \frac{\partial p}{\partial r} + \frac{\rho w^2}{r} - \frac{2\mu v}{r^2} + S^v, \quad (28)$$

$$\frac{1}{r} \left[ \frac{\partial}{\partial x} (\rho u r w) + \frac{\partial}{\partial r} (\rho v r w) - \frac{\partial}{\partial x} \left( r \mu \frac{\partial w}{\partial x} \right) - \frac{\partial}{\partial r} \left( r \mu \frac{\partial w}{\partial r} \right) \right] = - \frac{\rho v w}{r} - \frac{w}{r^2} \frac{\partial}{\partial r} (r \mu) + S^w, \quad (29)$$

$$\frac{1}{r} \left[ \frac{\partial}{\partial x} (\rho u r k) + \frac{\partial}{\partial r} (\rho v r k) - \frac{\partial}{\partial x} \left( r \frac{\mu}{\sigma_k} \frac{\partial k}{\partial x} \right) - \frac{\partial}{\partial r} \left( r \frac{\mu}{\sigma_k} \frac{\partial k}{\partial r} \right) \right] = G - C_D \rho \epsilon, \quad (30)$$

$$\frac{1}{r} \left[ \frac{\partial}{\partial x} (\rho u r \epsilon) + \frac{\partial}{\partial r} (\rho v r \epsilon) - \frac{\partial}{\partial x} \left( r \frac{\mu}{\sigma_\epsilon} \frac{\partial \epsilon}{\partial x} \right) - \frac{\partial}{\partial r} \left( r \frac{\mu}{\sigma_\epsilon} \frac{\partial \epsilon}{\partial r} \right) \right] = (C_1 \epsilon G - C_2 \rho \epsilon^2) / k, \quad (31)$$



where  $\mu$  is the effective viscosity, which is composed of laminar ( $\mu_l$ ) and turbulent ( $\mu_t$ ) parts and defined by

$$\mu = \mu_l + \mu_t = C_\mu \rho k^2 / \epsilon + \mu_l. \quad (32)$$

The values for the empirical constants are  $C_\mu = 0.09$ ,  $C_1 = 1.44$ ,  $C_2 = 1.92$ ,  $\sigma_k = 1.00$  and  $\sigma_\epsilon = 1.30$ , which are quoted in Lilley and Rhode (1982).

The terms  $S^u$ ,  $S^v$ ,  $S^w$  are parts of  $\nabla \cdot \mathcal{T}$ , and are defined by

$$\begin{aligned} S^u &= \frac{\partial}{\partial x} \left( \mu \frac{\partial u}{\partial x} \right) + \frac{1}{r} \frac{\partial}{\partial r} \left( r \mu \frac{\partial v}{\partial x} \right), \\ S^v &= \frac{\partial}{\partial x} \left( \mu \frac{\partial v}{\partial r} \right) + \frac{1}{r} \frac{\partial}{\partial r} \left( r \mu \frac{\partial v}{\partial r} \right), \\ S^w &= 0. \end{aligned} \quad (33)$$

The other parts of these terms are expressed in diffusion-term format and appear on the left-hand side of the governing equations.

The term  $G$  is the volumetric rate of generation of  $k$  and for Newtonian fluids

$$\begin{aligned} G &= T_{ij} \frac{\partial u_i}{\partial x_j} \\ &= 2\mu \left[ D_{ij} D_{ij} - \frac{1}{3} D_{ij}^2 \right]. \end{aligned} \quad (34)$$

For the linear  $k$ - $\epsilon$  model of incompressible fluids ( $D_{ii} = 0$ ),  $G$  becomes

$$\begin{aligned} G &= 2\mu [D_{ij} D_{ij}] \\ &= \mu \left[ 2 \left\{ \left( \frac{\partial u}{\partial x} \right)^2 + \left( \frac{\partial v}{\partial r} \right)^2 + \left( \frac{v}{r} \right)^2 \right\} + \left( \frac{\partial u}{\partial r} + \frac{\partial v}{\partial x} \right)^2 \right. \\ &\quad \left. + \left\{ r \frac{\partial}{\partial r} \left( \frac{w}{r} \right) \right\}^2 + \left( \frac{\partial w}{\partial x} \right)^2 \right]. \end{aligned} \quad (35)$$

For the nonlinear  $k$ - $\epsilon$  model, we write

$$(T_{ij})_{\text{total}} = (T_{ij})_{\text{linear}} + (T_{ij})_{\text{nonlinear}} = (T_{ij})_l + \hat{T}_{ij}, \quad (36)$$

where  $\hat{T}_{ij}$  is the nonlinear portion of  $T_{ij}$ , and is given by Eqs. (13) through (18).

The governing equations for the nonlinear  $k$ - $\epsilon$  model are the same as Eqs. (26) through (35), except the terms  $S^u$ ,  $S^v$ ,  $S^w$ , and  $G$  are replaced by

$$\begin{aligned} S^u &= S_l^u + \hat{S}^u, \\ S^v &= S_l^v + \hat{S}^v, \\ S^w &= S_l^w + \hat{S}^w, \\ G &= G_l + \hat{G}, \end{aligned} \quad (37)$$

where  $S_l^u$ ,  $S_l^v$ ,  $S_l^w$ , and  $G_l$  are linear parts of the quantities and given by Eqs. (33) and (35); the nonlinear parts are defined by

$$\begin{aligned} \hat{S}^u &= [\nabla \cdot \hat{\mathcal{T}}]_x = \frac{\partial}{\partial x} (\hat{T}_{xx}) + \frac{1}{r} \frac{\partial}{\partial r} (r \hat{T}_{rx}), \\ \hat{S}^v &= [\nabla \cdot \hat{\mathcal{T}}]_r = \frac{\partial}{\partial x} (\hat{T}_{xr}) + \frac{1}{r} \frac{\partial}{\partial r} (r \hat{T}_{rr}) - \frac{\hat{T}_{\theta\theta}}{r}, \\ \hat{S}^w &= [\nabla \cdot \hat{\mathcal{T}}]_\theta = \frac{\partial}{\partial x} (\hat{T}_{x\theta}) + \frac{1}{r^2} \frac{\partial}{\partial r} (r^2 \hat{T}_{r\theta}), \\ G &= \hat{\mathcal{T}} : \nabla \mathbf{v} = \hat{T}_{xx} \left( \frac{\partial u}{\partial x} \right) + \hat{T}_{rr} \left( \frac{\partial v}{\partial r} \right) + \hat{T}_{\theta\theta} \left( \frac{v}{r} \right) \\ &\quad + \hat{T}_{r\theta} \left[ r \frac{\partial}{\partial r} \left( \frac{w}{r} \right) \right] + \hat{T}_{\theta x} \left( \frac{\partial w}{\partial x} \right) + \hat{T}_{rx} \left( \frac{\partial u}{\partial r} + \frac{\partial v}{\partial x} \right). \end{aligned} \quad (38)$$

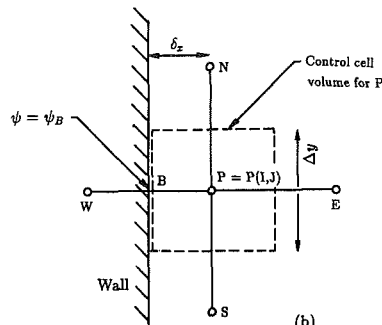
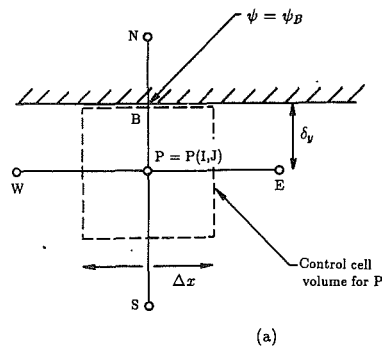


Fig. 1 Boundary conditions at solid walls. (a) Wall  $\psi$ -value prescription for northern wall. (b) Wall  $\psi$ -value prescription for western wall.

These nonlinear parts are simply added to the source terms of the linear  $k$ - $\epsilon$  model governing equations.

**2.1 Wall Functions.** The effect of swirl on wall function specificatin is described in the STARPIC code (Lilley and Rhode, 1982). Because of additional stress terms in the nonlinear  $k$ - $\epsilon$  model, modifications are made to accommodate these changes. Near the northern top wall (see Fig. 1(a)), the total tangential velocity  $V = (u^2 + w^2)^{1/2}$  is correlated by the universal velocity profile (Blackshall and Landis, 1969)

$$V^+ = \frac{1}{\kappa} \ln(EY^+), \quad (39)$$

where  $\kappa$  and  $E$  are constants. The dimensionless total velocity  $V^+$  and distance  $Y^+$  are normalized with respect to the total shear velocity  $(T_t/\rho)^{1/2}$ , viz.

$$V^+ = \frac{V}{\sqrt{T_t/\rho}}, \quad Y^+ = \frac{y\sqrt{T_t/\rho}}{\nu},$$

and the total tangential north wall shear stress  $T_t$  is

$$T_t = \sqrt{T_{rx}^2 + T_{r\theta}^2}.$$

A quantity  $T_k$  approximating  $T_t$  very near the wall can be formulated by observing that convection and diffusion of turbulence kinetic energy are nearly always negligible in this region. By deleting these terms from the  $k$ -transport equation and invoking isotropic viscosity  $\mu_{\text{eff}}$ , one obtains

$$T_k = (C_D C_\mu)^{1/2} \rho k. \quad (40)$$

Equation (39) can be written as

$$V(T_k \rho)^{1/2} / T_t = \frac{1}{\kappa} \ln[Ey(T_k/\rho)^{1/2} \nu], \quad (41)$$

and thus one obtains

$$T_t = -V_p \kappa \rho C_\mu^{1/4} C_D^{1/4} k_p^{1/2} / \ln(EY^+), \quad (42)$$

where the negative sign has been inserted since  $T_t$  and  $V_p$  must have opposite directions. The quantities with subscript  $p$  are evaluated at the near-wall point employed in numerical computations.

The  $T_{rx}$  component of  $T_t$  consists of

$$(T_{rx})_{\text{total}} = (T_{rx})_{\text{linear}} + (T_{rx})_{\text{nonlinear}}, \quad (43)$$

and

$$(T_{rx})_{\text{linear}} = \mu \left( \frac{\partial u}{\partial r} + \frac{\partial v}{\partial x} \right). \quad (44)$$

The values of  $\partial v / \partial x$  approach zero near the north wall. By multiplying the wall function (Eq. (42)) by the factor  $\cos \theta (= u/v)$  we obtain  $T_{rx}$ , where  $\theta$  is the angle between the total tangential velocity vector near the wall and the axial velocity vector. Combining these we get

$$T_{rx} = \mu \frac{\partial u}{\partial r} + (T_{rx})_{\text{nonlinear}} = \left[ -\kappa \rho C_\mu^{1/4} C_D^{1/4} k_p^{1/2} / \ln(EY^+) \right] u_p, \quad (45)$$

and the wall function for  $u$  is

$$\mu \frac{\partial u}{\partial r} = \left[ -\kappa \rho C_\mu^{1/4} C_D^{1/4} k_p^{1/2} / \ln(EY^+) \right] u_p - (T_{rx})_{\text{nonlinear}}. \quad (46)$$

Following the technique employed in the STARPIC code, the first and second terms on the right-hand side of the above equation correspond to  $S_p^\psi$  and  $S_U^\psi$  of the linearized source term ( $S_p^\psi \psi_p + S_U^\psi$ ), respectively.

For  $w$ -cells along the north wall

$$(T_{r\theta})_{\text{total}} = (T_{r\theta})_{\text{linear}} + (T_{r\theta})_{\text{nonlinear}}, \quad (47)$$

$$(T_{r\theta})_{\text{total}} = T_t \sin \theta = T_t \left( \frac{w}{V} \right), \quad (48)$$

$$(T_{r\theta})_{\text{linear}} = \mu \left( \frac{\partial w}{\partial r} - \frac{w}{r} \right). \quad (49)$$

By combining these equations, we obtain the north wall function for  $w$

$$\mu \frac{\partial w}{\partial r} = \left\{ \left[ -\kappa \rho C_\mu^{1/4} C_D^{1/4} k_p^{1/2} / \ln(EY_p^+) \right] + \frac{\mu}{r} \right\} w_p - (T_{r\theta})_{\text{nonlinear}}. \quad (50)$$

On the western wall (see Fig. 1(b)) the total tangential velocity is now  $V = (v^2 + w^2)^{1/2}$ , and

$$(T_{xr})_{\text{total}} = (T_{xr})_{\text{linear}} + (T_{xr})_{\text{nonlinear}}, \quad (51)$$

$$(T_{xr})_{\text{total}} = T_t \cos \phi = T_t \left( \frac{u}{V} \right), \quad (52)$$

$$(T_{xr})_{\text{linear}} = \mu_{\text{eff}} \frac{\partial v}{\partial x}, \quad (53)$$

where  $\phi = \arctan(w/v)$ . The western wall function for  $v$  is given by

$$\mu \frac{\partial v}{\partial x} = \left[ -\kappa \rho C_\mu^{1/4} C_D^{1/4} k_p^{1/2} / \ln(EY_p^+) \right] v_p - (T_{xr})_{\text{nonlinear}}. \quad (54)$$

Similarly the western wall function for  $w$  is

$$\mu \frac{\partial w}{\partial x} = \left[ -\kappa \rho C_\mu^{1/4} C_D^{1/4} k_p^{1/2} / \ln(EY_p^+) \right] w_p - (T_{r\theta})_{\text{nonlinear}}. \quad (55)$$

The wall flux for turbulent energy is zero. Zero normal gradient prescription for  $k$  for wall cells is through  $\alpha_{k,w}^\psi = 0$ , where  $\alpha$  is the coupling coefficient in the finite difference scheme. The effective wall boundary condition on  $\epsilon$  is

$$\epsilon = \frac{(C_\mu C_D)^{3/4} k_p^{3/2}}{C_D \kappa \delta_p}, \quad (56)$$

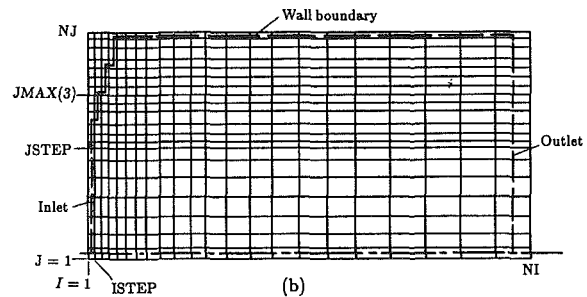
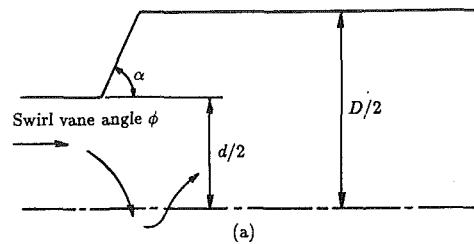


Fig. 2 Combustor geometry and flowfield investigated. Inlet Reynolds No. =  $1.26 \times 10^5$ . (a) Schematic of test section geometry. (b) An example of a non-uniform grid system employed to fit the flow domain.

where  $\delta_p$  is the distance from the wall to the near-wall point. In the code, this value is fixed for near-wall points via the linearized source procedure, viz.,  $S_U^\psi = \psi_F \cdot 10^{30}$ ,  $S_p^\psi = -10^{30}$ .

### 3 Numerical Method and Results

In this study, the computer source code developed by Lilley and Rhode (1982) is used. This code is a modified version of the Imperial College's TEACH (Teaching Elliptic Axisymmetry Characteristics Heuristically) computer program and is called STARPIC (Swirling Turbulent Axi-symmetric Recirculating flows in Practical Isothermal Combustor geometries). In this work, we have modified the STARPIC computer program by (i) allowing a new specification of the input data to change the combustor geometry and (ii) including the Reynolds stress tensor in a form of the nonlinear  $k-\epsilon$  model.

**3.1 The Grid System.** Figures 1(a) and 1(b) show the control cell volume at the northern wall and western wall, respectively. The points P, E, W, N, S represent the locations corresponding to the Center, East, West, North, and South of the cell, respectively. Point B represents the boundary location. At point P, all variables except the  $u$  and  $v$  velocity components are stored. The  $u$  velocity component is stored at a point somewhere between point P and point W. For the  $v$  velocity component, it is stored at a point somewhere between point P and point S.

The flow field is covered with a nonuniform grid system with finer spacing in the regions of large spatial gradients. A typical arrangement is shown in Fig. 2(b), in which NI = 23 (axial direction) and NJ = 21 (radial direction). Typically the boundary of the solution domain falls halfway between its immediate parallel gridlines. For the specification of the inlet pipe diameter, JSTEP gives J-index of horizontal line next to wall of, and within, smaller pipe. The information concerned with the position of the sloping sidewall boundary is specified via JMAX(I) for each I. JMAX(I) designates the maximum value of J-index within flow domain.

**3.2 Inlet Turbulent Intensity.** In the present computations, the turbulent intensity at inlet,  $k_{in}$ , is calculated from

$$k_{in} = \alpha_T U_{in}^2, \quad (57)$$

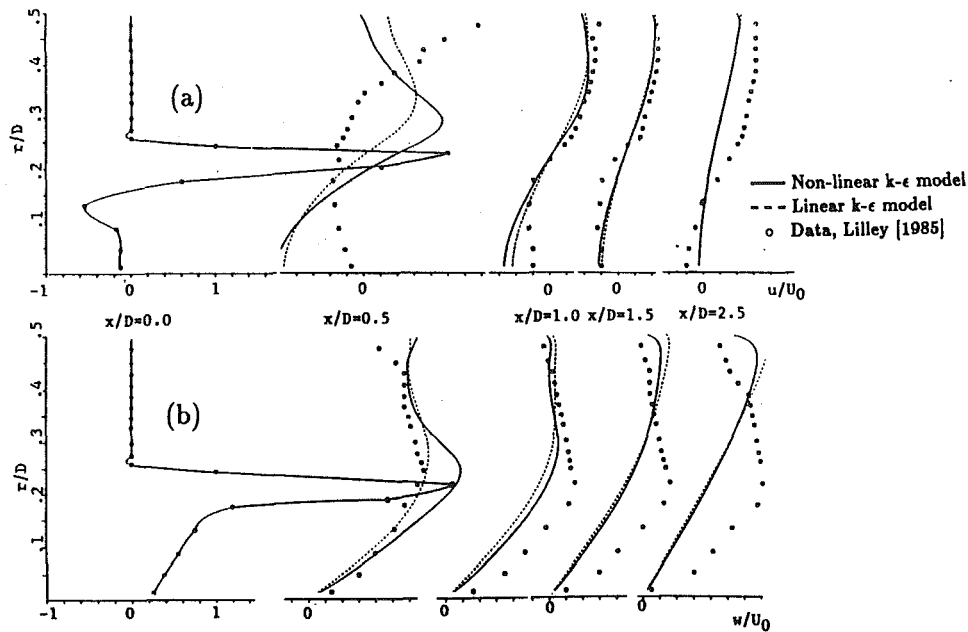


Fig. 3 Predicted axial and tangential velocity profiles at  $x/D = 0.0, 0.5, 1.0, 1.5, 2.5$ . (a) axial velocity, (b) tangential velocity. Inlet boundary conditions matched to the experimental data of Lilley (1985) at  $x/D = 0$ . Inlet sloping wall expansion angle,  $\alpha = 90$  deg, swirl vane angle  $\phi = 70$  deg.

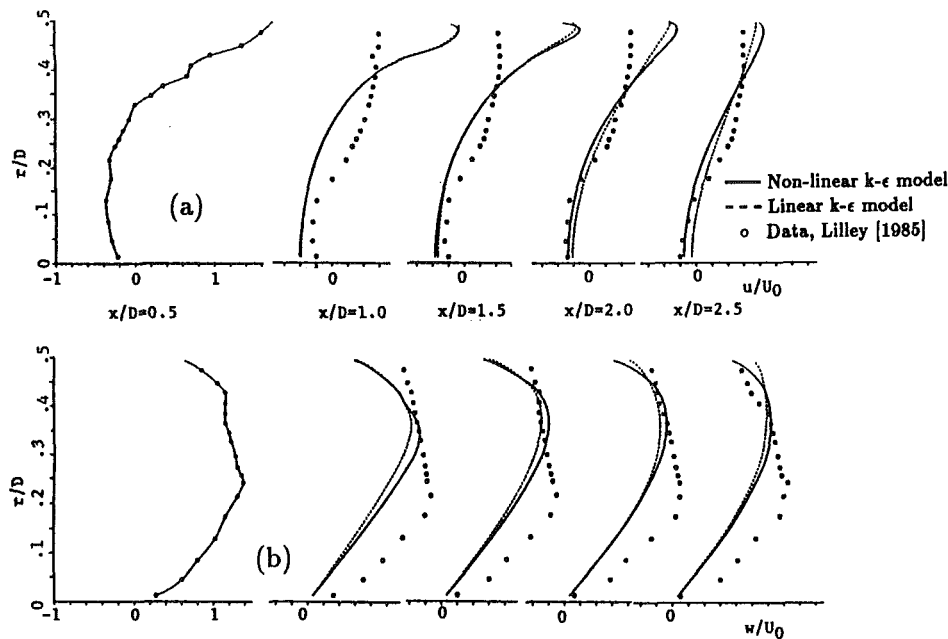


Fig. 4 Predicted axial and tangential velocity profiles at  $x/D = 0.5, 1.0, 1.5, 2.0, 2.5$ . (a) axial velocity, (b) tangential velocity. Inlet boundary conditions matched to the experimental data of Lilley (1985) at  $x/D = 0.5$ . Inlet sloping wall expansion angle,  $\alpha = 90$  deg, swirl vane angle  $\phi = 70$  deg.

where  $\alpha_T$  is the turbulent intensity factor at inlet, and  $U_{in}$  is the average velocity at the inlet. The dissipation rate  $\epsilon$  is obtained from a mixing-length assumption (Khalil, 1979)

$$\epsilon_{in} = \frac{(k_{in})^{1.5}}{\alpha_\lambda R_0}, \quad (58)$$

where  $\alpha_\lambda$  is the length scale factor at inlet.

**3.3 Solution Procedure.** In the computer code, the finite difference equations are solved via the primitive pressure-velocity approach. The details of the solution technique is de-

scribed in the work by Lilley and Rhode (1982). For the representation of the convective and diffusive terms over the cell control volume surfaces, a hybrid scheme is used, which is a combination of the central and upwind differences. An implicit line-by-line relaxation technique is employed in the solution procedure, using the tridiagonal matrix algorithm (TDMA). At each iteration it is necessary to employ some degree of under-relaxation to promote stability. To facilitate convergence, the swirl strength is increased through a range of swirl vane angles in steps until the final vane angle is reached. The solution is considered to be converged if the cumulative

sum of the absolute residuals throughout the fields for all variables is less than 0.5 percent of the inlet flow rate of the corresponding variables.

**3.4 Case 1—Lilley (1985).** The first problem to be considered in this study consists of the turbulent flow of an incompressible viscous fluid in a round pipe entering an expansion into another round pipe (see Fig. 2(a));  $d/2 = 3.125$  cm,  $D/2 = 6.25$  cm). The incoming flow has a swirl component of velocity via passage through swirl vanes at angle  $\phi$ , and the sidewall is at an angle  $\alpha$ , to the main flow direction—Lilley (1985) studied this problem using a standard  $k-\epsilon$  model. In particular, the effects of side-wall angle  $\alpha$ , degree of swirl  $\phi$ , turbulence intensity  $k_{in}$  of the inlet stream, and expansion ratio  $D/d$  on the flow field were studied. Figure 2(a) shows the geometry of the problem. In present example,  $d/2 = 3.125$  cm,  $D/2 = 6.25$  cm, and the inlet Reynolds number is  $1.26 \times 10^5$ . The turbulent intensity factor at inlet,  $\alpha_T$ , is taken to be 0.03 and the length scale factor at inlet,  $\alpha_\lambda$ , is 0.005 for the following computations.

Figure 3 shows the predicted velocity profiles, using both the standard  $k-\epsilon$  and the nonlinear  $k-\epsilon$  model, for the case of  $90^\circ$  expansion angle and  $70$  deg swirl vane angle. The inlet boundary condition is matched to the experimental data of Lilley (1985) at  $x/D = 0$ . Both the linear  $k-\epsilon$  model and the

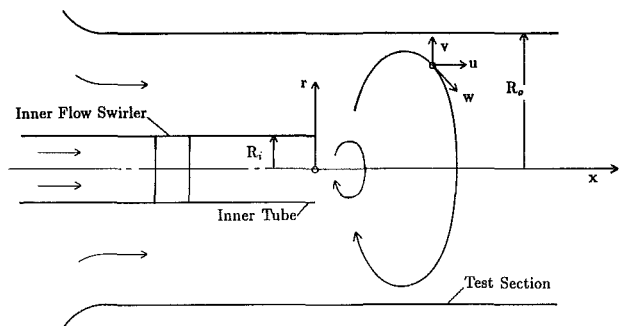


Fig. 5 Schematic of model swirl combustor (Vu and Gouldin 1982). Co-swirl condition is shown.  $R_i = 1.86$  cm,  $R_o = 7.25$  cm. Reynolds No. = 170,000.

nonlinear  $k-\epsilon$  model predict the trend of the flow development along the channel, except the axial velocity profile at  $x/D = 0.50$ . A significant change is noted in the axial velocity profiles between  $x/D = 0$  and  $x/D = 0.50$ . To see whether matching the experimental data at  $x/D = 0$  is appropriate or not for this problem, the inlet boundary condition is matched to the experimental data at  $x/D = 0.5$ . This result is shown in Fig. 4. The trend in the development of the axial velocity profile does not reflect complete agreement between the prediction and the experimental data. Figures 3 and 4 show no large difference in the velocity profiles for the linear model and the nonlinear model; in general, the nonlinear model shows a slightly better agreement with the experimental data in tangential velocity profiles.

**3.5 Case 2—Vu and Gouldin (1982).** The second problem considered is the turbulent flow of an incompressible viscous fluid in two confined co-axial swirling jets (Fig. 5). The outer swirl can be adjusted to co-swirl (streams rotating in the same direction) or counterswirl conditions. Vu and Gouldin (1982) made detailed measurements of velocity profiles using a directional Pitot probe and hot-wire anemometer. The radius of the inner tube,  $R_i = 1.86$  cm, is used for normalizing the axial and radial positions. The authors (Vu and Gouldin, 1982) gave a Reynolds number of 170,000 in the following sets of experiments. The velocity profiles for the axial and tangential components (normalized to the bulk average axial velocity of the inner jet) at various locations along the test sections are shown in Fig. 6. At the inlet ( $x/R_i = 0.1$ , where the inlet condition is matched to the experimental data), the outer axial velocity is almost uniform across the annulus whereas the inner axial velocity has a peak near  $R_i/2$ . The axial velocity profile has a minimum at the centerline ( $r = 0$ ) and the co-swirl interface ( $r = R_i$ ). The tangential velocity profile shows that the inner jet is approximately under solid-body rotation; the outer region can be approximated by a free vortex profile. Both the standard  $k-\epsilon$  model and the nonlinear  $k-\epsilon$  model over-predict the axial and tangential velocities in the central core. This may be interpreted as too small of a dissipation rate in the computations. In Fig. 6,  $\alpha_T = 0.03$  and  $\alpha_\lambda = 0.005$  are used. By changing the value of  $\alpha_\lambda$  from 0.005 to 0.10, Fig. 7 is obtained. Here,

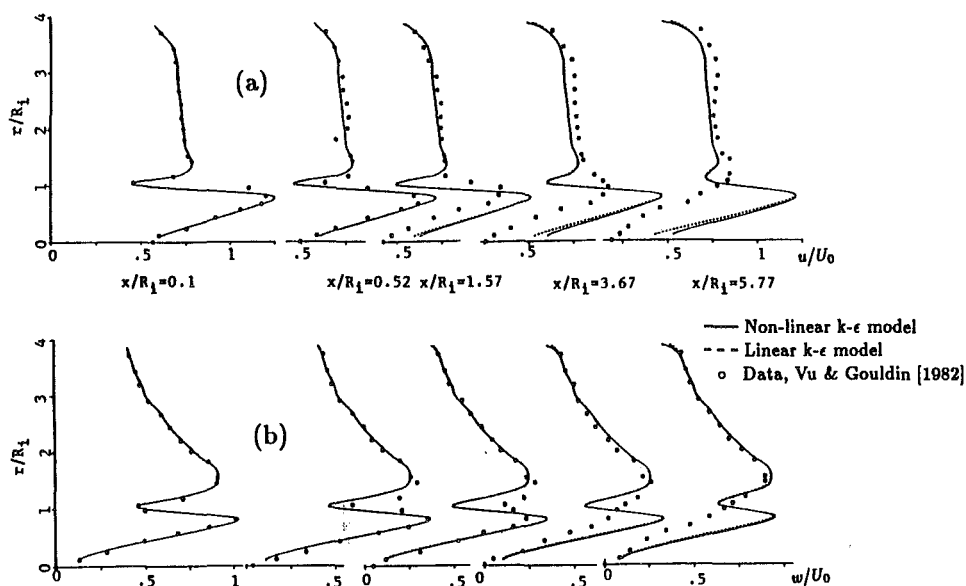


Fig. 6 Velocity profiles for coswirl condition at  $x/R_i = 0.10, 0.52, 1.57, 3.67,$  and  $5.77$ .  $U_0 = \langle U_i \rangle_{av} = 29.6$  m/s. (a) axial velocity, (b) tangential velocity. Inlet boundary conditions matched to the experimental data of Vu and Gouldin (1982) at  $x/D = 0.10$ . Turbulence intensity factor at inlet = 0.03, length scale factor at inlet = 0.005.

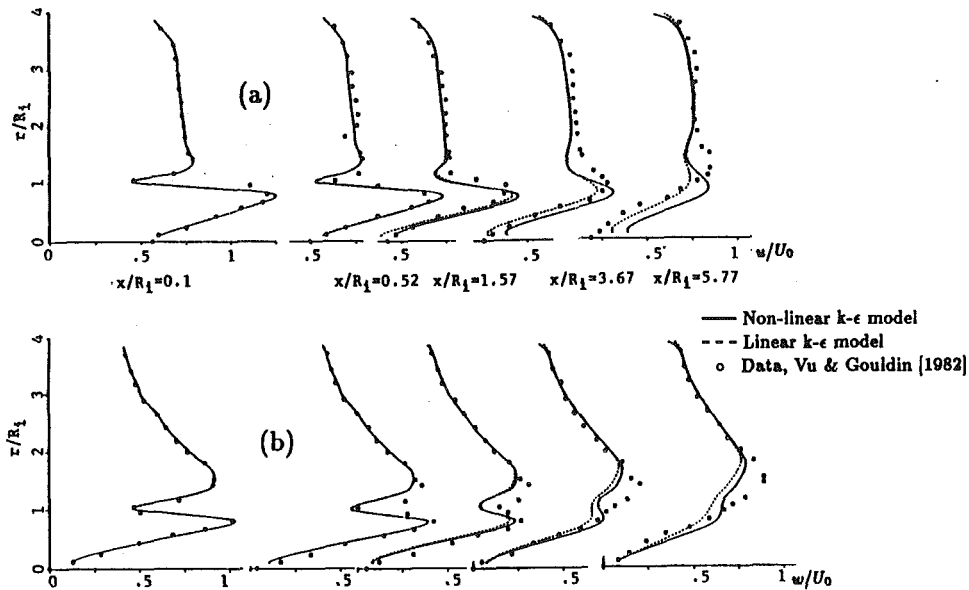


Fig. 7 Velocity profiles for coswirl condition at  $x/R_1 = 0.10, 0.52, 1.57, 3.67,$  and  $5.77$ .  $U_0 = (U_1)_{av} = 29.6$  m/s. (a) axial velocity, (b) tangential velocity. Inlet boundary conditions matched to the experimental data of Vu and Gouldin (1982) at  $x/D = 0.10$ . Turbulence intensity factor at inlet = 0.03, length scale factor at inlet = 0.10.

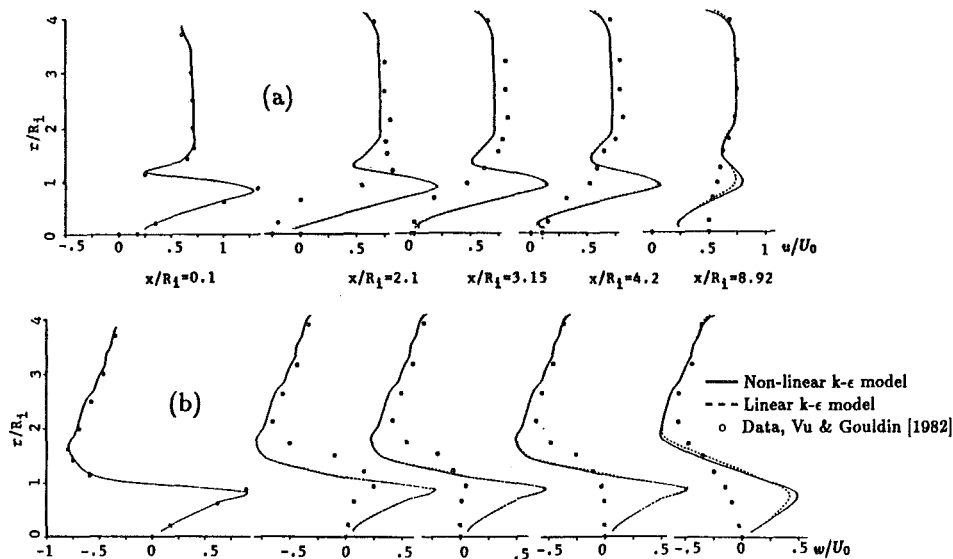


Fig. 8 Velocity profiles for coswirl condition at  $x/R_1 = 0.10, 2.10, 3.15, 4.20, 8.92$ .  $U_0 = (U_1)_{av} = 30.3$  m/s. (a) axial velocity, (b) tangential velocity. Inlet boundary conditions matched to the experimental data of Vu and Gouldin (1982) at  $x/D = 0.10$ . Turbulence intensity factor at inlet = 0.03, length scale factor at inlet = 0.005.

the agreement between the prediction and the experiment is much improved.

Figure 8 shows the axial and tangential velocity profiles for the case of counterswirl. The predicted velocity profiles again show persistence in velocity profiles along the tube in both axial and tangential profiles. In Fig. 9,  $\alpha_T = 0.05$  and  $\alpha_\lambda = 0.08$  are employed, resulting in better agreement between the prediction and the experiment. It is believed that further improvement in the agreement between the prediction and the experiment can be achieved by optimizing the values of  $\alpha_T$  and  $\alpha_\lambda$ .

The results of computations shown in Figs. 6 through 9 are based on the grid size of  $21 \times 23$ . No noticeable change in

the results of computations is observed when the grid size of  $41 \times 45$  is employed.

#### 4 Comments and Summary

Several points concerning the modeling and the numerical scheme need to be discussed in more detail. The values of universal constants  $C_D$  and  $C_E$  used in this study were the ones given by Speziale (1987). Speziale (1987) used the experimental data of Laufer (1951) (turbulent flow in a two-dimensional channel) to obtain these values. For the present problem, it might be more appropriate to use the experimental data of Laufer (1954) (turbulent flow in fully developed pipe flow) to obtain values of  $C_D$  and  $C_E$ . Furthermore, we have not per-

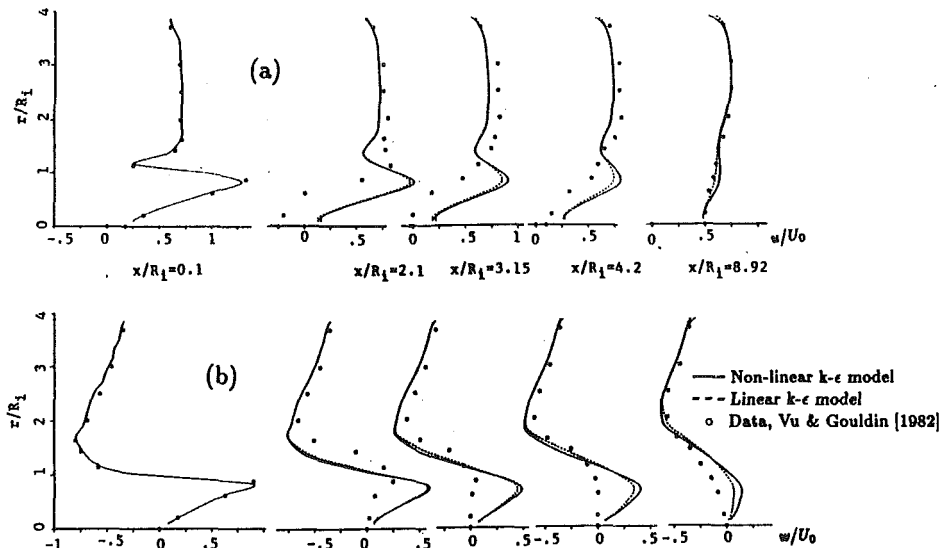


Fig. 9 Velocity profiles for counterswirl condition at  $x/R_1 = 0.10, 2.10, 3.15, 4.20, 8.92$ .  $U_0 = (U_i)_{av} = 30.3$  m/s. (a) axial velocity, (b) tangential velocity. Inlet boundary conditions matched to the experimental data of Vu and Gouldin (1982) at  $x/D = 0.10$ . Turbulence intensity factor at inlet = 0.05, length scale factor at inlet = 0.08.

formed an analysis to test the sensitivity of the computed results to the values of  $C_D$  and  $C_E$ . An alternative approach for estimating values of  $C_D$  and  $C_E$  is presented by Ahmadi and Chowdhury (1988). In their analysis, the limit of parallel flows, and in particular, the flows in the inertial sublayer (Tennekes and Lumley, 1972) are used to obtain values for some material parameters similar to  $C_D$  and  $C_E$ .

Furthermore, when the nonlinear  $k-\epsilon$  model is used in the equations of motion, the order of the partial differential equations increases by one. Therefore, additional boundary conditions are needed in turbulence modeling and non-Newtonian fluid mechanics, where the constitutive equations used are for fluids of differential types. This issue has been studied for these Rivlin-Ericksen fluids recently by Rajagopal (1984), Rajagopal and Gupta (1984), Kaloni (1989), and Bourgin and Tichy (1989). For the case of the nonlinear  $k-\epsilon$  model (Speziale and Ngo, 1988) the issue of additional boundary conditions was overcome by the application of the law of the wall (Rodi, 1982) at the solid boundaries. However, if we were to solve the governing equations fully, up to the wall, then the need for additional boundary condition arise. This is a subject matter of current research. It might be possible to develop a low-Reynolds number version of the nonlinear  $k-\epsilon$  model, similar to the model of Jones and Launder (1972, 1973) or perhaps one can use similar ideas from the non-Newtonian fluid mechanics.

The two test cases studied in this work do not seem to contain a very significant improvement in the theoretical results when the nonlinear  $k-\epsilon$  model is used. In the first case (sudden expansion with swirl), neither the linear model nor the nonlinear one performs well in predicting the axial and tangential velocity profiles near the inlet of the combustor chamber. For the second test case, both models seem to predict the general trend; furthermore, it appears that varying the turbulent intensity factor and the length scale factor may give better comparison with experiments. Nevertheless, the studies performed by Speziale and Ngo (1988), Ahmadi (1991), and Thangam and Hur (1991) clearly indicate that for problems when recirculating flows are of interest, such as the flow past a backward-facing step, the nonlinear  $k-\epsilon$  model does a better job of predicting the flow behavior. Chowdhury and Ahmadi (1992) studied a swirling axisymmetric flow with sudden expansion (similar to Case 1 in this study) using a different version of nonlinear  $k-$

$\epsilon$  models. The mean flow properties predicted by this model are in general better agreement with the experimental data than those predicted by a linear  $k-\epsilon$  model.

In this problem, we have used the computer code STARPIC (developed by Lilley and Rhode, 1982) without any modifications to the numerical scheme, accuracy, or efficiency of computation. The only modifications have been the inclusion of a nonlinear  $k-\epsilon$  model and a new scheme of specifying the input data to change the combustor geometry. However, the last few years have generated much work concerning such issues as accuracy, convergence, stability, numerical diffusion, etc. in TEACH-type calculations (cf. Sturgess et al., 1983; Syed and Chiapetta, 1985; Syed et al., 1985; and Van Doormaal et al., 1987). The importance of inlet boundary conditions on the solution was discussed by Sturgess et al. (1983) and Sloan et al. (1986). Leschziner and Rodi (1984) found that the inlet conditions for  $k$  and  $\epsilon$  played a crucial role in achieving predicted accuracy as turbulence modeling details. We also found that the solution was very sensitive to even small changes in the inlet conditions. Furthermore, the nonlinear  $k-\epsilon$  model has higher order terms and in this study the differentiation of these terms ( $\text{div } \vec{T}$ ), which appear in Eq. (1), is performed using a simple central difference scheme. This may have some influence on the accuracy and convergence of the numerical scheme. Hur et al. (1990) performed a numerical study of turbulent secondary flows in curved ducts using the nonlinear Reynolds stress given by Eq. (4). However, they avoided using the transport Eqs. (30)–(31) for  $k$  and  $\epsilon$ , reasoning that these modeled equations have weaknesses in performance. They specified  $k$  and  $l$  empirically, based on experimental data for turbulent flow in rectangular channels. In the present study, the modeled transport Eqs. (30)–(31) were used with either linear or nonlinear portion of the Reynolds stress given by Eq. (4). It is possible that weaknesses in the performance of Eqs. (30)–(31) may have overshadowed differences in the linear and nonlinear models.

## References

- Ahmadi, G., 1991, "A Thermodynamically Consistent Rate-Dependent Model for Turbulence, Part I—Formulation," *International Journal of Non-Linear Mechanics*, Vol. 26, pp. 595–607.
- Ahmadi, G., and Chowdhury, S. J., 1988, "A Rate-Dependent Algebraic Stress Model for Turbulence," Report No. MIE-163, Clarkson University, Apr.

- Blackshall, R. G., and Landis, F., 1969, "The Boundary-Layer Velocity Distribution in Turbulent Swirling Pipe Flow," *ASME Journal of Basic Engineering*, Vol. 91, pp. 728-733.
- Bishnoi, P. K., Ghia, U., and Ghia, K. N., 1991, "Prediction of Normal Reynolds Stresses with Nonlinear  $k-\epsilon$  Model of Turbulence," *Advances in Numerical Simulation of Turbulent Flows*, ASME FED-Vol. 117, pp. 25-34.
- Bourgin, P., and Tichy, J. A., 1989, "The Effect of an Additional Boundary Condition on the Plane Creeping Flow of a Second-Order Fluid," *International Journal of Non-Linear Mechanics*, Vol. 24, pp. 561-569.
- Chowdhury, S. J., and Ahmadi, G., 1992, "A Thermodynamically Consistent Rate-Dependent Model for Turbulence, Part II—Computational Results," *International Journal of Non-Linear Mechanics*, in press.
- Hur, N., Thangam, S., and Speziale, C. G., 1990, "Numerical Study of Turbulent Secondary Flows in Curved Ducts," *ASME JOURNAL OF FLUIDS ENGINEERING*, Vol. 112, pp. 205-211.
- Hwang, C. C., Zhu, Genxing, Massoudi, M., and Ekman, J. M., 1991, "Modification of the 'TEACH' Code for Use in a Study of Swirling Turbulent Flows," DOE/PETC Report, DOE/PETC/TR-91/3, March.
- Hwang, C. C., Zhu, Genxing, Massoudi, M., and Ekman, J. M., 1991, "Turbulence Modeling of the Flow Field in Combustors Using Non-Linear  $k-\epsilon$  Model," *Advances in Numerical Simulation of Turbulent Flows*, ASME FED-Vol. 117, pp. 35-42.
- Jones, W. P., and Launder, B. E., 1972, "The Prediction of Laminarization with a Two-Equation Model of Turbulence," *International Journal of Heat and Mass Transfer*, Vol. 15, pp. 301-314.
- Jones, W. P., and Launder, B. E., 1973, "The Calculation of Two-Reynolds Number Phenomena with a Two-Equation Model of Turbulence," *International Journal of Heat and Mass Transfer*, Vol. 16, p. 1119.
- Kaloni, P. N., 1989, "Some Remarks on Useful Theorem for the Second-Order Fluid," *Journal of Non-Newtonian Fluid Mechanics*, Vol. 31, pp. 115-120.
- Khalil, E. E., 1979, "Numerical Computation of Turbulent Flow Structure in a Cyclone Chamber," ASME Paper No. 79-HT-31.
- Laufer, J., 1951, "Investigation of Turbulent Flow in a Two-Dimensional Channel," NACA TN 1053.
- Laufer, J., 1954, "The Structure of Turbulence in Fully Developed Pipe Flow," NACA Report 1174.
- Launder, B. E., and Spalding, D. B., 1974, "The Numerical Computation of Turbulent Flows," *Computer Methods in Applied Mechanics and Engineering*, Vol. 3, pp. 269-289.
- Leschziner, M. A., and Rodi, W., 1984, "Computation of Strongly Swirling Axisymmetric Free Jets," *AIAA Journal*, Vol. 22, pp. 1742-1747.
- Lilley, D. G., 1985, "Investigation of Flow Fields Found in Typical Combustor Geometries," NASA CR-3869.
- Lilley, D. G., and Rhode, D. L., 1982, "A Computer Code for Swirling Turbulent Axisymmetric Recirculating Flows in Practical Isothermal Combustor Geometries," NASA CR-3442.
- Rajagopal, K. R., 1984, "On the Creeping Flow of the Second-Order Fluid," *Journal of Non-Newtonian Fluid Mechanics*, Vol. 15, pp. 239-246.
- Rajagopal, K. R., and Gupta, A. S., 1984, "An Exact Solution for the Flow of a Non-Newtonian Fluid Past an Infinite Porous Plate," *Meccanica*, Vol. 19, pp. 158-160.
- Rivlin, R. S., 1957, "The Relation Between the Flow of Non-Newtonian Fluids and Turbulent Newtonian Fluids," *Quarterly of Applied Mathematics*, Vol. 15, pp. 212-215.
- Rivlin, R. S., and Ericksen, J. L., 1955, "Stress Deformation Relation for Isotropic Materials," *Journal of Rational Mechanics and Analysis*, Vol. 4, pp. 323-325.
- Rodi, W., 1976, "A New Algebraic Relation for Calculating the Reynolds Stresses," *Zeitschrift fur Angewandte Mathematik und Mechanik*, Vol. 56, p. 219.
- Rodi, W., 1982, "Examples of Turbulence Models for Incompressible Flows," *AIAA Journal*, Vol. 20, pp. 872-879.
- Sloan, D. G., Smith, P. J., and Smoot, L. D., 1986, "Modeling of Swirl in Turbulent Flow Systems," *Progress in Energy and Combustion Science*, Vol. 12, pp. 163-250.
- Speziale, C. G., 1987, "On Nonlinear  $k-l$  and  $k-\epsilon$  Models of Turbulence," *Journal of Fluids Mechanics*, Vol. 178, pp. 459-475.
- Speziale, C. G., and Ngo, T., 1988, "Numerical Solution of Turbulent Flow Past a Backward Facing Step Using a Nonlinear  $k-\epsilon$  Model," *International Journal of Engineering Science*, Vol. 26, pp. 1099-1112.
- Sturgess, G. J., Syed, S. A., and McManus, K. R., 1983, "Importance of Inlet Boundary Conditions for Numerical Simulation of Combustor Flows," AIAA Paper No. AIAA-83-1263.
- Syed, S., and Chiappetta, L., 1985, "Finite Difference Methods for Reducing Numerical Diffusion in TEACH-Type Calculations," AIAA Paper No. AIAA-85-0057.
- Syed, S., Gosman, A., and Peric, M., 1985, "Assessment of Discretization Schemes to Reduce Numerical Diffusion in the Calculation of Complex Flows," AIAA Paper No. AIAA-85-0441.
- Tennekes, H., and Lumley, J. L., 1972, *A First Course in Turbulence*, MIT Press, Cambridge, MA.
- Thangam, S., and Hur, N., 1991, "A Highly-Resolved Numerical Study of Turbulent Separated Flow Past a Backward-Facing Step," *International Journal of Engineering Science*, Vol. 29, pp. 607-615.
- Van Doormaal, J. P., Turan, A., and Raithby, G. D., 1987, "Evaluation of New Techniques for the Calculation of Internal Recirculating Flows," AIAA Paper AIAA-87-0059.
- Vu, B. T., and Gouldin, F. C., 1982, "Flow Measurements in a Model Swirl Combustor," *AIAA Journal*, Vol. 20, pp. 642-651.

# Modeling and Computation of Flow in a Passage With 360-Degree Turning and Multiple Airfoils

W. Shyy

Department of Aerospace Engineering,  
Mechanics and Engineering Science,  
University of Florida,  
Gainesville, FL 32611-2031

T. C. Vu

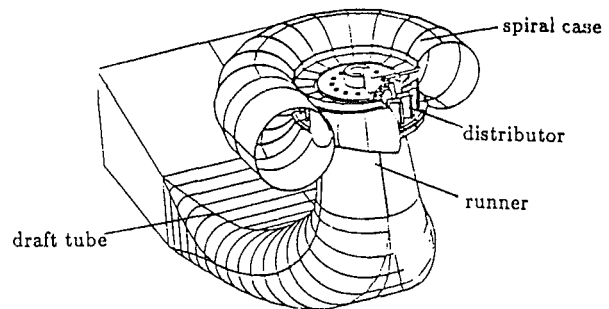
Hydro Business,  
GE Canada,  
Lachine, Quebec,  
Canada H8S 2S8

*The spiral casing of a hydraulic turbine is a complex flow device which contains a passage of 360-degree turning and multiple elements of airfoils (the so-called distributor). A three-dimensional flow analysis has been made to predict the flow behavior inside the casing and distributor. The physical model employs a two-level approach, comprising of (1) a global model that adequately accounts for the geometry of the spiral casing but smears out the details of the distributor, and represents the multiple airfoils by a porous medium treatment, and (2) a local model that performs detailed analysis of flow in the distributor region. The global analysis supplies the inlet flow condition for the individual cascade of distributor airfoils, while the distributor analysis yields the information needed for modeling the characteristics of the porous medium. Comparisons of pressure and velocity profiles between measurement and prediction have been made to assess the validity of the present approach. Flow characteristics in the spiral casing are also discussed.*

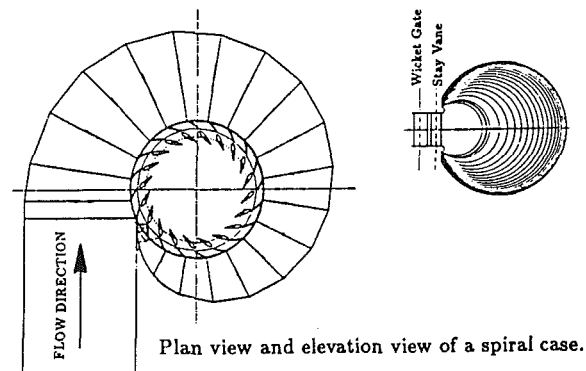
## 1 Introduction

Three-dimensional internal flows bounded by domains of large curvature and geometric variations are commonly encountered in fluid machinery. Numerous attempts with varying degrees of numerical sophistication have been made to predict the complex turbulent flow behavior in both rotating and non-rotating components, as documented in, e.g., Chang et al. (1985), Hah (1985), Holmes et al. (1988), Leschziner and Dimitriadis (1989), Löhner (1989), Quirk (1992), Shyy and Braaten (1986), and Towne (1984). In these studies, efforts are taken to accurately reproduce the geometric boundaries of the whole domain in detail. There are, however, cases where the number of solid bodies in the domain is so large that either extremely large computer memory and speed is required or some features of the problems, such as the three-dimensionality, must be simplified before a computation can be attempted. Examples can be found in runner-stator interactions (Rai, 1987), and combinations of film cooling, fuel spray nozzle, and splash plate in modern gas-turbine combustors (Shyy et al., 1989). The extent to which a problem can be simplified is, of course, case dependent.

In the present work, we report an attempt to predict the complicated three-dimensional turbulent flows within a device containing large curvature and a number of solid elements. The flow device investigated here is a spiral casing of a hydraulic turbine power plant. As schematically illustrated in Fig. 1, both in three-dimensional perspective and in two-dimensional projections, the spiral casing is a passage of 360 deg turning that directs water, coming from the dam, to enter from one end, and to exit circumferentially along the radially



Schematic representation of a hydraulic turbine

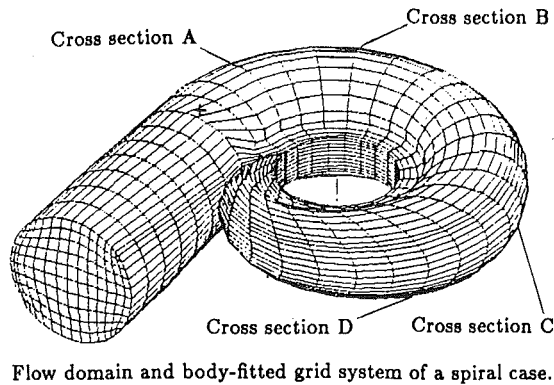


Plan view and elevation view of a spiral case.

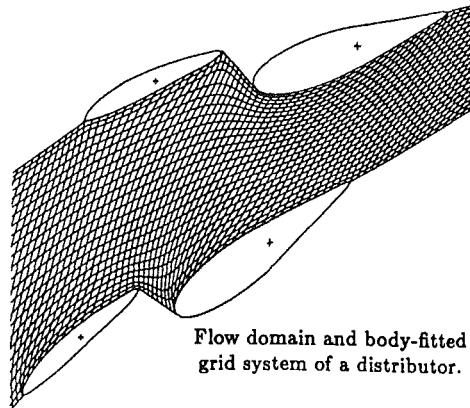
Contributed by the Fluids Engineering Division for publication in the JOURNAL OF FLUIDS ENGINEERING. Manuscript received by the Fluids Engineering Division September 5, 1991. Associate Technical Editor: R. K. Agarwal.

Fig. 1 Schematic illustrations of spiral casing





Flow domain and body-fitted grid system of a spiral case.



Flow domain and body-fitted grid system of a distributor.

Fig. 2 Representative grids of spiral casing and distributor

inward direction. In the exit region, there are twenty-four pairs of two-dimensional airfoils, forming the distributor, which serve to control the mass-flux distribution and angle of the water. The water, after leaving the distributor, enters the runner to drive the shaft and produce usable power. Representative geometries as well as body-fitted grids of both the spiral casing and the distributor are shown in Fig. 2. The spiral casing considered here is a Piquet type distributor with 360-degree turning and decreasing cross-sectional areas. The inlet is of a circular shape, and the outlet occupies the whole inner circumference. The distributor, consisting of a cascade of stay vanes and wicket gates, is housed in the outlet region of casing.

The flow in a combined spiral casing and distributor is difficult to model and predict. Since the spiral casing and the distributor closely affect each other, both must be treated in a coupled manner. We have found that in the computational model, without taking an appropriate account of the presence of the distributor, the flow in a spiral casing can be persistently oscillatory due to the lack of dissipation of the flow kinetic energy in the exit region. However, from the viewpoint of aiding the design practice for such devices on a routine basis, it is not feasible to model the whole spiral casing and distributor combination simultaneously with good grid resolution. In view of these considerations, instead of solving the whole problem all at once, an alternative method is devised utilizing different grid resolutions to satisfy the different needs of physical modeling in casing and in distributor. To predict the overall characteristics of the flow in the spiral casing, while accounting for the geometry of the casing in detail, it is not necessary to consider each individual airfoil element of the distributor. On the other hand, from the viewpoint of the distributor flow analysis, only the inlet condition of the distributor is needed from the global spiral casing flow analysis. Hence, a two-level approach is proposed: 1) To predict the flow characteristics inside the spiral casing, the distributor region is treated as a porous medium with the details of individual airfoils being

smear out; 2) Within the distributor region, analysis is conducted for flow between each pair of wicket gates and stay vanes to determine the local distributor performance and to provide input to the porous medium treatment. The information is exchanged and coupled between the two levels. We believe that the present type of approach can be useful for aiding a designer to understand the performance as well as the flow behavior of a given casing/distributor configuration without having to resort to exceedingly large computing resources. In the following, the construction of the model is discussed first. Comparisons will then be made between the measured and predicted velocity and pressure distributions. Some of the representative features of the flow solutions will also be highlighted.

## 2 Problem Formulation and Computational Techniques

The equations adopted are the Reynolds-averaged three-dimensional Navier-Stokes equations with an extra inclusion of the porous medium treatment based on Darcy's law. The equations for mass continuity and momentum conservation of the incompressible fluid are:

$$\nabla \cdot \mathbf{q} = 0$$

$$\mathbf{q} \cdot \nabla \mathbf{q} = -\frac{1}{\rho} \nabla p + \nu_{\text{eff}} \nabla^2 \mathbf{q} - K \mathbf{q}$$

where  $\mathbf{q}$  is the velocity vector with three velocity components,  $\nu_{\text{eff}}$  is the effective viscosity, and  $K$  is the Darcy's coefficient whose magnitude regulates the resistance exerted by the presence of porous medium in the distributor region. With regard to the turbulence closure, the  $\kappa$ - $\epsilon$  two-equation model with the wall function treatment proposed by Launder and Spalding (1974) is adopted to supply the information of eddy viscosity. By the nature of the Reynolds-averaging procedure, the mean flow quantities are solved. The basic computational procedure employed is an iterative algorithm cast in curvilinear coordinate system (Shyy et al., 1985; Shyy and Braaten, 1986).

As  $K$  becomes large, both convection and viscous terms in the momentum equations become negligible due to the small values of velocity, and the pressure term balances the Darcy's term. As  $K$  approaches zero, the original Navier-Stokes equations are recovered. In the present case,  $K$  is zero everywhere except in the distributor region. Within the distributor region,  $K$  varies according to the nature (e.g., number, shape, and thickness) of the airfoils, and the local angles of attack of the incoming flow. In order to determine  $K$ , the distributor flow analysis (Vu and Shyy, 1988) is conducted for flow in a passage bounded by a cascade of airfoils, as shown in Fig. 2. Since the inlet flow angles of the distributor vary along the circumferential direction, individual analysis for the flow between each pair of wicket gates and stay vanes is made with the inlet flow condition supplied by the spiral casing flow analysis. The total pressure loss profile of the distributor flow along the circumference of the spiral casing is then used to correlate the Darcy's coefficient,  $K$ . In the present work, the value of  $K$  is taken to be proportional to the square root of total pressure loss. This choice is made according to the relative agreement observed between the computation and the measurement for a base geometry and flow condition. The proportional constant is fixed by trying to match the prediction with the experimental measurement at one operating point. Once the correlation formula is determined, calculation is made to model other operating conditions with no change of any constants. In summary, the global casing model supplies the inlet condition to the local distributor flow analysis; the total pressure loss predicted by the distributor model, in turn yields guidance to determine the distribution of  $K$  in the porous medium treatment. Such a global-local iterative procedure continues till convergence is reached simultaneously at both levels.

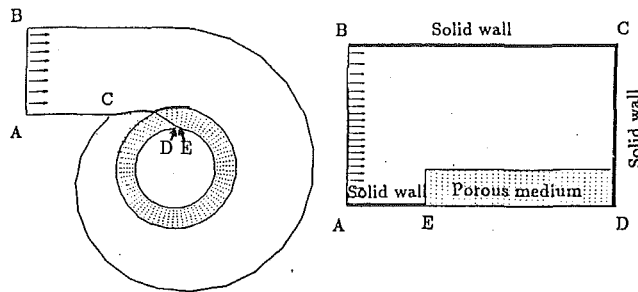


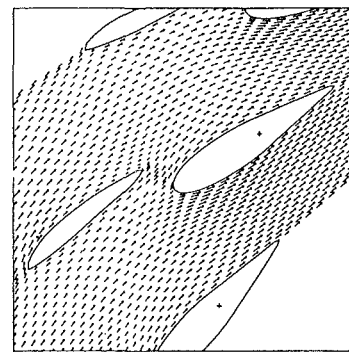
Fig. 3 Schematic representation of the flow domain for the spiral case

Figure 3 depicts the top view of the geometry and boundary conditions in both the physical and transformed computational domains. The velocity at the inlet, AB, is of a uniform profile, with a Reynolds number, based on the inlet diameter, of  $10^6$ . The dotted region is where the distributors are located and the only zone that the Darcy's coefficient,  $K$ , is nonzero. Other boundaries, including BC, CD, and AE, are all solid wall. The numerical procedure adopted for the computation is essentially the same as that used by Shyy and Braaten (1986) and Vu and Shyy (1990) where a pressure-correction type of semi-implicit finite volume/finite difference formulation is adopted for arbitrary curvilinear coordinates. The convection terms in the momentum equations are approximated by the second-order upwind scheme. The pressure as well as all the second-order derivative terms are discretized by the second-order central difference schemes. The results reported in the following are based on a 3-D grid of  $99 \times 21 \times 15$  nodes for the spiral casing, and a 2-D grid of  $25 \times 85$  nodes for the distributor. Typical CPU time of a complete calculation required for such a grid system is about 20 hours on a Silicon Graphics 4D/120. However, in general, much less time is needed to assess a design change since the calculation can be initiated from a solution obtained on an existing geometry.

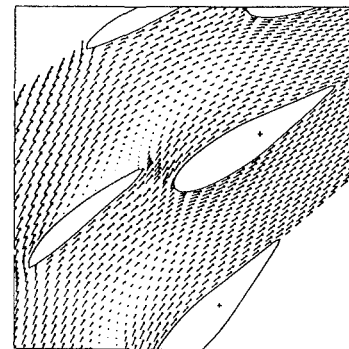
### 3 Results and Discussion

We first show some representative computed flow patterns in the distributor region based on the 2-D analysis presented by Vu and Shyy (1988). Figure 4 shows three calculated velocity fields based on inlet flow angles (between the inlet velocity vector and the tangent of the cascade), of 10-degree, 15-degree, and 25-degree. The flow characteristics are qualitatively different among the three cases. Under the favorable condition (25-degree), the flow is attached, resulting in a small amount of total pressure loss. As the inlet flow angle is reduced from 25-degree to 15-degree, flow is no longer attached and separation appears in the region above the stay vane. Hence the flow under such a condition produces a larger total pressure loss. With the inlet flow angle further reduced to 10-degree, massive separation results from the larger adverse pressure gradient, which also produces noticeable streamline curvatures downstream of the separation zone. The loss is obviously the highest for the lowest flow angle. The total pressure loss of the distributor flow, normalized by the fluid kinetic energy at the inlet is presented in Fig. 5. At very low inlet flow angle, where the pressure distribution is unfavorable, large total pressure loss, up to about 45, is observed. As the flow angle increases, the loss quickly decreases and the flow stabilizes as the inlet flow angle exceeds 25-degree.

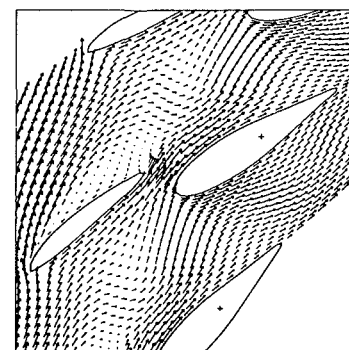
One of the key features in the present work is the supply of the inlet flow profiles of the distributor computation by the spiral casing analysis. The distributor flow analysis, in turn, yields information of the total losses within the distributor region. Based on this information, Darcy's resistance term is devised to represent the presence of the distributor. It is noted



25° Inlet Flow Angle



15° Inlet Flow Angle



10° Inlet Flow Angle

Fig. 4 Three representative flow solutions of distributor

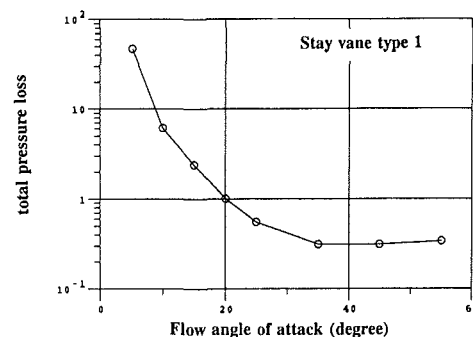


Fig. 5 Total pressure loss in the distributor versus flow attack angle

that, throughout the whole casing, the inlet angle of the distributor flow varies substantially along the circumferential direction. Figure 6 shows two profiles of inlet angle of the distributor flow, one at the mid-height location of the casing and the other averaged over the whole height of each cross-

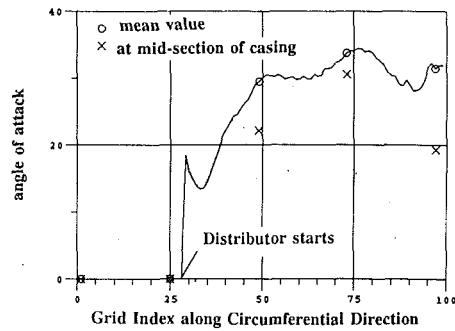


Fig. 6 Flow attack angle variation around distributor upstream

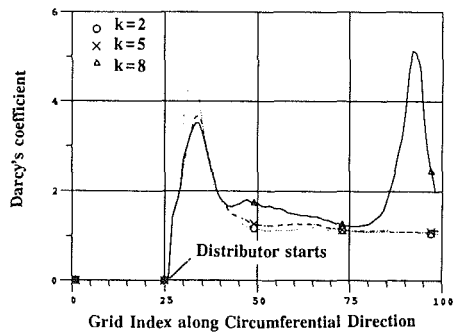


Fig. 7 Distribution of Darcy's coefficient along circumferential direction

section of the casing. The variation of the inlet flow angle of the distributor flow results from the change of flow rate along the circumferential direction of the casing, and the nonuniform total pressure loss within the distributor region. Although the geometry of the distributor used in the present study is not identical to the one reported by Vu and Shyy (1988), qualitative discussion given there is applicable here. Information related to experimental measurement can also be found in Vu and Shyy (1988, 1990).

As already stated, in the present model, Darcy's coefficient is determined from the local total pressure loss in the distributor region. Figure 7 exhibits three  $K$  profiles at different heights, from bottom to mid-height of the casing, along the circumferential direction. In the upstream portion of the casing, the inlet flow angles are low, resulting in high values of  $K$  for the distributor region. In the middle circumferential portion of the casing, as indicated by Fig. 6, the inlet angles of the distributor flow produce favorable conditions, resulting in lower total pressure losses and, accordingly, lower values of  $K$ . Toward the end circumferential portion of the casing, the inlet angles of the distributor flow vary substantially from bottom (high angle) to mid-height (low angle), and hence causes large differences in  $K$  to appear there.

Based on the combined casing/distributor flow analysis, a complete solution can be obtained for the whole passage. The numerical solutions have been compared to the in-house experimental measurements made with pitot tubes for various aspects of flow characteristics. We first compare the numerical prediction with the experimental measurement for the distributions of the static pressure, radial and tangential-velocity components on two cross-sectional planes. The data shown in Fig. 8 are for physical quantities predicted and measured on the cross-sectional planes A and B of Fig. 2; the plots are shown along the radial direction, from the outside wall (left end of figure) to the outlet (right end of figure) of the casing along the mid-height line. Figure 8 illustrates the ranges of agreements between the numerical prediction and the experimental measurement for these variables. Qualitatively, the static

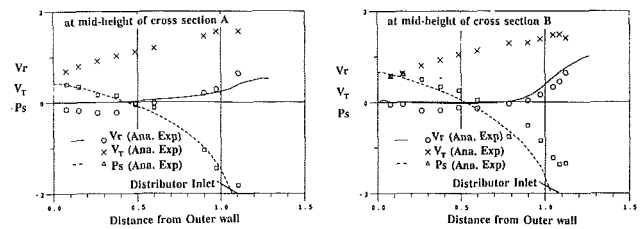


Fig. 8 Comparison of static pressure ( $P_s$ ), radial ( $V_r$ ) and tangential ( $V_t$ ) velocity components along radial direction (symbols: measurements; lines: predictions)

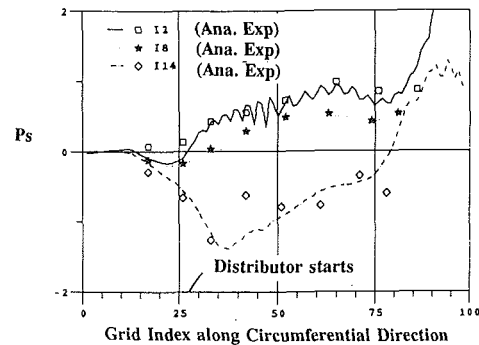


Fig. 9 Comparison of static pressure ( $P_s$ ) along circumferential direction (symbols: measurements; lines: predictions)

pressure generally decreases from the outside wall (upstream) toward the casing/distributor outlet (downstream). With regard to the velocity components, they also increase in magnitude along the same direction until reaching the distributor region. Within the distributor region, the radial velocity component increases in magnitude while the tangential velocity component becomes smaller, indicating that the flow is evolving toward a two-dimensional behavior due to the flow acceleration caused by the distributors.

Figure 9 compares the predicted and measured circumferential distribution of the static pressure at three locations, all on the mid-height plane. These three locations are, respectively, close to the outside wall, at the middle of the cross-section, and slightly upstream of the distributor. While there are quantitative differences between the measurements and the predictions, the overall characteristics are in agreement. The first portion of the spiral casing is just a circular duct, and hence the pressure there decreases along the streamwise direction. As the spiral casing starts to turn, the wall curvature causes a pressure gradient within each cross-section. Furthermore, the presence of the distributor produces more resistance to the flow field, resulting in an increasing pressure along the circumferential direction. In the end-wall region, the numerical solution predicts a more rapid increase of the static pressure, indicating that less fluid is predicted to be left in the end zone of the spiral casing. One can also clearly notice the pressure oscillations exhibited by the numerical solution in the region close to the outside wall. As discussed by Shyy and Vu (1991), this phenomenon is not a numerical phenomenon; it is caused by the way that the casing is manufactured. Due to its large size, the casing is made by joining many pieces of straight segments together, resulting in discontinuous slopes of the wall contours. This geometric characteristic is responsible for the apparent pressure oscillations observed along much of the outside wall. Shyy and Vu (1991) demonstrated that with smooth wall contours, pressure oscillations no longer appear.

Figure 10 shows both predicted and measured velocity fields on the middle top-view plane of the casing. Very close resemblance can be observed between the two. Since the Reynolds

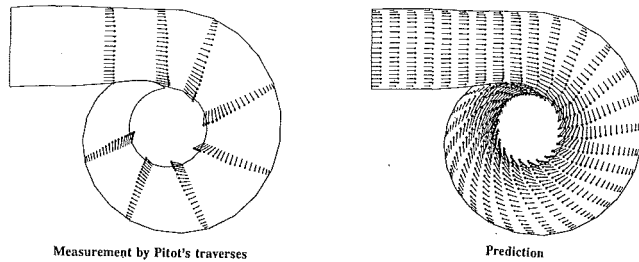


Fig. 10 Velocity vector distribution in the main flow direction at the middle section

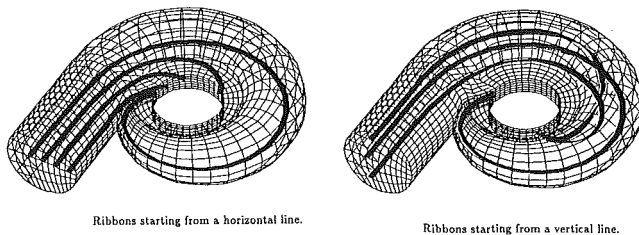


Fig. 11 Spiral case flow characteristics with ribbons representation

number is high, the pressure variation appears mainly along the radial, rather than the circumferential, direction in order to balance the curvature effect. Qualitatively, the overall convection field is of combined characteristics of a free vortex flow superimposed upon a sink flow. Three-dimensional illustrations of the fluid trajectories from inlet toward outlet in the form of the "ribbon" plots are shown in Fig. 11, which depicts the ribbons initiated along the middle line of the inlet section horizontally and vertically. As evidenced by the complicated mixing pattern exhibited in Fig. 11, the flow is highly three-dimensional.

Figure 12 gives representative views of the secondary flow patterns on four cross-sectional planes from upstream to downstream of the spiral casing, as indicated in Fig. 2. Several factors influence the development of the flow behavior. Since the outlet is located along the inner circumference of the spiral casing, a strong tendency exists to push the fluid to move radially inward. Furthermore, along the circumferential direction, the continuous reduction of cross-sectional area competes with the continuous loss of mass through the outlet; the balance of these factors determines whether the flow accelerates or decelerates in the streamwise direction, and interacts with the curvature of the spiral casing to produce the velocity pattern observed in Fig. 12. The strength of the secondary flow varies from cross-section to cross-section. At the beginning of the spiral casing, the flow is accelerated evenly along the casing height. As flow moves along the circumferential direction, double vortices are generated by the interaction between the casing curvature and the presence of the wall. From cross-sectional plane A to B (see Fig. 2) the secondary flow strengthens. The radial velocity component is very strong near the top and bottom of the casing and much weaker near the center. After the 180-degree turning, the core of the double swirls becomes smaller, as illustrated on cross-section C. Near the end of the casing where the flow continues accelerating, the double vortices completely disappear on cross-section D. The qualitative development of the secondary flow shown here is the same as the experimental observation made by Kurokawa and Nagahara (1986).

#### 4 Concluding Remarks

This paper reports an attempt at modeling and predicting the flow behavior in a spiral casing with an account of the

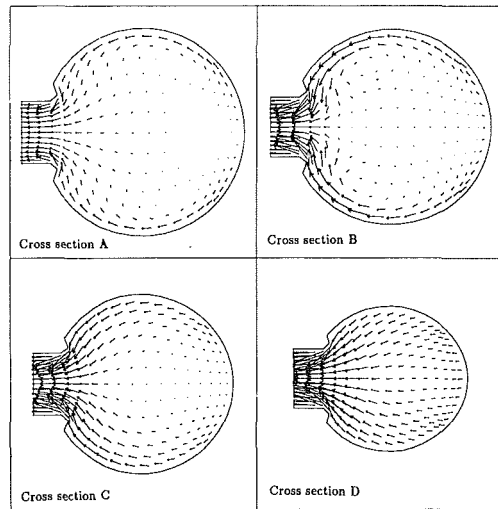


Fig. 12 Spiral case secondary flow characteristics at different cross sections

presence of the distributor. A two-level model is developed to devise a practical tool; the procedure outlined here has already been adopted as a part of design routine. The compromise as well as the features related to the treatment of the porous medium and the coupling between the global (spiral casing) and the local (distributor) analyses are discussed. Comparisons between the numerical prediction and the experimental measurement in terms of pressure and velocity profiles are made to assess the performance of the model. Based on the results obtained, the present approach appears to be capable of yielding useful design information without overloading the computing resources.

#### Acknowledgment

The present work has been supported by GE Canada. We are grateful to acknowledge the assistance of Mr. E. Desbeins for providing the experimental data, and Mrs. K. Heon for helping conduct the theory/data comparison. The software for grid generation was developed by the CASTOR project of Ecole Polytechnique de Montreal. Thanks are due also to Ms. Jan Machnik for her help in manuscript preparation.

#### References

- Chang, J. C. L., Kwak, D., Dao, S. C., and Rosen, R., 1985, "A Three-Dimensional Incompressible Flow Simulation Method and Its Application to the Space Shuttle Main Engine, Part II-Turbulent Flows," AIAA Paper 85-1670.
- Hah, C., 1984, "A Navier-Stokes Analysis of Three-Dimensional Turbulent Flows Inside Turbine Blade Rows at Design and Off-Design Conditions," *Journal of Engineering for Power*, Vol. 106, pp. 421-429.
- Holmes, D. G., Lamson, S., and Connell, S. D., 1988, "Quasi-3D Solutions for Transonic, Inviscid Flows by Adaptive Triangulation," ASME Paper 88-GT-83.
- Kurokawa, J., and Nagahara, H., 1986, "Flow Characteristics in Spiral Casing of Water Turbines," *IAHR Symposium 1986*, Vol. 2, Paper No. 62, Montreal, Canada.
- Lauder, B. E., and Spalding, D. B., 1974, "The Numerical Calculation of Turbulent Flows," *Computational Methods of Applied Mechanical Engineering*, Vol. 3, pp. 269-289.
- Leschziner, M. A., and Dimitriadis, K. P., 1989, "Computation of Three-Dimensional Turbulent Flow in Non-Orthogonal Junctions by a Branch-Coupling Method," *Computational Fluids*, Vol. 17, pp. 371-396.
- Löhner, R., 1989, "Adaptive H-Refinement on 3-D Unstructured Grids for Transient Problems," AIAA Paper No. 89-0653.
- Quirk, J. J., 1992, "An Alternative to Unstructured Grids for Computing

Gas Dynamic Flows around Arbitrary Complex Two-Dimensional Bodies," ICASE Report No. 92-7, NASA Langley Research Center.

Rai, M. M., 1987, "Unsteady Three-Dimensional Navier-Stokes Simulations of Turbine Rotor-Stator Interaction," AIAA Paper 87-2058.

Rhie, C. M., 1986, "A Pressure Based Navier-Stokes Solver Using the Multigrid Method," AIAA Paper 86-0207.

Shyy, W., and Braaten, M. E., 1986, "Three-Dimensional Analysis of the Flow in a Curved Hydraulic Turbine Draft Tube," *International Journal of Numerical Methods in Fluids*, Vol. 6, pp. 861-882.

Shyy, W., and Braaten, M. E., and Burrus, D., 1989, "Study of Three-Dimensional Gas-Turbine Combustor Flows," *International Journal of Heat and Mass Transfer*, Vol. 32, pp. 1155-1164.

Shyy, W., Tong, S. S., and Correa, S. M., 1985, "Numerical Recirculating

Flow Calculation Using a Body-Fitted Coordinate System," *Numerical Heat Transfer*, Vol. 8, pp. 99-113.

Shyy, W., and Vu, T. C., 1991, "On the Adoption of Velocity Variable and Grid System for Fluid Flow Computation in Curvilinear Coordinates," *Journal of Computational Physics*, Vol. 92, pp. 82-105.

Towne, C. E., 1984, "Computation of Viscous Flow in Curved Ducts and Comparison with Experimental Data," AIAA Paper 84-0531.

Vu, T. C., and Shyy, W., 1988, "Navier-Stokes Computation of Radial Inflow Turbine Distributor," *ASME JOURNAL OF FLUIDS ENGINEERING*, Vol. 110, pp. 29-32.

Vu, T. C., and Shyy, W., 1990, "Navier-Stokes Flow Analysis for Hydraulic Turbine Draft Tubes," *ASME JOURNAL OF FLUIDS ENGINEERING*, Vol. 112, pp. 199-204.

# LDV Measurements of Periodic Fully Developed Main and Secondary Flows in a Channel With Rib-Disturbed Walls

T.-M. Liou  
Professor.

Y.-Y. Wu  
Graduate Student.

Y. Chang  
Graduate Student.

Department of Power Mechanical  
Engineering,  
National Tsing Hua University,  
Hsinchu, Taiwan 30043

*Laser-Doppler velocimeter measurements of mean velocities, turbulence intensities, and Reynolds stresses are presented for periodic fully developed flows in a channel with square rib-disturbed walls on two opposite sides. Quantities such as the vorticity thickness and turbulent kinetic energy are used to characterize the flow. The investigated flow was periodic in space. The Reynolds number based on the channel hydraulic diameter was  $3.3 \times 10^4$ . The ratios of pitch to rib-height and rib-height to chamber-height were 10 and 0.133, respectively. Regions where maximum and minimum Reynolds stress and turbulent kinetic energy occurred were identified from the results. The growth rate of the shear layers of the present study was compared with that of a backward-facing step. The measured turbulence anisotropy and structure parameter distribution were used to examine the basic assumptions embedded in the  $k-\epsilon$  and  $k-\epsilon-A$  models. For a given axial station, the peak axial mean-velocity was found not to occur at the center point. The secondary flow was determined to be Prandtl's secondary flow of the second kind according to the measured streamwise mean vorticity and its production term.*

## Introduction

A noncircular cross-section channel with rib-disturbed walls is often used in heat exchanger systems for augmentation of the heat transfer. For instance, the internal cooling passages of the turbine blades can be approximately simulated as a rectangular channel with two opposite rib-disturbed walls. The main characteristic in modelling this kind of flow field is that an equivalent roughness factor often cannot be assumed for the discrete ribs since the ribs disturb the core flow significantly (Davalath and Bayazitoglu, 1987). Accordingly, the fundamental work on this type of flow field has tended to focus on the development of semi-empirical correlations (Bergles, 1988). To promote the advancement of numerical simulations on the ribbed-channel flows, detailed measurements of the flow structure over the repeated ribs are imperative.

For a rectangular duct with one surface roughened by a periodic rib structure, Drain and Martin (1985) performed laser-Doppler velocimetry (LDV) measurements for the fully developed flow condition. The measured data were compared with two-dimensional  $k-\epsilon$  predictions. The mean reattachment length was found to be seriously underestimated. Kobayashi et al. (1984, 1985) numerically studied the same type of flows using the  $k-\epsilon$  model and large eddy simulation. The distributions of two-dimensional mean velocities, turbulence energies, and shear stresses by both methods were quite dif-

ferent behind the ribs. Fodemski (1987) presented the fluid flow and temperature field for air flowing through a channel with one ribbed heated wall obtained using the  $k-\epsilon$  model. Qualitative comparison between the simulated (Fodemski, 1987) and laser holographic interferometry measured (Lockett and Collins, 1986) isotherms was made. Furthermore, the agreement between the predicted and measured Nusselt number distributions was found to be unsatisfactory behind the ribs. For a square duct with rib-roughened walls on two opposite sides, Yokosawa et al. (1989) measured the fully developed turbulent flow with a hot-wire anemometer. The coefficient of flow resistance and secondary flow pattern were presented.

It is clear from the above-mentioned studies that a better understanding of detailed flow structure in rib-disturbed channels by performing nonintrusive quantitative measurements of various turbulence parameters is needed for reducing the aforementioned discrepancies between the predicted and measured results. In addition, the quantitative data base for a rectangular channel with rib-disturbed walls on two opposite sides is still scarce. Consequently, the present paper aims at experimentally characterizing the complex flow structure in a rectangular channel with periodic rib turbulators on two opposite walls in terms of the mean velocity vector, reattachment length, vorticity thickness, and contour maps of various turbulent parameters. Both periodic fully developed mean and secondary flows have been measured. Furthermore, the isotropy of turbulence and the structure parameter distribution are examined to evaluate the basic assumptions embedded in  $k-\epsilon$  turbulence models. Non-intrusive measurements were made using LDV

Contributed by the Fluids Engineering Division for publication in the JOURNAL OF FLUIDS ENGINEERING. Manuscript received by the Fluids Engineering Division November 4, 1991. Associate Technical Editor: D. M. Bushnell.

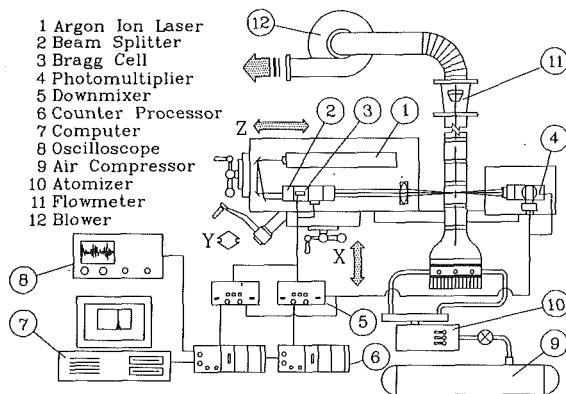


Fig. 1 Schematic drawing of overall experimental system

in the present work, since the flow reversal behind and in front of the rib turbulators and the large turbulence fluctuations along the separated shear layers make the use of the hot-wire technique impractical. Regions where the LDV measurements were inhibited were observed with flow visualization.

### Experimental Program

**Experimental Apparatus.** The flow system and LDV experimental setup in the present work, Fig. 1, is similar to that described in Liou et al. (1990a). Please refer to this earlier paper for more detail. The LDV optics is a two-color four-beam two-component system. A 4-W argon-ion laser with 514.5 nm (green) and 488 nm (blue) lines provided the coherent light sources. Both forward and off-axis scattering configurations were used in the experiment; the former gave a probe volume of 1.69 mm × 0.164 mm and the latter 0.74 mm × 0.164 mm inside the test section. The entire LDV system was mounted on a milling machine with four vibration-isolation mounts, allowing the probe volume to be positioned with 0.01 mm resolution. The light scattered from salt particles with a nominal 0.8 μm was collected into a photomultiplier and subsequently downmixed to the appropriate frequency shift of 0.1 to 10 MHz. Then two counter processors with 1 ns resolution were used to process the Doppler signals and feed the digital outputs into a microcomputer for storage and analysis. Depending on the location of the probe volume in the flow, typical coincidence rates were between 500 and 3000 s<sup>-1</sup> with a 50 μs coincidence window.

**Test Model and Conditions.** The test channel, shown in Fig. 2, was 900-mm in length and 60 mm × 30 mm in cross-sectional area, and made of 5-mm Plexiglas. The top and bottom walls of this channel were covered by square ribs of size 4 mm × 4 mm ( $W_r/H = 1$  and  $H/2B = 0.133$ ). The leading

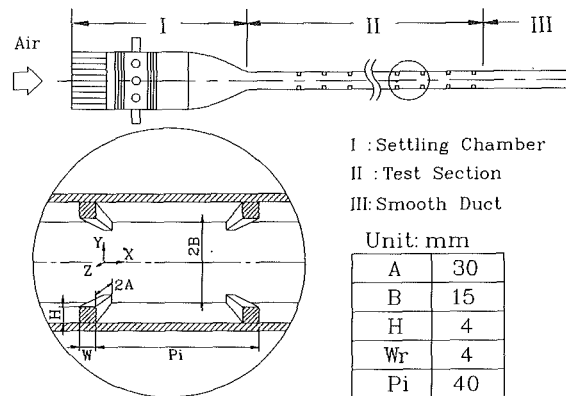


Fig. 2 Sketch of configuration, dimensions, and coordinate system of rectangular duct with repeated rib pairs (Uncertainty in H: ±0.1mm, in  $W_r$ : ±0.1mm, in A and B: ±0.3 mm, in axial position: ±0.1mm, in transverse position: ±0.1mm, in spanwise position: ±0.1mm)

edges of the first pair of ribs were placed 100mm downstream of the bell-shaped 10:1 contraction.

It is expected that the flow pattern will repeat itself from pitch to pitch, i.e., become periodic when fully developed (at a sufficient distance downstream of the first pair of ribs). Note that the flow is periodic in space, not time. Along the central plane  $Z/A = 0$ , measurements of the periodic fully developed flow were obtained at 23 stations on a grid with 0.5H spacing between the 10th and 11th rib pairs. Verification of the periodic fully developed condition is shown in Fig. 3 for a typical station  $X/H = -1.0$ . The repeatability is found to be within ±2 percent for both mean and fluctuating components. At each station the measurements were made at 13 to 21 locations. Because the cross-sectional aspect ratio of the test channel was 2:1, the velocity measurements were also taken in three transverse planes at  $X/H = -0.5, 2.0,$  and  $7.0$  (Fig. 2). In each transverse plane the measurements were made at 104 to 130 points in the (+Y, -Z) quadrant, since the flow was determined to be reasonably symmetric across the  $Z = 0$  plane (Fig. 4) and  $Y = 0$  plane. Quadrant to quadrant average variations were within ±0.5 percent of  $U_{REF}$ . The bulk mean velocity  $U_{REF} = 12.95$  m/s was used to non-dimensionalize the experimental results and corresponded to a Reynolds number of  $3.3 \times 10^4$ , where the hydraulic diameter of the channel was 40 mm.

### Results and Discussion

**Uncertainty Estimates.** Representative values of uncertainty estimates are noted in figure captions. More detailed uncertainty estimates and velocity bias correction are included in Liou et al. (1988, 1990a). There were typically 4096 realizations averaged at each measuring location. The statistical

### Nomenclature

A = half width of duct (30mm)  
 B = half height of duct (15mm)  
 $D_h$  = duct hydraulic diameter (40mm)  
 H = rib height (4mm)  
 k = turbulent kinetic energy,  $k \equiv 3/4(\overline{u^2} + \overline{v^2})$   
 $L_R$  = reattachment length  
 $P_i$  = pitch length (40mm)  
 PR = pitch ratio ( $\equiv P_i/W_r = 10$ )  
 Re = Reynolds number ( $\equiv \rho U_{REF} D_h / \mu_i$ )

U = streamwise mean velocity  
 u = streamwise velocity fluctuation  
 $u'$  = streamwise turbulence intensity ( $\equiv (\overline{u^2})^{1/2}$ )  
 $U_{REF}$  = duct bulk mean velocity,  $U_{REF} = 12.95$  (m/s)  
 $-\overline{uv}$  = turbulent shear stress  
 V = transverse mean velocity  
 v = transverse velocity fluctuation  
 $v'$  = transverse turbulence intensity ( $\equiv (\overline{v^2})^{1/2}$ )

W = spanwise mean velocity  
 w = spanwise velocity fluctuation  
 $w'$  = spanwise turbulence intensity ( $\equiv (\overline{w^2})^{1/2}$ )  
 $W_r$  = rib width (4mm)  
 X = streamwise coordinate  
 Y = transverse coordinate  
 Z = spanwise coordinate  
 $\epsilon$  = dissipation rate of turbulent kinetic energy  
 $\Lambda$  = vorticity thickness  
 $\rho$  = air density  
 $\mu_i$  = laminar viscosity

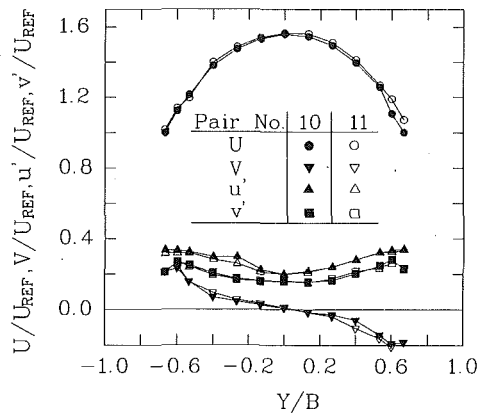


Fig. 3 Verification of periodic fully developed flow condition (Uncertainty in  $U/U_{REF}$  and  $V/U_{REF}$ : less than  $\pm 3.2$  percent, in  $u'/U_{REF}$  and  $v'/U_{REF}$ : less than  $\pm 4.4$  percent)

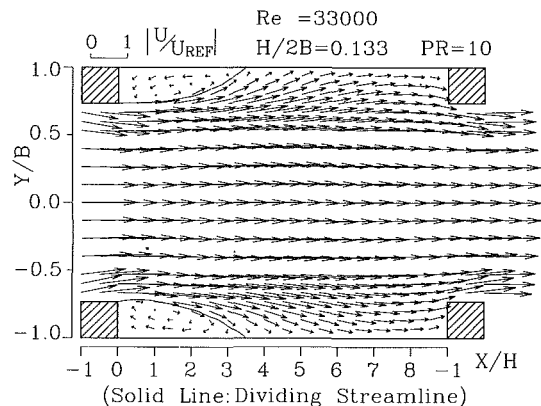


Fig. 5 Mean flow pattern in terms of velocity vectors (Uncertainty in  $U/U_{REF}$ : less than  $\pm 3.2$  percent)

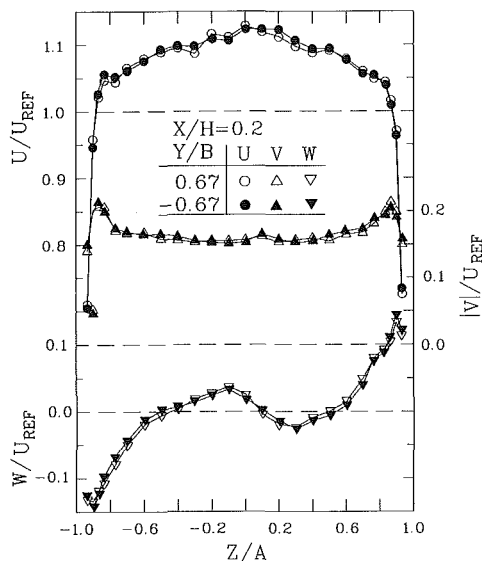


Fig. 4 Spanwise distributions of axial ( $U$ ), transverse ( $V$ ), and spanwise ( $W$ ) mean-velocity profiles at  $X/H = 0.2$  (Uncertainty: see Fig. 3 caption)

errors in the mean velocity and turbulence intensity were less than 1.8 and 2.2 percent, respectively, for a 95 percent confidence level. The well known weighting method of McLaughlin and Tiederman and the constant time-interval sampling mode were used to correct velocity bias for regions where local turbulence intensity was below and above 25 percent, respectively. The difference between corrected and uncorrected data sets was found to be below 2.6 percent. The counter processor with 1 ns resolution, together with a Bragg cell and an electronic downmixer, gave a typical error within 0.2 percent. For the range of atomizer pressure setting used, the saline solution was mixed to produce particles from 0.5 to 1.2  $\mu\text{m}$ . This particle diameter range is appropriate in gas flows in which turbulence frequencies exceeding 1 KHz are to be followed (Durst et al., 1976).

#### Flow Field in Longitudinal Plane $Z = 0$

**Mean Flow.** The vector plot in Fig. 5 shows flow contraction between the upper and the lower ribs as well as flow expansion and separation downstream of rib pairs for periodic fully developed flow in a one-pitch module. The acceleration of core flow by the geometric contraction can be more easily seen from the contour map of the nondimensionalized streamwise and transverse mean velocity components. This is shown

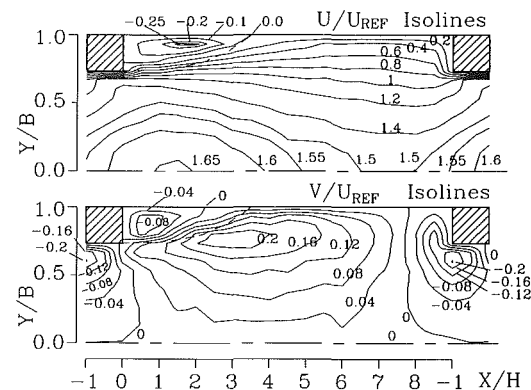


Fig. 6 Streamwise and transverse mean-velocity contours (Uncertainty: see Fig. 3 caption)

in Fig. 6. The acceleration starts from about  $X/H = 7$  ( $U/U_{REF} = 1.45$ ) to  $X/H = 1.5$  ( $U/U_{REF} = 1.65$ ). Also note that  $V/U_{REF}$  changes sign around  $X/H = 7.8$ , indicating transition of flow from expansion to contraction, that is, the extent of the upstream effect of the successive rib pair. The dividing streamline separates the core flow from the main recirculating flow behind the rib and reattaches onto the wall at  $X = 3.5 \pm 0.2H$  which is close to the  $3.7 \pm 0.3H$  measured by Hijikata et al. (1984) using a hot-wire anemometer for a similar flow field with larger pitch ( $PR = 15$ ) and rib height ( $H/2B = 0.2$ ). The center of the main recirculation zone is located approximately at  $X/H = 1.3$  and  $Y/H = \pm 0.8$ . Corner vortices in front of and behind the rib, which were not measured by the LDV, can be seen in oil-film drop flow-visualization and are  $0.4 \pm 0.2$  mm and  $0.8 \pm 0.2$  mm long, respectively.

**Turbulence.** The contour maps of the turbulent kinetic energy and Reynolds shear stress are shown in Fig. 7. It is seen that the shear stress is high in the regions where the mean-velocity gradient is steep (Fig. 6). The maximum shear stress at each streamwise station  $X/H$  first occurs along the dividing streamline for  $0 < X/H < 3$  and then along a horizontal band at a distance  $0.7 \pm 0.2H$  away from the wall ( $Y/B = 1.0$ ) for  $X/H \geq 3$ . In the meantime the value of maximum  $-\overline{uv}/U_{REF}^2$  increases up to 0.08 as  $X/H$  increases from 0 to 3, but subsequently decreases with increasing  $X/H$ . Moreover, the shear stress decreases toward the centerline ( $Y/B = 0$ ) and toward the concave corner in the separated recirculating zone. Similar behavior also occurs for  $k/U_{REF}^2$ , Fig. 7, since the production of turbulent kinetic energy is related to the product of shear stresses and the mean velocity gradients. There are two more aspects worth pointing out. First, the peak of maximum tur-



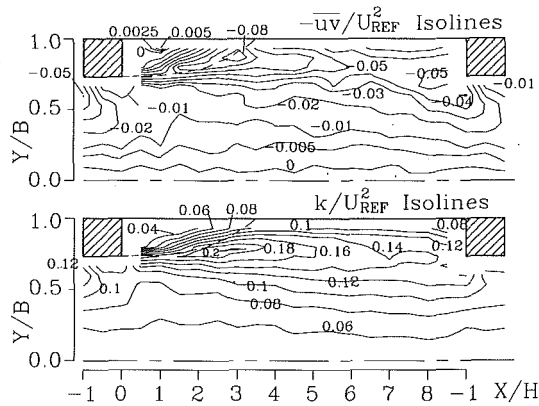


Fig. 7 Contours of Reynolds shear stress and turbulent kinetic energy (Uncertainty in  $|\overline{uv}/U_{REF}^2$ : less than  $\pm 4.8$  percent, in  $k/U_{REF}^2$ : less than  $\pm 7.4$  percent)

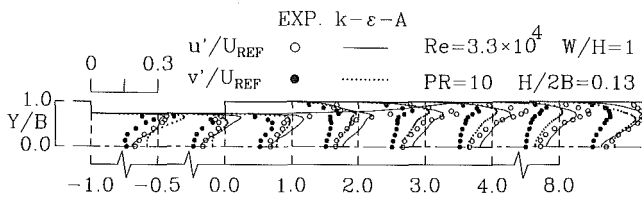


Fig. 8 Measured and computed streamwise and transverse turbulence intensity profiles in one-pitch module (Uncertainty: see Fig. 3 caption)

bulent kinetic energy is 20 percent of  $U_{REF}^2$  and occurs approximately  $0.6 \pm 0.3$  rib heights upstream of reattachment ( $X/H = 3.5$ ). Similar results have also been measured by others in sudden expansion pipe or channel flows where the peak of streamwise turbulence intensity was found to occur at approximately one step height upstream of reattachment (Eaton and Johnston, 1981). Second, the minimum  $K/U_{REF}^2$  in the entire pitch module occurs inside the separated recirculating zone and near the concave corner ( $X/H = 0$ ,  $Y/B = 1.0$ ), and has a value 0.04 which is only one-fifth of the aforementioned peak value. This provides a rationale for the poor heat transfer measured in the concave corner formed by the intersection of the rib rear edge and channel wall (Liou and Hwang, 1991; Lockett and Collins, 1990).

**Isotropy.** A check of isotropy for the turbulence flow field investigated is useful in guiding turbulence modelling efforts. Figure 8 depicts the distributions of both axial and transverse turbulence intensities throughout the entire pitch module. For regions around the centerline  $u'$  is found to be 1.5 times  $v'$  and for other regions  $u' \approx 2v'$ . In other words, Fig. 8 shows that the turbulence is anisotropic with  $\overline{u^2} = 2.25$  to  $4v^2$  in the  $Z = 0$  plane. Consequently, the standard  $k-\epsilon$  turbulence model, which can not distinguish  $\overline{u^2}$  from  $\overline{v^2}$ , is not appropriate to be applied to the flow field investigated in this work. The predicted results using a two-dimensional algebraic Reynolds stress model (referred to as the  $k-\epsilon-A$  model in this study), described in detail in Liou et al. (1990b), are indicated in Fig. 8 and are found to be in fair agreement with the measured data. The quantitative discrepancies between the computed and measured results shown in Fig. 8 are partly due to the three-dimensional effect of the flow field, as will be shown shortly, and partly attributable to the basic assumption that  $\overline{uv}$  is proportional to  $k$ , an assumption embedded in the  $k-\epsilon-A$  model. Figure 9 depicts the contour map of the structure parameter  $|\overline{uv}/k|$ . As one can see the measured  $|\overline{uv}/k|$  is in the range of 0.1 to 0.4, whereas it is often specified by researchers as 0.3 (Harsha et al., 1970) or 0.24 (Launder, 1975).

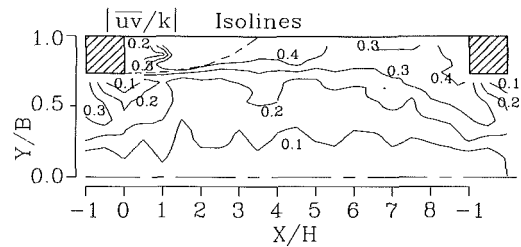


Fig. 9 Structure parameter contours (Uncertainty in  $|\overline{uv}/k|$ : less than  $\pm 8.8$  percent)

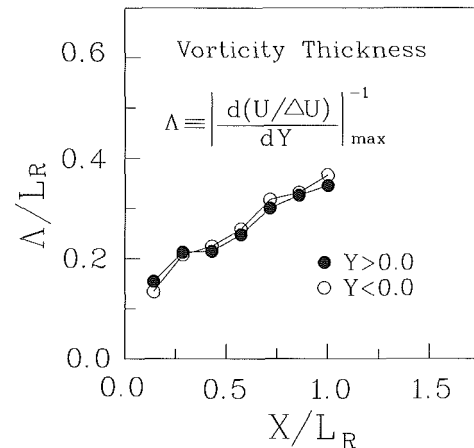


Fig. 10 Vorticity thickness as a function of axial distance (Uncertainty in  $\Lambda$ : less than  $\pm 5.2$  percent)

**Vorticity Thickness.** The vorticity thickness (Ellzey et al., 1988; Westphal et al. 1981), an index of shear layer growth, is defined as

$$\Lambda = \left| \frac{\partial(U/\Delta U)}{\partial Y} \right|_{\max}^{-1}$$

$\Delta U$  is the largest (local) velocity difference across the shear layer ( $U_{\max} - U_{\min}$ ). Figure 10 shows the variation of  $\Lambda$  downstream of the rib. The vorticity thickness of the separation bubble is found to grow approximately linearly with axial distance. The growth rate  $d\Lambda/dX$  is about 0.58 which is two times that of the backward-facing step (Ellzey et al., 1988). According to a review of research on subsonic turbulent flow reattachment by Eaton and Johnston (1981), the mixing layer growth rates are increased by increasing the freestream turbulence level. For the present cyclic fully developed flow, the turbulence intensities  $u'/U_{REF}$  and  $v'/U_{REF}$  in the region between the upper and lower ribs are typically 20 to 30 percent (Fig. 8), which is considerably higher than the upstream turbulence level of the backward-facing step flows investigated previously. This rapid growth of the mixing layer and, to some extent, the significant three dimensionality of the flow field (as will be shown in the following section) account for the short reattachment length found in the present study, which is one-third to one-half of the reattachment length found in the backward-facing step flow (Eaton and Johnston, 1981).

**Spanwise Flow Structure.** Secondary flow has been assumed to be responsible for the insensitivity of heat transfer performance to the angle of attack of the rib (Han, 1988; Han and Park, 1988), although without any direct evidence. Consequently, a direct measurement of secondary flow in the ribbed channel is worthwhile and the measured results of  $V$  and  $W$  are shown in Fig. 11 in terms of a vector plot. There is only one secondary flow cell in each quadrant of a channel cross

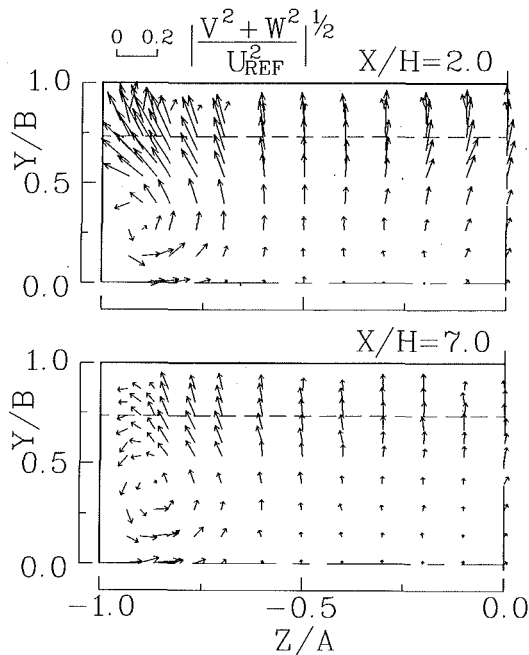


Fig. 11 Secondary-flow vectors in  $X/H = 2.0$  and  $7.0$  planes (Uncertainty in  $(V^2 + W^2)/U_{REF}^2$ : less than  $\pm 3.2$  percent)

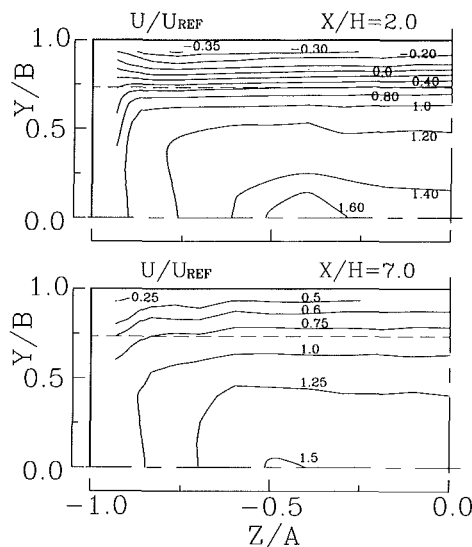


Fig. 12 Streamwise mean-velocity contours in  $X/H = 2.0$  and  $7.0$  planes (Uncertainty: see Fig. 3 caption)

section, a result different from the well-known two secondary flow cells in each quadrant of a channel cross section in the smooth channel (Fujita et al., 1989; Speziale, 1986). Moreover, the magnitudes of  $V$  and  $W$  in Fig. 11 are approximately ten times those in the smooth channel (Fujita et al., 1989; Speziale, 1986). The center of the secondary flow cell is toward the side wall, ( $Y/B = 0.35$ ,  $Z/A = -0.9$ ) for  $X/H = 2.0$  and ( $Y/B = 0.42$ ,  $Z/A = -0.99$ ) for  $X/H = 7.0$ , and the extent of the cell is about one half of a quadrant. Figure 11 also depicts the secondary flow in the  $X/H = 2.0$  plane (across the separating bubbles), which is two to three times stronger than that in the  $X/H = 7.0$  plane (across the redeveloping region). As for the spanwise distribution of the streamwise mean velocity, Fig. 12, another contrast between the ribbed and the smooth channels is revealed. The maximum  $U/U_{REF}$  at a given  $X/H$  station no longer occurs at the center point ( $Y/B = 0$ ,  $Z/A = 0$ ), as in the smooth channel case, but instead occurs at ( $Y/$

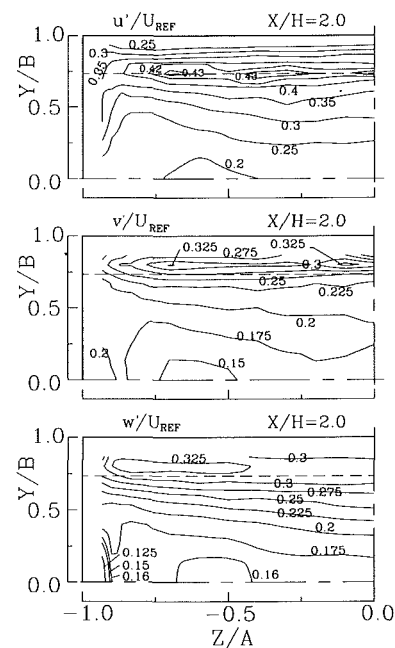


Fig. 13 Streamwise, transverse, and spanwise turbulent-intensity contours (Uncertainty in  $u'/U_{REF}$  and  $v'/U_{REF}$ : less than  $\pm 4.4$  percent, in  $w'/U_{REF}$ : less than  $\pm 5.8$  percent)

$B = 0$ ,  $Z/A = \pm 0.27$ ) in the  $X/H = -0.5$  plane (not shown) and at ( $Y/B = 0$ ,  $Z/A = \pm 0.46$ ) in the  $X/H = 7.0$  plane.

Figure 13 depicts the streamwise, transverse, and spanwise turbulence intensity contours. The shapes of the  $u'/U_{REF}$ ,  $v'/U_{REF}$ , and  $w'/U_{REF}$  contours are similar and maximum values of all three components are found to occur along a horizontal band separated from the ribbed wall at a distance the same as, or slightly lower than, the rib height. Quantitatively, the values of  $v'/U_{REF}$  and  $w'/U_{REF}$  are less than those of  $u'/U_{REF}$  at all measured  $X/H$  stations. These observations may suggest that the  $v'/U_{REF}$  and  $w'/U_{REF}$  fluctuations receive their energy from the  $u'/U_{REF}$  fluctuations by means of pressure interactions (Tennekes and Lumley, 1970). Figure 13 also shows anisotropy of the turbulence, which is consistent with the observation made earlier from Fig. 8. The  $v'/U_{REF}$  and  $w'/U_{REF}$  contours differ mainly in the regions near the side wall,  $-1 < Z/A < -0.7$  in Fig. 13, and one rib height from the ribbed wall,  $0.7 < Y/B < 1.0$ . Note that the secondary flow is most pronounced in these regions, as shown in Fig. 11. Consequently, the secondary flows may be triggered by the anisotropy of  $v'/U_{REF}$  and  $w'/U_{REF}$  in these regions. Such turbulence-generated secondary flows are generally called Prandtl's secondary flows of the second kind (Perkins, 1970) and represent streamwise mean vorticity ( $\Omega$ ) production. Figure 14 presents the generated  $\Omega$  and the dominant vorticity production term  $\partial^2 (v^2 - w^2)/\partial y \partial z$  of secondary flows of Prandtl's second kind. Consistency is clearly demonstrated as one compares Fig. 14(a) with Fig. 14(b), Fig. 13 ( $v'/U_{REF}$  and  $w'/U_{REF}$ ), and Fig. 11. Further, the vorticity production term shown in Fig. 14(b) is found to be an order of magnitude larger than that in the corresponding smooth channel (Brundrett and Baines, 1964).

## Summary and Conclusions

The main and secondary flow fields in a rectangular channel with ribs on two opposite walls under a cyclic fully developed condition have been characterized using laser-Doppler velocimetry and flow visualization. In the  $Z = 0$  plane, the separated mixing layers immediately downstream of the rib pair are found to grow linearly with axial distance and faster than

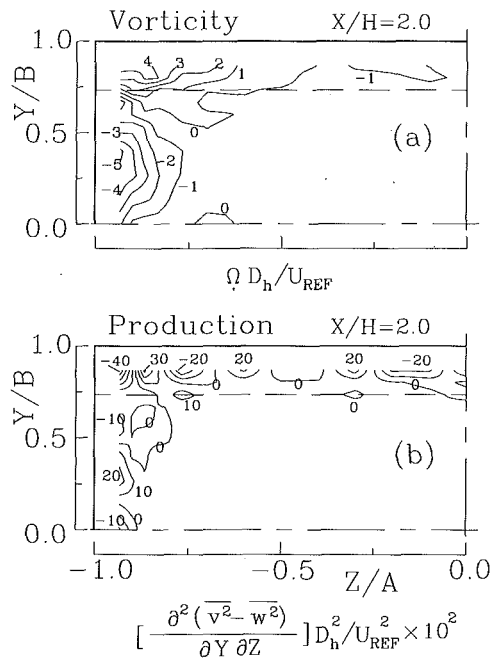


Fig. 14 (a) Streamwise mean-vorticity contour; (b) production term of Prandtl's secondary flows of the second kind (Uncertainty in  $\Omega$ : less than  $\pm 9.6$  percent, in  $\partial^2(\bar{v}^2 - \bar{w}^2)/\partial Y \partial Z$ : less than  $\pm 10.4$  percent)

those of a backward-facing step, resulting in a shorter reattachment length. Both Reynolds shear stresses and turbulent kinetic energy have maximum values distributing along horizontal bands at a distance of about  $0.7H$  from the ribbed walls and minimum values in the regions near the channel centerline and concave corners within the separating bubbles. These results should provide useful information for heat transfer studies in this area. The degree of turbulence anisotropy and the distribution of the structure parameter measured in the present work also provide important data base for examining the basic assumptions embedded in the standard  $k-\epsilon$  model and the  $k-\epsilon-A$  model.

At a given  $X/H$  station the streamwise mean-velocity contours show two peaks occurring at ( $Y/B = 0, 0.25 < |Z/A| < 0.5$ ), a result not reported previously and differing from the smooth-wall channel case. The secondary flow field contains one recirculating cell, instead of the two cells in the smooth-wall channel case, for each quadrant. The streamwise mean vorticity is found to be Prandtl's secondary flow of the second kind and is most pronounced in the regions where the transverse and spanwise turbulence intensity contours indicate major differences.

## References

- Bergles, A. E., 1988, "Some Perspectives on Enhanced Heat Transfer—Second-Generation Heat Transfer Technology," *ASME Journal of Heat Transfer*, Vol. 110, pp. 1082–1096.
- Brundrett, E., and Baines, W. D., 1964, "The Production and Diffusion of Vorticity in Duct Flow," *Journal of Fluid Mechanics*, Vol. 19, pp. 375–394.
- Davalath, J., and Bayazitoglu, Y., 1987, "Forced Convection Cooling Across Rectangular Blocks," *ASME Journal of Heat Transfer*, Vol. 109, pp. 321–328.
- Drain, L. E., and Martin, S., 1985, "Two Component Velocity Measurements of Turbulent Flow in A Ribbed-Wall Flow Channel," *International Conference*

on Laser Anemometry—Advances and Application, Manchester, U.K., 16th–18th, Dec.

Durst, F., Melling, A., and Whitelaw, J. H., 1976, *Principles and Practice of Laser-Doppler Anemometry*, Academic Press, New York, Chapter 9.

Eaton, J. K., and Johnston, J. P., 1981, "A Review of Research on Subsonic Turbulent Flow Reattachment," *AIAA Journal*, Vol. 19, No. 9, pp. 1093–1100.

Ellzey, J. L., and Berbee, J. G., 1988, "Aspect Ratio and Reynolds Number Effects on the Flow Behind a Rearward-Facing Step," *AIAA 26th Aerospace Sciences Meeting*, AIAA-88-0612.

Fodemski, T. R., 1987, "The Simulation of Flow and Heat Transfer in Channels with Ribbed Surface," *2nd International Symposium on Transport Phenomena in Turbulent Flows*, Tokyo, Japan.

Fujita, H., Yokosawa, H., and Hirota, M., 1989, "Secondary Flow of the Second Kind in Rectangular Ducts with One Kind of Rough Wall," *Experimental Thermal and Fluid Science*, Vol. 2, pp. 72–80.

Han, J. C., 1988, "Heat Transfer and Friction Characteristics in Rectangular Channel with Rib Turbulators," *ASME Journal of Heat Transfer*, Vol. 110, pp. 321–328.

Han, J. C., and Park, J. S., 1988, "Developing Heat Transfer in Rectangular Channels with Rib Turbulators," *International Journal of Heat and Mass Transfer*, Vol. 31, No. 1, pp. 183–195.

Harsha, P. T., and Lee, S. C., 1970, "Correlation Between Turbulent Shear Stress and Turbulent Kinetic Energy," *AIAA Journal*, Vol. 8, No. 8, pp. 1508–1510.

Hijikata, K., Mori, Y., and Ishiguro, H., 1984, "Turbulent Structure and Heat Transfer of Pipe Flow with Cascade Smooth Turbulence Surface Promoters," *Transactions of Japan Society of Mechanical Engineers*, Vol. 50, No. 458, pp. 2555–2562.

Kobayashi, T., Kano, M., and Ishihara, T., 1984, "Prediction of Turbulent Flow in Two-Dimensional Channels with Turbulence Promoters, 1st Report: Numerical Predictions by Large Eddy Simulation," *Bulletin of Japan Society of Mechanical Engineers*, Vol. 27, No. 231, pp. 1893–1898.

Kobayashi, T., Kano, M., and Ishihara, T., 1985, "Prediction of Turbulent Flow in Two-Dimensional Channels with Turbulence Promoters, 2nd Report: Numerical Predictions by  $k-\epsilon$  Model and Comparison with Experimental Results," *Bulletin of Japan Society of Mechanical Engineers*, Vol. 28, No. 246, pp. 2940–2947.

Lauder, B. E., Reece, G. J., and Rodi, W., 1975, "Progress in the Development of a Reynolds-Stress Turbulence Closure," *Journal of Fluids Mechanics*, Vol. 68, part 3, pp. 537–566.

Liou, T. M., and Kao, C. F., 1988, "Symmetric and Asymmetric Turbulent Flows in a Rectangular Duct with a Pair of Ribs," *ASME JOURNAL OF FLUIDS ENGINEERING*, Vol. 110, pp. 373–379.

Liou, T.-M., Chang, Y., and Hwang, D.-W., 1990a, "Experimental and Computational Study of Turbulent Flows in a Channel with Two Pairs of Turbulence Promoters in Tandem," *ASME JOURNAL OF FLUIDS ENGINEERING*, Vol. 112, pp. 302–310.

Liou, T.-M., Hwang, Y.-H., and Wu, S.-M., 1990b, "The Three-Dimensional Jet-Jet Impingement Flow in a Closed-End Cylindrical Duct," *ASME JOURNAL OF FLUIDS ENGINEERING*, Vol. 112, pp. 171–178.

Liou, T.-M., and Hwang, J.-J., 1991, "Turbulent Heat Transfer Augmentation and Friction in Periodic Fully Developed Channel Flows," *ASME Journal of Heat Transfer*, Vol. 114, No. 1, pp. 56–64.

Lockett, J. F., and Collins, M. W., 1986, "Holographic Interferometry and Its Applications to Turbulent Convective Heat Transfer," *International Journal of Optical Sensors*, Vol. 1, No. 3, pp. 191–244.

Lockett, J. F., and Collins, M. W., 1990, "Holographic Interferometry Applied to Rib-Roughness Heat Transfer in Turbulent Flow," *International Journal of Heat and Mass Transfer*, Vol. 33, pp. 2439–2449.

McLaughlin, D. K., and Tiederman, W. G., 1973, "Biasing Correlation for Individual Realization of Laser Anemometer Measurement in Turbulent Flows," *The Physics of Fluids*, Vol. 16, No. 12, pp. 2082–2088.

Perkins, H. J., 1970, "The Formation of Streamwise Vorticity in Turbulent Flow," *Journal of Fluid Mechanics*, Vol. 44, pp. 721–740.

Speziale, C. G., 1986, "The Dissipation Ratio Correlation and Turbulent Secondary Flows in Noncircular Ducts," *ASME JOURNAL OF FLUIDS ENGINEERING*, Vol. 108, pp. 118–120.

Tennekes, H., and Lumley, J. L., 1972, *A First Course in Turbulence*, The MIT Press.

Yokosawa, H., Fujita, H., Hirota, M., and Iwata, S., 1989, "Measurement of Turbulent Flow in a Square Duct with Roughened Walls on Two Opposite Sides," *International Journal of Heat and Fluid Flow*, Vol. 10, No. 2, pp. 125–130.

Westphal, R. V., Eaton, J. K., and Johnston, J. P., 1981, "A New Probe for Measurement of Velocity and Wall Shear Stress in Unsteady, Reversing Flow," *ASME JOURNAL OF FLUIDS ENGINEERING*, Vol. 103, pp. 478–482.

# Real Gas Effects for Compressible Nozzle Flows

D. Drikakis<sup>1</sup>

S. Tsangaris

Department of Mechanical Engineering,  
National Technical University of Athens,  
Athens, Greece

*Numerical simulation of compressible nozzle flows of real gas with or without the addition of heat is presented. A generalized real gas method, using an upwind scheme and curvilinear coordinates, is applied to solve the unsteady compressible Euler equations in axisymmetric form. The present method is an extension of a previous 2D method, which was developed to solve the problem for a gas having the general equation of state in the form  $p = p(\rho, i)$ . In the present work the method is generalized for an arbitrary P-V-T equation of state introducing an iterative procedure for the determination of the temperature from the specific internal energy and the flow variables. The solution procedure is applied for the study of real gas effects in an axisymmetric nozzle flow.*

## 1 Introduction

The numerical solution of the compressible Euler equations has been reported by several authors, but all of these methods were developed mainly for perfect air. The incorporation of the real gas effects requires the introduction of a general equation of state. In the present paper a generalized method is presented for the simulation of real gas flows and test cases are presented for nozzle flows.

In recent years efforts have been made by many authors for the construction of algorithms for the solution of the equations of gas dynamics with real gas effects (Collela and Glaz, 1985; Liou et al., 1990; Grossman and Walters, 1989; Glaister, 1988; Drikakis and Tsangaris, 1991). These efforts mainly originated in the numerical investigation of hypersonic flow fields using an equation of state in the form  $p = p(\rho, i)$ , where  $p$ ,  $\rho$ ,  $i$  are the pressure, density, and specific internal energy of the gas. In the aforementioned papers modern numerical methods, as Flux Vector Splitting methods and Riemann solvers, have been modified for hypersonic flow simulation. All the above methodologies concern a  $p = p(\rho, i)$  E.O.S. and they can not directly be used for a P-V-T equation of state.

Drikakis and Tsangaris (1991) developed a real gas method, in combination with a Riemann solver, for the discretization of the inviscid fluxes, introducing thermodynamic parameters, such as the pressure derivatives with respect to density and specific internal energy. This method can not directly be used for an arbitrary P-V-T E.O.S., because it needs the definition of the pressure as a function of the density and the specific internal energy. In the present paper, this method is extended to apply to any P-V-T equation of state by an iterative procedure for the determination of the temperature from the specific internal energy. On the other hand, the extension of the 2-D method in axisymmetric form, with source terms, is presented. The solution of the inviscid axisymmetric gas dynamic

equations with source terms is obtained by a Godunov type, finite volume scheme. The variation of the pressure along a characteristic line is calculated in terms of the thermodynamic parameters. The present method is general because it does not make any assumption in the real gas manipulation, formulating the real gas problem along the characteristic lines in conservative form. The method has the advantage that it can also be used for P-V-T equations of state, while the methods mentioned in the literature have been developed on the basis that pressure is a function of the density and the specific internal energy or on the basis of an "equivalent" ratio of specific heats.

The solution procedure is used for the numerical simulation of real gas effects in an axisymmetric convergent-divergent nozzle. Results and differences from the perfect gas assumption are presented for nitrogen and superheated steam flow. The study of real gas effects is also presented for the gas flow with the addition of heat. The introduction of the heat source terms causes large variations in the gas flow, especially in the temperature field.

## 2 Governing Equations

The Euler equations for axisymmetric gas flow with real gas effects and source terms, such as a volumetric heat addition, are solved. The equations can be written in an extended conservation law form for a generalized coordinate system as:

$$U_t + E_\xi + G_\zeta + r\tilde{H} = Q \quad (1a)$$

where

$$U = J(\rho, \rho u, \rho w, e)^T$$

$$E = J(\rho \tilde{U}, \rho \tilde{U} u + p \xi_x, \rho w \tilde{U} + p \xi_z, (e + p) \tilde{U})^T$$

$$G = J(\rho \tilde{W}, \rho u \tilde{W} + p \zeta_x, \rho w \tilde{W} + p \zeta_z, (e + p) \tilde{W})^T$$

<sup>1</sup>Present address: Lehrstuhl für Strömungsmechanik, Universität Erlangen-Nürnberg, D-8520, Erlangen, Germany.

Contributed by the Fluids Engineering Division for publication in the JOURNAL OF FLUIDS ENGINEERING. Manuscript received by the Fluids Engineering Division March 30, 1991. Associate Technical Editor: C. J. Freitas.

$$\vec{H} = \frac{J}{z} (\rho w, \rho u w, \rho w^2, (e+p)w)^T$$

$$\vec{U} = u\xi_x + w\xi_z$$

$$\vec{W} = u\zeta_x + w\zeta_z$$

$$e = \rho i + .5\rho(u^2 + w^2) \quad (1b)$$

If  $r=1$  the equation is in axisymmetric form. If  $r=0$  it is in 2-D form. The source term  $Q$  contains a volumetric heat addition.

$$Q = J(0, 0, 0, q)^T$$

Body fitted arbitrary coordinates  $\xi, \zeta$  are used and the Jacobian of the transformation  $\xi = \xi(x, z), \zeta = \zeta(x, z)$  from Cartesian coordinates  $x, z$  to generalized coordinates  $\xi, \zeta$  is written as:

$$J = x_\xi z_\zeta - z_\xi x_\zeta$$

The quantities  $\rho, p, u, w$  represent the density, the pressure and the Cartesian velocity components respectively and  $e, i$  represent the total energy and the specific internal energy. The indices  $(\cdot)_\xi, (\cdot)_\zeta$  denote partial derivatives with respect to  $\xi, \zeta$ . The formulation of the governing equations is completed by a general equation of state in the form:

$$p = p(\rho, i) \quad \text{or} \quad p = p(\rho, T)$$

where  $T$  is the temperature of the gas.

The solution is obtained by an implicit procedure. The first order in time discretized implicit form of Eq. (1) is written as:

$$\frac{U^{n+1} - U^n}{\Delta t} + E_\xi^{n+1} + G_\zeta^{n+1} + r\vec{H}^n = Q \quad (2)$$

A Newton method can be constructed for  $U^{n+1}$  by linearizing the fluxes in Eq. (2) about the known time level  $n$ . Then Eq. (2) is written as follows:

$$\frac{\Delta U}{\Delta t} + (A^n \Delta U)_\xi + (C^n \Delta U)_\zeta = RHS \quad (3a)$$

where

$$RHS = - (E_\xi^n + G_\zeta^n + r\vec{H}^n) + Q \quad (3b)$$

$A, C$  are the Jacobians of the flux vectors  $E, G$ , respectively, and  $\Delta U$  is the time variation of the solution.

The fluxes on the right-hand side are calculated at the cell faces of the finite volume by a linear, locally one dimensional Riemann solver (Godunov type differencing) (Eberle, 1985). The characteristic flux averaging scheme is of third accuracy

in space and locally monotonic. The Jacobians of the fluxes of the left-hand side are formulated for a general equation of state.

### 3 Real Gas Formulation

The Euler equations are splitted into two one-dimensional equations.

$$U_t + E_\xi = 0$$

$$U_t + G_\zeta = 0$$

The Riemann invariants are a transformation of nonconservative Euler equations on the characteristic directions. These invariants are given by the following expressions:

$$p - p_0 - s^2(\rho - \rho_0) = 0 \quad (4a)$$

$$(w - w_0)\bar{x} - (u - u_0)\bar{z} = 0 \quad (4b)$$

$$p - p_1 + \rho s[\bar{x}(u - u_1) + \bar{z}(w - w_1)] = 0 \quad (4c)$$

$$p - p_2 + \rho s[-\bar{x}(u - u_2) - \bar{z}(w - w_2)] = 0 \quad (4d)$$

The subscripts indicate the point locations (points on the characteristic lines) at which  $p_j, \rho_j, u_j, w_j, j=0, 1, 2$ , should be interpolated.

Since we make use of the homogeneous property, the invariants have to be inverted into conservative variables. Considering that the pressure can be written as a function of the density and specific internal energy,  $p = p(\rho, i)$ , we obtain:

$$\Delta p = p_\rho \Delta \rho + p_i \Delta i \quad (5)$$

Our goal is to formulate the equations by means of the pressure derivatives  $p_\rho$  and  $p_i$ . The development of the method for a general equation of state is analytically presented in the literature (Drikakis and Tsangaris, 1991).

Finally, we find the conservative cell face flow values  $\rho, l = \rho u, n = \rho w, e$  from which the Euler fluxes on the right-hand side of Eq. (3), can be calculated. All the conservative values are given by the following equations:

$$\rho = \rho_0 + \bar{\rho} + r_1 + r_2 \quad (6a)$$

$$l = l_0 + r_1(u + s\bar{x}) + r_2(u - s\bar{x}) + \bar{x}d + u\bar{\rho} \quad (6b)$$

$$n = n_0 + r_1(w + s\bar{z}) + r_2(w - s\bar{z}) + \bar{z}d + w\bar{\rho} \quad (6c)$$

$$e = d\lambda_0 + (H + s\lambda_0)\rho_1 + (H - s\lambda_0)\rho_2 + \bar{e} + \bar{\rho} \left( q^2 + \rho \frac{Q}{p_i} \right) - \rho_0 \frac{p}{p_i} Q \quad (6d)$$

with

### Nomenclature

$A, C$  = Jacobians of the flux vectors  
 $e$  = total energy per unit volume  
 $E, G$  = flux vectors  
 $i$  = specific internal energy  
 $J$  = Jacobian matrix  
 $H$  = total enthalpy  
 $p$  = pressure  
 $p_i$  = pressure derivative with respect to internal energy

$p_\rho$  = pressure derivative with respect to density  
 $\rho$  = density  
 $s$  = sound velocity  
 $T$  = gas temperature  
 $u, w$  = Cartesian velocity components  
 $U$  = conservative solution vector

$\Delta U$  = time variation of the conservative solution vector  
 $\xi, \zeta$  = Body fitted coordinates  
 $x, z$  = Cartesian coordinates  
 $\lambda_k$  = eigenvalues

#### Indices

$n$  = iteration level

$$\tilde{p} = \frac{p_i}{\rho s^2} \left( \tilde{e} - e_0 - \rho_0 Q \frac{\rho}{p_i} \right) \quad (7a)$$

$$\tilde{e} = ul_0 + wn_0 \quad (7b)$$

$$d = \rho_0 \lambda_0 - l_0 \tilde{x} - n_0 \tilde{z} \quad (7c)$$

and

$$\lambda_0 = u\tilde{x} + w\tilde{z}$$

$$r_1 = \frac{0.5}{s^2} \left\{ \rho_1 (-s\lambda_0 + Q) + l_1 \left( -u \frac{p_i}{\rho} + s\tilde{x} \right) + n_1 \left( -w \frac{p_i}{\rho} + s\tilde{z} \right) + e_1 \frac{p_i}{\rho} \right\} \quad (7d)$$

$$r_2 = \frac{0.5}{s^2} \left\{ \rho_2 (s\lambda_0 + Q) - l_2 \left( -u \frac{p_i}{\rho} + s\tilde{x} \right) + n_2 \left( -w \frac{p_i}{\rho} + s\tilde{z} \right) + e_2 \frac{p_i}{\rho} \right\} \quad (7e)$$

$H$  is the total enthalpy while the sound velocity  $s$  and the term  $Q$  are given as:

$$s^2 = p \frac{p_i}{\rho^2} + p_\rho \quad (8a)$$

and

$$Q = p_\rho + p_i \frac{q^2}{2\rho} - i \frac{p_i}{\rho} \quad (8b)$$

The  $\tilde{x}$ ,  $\tilde{z}$  terms contain metric derivatives:

$$\tilde{x} = \frac{\xi_x}{\sqrt{\xi_x^2 + \xi_z^2}}, \quad \tilde{z} = \frac{\xi_z}{\sqrt{\xi_x^2 + \xi_z^2}}$$

The implementation of the method in the right-hand side of the equation, in order to include real gas effects, is obtained by the derivation of the Jacobian matrices and the eigenvectors for a general equation of state. For this reason, as with the expressions on the right-hand side, the matrices on the left-hand side are defined by introducing the pressure derivatives. The Jacobian matrix  $A$  is defined as follows:

$$A = \frac{\partial E}{\partial U} = \left( \frac{\partial E}{\partial \rho}, \frac{\partial E}{\partial l}, \frac{\partial E}{\partial n}, \frac{\partial E}{\partial e} \right)$$

In accordance with the assumption that the pressure is a function of the density and the internal energy, the partial derivatives for the pressure are given by the following relations:

$$\frac{\partial p}{\partial \rho}(\rho, i)|_{l, n, e} = \frac{\partial p}{\partial \rho}(\rho, i)|_i + \frac{\partial i}{\partial \rho}(\rho, l, n, e)|_{l, n, e} \frac{\partial p}{\partial i}(\rho, i)|_\rho$$

$$\frac{\partial p}{\partial l}(\rho, i)|_{\rho, n, e} = \frac{\partial p}{\partial l}(\rho, i)|_\rho \frac{\partial i}{\partial l}(\rho, l, n, e)|_{\rho, n, e}$$

$$\frac{\partial p}{\partial n}(\rho, i)|_{\rho, l, e} = \frac{\partial p}{\partial n}(\rho, i)|_\rho \frac{\partial i}{\partial n}(\rho, l, n, e)|_{\rho, l, e}$$

$$\frac{\partial p}{\partial e}(\rho, i)|_{\rho, l, n} = \frac{\partial p}{\partial e}(\rho, i)|_\rho \frac{\partial i}{\partial e}(\rho, l, n, e)|_{\rho, l, n}$$

and the internal energy is defined by:

$$i(\rho, l, n, e) = \frac{e}{\rho} - 0.5 \frac{(l^2 + n^2)}{\rho^2}$$

The analytical expressions of Jacobian matrices and the eigenvectors for a real gas can be found in reference (Drikakis and Tsangaris, 1991).

The above formulation of the method imposes the calculation of the thermodynamic derivatives of the pressure. These derivatives are approximated by the values of the pressure, density and the specific internal energy on the left and right states of the volume cell face. These approximations are defined as follows:

$$p_i = \frac{1}{\Delta i} \left\{ \frac{1}{2} (p(\rho_R, i_R) + p(\rho_L, i_R)) - \frac{1}{2} (p(\rho_R, i_L) + p(\rho_L, i_L)) \right\} \quad (9a)$$

$$p_\rho = \frac{1}{\Delta \rho} \left\{ \frac{1}{2} (p(\rho_R, i_R) + p(\rho_R, i_L)) - \frac{1}{2} (p(\rho_L, i_R) + p(\rho_L, i_L)) \right\} \quad (9b)$$

for  $\Delta i \neq 0$ ,  $\Delta \rho \neq 0$  and

$$p_i = \frac{1}{2} \{ p_\rho(\rho_L, i) + p_\rho(\rho_R, i) \} \quad (9c)$$

$$p_\rho = \frac{1}{2} \{ p_\rho(\rho, i_L) + p_\rho(\rho, i_R) \} \quad (9d)$$

for  $\Delta i = 0$ ,  $\Delta \rho = 0$ , respectively.

Where

$$\Delta(\cdot) = (\cdot)_R - (\cdot)_L$$

The indices  $R$ ,  $L$  represent, for a cell face  $i + 1/2$ , the volumes  $i + 1$ ,  $i$ , respectively (Fig. 1(a)).

#### 4 Coupling of the Temperature With the Specific Internal Energy

The equations of state for real gases are defined either by the density and the specific internal energy or by the density (or specific volume) and the temperature (P-V-T equation of state). To the second category belong the best known equations of state. In this case the calculation of the temperature of the gas is needed because from the conservative variables only the internal energy can be defined. For a real gas the specific internal energy is defined by the following relation:

$$i(\rho, T) = \int \left( \frac{\partial i}{\partial v} \right)_T dv + \int \left( \frac{\partial i}{\partial T} \right)_v dT \quad (10a)$$

The derivative in the second term of the above relation is the specific heat for constant volume  $v$ .

The derivative of the internal energy in the first term can be calculated by the pressure and the pressure derivative with respect to temperature as follows:

$$\left( \frac{\partial i}{\partial v} \right)_T = T \left( \frac{\partial p}{\partial T} \right)_v - p \quad (10b)$$

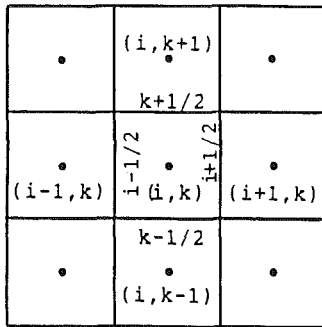
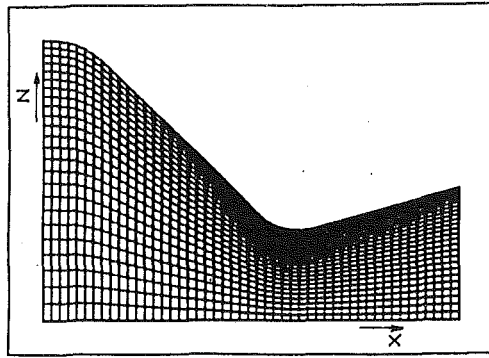


Fig. 1 Typical control volume and labeling scheme-Computational mesh 50 x 25 for the JPL nozzle

The specific heat for constant volume  $c_v$  for a real gas depends on the specific volume and the temperature, while for a perfect gas depends on the temperature alone. On the other hand, if the temperature of the gas is greater than the critical temperature ( $T_c$ ) the variations of the  $c_v$  are not large (Hittmair and Adam, 1971). Thus a first approximation can be considered with constant  $c_v$ .

For the Van der Waals equation of state:

$$p = \frac{RT}{v-b} - \frac{a}{v^2}$$

and using Eqs. (10a, b), the specific internal energy can be defined as follows:

$$i(T, v) - i(T_0, v_0) = \int_{v_0}^v c_v dT - a \left( \frac{1}{v} - \frac{1}{v_0} \right) \quad (11a)$$

Thus a value for the temperature can be defined by the known specific internal energy. If we consider that  $c_v$  is a function of the pressure and the density, an iterative procedure is needed in order to satisfy Eq. (11a). An iterative procedure, such as the Newton-Raphson technique, is also necessary if the internal energy from the Eq. (10a) is a complex function of the temperature. For instance if we consider the Benedict-Webb-Rubin equation of state and assuming, for the sake of simplicity, that  $T > T_c$ , the Eq. (10a) is written as follows:

$$i = T - T^{-2} f_1(v) + f_2(v) \quad (11b)$$

where  $f_1(v)$ ,  $f_2(v)$  are functions of the specific volume. From Eqs. (11a) or (11b) by an iterative procedure we can find the temperature and consequently the pressure from the P-V-T equation of state.

## 5 Heat Addition

In the computational method, source terms have also been introduced in order to simulate real gas flows with the addition

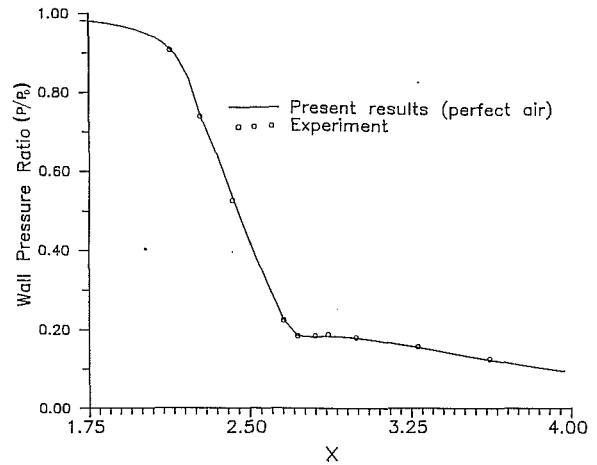


Fig. 2 Wall pressure distribution. Perfect air

of heat. As it seems from the results in the following section of the real gas effects are stronger when heat is added in the gas flow. The source term is defined in terms of an algebraic function  $F(x, y)$  as (Merkle and Choi, 1987):

$$q = P \min \{ 2F^{3/2} - 3F + 1, 1 \}$$

where

$$F(x, y) = \frac{(x-x_1)^2 + (z-z_1)^2}{(x_2-x_1)^2 + (z_2-z_1)^2}$$

$(x_1, z_1)$  is the position of the maximum heat addition. The source term is normalized by the coordinate  $(x_2, z_2)$ . In the nozzle calculations we consider the position of the maximum heat addition at the axis of the nozzle in the throat region. The parameter  $P$  is defined as input parameter. For the present test cases  $P = 1 \times 10^7 \text{ W/m}^3$ .

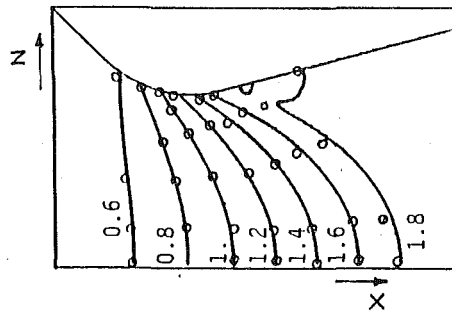
## 6 Results and Discussion

The computational code in axisymmetric form is used for the simulation of the gas flow into JPL nozzle (Fig. 1(b)). For the present conical nozzle with angles of convergence 45 deg and divergence 15 deg, experiments for the perfect air have been performed by Cuffel et al. (1969). The computational mesh is 50 x 25 grid points. Grid dependence studies (Drikakis, 1991) have shown that finer meshes do not influence the accuracy of the solution in the case of the axisymmetric nozzle flow. The present flow is a steady flow problem. In order to accelerate the convergence to steady state solution, the local time stepping technique is used. The time step is varied in the computational domain by the following relation:

$$\Delta t = \frac{\text{CFL}}{\max(|\lambda_j|)}$$

where  $\lambda_j$ ,  $j=0, 1, 2$  are the eigenvalues of the equations while CFL is the Courant-Friedrichs-Lewy number. The unfactored implicit procedure allows the use of CFL numbers up to 150. The CPU time on a workstation computer system (main processor consists of the R3000 and R3010 floating point coprocessor with 20-MHz clock frequency) is 30 min for the perfect gas case.

Comparison, in Fig. 2, of the ratio of static pressure to stagnation pressure along the wall with the corresponding experimental results shows the reliability of the numerical method. In Fig. 3 comparison is also presented with the experimental results for the Mach number distributions.



— Present Results  
 o Experiment

Fig. 3 Iso-Mach lines. Perfect air

Table 1 Summary table of the equations for the test problems

Euler equations written in curvilinear coordinates system and axisymmetric form.

$$U_i + E_{\xi} + G_{\zeta} + r\ddot{H} = Q$$

Van der Waals EOS

$$p = \frac{RT}{v-b} - \frac{a}{v^2}$$

Benedict-Webb-Rubin EOS ( $A_0, B_0, C_0, a, b, c, \gamma, \alpha$  constants)

$$p = \frac{RT}{v} + \left( B_0 RT - A_0 - \frac{C_0}{T^2} \right) \frac{1}{v^2} + (bRT - a) \frac{1}{v^3} + \frac{a\alpha}{v^6} + \frac{c \left( 1 + \frac{\gamma}{v^2} \right)}{T^2} \frac{1}{v^3} \exp \left( -\frac{\gamma}{v^2} \right)$$

Coupling of the specific internal energy with the temperature

$$i(T, v) - i(T_0, v_0) = \int_{T_0}^T c_v dT - a \left( \frac{1}{v} - \frac{1}{v_0} \right)$$

As a first test case for the real gas flow in the JPL nozzle, the nitrogen flow has been studied. For the present cases the Van der Waals E.O.S., the Benedict-Webb-Rubin E.O.S. and the constant compressibility factor have been used. The set of equations which are solved for the test problems is summarized in Table 1.

In Figs. 4(a) and 4(b), comparisons of the pressure and the temperature distributions at the wall are presented. In those figures comparisons between "perfect" nitrogen with Van der Waals E.O.S., Benedict-Webb-Rubin (BWR) E.O.S. and nitrogen with a constant compressibility factor  $z = pv/RT = 0.3$  are presented. From these figures we observe small differences in the temperature distributions, between the two equations of state (Van der Waals, BWR) and the perfect gas assumption. Greater differences are presented for the constant compressibility factor  $z = 0.3$  especially in the temperature distribution. A significant result is that the ideal gas assumption underpredicts the temperature distribution in the supersonic region of nozzle. The influence of real gas on the supersonic region is stronger because of the compressibility effect.

The pressure rise in the throat region just downstream of the tangency is larger for  $z = 0.3$ . This result is important because the pressure rise influences significantly the boundary layer and the heat transfer in high temperature gas flows. For the above test cases the calculation of the temperature is obtained for each computational volume by an iterative process (Newton-Raphson) and for each time step. This increase the computational cost by a factor of two.

Another test case is the flow of superheated steam through

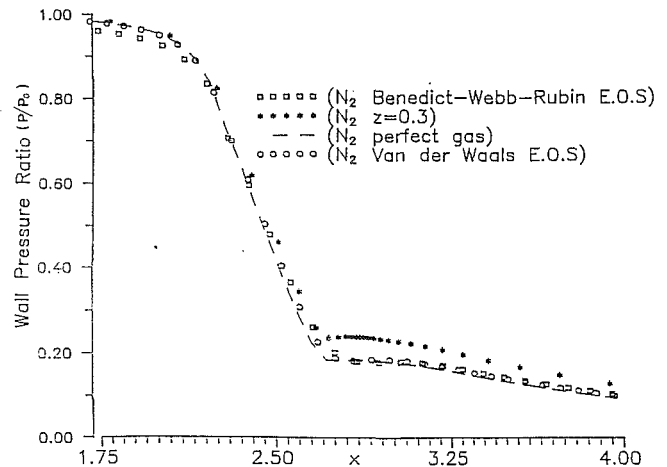


Fig. 4(a)

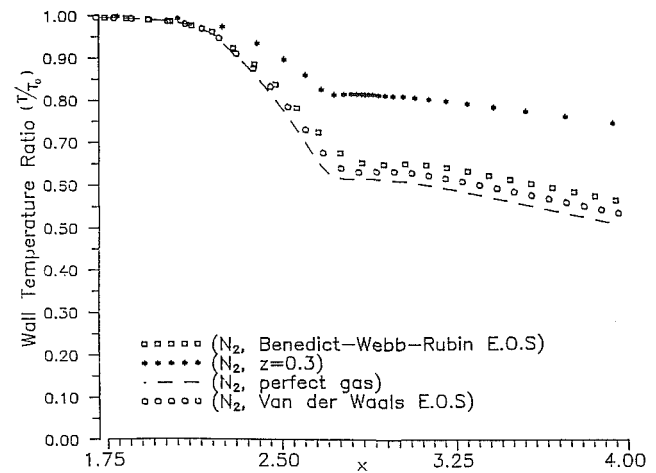


Fig. 4(b)

Fig. 4(a,b) Wall pressure and temperature distributions for nitrogen ( $N_2$ )

the JPL nozzle. The real gas behavior of the steam is described by thermodynamic relations (Galits, 1990) which have been incorporated as thermodynamic subroutines in the computational code in order to obtain real gas flow simulation. These subroutines also define the specific heats for constant volume and pressure as function of the  $p, T$ :

$$c_v = c_v(p, T), \quad c_p = c_p(p, T)$$

The flow of superheated steam has also been studied with the addition of heat using the source term. In Fig. 5 the pressure distributions for perfect and real steam are shown and the differences are small. In the case of heat addition, not shown here, the pressure rise is larger than the corresponding rise in the case with no heat addition. On the other hand, large differences between steam as perfect gas and steam as real gas are presented in the temperature field (Fig. 6). The influence of real gas effect is stronger in the case of heat addition (Fig. 6). Finally in Fig. 7 differences for perfect and real steam (without heat addition) in the location of the isotherm lines are shown. The real gas effects are significant especially in the divergent region (supersonic) of the nozzle where the compressibility is stronger.

## 7 Conclusions

A previous real gas method (Drikakis and Tsangaris, 1991)



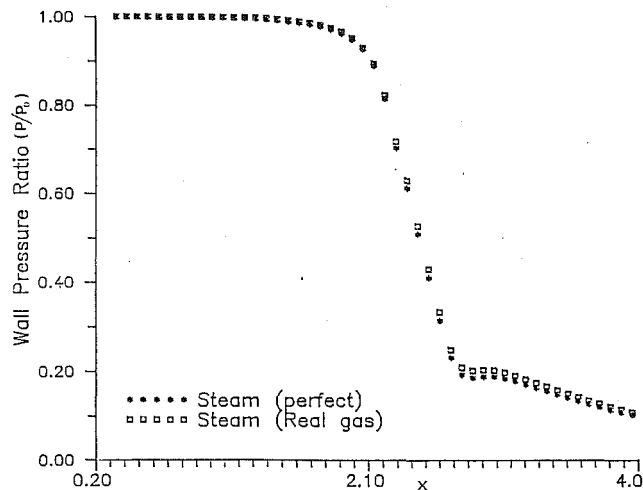


Fig. 5 Wall pressure distributions for superheated steam

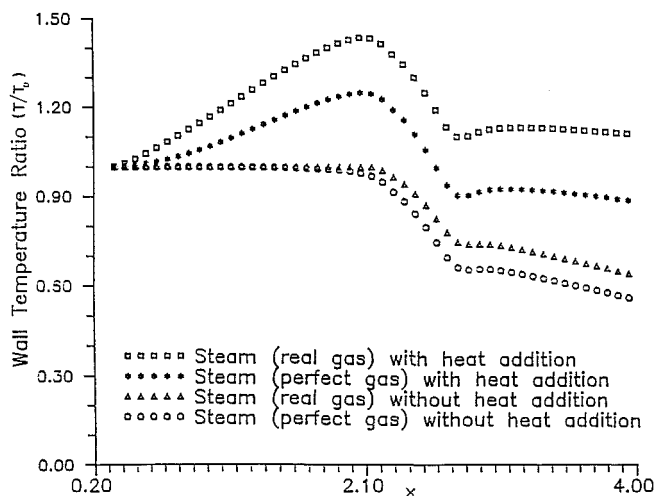


Fig. 6 Wall temperature distributions for superheated steam

is generalized for any P-V-T equation of state. Using the present method it is not necessary to consider the pressure as a function of the density and the specific internal energy. The pressure can be a complex function of the density or the specific volume and the temperature. In this case thermodynamic equations are used in order to correlate the thermodynamic and the flow variables. Numerical simulation of the nitrogen and

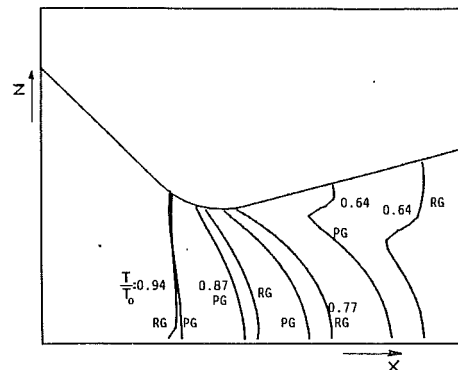


Fig. 7 Iso-temperature lines for superheated steam (PG = perfect gas, RG = real gas)

steam flow in an axisymmetric nozzle shows that the ideal gas assumption underpredicts the temperature distribution along the wall of the nozzle, while there are significant differences between perfect and real gas in the temperature profiles. Differences between perfect and real gas in the pressure distribution are small. On the other hand, in the case of heat addition the influence of the real gas on the temperature distribution is more intense; that means that the reformulation of the computational methods for real gases is necessary for the understanding of the complex gas flows.

## References

- Colella, P., and Glaz, P. M., 1985, "Efficient Solution Algorithms for the Riemann Problem for Real Gases," *Journal of Computational Physics*, Vol. 59, pp. 264-289.
- Cuffel, R. F., Back, H. L. and Massier, P. F., 1969, "Transonic Flowfield in a Supersonic Nozzles with small Throat Radius of Curvature," *AIAA Journal*, Vol. 7, No. 7, pp. 1364-1368.
- Drikakis, D., and Tsangaris, S., 1991, "An Implicit Characteristic Flux Averaging Scheme for the Euler Equations with Real Gases," *International Journal for Numerical Methods in Fluids*, Vol. 12, pp. 711-726.
- Eberle, A., 1985, "3D Euler Calculations Using Characteristic Flux Extrapolation," AIAA paper-85-0119.
- Galis, M., 1990, Diploma Dissertation NTUA.
- Glaister, P., 1988, "An Approximate Linearized Riemann Solver for the Euler Equations for Real Gases," *Journal of Computational Physics*, Vol. 74, pp. 361-383.
- Grossman, B., and Walters, R. W., 1989, "Analysis of Flux Split Algorithms for Euler Equations with Real Gases," *AIAA Journal*, Vol. 27, No. 5, pp. 524-532.
- Hittmair, O., and Adam, J., 1971, "Wärmetheorie" Friedrich Vieweg and Sohn GmbH, Verlag, Braunschweig.
- Liou, M. S., Van Leer, B., and Shuen, J. S., 1990, "Splitting of Inviscid Fluxes for Real Gases," *Journal of Computational Physics*, Vol. 87, pp. 1-24.
- Merkle, C. L., and Choi, Y. H., 1987, "Computation of Low-Speed Flow with Heat Addition," *AIAA Journal*, Vol. 25, No. 6, pp. 831-841.

# An Inverse Inviscid Method for the Design of Quasi-Three-Dimensional Turbomachinery Cascades

E. Bonataki  
Research Assistant.

P. Chaviaropoulos  
Research Engineer.

K. D. Papailiou  
Professor.

National Technical University of Athens,  
Laboratory of Thermal Turbomachines,  
15710 Athens, Greece

*The calculation of the blade shape, when the desired velocity distribution is imposed, has been the object of numerous investigations in the past. The object of this paper is to present a new method suitable for the design of turbomachinery stator and rotor blade sections, lying on an arbitrary axisymmetric stream-surface with varying streamtube width. The flow is considered irrotational in the absolute frame of reference and compressible. The given data are the streamtube geometry, the number of blades, the inlet flow conditions and the suction and pressure side velocity distributions as functions of the normalized arc-length. The output of the computation is the blade shape that satisfies the above data. The method solves an elliptic type partial differential equation for the velocity modulus with Dirichlet and periodic type boundary conditions on the (potential function, stream function)-plane ( $\Phi$ ,  $\Psi$ ). The flow angle field is subsequently calculated solving an ordinary differential equation along the iso- $\Phi$  or iso- $\Psi$  lines. The blade coordinates are, finally, computed by numerical integration. A set of closure conditions has been developed and discussed in the paper. The method is validated on several test cases and a discussion is held concerning its application and limitations.*

## Introduction

The design of each blade row of a turbomachinery component is usually carried out in two steps. A meridional plane calculation is initially performed, which specifies the position of the axisymmetric streamtubes, along which the blade sections will be placed. Then, a blade section design method is employed in order to specify the blade geometry. Such blade section design methods have already been developed, in the past for both incompressible and compressible flows. Most of them apply to plane cascades only and use a variety of numerical techniques.

The present work started four years ago, following an unsuccessful effort to utilize Wilkinson's (1967) method for plane cascades in incompressible flow. Earlier work (Papailiou, 1967) had already convinced the authors that the flexibility offered by an inverse method was necessary in order to obtain optimized blade shapes. In setting out to develop such a method, two additional requirements were imposed, namely, that this inverse inviscid method should support the design optimization procedure presented by Bouras et al. (1991) and that it should be capable to deal with the general case of an arbitrary rotating cascade.

Reviewing the existing literature, it was decided to follow the work of Schmidt (1980) and Zannetti (1986), which matched our background accordingly. The corresponding methodology can be traced back to Stanitz (1953).

Contributed by the Fluids Engineering Division of THE AMERICAN SOCIETY OF MECHANICAL ENGINEERS and presented at the International Symposium on Methods in Turbomachinery, Portland, OR, June 23-26, 1991. Manuscript received by the Fluids Engineering Division August 6, 1991. Associate Technical Editor: W. Tabakoff.

The present inverse inviscid flow calculation method is addressing the rotating cascade case lying on an arbitrary axisymmetric surface with varying streamtube width. It makes use of Schmidt's equations but it then diverges, as will be seen, in the formulation of the problem, the numerical techniques used, as well as the closure conditions.

## Position of the Problem and Development of the Equations

Our task will be to compute a closed blade section shape of a peripheral cascade (Fig. 1), given the stream surface shape, the streamtube width variation with the meridional distance ( $m$ ), the approximate number of blades  $N$ , the inlet stagnation conditions ( $P_{T1}$ ,  $T_{T1}$ ) and velocity vector  $\mathbf{W}$ , the meridional

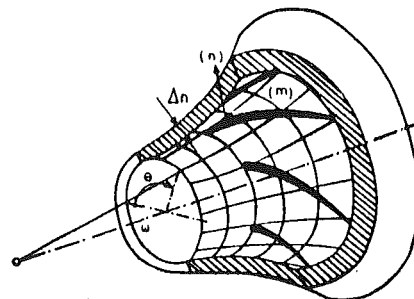


Fig. 1 Schematic representation of an annular cascade

position of the inlet stagnation point  $m_1$ , the rotational speed  $\omega$  and the desired outlet flow angle  $\beta_2$ . Assumed given, as well, are the suction side velocity distribution and an approximate pressure side velocity distribution versus arc length. The number of blades and the pressure side velocity distribution will change during the computation, in order to obtain a closed profile, with the constraint to alter them as little as possible.

The flow is considered steady, inviscid compressible subsonic at the inlet and irrotational in the absolute frame of reference.

The  $(\Phi, \Psi)$  natural coordinates which form the transformed plane (Fig. 2) are defined by the relations

$$\nabla_s \Phi = (\mathbf{W} + \omega \times \mathbf{r}) \quad (1)$$

$$\mathbf{n} \times \nabla_s \Psi = \rho(\Delta n) \mathbf{W} \quad (2)$$

where  $\mathbf{n}$  is the unit vector normal to the axisymmetric surface and  $\nabla_s(\cdot)$  is the surface gradient operator. In this transformed plane (Fig. 2(b)), which corresponds to the physical plane presented in (Fig. 2(a)), the continuity and rotation free equations may be written in the form (Bonataki, 1991)

$$A1(\ln W)_{\phi\phi} + A2(\ln W)_{\phi}^2 + A3(\ln W)_{\phi} + A4(\ln W)_{\psi\psi} + A5(\ln W)_{\psi}^2 + A6(\ln W)_{\psi} + A7(\ln W)_{\phi\psi} + A8(\ln W)_{\phi}(\ln W)_{\psi} + A9 = 0 \quad (3)$$

$$\frac{\partial \beta}{\partial \Phi} = F1(W, \beta, R, (\Delta n)) \quad (4)$$

$$\frac{\partial \beta}{\partial \Psi} = F2(W, \beta, R, (\Delta n)) \quad (5)$$

The expression for the coefficients  $A1$  to  $A9$  and  $F1, F2$  functions are given by Bonataki et al. (1991). In the above form  $\Phi$  and  $\Psi$  have been introduced as independent variables, while the velocity modulus and the flow angle are the dependent ones. During the calculation procedure only one of Eqs. (4) and (5) is utilized, as they are equivalent.

### The Boundary Conditions on the $(\Phi, \Psi)$ -Plane

Having performed the transformation from the physical to the  $(\Phi, \Psi)$ -plane (Fig. 2), the next steps is to investigate the corresponding boundary conditions. We consider

(a) The integral mass flux conservation equation, in the form

$$\rho_2 W_2 = \rho_1 W_1 \frac{R_1 \cos \beta_1 (\Delta n)_1}{R_2 \cos \beta_2 (\Delta n)_2} \quad (6)$$

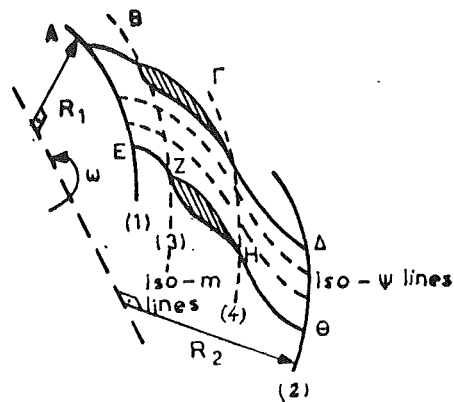
(b) The integral momentum equation in the following form

$$\Gamma = \int_{\text{blade}} \mathbf{V} \cdot d\mathbf{s} = \int_{\text{blade}} W ds + \Gamma 1 = \frac{2\pi}{N} (R_1 V u_1 - R_2 V u_2) \quad (7)$$

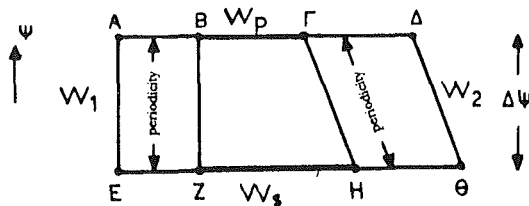
where

$$\Gamma 1 = \int_{\text{blade}} \omega R^2 d\theta \quad (7a)$$

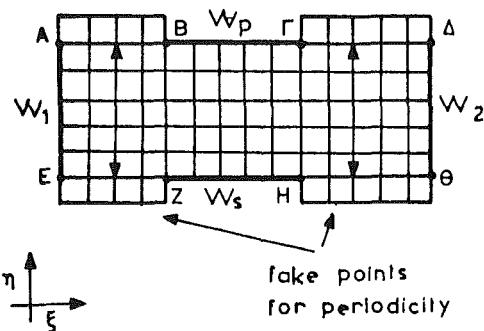
(c) The isentropic flow relations, combined with the energy conservation equation (conservation of the relative total



(a) The physical plane



(b) The  $(\Phi, \Psi)$ -plane



(c) The computational plane

Fig. 2 Schematic representation of a blade passage of an annular cascade

enthalpy) along a meridional streamline, result to the following expression

$$\frac{\rho_2}{\rho_1} = \left( 1 + \frac{W_1^2 - U_1^2}{2 \cdot C_p T_1} - \frac{W_2^2 - U_2^2}{2 \cdot C_p T_1} \right)^{1/\gamma-1} \quad (8)$$

Making use of the above equations, it is possible to calculate the flow conditions at the cascade exit ( $\rho_2, W_2$ ). It is not possible, however, to specify "a priori" the value of the cir-

### Nomenclature

$A1...A9$  = differential equation coefficients  
 $C_p$  = specific heat at constant pressure  
 $m$  = meridional distance  
 $n$  = outward unit vector  
 $N$  = number of blades  
 $p$  = pressure  
 $R$  = radius modulus  
 $r$  = radius vector  
 $T$  = temperature

$U$  = peripheral velocity  
 $V$  = absolute velocity  
 $W$  = relative velocity  
 $\beta$  = flow angle  
 $\gamma$  = isentropic exponent  
 $\Gamma$  = circulation  
 $\Delta n$  = streamtube thickness  
 $\theta$  = peripheral distance  
 $\rho$  = density  
 $\Phi$  = potential of the absolute flow

$\Psi$  = stream function  
 $\omega$  = rotational speed

### Subscripts

$m$  = meridional component  
 $T$  = total thermodynamic quantities  
 $u$  = peripheral component  
 $1$  = inlet quantities  
 $2$  = outlet quantities

ulation  $\Gamma$ , using the problem data and Eq. (7), if a rotating cascade is considered. For doing this, the integral  $\Gamma I$  must be known, which, in our case, may be computed only when the cascade geometry is known. This explains one of the difficulties of the inverse methodology applied to arbitrary rotating cascades, as, only when the radius  $R$  is constant the value of  $\Gamma I$  is zero. During the computational procedure the integral  $\Gamma I$  will be given an initial reasonable value and corrected accordingly, each time a blade shape is computed. In any case, the value of  $\Gamma$  must be compatible with the imposed value of the outlet flow angle  $\beta_2$ , so that, if the suction side velocity distribution (being the most sensitive) must be maintained, the pressure side velocity distribution must be chosen to satisfy this value of  $\Gamma$ .

Considering, again, Fig. 2, periodic conditions are imposed along the  $((AB), (EZ))$  and  $((\Gamma\Delta), (H\Theta))$  pairs of boundaries.  $W(\Phi)$  is specified along the suction and pressure side solid boundaries and the corresponding value of  $\Phi$  is calculated from the following relation

$$d\Phi = W ds + \omega R^2 d\theta \quad (9)$$

Along the inlet and outlet stations the flow is uniform with velocities and flow angles,  $W_1, W_2$  and  $\beta_1, \beta_2$ , correspondingly. Consequently, if  $\Psi_E = \Psi_Z = \Psi_H = \Psi_\theta = 0$  is the streamfunction value characterizing the lower boundary, then the one characterizing the upper boundary is, according to Eq. (2),

$$\begin{aligned} \Delta\Psi \Big|_E^A &= \rho_1 W_1 \cos \beta_1 \frac{2\pi R_1}{N} (\Delta n)_1 \\ &= \rho_2 W_2 \cos \beta_2 \frac{2\pi R_2}{N} (\Delta n)_2 = \Delta\Psi \Big|_\theta^A \quad (10) \end{aligned}$$

the upper boundary being a streamline,  $\Psi_A = \Psi_B = \Psi_\Gamma = \Psi_\Delta$ .

### The Numerical Integration of the Equations

Equations (3) and (4) or (5) are solved in the  $(\Phi, \Psi)$ -plane, which in general is nonorthogonal. If one considers suction and pressure side extensions of equal length in the periodic zones (to facilitate the application of the periodicity conditions), then the computational domain on the  $(\Phi, \Psi)$ -plane takes a trapezoidal form (Fig. 2). A nonuniform discretization of the  $(\Phi, \Psi)$  boundary regions was found to be efficient, permitting the stretching of the grid lines in the near-leading and near-trailing edge regions of the blade section, where the velocity gradients are large. In view of the above, the resulting grid on the  $(\Phi, \Psi)$ -plane, composed only of straight lines, is generally skewed and stretched. In order to increase the generality of the solver and the accuracy of the solution, avoiding at the same time complexities (such as patched grid techniques), an additional body-fitted coordinate transformation is performed, which maps the  $(\Phi, \Psi)$ -plane to an orthogonal  $(\xi, n)$ -plane with square cells (Fig. 2).

The resulting equation on  $W$  in the  $(\xi, n)$ -plane is discretized using of second-order accurate finite-difference/finite volume centered schemes. The discrete equation is, then, linearized transferring all nonlinear terms  $(\ln W)^2$ , for example to the right-hand side (fixed point algorithm). The resulting system of algebraic equations, which has a 9-diagonal banded, non-symmetric characteristic matrix, is solved iteratively using the MSIP method (Zedan and Schneider, 1983; Chaviaropoulos et al., 1986).

Once the velocity field is computed, the flow angle field is obtained integrating the ordinary differential Eqs. (4) or (5), along the iso- $n$  or the iso- $\xi$  lines. A fourth-order Runge-Kutta method is used for this step. In practice, Eq. (4) is first integrated along the cascade mean streamline and the computed  $\beta$ -mean streamline values are used as initial conditions for the integration of Eq. (5) along the iso- $\xi$  lines. The above procedure

provides the complete  $\beta(\Phi, \Psi)$  field and, consequently, the blade coordinates.

### The Computational Algorithm

A computational algorithm was constructed, outlined by the following steps (without considering the conditions for the profile closure, which will be examined later).

**Step 1:** The exit plane flow quantities are calculated through Eqs. (6) and (8). A value for the integral  $\Gamma I$  is assumed and a velocity distribution for the pressure side compatible with the value of the circulation  $\Gamma$  issued from Eq. (7) is established. The values of the potential differences  $\Delta\Phi|_A^B$  and  $\Delta\Phi|_\theta^A$  are specified.

**Step 2:** A first approximation of the  $(\Phi, \Psi)$ -plane contour is considered and the boundary conditions for the velocity (through Eqs. (9) and (10)) and the angle (utilizing plausible angle distributions), are specified. The interior grid points of the region (B $\Gamma$ HZ) are established using a simple linear procedure. In the upstream (ABZE) and downstream ( $\Gamma\Delta\Theta$ H) regions, the grid is constructed, in a way that periodic conditions can be checked without interpolation. The complete velocity and flow angle fields are initialized making use of the values at the boundaries, through a linear interpolation. An initial estimate of  $(\Delta n)$  and  $R$  for each node is made, as well.

**Step 3:** The coefficients  $A_i (i = 1, 9)$  appearing in Eq. (3) are calculated.

**Step 4:** Equation (3) is solved for  $W(\Phi, \Psi)$  using the numerical scheme described in the previous section. At the end of the computational procedure involved in this step, the values of  $W$  at the periodic boundaries will have been updated along with the complete velocity field.

**Step 5:** The flow angle  $\beta(\Phi, \Psi)$  is computed after numerical integration of equations (4) and/or (5) in the manner described in the previous section. During this procedure, new angle values are computed at the boundaries, as well.

**Step 6:** The blade section shape  $\theta = \theta(m)$  is computed using the following geometrical relations, valid along a streamline

$$m = \int \cos ds = m(s) \quad (11)$$

$$\theta = \int \frac{\sin \beta}{R} ds = \theta(s) \quad (12)$$

Utilizing these relations, the values of  $m$  and  $\theta$  are computed along streamlines for the whole flow field, as well. An interpolation procedure is used in order to estimate the new set of values  $R(m(s))$  and  $\Delta n(m(s))$ , which will be used, along with the updated values of the angles.

The exit conditions are calculated at station (2), using the same procedure as in STEP 1. The integral  $\Gamma I$  is then computed and its new value is used to update  $\Gamma$ . The pressure side velocity distribution is in turn modified in order to satisfy the new value of the circulation. The boundaries and associated conditions can then be established for a new  $(\Phi, \Psi)$ -plane. A new grid is thus generated on the  $(\Phi, \Psi)$ -plane, moving along  $\Psi$ -lines and computing each time the value of  $\Phi$  corresponding to the previously updated values of the velocity field.

**Step 7:** Steps 3 to 6 are repeated until convergence is achieved.

As observed before, the blade section shape obtained from the above described computational procedure is not necessarily closed.

### Results and Discussion

Even before starting discussing various aspects of the method, it will be useful to present some calculation results. It is easier to present them for a plane two-dimensional cascade. Figure 3 presents a turbine cascade in the physical plane and the

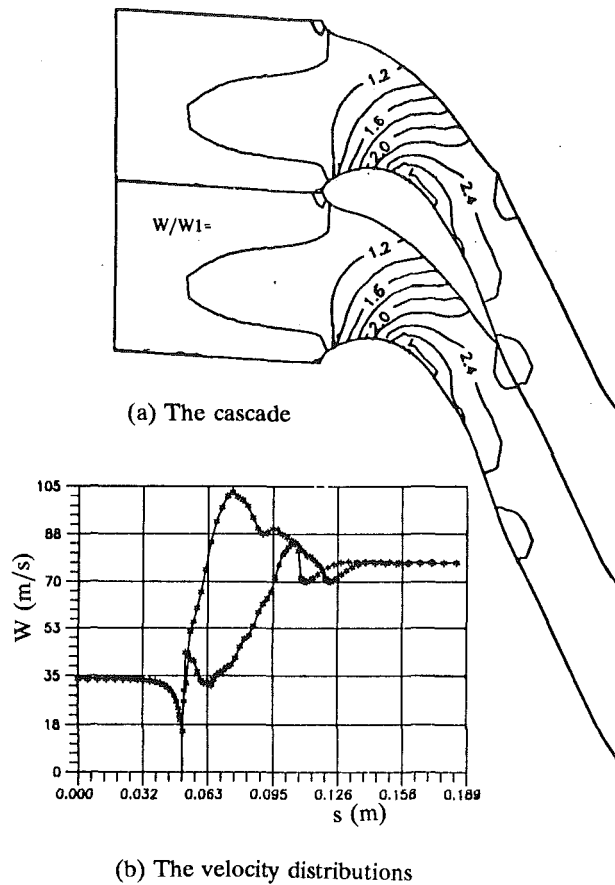


Fig. 3 An example of a cascade and its velocity distributions

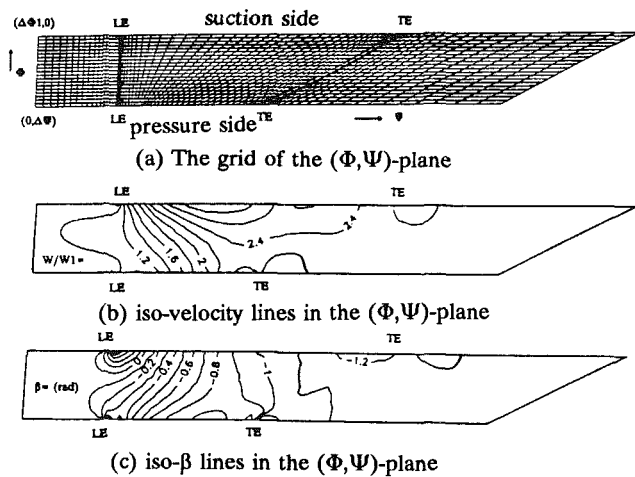


Fig. 4 The corresponding to Fig. 3  $(\Phi, \Psi)$ -plane and some computational results

corresponding velocity distributions along the lower and upper boundaries calculated with a direct method. The generated grid is shown in Fig. 4, along with the fields of  $W(\Phi, \Psi)$  and  $\beta(\Phi, \Psi)$ . The resulting velocity field  $W(m, R\theta)$  has been plotted in Fig. 3(a). As demonstrated above, one of the attractive features of the present method is the simplicity of the employed grid, which can be generated using simple algebraic techniques.

Several stationary cascade and isolated airfoil test cases were used in order to validate the accuracy and capabilities of the present inverse calculation method. The considered cases were selected in order to cover as many geometrical configurations as possible and the complete Mach number range of application of the method. Exact cases were used whenever that was pos-

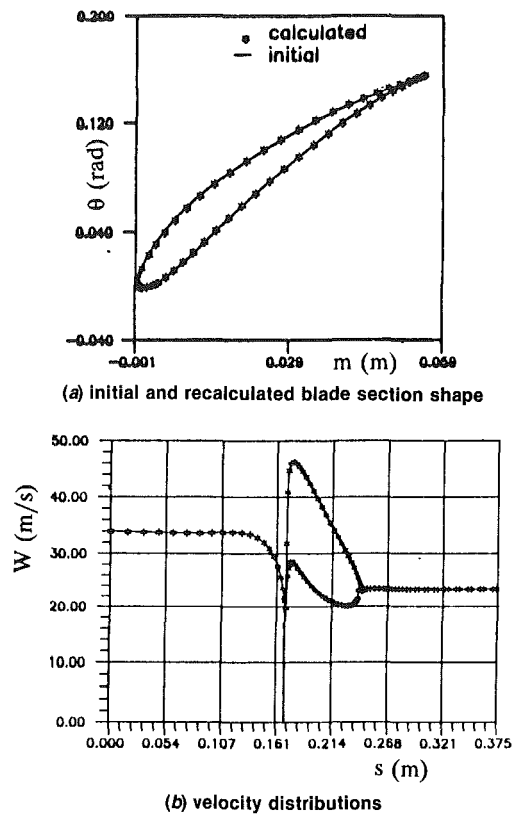


Fig. 5.1 The Gostelov cascade (test case 1)

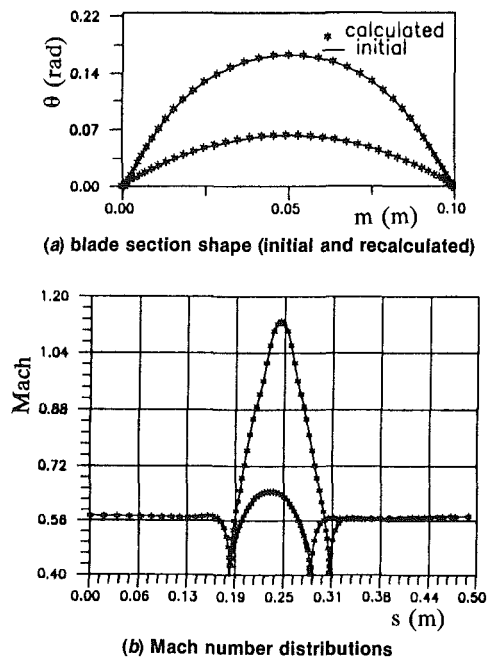
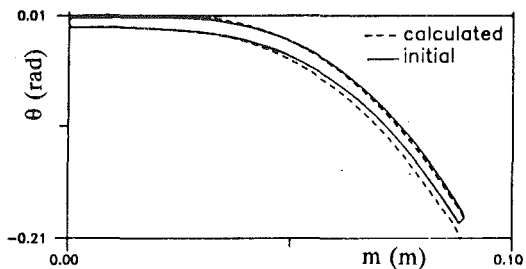
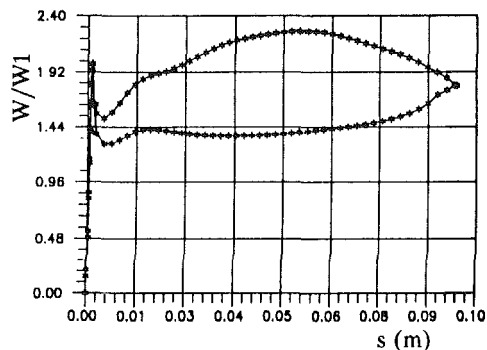


Fig. 5.2 The Hobson cascade (test case 2)

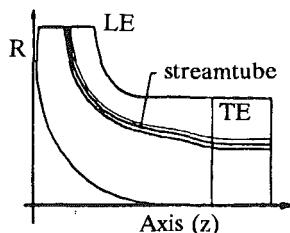
sible, while a direct method of calculation was used, when the velocity distributions corresponding to a given blade shape, were not known. Inevitably, slight inaccuracies in the results of the direct calculation method resulted in inaccuracies of the computed blade shape by the inverse method. A complete outline of the test cases utilized for the validation of the method are reported by Bonataki (1991). In order to demonstrate the capability of the method, some "reproduction" cases were chosen and presented here (Fig. 5). Besides the turbine case



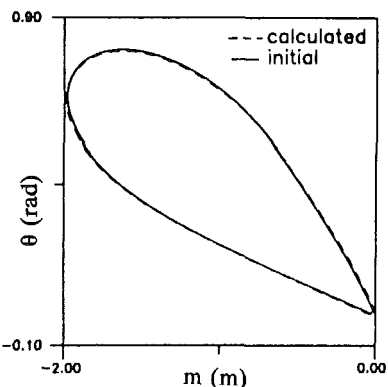
(a) Initial and recalculated blade section shape



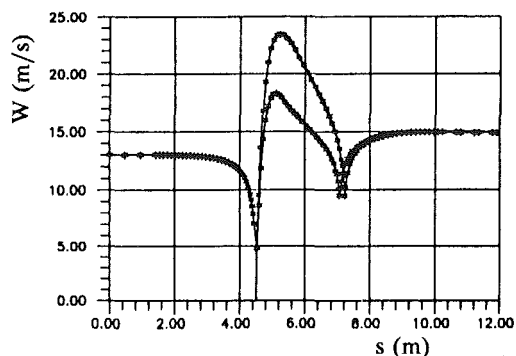
(b) velocity distributions



(c) Meridional plane and streamtube variation  
Fig. 5.3 A radial inflow turbine (test case 3)

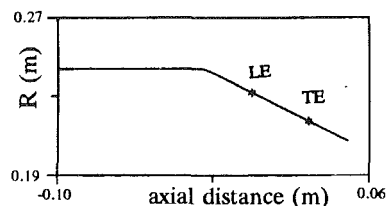


(a) Initial and recalculated profile

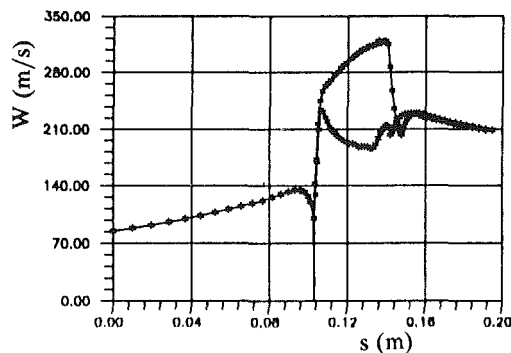


(b) Velocity distributions

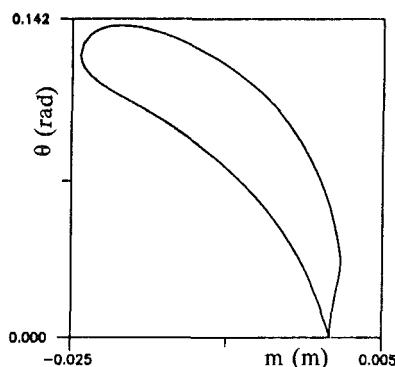
Fig. 5.4 A wind turbine hub blading (test case 4)



(a) The generatrix of the axisymmetric streamsurface



(b) Velocity distributions



(c) Calculated profile

Fig. 5.5 Rotating turbine with variable  $R(m)$  distribution (test case 5)

presented above the validation test involves, the Gostelow (1963) exact case (incompressible flow, compressor cascade), the Hobson (Jones, 1985) exact case (high Mach number, high turning, low pitch to chord ratio), a radial inflow turbine case (Katsanis, 1969) (strong variation of  $R(m)$ ), a hub wind turbine case (Boletis, et al., 1988) (high pitch to chord ratio, high stagger), a second rotating turbine case (variation of  $R(m)$ ). Good results are obtained for all cases demonstrating that the present inverse calculation procedure is numerically sound.

In view of the cases considered up to now, one may state that, for the present method slightly supersonic Mach numbers are permitted, while the inlet and outlet conditions must be always kept subsonic. Camber presents no problem, while large pitch to chord ratios certainly up to 10 may be accommodated.

Typically, the number of grid points utilized for the calculations presented above is  $(78 \times 15)$  and the computed time needed for the complete solution was 20 CPU sec in an ALIANT FX-80 computer.

It has been already stated that, if this procedure is applied using two arbitrary suction and pressure side velocity distributions, it does not necessarily produce a closed blade section. The conditions for blade section closure have been expressed in various ways up to now. Generally speaking, three integral or global conditions must be satisfied (Papailiou, 1967; Volpe, 1990; Goldstein (unpublished lecture)). For transonic flow, no explicit expression for these conditions has been derived to our

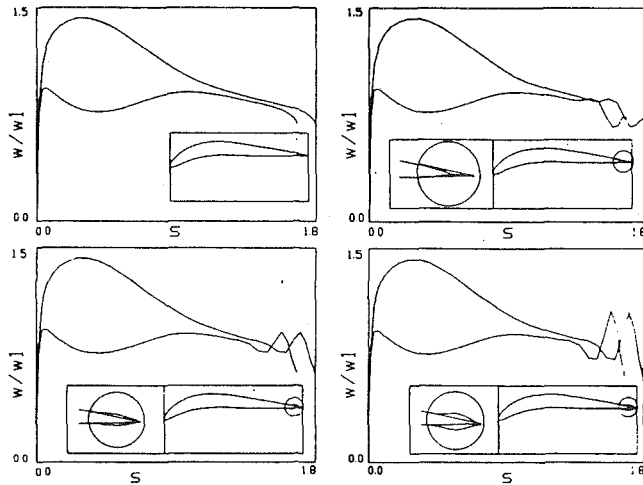


Fig. 6 Study of the variation of the velocity distribution produced by a local change of the blade shape near the trailing edge

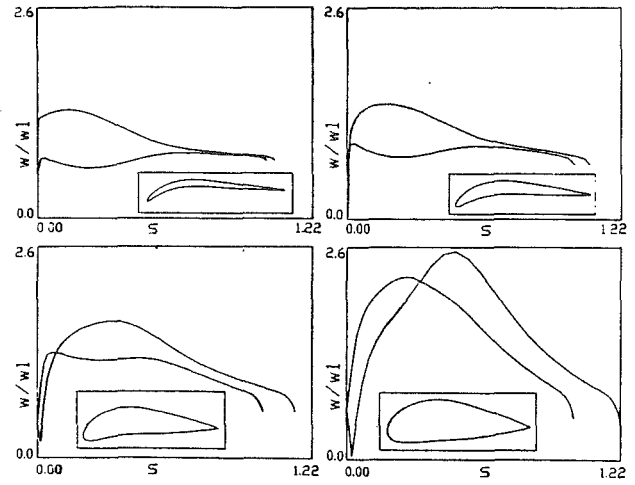


Fig. 8 Study of the dependence of the velocity distribution produced by a uniform change of the blade thickness

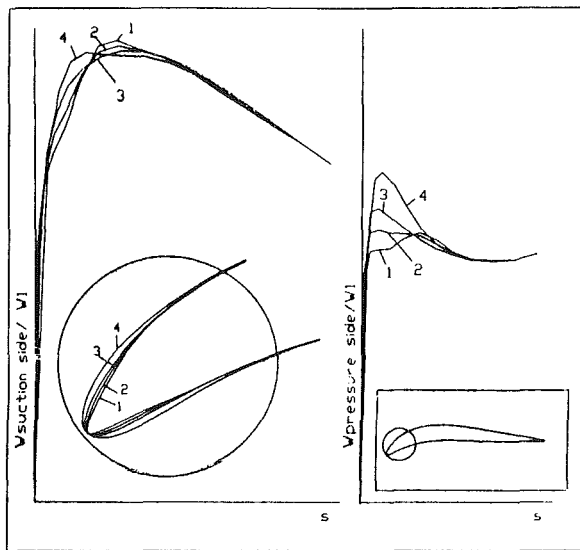


Fig. 7 Study of the variation of the velocity distribution produced by a local change of the blade shape near the leading edge.

knowledge for both the single airfoil case and the arbitrary quasi-three dimensional cascade case.

An extensive investigation was undertaken in the present work, in order to decide about the appropriate overall parameters, which should be employed for controlling the closure of the profile. Rather than utilizing the usual integral conditions, it was decided to employ two parameters, which were sensitive and convenient. Finally, the ratio of the pressure to suction side arc length and the pitch to chord ratio were chosen. This last parameter can be controlled by modifying either the number of blades or the blade chord. Numerical tests have demonstrated that the above chosen parameters control the relative movement of the pressure and suction side trailing edge points in two directions, which are quasi-perpendicular. Consequently, it is not only possible to have these points coincide (closed blade) but to position them at a desired distance, as well. This last possibility is used in order to obtain a closed blade after subtracting from the calculated shape the displacement thickness, when a viscous-inviscid interaction method is used. In practice it has been seen that very few iterations are required for profile closure.

In order to facilitate the numerical calculation, the analytical solution for the flow around a cylinder in the vicinity of the forward stagnation point has been implemented in the cal-

culcation method. The knowledge of an analytic solution in a region, where gradients are particularly important, facilitates the numerical procedure. On the other hand, as this solution relates the local radius of curvature with the velocity slope in the stagnation point region, the nose of the profile can be a priori imposed as desired. The same considerations are valid for the trailing edge region. However, it was found that in practice such measures were not necessary for both rounded and wedge trailing edge shapes.

When choosing a pair of suction and pressure side velocity distributions, some other aspects of the blade shape can be considered beforehand, as well. The resulting blade shape thickness is one of the most important aspects, on which constraints are quite often imposed. In fact, it is possible to anticipate such constraints by choosing appropriate blade surface velocity distributions.

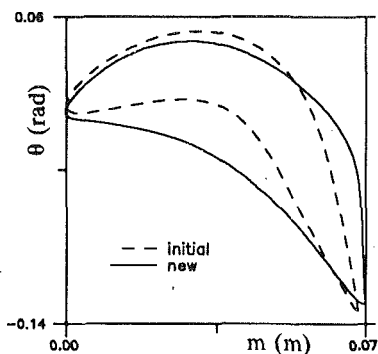
In Figs. 6, 7, and 8 the computational results are presented from a study performed on the geometry of a straight cascade, concerning trailing edge, leading edge and thickness influence on velocity distributions. Although a particular cascade geometry is addressed, the conclusions that are drawn apply to the general case.

The above study may provide information on how one may deal with the choice of the leading and trailing edge velocity distributions, as well as, with certain aspects of the mechanical constraints imposed during the blade design phase. As one example we present in Fig. 9 a turbine blade which was used as starting point and the thicker blade that was obtained by increasing the level of the suction and pressure side velocity distributions while keeping, at the same time, the initial inlet and outlet flow conditions. This particular design is quite revealing, because changes in the velocity distribution were introduced in such a way, so that the maximum velocity along the blade surfaces was not increased. On the other hand, the linear part of the inlet velocity was kept intact, so that the radius of curvature at the inlet was conserved. This particular design was obtained by applying the closure conditions as mentioned above and demanding that the suction side trailing edge point coincides with the corresponding pressure side one.

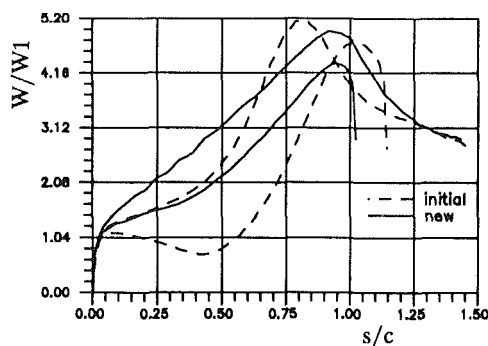
## Conclusions

A new inverse inviscid calculation method for designing arbitrary stationary and rotating subsonic or slightly transonic axisymmetric cascades, has been presented.

The method was developed to match the corresponding inverse viscous method for the design of optimum blade shapes presented by Bouras et al. (1991).



(a) Initial and new profile



(b) Initial and new velocity distributions

Fig. 9 Design of a thicker profile using the present inverse inviscid flow method

One of the advantages of this method is that there is no need for an initial blade shape to start with. Additionally, the problem is formulated on the  $(\Phi, \Psi)$ -plane and solved imposing periodic type boundary conditions upstream and downstream of the blade section. So the velocity distributions along periodic boundaries are updated during the solution for the velocity field and no particular iterations are needed to calculate the velocity distribution there.

The numerical results presented, concern a variety of geometries and flow conditions. The flexibility and the limitations of the method have been, thus, demonstrated.

Another important feature of this work is the way that profile closure is achieved. Two geometrical parameters, the pitch to chord ratio and the chord length, are used as control parameters. Changing these two parameters, iteratively, the profile closes in a few iterations.

Additionally, an analysis was attempted, providing information on the influence of the imposed velocity distributions to the geometrical aspects of the blade section shape. These aspects are essential to the designer for structural reasons. As a conclusion it is stated that the leading edge curvature is related to the velocity distribution slope there. The trailing edge shape depends on the velocity distribution at this region. Finally, the thickness of the profile is directly relative to the mean value of the velocity distributions.

## Acknowledgments

We wish to express our thanks to the DG XII of the EEC for financing the present work in the context of the "Aerodynamic Investigation of Horizontal Axis Wind Energy Machine Rotors" Project, without which this work would have not been completed.

## References

- Boletis, E., Chaviaropoulos, P., Bonataki, E., Bouras, B., and Papailiou, K. D., 1988, "A Complete Inverse Calculation Procedure for the Optimization of Horizontal-Axis Wind Turbine Airfoils," *Proceedings of European Community Wind Energy Conference*, 6-10 June, Herning, Denmark.
- Bonataki, E., 1991, "Inviscid Subsonic Inverse Method for the Design of Blade Sections along Arbitrary Axisymmetric Stream Surfaces with Varying Stream Tube Width," Ph.D. thesis, NTUA, Greece.
- Bonataki, E., Chaviaropoulos, P., and Papailiou, K. D., 1991, "An Inverse Inviscid Method for the Design of Quasi-Three Dimensional Turbomachinery Cascades," *Proceedings of International Symposium on Numerical Simulations in Turbomachinery*, Joint ASME-JSME Fluids Engineering Meeting, Portland, Oregon, June 23-26.
- Bouras, B., Karagiannis, F., Chaviaropoulos, P., and Papailiou, K. D., 1991, "Arbitrary Blade Section Design Based on Viscous Considerations. Blade Optimization," *Proceedings of International Symposium on Numerical Simulations in Turbomachinery*, Joint ASME-JSME Fluids Engineering Meeting, Portland, OR, June 23-26.
- Chaviaropoulos, P., Giannakoglou, K., and Papailiou, K. D., 1986, "Numerical Computation of Three-Dimensional Rotational Inviscid Subsonic Flows, Using the Decomposition of the Flow Field into a Potential and a Rotational Part," ASME Paper No. 86-GT-169.
- Goldstein, A., Unpublished lecture.
- Gostelow, J. P., 1963, "Potential Flow Through Cascades—A Comparison Between Exact and Approximate Solutions," A.R.C., CP No. 807.
- Jones, D. J., 1985, "Test Cases for Inviscid Flow Field Methods, Reference Test Cases and Contributors," AGARD AR-211.
- Katsanis, T., 1969, "Fortran Program for Calculating Transonic Velocities on a Blade-to-Blade Stream Surface of a Turbomachine," NASA TN D-5427.
- Papailiou, K. D., 1967, "Blade Optimization Based on Boundary Layer Concepts," VKI CN60.
- Papailiou, K. D., 1988, "Boundary Layer Optimization for the Design of High Turning Axial Flow Compressor Blades," ASME Paper No. 70-GT-88.
- Schmidt, E., 1980, "Computation of Supercritical Compressor and Turbine Cascades With a Design Method for Transonic Flows," ASME *Journal of Engineering for Power*, Vol. 102, pp. 68-74.
- Schmidt, E., and Berger, P., 1986, "Inverse Design of Supercritical Nozzles and Cascades," *International Journal of Numerical Methods in Engineering*, Vol. 22, pp. 417-432.
- Schmidt, E., 1988, "Inverse Methods for Blade Design, Controlled Diffusion Blading for Supercritical Compressor Flow," VKI-LS 1988-03 Transonic Compressors.
- Schmidt, E., and Klimetzek, F., 1989, "Inverse Computation of Transonic Internal Flows With Application for Multi-Point-Design of Supercritical Compressor Blades," Presented at the Specialists Meeting on Computational Methods for Aerodynamic Design (Inverse) and Optimization, Loen, Norway.
- Stanitz, J. D., 1953, "Design of Two-Dimensional Channels with Prescribed Velocity Distributions along the Channel Walls," NACA Report 1115.
- Vople, G., 1990, "Geometric and Surface Pressure Perturbations in Airfoil Design," AGARD VKI Special Course on Inverse Methods in Airfoil Design, 14-18 May 1990, Belgium.
- Wilkinson, D. H., 1967, "A Numerical Solution of the Analysis and Design Problems for the Flow Part One or More Airfoils," A.R.C. Reports and Memoranda N.3545.
- Zannetti, L., 1986, "A Natural Formulation for the Solution of Two-Dimensional or Axisymmetric Inverse Problems," *International Journal of Numerical Methods in Engineering*, Vol. 22, pp. 451-463.
- Zedan, M., and Schneider, G. E., 1983, "A Three-Dimensional Modified Strongly Implicit Procedure for Heat Conduction," *AIAA Journal*, Vol. 21.



F. Bakhtar

R. A. Webb

School of Manufacturing  
and Mechanical Engineering,  
University of Birmingham,  
Birmingham B15 2TT, U.K.

M. H. Shojaee-Fard

University of Science and Technology,  
Tehran, Iran

M. A. Siraj

Faculty of Engineering,  
University of Khartoum, Sudan

# An Investigation of Nucleating Flows of Steam in a Cascade of Turbine Blading

*During the course of expansion in turbines steam first supercools and then nucleates to become a wet mixture. To reproduce turbine nucleating conditions realistically requires a supply of supercooled vapor. This can be achieved under blow-down conditions and an experimental facility for such studies has been constructed. The results of the first experimental investigation of nucleating flows of steam in a cascade of nozzle blading using the equipment are presented. The experimental results presented consist of surface pressure measurements, Mach-Zehnder and shadow photography. Comparisons with theoretical solutions show reasonable agreement.*

## Introduction

This paper is one of a set describing the results obtained on a novel experimental facility constructed to study the problems associated with the flow of nucleating and wet steam in turbines. It is accepted in the literature that turbine stages operating on wet steam have a lower thermodynamic efficiency than those in which steam is superheated. The difference is loosely attributed to wetness losses but the mechanisms underlying them are insufficiently understood. The rule still quoted for estimating the performance of wet turbine stages is an empirical formula proposed by Baumann in 1921. It was estimated by Traupel (1979) that some 80 percent of the power consumed in the world is developed in steam driven power stations. Thus any progress in understanding leading to improved performance, however small, will yield substantial economic dividends.

The development of nucleation theory has been of help to the study of wetness problems in turbines, as the equations describing droplet formation and growth can be combined with the standard gas dynamic conservation equations to form a set and treated numerically. With progress in the development of numerical methods, treatments of two-dimensional flows of nucleating and wet steam are becoming available (Bakhtar and Mohammadi Tochai, 1990; Yeoh and Young, 1984; Bakhtar and Bamkole, 1989 and Bakhtar and So, 1991). However, before they can be employed as design tools with any confidence, it is necessary that they be validated against direct observations, but experimental measurements suitable for this purpose are scarce. For example, in the study of nucleating flow of steam in the blade-to-blade plane by the time-marching

method reported by Bakhtar and Mohammadi Tochai (1980), although differences were exhibited by the nucleating and superheated solutions, the findings could not be confirmed by experimental measurements due to lack of direct observations.

Experimental investigations of condensing flows in turbines are hindered by the fact that at low and moderate pressures the supercooling associated with the first reversion of steam is substantial. For this reason the zones of rapid condensation in steady state tunnels occur in the supersonic parts of the flow. This is in contrast to conditions in turbines where because of work extraction steam can nucleate without attaining the speed of sound. Thus the turbine nucleating and wet steam flow conditions cannot be reproduced in steady state tunnels realistically. To produce nucleation in subsonic flow requires a supply of supercooled steam. It has already been demonstrated that such a supply can be produced under blow down conditions (Bakhtar and Heaton 1986). This has been followed by the construction of a short duration tunnel working on this principle (Bakhtar et al., 1991) and this paper gives some of the special features of the equipment and the first set of experimental results which have been obtained.

## Description of the Equipment

**Principle of Operation.** The principle of operation of the equipment may be described with reference to the enthalpy-entropy diagram shown as Fig. 1(a). If a receiver is charged with steam at  $P_1$  and then vented until the pressure drops to  $P_2$  the steam remaining in the tank will have expanded to expel the fluid which has been discharged. Under these circumstances the vapor temperature drops faster than its saturation temperature. Thus if the initial and final states of the fluid are represented by A and B, respectively, the fluid will be less superheated at B than at A. Now to generate supercooled

Contributed by the Fluids Engineering Division for publication in the JOURNAL OF FLUIDS ENGINEERING. Manuscript received by the Fluids Engineering Division September 2, 1991. Associate Technical Editor: W. Tabakoff.

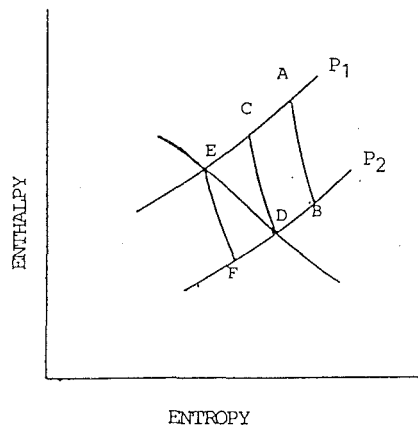


Fig. 1(a) Expansion paths

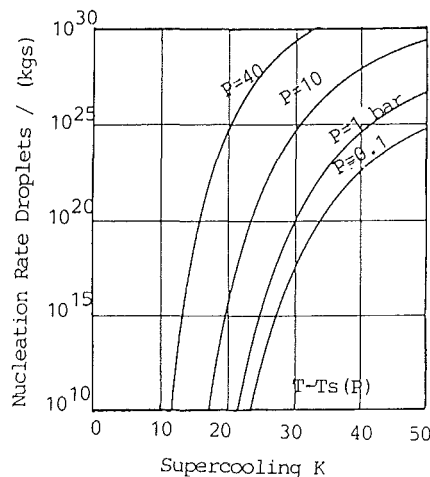


Fig. 1(b) Variations of nucleation rate with pressure and degrees of supercooling

steam, if the tank is initially charged with saturated steam at  $P_1$  as represented by point E and then vented, without nucleation on attaining pressure  $P_2$  the tank contents will be supercooled at F. The variations of nucleation rate with supercooling at constant pressure, calculated from equations currently in use by the authors (Bakhtar and Zidi, 1990), have been plotted in Fig. 1(b). For flowing steam, the limiting supersaturation at 1 bar is over 30K and with reference to the line showing nucleation at 1 bar in Fig. 1(b), it will be seen that the nucleation rate for this condition is approximately  $10^{20}$  droplets per kg per second. But at 1 bar and 22K of supercooling the nucleation rate is  $10^{10}$ . Thus returning to Fig. 1(a) if on expansion to point F the steam is supercooled by 20K it can be retained at this condition for a considerable period without the danger of reversion. Supercooled steam thus produced can be used for experimental purposes and only a moderate further expansion is sufficient to cause it to nucleate.

**General Arrangement** The general features of the equipment are shown schematically in Fig. 2. Except for the length of the tank, the diagram is approximately to scale indicating the relative sizes of the components. The receiver is a tank of

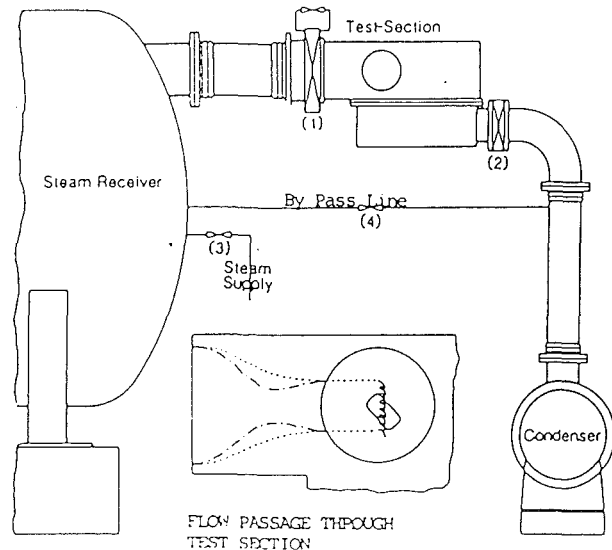


Fig. 2 General arrangement

28 m<sup>3</sup> capacity. Valve (1) is a quick acting valve with a typical opening time of 70ms and release the flow through the test section to the condenser. The test section is essentially a stainless steel fabrication which holds two cover plates 76mm apart. The blade profiles to be investigated are mounted on circular supporting plates which fit into the test section. Valve (2) is a butterfly valve and used for setting the downstream pressure.

With the general principle as described to generate supercooled steam the receiver is first charged with saturated steam and then vented to the condenser. This has the effect of expanding the content to predetermined degrees of supercooling without the penalty of giving it kinetic energy. Supercooled steam thus generated then passes to the test section. The opening of the quick-acting valve is followed by starting transients which then decay. Thereafter a quasi-steady flow is established in the test section which can be studied.

To minimize thermal contact between the tank walls and the steam content a thin aluminium shield is fitted close to the inside surface of the tank.

The receiver volume was sufficient to choke a throat area of 4500 mm<sup>2</sup> with a drop in stagnation pressure of 1 percent per second. The total throat area of the cascade used in the present study was approximately half the above value. Hence once a quasi-steady state was reached the drop in the upstream stagnation pressure was corresponding slower.

To supply the blades with supercooled steam, as shown by the dotted lines in the view of the flow passage through the test section in Fig. 2, the flow passage between the test section inlet and the cascade of the blades is arranged as a contraction. It is also possible to feed the cascade with wet steam with predetermined droplet sizes. For this purpose, as shown by the chain dotted line in the diagram, the inlet passage can be arranged as a venturi. With steam supercooled at inlet, expansion in the convergent part of the venturi will cause it to nucleate. Then application of suction to the walls of the diverging section ensures that the droplets are retained.

**Main Features of the Test Section.** A photographic view of a cascade of blades is given in Fig. 3. The profiles were

## Nomenclature

$J$  = nucleation rate  
 $P$  = pressure  
 $T$  = temperature

$T_s(P)$  = saturation temperature corresponding to pressure  $P$

### Suffixes

0 = stagnation condition

$s$  = static  
 2 = downstream

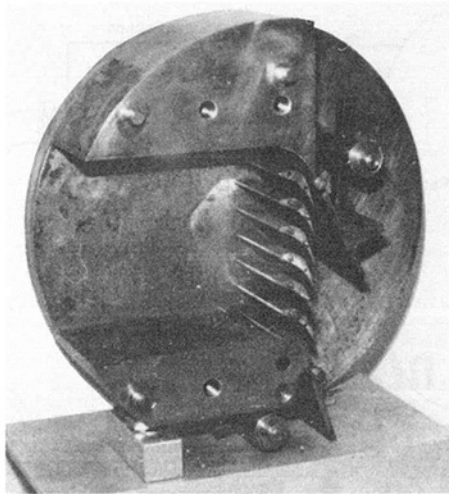


Fig. 3 Cascade assembly with cover removed

based on a typical nozzle section of an operating turbine, and were of 76mm length and 35.76mm chord. The pitch and axial chord were 18.26 and 25.27mm, respectively. The cascade consisted of six blades and two half profiles forming seven passages. The central passage was the effective test section and was the focus of the instrumentation. To cater for different measurements, the central three blades were formed into a separate interchangeable unit. Two such units were used in the present investigation one for surface pressure measurements, the other for optical observations.

To carry out surface pressure measurements, tapping points were drilled into the blade surfaces either side of the central passage and into the side walls. The latter tapping points were drilled along the mid passage line as well as upstream and downstream of the blades. Near the trailing edge, the thickness of the blade section was not sufficient to support tapping points. To obtain some pressure measurements in this zone, a number of tapping points were drilled into the side walls. The arrangement of the tapping points relative to the central passage is shown diagrammatically in Fig. 4.

**The Quick Acting Valve.** The quick acting valve consisted essentially of a shutter with a rectangular opening and tapered seating surfaces. In the open position the opening aligned with similar openings in the flanges either side of it. In the fully closed position the tapered surfaces of the shutter were pulled against similarly shaped seats. The valve was actuated by a pneumatic impact cylinder. External damping was provided to arrest the shutter at the end of its stroke and the whole system was designed as a self contained stress loop to minimize the transmission of impulsive forces to the rest of the test section.

#### Instrumentation

(a) *Surface Pressure Measurements.* To take surface pressure measurements during the short run times, each tapping point was connected by a hypodermic tube to a separate pressure transducer. These were piezo-resistive instruments each built integral with its own amplifier. To prevent formation of vapor bubbles and protect the transducer elements from exposure to steam the connecting lines were kept full of oil and purged when necessary. For this purpose the transducers were mounted each in a separate cell in a special manifold block. The cells were each fitted with an individual purge line. The connecting lines were typically 0.5m in length and it is estimated that the system has a response time of approximately 1ms. The transducers were calibrated in situ through the data acquisition system and the measurements were accurate to within  $\pm 0.01$

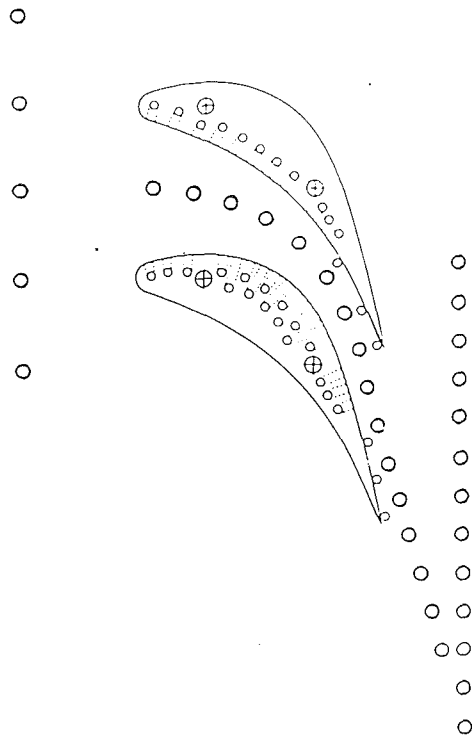


Fig. 4 Arrangement of wall and blade surface tapping points

bar. This is regarded as the uncertainty in the measured pressures.

(b) *Temperature Measurement.* The temperature of steam in the tank when superheated was measured by two shielded thermocouples positioned approximately one meter from the wall but the temperature of supercooled steam cannot be measured by thermocouples directly. This is because steam condenses on the surface of the instrument and the thermocouple will indicate the saturation temperature. The procedure used for evaluating the temperature of supercooled steam is given in the Appendix. It is estimated that the deduced stagnation temperatures of steam were to within  $\pm 1$  K.

(c) *Mach Zehnder Interferometry.* The interferometer used was a standard instrument. Due to the short duration of the run time it was not possible to observe the flow for setting up purposes. Furthermore the sudden opening of the quick acting valve causes the equipment to vibrate. To minimize the problems the light source used was a pulsed laser with a pulse duration of 50 ns.

**Data Acquisition.** Recording of data was controlled by a micro-computer via an interface. The signals from the instruments after individual processing were fed each to a separate sample and hold module. To take a set of readings all the sample and hold units were signalled from the processor simultaneously and subsequently scanned. For the latter purpose the analogue signals were converted into digital form and stored in the computer memory. Having completed a set of readings the sample and hold units could be signalled once more and the procedure repeated.

The time required to record one signal was 25  $\mu$ s. Thus a set of 96 readings could be recorded in 2.4 ms. The computer memory was sufficient to record the data for 0.5 s during which a large number of sets of readings could be recorded. The start of data logging was triggered by an optical signal from the movement of the quick acting valve. An adjustable delay was interposed between the receipt of the signal and the start of the data acquisition to allow for the transients to decay.

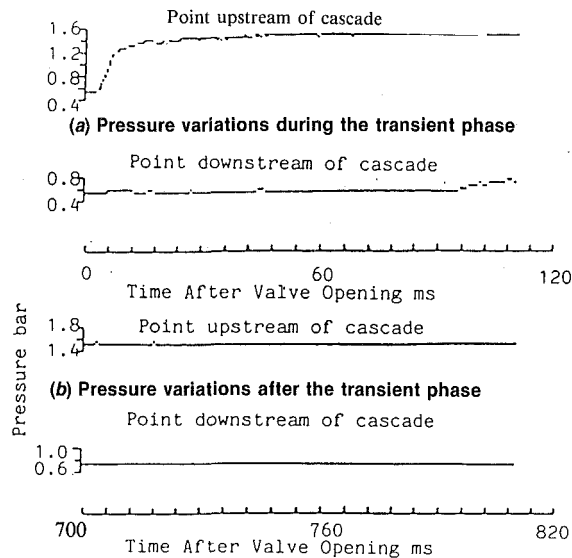


Fig. 5 Variations of typical wall pressures with time (Uncertainty in pressures  $\pm 0.01$  bar, in time  $\pm 0.05$  ms)

### Experimental Results and Comparison With Theory

**Establishment of Quasi-Steady State.** The variations of pressure with time at typical locations upstream and downstream of the cascade are given in Fig. 5. As shown in Fig. 5(a) the conditions undergo a transient change initially which was found to last up to 700 ms. Thereafter they became steady. As already stated the computer memory was sufficient to store the readings for 500 ms. Providing a delay of 700 ms was allowed before the data was recorded, no perceptible change in the reading was noted.

**Establishment of Periodic Conditions.** The periodicity of the flow was monitored from the wall pressure tappings downstream of the cascade. The tail-boards were adjusted until the conditions were regarded as the best which could be obtained. The quantity of periodicity achieved can be seen from the typical Mach Zehnder and Shadowgraphs to be presented in the following paragraphs.

**Procedural Details.** It was originally envisaged to supercool the steam by using the bypass line prior to its release to the test section. Because of the high rate of heat transfer between the steam and the tank walls it was found more efficient to blow down the tank through the test section and to trigger the data acquisition when the required conditions were reached.

**Theoretical Analysis.** Two-dimensional two-phase flows of steam are capable of treatment by the time-marching method. Computer programs for the treatment of such flows using this technique were developed in earlier studies. Although further development of the treatment is necessary before it can be regarded as a reliable design tool, nevertheless the experience so far has shown the technique to be promising and solutions using the program have been used to compare with the experimental results to be presented. The procedure which is based on Denton's method is essentially that described by Bakhtar and Mohammadi Tochai (1980). Following publication of improved procedures by Denton (1982), the basic algorithm currently adopted is that described by Bakhtar and So (1991).

**Features of the Flow.** A comparison between typical measured surface pressure distributions for superheated and nucleating flows is given in Fig. 6. The distributions are almost identical on the pressure surface but there is a departure between the two on the suction surface. This occurs just downstream of the throat and corresponds with the zone of rapid condensation.

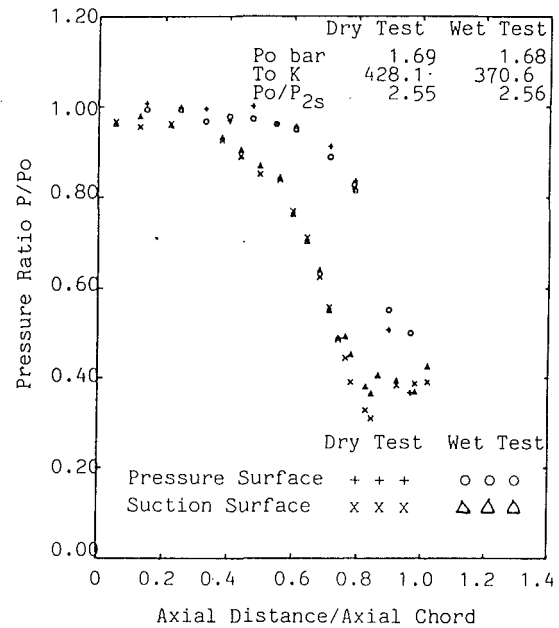


Fig. 6 Comparison of typical superheated and nucleating surface pressure distributions (Uncertainty in pressures  $\pm 0.01$  bar, in nondimensional distances  $\pm 0.005$ )

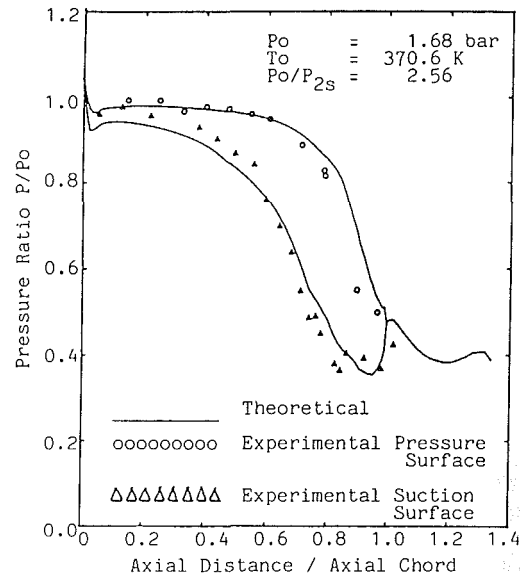


Fig. 7 Comparison of theoretical and measured surface pressures in nucleating test (Uncertainty in measured pressures  $\pm 0.01$  bar, in nondimensional distances  $\pm 0.005$ )

The measured and predicted surface pressure distributions of the nucleating test are compared in Fig. 7. The theoretical surface pressure distributions from the dry and nucleating solutions are compared in Fig. 8. It will be seen from Fig. 7 and comparison of Figs. 6 and 8 that the influence of condensation on the pressure distributions is predicted reasonably well by the theoretical solution. But with reference to Fig. 7, the pressure change associated with rapid condensation is smeared and appears as a knee in the theoretical solution.

Typical shadow graphs of superheated and nucleating flows are given as Figs. 9 and 10 respectively. The trailing edge shocks are clearly visible in the photograph of the superheated test. The trailing edge shocks are weaker but still visible in the photograph of the nucleating test. A further dark line can be seen in the nucleating photograph downstream of the throat which is absent from Fig. 9. This corresponds in location with the departure between the measured pressure distributions on

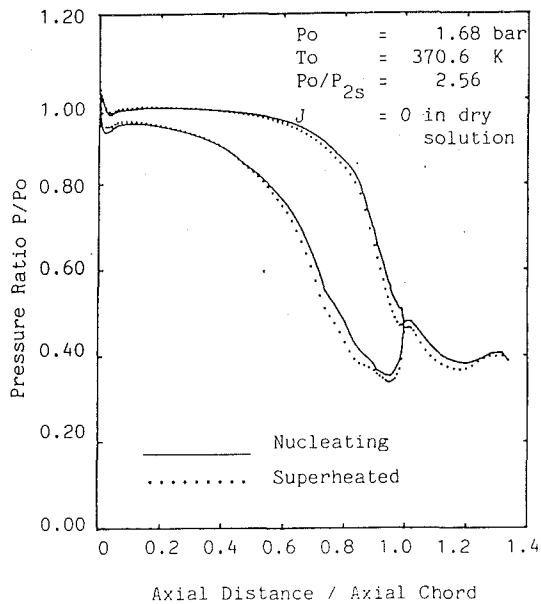


Fig. 8 Comparison between theoretical nucleating and dry surface pressure distributions



Fig. 9 Superheated flow  $P_o = 1.69 \text{ bar}$   $T_o = 421.2 \text{ K}$   $P_o/P_{2s} = 3.41$

the suction surface and is a further indication of the zone of rapid condensation. The dark lines downstream of the trailing edge in Fig. 10 are caused by the presence of water films on the windows. The patterns upstream of the leading edge are also caused by water films and rivulets on the windows. The dark line starting from the suction surface at approximately



Fig. 10 Nucleating flow  $P_o = 1.69 \text{ bar}$   $T_o = 372.2 \text{ K}$   $P_o/P_{2s} = 2.86$

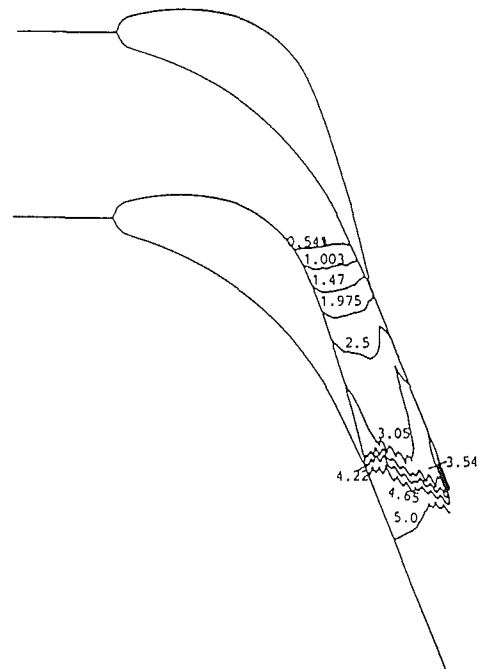


Fig. 11 Contours of constant wetness fraction in theoretical solution

half a chord length and continuing into the flow is caused by deposits formed on the windows in earlier tests. Contours of constant wetness fraction from the theoretical solution are given in Fig. 11. The rapid condensation zone occurs just upstream of 1 percent constant wetness line. The correspondence between this zone and the dark line in the shadowgraph is also evident.



Fig. 12 Superheated flow  $P_o = 1.69 \text{ bar}$   $T_o = 424.2\text{K}$   $P_o/P_{2s} = 3.41$

The measured pressure distributions along the mid-passage line also differed after the rapid condensation zone. Because of the large spacing between the tapping points in this zone, the existence of a pressure change in the nucleating test could not be detected from the measurements. Nevertheless the departure between the condensing and superheated distributions was substantial.

The closest tapping points in the vicinity of the condensation zone were on the suction surface and the measurements plotted in Fig. 6 do in fact indicate a pressure rise. But it is not certain whether these measurements give a true indication of the steepness of the pressure change in the condensation zone. No pressure rise is indicated in this zone by the theoretical solutions but it is already known that the time-marching method smears such pressure changes.

Typical Mach-Zehner photographs of superheated and nucleating flows are given in Figs. 12 and 13, respectively. In the zone of rapid condensation the fringe spacing is larger in Fig. 13 in comparison with the pattern in the corresponding location in the superheated photograph. In addition, the fringe patterns show a distortion just above the suction surface and upstream of the trailing edge which is not evident in the photograph of the superheated test. This feature became more pronounced with increases in the supercooling of the flow initially but then diminished. A hint for the possible explanation of this behavior is apparent in the contours of constant wetness in the corresponding location in Fig. 11. The possible cause might be the interaction between the trailing edge shock wave, rate of heat release, consequent changes in fluid density and the flow streamlines.

A further difference was in the shock patterns and that the shocks were weaker in nucleating flows. This is due to the fact

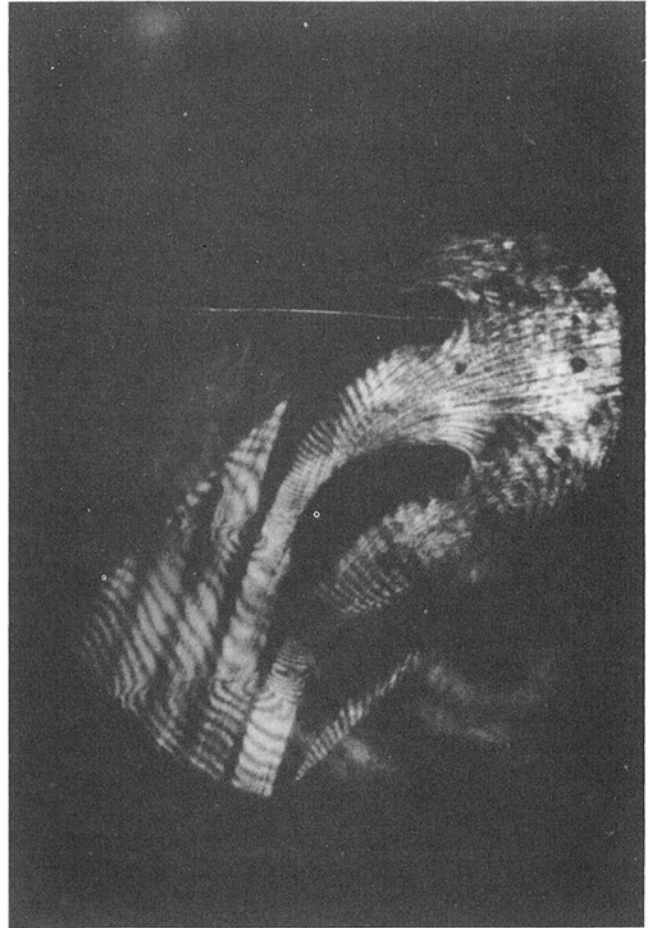


Fig. 13 Nucleating flow  $P_o = 1.69 \text{ bar}$   $T_o = 372.2\text{K}$   $P_o/P_{2s} = 3.14$

that two-phase flows generally choke at a velocity below the frozen speed of sound. Consequently in flows with supersonic outlet the sonic line shifts downstream and on reaching the trailing edge the flow Mach numbers are lower leading to weaker shock waves.

**Effect of Inlet Temperature.** With the inlet and outlet pressures maintained nearly constant the measured surface pressure distributions at a series of inlet temperatures are compared in Fig. 14. Over the range of inlet stagnation temperatures corresponding to 4K superheat and the maximum supercooling of 17.5K attainable there was little change in the location of the zone of rapid condensation. This result is also predicted by the theoretical solutions and can be attributed to two factors. The first is the rapid increase in the rate of expansion as the flow approaches the throat followed by a sudden drop. As the limiting supersaturation is governed by the rate of expansion any nucleation started in the earlier regions will be dominated by the rapid expansion just before the throat. The second factor is the influence of heat addition to a flowing vapor in the high subsonic Mach number range. It has been shown (Bakhtar and Young, 1978) that for steam flowing in a constant area duct in a Mach number range of approximately 0.9-1 any heat release due to condensation will cause the supercooling to increase. Thus in the above tests if the steam were still substantially supercooled on reaching a Mach number of 0.9 any heat release due to condensation will have increased the supercooling until the throat was reached.

It was also found that the flow remained almost choked over a wide range of outlet pressures and thus under these conditions the location of rapid condensation zone and the



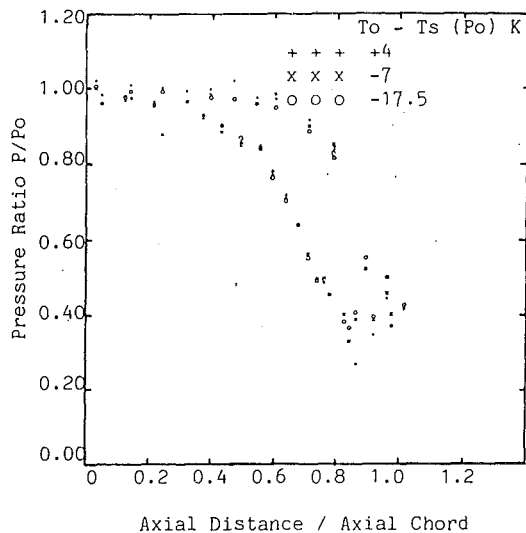


Fig. 14 Effect of inlet temperature on pressure distribution (Uncertainty in temperatures  $\pm 1\text{K}$ , pressures  $\pm .01$  bar in non-dimensional distances  $\pm .005$ )

pressure change associated with it was little affected by the downstream pressure.

### General Comments and Conclusions

The problems associated with supercooling and reversion of flowing steam in turbines add further complexity to an already difficult subject but the existence of complications should present no barriers to their solution. It has been demonstrated that nucleating flow conditions experienced in turbine blading can be reproduced satisfactorily for systematic study by the blow down technique. The equipment constructed has performed well and extraction of data during the short run times has presented no particular difficulty.

Two-dimensional blade-to-blade flows of nucleating steam can be treated by the time-marching method. A full examination of the method of treatment available and comparison with the experimental results is beyond the scope of the present paper. It will, however have been noted that the general features of the flow are predicted by the method reasonably well and the technique is very promising.

It is accepted that the measurements have been limited to one geometry but within this limitation the condensing flows have exhibited features which have been absent from the superheated tests. The most notable difference has been the pressure rise associated with the zone of rapid condensation, its occurrence just downstream of the throat and its insensitivity to the inlet temperature. Differences were also observed in the shock patterns downstream of the throat between superheated and nucleating tests with transonic outlets. It must, however, be said that the outlet Mach number corresponding to a given pressure ratio differs, between dry and nucleating flows. The actual flow pattern in a nucleating test is complicated by the interaction between the aerodynamic and thermodynamic changes and warrants a separate study.

The only observation of boundary layer behaviour in the present study has been limited to the optical photographs and these are inconclusive as to whether the pressure changes caused by condensation have affected the boundary layers adversely. However, an examination of the records indicates that such problems are more likely to occur in condensing flows with sub-sonic outlet velocities.

The observations reported are the results of the first inves-

tigation carried out using the facility. The equipment constitutes a variable density tunnel and offers a unique opportunity for wetness problems in steam turbines to be studied and the associated losses minimized.

### Acknowledgments

The investigations were carried out in the Department of Mechanical Engineering of the University of Birmingham and supported by grants AR/C/22080 and AR/065961 from the Science and Engineering Research Council. The generous help of Messrs, NEI Parsons in the provision of the pulsed laser is gratefully acknowledged. The authors are also grateful for the assistance of Drs. K. K. Abbas and M. R. Mahpaykar in the provision of the theoretical results presented.

### References

- Bakhtar, F., and Bamkole, B. O., 1989, "An Examination of the Through Flow of Nucleating Steam in a Turbine Stage by a Time-Marching Method," *Proceedings Institution of Mechanical Engineers*, Vol. 203, A4, pp. 233-243.
- Bakhtar, F., and Heaton, A. V., 1986, "On the Potential of Blow-Down conditions in studies of Nucleating and Two-Phase Flows of Steam," *Proceedings 8th International Heat Transfer Conference*, Aug., San Francisco, pp. 2277-2282.
- Bakhtar, F., and Mohammadi Tochai, M. T., 1980, "An Investigation of Two-Dimensional Flows of Nucleating and Wet Steam by the Time-Marching Method," *International Journal of Heat and Fluid Flow*, Vol. 2, No. 1, pp. 5-18.
- Bakhtar, F., and So, K. S., 1991, "A Study of Nucleating Flow of Steam in a Cascade of Supersonic Blading by the Time-Marching Method," *International Journal of Heat and Fluid Flow*, Vol. 12, No. 1, pp. 54-62.
- Bakhtar, F., and Young, J. B., 1978, "A Study of Choking Conditions in the Flow of Wet Steam," *Proceedings Institution of Mechanical Engineers*, Vol. 192, No. 21, pp. 237-242.
- Bakhtar, F., Webb, R. A., Shojaee-Fard, M. H., and Siraj, M.A., 1991, "An Experimental Facility for Studies of Nucleating and Wet Steam Flows in Turbine Blading," *Proceedings Institution of Mechanical Engineers*, European Conference on Turbomachinery Mechanical Engineering Publications, C423/003, pp. 191-199.
- Bakhtar, F., and Zidi, K., 1990, "Nucleation Phenomena in Flowing High-Pressure Steam Part 2-Theoretical Analysis," *Proceedings Institution of Mechanical Engineers A*, Vol. 204, pp. 233-242.
- Denton, J. D., 1982, "An Improved Time-Marching Method for Turbomachinery Flow Calculations," ASME Paper 82-GT-239.
- Traupel, W., 1979, "Steam Turbines, Yesterday, Today and Tomorrow," *Proceedings Institution of Mechanical Engineers*, Vol. 193, p. 391.
- Yoeh, C. C., and Young, J. B., 1984, "Non-Equilibrium Through Fluid Flow Analysis of Low Pressure Wet Steam Turbines," *ASME Journal of Engineering for Power*, Vol. 106, p. 716.

## APPENDIX

### Determination of Supercooled Stagnation Temperatures

To estimate the temperature of supercooled steam in the tank it was necessary to establish the pressure temperature relationship in the tank during the blow-down. With reference to Fig. 1, this was done by starting from initially superheated steam as from point C and blowing down until the contents of the tank fogged at D. This indicated that the steam had become saturated. Hence by measuring the pressure at D the temperature was inferred. Now if the expansion is started from a saturated initial condition as that represented by E and the tank vented over the same pressure ratio to F, assuming that over the range of conditions the same condition law can be applied to both expansions the ratio of  $T_F/T_E$  can be taken to be the same as  $T_D/T_C$ . With  $T_C$ ,  $T_D$  and  $T_E$  known  $T_F$  can be deduced.

To obtain a calibration chart the process of expansion of initially superheated vapour was repeated over a range of initial superheated and the ratios of temperatures at end of expansions to those at the beginnings ( $T_D/T_C$ ) were plotted against the pressure ratio  $P_D/P_C$ .

## Y. Tsujimoto

Visiting Researcher  
National Aerospace Laboratory,  
Kakuda Research Center,  
Miyagi, Japan  
On leave from Osaka University,  
Engineering Science (Professor),  
Toyonaka, Osaka, 560 Japan

## K. Kamijo

Head of Rocket Fluid Systems Section,  
National Aerospace Laboratory,  
Kakuda Research Center,  
Kimigaya, Kakuda, Miyagi, 981-15 Japan  
Mem. ASME

## Y. Yoshida

Research Associate,  
Osaka University, Engineering Science,  
Toyonaka, Osaka, 560 Japan

# A Theoretical Analysis of Rotating Cavitation in Inducers

*Rotating cavitation was analyzed using an actuator disk method. Quasi-steady pressure performance of the impeller, mass flow gain factor, and cavitation compliance of the cavity were taken into account. Three types of destabilizing modes were predicted: rotating cavitation propagating faster than the rotational speed of the impeller, rotating cavitation propagating in the direction opposite that of the impeller, and rotating stall propagating slower than the rotational speed of the impeller. It was shown that both types of rotating cavitation were caused by the positive mass flow gain factor, while the rotating stall was caused by the positive slope of the pressure performance. Stability and propagation velocity maps are presented for the two types of rotating cavitation in the mass flow gain factor-cavitation compliance plane. The correlation between theoretical results and experimental observations is discussed.*

## Introduction

During the development stage of the liquid oxygen turbo-pump for the LE-7 the main engine of the H-II rocket, the next generation Japanese launch vehicle, supersynchronous vibrations with frequencies 1.0 to 1.2 times as large as those of the shaft rotational frequency were experienced. The cause of these vibrations was attributed to rotating cavitation in the pump inducer, and a simple modification of the inducer casing based on this supposition almost completely suppressed the vibrations. Details are reported by Kamijo et al. (1992). Rotating cavitation has been studied experimentally (Kamijo et al., 1977, 1980) but its mechanisms are not yet fully understood. In the present study a theoretical analysis is carried out to elucidate the fundamental mechanisms, characteristics of rotating cavitation, and how it is related to rotating stall.

Surge and rotating stall have been extensively studied, and it is well known that both phenomena are caused by the positive slope of the head-capacity curve. On the other hand, in the presence of cavitation, a surge can occur even with a negative slope. This is known as "cavitation surge" and extensive studies have been made on its relation to POGO instability (NASA, 1970). Cavitation surge (Young et al., 1972) is known to be caused by an increase of the cavity volume related to a decrease in the flow rate. This effect is represented by a positive "mass flow gain factor." This parameter was closely investigated by Acosta and Brennen, for example, Brennen and Acosta (1976). An excellent review of these instabilities has been given by Greitzer (1981). Considering that the positive slope causes both surge and rotating stall, it is probable that the positive mass

flow gain factor can cause both cavitation surge and rotating cavitation.

It is assumed that the flow is inviscid and two-dimensional upstream and downstream of the impeller, but the effects of the change in the height of the impeller blades and the losses in the impeller are taken into account. It is also assumed that the flow in the impeller is perfectly guided by the impeller blades; thus, an actuator disk analysis was employed. The problem is linearized based on the assumption that the disturbances are small.

## Characteristics of Rotating Cavitation

The following characteristics of rotating cavitations have been found from experiments (Kamijo et al., 1977, 1980) based on visual flow observations and unsteady pressure measurements of helical inducers.

(1) In a certain range of flow coefficient and cavitation number including the design point, the cavitating region propagates from blade to blade in the direction of impeller rotation, as shown in Fig. 1. That is, the absolute propagation velocity exceeds the rotational velocity of the impeller as also found in a centrifugal impeller by Yamamoto (1980). These characteristics are completely different from those of rotating stall, which occurs at smaller flow rate with positive slope of pressure performance and propagates slower than impeller rotation.

(2) The frequency of inlet pressure fluctuation agrees well with that of cavity propagation. This frequency component is insignificant at the outlet, see Fig. 2.

From these observations, it was concluded that rotating cavitation is a phenomenon related mainly to the flow condition at the inlet. These characteristics, which had been found by Kamijo et al. (1977, 1980), served as a key to identify the cause

Contributed by the Fluids Engineering Division for publication in the JOURNAL OF FLUIDS ENGINEERING. Manuscript received by the Fluids Engineering Division December 17, 1991. Associate Technical Editor: A. Prosperetti.



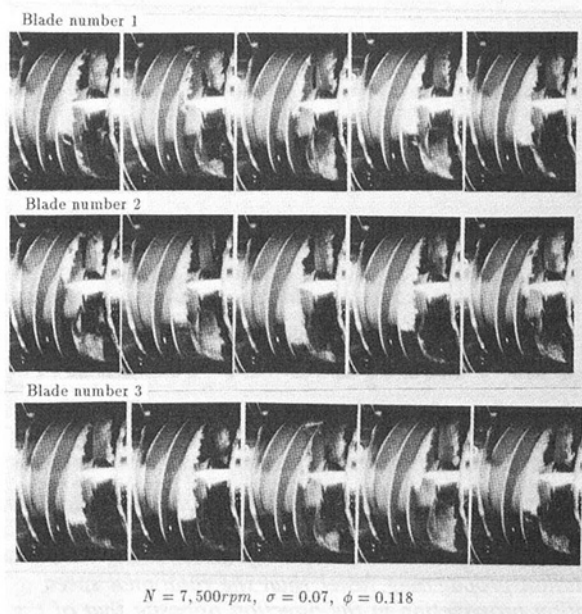


Fig. 1 Sequence of cavity fluctuations on three blades in rotating cavitation. (Pictures were picked up at every 1/3 turn of the blades and arranged so as to show the cavity size on each blade at every turn. The blade passes in the sequence of blade number 1, 2, 3).

of the supersynchronous shaft vibrations of the LOX turbopump for the LE-7 and led to their successful suppression (Kamijo et al., 1992).

### Disturbances in Upstream and Downstream Fields

In order to simulate rotating cavitation, we consider a linear cascade at  $x = 0$  with inlet and outlet vane angles  $\beta_1^*$  and  $\beta_2^*$ , respectively, moving with a velocity of  $U_T$  in  $y$  direction, as shown in Fig. 3. The average velocity ( $U, V$ ) is assumed to be  $(U_1, 0)$  for  $x < 0$  (upstream), and  $(U_2, U_2 \tan \gamma)$  for  $x > 0$  (downstream). The flow height is assumed to be 1 for  $x < 0$  and  $1/b$  in for  $x > 0$ , thus  $U_2 = bU_1$ . If we impose the condition that the disturbances should be finite at infinity, the pressure and velocity disturbances,  $\delta p$  and  $(\delta u, \delta v)$ , respectively, can be expressed as follows, as shown, for example, by Tsujimoto and Murata (1978).

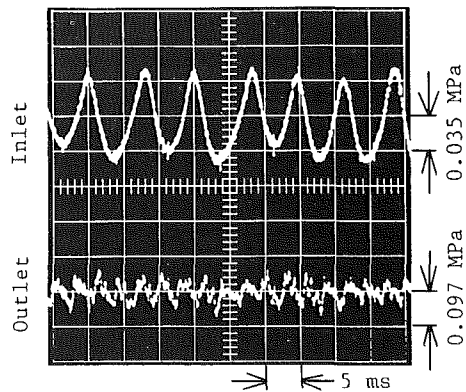


Fig. 2 Pressure oscillations in rotating cavitation. (Uncertainties in pressure are  $0.035 \text{ MPa} \pm 0.0007 \text{ MPa}$  (inlet) and  $0.097 \text{ MPa} \pm 0.0019 \text{ MPa}$  (outlet) and that in time is  $5 \text{ ms} \pm 0.15 \text{ ms}$  at 20:1 odds).

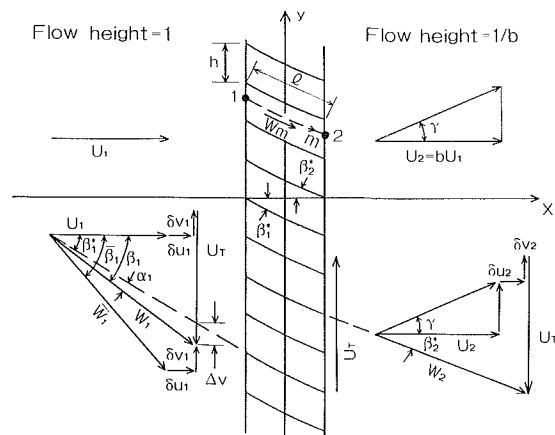


Fig. 3 Analytical model

$x < 0$

$$\left. \begin{aligned} \delta p / \rho U_1^2 &= A_1 \exp 2\pi j (nt - y/s) e^{(2\pi x)/s} \\ \delta u / U_1 &= B_1 \exp 2\pi j (nt - y/s) e^{(2\pi x)/s} \\ \delta v / U_1 &= D_1 \exp 2\pi j (nt - y/s) e^{(2\pi x)/s} \end{aligned} \right\} \quad (1)$$

### Nomenclature

- $a$  = nondimensional cavity volume
- $A, B, C, D, E$  = amplitudes of nondimensional disturbances
- $b$  = ratio of flow channel heights
- $F_3, F_4, F_5$  = cavitation characteristics, Eq. (9)'
- $h$  = blade spacing
- $j$  = imaginary unit
- $k$  = reduced frequency,  $k^* = k_R^* + jk_I^* = k / \tan \beta_1$
- $K$  = cavitation compliance,  $= -\partial a / \partial \sigma$
- $l$  = chord length
- $\mathcal{L}_u, \mathcal{L}_v$  = loss coefficients, Eq. (6)'
- $M$  = mass flow gain factor,  $= \partial a / \partial \alpha$
- $n$  = complex frequency
- $p$  = pressure
- $s$  = wavelength of disturbances
- $t$  = time
- $U, V$  = mean velocities in  $x$  and  $y$  directions
- $u, v$  = velocities in  $x$  and  $y$  directions
- $U_T$  = translating velocity of cascade

- $V_c$  = cavity volume
- $W$  = relative velocity
- $\alpha_1$  = incidence angle
- $\beta_1$  = relative inlet flow angle
- $\beta_1^*$  = mean relative inlet flow angle
- $\beta_1^*, \beta_2^*$  = inlet and outlet blade angle
- $\gamma$  = downstream mean flow angle
- $\delta$  = disturbance
- $\Delta v$  = incidence velocity
- $\zeta_s, \zeta_Q$  = incidence and through flow loss coefficients
- $\sigma$  = cavitation number,  $= (p_1 - p_c) / (\rho W_1^2 / 2)$
- $\phi$  = velocity potential, flow coefficient
- $\Omega_h'$  = nondimensional blade spacing,  $= 2\pi h / s$
- $\Omega_l'$  = nondimensional inertial chord length,  $= 2\pi l^* / s$

### Subscripts

- 1, 2 = upstream, downstream

$x > 0$

$$\left. \begin{aligned} \delta p / \rho U_2^2 &= A_2 \exp 2\pi j (nt - y/s) e^{(-2\pi x)/s} \\ \delta u / U_2 &= B_2 \exp 2\pi j (nt - y/s) e^{(-2\pi x)/s} \\ &\quad + C_2 \exp 2\pi j (nt - y/s) e^{(-j2\pi x)(k/b - \tan \gamma)/s} \\ \delta v / U_2 &= D_2 \exp 2\pi j (nt - y/s) e^{(-2\pi x)/s} \\ &\quad + E_2 \exp 2\pi j (nt - y/s) e^{(-j2\pi x)(k/b - \tan \gamma)/s} \end{aligned} \right\} \quad (2)$$

where  $s > 0$  is the wavelength of the disturbance, and the real part of the complex number  $n$  gives the frequency, and its imaginary part yields the damping rate. From the linearized momentum equation for  $x > 0$  and  $x < 0$ , we obtain the following relations.

$$\left. \begin{aligned} B_1 &= -\frac{1}{1+jk} A_1 \\ B_2 &= \frac{-1}{1-j(k/b - \tan \gamma)} A_2 \\ D_1 &= \frac{j}{1+jk} A_1 \\ D_2 &= \frac{-j}{1-j(k/b - \tan \gamma)} A_2 \end{aligned} \right\} \quad (3)$$

where  $k = sn/U_1$  is a reduced frequency. The velocity fields represented by  $B_{1,2}$  and  $D_{1,2}$  are irrotational, while that represented by  $C_2$  and  $E_2$  is rotational and represents the effects of vorticity shed from the cascade. The continuity equation for  $x > 0$  requires that

$$E_2 = -(k/b - \tan \gamma) C_2 \quad (4)$$

We now have five relations of Eqs. (3) and (4), for eight unknown disturbance amplitudes in Eqs. (1) and (2). The missing three conditions are obtained from the cascade characteristics, which will be given in the following section.

### Cascade Characteristics

**Pressure Increase.** Since it is experimentally found by Kamijo et al. (1977, 1980) that the degradation of pressure performance due to cavitation is small in the range of  $\sigma$  where rotating cavitation is observed, we neglect the effect of cavitation in estimating the pressure increase in the impeller. We apply the unsteady Bernoulli equation in a frame moving with the cascade, taking into account a through flow loss proportional to  $(U_1 + \delta u_1)^2$  and an incidence loss proportional to  $(\Delta v)^2$ . Then we obtain:

$$\frac{p_2 - p_1}{\rho} = \frac{1}{2} (W_1^2 - W_2^2) - \frac{\partial^*}{\partial t^*} (\phi_2 - \phi_1) - \zeta_Q (U_1 + \delta u_1)^2 - \zeta_S (U_1 + \delta u_1)^2 (\tan \beta_1^* - \tan \beta_1)^2 \quad (5)$$

where  $\phi$  is the velocity potential and  $\partial^*/\partial t^*$  denotes time differential in the moving frame. Since cavities occur at the inlet, it is appropriate to relate the velocity in the cascade to that at the outlet. Thus we can express the velocity potential difference:

$$\begin{aligned} \phi_2 - \phi_1 &= \int_1^2 W_m dm = (U_2 + \delta u_2) \int_1^2 \frac{b(m)/b}{\cos \beta(m)} dm \\ &\cong (U_2 + \delta u_2) l^* \end{aligned}$$

Putting the above expression into Eq. (5) and linearizing it, we arrive at the following expression for the unsteady component:

$$\frac{\delta p_2 - \delta p_1}{\rho U_1^2} = (1 - \mathcal{L}_u) \frac{\delta u_1}{U_1} - (\tan \bar{\beta}_1 + \mathcal{L}_v) \frac{\delta v_1}{U_1} - \left( \frac{b}{\cos^2 \beta_2^*} + j\Omega_l \right) \frac{\delta u_2}{U_1} \quad (6)$$

where

$$\left. \begin{aligned} \mathcal{L}_u &= 2\zeta_Q + 2\zeta_S \tan \beta_1^* (\tan \beta_1^* - \tan \bar{\beta}_1) \\ \mathcal{L}_v &= 2\zeta_S (\tan \beta_1^* - \tan \bar{\beta}_1) \\ \Omega_l &= 2\pi (l^*/s) (k - \tan \bar{\beta}_1) = \Omega_l' (k - \tan \bar{\beta}_1) \\ l^* &= (1+b)l / (2b \cos \bar{\beta}), \quad \bar{\beta} = (\beta_1^* + \beta_2^*)/2 \end{aligned} \right\} \quad (6')$$

**Change in Cavity Volume.** The cavity volume,  $V_c$ , per blade and per unit span is normalized as  $a = V_c/h^2$  using the blade spacing,  $h$ . It is assumed that the normalized volume,  $a$ , is a function of the incidence angle,  $\alpha_1$ , and of the cavitation number,  $\sigma = (p_1 - p_c) / (\rho W_1^2/2)$ , and thus  $a = a(\sigma, \alpha_1)$ . Then the change in the cavity volume  $V_c$  due to the change in the inlet conditions is given by (see Brennen and Acosta, 1976).

$$\delta V_c = h^2 \left[ \left( \frac{\partial a}{\partial \sigma} \right) \left( \frac{\partial \sigma}{\partial W_1} \delta W_1 + \frac{\partial \sigma}{\partial p_1} \delta p_1 \right) + \frac{\partial a}{\partial \alpha_1} \delta \alpha_1 \right] \quad (7)$$

The mass continuity relation applied in the moving frame yields

$$h(\delta u_2/b - \delta u_1) = \frac{\partial^*}{\partial t^*} (\delta V_c) \quad (8)$$

We estimate  $\delta W_1$  and  $\delta \alpha_1$  in Eq. (7) from the velocity triangle. Then Eq. (8) with Eq. (7) results in the following expression for the unsteady part of the continuity relation.

$$\frac{1}{b} \frac{\delta u_2}{U_1} - \frac{\delta u_1}{U_1} = j\Omega_h \left( F_3 \frac{\delta u_1}{U_1} + F_4 \frac{\delta v_1}{U_1} + F_5 \frac{\delta p_1}{\rho U_1^2} \right) \quad (9)$$

where,

$$\left. \begin{aligned} F_3 &= 2\sigma K \cos^2 \bar{\beta}_1 - M \sin \bar{\beta}_1 \cos \bar{\beta}_1 \\ F_4 &= -2\sigma K \cos \bar{\beta}_1 \sin \bar{\beta}_1 - M \cos^2 \bar{\beta}_1 \\ F_5 &= -2 \cos^2 \bar{\beta}_1 K \\ \Omega_h &= 2\pi (h/s) (k - \tan \bar{\beta}_1) = \Omega_h' (k - \tan \bar{\beta}_1) \end{aligned} \right\} \quad (9')$$

with the mass flow gain factor  $M \equiv \partial a / \partial \alpha$  and the cavitation compliance  $K \equiv -\partial a / \partial \sigma$ .

**Kutta's Condition.** If we assume that the relative flow is tangential to the blade surface, the velocity triangle at the outlet yields:

$$\tan \gamma + \tan \beta_2^* = (1/b) \tan \bar{\beta}_1 \quad (10)$$

for the steady component and

$$\delta v_2 / U_1 = -(\delta u_2 / U_1) \tan \beta_2^* \quad (11)$$

for the unsteady component.

### Characteristic Equation and Characteristic Roots

Conditions (3) and (4), along with the pressure increase of Eq. (6), the continuity equation (9) and Kutta's condition of Eq. (11) yield eight linear, homogeneous equations in terms of the eight unknown disturbance amplitudes. The following characteristic equation is obtained from the determinant of the coefficient matrix of the above equations.

$$b \left\{ (1 + \Omega_l') (k - \tan \bar{\beta}_1) - \frac{jb}{\cos^2 \beta_2^*} \right\} \left\{ 1 + \Omega_h' (k - \tan \bar{\beta}_1) (F_4 + kF_5) + j\Omega_h' (k - \tan \bar{\beta}_1) (F_3 - F_5) \right\} + k - \tan \bar{\beta}_1 - \mathcal{L}_v - j\mathcal{L}_u = 0 \quad (12)$$

The foregoing is a third-order equation in terms of  $k$ , which gives three complex characteristic roots for  $k$ . We introduce

$$k^* \equiv k_R^* + jk_I^* \equiv k / \tan \bar{\beta}_1$$

and write

$$\begin{aligned} \exp 2\pi j (nt - y/s) &= \exp \{ [-2\pi (U_1/s) \tan \bar{\beta}_1 k_I^*] t \} \\ &\quad \times \exp [2\pi j (U_1/s) \tan \bar{\beta}_1 k_R^* \{ t - y / (U_T \cdot k_R^*) \}] \end{aligned}$$

in expressions of Eqs. (1) and (2). This shows that  $k_R^*$  is the propagation velocity ratio (phase velocity of the disturbance/peripheral velocity  $U_T$  of the cascade) and  $k_I^*$  is the damping rate of the disturbance.

### Special Cases

**Rotating Stall.** We now consider a case without cavitation. With  $F_3 = F_4 = F_5 = 0$ , Eq. (12) results in

$$k^* = \left\{ 1 - \frac{2F_5(1 - \tan \beta_1^*/\tan \bar{\beta}_1)}{1 + b(1 + \Omega_i')} \right\} + j \left( \frac{b^2/\cos^2 \beta_2^* + \mathcal{L}_u}{1 + b(1 + \Omega_i')} \right) \cot \bar{\beta}_1 \quad (13)$$

It is clearly shown that the propagation velocity ratio  $k_R^*$  is smaller than 1 since  $\bar{\beta}_1 > \beta_1^*$  at the flow rates where rotating stall occurs. It can be shown that the onset condition can otherwise be written as follows:

$$\frac{\partial \psi_{1s}}{\partial \phi} = \frac{\partial}{\partial \phi} \left( \frac{p_2 - p_{11}}{\rho U_T^2} \right) = - \left( \frac{b^2}{\cos^2 \beta_2^*} + \mathcal{L}_u \right) \cot \bar{\beta}_1 = - (1 + b + b\Omega_i') k_I^* > 0 \quad (14)$$

where  $p_{11}$  = inlet total pressure and  $\phi = U_1/U_T = \cot \bar{\beta}_1$  = flow coefficient. This is in agreement with conventional results for rotating stall, as described by Greitzer (1981).

**Rotating Cavitation.** As shown in Fig. 2, the outlet pressure fluctuation due to rotating cavitation is significantly smaller than that at the inlet. As will be shown later, Eq. (12) predicts smaller outlet velocity and pressure fluctuations than those at the inlet. Therefore, we put  $\delta u_2 = 0$  in the continuity Eq. (9), which results in

$$\Omega_i'(k^* - 1)[j(F_5 - F_3) - k^*F_5 \tan \bar{\beta}_1 - F_4] \times \tan \bar{\beta}_1 - 1 = 0 \quad (15)$$

On the other hand, at the limit cases of  $\beta_2^* \rightarrow 90$  deg or  $\Omega_i' \rightarrow \infty$ , Eq. (12) reduces to Eq. (15) or the equation multiplied by  $(k^* - 1)$  on both sides of Eq. (15), respectively. The characteristic roots of the latter equation are  $k^* = 1$  and the two roots of Eq. (15). Equation (13) yields  $k^* = 1$  at the limit  $\Omega_i' \rightarrow \infty$ . Hence,  $k^* = 1$  corresponds to rotating stall and the two roots of Eq. (15) represent rotating cavitation. For inducers, since  $\Omega_i'$  and the negative slope of the head-capacity curve are sufficiently large, two of the three roots of Eq. (12) agree fairly well with those of Eq. (15), as will be shown later. Thus, the inertia of the fluid in the impeller and the negative slope are responsible for the smaller fluctuations at the outlet. Here we study the characteristics of rotating cavitation by examining Eq. (15).

In the case  $K = 0$ , Eq. (15) reduces to a first-order equation which yields

$$k^* = \left( 1 + \frac{\cot \bar{\beta}_1}{M\Omega_h'} \right) - j \frac{1}{M\Omega_h'} \quad (16)$$

This shows that a rotating cavitation with  $k_R^* > 1$  appears whenever  $K = 0$  and  $M > 0$ .

Next, we consider the case of neutral stability ( $k_I^* = 0$ ). Since  $k^* = k_R^*$  is real, the imaginary part of Eq. (15) gives the condition  $F_5 = F_3$  for neutral stability. If we use the relations of Eq. (9)' and consider the result of Eq. (16), the rotating cavitation onset condition can be given as follows.

$$M > 2K(1 + \sigma) \cot \bar{\beta}_1 \quad (17)$$

This relation shows clearly that positive  $M$  causes rotating cavitation and that positive  $K$  has the effect of reducing the region of the rotating cavitation onset. Surge analyses, for example Young et al. (1972) and Shimura and Kamijo (1982), show that positive  $K$  has a stabilizing effect on the system while

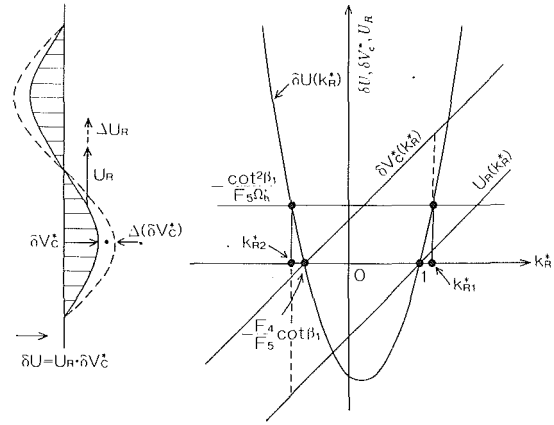


Fig. 4 Explanation how propagation velocities are determined

positive  $M$  has a destabilizing effect. This is in accord with the present result of Eq. (17).

The propagating velocity ratio,  $k_R^*$ , is determined from the real part of Eq. (15). After some rearrangements we can express this equation as follows:

$$\delta U(k_R^*) \equiv U_R(k_R^*) \cdot \delta V_c^*(k_R^*) = (k_R^* - 1) \left[ k_R^* + \frac{F_4}{F_5} \cot \bar{\beta}_1 \right] = - \frac{\cos^2 \bar{\beta}_1}{F_5 \Omega_h'} \quad (18)$$

Figure 4 shows that we have two types of rotating cavitation with  $k_{R1}^* > 1$ ,  $k_{R2}^* < -F_4 \cot \bar{\beta}_1 / F_5 = -(\sigma + M/2K \cot \bar{\beta}_1)$ . We express these characteristic roots by  $k_1^*$  and  $k_2^*$ , respectively. On the other hand, as shown by Eq. (13), rotating stall has a characteristic root of  $k_R^* < 1$ , which is represented by  $k_3^*$ .

Next, we consider the physical difference between  $k_1^*$  and  $k_2^*$ . Equation (18) is equivalent to Eq. (15) which comes from Eq. (9): thus Eq. (18) is basically equivalent to the continuity Eq. (8).  $U_R \equiv k_R^* - 1$  appears from  $\partial^*/\partial t^*$  of Eq. (8) and is equal to the propagation velocity ratio relative to the moving cascade.  $\delta V_c^* \equiv k_R^* + (F_4/F_5) \cot \bar{\beta}_1$  corresponds to the cavity volume change,  $\delta V_c$ , due to  $\delta u_1/U_1 = 1$ . Owing to the inertia effects in the inlet flow field,  $\delta p_1/\delta u_1$  is a function of  $k^*$ , as can be seen from Eqs. (1) and (3). Hence, Eq. (9) shows that  $\delta V_c^*$  is also a function of  $k^*$ . Thus,  $\delta U = U_R \cdot \delta V_c^*$  represents the change in the axial velocity due to the change of the cavity volume,  $\delta V_c^*$ , in the rotating frame, and Eq. (18) requires that  $\delta U$  should be equal to  $-\cot^2 \bar{\beta}_1 / F_5 \Omega_h'$  which corresponds to the assumed axial velocity,  $\delta u_1/U_1 = 1$ . The change in  $k_R^*$  results in the change in  $\delta V_c^*$  and  $U_R$ :  $k_R^*$  is determined so that Eq. (18) is satisfied.

Considering that  $\Delta(\delta U) = U_R \cdot \Delta(\delta V_c^*) + (\delta V_c^*) \cdot \Delta U_R$  and that  $|U_R(k_{R1}^*)| \ll |\delta V_c^*(k_{R1}^*)|$  and  $|\delta V_c^*(k_{R2}^*)| \ll |U_R(k_{R2}^*)|$  (see Fig. 4), we find that  $k_1^*$  represents the rotating cavitation which is balanced mainly by the change in the relative propagation velocity ( $\Delta U_R$ ), and that  $k_2^*$  is the other rotating cavitation mainly balanced by the change in the amplitude of volume fluctuation ( $\Delta(\delta V_c^*)$ ). Figure 4 suggests that the volume change  $\delta V_c^*$  for  $k_2^*$  is significantly smaller than that for  $k_1^*$ . In the case  $K = 0$  (i.e.,  $F_5 = 0$ ),  $\delta V_c^*$  is independent of  $\delta p_1$  and hence of  $k^*$ . Therefore the balancing mechanism for  $k_2^*$  is lost and only  $k_1^*$  appears for the case of  $K = 0$ , as shown by Eq. (16).

## Results and Discussions

**Examination of Three Roots of Equation (12).** The present analysis is applied to the inducer tested by Kamijo et al. (1977, 1980), and the calculation was carried out at the mean radius ( $0.794 \times$  tip radius) of the inducer. The standard values of the parameters used in the calculation are shown in Fig. 5(a). The static performances of the inducer is shown in Fig. 6. In

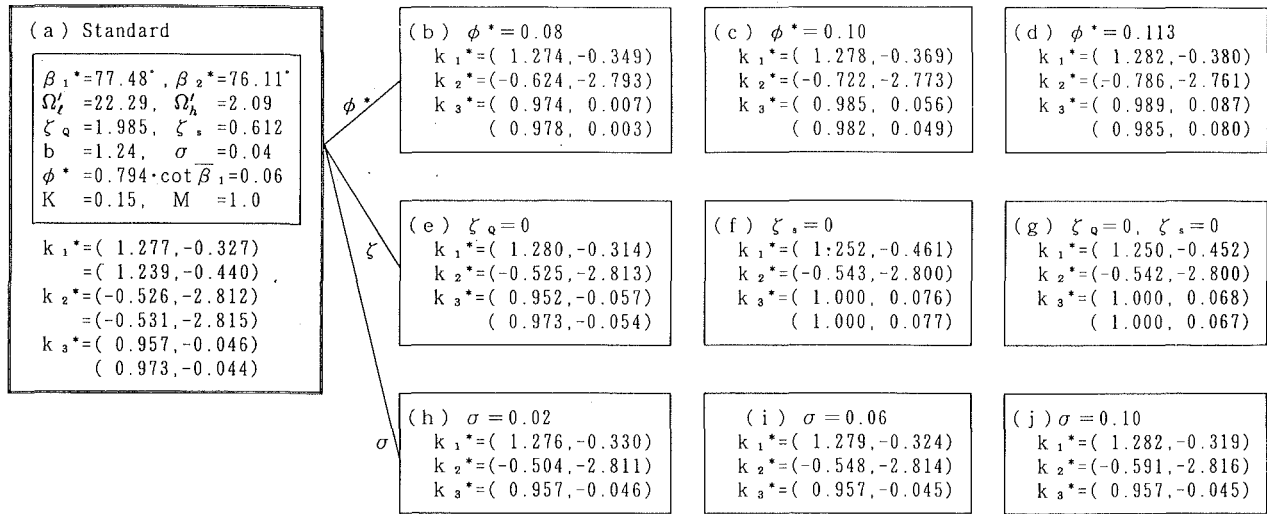


Fig. 5 Parameters and results of calculation

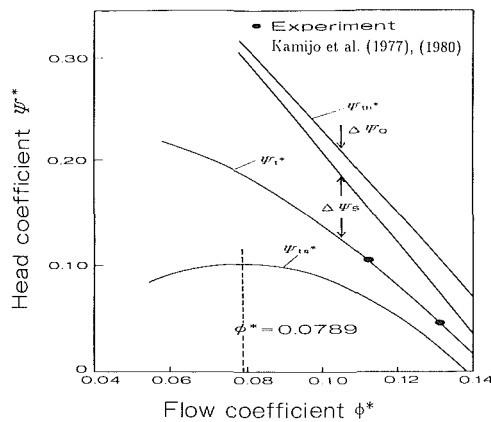


Fig. 6 Static performance of inducer

the figure,  $\phi^*$  and  $\psi^*$  are flow and pressure coefficients normalized by the inducer tip velocity.  $\psi_{th}^*$  is the Euler's head at the mean radius,  $\psi_i^*$  is the total head and  $\psi_{is}^*$  is the inlet total to outlet static pressure coefficient.

Figure 5(b)-(j) show the three roots,  $k_i^* = (k_{Ri}^*, k_{Ii}^*)$ , of Eq. (12), with the value of the parameter which is different from the standard values shown in (a). They can be assigned to  $k_1^*$ ,  $k_2^*$ , and  $k_3^*$  following the criteria ( $k_{R1}^* > 1$ ,  $k_{R2}^* < 0$  and  $k_{R3}^* < 1$ ) given in the preceding section. The values in the lower lines of  $k_1^*$  and  $k_2^*$  in (a) are given by Eq. (15), and the values in the lower line of  $k_3^*$  in (a)-(g) are given by Eq. (13).

As shown in Fig. 5(a), the values of  $k_1^*$  and  $k_2^*$  are close to those obtained by Eq. (15), and  $k_3^*$  is close to those obtained by Eq. (13). This suggests that  $k_1^*$  and  $k_2^*$  represent the rotating cavitations and  $k_3^*$  the rotating stall, and that they can be approximately treated by the methods outlined in the preceding section. For the standard case (a), the imaginary parts of  $k_1^*$ ,  $k_2^*$ , and  $k_3^*$  are all negative, showing that both rotating cavitation and rotating stall are amplified simultaneously. The fact that the root  $k_3^*$ , which represents rotating stall estimated under the effects of cavitation, is close to the noncavitating rotating stall solution of Eq. (13) means that the rotating stall is not largely affected by the cavitation. As shown in Fig. 5(b)-(g), the rotating stall is damped ( $k_{R3}^* > 0$ ) when  $\phi^*$  increases or  $\zeta_s$  is neglected, which can be explained by Fig. 6 and Eqs. (13) and (14). On the other hand, the values of  $k_1^*$  and  $k_2^*$  are almost independent of the values of  $\phi^*$ ,  $\zeta_q$ ,  $\zeta_s$  and  $\sigma$ , so long as the values of  $K$  and  $M$  are kept constant. Rotating cavitations are amplified even with a negative slope of  $\psi_{is}^*$  at

Table 1 Amplitudes of pressure and axial velocity fluctuations (Assumption of  $|\delta p_1/\rho U_1^2| = 1$ )

	$k^* = k_1^*$	$k^* = k_2^*$	$k^* = k_3^*$
$ \delta p_2/\rho U_2^2 $	(0.0591)	(0.00836)	(0.0497)
$ \delta u_1/U_1 $	(0.0563)	(0.00257)	(0.0783)
$ \delta u_2/U_2 $	(0.0129)	(0.00020)	(0.0743)

larger  $\phi^*$  or without  $\zeta_s$ , which is quite different from the case of rotating stall.

From these numerical results and the discussions in the preceding section, we can conclude that rotating cavitation and rotating stall are, practically, mutually independent and completely different phenomena, in the sense that their causes are different and that they behave differently, although both can be treated by and deduced from the same characteristic Eq. (12).

Table 1 shows the amplitudes of the pressure and axial velocity fluctuations at the inlet and the outlet of the cascade, for the case of Fig. 5(a) and corresponding to  $\delta p_1/\rho U_1^2 = 1$ . For each case  $\delta p_2$  is much smaller than  $\delta p_1$ . For rotating cavitation ( $k_1^*$  and  $k_2^*$ ),  $\delta u_2$  is small compared with  $\delta u_1$ , showing that the fluctuation at the inlet is almost absorbed by the change of cavity volume. This supports the experimentally obtained conclusion (Kamijo et al., 1977, 1980) that "rotating cavitations are related mainly to the inlet flow conditions." On the other hand, for rotating stall ( $k_3^*$ ),  $\delta u_2$  is nearly equal to  $\delta u_1$ , with a small effect of the cavity volume change.

As shown above, direct effects of  $\phi^*$  and  $\sigma$  on  $k_1^*$  and  $k_2^*$  are small. The discussions in the section "Rotating Cavitation" showed that  $k_1^*$  and  $k_2^*$  are mainly dependent on  $M$  and  $K$ . Since  $M$  and  $K$  are functions of  $\phi^*$  and  $\sigma$ , rotating cavitations are affected by  $\phi^*$  and  $\sigma$  through  $M$  and  $K$ .

**Characteristic Roots of Rotating Cavitations.** Contour maps of  $k_1^*$  and  $k_2^*$  in the  $M$ - $K$  plane are shown in Figs. 7 and 8. Values of parameters not specified in the figures are the same as those in Fig. 5(a). The solid lines are obtained from Eq. (12), while the broken lines are determined from Eq. (15). The difference between these results are small, showing that Eq. (15) simulates rotating cavitations very well. The neutral stability curve is shown by the solid line of  $k_I^* = 0$ , which is close to the criteria of Eq. (17). The rotating cavitations are amplified in the region under the neutral stability curve.

In order to make comparisons with experimental results, calculations were also made as for  $\sigma = 0.06$  and  $0.02$ . It was found that the contour maps are almost unchanged. Hence,

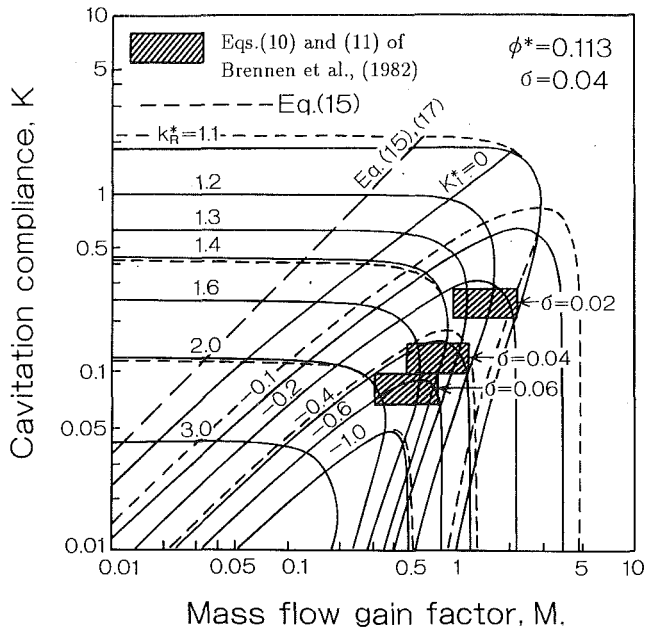


Fig. 7 Contour map of  $k_1^*$  rotating cavitation

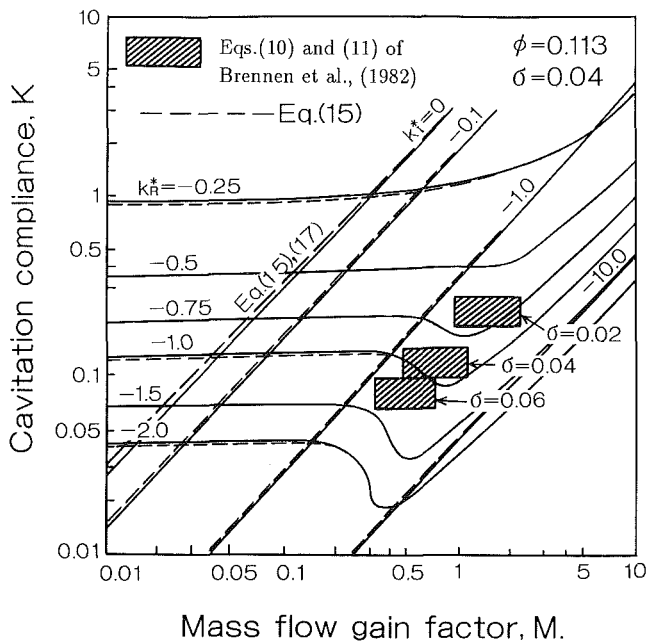


Fig. 8 Contour map of  $k_2^*$  rotating cavitation

the ranges of  $M$  and  $K$  for three values of  $\sigma$  are shown in Figs. 7 and 8, estimated from Eqs. (10) and (11) of Brennen et al. (1982). These equations are based on a bubbly flow model (Brennen, 1978), with the values of two parameters in the model determined so that the results can best fit the experimental data (Ng and Brennen, 1978) obtained with inducers similar to the present case, under surge mode flow oscillations.

For  $k_1^*$  shown in Fig. 7, the propagation velocity for  $\sigma = 0.02$  is  $k_R^* = 1.1 \sim 1.4$ , which is close to the experimental value of  $k_R^* = 1.16$  (Kamijo et al., 1977, 1980). As we reduce the cavitation number  $\sigma$ , the estimated ranges of  $M$  and  $K$  shifts to the location with smaller propagation velocity ratio  $k_R^*$ . The experiments (Kamijo et al. 1977, 1980) showed a similar tendency. Figure 9 shows the supersynchronous shaft vibration of LE-7 LOX turbopump caused by the  $k_1^*$  rotating cavitation. The reduction of the supersynchronous frequency

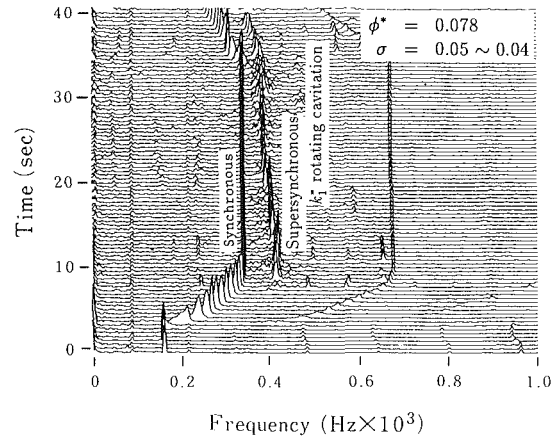


Fig. 9 Fourier analysis of LE-7 LOX turbopump shaft vibrations. (Uncertainty in frequency is  $10^3 \text{ Hz} \pm 0.1 \text{ Hz}$  and that in time is  $40 \text{ s} \pm 0.2 \text{ s}$  at 20:1 odds).

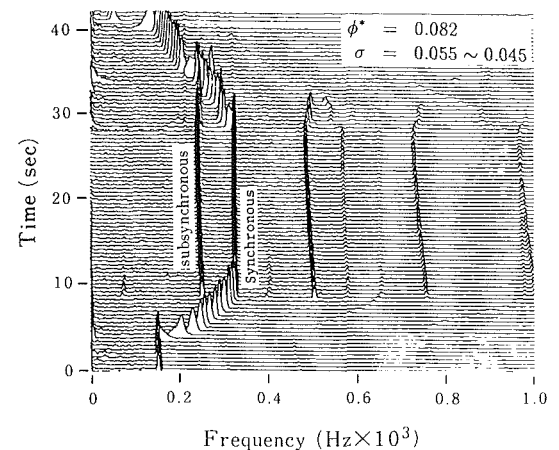


Fig. 10 Fourier analysis of LE-7 LOX turbopump shaft vibrations. (Uncertainty in frequency is  $10^3 \text{ Hz} \pm 0.1 \text{ Hz}$  and that in time is  $40 \text{ s} \pm 0.2 \text{ s}$  at 20:1 odds).

with time is caused by the reduction of the inlet pressure with time, showing the above-mentioned tendency.

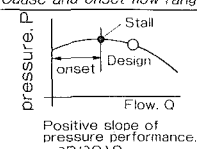
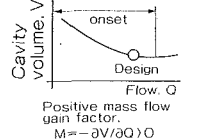
Since  $k_{R2}^* < 0$ , the characteristic root  $k_2^*$  corresponds to a rotating cavitation which propagates in the direction opposite that of the impeller rotation. In the LOX turbopump for the LE-7, unidentified subsynchronous vibrations as shown in Fig. 10 were often observed with the inducer which suffers from rotating cavitation of  $k_{R1}^* = 1.0 \sim 1.2$ . The subsynchronous vibration disappeared completely when the  $k_1^*$  rotating cavitation was suppressed. The frequency of the subsynchronous vibration in Fig. 10 is about 0.8 times the frequency of the component synchronous to the impeller rotation, which is close to the value of  $k_{R2}^*$  obtained from Eq. (12) using the values of  $K$  and  $M$  estimated from Brennen et al. (1982). These facts suggest the existence of  $k_2^*$  rotating cavitation, but unfortunately the rotational direction of the vibration was not observed in the experiment. Further study is needed before we can conclude that the subsynchronous vibration is caused by the  $k_2^*$  rotating cavitation.

## Conclusions

Major findings of the present study are:

1. Rotating cavitation is a completely different phenomenon from rotating stall. Rotating stall is not significantly affected by the existence of cavitation.
2. Rotating cavitation is caused by the positive mass flow

**Table 2 Relation between flow instabilities in turbomachinery**

Cause and onset flow range	Local instability	System instability
 <p>pressure, <math>P</math></p> <p>Flow, <math>Q</math></p> <p>Positive slope of pressure performance. <math>\partial P / \partial Q &gt; 0</math></p>	Rotating stall	Surge
 <p>Cavity volume, <math>V</math></p> <p>Flow, <math>Q</math></p> <p>Positive mass flow gain factor. <math>M = -\partial V / \partial Q &gt; 0</math></p>	Rotating cavitation	Cavitation surge

gain factor  $M$ , while rotating stall by the positive slope of the pressure performance.

- Two modes of rotating cavitations are predicted; one of them propagates faster than the impeller rotation, and the other propagates in the direction opposite to it. Namely, they have the propagation velocity ratio  $k_R^* > 1$  or  $k_R^* < 0$ , while for the rotating stall  $k_R^* < 1$ .
- Rotating cavitations are almost unaffected by the flow coefficient, impeller loss, and cavitation number, so long as the mass flow gain factor  $M$  and the cavitation compliance  $K$  are kept constant.
- Contour maps of the propagation velocity ratio and the damping rate are given for the two types of the rotating cavitations, in the  $M - K$  plane.
- The propagation velocity ratio for the forward rotating cavitation is in fair agreement with experiments. Possibility of the backward rotating cavitation is discussed.
- From these results and the discussions in the introduction, the relations between flow instabilities in turbomachinery can be summarized as shown in Table 2.

For rotating stalls, it is known (Greitzer, 1981) that linear analyses are applicable only for the prediction of inception—once they occur, the disturbances are by no means small. Unfortunately, experimental data for rotating cavitations are not sufficient at present to determine the applicability limit of the present linear analysis. However, the authors believe that the various simplifications, including linearization, adopted in the present analysis have made it possible to elucidate the fun-

damental mechanisms and the nature of rotating cavitation. Further study is needed for closer comparisons with experiments (especially for the backward propagating mode), quantitative estimation of  $M$  and  $K$  (including the nonuniformity and the unsteadiness of the disturbance), and the construction of a more sophisticated model including the effects of nonlinearity of the problem, the finiteness of the blade spacing, and the three dimensionality of the flow.

### Acknowledgment

The authors would like to express their sincere gratitude to Mrs. Y. Sato at Kakuda Research Center of NAL. Her support in numerical calculation, drawing, and preparation of the manuscript is greatly appreciated.

### References

- Brennen, C. E., 1978, "Bubbly Flow Model for the Dynamic Characteristics of Cavitating Pumps," *Journal of Fluid Mechanics*, Vol. 89-2, pp. 223-240.
- Brennen, C., and Acosta, A. J., 1976, "The Dynamic Transfer Function for a Cavitating Inducer," *ASME JOURNAL OF FLUIDS ENGINEERING*, pp. 182-191.
- Brennen, C. E., Meissner, C., Lo, E. Y., and Hoffman, G. S., 1982, "Scale Effects in the Dynamic Transfer Functions for Cavitating Inducers," *ASME JOURNAL OF FLUIDS ENGINEERING*, Vol. 104, No. 4, pp. 428-433.
- Greitzer, E. M., 1981, "The Stability of Pumping Systems—The 1980 Freeman Scholar Lecture," *ASME JOURNAL OF FLUIDS ENGINEERING*, Vol. 103, No. 2, pp. 193-242.
- Kamijo, K., Shimura, T., and Watanabe, M., 1977, "An Experimental Investigation of Cavitating Inducer Instability," *ASME Paper No. 77-WA/FW-14*, and also, 1980, "A Visual Observation of Cavitating Inducer Instability," *NAL TR-598T*.
- Kamijo, K., Yoshida, M., and Tsujimoto, Y., 1992, "Hydraulic and Mechanical Performance of LE-7 LOX Pump Inducer," *AIAA Paper 92-3133*, 28th Joint Propulsion Conference and Exhibit, July 6-8, Nashville, TN.
- NASA, 1970, "Prevention of Coupled Structure—Propulsion Instability (POGO)," *NASA Space Vehicle Design Criteria (Structures)*, NASA SP-8055.
- Ng, S. L., and Brennen, C. E., 1978, "Experiments on the Dynamic Behavior of Cavitating Pumps," *ASME JOURNAL OF FLUIDS ENGINEERING*, Vol. 100, pp. 166-176.
- Shimura, T., and Kamijo, K., 1982, "A Study on Dynamic Characteristics of Liquid Oxygen Pumps for Rocket Engines (1st Report), *NAL TR-725*, (in Japanese).
- Tsujimoto, Y., and Murata, S., 1978, "Three Dimensional Unsteady Actuator Disk Theory for Subsonic Viscous Flows," *ZAMM*, Vol. 58, pp. 561-569.
- Yamamoto, K., 1980, "An Experimental Study on Instability in a Cavitating Centrifugal Pump with a Volute Suction Nozzle," *Proceedings IAHR Symposium*, Tokyo, pp. 303-312.
- Young, W. E., et al., 1972, "Study of Cavitating Inducer Instabilities, Final Report," *NASA-CR-123939*.

# The Accuracy of a Three-Component Laser Doppler Velocimeter System Using a Single-Lens Approach

P-A. Chevrin

SNECMA,  
77550 Moissy-Cramayel, France

H. L. Petrie

S. Deutsch

Applied Research Laboratory,  
The Pennsylvania State University,  
State College, PA 16804

*An analysis of the effects of misalignment on the on-axis velocity component measurements made with a three-component LDV system using two colors and five beams issuing from a single lens is discussed. A slight misalignment of the center beam from the optical axis is shown to cause large changes in the measured "on-axis" component of velocity. The effect of misalignment on the ensemble averaged velocity statistics in turbulent flows is also considered. The error analysis of Neti and Clark (1979) is applicable to on-axis component of the present system and it shows that even when the system is perfectly aligned, the relative uncertainty of the on-axis component of velocity is much larger than that of the other components of velocity. Measurements taken in a laminar pipe flow support this conclusion.*

## 1 Introduction

Many flows of practical interest are three-dimensional in nature. Measurement of only one or two components of velocity is insufficient to characterize these flow fields and can even be misleading. Complete understanding of three-dimensional flows often requires simultaneous measurement of all three components of velocity. The laser Doppler velocimeter, in addition to being a nonintrusive technique which does not suffer from sensitivity to either pressure or temperature, is now commonly used to perform this kind of measurement. Various three velocity component measurement schemes have been proposed and a number of them have been tested. Bell et al. (1985) and Boutier (1987) provide a critical review of the different systems. Meyers (1988) presents a brief historical overview of the development of LDV systems and discusses the difficulties associated with measurement of the third, on-axis velocity component by various approaches.

In most experimental situations, measuring three orthogonal components of velocity directly is not possible. For these cases, the LDV system is used to measure nonorthogonal velocity components and, using the appropriate matrix transformation, the velocity components in the desired coordinate system are reconstructed. Among the possible configurations of a three component LV system the three-color, dual-beam system, as described by Buchhave (1983) or Menon (1986) is attractive. This system consists of three single channel systems, built around two optical axes which generally lie at an angle of at least 30 deg to each other. Although such a system offers the best performance in terms of dynamic range, it is cumbersome

and sometimes cannot be used in situations where space or optical access are limited. Another technique to measure three velocity components uses frequency shift, rather than color separation, to differentiate between the velocity components. In this approach, each beam pair uses a sufficiently different frequency shift, so that retrieval of the individual contribution of each component can be made by appropriate filtering of the Doppler signal. The most popular arrangement consists of a conventional two-color, dual-beam system with an off-axis channel oriented at an angle relative to the axis of the two-color system. Examples of such arrangements and error estimates for them can be found in Neti and Clark (1979), Orloff and Snyder (1982), Snyder et al. (1984), and Ozcan (1987). Access, as noted previously for three-color systems, however, remains a problem in this case.

In an alternative design, the system has just one focusing lens. This approach uses only two laser lines, usually the blue (488 nm) and green (514.5 nm) wavelengths of an Argon laser. Only five beams oriented symmetrically with respect to the optical axis are needed. This five-beam system overcomes problems of spatial and optical access common to the other approaches. Such systems are commercially available. The first applications of the technique are due to Schock et al. (1983) and to Meyers and Hepner (1984).

The accuracy of the on-axis component of velocity measurement with this five beam single lens approach is the subject of this paper. In Section 2 the effect of a slight error in the beam half angle is studied. Section 3 considers errors due to a misaligned center beam which is key to the system. It is shown that misalignment can contribute to large errors in the measured on-axis component of velocity. The effect on the measurement of ensemble-averaged quantities in turbulent flows is then considered. An analysis similar to that of Neti

Contributed by the Fluids Engineering Division for publication in the JOURNAL OF FLUIDS ENGINEERING. Manuscript received by the Fluids Engineering Division August 28, 1991. Associate Technical Editor: D. P. Telionis.

and Clark (1979) is extended in Section 4 to the LV system considered here. It is shown that even when the system is perfectly aligned the random error in the on-axis component of velocity is much larger than that on the other components of velocity, regardless of the type of signal processor used. In practice, the resulting large uncertainties in the on axis component preclude the use of such a system for accurate turbulence measurements involving the on-axis component.

## 2 Principle of the Basic System

The five-beam, two-color system, which was employed in our Laboratory and is studied in this paper, has a single focusing lens. Two blue wavelength beams lie in a horizontal plane, and three green wavelength beams are in the vertical plane with one green beam directed along the optical axis. The two blue beams comprise a standard dual-beam, one-component fringe mode system, with one beam frequency shifted and will not be considered further. We assume for convenience that the blue beam pair are used to measure the  $X$  component of velocity,  $U$ . The three green beams are assumed to be perfectly aligned in the sense that they lie in one vertical plane and the center beam evenly bisects the top and bottom green beams. These three green beams, which are denoted as the top, center, and bottom beams, can be considered to comprise two dual-beam systems with one center beam common to each system. The combination of the top and center beams is used to measure a velocity component  $V_1$ , while the combination of the center and bottom beams is used to measure a second component  $V_2$  as shown in Fig. 1. These two components are not orthogonal, but given their orientation, it is possible to calculate the velocity component perpendicular to the optical axis,  $W$ , and the on-axis velocity component,  $V$ . As discussed by Meyers (1988), this approach is similar to a number of other LDV systems configured to measure a portion of the on-axis  $V$  component using fringe mode systems at what is usually a shallow angle to the  $V$  component axis. A common problem is that the resultant fringes are widely spaced. A larger fringe spacing means a reduction in the sensitivity of the system.

For the signal processor to differentiate between a Doppler signal coming from the top-center beam combination from that coming from the center-bottom configuration, a large frequency difference must exist between the top and bottom beams. This is achieved by passing the top and bottom beams through Bragg cell modules to produce frequency shifts  $f_{st}$  and  $f_{sb}$ . The shifts,  $f_{st}$  and  $f_{sb}$ , must be sufficiently far apart so that the separation of the Doppler frequency range in the top and bottom channels do not overlap in the presence of tur-

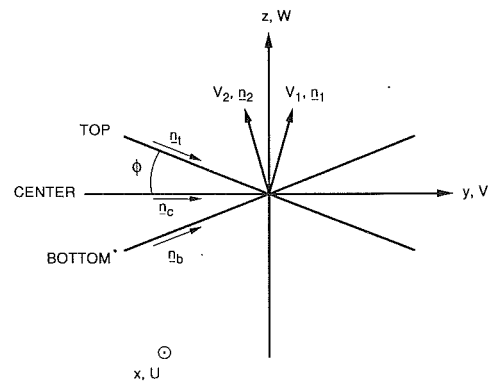


Fig. 1 Orientation of the top, center, and bottom beams and the coordinate system used. Unit vectors and velocities measured by the top-center and bottom-center beam combinations are shown.

bulent fluctuations. In the present system, the top beam is down shifted by 60 MHz and the bottom beam is oppositely shifted by 40 MHz.

The velocity component  $W$  in Fig. 1 can be measured using signals from the top and bottom beams only, as in any dual beam fringe mode LDV system equipped with frequency shift. In this case, the Doppler frequency of a particle passing through this probe volume will have a frequency shaft  $f_{st} + f_{sb} = 100$  MHz. This signal is separated from the signals resulting from the other two beam combinations by a 80 to 110 MHz band pass filter and is then downmixed prior to processing. As mentioned above, it is possible to determine the  $W$  component using the top-center and bottom-center beam combinations.

Measurement of the on-axis component of velocity,  $V$ , requires the center beam. This component is measured as the projection on the optical axis of the vector difference of the velocity seen by the top-center combination and that seen by the center-bottom combination (Fig. 1). Since the center beam is not frequency shifted, the signal generated by the combination of the top and center beams has a frequency:

$$f_1 = f_{st} - \mathbf{V} \cdot \frac{\mathbf{n}_1}{d} \quad (1)$$

where  $\mathbf{V}$  is the local velocity vector,  $\mathbf{n}_1$  is the unit vector normal to the bisector of the top and center beams, and  $d$  is the fringe spacing of the interference pattern created by the top and center beams. Note that since we have assumed the system to be perfectly aligned, the fringe spacing of the top and center beam

## Nomenclature

$a, b, c$  = coefficient indicating contribution of  $U, V$ , and  $W$  to  $V_m$   
 $d$  = fringe spacing  
 $d_o$  = equivalent virtual fringe spacing of on-axis component  
 $d_v$  = virtual fringe spacing of misaligned system  
 $f$  = doppler frequency sent to the signal processor  
 $f_D$  = a difference frequency,  $f_1 - f_2$   
 $f_s$  = a bragg cell shift frequency  
 $\mathbf{n}$  = a unit vector  
 $n_x, n_y, n_z$  = orthogonal components of a general unit vector,  $\mathbf{n}_v$

$U, V, W$  = the  $x, y$ , and  $z$  components of velocity (Fig. 1)  
 $u, v, w$  = velocity fluctuations from mean of each component  
 $\mathbf{V}$  = a general velocity vector  
 $V_m, v_m$  = measured on-axis velocity and velocity fluctuation from measured mean  
 $\alpha$  = angle between  $y$ - $z$  plane projection of a general vector,  $\mathbf{V}$ , and the  $y$  axis (Fig. 2)  
 $\epsilon$  and  $\epsilon'$  = small centerbeam misalignment angles (Fig. 3)  
 $\theta$  = angle from  $z$  axis to centerbeam (Fig. 3)  
 $\psi$  = angle from  $x$  axis to  $x$ - $y$  plane projection of centerbeam (Fig. 3)

$\kappa$  = angle between misaligned centerbeam and outerbeams  
 $\lambda$  = wavelength of light  
 $\phi$  = the half-angle between the outerbeams (Fig. 1)

## Subscripts

$b, c, t$  = bottom, center, and top beam quantity  
 $m$  = quantity measured by misaligned system  
 $1, 2$  = center-top beam component and center-bottom beam component quantities (Fig. 1)

## Other Symbols

$\bar{\quad}$  = mean quantity, overbar  
 $\underline{\quad}$  = vector quantity, underline



combination is equal to that of the center and bottom beam combination, therefore:

$$f_2 = f_{sb} - \frac{\mathbf{V}\mathbf{n}_2}{d} \quad (2)$$

where  $\mathbf{n}_2$  is the unit vector normal to the bisector of the center and bottom beams. Subtracting (2) from (1), we obtain:

$$f_D = f_1 - f_2 = f_{st} - f_{sb} - \frac{\mathbf{V}(\mathbf{n}_1 - \mathbf{n}_2)}{d}$$

After removing the composite shifting frequency ( $f_{st} - f_{sb}$ ) from the signal, the frequency sent to the signal processor,  $f$ , is obtained. Since,  $\mathbf{n}_1$  and  $\mathbf{n}_2$  have cosine directors ( $\pi/2 - \phi/2$ ) and ( $\pi/2 + \phi/2$ ), respectively, where  $\phi$  is the beam half-angle (Fig. 1), their vector difference has a magnitude equal to  $2\sin(\phi/2)$  and is directed along the optical axis. The frequency,  $f$ , sent to the processor is equal to:

$$f = \frac{2V\sin(\phi/2)}{d}$$

where the fringe spacing  $d$  is given by:

$$d = \frac{\lambda}{2\sin(\phi/2)}$$

with  $\lambda$ , the wavelength.

Thus the measured on-axis component of velocity is given by:

$$V_m = \frac{f\lambda}{4\sin^2(\phi/2)} = fd_0$$

where  $d_0$  is the equivalent or virtual fringe spacing of the on axis component. This virtual fringe spacing is larger than the fringe spacing in the top-bottom beam  $W$  component dual beam system by a factor  $\sin(\phi)/(2\sin^2(\phi/2))$  or by a factor of 14.7 in the system used in our laboratory with  $\phi = 7.79$  deg. As can be seen,  $V_m$  critically depends on the correct estimation of the beam half-angle  $\phi$ , especially when this angle is small. Assuming all other contributions to  $V_m$  are kept constant, a small error  $d\phi$  leads to an error in  $V_m$  equal to  $dV_m$ :

$$dV_m = \frac{f\lambda}{2} \frac{\cos\phi/2}{\sin^3\phi/2} d\phi \sim \frac{d\phi/2}{\sin^3\phi/2}$$

Thus,  $dV_m$  can be very large since  $\phi$  is small. This result shows not only the importance of a correct alignment of the outer beams, it also emphasizes the need for careful calibration of the beam angles. The next section shows that nearly perfect alignment of the center laser beam is essential for a proper operation of the system. Since perfect alignment of the center beam is never the case, it is necessary to accurately evaluate its orientation and to take it into account for the calibration of the on-axis component of velocity.

### 3 Systematic Error Due to Misalignment of the Center Beam

**3.1 Influence on Instantaneous Velocity.** In the following, it is assumed that the outer beams are correctly aligned and that all three beams cross at the same point, a requirement which must be satisfied to produce a fringe pattern. Therefore, an adequate Doppler signal is generated when a particle passes through the probe volume.

The misalignment of the center beam is characterized by the orientation of the unit vector in the direction of the center beam. The definition of angles and orientation of the axes is shown on Figs. 1 and 2. The angle  $\phi$  lies between the properly aligned top and bottom beams and the  $y$  axis. The angles  $\theta$  and  $\psi$  describe the center beam misalignment.

The unit vectors  $\mathbf{n}_t$  and  $\mathbf{n}_b$  characterizing the top and bottom beams have the components:

$$\mathbf{n}_t = (0, \cos\phi, -\sin\phi)$$

and

$$\mathbf{n}_b = (0, \cos\phi, \sin\phi)$$

The unit vector characterizing the direction of the center beam is given by:

$$\mathbf{n}_c = (\sin\theta\cos\psi, \sin\theta\sin\psi, \cos\theta)$$

As in the previous section, all quantities related to the top and center beam combination are subscripted by 1, and all those related to the center and bottom beam combination are subscripted by 2. The unit vectors of the velocities measured by these beam pairs,  $\mathbf{n}_1$  and  $\mathbf{n}_2$ , are:

$$\mathbf{n}_1 = \frac{\mathbf{n}_c - \mathbf{n}_t}{\|\mathbf{n}_c - \mathbf{n}_t\|} = \frac{(\sin\theta\cos\psi, \sin\theta\sin\psi - \cos\phi, \cos\theta + \sin\phi)}{\sqrt{2(1 - \sin\theta\cos\psi\cos\phi + \cos\theta\sin\phi)}}$$

$$\mathbf{n}_2 = \frac{\mathbf{n}_b - \mathbf{n}_c}{\|\mathbf{n}_b - \mathbf{n}_c\|} = \frac{(-\sin\theta\cos\psi, \cos\phi - \sin\theta\sin\psi, \sin\phi - \cos\theta)}{\sqrt{2(1 - \sin\theta\sin\psi\cos\phi - \cos\theta\sin\phi)}}$$

The angle between  $\mathbf{n}_c$  and  $\mathbf{n}_1$ ,  $\kappa_1$ , is expressed as:

$$\cos(\kappa_1) = \cos(\mathbf{n}_c, \mathbf{n}_1) = \cos\phi\sin\theta\sin\psi - \sin\phi\cos\theta$$

Similarly, the angle between  $\mathbf{n}_b$  and  $\mathbf{n}_c$  is given by:

$$\cos(\kappa_2) = \cos(\mathbf{n}_b, \mathbf{n}_c) = \cos\phi\sin\theta\sin\psi + \sin\phi\cos\theta$$

The interference pattern created by the top and center beams in the probe volume has a fringe spacing  $d_1$ :

$$d_1 = \frac{\lambda}{2\sin(\kappa_1/2)} = \frac{\lambda}{\sqrt{2(1 - \cos\phi\sin\theta\sin\psi + \cos\theta\sin\phi)}}$$

and similarly:

$$d_2 = \frac{\lambda}{2\sin(\kappa_2/2)} = \frac{\lambda}{\sqrt{2(1 - \cos\phi\sin\theta\sin\psi - \cos\theta\sin\phi)}}$$

The combined Doppler frequency for some velocity vector  $\mathbf{V} = U\mathbf{i} + V\mathbf{j} + W\mathbf{k}$  from Eqs. (1) and (2) is:

$$f_1 - f_2 = (f_{st} - f_{sb}) - \mathbf{V} \cdot \left( \frac{\mathbf{n}_1}{d_1} - \frac{\mathbf{n}_2}{d_2} \right)$$

which after downmixing with the frequency ( $f_{st} - f_{sb}$ ) results in the frequency  $f$  which is sent to the processor:

$$f = \mathbf{V} \cdot \left( \frac{\mathbf{n}_1}{d_1} - \frac{\mathbf{n}_2}{d_2} \right)$$

If we define the quantities  $d_v$  and  $n_v$  as follows:

$$d_v = \left\| \frac{\mathbf{n}_1}{d_1} - \frac{\mathbf{n}_2}{d_2} \right\| = \frac{2}{\lambda} \sqrt{1 - 2\cos\phi\sin\theta\sin\psi + \cos^2\phi}$$

and:

$$\mathbf{n}_v = d_v \left( \frac{\mathbf{n}_1}{d_1} - \frac{\mathbf{n}_2}{d_2} \right) = \frac{2d_v}{\lambda} (\sin\theta\cos\psi, \sin\theta\sin\psi - \cos\phi, \cos\theta)$$

then the usual expression for the Doppler frequency results:

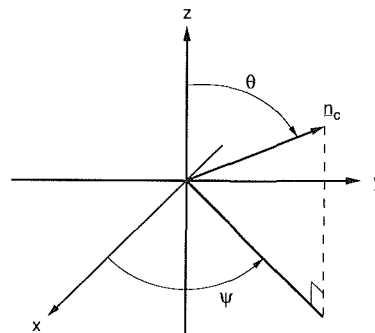


Fig. 2 Definition of angles describing a misaligned center beam. Misalignment is exaggerated for illustration purposes.

$$f = \frac{\mathbf{V} \cdot \mathbf{n}_v}{d_v}$$

These expressions show that  $d_v$  can be considered as the “virtual” fringe spacing of the misaligned system, while  $\mathbf{n}_v$  is the direction of the velocity component actually measured and has orthogonal components  $n_x$ ,  $n_y$ , and  $n_z$ . The measured frequency is equal to:

$$f = \frac{n_x U + n_y V + n_z W}{d_v} \quad (3)$$

If beam misalignment is ignored, then the fringe spacing used for the calculation of velocity is  $d_o$ :

$$d_o = \frac{\lambda}{4 \sin^2(\phi/2)}$$

so that the on-axis velocity component is measured as  $V_m$ :

$$V_m = f d_o$$

Replacing  $f$  by its value in (3), we find:

$$V_m = \frac{n_x U + n_y V + n_z W}{d_v} d_o \quad (4)$$

This equation shows that the apparent on-axis velocity component  $V_m$  depends linearly on the actual components of velocity  $U$ ,  $V$ , and  $W$ , with coefficients:

$$a = n_x \frac{d_o}{d_v}, \quad b = n_y \frac{d_o}{d_v} \quad \text{and} \quad c = n_z \frac{d_o}{d_v}$$

Replacing  $\mathbf{n}_v$ ,  $d_o$  and  $d_v$  by their expressions as functions of  $\phi$ ,  $\theta$ , and  $\psi$ , we find the following relations:

$$a = \frac{\sin \theta \cos \psi}{2 \sin^2 \phi / 2}$$

$$b = \frac{\sin \theta \sin \psi - \cos \phi}{2 \sin^2 \phi / 2}$$

$$c = \frac{\cos \theta}{2 \sin^2 \phi / 2}$$

For small misalignments,  $\theta = \pi/2 + \epsilon$  and  $\psi = \pi/2 + \epsilon'$ , so that  $a$ ,  $b$ , and  $c$  are:

$$\begin{aligned} a &= \frac{-\epsilon'}{2 \sin^2 \phi / 2} \\ b &= 1 \\ c &= \frac{-\epsilon}{2 \sin^2 \phi / 2} \end{aligned} \quad (5)$$

Then, to order  $0(\epsilon^2, \epsilon'^2)$   $a$  and  $c$  are linear functions of the misalignment angles  $\epsilon$  and  $\epsilon'$ .

The LDV system evaluated in our laboratory uses a half-angle of  $\phi = 7.79$  deg, which gives for a misalignment  $\epsilon = \epsilon' = 0.1$  deg,  $a = c = 0.189$ ,  $b = 1.0$ . In most applications, the optical axis of the LDV system is nearly perpendicular to the flow velocity and  $U$  or  $W$  are the dominant velocity components. Thus, the effect of misalignment is not negligible; a misalignment of only 0.1 deg in each direction leads to measuring the following apparent on-axis velocity:

$$V_m = 0.189 U + V + 0.189 W$$

Since  $V$  often has a mean value near zero and either  $U$  or  $W$  are relatively large, the error is often substantial.

**3.2 Influence on Velocity Statistics.** When the flow is turbulent, the ensemble average of the velocity of individual particles over a large number of realizations is used to obtain statistical quantities, such as mean velocity and turbulent stresses. Because of the linearity of the averaging operator,

the mean velocity  $\bar{V}$  is affected by misalignment errors in the same manner as the instantaneous velocity  $V$ . However, higher order statistical moments do not in general depend linearly on the instantaneous velocity. Using the relations determined in the previous section, one can derive expressions providing the correct values of the velocity statistics as functions of the measured velocity statistics.

To avoid unnecessary algebra, the simple case of a turbulent pipe flow is considered.  $U$  is the streamwise velocity component,  $V$ , the radial velocity component and,  $W$ , the circumferential velocity component. Taking the average of Eq. (4), we obtain for the measured on axis component of velocity:

$$\bar{V}_m = a \bar{U} + b \bar{V} + c \bar{W}$$

Since  $a$ ,  $b$ , and  $c$  are deterministic quantities, we can write:

$$\bar{V}_m = a \bar{U} + b \bar{V} + c \bar{W}$$

But in pipe flow, the mean radial and circumferential velocities are zero, so that:

$$\bar{V}_m = a \bar{U} \quad (6)$$

The fluctuating part of the measured radial velocity component  $V_m$  can be expressed as:

$$v_m = V_m - \bar{V}_m = au + bv + cw,$$

where,  $u$ ,  $v$ , and  $w$  are the fluctuating parts of the actual velocity components  $U$ ,  $V$ , and  $W$ . The variance of  $v_m$  can then be evaluated as:

$$\overline{v_m^2} = \overline{(au + bv + cw)^2}$$

which yields, after taking into account the various symmetries of the flow:

$$\overline{v_m^2} = a^2 \overline{u^2} + b^2 \overline{v^2} + c^2 \overline{w^2} + 2ac \overline{uw}$$

Since  $a$  and  $c$  are first-order functions of the misalignment angles, the systematic error involved in the measurement of  $\overline{v_m^2}$  is of second order. Assuming, as a simple example, that all normal stresses are approximately equal to the shear stress with  $\epsilon = \epsilon' = 0.1$  deg then the systematic error in  $\overline{v_m^2}$  is about 14 percent.

Similar calculations lead to the following expressions for the turbulent stresses in the pipe flow:

$$\begin{aligned} \overline{uv_m} &= a \overline{u^2} + b \overline{uv} \\ \overline{wv_m} &= c \overline{w^2} \end{aligned} \quad (7)$$

In a pipe flow,  $\overline{u^2}$  is usually much larger than  $\overline{uv}$  (Laufer, 1954). The worst case occurs close to the wall at  $y^+ = 15$  where  $\overline{uv}/u_\tau^2 = 0.6$ ,  $\overline{u^2}/u_\tau^2 = 8$  thus  $\overline{u^2} = 13 \overline{uv}$  and the measured Reynolds stress  $\overline{uv_m}$  can be as large as  $\overline{uv_m} = (13a + b) \overline{uv} = 3.5 \overline{uv}$  for  $\epsilon = \epsilon' = 0.1$  deg. Of course, noise and error are random factors that will reduce the correlation between any two velocity components and this could offset or reduce the effects of misalignment on the Reynold shear stress results. Therefore, fortuitous near agreement between measured and expected results is possible in a misaligned system and careful consideration of the results is essential.

The above analysis is easily extended to the general case. The results are of the same nature. This must be primary concern when turbulent quantities are measured in a strongly three-dimensional flow. In such a case, unless appropriate corrections are used, the measured velocity correlations can be in serious error. In practice, alignment of a 3D LDV system is a time-consuming process, and some misalignment of the beams seems inevitable. The only efficient way to avoid problems seems to be to accurately calibrate the device.

**3.3 Calibration of the Beam Angles.** The results of the two previous sections emphasize the need for calibration of a five-beam, two color system. Various calibration schemes have been proposed. One of the most common techniques involves the use of a rotating wheel (e.g., Snyder et al., 1984). Another

technique was suggested by Boutier and Lefevre (1986), and makes use of a theodolite to measure the beam angles. A theodolite is an instrument used by surveyors to measure orthogonal angles with great accuracy (as high as  $6 \times 10^{-5}$  degrees). This technique has the advantage over the other schemes in that it directly measures the primary parameters of the LV system (beam angles), rather than the secondary parameters (elements of the rotation matrix). By using this method, the real on-axis velocity component can be computed directly and no correction to the system is necessary. Other sources of systematic errors can then be treated separately.

In many simple flows such as a pipe flow, only one mean velocity component and one Reynolds shear stress term will be nonzero. Such flows can be used to evaluate system alignment but this does not solve the problem of achieving alignment. Dealing with the misalignment may be a more practical alternative. If other sources of systematic errors can be neglected, it is possible to use a rotating wheel or a simple flow to check the values of the misalignment angles. For the pipe flow case, since the streamwise and circumferential velocities are not affected by misalignment of the center beam, Eq. (6) can be used to compute the error coefficient  $a$ , while Eq. (7) can be used to compute the error coefficient  $c$ . These quantities can then be compared to those obtained by using Eq. (5) directly, with  $\epsilon$  and  $\epsilon'$  given by the measurement of the beam angles.

#### 4 Random Error on the On-Axis Component

The value of the beam half-angle  $\phi$  has a great potential influence on the random measurement error. Meyers (1988) simulated a Doppler burst signal and how it is processed by a counter processor for a range of signal bandwidths and amplitudes and a fixed high visibility. The results of this simulation indicate that the random error increases nearly in direct proportion to the fringe spacing. The virtual fringe spacing of the on axis component increases as  $1/\sin^2(\phi/2)$  and is large for the present five-beam system.

A simple analysis of the five-beam system itself shows some specific limitations of the system for on axis turbulence measurements. The LDV set-up is the same as in the previous section and the system is assumed to be aligned. In the absence of frequency shift, the expressions for the velocity components  $W$  and  $V$  are as follows:

$$\begin{aligned} W &= \|\mathbf{V}\| \sin \alpha \\ V &= \|\mathbf{V}\| \cos \alpha \end{aligned} \quad (8)$$

where  $\alpha$  is the angle between the velocity vector  $\mathbf{V}$  and the  $y$  axis which is also the optical axis of the system in the  $y$ - $z$  plane (Fig. 3). In this case  $\mathbf{V}$  is the projection of a general 3D velocity vector onto the  $y$ - $z$  plane. With the beams perfectly aligned, the velocities actually measured are  $V_1$  and  $V_2$  and are given by:

$$\begin{aligned} V_1 &= \|\mathbf{V}\| \sin(\alpha + \phi/2) \\ V_2 &= \|\mathbf{V}\| \sin(\alpha - \phi/2) \end{aligned} \quad (9)$$

Eliminating  $\|\mathbf{V}\|$  between (8) and (9) gives the following expression for the on-axis component,  $V$ :

$$V = \frac{V_1 - V_2}{2 \sin(\phi/2)} \quad (10)$$

Expression (10) for the on-axis component is the same as with the system considered by Neti and Clark (1979). Since  $V_1$  and  $V_2$  are determined by the same process their relative accuracies are the same and the fractional error in the on-axis component is, from Neti and Clark (1979):

$$\frac{dV}{V} = \frac{dV_1}{V_1 \sqrt{2} [(V/W) \tan(\phi/2)]} \quad (11)$$

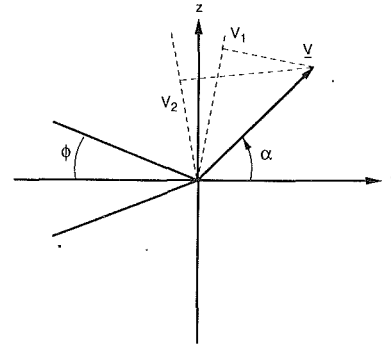


Fig. 3 Definition of angles for the random error analysis

Thus, the relative accuracy of the on axis  $V$  component of velocity is degraded by small  $\phi$  and small  $V/W$ . As an approximation, the relative accuracy of the various fringe mode measurements of the five beam system should be comparable within reasonable limits so that  $dV_1/V_1 \approx dU/U \approx dW/W$ . For a case when the  $V$  and  $W$  components are similar in magnitude,  $V/W \approx 1$ , the relative error in the on axis component is larger than the error in the other components by factor of  $[\sqrt{2} \tan(\phi/2)]^{-1}$ . This result is independent of the type of signal processor used and the same deviations of the measured result about a mean value would occur with any signal processor provided other factors such as signal to noise ratio and bandwidth are appropriate to the processor.

The LDV system used by Chevrin (1988) in a pipe flow had a beam half-angle of  $\phi = 7.79$  deg and was oriented so that the mean  $V$  and  $W$  were the same. Therefore, from expression (11) the relative accuracy on the on-axis component is expected to be 10.4 times as large as with other velocity components. An experimental check of this result was made using the three-component LDV in the center region of a laminar pipe flow. The small velocity gradient in this region guarantees no occurrence of velocity gradient broadening. A complete description of the experimental setup is given in Chevrin et al. (1989). The mean velocity in the tunnel was close to 5 m/s and the working fluid was glycerin. The turbulence intensity of the streamwise velocity component,  $U$ , and circumferential velocity components,  $W$ , nondimensionalized with mean streamwise velocity were between 0.5 percent and 0.6 percent. This value is typical of the noise of a one-component backscatter system equipped with a counter-type processor, when it is used to measure moderate velocities in liquids. The measured turbulence intensity in the on-axis component was slightly more than 5 percent, or approximately ten times as large as the other components. This experimentally observed increase in uncertainty agrees well with the expected result.

#### 5 Conclusions

Three-component LV systems using a single lens five-beam approach are sensitive to errors in the half angle and misalignment of the center beam. This is particularly true when the Reynolds stress tensor must be measured. It was shown in this paper that large errors can be introduced, even with misalignment angles as small as 0.1 deg. The only way to eliminate this error is to explicitly take into account the misalignment angles after an accurate calibration procedure.

The evaluation of the random error for this three-component LV system indicates that the relative uncertainty of the on-axis component of velocity is much worse than on the two other components and an estimate of the uncertainty is given. In practice, the relative accuracy in laminar flow was observed to be ten times that of the other components which is in good agreement with the uncertainty estimate. Although this result

emphasizes the limitations inherent in the use of such a system for the measurement of turbulence quantities, the system may still be useful, in a number of scenarios, for researchers who are aware of its limitations and how to estimate and correct for them.

## References

- Bell, J. H., Rodman, L. C., and Metha, R. D., 1985, "Aspects of the Design and Performance of a 3-Component LDV System," ICIASF.
- Bouties, A., 1987, "Three Dimensional Laser Velocimeter Systems," LDA International Conference, Glasgow, UK.
- Boutier, A., and Lefevre, J., 1986, "Accurate Calibration of 3D Fringe Laser Velocimeters with a Theodolite," *3rd Symposium on Applications of Laser Anemometry to Fluid Mechanics*, Lisbon, Portugal.
- Buchhave, P., "Three-Component LDA Measurements," DISA Information, July 1983.
- Chevrin, P. A., Petrie, H., and Deutsch, S., 1989, "Measurement of Spatial Correlations in the Near-Wall Region of a Fully Developed Turbulent Pipe Flow by LDV," 3rd International Conference on Laser Anemometry, Swansea, UK.
- Laufer, J., 1954, "The Structure of Turbulence in Fully Developed Pipe Flow," NBS Report No. 1174.
- Menon, R. K., 1986, "Three-Component Velocity Measurement using LDV," *Flow Lines-TSI Magazine*, Fall, 1986.
- Meyers, J. F., 1988, "Laser Velocimetry: The Elusive Third Component," *Finite Elements in Analysis and Design*, Vol. 4, pp. 51-64.
- Meyers, J. F., and Hepner, T. E., 1984, "Velocity Vector Analysis in a Juncture Flow Using a Three-Component Laser Velocimeter," *Proceedings of the Second International Symposium on Applications of Laser Anemometry to Fluid Mechanics*, Lisbon, Portugal.
- Neti, S., and Clark, W., 1979, "On-Axis Velocity Component Measurement with Laser Velocimeters," *AIAA Journal*, Vol. 17, No. 9, pp. 1013-1015.
- Orloff, K. L., and Snyder, P. K., 1982, "Laser Anemometer Measurements Using Nonorthogonal Velocity Components: Error Estimates," *Applied Optics*, Vol. 21, No. 2, pp. 339-344.
- Ozcan, O., 1987, "Description and Measurement Accuracy of a 3D LDA System," ASME Applied Mechanics, Bioengineering and Fluids Engineering Conference, Cincinnati, Ohio, eds. R. A. Bajura and M. L. Billet.
- Schock, H. J., Regan, C. A., Rice, W. J., and Chlebeck, R. A., 1983, "Multicomponent Velocity Measurements in a Piston-Cylinder Configuration Using Laser Velocimetry," *TSI Quarterly*, Vol. 9, Issue 4.
- Snyder, P. K., Orloff, K. L., and Reinath, M. S., 1984, "Reduction of Flow Uncertainties in Laser Velocimeters with Nonorthogonal Components," *AIAA Journal*, Vol. 22, No. 8, pp. 1115-1123.

J. John  
Graduate Research Assistant.

T. Schobeiri  
Associate Professor,  
Turbomachinery Committee.  
Mem. ASME

Turbomachinery Laboratory,  
Department of Mechanical Engineering,  
Texas A&M University,  
College Station, Texas, 77843-3123

# A Simple and Accurate Method of Calibrating X-Probes

*This paper presents an improved method of calibrating hot-film X-probes in incompressible flow. The yaw response of a hot-film X-probe was investigated for different velocities and found to be strongly velocity dependent at low velocities. A simple relation was developed to correct for the variation of yaw response at low velocities. The method using the yaw correction is compared with the single-velocity yaw calibration method. The correction to the yaw response considerably improves accuracy at low velocities.*

## Introduction

X-probes are widely used for measuring two components of the flow velocity. Various methods are employed for interpreting the signals from two sensor probes and almost all methods relate the output voltage to the effective cooling velocity  $V_e$ . The effective velocity is related to the actual flow velocity  $V$  in different forms. The most accurate representation of the directional response of a hot-wire or hot-film

$$V_e^2 = V_N^2 + k^2 V_T^2 \quad (1)$$

was introduced by Hinze (1959) and Champagne et al. (1967). This equation takes into account the cooling due to both normal and tangential velocity components. Webster (1962) experimentally found the values of  $k$  for various  $l/d$  ratios for a single hot-wire sensor. Jorgensen (1971) investigated the dependence of  $k$  on yaw angle and found that the value of  $k$  varies with the yaw angle. Bradshaw (1971) introduced a calibration method based on an effective angle defined as:

$$V_e = V \cos \alpha_e \quad (2)$$

Brunn et al. (1990) used a conventional calibration method with a constant  $k$ -factor in Eq. (1) and compared it with Bradshaw's method, which is based on Eq. (2). As a result, Brunn showed that the conventional method based on Eq. (1) gives the smallest error over the complete angle range.

Lekakis (1988) obtained the  $k$  values at a given velocity from a yaw calibration and found that a constant value for  $k$ , determined by a least square-fit of all  $k$  values, provides a good representation of the probe angular response. In a similar way, he determined the value of  $k$  for different velocities. Using the above  $k$  values, Lekakis developed an analytical method for the calculation of the velocity and its components.

The use of constant  $k$  at a given velocity, which is common to the previously described methods, introduces significant errors particularly at higher yaw angles. Schröder (1985) employed a simple calibration method by introducing an ideal flow angle, for which  $k$  was equal to zero and applied the method to X-hot-wire probes. A yaw calibration covering the entire angle range was performed at a single velocity. Com-

pared to constant  $k$ -factor based methods, the method by Schröder was more accurate to a wide range of yaw angles ( $-40 \text{ deg} < \alpha < 40 \text{ deg}$ ). A more detailed description of this method is given later.

Another alternative to reduce calibration errors is to utilize a full-range velocity-angle calibration technique in conjunction with look-up tables. Such a calibration technique was first introduced by Willmarth and Bogar (1977), further developed by Johnson and Eckelmann (1984) and Leuptow et al. (1988), and modified by Browne et al. (1989). The generation of such tables as a result of a full-range velocity-angle calibration, however, requires a significant amount of calibration time and effort. Furthermore, the implementation of the above tables into a corresponding data reduction and analysis program necessitates excessive computational overhead particularly in connection with unsteady flow measurements. This situation motivated the authors to develop a simple method that significantly reduces the calibration time and accounts for high accuracy. The need for developing such a method was particularly indicated for flow situations, where the angle as well as the velocity undergo significant changes. Such situations are frequently encountered in turbomachinery wake flows immediately downstream of the stator or rotor trailing edge plane. Similar flow situations are also observed in wakes immediately downstream of a stationary or rotating cylinder.

This paper presents an improved yaw calibration technique based on the ideal flow angle previously mentioned. A correction procedure is introduced which allows accurate measurement at lower velocities. The calibration technique is applicable to X-hot-wire and hot-film probes; however, the measurements presented in this paper were performed with a hot-film probe.

## Description of Calibration Facility

The calibration was performed in a uniform low-turbulence jet issuing from a nozzle with an area ratio of 16. A schematic of the calibration facility is shown in Fig. 1. Compressed air from an air supply passes through a pressure regulator, filter and a flow control valve and enters a settling chamber and a pipe consisting of three segments with a diameter of 150 mm. The nozzle, with an outlet diameter of 38.1 mm, is attached

Contributed by the Fluids Engineering Division for publication in the JOURNAL OF FLUIDS ENGINEERING. Manuscript received by the Fluids Engineering Division October 30, 1991. Associate Technical Editor: D. M. Bushnell.

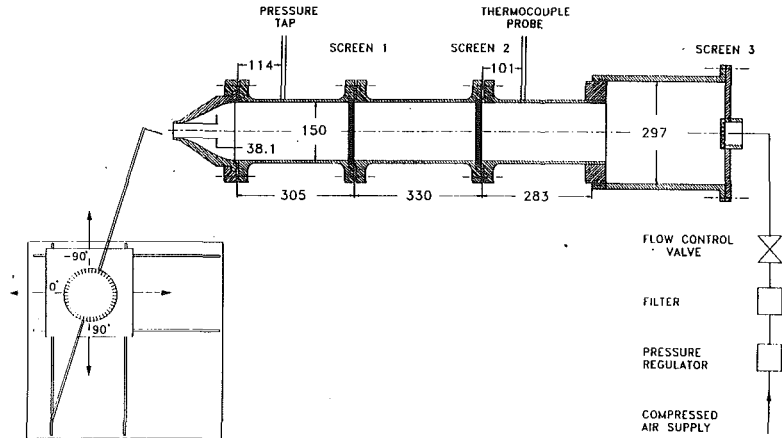


Fig. 1 Calibration set-up for X-probe calibration, dimensions in mm

to the exit of the pipe. Screens are located between flanges of pipe sections to reduce the turbulence level, which is about 0.35 percent at the measuring location. The pressure drop across the nozzle is measured using a high precision differential pressure transducer and the air temperature is measured by a thermocouple located upstream of the nozzle. Calibration measurements were performed with an X-hot-film probe, which was connected to the two channels of a TSI IFA 100 constant temperature anemometer system. The diameter of the platinum hot-film sensor was  $25 \mu\text{m}$  with the two sensors separated by a distance of approximately 1 mm. The sensors were operated at an overheat ratio of 1.5. The analog signals from the pressure transducer, thermocouple and hot-film anemometer were transferred to the input channels of an A/D board plugged into the expansion slot of a personal computer, which is used for the data acquisition and analysis.

The probe geometry, the flow velocity  $V$  and direction  $\alpha$  as well as the components  $V_x$  and  $V_y$  are shown in Fig. 2. Each of the sensors of the X-hot-film probe under investigation had an angle  $\alpha_s = 45$  deg to the X-axis. The components of the velocity  $V$  along and perpendicular to the probe axis are  $V_x$  and  $V_y$ , respectively.

### Description of Calibration Technique

A brief description of the calibration technique for a single freestream velocity is given in this section. It is followed by a description of the calibration procedure, a discussion of calibration uncertainty, and the yaw angle correction at different velocities.

**Calibration at Single Freestream Velocity, Equations.** The effective cooling velocity  $V_{ej}$  is approximated as a fourth-order polynomial function of the anemometer output voltage  $E_j$ .

$$V_{ej} = a_{0j} + a_{1j}E_j + a_{2j}E_j^2 + a_{3j}E_j^3 + a_{4j}E_j^4 \quad (3)$$

where the coefficients  $a_{ij}$  are obtained by a least-squares fit. The angle response equations for sensors 1 and 2 are derived from Eq. (1).

$$V_{e1}^2 = V^2[\sin^2(\alpha_s + \alpha) + k_1^2 \cos^2(\alpha_s + \alpha)] \quad (4)$$

$$V_{e2}^2 = V^2[\sin^2(\alpha_s - \alpha) + k_2^2 \cos^2(\alpha_s - \alpha)] \quad (5)$$

$V_{e1}$  and  $V_{e2}$  are the effective cooling velocities and  $k_1$  and  $k_2$  are the yaw coefficients for sensors 1 and 2. As mentioned in the introduction, Schröder (1985) defined an ideal angle  $\alpha_{id}$  for which  $k_j$  is equal to zero. Applying this definition to Eqs. (4) and (5) leads to

### Nomenclature

$a_{ij}$  = coefficients of polynomial for sensor  $j$  in Eq. (3)  
 $b_i$  = coefficients of polynomial in Eq. (9)  
 $c_i$  = coefficients of polynomial in Eq. (10)  
 $d_i$  = coefficients of polynomial in Eq. (12)  
 $d$  = diameter of hot-wire or hot-film  
 $e_i$  = coefficients of polynomial in Eq. (17)  
 $E_b$  = anemometer bridge output voltage  
 $E_i$  = anemometer output voltage of sensor  $j$  after temperature compensation  
 $E_{mj}$  = measured anemometer output voltage of sensor  $j$   
 $H$  = yaw calibration function defined by Eq. (8)  
 $H^*$  = modified yaw calibration function defined by Eq. (11)

$k$  = yaw sensitivity coefficient to account for tangential cooling  
 $k_j$  = yaw sensitivity coefficient of sensor  $j$   
 $l$  = length of hot-wire or hot-film  
 $m$  = yaw correction parameter in Eq. (16)  
 $n$  = exponent in the modified King's law relationship  
 $T$  = temperature of fluid  
 $T_s$  = operating temperature of sensor  
 $T_c$  = temperature of fluid at calibration  
 $V$  = resultant velocity  
 $V_{ej}$  = effective velocity of sensor  $j$   
 $V_N$  = velocity component normal to sensor  
 $V_T$  = velocity component tangential to sensor  
 $V_x$  = velocity component along X-axis

$V_y$  = velocity component along Y-axis  
 $\alpha$  = angle between resultant velocity vector and X-axis  
 $\alpha_e$  = effective angle  
 $\alpha_{id}$  = yaw calibration function defined by Eq. (6) or (7)  
 $\alpha_s$  = angle between wire and X-axis  
 $\Delta Q$  = uncertainty in quantity  $Q$ ;  $Q = V, V_e, \alpha_{id}$  or  $H^*$   
 $\Delta\alpha$  = difference between actual and calculated  $\alpha$   
 $\epsilon_V$  = percentage deviation of  $V$   
 $\epsilon_{V_x}$  = percentage deviation of  $V_x$   
 $\epsilon_{V_y}$  = percentage deviation of  $V_y$

### Subscripts

$a$  = actual  
 $c$  = calculated  
 $i$  = index for the coefficients  
 $j$  = index for the sensor,  $j = 1, 2$   
 $\text{max}$  = maximum

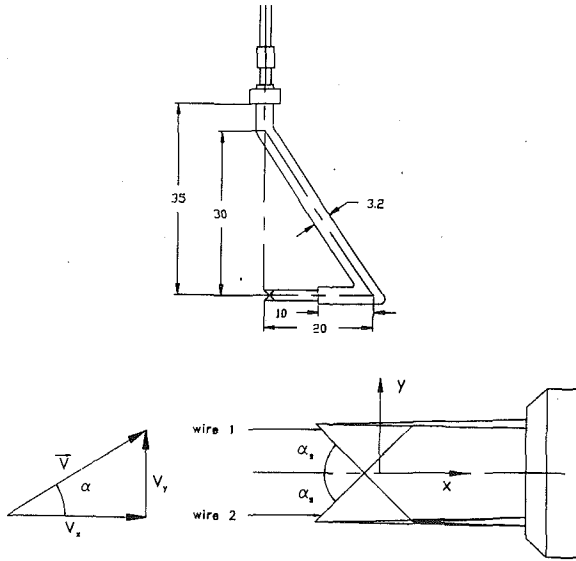


Fig. 2 Probe geometry and flow coordinates, dimensions in mm

$$\alpha_{id} = \tan^{-1} \left( \frac{V_{e1} - V_{e2}}{V_{e1} + V_{e2}} \tan \alpha_s \right) \quad (6)$$

For probes with  $\alpha_s = 45$  deg, Eq. (6) can be written as:

$$\alpha_{id} = \tan^{-1} \left( \frac{V_{e1}}{V_{e2}} \right) - 45 \quad (7)$$

Schröder also introduced a nondimensional parameter  $H$  that relates the effective cooling velocities to the actual velocity. It is defined by:

$$H = \frac{V^2}{V_{e1}^2 + V_{e2}^2} \quad (8)$$

The yaw angle calibration determines the values of  $\alpha_{id}$  and  $H$  for various  $\alpha$ .  $H$  and  $\alpha$  are represented by a fifth-order polynomial function of  $\alpha_{id}$  by a least-squares fit. i.e.,

$$H = b_0 + b_1 \alpha_{id} + b_2 \alpha_{id}^2 + b_3 \alpha_{id}^3 + b_4 \alpha_{id}^4 + b_5 \alpha_{id}^5 \quad (9)$$

$$\alpha = c_0 + c_1 \alpha_{id} + c_2 \alpha_{id}^2 + c_3 \alpha_{id}^3 + c_4 \alpha_{id}^4 + c_5 \alpha_{id}^5 \quad (10)$$

In order to increase the curve fit accuracy we introduced a new function  $H^*$  defined by:

$$H^* = \frac{V \cos \alpha}{\sqrt{V_{e1}^2 + V_{e2}^2}} \quad (11)$$

Similar to  $H$ , the new function  $H^*$  is also represented by a fifth order polynomial function of  $\alpha_{id}$ . i.e.,

$$H^* = d_0 + d_1 \alpha_{id} + d_2 \alpha_{id}^2 + d_3 \alpha_{id}^3 + d_4 \alpha_{id}^4 + d_5 \alpha_{id}^5 \quad (12)$$

The variation of  $\alpha$  with  $\alpha_{id}$  is shown in Fig. 3. The values of  $H$  and  $H^*$  are plotted against  $\alpha_{id}$  in Fig. 4. The solid lines in Figs. 3 and 4 show the fifth-order polynomial curve fit. As seen from Fig. 4, the function  $H^*$  gave lower scatter of data points compared to the function  $H$ . It can be seen from Fig. 3 that the difference between  $\alpha_{id}$  and  $\alpha$  is very high at higher absolute values of  $\alpha$ .

**Calibration Procedure.** The velocity calibration to obtain the coefficients of Eq. (3) for each of the sensors is done by keeping the sensors normal to the flow and varying the velocity. The yaw angle calibration is carried out for  $\alpha$  from  $-40$  deg to  $40$  deg at a constant velocity  $V$ . The function  $H^*$  and  $\alpha_{id}$  are calculated from Eqs. (11) and (7). The coefficients  $c_i$  in Eq. (10) and  $d_i$  in Eq. (12) are found by least-squares fit of  $\alpha_{id}$  against  $\alpha$  and  $H^*$ , respectively. The values of  $\alpha_{id}$  and  $H^*$  are found to have good reproducibility. As compared to  $\alpha_{id}$  and  $H^*$ , the coefficients of velocity calibration in Eq. (3) can

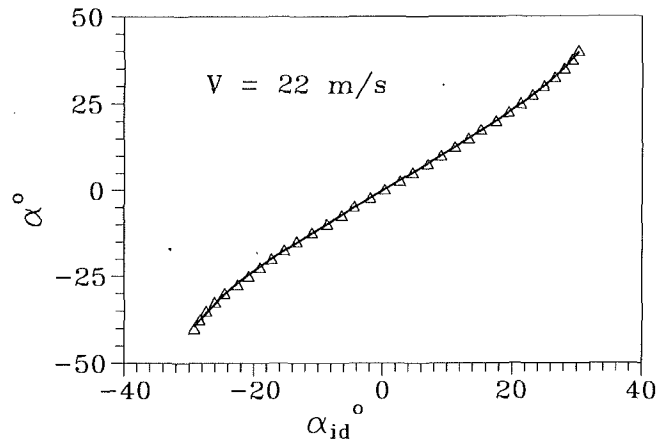


Fig. 3 Variation of  $\alpha$  with  $\alpha_{id}$  obtained from yaw calibration at 22 m/s. For uncertainty estimates see Table 1.

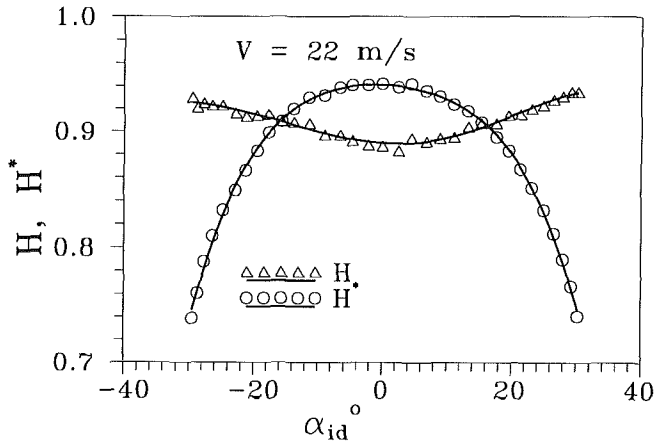


Fig. 4 Variation of  $H$  and  $H^*$  with  $\alpha_{id}$  obtained from yaw calibration at 22 m/s. For uncertainty estimates see Table 1.

drift and frequent calibration is essential. It is always preferable to perform the calibration in the test section where actual measurements are carried out. Many times the specific geometry of the test section and the probes makes it impossible to yaw the probe such that the sensors are normal to the flow. However, the velocity calibration can be conducted simultaneously for both the sensors at any angle  $\alpha$ , provided  $c_i$  and  $d_i$  are already determined by yaw angle calibration and the velocity  $V$  is known and can be varied. For a known angle  $\alpha$ ,  $\alpha_{id}$  is obtained from Eq. (10) using the Newton-Raphson method. The corresponding value of  $H^*$  is determined using Eq. (12). The effective cooling velocities are obtained from the following relations derived from Eqs. (7) and (11).

$$V_{e1} = \frac{V \cos \alpha \tan(\alpha_{id} + 45)}{H^* \sqrt{1 + \tan^2(\alpha_{id} + 45)}} \quad (13)$$

$$V_{e2} = \frac{V \cos \alpha}{H^* \sqrt{1 + \tan^2(\alpha_{id} + 45)}} \quad (14)$$

Velocity calibrations with  $\alpha = -45, 0$ , and  $+45$  deg are shown in Fig. 5. The flow velocity  $V$  is normal to sensors 1 and 2 when  $\alpha$  is  $+45$  and  $-45$  deg, respectively. The two calibration curves for each of the sensors are almost identical, which proves the validity of above mentioned calibration procedure.

**Calibration Uncertainty.** The calibration uncertainties of the various quantities are estimated according to the method suggested by Yavuzkurt (1984) which is based on the uncertainty analysis by Moffat (1982). The uncertainties for four different velocities are shown in Table 1. The main contribution to the uncertainty comes from the differential pressure trans-

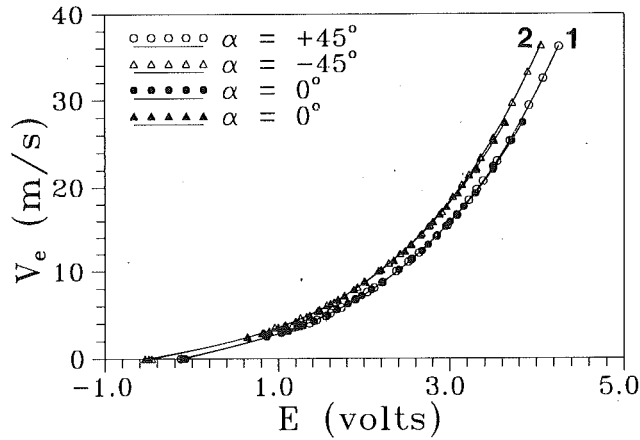


Fig. 5 Effective velocities of sensors 1 and 2. For uncertainty estimates see Table 1.

$V$ m/s	$\Delta V/V$ %	$\Delta V_e/V_e$ %	$\Delta \alpha_{id}/\alpha_{id}$ %	$\Delta H^*/H^*$ %
5	2.00	2.30	3.30	2.95
10	0.50	1.30	1.80	1.28
20	0.10	1.22	1.71	1.09
30	0.06	1.20	1.70	1.07

ducer which has an uncertainty of  $\pm 0.6$  Pa. However, significantly lower uncertainties can be achieved by using transducers or manometers with lower uncertainties.

**Yaw Calibration at Different Velocities and Yaw Angle Correction.** To investigate the effect of velocity on the yaw response, a yaw angle calibration was carried out at different velocities and the results are plotted in Fig. 6. Note that the value of  $\alpha_{id}$  varies with  $\alpha$  and velocity  $V$ . For a given  $\alpha$ , the variation of  $\alpha_{id}$  increases with decreasing velocity. The above variation is greater at a higher absolute value of  $\alpha$ . This can be explained in terms of the  $k$ -factors of each sensor. A preliminary investigation showed that for a given  $\alpha$ , the  $k$  remains almost constant for velocities above 17 m/s and for  $-20$  deg  $< \alpha < +20$  deg. Lekakis et al. (1989) found that  $k$  is constant for flow velocities higher than approximately 15–20 m/s. The relation between  $\alpha_{id}$  and  $k_1$  and  $k_2$  can be obtained from Eqs. (4), (5), and (7). i.e.,

$$\tan(\alpha_{id} + 45) = \frac{\sqrt{\sin^2(45 + \alpha) + k_1^2 \cos^2(45 + \alpha)}}{\sqrt{\sin^2(45 + \alpha) + k_2^2 \cos^2(45 - \alpha)}} \quad (15)$$

Since  $k_1$  and  $k_2$  are functions of  $V$  and  $\alpha$ , the left hand side of Eq. (15) is a function of  $V$  for a particular  $\alpha$ . Based on the assumption of a power law relationship between Eq. (15) and  $V$ , Eq. (16) can be derived to compensate for the deviation of  $\alpha_{id}$ . When using the result of yaw angle calibration at a velocity above 20 m/s to any other velocity below 15 m/s,  $\alpha_{id}$  was corrected using the following relation.

$$\frac{\tan(\alpha_{id}^* + 45)}{\tan(\alpha_{id} + 45)} = \left(\frac{V^*}{V}\right)^m \quad (16)$$

The superscript  $*$  denotes the quantities at the reference velocity at which the yaw angle calibration was carried out. The power  $m$  is a function of  $\alpha$  and can be least-square-fitted by a third-order polynomial as shown in Fig. 7. i.e.,

$$m = e_0 + e_1\alpha + e_2\alpha^2 + e_3\alpha^3 \quad (17)$$

Figure 7 was obtained using a reference velocity yaw angle calibration at 22 m/s and two other calibrations at 5 m/s and 10 m/s.

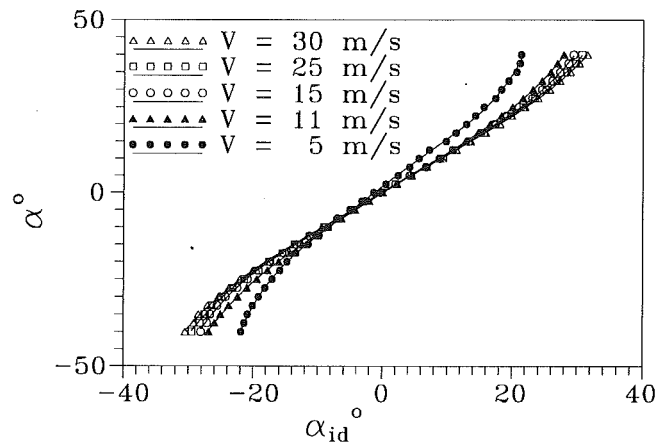


Fig. 6 Distribution of  $\alpha_{id}$  versus  $\alpha$  for different velocities. For uncertainty estimates see Table 1.

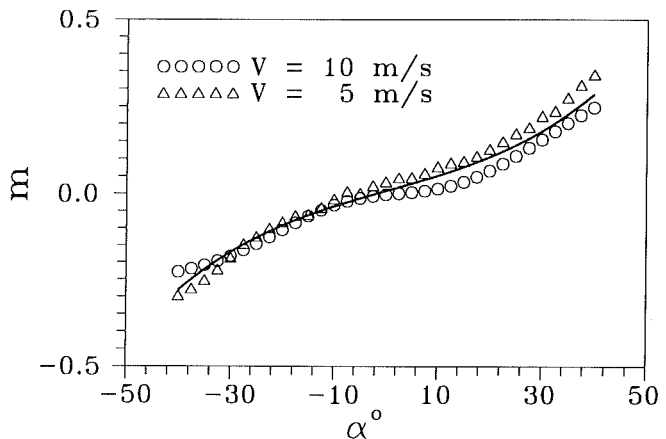


Fig. 7 Variation of yaw correction parameter  $m$  with  $\alpha$ . For uncertainty estimates see Table 1.

## Reduction Method

This section briefly describes the steps to calculate the velocity components from the voltage outputs of the two sensors obtained during an actual measurements. The first step is to compensate the anemometer output voltage  $E_{mj}$  of each sensor for the change in fluid temperature. An equation for temperature compensation is obtained from the modified form of King's law,  $E_b^2 = (A + B \cdot V^n)(T_s - T)$ . As shown by Lekakis (1988), the temperature dependency of the constants  $A$  and  $B$  can be neglected for a hot-film sensor of 25  $\mu\text{m}$  diameter at velocities above 1 m/s. This leads to a temperature compensation formula given by

$$E_j = E_{mj} \sqrt{\frac{T_s - T}{T_s - T_c}} \quad (18)$$

where  $T_s$ ,  $T_c$ , and  $T$  are the sensor operating temperature, calibration temperature and the temperature of the fluid during actual measurement, respectively. As a second step, the instantaneous effective velocities  $V_{e1}$  and  $V_{e2}$  are calculated from instantaneous temperature-compensated voltages using Eq. (3). The instantaneous value of  $\alpha_{id}$  is obtained from  $V_{e1}$  and  $V_{e2}$  using Eq. (7) while  $\alpha$  and  $H^*$  are calculated using Eq. (10) and Eq. (12). The magnitude of instantaneous velocity  $V$  is determined using Eq. (11) and its components  $V_x$  and  $V_y$  are calculated from its magnitude and direction  $\alpha$ .

If the velocity  $V$  is below 15 m/s,  $\alpha_{id}$  is corrected by Eq. (16) by using the yaw correction parameter  $m$  obtained from Eq. (17). From the new  $\alpha_{id}$ , instantaneous values of  $\alpha$ ,  $H^*$ , and  $V$  are computed again using Eqs. (10), (12), and (11),



**Table 2 Maximum deviation between actual and calculated values of velocities and angle for the case without yaw angle correction**

Angle $\alpha$ o	Velocity $V$ m/s	$\epsilon_{V_{max}}$ %	$\epsilon_{V_x, max}$ %	$\epsilon_{V_y, max}$ %	$\Delta\alpha_{max}$ o
-20-+20	20-30	1.3	1.2	3.0	.5
$\pm 20-\pm 30$	20-30	2.0	2.7	3.8	.9
-20-+20	10	1.3	1.5	8.0	1.9
$\pm 20-\pm 30$	10	1.1	3.9	10.0	3.5

**Table 3 Maximum deviation between actual and calculated values of velocities and angle for the case with yaw angle correction**

Angle $\alpha$ o	Velocity $V$ m/s	$\epsilon_{V_{max}}$ %	$\epsilon_{V_x, max}$ %	$\epsilon_{V_y, max}$ %	$\Delta\alpha_{max}$ o
-20-+20	10	1.25	1.27	3.0	.74
$\pm 20-\pm 30$	10	1.0	1.7	3.6	1.1

respectively. The instantaneous velocity components  $V_x$  and  $V_y$  are calculated as before.

### Correction Results, Comparison

In this section, the results of the single velocity calibration without the yaw correction are compared to those with the yaw correction. After the calibration was complete, 50 new sets of data independent from that of calibration were taken covering a velocity range of 10-30 m/s and angle  $-30 \text{ deg} < \alpha < +30 \text{ deg}$ . The actual values of  $V$ ,  $V_x$ , and  $V_y$  are obtained from the measured pressure drop across the nozzle, temperature of the air and on  $\alpha$  value obtained from the vernier of the rotary table. The absolute percentage deviation between actual and calculated  $V$  is given by

$$\epsilon_V = \frac{|V_a - V_c|}{V_a} \times 100 \quad (19)$$

where  $V_a$  and  $V_c$  are the actual and calculated values of  $V$ . Similarly, percentage deviations of  $V_x$  and  $V_y$ , denoted by  $\epsilon_{V_x}$  and  $\epsilon_{V_y}$  are computed. The absolute difference between actual and calculated  $\alpha$  is denoted by  $\Delta\alpha$ .

Table 2 shows the maximum deviations of  $V$ ,  $V_x$ ,  $V_y$ , and  $\alpha$  when the yaw angle calibration at 22 m/s is used. These deviations were expected from the results plotted in Fig. 6. At the velocity of 10 m/s,  $\Delta\alpha_{max}$  is higher than values obtained for the velocity range of 20-30 m/s. These large angle deviations result in significant errors for velocity particularly for the  $y$ -direction component. Table 3 shows the result for 10 m/s velocity when the yaw correction is applied. The error decreases significantly and the deviations are of the same order as those obtained for the 20-30 m/s range.

### Conclusion

Among the various methods available for  $X$ -probe calibration, the one using the  $\alpha_{id}$  concept was studied for yaw response at different velocities. It was found that significant errors can be introduced into the velocity components if the results of the yaw angle calibration at high velocities (above 20 m/s) are used for low velocities. A formula to correct the yaw response at low velocities is introduced. This correction was applied to a set of data and the deviation between actual and calculated values of velocity components was determined. The correction applied to the lower velocity range significantly improves the accuracy of the velocity components (to the same order as obtained in the higher velocity range). The present method is faster, easier to implement and requires fewer steps compared to full velocity yaw angle calibration methods.

### References

- Bradshaw, P., 1971, *An Introduction to Turbulence and Its Measurement*, Pergamon Press, Oxford.
- Browne, L. W. B., Antonia, R. A., and Chua, L. P., 1989, "Calibration of  $X$ -probes for Turbulent Flow Measurements," *Experiments in Fluids*, Vol. 7, pp. 201-208.
- Brunn, H. H., Nabhani, N., Al-Kayiem, H. H., Fardad, A. A., Khan, M. A., and Hogarth, E., 1990, "Calibration and Analysis of X Hot-wire Probe Signals," *Measurements of Science Technology*, Vol. 1, pp. 782-785.
- Champagne, F. H., Sleicher, C. A., and Wehrmann, O. H., 1967, "Turbulence Measurements with Inclined Hot-wires, Part 1: Heat Transfer Experiments with Inclined Hot-wire," *Journal of Fluid Mechanics*, Vol. 28, pp. 153-175.
- Hinze, J. O., 1959, *Turbulence*, McGraw-Hill, New York.
- Johnson, F. D., and Eckelmann, H., 1984, "A Variable Angle Method of Calibration for  $X$ -probes Applied to Wall-bounded Turbulent Shear Flow," *Experiments in Fluids*, Vol. 2, pp. 121-130.
- Jorgensen, F. E., 1971, "Directional Sensitivity of Wire and Fibre Film Probes," *DISA Information*, Vol. 11, pp. 31-37.
- Lekakis, I. C., 1988, "Coherent Structures in Fully Developed Turbulent Pipe Flow," Ph.D. thesis, Univ. of Illinois at Urbana Champaign, USA.
- Lekakis, I. C., Adrian, R. J., and Jones, B. G., 1989, "Measurement of Velocity Vectors with Orthogonal and Non-orthogonal Triple-sensor Probes," *Experiments in Fluids*, Vol. 7, pp. 228-240.
- Leuptow, R. M., Breuer, K. S., and Haritonidis, J. H., 1988, "Computer-Aided Calibration of  $X$ -probes Using a Look-up Table," *Experiments in Fluids*, Vol. 6, pp. 115-118.
- Moffat, R. J., 1982, "Contributions to the Theory of Single-Sample Uncertainty Analysis," *ASME JOURNAL OF FLUIDS ENGINEERING*, Vol. 104, pp. 250-260.
- Schröder, T., 1985, "Entwicklung des instationären Nachlaufs hinter quer zur Strömungsrichtung bewegten Zylindern und dessen Einfluß auf das Umschlagverhalten von ebenen Grenzschichten stromabwärts angeordneter Versuchskörper," Dissertation D-17, Technische Hochschule Darmstadt, Germany.
- Webster, C. A. G., 1962, "A Note on the Sensitivity to Yaw of a Hot-wire Anemometer," *Journal of Fluid Mechanics*, Vol. 13, pp. 307-312.
- Willmarth, W. W., Bogar, T. J., 1977, "Survey and New Measurements of Turbulent Structure Near the Wall," *Physics of Fluids*, Vol. 20, p. S9-S21.
- Yavuzkurt, S., 1984, "A Guide to Uncertainty Analysis of Hot-wire Data," *ASME JOURNAL OF FLUIDS ENGINEERING*, Vol. 106, pp. 181-186.

# A New Approach to the Dynamic Parameter Estimation of a Viscoelastic System

**S. Bennis**

Professor,  
Ecole de Technologie Supérieure,  
Montréal, Québec, Canada  
H2T 2C8

*This work involves the study of newtonian transitory flow regimes in a rigid tube that has been extended to include an elastic enclosure. Three different techniques have been applied and compared. The first approach is the classical one, in which the calculations, which are based on the Laplace transform, enable direct integration of the Navier-Stokes equations and make it possible to determine longitudinal velocity and fluid flow. The solution, however, involves real or complex parameters that are solutions to a nonlinear equation involving Bessel functions. Where the flow regime in the tube is oscillating, we find a natural frequency of oscillation there, and a flow damping ratio. A comparison will be made with the other two methods partly on the basis of these two parameters.*

*The second is an approach based on time series analysis of flow in the tube, and consists in applying auto-regressive moving-average (ARMA) models to the fluid flow in order to identify the natural frequency and the damping coefficient of the flow. The flow series analyzed by this method come from two sources:*

- 1. The flow series obtained from the theoretical solution using the first method; these flow series were artificially contaminated with random noise to simulate real situations.*

- 2. The flow series obtained experimentally by direct measurement and integration of the velocity profile in the tube.*

*Finally, with the third technique, the experimental method, we have succeeded in validating the first two approaches. The approach based on the analysis of the time series through the use of ARMA models appears to perform best and is the simplest to use.*

## 1 Introduction

The classical analysis of a complex hydraulic system requires the formation of a mathematical model based on Navier-Stokes equations of motion and a knowledge of the fluid and material characteristics of the system components. An analytical solution of this model is theoretically feasible. In most applications, however, the analyst must introduce major simplifications and assumptions in order to solve the model. Numerical solutions are also possible, but these involve convergence problems and extensive computer time. These difficulties are multiplied if the system geometry is complex and if the material and fluid characteristics are not classical and linear. In biomedical applications, for instance, the physical characteristics of the components and fluids are difficult to measure and the analyst must rely on remote external readings or on measurements taken from nonliving components, and this affects the accuracy of the results.

Our approach to the problem is different from this, in that

the hydraulic model under study here is considered as a "black box," where only the entry and exit signals are used to determine the impulse response of the system based on ARMA (auto-regressive moving average) models. The proposed model consists of an elastic enclosure connected by a rigid tube to a second enclosure that is subjected to a variable pressure. This approach may be easily applied in cases where the fluid filler is nonnewtonian and the enclosure viscoelastic. For the sake of simplicity and due to lack of space, we have chosen to limit ourselves to a relatively simple case in order to provide a clear illustration of the proposed methodology.

The modeling methodology we propose is based on sampling real-time signals of the fluid-flow variables of the system. These discrete time series are then fitted to an auto-regressive series, the coefficients of which identify the dynamic parameters of the system. This time series is purely data-based and, as such, it incorporates all effects influencing system behavior and consequently truly reflects its dynamic properties without recourse to any knowledge of the material and fluid properties or to any standard simplifications of the system.

Other, more general studies involving non-newtonian fluids and viscoelastic materials have already been carried out (Briley

Contributed by the Fluids Engineering Division for publication in the JOURNAL OF FLUIDS ENGINEERING. Manuscript received by the Fluids Engineering Division October 15, 1991. Associate Technical Editor: J. Humphrey.

and McDonald, 1984), (Barnes et al., 1971) and (Obrecht, 1976). In particular, Lieber and Giddens (1987) consider the treatment of velocity disturbances in pulsatile flow; but without taking into account the elastic enclosure. More recently, Giddens and Nerem (1988) have studied flow in the cardiovascular system. For a fluid mechanician, this means solving the three-dimensional Navier-Stokes equations for a system of viscoelastic tubes and enclosures. The complexity of the problem led them to conclude: "we clearly do not have the capability to do such calculations currently, such a computational approach is realizable within the next generation." The study presented here is original in the following ways:

1. The direct integration of the Navier-Stokes equations and the use of nonlinear least squares methods make it possible to obtain an explicit and accurate solution in the case where the fluid is newtonian and the enclosure elastic.
2. The use of the ARMA process is a new approach to the problem, and may be easily applied to more complex systems where the fluid is nonnewtonian and the material viscoelastic.
3. The experimental approach based on laser velocity measurement enables validation of the first two: the classical and the time series analysis approaches.

A possible application of this system would be in non traumatic in vivo measurement. The elastic enclosure described here may be considered as the membrane of a pressure gauge, connected by a tube to the measurement zone. In some zones, however, it is not possible to mount a miniature receiver on the end of a catheter because of its size, and the traditional method of exploration must be used. This involves perforation by means of a very small diameter catheter which is connected to a pressure pick-up. However, the quality of the data collected by this system, which comprises the receiver and its connection to the measurement zone, is dependent on how well the dynamic behaviour of the system is known.

Another similar application for this system involves the measurement of pressure in flexible walls. Morgan and Parker (1989) studied a one-dimensional model to describe the flow through a collapsible tube whose ends are tethered to rigid tubes and which is enclosed in a pressurized chamber. It is often impossible to attach a receiver directly to a flexible wall. In these cases, a hydraulic link is added to connect the pressure measurement device to the receiver, which then behaves like an elastic enclosure. In order to obtain an accurate reading of the pressure, the behavior of the entire hydraulic system must be known.

## 2 Analytical Approach

### 2.1 Establishment and Solution of the Movement Equation.

The system consists of a rigid tube of length  $L$  and radius  $a$ , connected at one end to an elastic enclosure and free at the

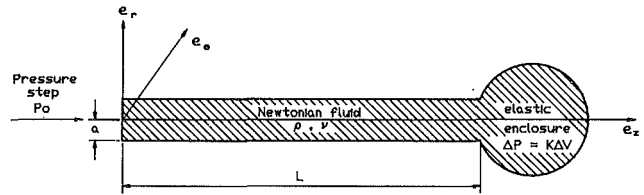


Fig. 1 Studied system

other end. The system is filled with a fluid of density  $\rho$  and kinematic viscosity  $\nu$ . A step change in pressure  $P_0$  is applied to the system at the free end resulting in a transient flow of the fluid in the system depicted in Fig. 1.

The following assumptions are introduced:

1. the flow is laminar and unidirectional,
2. the fluid is incompressible and newtonian,
3. the volume variations in the elastic enclosure are small and then proportional to the pressure variations,
4. the effects of the tube extremities are neglected.

The mathematical model for this case is written as follows (see Appendix A):

$$\frac{\partial W}{\partial t} = \frac{P_0}{\rho L} - \frac{2\pi K}{\rho L} \int_0^t \int_0^a W(r, t) r dr dt + \frac{\nu}{r} \frac{\partial}{\partial r} \left( r \frac{\partial W}{\partial r} \right) \quad (1)$$

the boundary conditions are:  $W(a, t) = 0$ ,  $W(r, 0) = 0$  and  $\partial W / \partial r|_{r=0} = 0$  where:

$W(r, t)$  is the longitudinal fluid velocity component  
 $r$  is the radial distance from the tube's centre  
 $t$  is the time and  $K$  is the stiffness coefficient of the enclosure.

The solution of Eq. (1) is (see Appendix A):

$$W(r, \tau) = 16\beta\gamma \sum_1^{\infty} \frac{1}{\phi(\chi_i)} \frac{J_0\left(\frac{r}{a} \chi_i\right) - J_0(\chi_i)}{J_0(\chi_i)} e^{-\chi_i^2 \tau} \quad (2)$$

where:  $\tau = \frac{\nu}{a^2} t$ ,  $\beta = \frac{a^2 P_0}{4\rho\nu L}$ ,  $\gamma = \frac{\pi a^6 K}{\rho\nu^2 L}$ ,  $\phi(\chi_i) = 12\gamma\chi_i^2 - (\chi_i^4 + \gamma)^2$

the discrete values of  $\chi_i$  are the roots of the following equation:

$$\gamma = \chi^4 \frac{J_0(\chi)}{J_2(\chi)}, \quad (3)$$

and  $J_0$  and  $J_2$  are the Bessel functions of orders 0 and 2.

The function  $\varphi(\chi) = \chi^4 (J_0(\chi)/J_2(\chi))$  is represented in Fig. 2.

There is a critical value of  $\gamma$ ,  $\gamma_c = 11,799754 \pm 10^{-6}$  such that:

## Nomenclature

$a, L$ = radius and length of the rigid tube	$Q$ = fluid flow	$\Omega$ = damped frequency
$\rho, \nu$ = density and kinematic viscosity of the fluid	$r$ = radial distance from the tube's centre	$\omega\sqrt{1-\xi^2}$
$P_0$ = applied pressure at the free end	$t, T$ = time parameters	$X$ = real and complex roots (theoretical solution)
$H_0$ = applied pressure at the free-end expressed in m ( $H_0 = P_0/\rho g$ )	$K$ = enclosure stiffness coefficient	$\psi_i$ = phase angle
$W(r, t)$ = fluid velocity	$\omega$ = natural frequency of the fluid flow	$\phi_i$ = coefficient of the AR model
	$\xi$ = damping ratio	$\theta_i$ = coefficient of the MA model
	$\sigma$ = decay rate $\omega\xi$	$\epsilon$ = white noise
	$\gamma$ = operating parameter	$\lambda_i$ = root of the characteristic equation (AR model)
		$B$ = backward shift operator

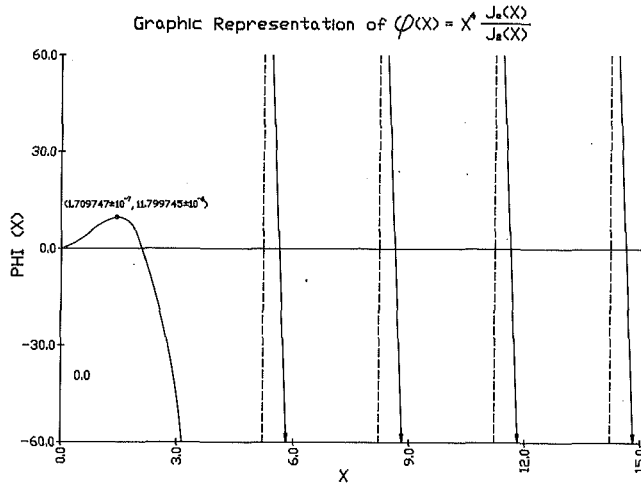


Fig. 2

- if  $\gamma < \gamma_c$ , then Eq. (3) allows entirely real and simple roots, such as:  $x_1 < x_2 < x_3 < x_4 < x_5 < \dots$
- if  $\gamma = \gamma_c$ , then Eq. (3) allows a double root ( $X_c = 1,7097475 \pm 10^{-6}$ ) and an infinite number of real roots, such as:  $x_c < x_3 < x_4 < x_5 < \dots$
- if  $\gamma > \gamma_c$ , then Eq. (3) allows two conjugated complex roots ( $x_1; x_2 = \bar{x}_1$ ) and an infinite number of real roots, such as:

$$|x_1| = |\bar{x}_2| < x_3 < x_4 < x_5 \dots$$

It is clear from Fig. 2 that the roots are calculated automatically and placed in increasing modular order. The parameter  $\gamma$  can be interpreted as the ratio of the inertial force to the fluid friction force. When  $\gamma \leq \gamma_c$ , the frictional force predominates relative to the inertial force. All the roots  $x_i$  are real, and the damped flow is non oscillating and always moves in the same direction. When  $\gamma > \gamma_c$ , the inertial force predominates relative to the frictional force. The existence of complex roots is evidence of an oscillating motion and flow inversions in the tube. This motion will be studied in detail below.

There are two main reasons for stressing the oscillating motion pattern:

1. The damped, nonoscillating pattern presents no calculation difficulty. The real roots can be calculated by simple dichotomic methods (Obrecht, 1976). In the case of the oscillating pattern, the complex roots must be calculated by more elaborate techniques. Two nonlinear least squares procedures may be used: Gauss-Newton linearization and the gradient method, also known as the steepest-descent method. The practical advantage of the Gauss-Newton method is that it tends to converge rapidly to the least-squares (LS) estimates, if it converges; the disadvantage is that it may not converge at all. The practical advantage of the gradient method is that, in theory, it will converge to LS estimates; however, it may converge so slowly that it becomes impractical to use (Sharf and D'Eleuterio, 1989).

2. The range of nonoscillating flows ( $0 \leq \gamma \leq 11,799745 \pm 10^{-6}$ ) is much more limited relative to oscillating flows ( $11,799745 < \gamma < \infty$ ).

**2.2 Flow for an Operating Parameter  $\gamma > \gamma_c$ :** From relation (2), it is possible to calculate the flow in the form (see Appendix B):

$$Q(\tau) = \frac{4\pi a^4 g H_0}{L\nu} \sum_i \frac{\chi_i^4}{\phi(\chi_i)} e^{-\chi_i^2 \tau} \quad (4)$$

where:  $H_0 = P_0/\rho g$

In order to establish the link between the solution obtained

here by direct integration of the Navier-Stokes equations and the solution obtained by time series analysis using ARMA models in Section 3, we write Eq. (4) in a simplified form.

The previous analysis leads us to separate the sum of the terms of order  $i \geq 3$  that include only real roots, from the terms that include two complex conjugated roots ( $x_1, x_2 = \bar{x}_1$ ):

Taking into account that  $|x_1| < x_3 < x_4 < x_5 < \dots$ , and  $|e^{-x_1 \tau}| > e^{-x_3 \tau} > e^{-x_4 \tau} > \dots$  therefore  $T^*$  exists, such that for  $T > T^*$ , flow  $Q(T)$  is expressed by:

$$Q(\tau) = \frac{4\pi a^4 g H_0}{L\nu} \left[ \frac{\chi_1^4}{\phi(\chi_1)} e^{-\chi_1^2 \tau} + \frac{\bar{\chi}_1^4}{\phi(\bar{\chi}_1)} e^{-\bar{\chi}_1^2 \tau} \right] \quad (5)$$

Knowing that:

$$G = \sum_3 \frac{\chi_i^4}{\phi(\chi_i)} e^{-\chi_i^2 \tau} = \frac{\chi_3^4}{\phi(\chi_3)} e^{-\chi_3^2 \tau} \left[ 1 + \sum \frac{\phi(\chi_3) \chi_i^4 e^{-\chi_i^2 \tau}}{\phi(\chi_i) \chi_3^4 e^{-\chi_3^2 \tau}} \right] \quad (6)$$

decreases very rapidly as  $T$  increases,  $G$  may be considered to be of the order of size of the term in  $x_3$ , which makes it possible to calculate numerically the duration  $T^*$  of the initial phase, beyond which the movement limit will be considered to have been established.

When  $T > T^*$ , Eq. (4) assumes the following form:

$$Q(\tau) = \left[ \frac{4\pi a^4 g H_0}{L\nu} M_q \right] \cos(V\tau - \psi) e^{-U\tau} \quad (7)$$

$$\left. \begin{aligned} \frac{\chi_1^4}{\phi(\chi_1)} = A + iB, \quad \frac{\bar{\chi}_1^4}{\phi(\bar{\chi}_1)} = A - iB \\ M_q = 2[A^2 + B^2]^{1/2} \end{aligned} \right\}$$

where:

$$\tan \psi = B/A \quad (8)$$

$$\chi_1^2 = U + iV, \quad \bar{\chi}_1^2 = U - iV$$

$$U = \sigma \left( \frac{a^2}{\nu} \right), \quad V = \Omega \left( \frac{a^2}{\nu} \right)$$

and:

$\Omega$  is the damped frequency of motion =  $\omega \sqrt{1 - \xi^2}$

$\sigma$  is the decay rate =  $\xi \omega$

$\omega$  is the natural frequency

$\xi$  is the damping ratio

Once the fluid flow time series is established from Eq. (4), it is possible to estimate variables  $V$  and  $U$  and, consequently, estimates for the decay rate  $\sigma$ , and the damped frequency of motion  $\Omega$  can be established. These estimates are then used to calculate the damping ratio  $\xi$  and the natural frequency  $\omega$  of the system. A comparison will be made with the other two methods in part on the basis of these two parameters. The determination of the rate of flow (Eq. (4)), however, requires elaborate calculation techniques including determination of the complex roots  $x_i$ . For this reason, we propose time series modelling that provides information regarding the natural frequency and damping ratio of the system directly from measures on the system and without the need for developing a mathematical model for the fluid flow time history.

### 3 The Auto-Regressive (AR) Time Series

The flow series analyzed here may be obtained from two different sources:

1. They are generated based on the theoretical solution (4) proposed in Section 2.2;

2. They are calculated numerically by integrating the velocity profiles measured experimentally.

In both cases, the observable variable  $Q(t)$  can easily be recorded and sampled at uniformly spaced time ( $\Delta$ ) intervals,  $t, t-1, \dots, t-n$ . Using the finite difference technique, an

auto-regressive moving average (ARMA) series (Box and Jenkins, 1976) can be fitted to the time samples as follows:

$$Q(t) - \phi_1 Q(t-1) - \phi_2 Q(t-2) \dots - \phi_n Q(t-n) = \epsilon(t) - \theta_1 \epsilon(t-1) - \dots - \theta_m \epsilon(t-m) \quad (9)$$

where:  $\epsilon(t)$  is a stochastic process with zero mean and constant variance  $\phi_i$  and  $\theta_i$  are series coefficients.

Introducing the backward shift operator  $B$ , where  $B^r Q(t) = Q(t-r)$  Eq. (9) can be written:

$$(1 - \phi_1 B - \phi_2 B^2 \dots - \phi_n B^n) Q(t) = (1 - \theta_1 B - \theta_2 B^2 \dots - \theta_m B^m) \epsilon(t) \quad (10)$$

The right-hand side of Eq. (10) can be factorized as follows:

$$(1 - \phi_1 B - \phi_2 B^2 \dots - \phi_n B^n) Q(t) = (1 - \lambda_1 B) (1 - \lambda_2 B) \dots (1 - \lambda_n B) Q(t) \quad (11)$$

where  $\lambda_i$  are real or complex numbers.

We are not concerned here with the left-hand side of Eq. (10) for two reasons:

1. In order to calculate the dynamic parameters  $\sigma$ ,  $\xi$ ,  $\omega$  of the system, only the auto-regressive component that represents the evolution of an unforced system is required (Pandit and Wu, 1983).

2.  $\epsilon(t)$  may be interpreted as the random perturbation of the system. In the case studied here, perturbation takes the form of a step of pressure. Therefore we do not consider the moving average (MA) part of the model.

Equation (11) represents the auto-regressive (AR) part of the time series. This AR part has  $h$  real roots  $\lambda_r$  and  $2s$  complex roots  $\lambda_i$  and their conjugate  $\bar{\lambda}_j$ , and can be written in the following form:

$$\left[ \prod_{r=1}^h (1 - \lambda_r B) \right] \left[ \prod_{j=1}^s \{1 - \lambda_j B\} \{1 - \bar{\lambda}_j B\} \right] Q(t) = 0 \quad (12)$$

The general solution of Eq. (12) may be written in the form (D'Azzo and Houpis, 1988):

$$Q(K\Delta t) = \sum_{j=1}^h D_j \lambda_j^{K\Delta t} + \sum_{j=1}^{2s} F_j \lambda_j^{K\Delta t} \quad (13)$$

where  $t = K\Delta t$ ;  $K$  is an integer and  $\Delta t$  is the sampling period.  $D_j$  is a real number and  $F_j$  is a complex number.

If  $\lambda_j$  is a complex number, it is always possible to make:

$$\lambda_j = e^{\mu_j} \quad (14)$$

or:

$$\mu_j = L_n \lambda_j \quad (15)$$

$\mu_j$  is a complex number that can always be put in the form:

$$\mu_j = \sigma_j + i\Omega_j \quad (16)$$

We shall see later that  $\sigma_j$  and  $\Omega_j$  have the same physical significance and value as the  $\sigma$  and  $\Omega$  introduced in Section 2.2.

Taking into account (15) and (17), Eq. (14) may be written in the form:

$$Q(k\Delta t) = \sum_{j=1}^h D_j \lambda_j^{K\Delta t} + \sum_{j=1}^s [F_j e^{(\sigma_j + i\Omega_j)k\Delta t} + \bar{F}_j e^{(\sigma_j - i\Omega_j)k\Delta t}] \quad (17)$$

where  $\bar{F}_j$  is the complex conjugate of  $F_j$ .

If, in addition, we have stable damped oscillating flow, terms containing real roots disappear as time increases, and Eq. (18) can be written (see Section 2.2):

$$Q(k\Delta t) = \sum_{j=1}^s [F_j e^{(\sigma_j + i\Omega_j)k\Delta t} + \bar{F}_j e^{(\sigma_j - i\Omega_j)k\Delta t}] \quad (18)$$

For a system with one degree of freedom ( $j = 1$ ), the indices no longer need to be included and the time flow rate can simply be represented by the equation:

$$Q(k\Delta t) = F e^{(\sigma + i\Omega)k\Delta t} + \bar{F} e^{(\sigma - i\Omega)k\Delta t} \quad (19)$$

If we make:

$$F = A + iB \text{ and } \bar{F} = A - iB$$

then Eq. (19) is written:

$$Q(k\Delta t) = \{ F [\cos(\Omega K\Delta t) - i \sin(\Omega K\Delta t)] + \bar{F} [\cos(\Omega K\Delta t) + i \sin(\Omega K\Delta t)] \} e^{-\sigma k\Delta t} \quad (20)$$

or:

$$Q(k\Delta t) = 2[A \cos(\Omega K\Delta t) + B \sin(\Omega K\Delta t)] e^{-\sigma k\Delta t} \quad (21)$$

If we make:

$$C = 2\sqrt{A^2 + B^2}, \quad \text{tg}\psi = \frac{B}{A}, \quad M = 2C \quad (22)$$

then Eq. (20) is written:

$$Q(k\Delta t) = M \cos(\Omega K\Delta t - \psi) e^{-\sigma k\Delta t} \quad (23)$$

Equation (23) is similar to Eq. (7). The natural frequency  $\omega$  of the system and the damping ratio  $\xi$  can therefore be calculated directly from the complex root  $\lambda$  of the auto-regressive Eq. (11). Thus, from Eqs. (15) and (16), we have:

$$\ln \lambda = \sigma + i\Omega \quad (24)$$

or:

$$\ln \lambda = -\xi \omega + i\omega \sqrt{1 - \xi^2} \quad (25)$$

Estimates of  $\omega$  and  $\xi$  can therefore be obtained directly from a series of measurements of fluid flow and without recourse to the physical characteristics of the system and without solving the Navier-Stokes equations.

## 4 Experimental Method

In the third, or experimental, approach, a hydraulic model has been designed and built to validate the theoretical assertions.

**4.1 Description of the Apparatus.** The experimental model, built according to the working hypotheses, includes the following elements (Fig. 3):

**4.1.1 Elastic Chamber.** This is a plexiglass chamber in the shape of a truncated cone 200 mm in length and 10 mm thick. The diameters of the two bases are 16 mm and 150 mm. A threaded ring provides a way of fixing the elastic enclosure, 2 mm thick, to the large base of the cone (Fig. 4).

**4.1.2 Fluid Air Float Reservoir.** This is a very large plexiglass container. Its walls are thick (40 mm) and impervious, and do not become deformed by the pressures applied to the fluid contained within them.

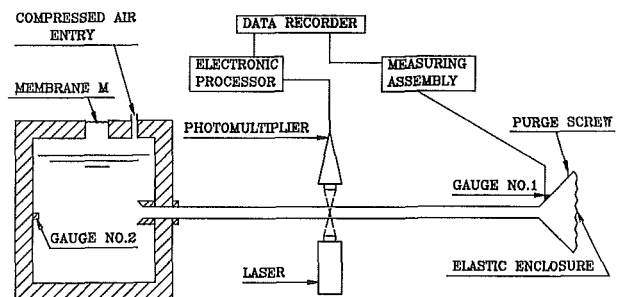


Fig. 3 Schematic diagram of the assembly

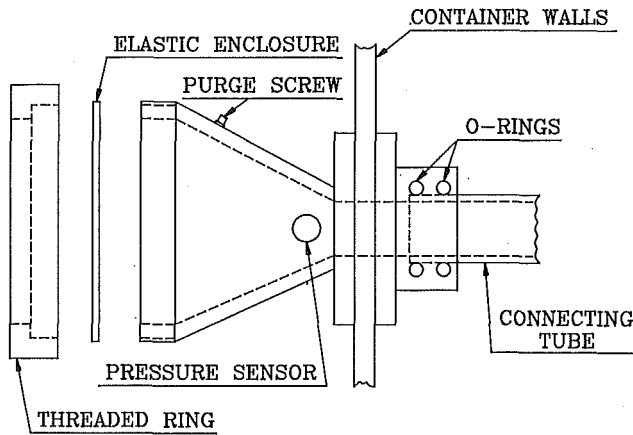


Fig. 4 Elastic chamber

**4.13 Experimental Tube.** This is a rigid horizontal cylindrical tube made of plexiglass with a circular cross-section having an interior radius of 8 mm, a thickness of 2 mm, and a length of 2.75 m. It is transparent, which enables the measurement of speeds by optical means. To decrease the extremity effects, this tube has been equipped with a convergence at the upper end and a divergence at the lower end.

**4.2 Principle of Operation.** An overpressure is applied to the free surface of the large container by applying compressed air at a regulated pressure. Once equilibrium has been achieved, a step-changing pressure is applied, bringing the free surface abruptly back to atmospheric pressure. The flow in the tube is therefore directly influenced by the return force of the elastic at the downstream enclosure.

During the flow, the pressure variations at the entry and exit points of the tube are recorded, and the evolution of the velocity profiles is measured at the middle of the tube.

**4.3 System of Measurement.** Pressure is measured at two points:

- Gauge No. 1 provides a means to track the evolution of the pressure in the elastic chamber;
- Gauge No. 2 enables control of the quality of the step pressure produced (the trials where the descending front of the step is not very stiff were systematically rejected).

We used H.B.M.-type gauges (Hottinger Baldwin Messtechnik) with a cupro-beryllium membrane. Their operating range is between 0.1 and 100 kPa, and their linearity loss is within 0.1 percent.

Speeds are measured with a Disa-Mark II laser velocimeter with a power of 35 megawatts.

This system of measurement is particularly well suited to our needs in this study because of its short response time, resulting in a large spatial resolution (<0.33 mm) and no turbulence inside the flow.

The velocimeter is of the frequency-tracking type. Since the flow sometimes oscillates, this velocimeter is equipped with a Bragg-cell frequency slippage system in order to detect the phase and the direction of the flow. We chose to use a fringed apparatus with light diffused to the front.

**Mechanical Characteristics of the Enclosure.** The development of a simple device has made it possible to determine the static properties of the elastic enclosure. The principle, which uses the simultaneous observation of the variations in volume and pressure in the enclosure, is the following: an overpressure  $P_0$  is applied to the free surface of the large container, after which there is a pause until equilibrium is achieved throughout the system. Using a graduated syringe, a volume  $V$  is taken from the elastic chamber after it has been isolated from the large container. The variation in the corre-

sponding pressure  $P$  indicated by Gauge No. 1 is noted, and the coefficient  $K$  is calculated using the ratio:

$$\frac{\Delta P}{\Delta V} = K \quad (26)$$

The step pressure supplied a linear response with a relative error of 1 percent.

## 5 Results

The characteristics of the apparatus in Fig. 3 are:

- tube radius  $a = 0.8$  mm
- tube length  $L = 2.75$  m
- fluid density  $\rho = 10^3$  kg/m<sup>3</sup>
- kinematic viscosity of the fluid  $\nu = 8.95 \times 10^{-7}$  m<sup>2</sup>/s
- coefficient of elasticity  $K = 1.9 \times 10^{11}$  N/m<sup>5</sup>
- factor  $H_0 = 1$  m

The analytical solution is used to simulate a time flow history for the case discussed here. This time flow history is then sampled at one second time intervals ( $Q(j\Delta t)$ ,  $j = 1$  to 200). To ensure that the terms containing the real roots  $x_j$  of Eq. (4) are sufficiently small with respect to the terms containing the complex conjugate roots  $x_1$  and  $\bar{x}_1$ , the first sample  $Q(\Delta t)$  is recorded 3 seconds after the start of the simulated time flow.

The reduced time  $T^*$  (introduced in Section 2.2) corresponds to  $t = 3$  s, where the term  $G$  of Eq. (6) is of the order of  $10^{-7}$ . If we use flow expression (5), neglecting term  $G$  induces an error of  $2.10^{-8}$  m<sup>3</sup>/s on the maximal value of the fluid flow ( $2.10^{-5}$  m<sup>3</sup>/s) in the case studied here.

The 200 samples now represent an ideal flow which we refer to here as case (1). To demonstrate the ability of this time model to provide good estimates of the dynamics parameters, we superposed on case (1) white noise signals of zero average and standard deviation  $10^{-7}$ ,  $5 \times 10^{-7}$  and  $8.6 \times 10^{-7}$ . These three cases are identified as cases (2), (3) and (4), respectively. They represent maximum variations in the signal's maximum amplitude in case (1) of 0.5%, 3% and 5% respectively. Time signals for the four cases are then fitted to an auto-regressive time series of the second order which takes the following form:

$$Q(K\Delta t) - \phi_1 Q((K-1)\Delta t) - \phi_2 Q((K-2)\Delta t) = \epsilon(t) \quad (27)$$

For each of the four cases indicated, we have two hundred time samples:  $Q(\Delta t)$ ,  $Q(2\Delta t)$  ...  $Q(200\Delta t)$ . Using Eq. (14) we can establish the following relations:

$$\begin{aligned} Q(3\Delta t) - \phi_1 Q(2\Delta t) - \phi_2 Q(\Delta t) &= \epsilon(3) \\ &\vdots \\ &\vdots \end{aligned} \quad (28)$$

$$Q(200\Delta t) - \phi_1 Q(199\Delta t) - \phi_2 Q(198\Delta t) = \epsilon(200)$$

The best estimates of the coefficients  $\phi_1$  and  $\phi_2$ , for this case, give optimum errors  $\epsilon_i$ ,  $i = 3, \dots, 200$ . The standard recursive least square procedure (Ljunhg, 1987) is used to estimate the required values  $\phi_1$  and  $\phi_2$ . This procedure does not necessitate any matrix inversion, and thus provides an acceptable level of precision and is one that does not take up extensive memory space.

When the procedure is applied to case (1), we obtain:

$$Q(K\Delta t) + 1.829865Q((K-1)\Delta t) + 0.9456138Q(K-2)\Delta t = 0$$

As with Eq. (8), this characteristic equation can be factorized into the following form:

$$(1 - \lambda B)(1 - \bar{\lambda} B)Q_t = 0$$

where:

$$\lambda = -0.913094 + i0.32869$$

and  $\bar{\lambda}$  is the conjugate of  $\lambda$ . For  $\Delta = 1$  s and from Eqs. (10) and (13), we obtain:

$$\lambda = e^{\mu} = e^{\sigma + i\Omega} = e^{\sigma} (\cos\Omega + i\sin\Omega)$$

We thus have:

$$\sigma = -\xi\omega = -0.027988 \quad \Omega = \omega\sqrt{1-\xi^2} = 2.79614 \text{ rad/s}$$

or:

$$\omega = 2.796 \text{ rad/s}, \quad \xi = 1.001 \text{ percent}$$

These values, as expected, are exactly equal to those obtained from the theoretical analysis. The procedure is then applied to the other cases that include noisy data. The results obtained for cases (2), (3), and (4) are presented in Table 1.

The comparisons between theoretical evolutions and experimental values are shown in Figs. (5), (6), (7), and (8), respectively, for:

- the evolution of velocity profiles calculated from Eq. (2) and values measured by a laser velocimeter;
- the evolution of pressure in the elastic enclosure calculated from Eqs. (A.5), (A.9), and (2) and measured by gauge No. 1;
- theoretical and experimental central velocity ( $W(0, t)$ );
- the evolution of fluid flow calculated from Eq. (4) and values obtained by numerical integration of the velocity profiles measured experimentally by a laser velocimeter.

The agreement between the theoretical and experimental values, represented by points, seems to be satisfactory in general.

In order to compare the results from the three different sources: theoretical, experimental and time-series analysis (ARMA), we have calculated the natural frequency and the damping ratio based on the experimental results. For this calculation, the fluid flow was obtained in different time frames through numerical integration of the velocity profiles measured experimentally by a laser velocimeter. We then applied, on this measured flow series, the same type of ARMA model as the one applied previously on the series generated synthetically, to obtain the Natural Frequency, the Damping Ratio, the Damped Frequency and the Decay Rate. These results are presented in the final column of Table 1. While the experimental results again seem to agree well with the theoretical results, we find that case 3, in which the white noise signal in the simulated noisy data is of zero average and standard deviation  $5.10^{-7}$  (3 percent of maximum amplitude), is the one that is the closest to the experimental results.

## 6 Conclusion

The theoretical study has allowed us to obtain the exact solution to the problem from the direct integration of the Navier-Stokes equations.

The applicability of AR time series methodology in providing system dynamic parameters has been demonstrated. In both noise-free and noisy cases, the estimated parameters are remarkably accurate, the variation from theoretical values being consistently less than 2 percent for damping ratio values and 0.005 percent for natural frequencies. The time series is purely data-based and, as such, it incorporates all the effects influ-

$$\gamma = 307$$

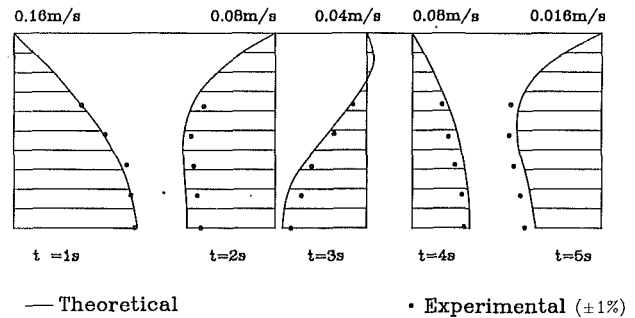


Fig. 5 Evaluation of velocity profiles

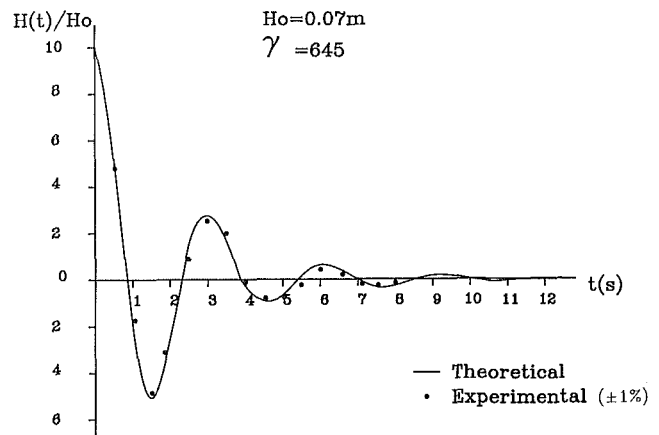


Fig. 6 Evolution of pressure

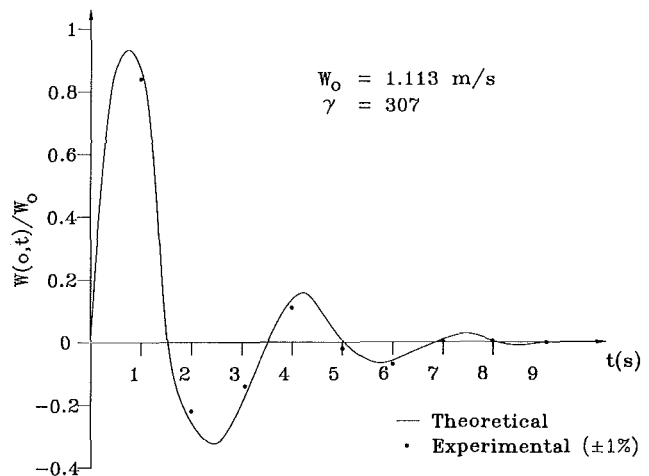


Fig. 7 Evolution of central velocity ( $W(0, t)$ )

Table 1 Comparison of theoretical, experimental, and simulated results (values  $\pm 10^{-5}$ )

	Theoretical data	Simulated noise-free data	Simulated noisy data			Experimental data
		Case (1)	Case (2)	Case (3)	Case (4)	
Decay rate	0.02799	0.0279988	0.02799	0.02829	0.02998	0.0284
Damped frequency	2.796596	2.79614	2.79601	2.79606	2.79604	2.79627
Natural frequency	2.79610	2.79628	2.79623	2.79621	2.79620	2.79642
Damping ratio	1.001 %	1.001 %	1.001 %	1.012 %	1.072 %	1.014 %

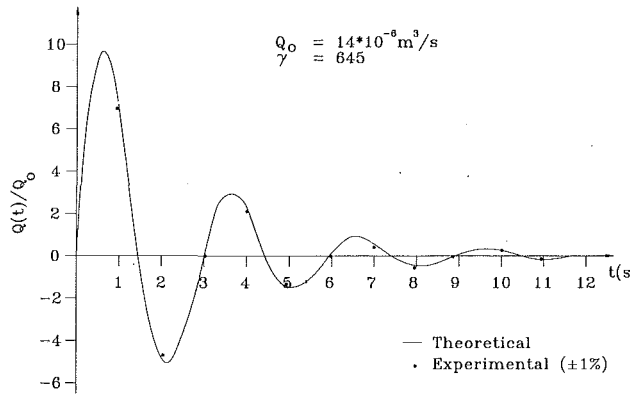


Fig. 8 Evolution of fluid flow

encing the system's behaviour and, consequently, only reflects its dynamic properties. This method thus provides a complete estimate of dynamic parameters without the need to measure physical parameters.

The operation of an experimental model has provided a means for verifying the validity of our theoretical assertions. The results, from various sources, are found to be in good agreement in each case, which is a good test of their quality individually.

Such an approach should provide a great deal of information that is useful to physiologists who need to know with increasing precision, and without surgical intervention, the condition of the various organs and fluids of the body, in order to prevent the ultimate consequences of their deterioration.

The authors are soon planning to apply the method to measurements from real applications in various domains.

### Acknowledgments

I wish to thank the reviewers for several useful comments and suggestions. This project was supported by a grant from the Natural Sciences and Engineering Research Council of Canada.

### References

- Barnes, H. H., Townsend, P., and Walters, K., 1971, "On Pulsatile Flow of Non Newtonian Liquid," *Rheologica Acta*, Vol. 10, pp. 517-527.
- Bennis, S., 1983, "Écoulements transitoires dans un tube rigide prolongé par une enceinte viscoélastique," Thèse de doctorat en mécanique Institut national Polytechnique, Toulouse.
- Box, G. E. P., and Jenkins, G. M., 1976, "Time Series Analysis; Forecasting and Control," 2nd ed., Holden Day, San Francisco.
- Briley, W. R., and MacDonald, H., 1984, "Three-Dimensional Viscous Flows with Large Secondary Velocity," *Journal of Fluid Mechanics*, Vol. 144, pp. 47-77.
- D'Azzo, J. J., and Houpis, C. H., 1988, "Linear Control System Analysis and Design," McGraw-Hill Electrical Engineering Series, pp. 178-179.
- Giddens, D. P., and Nerem, R. M., 1988, "Challenging Computational Problems in Cardiovascular Fluid Mechanics," *Computational Methods in Bioengineering*, Presented at the Winter Annual Meeting of the ASME, pp. 21-28.
- Lieber, B. B., and Giddens, D. P., 1987, "On the Treatment of Velocity Disturbances in Pulsatile Flow," *Proceedings of the International Conference on Fluid Mechanics*, Peking Press, Beijing, pp. 1005-1009.
- Ljung, L., 1987, "System Identification: Theory for the User," Prentice-Hall, Englewood Cliffs, N.J.
- Morgan, P., and Parker, K. H., 1989, "Mathematical Model of Flow Through a Collapsible Tube. I. Model and Steady Flow Results," *Journal of Biomechanics*, Vol. 22, No. 11-12, pp. 1263-1270.
- Obrecht, B., 1976, "Comportement dynamique de systèmes en régime non permanent. Étude d'un modèle théorique et d'un modèle hydraulique, application à la biomécanique," Thèse de doctorat ès sciences physiques, Strasbourg.
- Pandit, S. M., and Wu, S. M., 1983, "Time Series and System Analysis with Application," Wiley, son.
- Sharf, I., and D'Eleuterio, G. M. T., 1989, "Parallel Simulation Dynamics for Rigid Multibody Chains," The 1989 ASME Design Technical Conferences, Mechanical Vibration and Noise, Vol. 18-5, pp. 265-272, Montreal, Canada.
- Zienkiewicz, O. C., and Cheung, Y. K., 1967, "The Finite Element Method in Structural and Continuum Mechanics," McGraw-Hill, London.

## APPENDIX A

### Establishment and Resolution of the Equation of Movement

Based on the hypotheses formulated in Section 2, the Navier-Stokes equations are written by projection on a system of cylindrical coordinates ( $e_r, e_\theta, e_z$ ):

$$\frac{\partial p}{\partial x} = 0 \quad (\text{A.1})$$

$$\frac{\partial p}{\partial y} - \rho g = 0 \quad (\text{A.2})$$

$$\frac{\partial w}{\partial t} = -\frac{1}{\rho} \frac{\partial p}{\partial z} + \nu \frac{1}{r} \frac{\partial}{\partial r} \left( r \frac{\partial w}{\partial r} \right) \quad (\text{A.3})$$

It is agreed that the motor pressure applied the tube be called  $P^*$ , which is, in fact, the difference between the value  $P_0$  on the pressure scale at the free end of the tube and the counter-pressure  $P$  that exists in the elastic enclosure at the other end:

$$P^* = P_0 - P \quad (\text{A.4})$$

Also, the pressure variation  $\Delta P$  in the elastic enclosure is proportional to the variation in volume  $\Delta V$  of this enclosure:

$$\Delta P = K \Delta V \quad (\text{A.5})$$

The coefficient  $K$  is directly related to Young's modulus  $E$  and to the geometry of the enclosure. In the case of small deformities (linear elasticity), the coefficient  $K$  is constant (Zienkiewicz and Cheung, 1967):

$$-\frac{\partial P^*}{\partial z} = \frac{\Delta P^*(t)}{L} = \frac{P_0}{L} - \frac{K \Delta V(t)}{L} \quad (\text{A.6})$$

The volume of flow  $\Delta V(t)$  from the initial moment to moment  $t$  is:

$$\Delta V(t) = \int_0^t Q(t) dt \quad (\text{A.7})$$

where  $Q(t)$  represents the flow that is given as a function of the velocity  $W(r, t)$  by:

$$Q(t) = \int_0^{2\pi} \int_0^a W(r, t) r dr d\theta \quad (\text{A.8})$$

where:

$$\Delta V(t) = 2\pi \int_0^t \int_0^a W(r, t) r dr dt \quad (\text{A.9})$$

Based on relations (A.6) and (A.9), Eq. (A.3) gives us the integro-differential equation of the movement:

$$\frac{\partial W}{\partial t} = \frac{P_0}{\rho L} - \frac{2\pi K}{\rho L} \int_0^t \int_0^a W(r, t) r dr dt + \frac{\nu}{r} \frac{\partial}{\partial r} \left( r \frac{\partial W}{\partial r} \right) \quad (\text{A.10})$$

with these conditions at the limits:

$$W(a, t) = 0 \quad W(r, 0) = 0 \quad \left. \frac{\partial W}{\partial r} \right|_{r=0} = 0 \quad (\text{A.11})$$

To simplify the notation, let us make:

$$\frac{P_0}{\rho L} = A \quad \frac{2\pi K}{\rho L} = b \quad (\text{A.12})$$

The Laplace transform  $W(r, t)$  is written:

$$W(r, s) = \int_0^\infty e^{-st} W(r, t) dt \quad (\text{A.13})$$

With the initial condition ( $W(r, 0) = 0$ ), the transform of Eq. (A.10) is written:

$$\frac{d^2 W}{dr^2} + \frac{1}{r} \frac{dW}{dr} - \frac{s}{\nu} W = -\frac{A}{s\nu} + \frac{b}{\nu s} \int_0^a W r dr \quad (\text{A.14})$$



It will be noted that in relation (A.14) there is a Bessel equation, whose general solution is given by:

$$W(r, s) = CJ_0\left(i\sqrt{\frac{s}{\nu}}r\right) + EY_0\left(i\sqrt{\frac{s}{\nu}}r\right) + \frac{A}{s^2 + \frac{a^2}{2}} + \frac{b}{s^2} \int_0^a W(r, s) r dr \quad (\text{A.15})$$

where  $Y_0$  is the modified second species Bessel function of order 0.

Based on the condition with limits:

$$\left. \frac{\partial W}{\partial r} \right|_{r=0} = 0,$$

the velocity must have a finite value for  $r = 0$ , and consequently  $E = 0$ .

Let us calculate the integral:

$$I_1 = \int_0^a W(r, s) r dr$$

By multiplying by  $r$  the relation (A.15), and after integration with respect to variable  $r$ , we obtain:

$$I_1 = \int_0^a r J_0\left(i\sqrt{\frac{s}{\nu}}r\right) dr + \frac{A}{s^2} \int_0^a r dr - \frac{b}{s^2} I_1 \int_0^a r dr \quad (\text{A.16})$$

Let us now calculate:

$$I_2 = \int_0^a r J_0\left(i\sqrt{\frac{s}{\nu}}r\right) dr$$

For this calculation, let us change the variable:

$$\chi = ir \sqrt{\frac{s}{\nu}} \quad (\text{A.17})$$

$$I_2 \text{ becomes: } I_2 = \left(\frac{1}{i\sqrt{\frac{s}{\nu}}}\right)^2 \int_0^{i\sqrt{\frac{s}{\nu}}a} \chi J_0(\chi) d\chi \quad (\text{A.18})$$

Based on the recursion relations between  $J_0$  and  $J_1$ , we obtain:

$$I_2 = \frac{a}{i\sqrt{\frac{s}{\nu}}} J_1\left(i\sqrt{\frac{s}{\nu}}a\right) \quad (\text{A.19})$$

Combining (A.19) with (A.16), we obtain the value of the integral  $I_1$ , which is:

$$I_1 = \frac{\frac{a^2 A}{2s^2} + \frac{aC}{i\sqrt{\frac{s}{\nu}}} J_1\left(i\sqrt{\frac{s}{\nu}}a\right)}{1 + \frac{a^2 b}{2s^2}} \quad (\text{A.20})$$

This relation is combined with (A.15) to obtain:

$$W(r, s) = C \left[ J_0\left(i\sqrt{\frac{s}{\nu}}r\right) - \frac{ba}{i\sqrt{\frac{s}{\nu}}} \frac{J_1\left(i\sqrt{\frac{s}{\nu}}a\right)}{s^2 + \frac{a^2 b}{2}} \right] + \frac{A}{s^2 + \frac{a^2}{2}} \quad (\text{A.21})$$

$$C = \frac{A}{s^2 + \frac{a^2}{2} b} - \frac{J_0\left(i\sqrt{\frac{s}{\nu}}\right) - \frac{ba}{i\sqrt{\frac{s}{\nu}}} \frac{J_1\left(i\sqrt{\frac{s}{\nu}}\right)}{s^2 + \frac{a^2}{2} b}}{s^2 + \frac{a^2}{2} b} \quad (\text{A.22})$$

The integration constant  $C$  is determined by translating the fact that the fluid adheres to the wall ( $W(a, t) = 0$ ):

By replacing constant  $C$  with its value in (A.21), the velocity becomes:

$$W(r, s) = A \frac{ia\sqrt{\frac{s}{\nu}} \left[ J_0\left(i\sqrt{\frac{s}{\nu}}a\right) - J_0\left(i\sqrt{\frac{s}{\nu}}r\right) \right]}{ia\sqrt{\frac{s}{\nu}} \left[ s^2 + \frac{a^2}{2} b \right] J_0\left(i\sqrt{\frac{s}{\nu}}a\right) - ba^2 J_1\left(i\sqrt{\frac{s}{\nu}}a\right)} \quad (\text{A.23})$$

$$\text{Let us make } H(s) = ia\sqrt{\frac{s}{\nu}} \left[ J_0\left(i\sqrt{\frac{s}{\nu}}a\right) - J_0\left(i\sqrt{\frac{s}{\nu}}r\right) \right]$$

$$\text{And } G(s) = ia\sqrt{\frac{s}{\nu}} \left[ s^2 + \frac{a^2}{2} b \right] J_0\left(i\sqrt{\frac{s}{\nu}}a\right) - ba^2 J_1\left(i\sqrt{\frac{s}{\nu}}a\right)$$

The relation (A.23) is written in the form:

$$W(r, s) = \frac{H(s)}{G(s)} \quad (\text{A.24})$$

By applying the theorem of residuals, the transform of  $W(r, s)$  is expressed by:

$$W(r, t) = \sum_{i=1}^{\infty} \frac{H(s_i)}{G'(s_i)} e^{s_i t} \quad (\text{A.25})$$

where  $s_i$  are the roots of  $G(s) = 0$ , and are therefore such that:

$$ia\sqrt{\frac{s_i}{\nu}} \left[ s_i^2 + \frac{a^2}{2} b \right] J_0\left(i\sqrt{\frac{s_i}{\nu}}a\right) - ba^2 J_1\left(i\sqrt{\frac{s_i}{\nu}}a\right) = 0 \quad (\text{A.26})$$

By deriving the denominator of (A.23), it can easily be shown that:

$$G'(s_i) = \frac{\chi_i \nu^3}{2ba^8} J_0(\chi_i) \Phi(\chi_i) \quad (\text{A.27})$$

in which:

$$\Phi(\chi_i) = 12\gamma\chi_i^2 - (\chi_i^4 + \gamma)^2 \quad \chi_i = ia\sqrt{\frac{s_i}{\nu}} \quad \gamma = \frac{\pi a^6 K}{\rho \nu^2 L} \quad (\text{A.28})$$

Taking into account (A.28), Eq. (A.25) is written:

$$W(r, \tau) = 16\beta\gamma \sum_{i=1}^{\infty} \frac{1}{\Phi(\chi_i)} \frac{J_0\left(\frac{r}{a}\chi_i\right) - J_0(\chi_i)}{J_0(\chi_i)} e^{-\chi_i^2 \tau} \quad (\text{A.29})$$

$$\beta = \frac{a^2 P_0}{4\rho \nu l}$$

where:  $\tau = (\nu/a^2)t$  and  $\chi_i$  are the roots of Eq. (A.26), which can be put in the form:

$$\gamma = \chi^4 \frac{J_0(\chi)}{J_2(\chi)} \quad (\text{A.30})$$

Equation (A.29) seems at first glance not to satisfy the initial

condition  $W(r, 0) = 0$ . If we remember that this initial condition was used in (A.14) to obtain solution (A.29), then this latter relation must satisfy this condition. On the other hand, with some quite laborious calculations (Bennis, 1983) we can show that:

$$\sum_{i=1}^{\infty} \frac{1}{\Phi(\chi_i)} \frac{J_0\left(\frac{r}{a} \chi_i\right) - J_0(\chi_i)}{J_0(\chi_i)} = 0 \quad (\text{A.31})$$

and thus:  $\dot{W}(r, 0) = 0$

## APPENDIX B

### Calculation of Instantaneous Flow

The longitudinal fluid velocity is given by Eq. (2):

$$W(r, \tau) = 16\beta\gamma \sum_{i=1}^{\infty} \frac{1}{\Phi(\chi_i)} \frac{J_0\left(\frac{r}{a} \chi_i\right) - J_0(\chi_i)}{J_0(\chi_i)} e^{-\chi_i^2 \tau} \quad (\text{B.1})$$

The expression for instantaneous flow is given by:

$$Q(\tau) = \int_0^{2\pi} \int_0^a W(r, \tau) r dr d\theta \quad (\text{B.2})$$

Suppose, by replacing the instantaneous velocity by its expression (B.1):

$$Q(\tau) = 32\pi\beta\gamma \sum_{i=1}^{\infty} \frac{e^{-\chi_i^2 \tau}}{\Phi(\chi_i) J_0(\chi_i)} \int_0^a \left[ J_0\left(\frac{r}{a} \chi_i\right) - J_0(\chi_i) \right] r dr \quad (\text{B.3})$$

and we make:  $y = r/a \chi_i$  we obtain:

$$\int_0^a \left[ J_0\left(\frac{r}{a} \chi_i\right) - J_0(\chi_i) \right] r dr = \frac{a^2}{\chi_i^2} \int_0^{\chi_i} [J_0(y) - J_0(\chi_i)] y dy \quad (\text{B.4})$$

Using the relation:

$$J_\nu(z) = \left(\frac{z}{2}\right)^\nu \sum_{p=0}^{\infty} \frac{(-1)^p}{p!} \frac{\left(\frac{z}{2}\right)^{2p}}{\Gamma(\nu+p+1)} \quad (\text{B.5})$$

where:  $\Gamma(\nu+p+1) = (\nu+p)!$  (B.6)

we have:  $\int_0^{\chi_i} y J_0(y) dy = 2 \left(\frac{\chi_i}{2}\right)^2 \sum_k \frac{(-1)^k}{k!(k+1)!} \times \left(\frac{\chi_i}{2}\right)^{2k} = \chi_i J_1(\chi_i)$  (B.7)

On the other hand:

$$\int_0^{\chi_i} y J_0(\chi_i) dy = \frac{\chi_i^2}{2} J_0(\chi_i) \quad (\text{B.8})$$

from which, by substituting (B.7) and (B.8) into (B.3), we obtain:

$$Q(\tau) = 16\pi a^2 \beta \gamma \sum_{i=1}^{\infty} \frac{1}{\Phi(\chi_i)} \frac{2J_1(\chi_i) - \chi_i J_0(\chi_i)}{\chi_i J_0(\chi_i)} e^{-\chi_i^2 \tau} \quad (\text{B.9})$$

Taking into account the relation that exists between  $J_0$ ,  $J_1$  and  $J_2$ :

$$2J_1(x) - xJ_0(x) = xJ_2(x)$$

Again, Eq. (A.9) is written:

$$Q(\tau) = 16\pi a^2 \beta \gamma \sum_{i=1}^{\infty} \frac{1}{\Phi(\chi_i)} \frac{J_2(\chi_i)}{J_1(\chi_i)} e^{-\chi_i^2 \tau} \quad (\text{B.10})$$

By replacing  $(J_2(\chi)/J_1(\chi)) = \chi^4/\gamma$  based on relation (3), and by replacing  $\beta$  by its value  $\beta = a^2 P_0 / 4\rho\nu L$ , Eq. (B.10) is written:

$$Q(\tau) = \frac{4\pi a^4 P_0}{\rho L \nu} \sum_{i=1}^{\infty} \frac{\chi_i^4}{\Phi(\chi_i)} e^{-\chi_i^2 \tau} \quad (\text{B.11})$$

## A Relative Examination of $C_D - Re$ Relationships Used in Particle Trajectory Calculations

D. D. Kladas<sup>1</sup> and D. P. Georgiou<sup>1</sup>

### Nomenclature

$A, B, C$  = constants (Eq. (5))  
 $b$  = height (Fig. 3)  
 $C_n$  = Cunningham correction factor  
 $C_D$  = drag coefficient  
 $dp$  = particle diameter  
 $f$  = dimensionless radial distance  
 $L$  = characteristic length  
 $M$  = Mach number  
 $m$  = exponent, Eq. (5)  
 $n$  = exponent, Eq. (5)  
 $Pr$  = Prandtl number  
 $Re_p$  = particle Reynolds number  
 $r$  = radial coordinate  
 $r_0$  = initial radial coordinate  
 $Stk$  = particle Stokes number  
 $T$  = absolute temperature  
 $V$  = velocity, absolute  
 $V_\infty$  = free-stream velocity  
 $\gamma$  = gas specific heat ratio  
 $\theta$  = angular coordinate  
 $\mu$  = dynamic viscosity  
 $\rho$  = density

### Introduction

For a large variety of gas - particle flows, realistic simulation of particle behavior in the flowfield is needed to calculate accurate particle trajectories. The accuracy depends largely on the flowfield (loading, compressibility, unsteadiness, turbulence level), the forces acting on the particles (drag, gravity, buoyancy, Basset, Saffman lift, apparent mass, thermophoresis), and the particle size, density, and shape. Previous investigators have employed simplified (and indeed justified) models in which spherical particles move in a steady, incompressible, single phase flow.

<sup>1</sup>Research Associate and Assistant Professor, respectively, Department of Mechanical Engineering, Thermal Engines Laboratory, University of Patras, Rion, Greece.

Contributed by the Fluids Engineering Division of THE AMERICAN SOCIETY OF MECHANICAL ENGINEERS. Manuscript received by the Fluids Engineering Division August 9, 1991. Associate Technical Editor: F. T. Dodge.

In trajectory calculations, the flowfield is known in either an analytical or a discrete (mesh) form. The particle equations of motion are integrated numerically using appropriately small steps. The predominant force acting on a particle is the drag force represented by a drag coefficient,  $C_D$ , whose value depends mainly on the particle Reynolds number,  $Re_p$ . At each step during the trajectory calculation, its value is input to the equations of motion that are being integrated. The dependence on  $Re_p$  asks for accurate  $C_D - Re_p$  relationships.

The present note examines the relative accuracy of 19 such relationships met in the literature. Two sample flowfields are considered: (i) a swirling flowfield similar to that found in cyclone separators and (ii) a cylinder in crossflow. The accuracy of fit of the various formulae to experimental data is reflected on the trajectory results, which in turn may be critical in the design process and performance prediction analysis. It must be here emphasized that trajectory predictions compared to the mean prediction of 19 formulae do not necessarily define a measure of accuracy or confidence of a particular drag formula, but only gives a measure of standard deviation.

### Equations of Motion

The gas-particle interaction in single phase flow, (where coupling between the solid and the fluid phases is not needed when the density ratio is less than 0.001), is described with the particle Reynolds and Stokes numbers:

$$Re_p = \frac{\rho_p dp |V - V_p|}{\mu} \quad (1)$$

$$Stk = \frac{\rho_p V_\infty dp C_n}{18 \mu L} \quad (2)$$

In a given two-dimensional flowfield where only the drag force is assumed to act on the particle, the equation of motion is:

$$\frac{dV_p}{dt} = \frac{18\mu}{\rho_p dp^2 C_n} g(Re) \cdot (V - V_p) \quad (3)$$

The particle drag coefficient generally depends on a number of parameters (Walsh, 1976):

$$C_D = g(Re_p, M, \gamma, Pr, T/T_p) \quad (4a)$$

In the case of incompressible flow, the calculations are carried out using explicit  $C_D - Re_p$  relations in the equation of motion:

$$C_D = g(Re_p) \quad (4b)$$

### Literature Survey

Morsi and Alexander (1972) proposed a polynomial fit of the form:

$$C_D = A + B \cdot \text{Re}_p^m + C \cdot \text{Re}_p^n \quad (5)$$

Several investigators (Michaelides, 1988; Rudinger, 1976; Elfeki et al., 1987; Walsh, 1976; Husein, et al., 1973, 1974) have suggested different values for  $A$ ,  $B$ ,  $C$ ,  $m$  and  $n$  for appropriate  $\text{Re}_p$  ranges, listed in Table 1.

A similar polynomial fit has been suggested by Tilly (1969) for studies of surface erosion:

$$C_D = \frac{24}{\text{Re}_p} (1 + 0.197 \text{Re}_p^{0.63} + 0.00026 \text{Re}_p^{1.38}) \quad (0-2.E5)$$

where the number in parenthesis indicate the applicable particle Reynolds number range. Dring and Suo (1978) employ the following formula to study the particle motion in a swirling flowfield:

$$C_D = \begin{cases} 4.5 + 24/\text{Re}_p & (0-1) \\ 10^{**} \log 28.5 - 0.842 \log \text{Re}_p & (0-60) \\ \quad + 0.06919 (\log \text{Re}_p)^2 & (0-60) \\ 10^{**} 2.0065 - 1.383 \log \text{Re}_p & (60-3000) \\ \quad + 0.19887 (\log \text{Re}_p)^2 & (60-3000) \\ 0.4 & (>3000) \end{cases}$$

whereas Clevenger and Tabakoff (1976) study dust particle trajectories in a turbomachine using:

$$C_D = \begin{cases} 4.5 + 24/\text{Re}_p & (0-1) \\ 28.5 - 24(\log \text{Re}_p) + 9.0682(\log \text{Re}_p)^2 & (1-3000) \\ -1.7713(\log \text{Re}_p)^3 + 0.1718(\log \text{Re}_p)^4 & (1-3000) \\ -0.0065(\log \text{Re}_p)^5 & (1-3000) \\ 0.4 & (3000-2.E5) \end{cases}$$

Flagan (1988) proposes the use of the following relation for cyclone separator work:

$$C_D = \begin{cases} 24/\text{Re}_p & (<0.1) \\ \frac{24}{\text{Re}_p} \left( 1 + \frac{3}{16} \text{Re}_p + \frac{9}{120} \text{Re}_p^2 \ln(2\text{Re}_p) \right) & (0.1-2) \\ \frac{24}{\text{Re}_p} (1 + 0.15 \text{Re}_p^{0.687}) & (2-500) \\ 0.44 & (500-2.E5) \end{cases}$$

Pinkus (1983) studies the motion of steam droplets through a blade channel using:

$$C_D = \begin{cases} 24/\text{Re}_p & (<0.6) \\ 0.05 \exp(6.193 \text{Re}_p^{-0.1496}) & (0.6-1500) \\ 0.398 & (>1500) \end{cases}$$

Finally, White (1974) proposes a single drag formula over a wide range of Reynolds numbers:

$$C_D = 0.4 + (24/\text{Re}_p) + \frac{6}{1 + \sqrt{\text{Re}_p}} \quad (0-2.E5)$$

Figure 1 shows existing experimental data for smooth spheres compared with some of the expressions listed above. The Stokes regime ( $\text{Re}_p < 0.2$ ) is approximated well by all formulae. Allen's regime ( $0.2 < \text{Re}_p \leq 500$ ) and Newton's regime ( $\text{Re}_p > 500$ ) are more difficult to approximate. Therefore, some disagreement is expected in trajectory calculations in these regions.

A preliminary study on the relative accuracy of fit used the experimental data presented by Morsi and Alexander (1972) for  $0 < \text{Re}_p < 200000$ . The formulae fit the data with varying degree of accuracy. To test the degree of deviation involved,

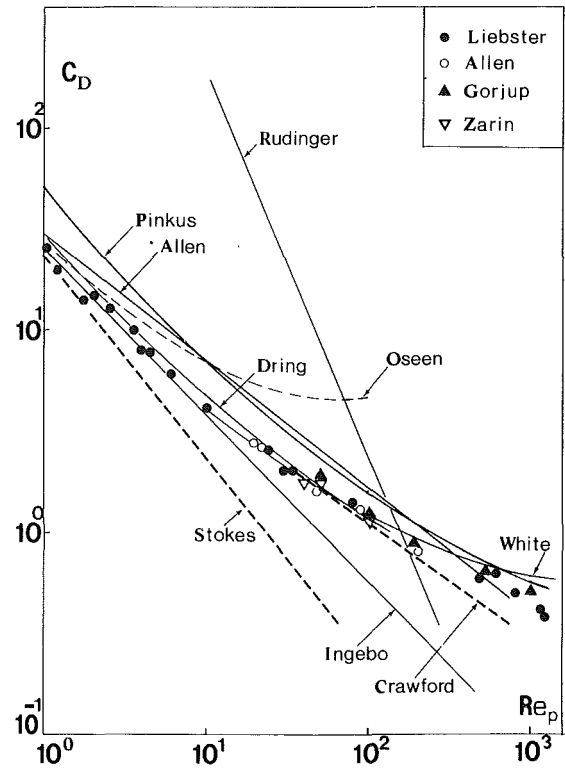


Fig. 1 Drag coefficient of spheres versus particle Re number

two flowfields are examined here. Since experimental data are not available, the trajectory results are compared to the mean prediction from all 19 formulae tested.

### The Swirling Flowfield

The analysis of the flowfield, which simulates a free-vortex flow met in cyclone separators, can be found in detail in a paper by Dring and Suo (1978) in which the particle trajectory equation was formulated in the Stokes regime only. The assumption of free-vortex flow simplifies the analysis since only the radial component of the relative motion between the particle and the fluid needs to be considered. In polar coordinates, the equation of the trajectory of a particle under the action of the drag force alone is, in the general case ( $f = r/r_0$ ):

$$f'' + \left( \lambda \cdot C_D - \frac{2}{f r_0} \right) r_0 (f')^2 - f = 0 \quad (6)$$

where

$$\lambda = \frac{3}{4} \cdot \frac{\rho}{\rho_p} \cdot \frac{1}{d_p}$$

Equation (6) was integrated numerically using a fourth-order Runge-Kutta scheme at one degree steps. The nondimensional radial distance ( $f$ ) of the particle was initiated at the value  $f = 1$  ( $r = r_s$ ). The integration was terminated at  $f = f^*$ , when  $\theta = 90$  deg.

Figure 2 shows the results of the calculations for fly ash particles ( $\rho_p = 2000 \text{ Kg/m}^3$ ). The expression used by Michaelides (1988) underestimates  $f^*$  by 21 percent, whereas that suggested by Rudinger (1976) overpredicts it by 64 percent. The percentage deviation (percent  $E_S$ ) from the mean value of  $f^*$  increases with Stokes number. Most predictions are within 5 percent of this mean. However, the formulae used by Michaelides (1988) and Pinkus (1983) show errors up to 20 percent

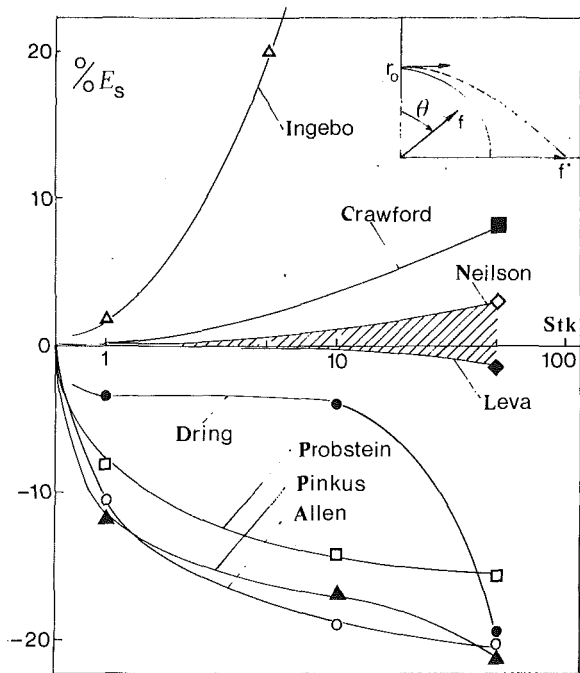


Fig. 2 Percentage deviation from the mean result - swirling flowfield

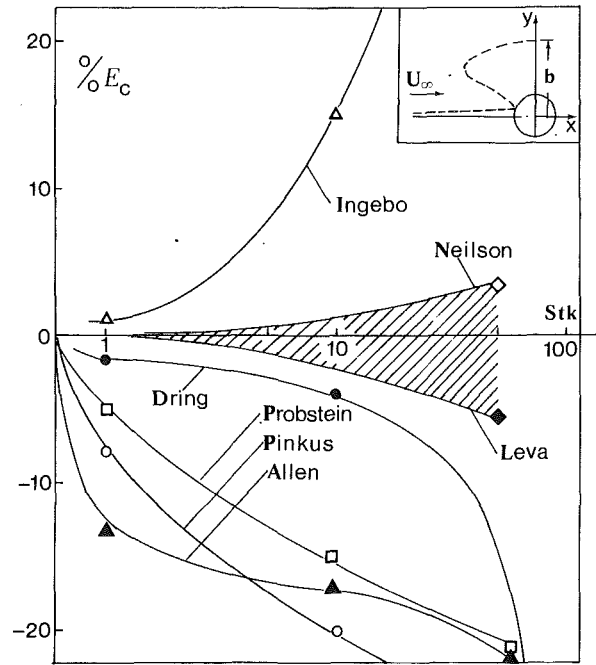


Fig. 3 Percentage deviation from the mean result - cylinder flowfield

for  $Stk < 50$ . In particular, Ingebo's formula (Rudinger, 1976) results to very large errors which increase enormously at large Stokes numbers. Also, the relationship used by Dring and Suo (1978) deviates suddenly the mean prediction at large Stokes numbers. High particle Reynolds number are encountered during the trajectory at about  $40 \text{ deg} < \theta < 50 \text{ deg}$ . These large deviations lead to considerable errors in cyclone wall impact location and efficiency prediction.

### Cylinder in Crossflow

The potential flowfield around a cylinder in crossflow can be found in standard textbooks. The particles assume local flow velocity and direction three diameters upstream and proceed to impact the cylinder. A preliminary examination showed that the point of the first impact on the frontal cylinder surface was predicted equally by all 19 drag expressions. This was because low particle Reynolds numbers ( $Re_p < 1$ ) were encountered in this part of the motion. To examine trajectories at higher  $Re_p$  values, where the formulas disagree, it was necessary to consider the subsequent motion of the particle after its impact. (This might simulate the trajectory of fly ash particles towards the leading edge of a turbine blade in a cascade.) The height  $b$ , above the cylinder axis, is therefore critical for the trajectory analysis.

The velocity and direction of the particle after impact are found by using standard empirical relationships obtained by Elfeki and Tabakoff (1987). The equations of motion are integrated by a R-K scheme. When a particle hits the cylinder, its velocity and direction after the impact are input to the trajectory code as the new initial conditions. The calculations stop when the particle passes directly above the cylinder at  $x = 0$ .

The results for  $Stk = 50$  are shown in Fig. 3. Again, the two extreme cases are those of Michaelides (1988) and Ingebo (Rudinger, 1976). The former underestimates  $b$  by 28 percent whereas the later overestimates it by 48 percent. All other trajectories lie within these limits. Following the impact, values of  $Re$  up to 140 were encountered. The percentage deviation (percent  $E_c$ ) from the mean value of  $b$  obtained from the 19

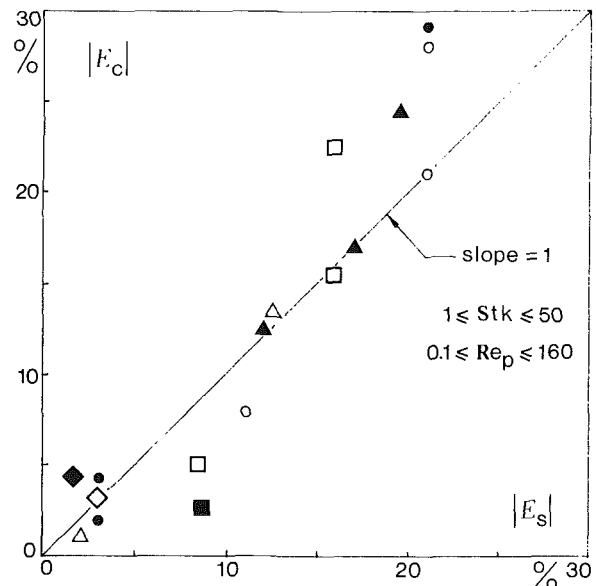


Fig. 4 Comparison of absolute percentage deviations from the mean for the two flowfields

expressions, increases with Stokes number. Deviation in most cases is in the range +5 percent for  $Stk < 50$ . Again, the formulas used by Michaelides (1988) and Pinkus (1983) underestimate  $b$  by about 25 percent. Ingebo's formula (Rudinger, 1976) results again to large errors.

It is interesting to note the similarity of Figs. 2 and 3 for the two different flowfield cases. An examination shows that the relationships of Michaelides (1988), Rudinger (1976), Dring et al. (1978), and Pinkus (1983) deviate almost equally from the mean prediction. A comparison of percentage deviations (on an absolute basis) is shown in Fig. 4 for a range of  $Re_p$  values. As it can be seen, the percentage deviation of the drag formulas used by Rudinger (1976), Dring (1978) and Pinkus (1983) is nearly the same in both flowfields. This indicates that

the prediction of the particle drag coefficient does not depend on whether the particle is in swirling or in stagnation flow.

### Conclusions

(1) Fifteen of the nineteen  $C_D - Re_p$  relationships tested yield trajectory results which are within 10 percent of the mean value, for particle Stokes numbers up to 50. However, four drag formulae showed, in both a free-vortex and a cylinder flowfield, deviations larger than 20 percent from the mean prediction.

(2) Large deviations from the mean are obtained for particle Reynolds numbers in the Allen regime (0.2 – 500). The deviations increase with particle Stokes number.

(3) The predictions do not seem to depend on the flowfield character. The same four formulae deviated from the mean prediction almost equally in both the swirling and the cylinder flowfields.

### References

Clevenger, W. B., and Tabakoff, W., 1976, "Dust Particle Trajectories in Aircraft Radial Turbines," *AIAA Journal*, pp. 786-791.

Dring, R. P., and Suo, M., 1978, "Particle Trajectories in Swirling Flows," *Journal of Energy*, Vol. 2, pp. 232-237.

Elfeki, S., and Tabakoff, W., 1987, "Erosion Study of Radial Flow Compressor With Splitters," *ASME Journal of Turbomachinery*, Vol. 109, pp. 62-69.

Flagan, R. C., and Seinfeld, J. H., 1988, *Fundamentals of Air Pollution Engineering*, Prentice Hall, N.J., pp. 137-142.

Hussein, M. F., and Tabakoff, W., 1973, "Dynamic Behaviour of Solid Particles Suspended by Polluted Flow in a Turbine Stage," *Journal of Aircraft*, Vol. 10, pp. 434-440.

Hussein, M. F., and Tabakoff, W., 1974, "Computation and Plotting of Solid Particle Flow in Rotating Cascades," *Computers and Fluids*, Vol. 2, pp. 1-15.

Michaelides, E. E., 1988, "On the Drag Coefficient and the Correct Integration of the Equation of Motion of Particles in Gases," *ASME JOURNAL OF FLUIDS ENGINEERING*, Vol. 110, pp. 339-341.

Morsi, S. A., and Alexander, A. J., 1972, "An Investigation of Particle Trajectories In Two-Phase Flow Systems," *Journal of Fluid Mechanics*, Vol. 55, Part 2, pp. 193-208.

Pinkus, O., 1983, "Liquid Particle Dynamics and Rate of Evaporation in the Rotating Field in Centrifugal Compressors," *ASME Journal of Engineering for Power*, Vol. 105, pp. 80-87.

Rudinger, G., 1976, *Flow of Solid Particles in Gases*, AGARDograph AG-222, pp. 59-60.

Tilly, G. P., 1969, "Erosion Caused By Solid Particles," *Wear*, Vol. 14, pp. 63-79.

Walsh, M., 1976, "Influence of Particle Drag Coefficient on Particle Motion in High-Speed Flow with Typical LDV Application," NASA TN-D-8120.

White, F., 1974, *Viscous Fluid Flow*, McGraw-Hill, pp. 172-184.

## APPENDIX

Table 1 Polynomial form

A	B	C	m	n	Re range
0	24	0	-1	-2	0-0.1
3.69	22.73	0.093	-1	-2	0.1-1
0.36	38.80	-12.65	-1	-2	1-10
0.6167	46.50	-166.67	-1	-2	10-100
0.3644	98.33	-2778	-1	-2	100-1000
0.3571	148.62	-47500	-1	-2	1000-5000
0.46	-490.546	57.87 × 10	-1	-2	5000-10000
0	24	0	-1	0	0-0.1
4.5	24	0	-1	0	0.1-1
0	24	3.6	-1	-0.313	1-1000
0	24	0	-1	0	0-1
0	30	0	-0.625	0	1-800
0.44	0	0	0	0	800-2 × 10
0.2	0	0	0	0	> 2 × 10
0	24	4	-1	-0.3333	?
0	24	0	-1	0	0-0.1
4.5	24	0	-1	0	1-4
0.3246	21.9416	0	-0.718	0	4-2000
0.4	0	0	0	0	> 2000
0.48	28	0	-0.85	0	
0	27	0	-0.84	0	0.1-500
0	24	2.4	-1	-0.01	0.2-2
0	24	2.64	-1	-0.19	2-21
0	24	4.536	-1	-0.37	21-200
0	24	3.6	-1	-0.313	0-200
0.324	21.9416	0	-0.718	0	200-2500
0.4	0	0	0	0	> 2500
2	24	0	-1	0	0-10
0.344	67.3	-287.4	-1	-2	10-700
0.44	0	0	0	0	> 700
0	24	0	-1	0	
0.4	24	4	-1	-0.5	?
0.23	21.5	6.5	-1	-0.5	
0	24	0	-1	0	0-1
0	24	0	-0.6	0	1-1000
0.44	0	0	0	0	> 1000
0	24	0	-1	0	0-1
0	18.48	0	-0.6	0	1-500
0.44					> 500

# A Unifying Method for Sizing Throttling Valves Under Laminar or Transitional Flow Conditions

H. D. Baumann<sup>1</sup>

The mass flow passing through a given valve will decrease in Reynolds number ranges below approximately 10,000 due to the transition from fully developed turbulent to laminar flow. The objective of this study is to provide a uniform prediction method to establish, with reasonable accuracy, the ratio between the turbulent and transitional or laminar flow rate passing through a given valve, taking into account the valve's hydraulic diameter and the initial turbulent velocity head loss coefficient. Experimental data from prior research tends to support a proposed "unified sizing method" that is applicable for all single-stage valves regardless of size or type.

## Nomenclature

- $A$  = area of pipe, m<sup>2</sup>  
 $A_0$  = flow area through valve trim, m<sup>2</sup>  
 $C_{vT}$  = flow coefficient of valve established under turbulent flow conditions  $2.4 \times 10^{-5} (\text{m}^3/\text{s})(\text{Kg}/\text{m}^3)^{0.5} / (\text{N}/\text{m}^2)^{0.5}$   
 $d$  = valve size, mm  
 $D$  = diameter of pipe  
 $D_H$  = hydraulic diameter of valve trim flow passage  
 $D_0$  = equivalent orificial diameter of trim flow area  
 $f$  = friction factor,  $K/(L/D)$   
 $F_d$  = valve style modifier,  $D_H/D_0$   
 $F_L$  = liquid pressure recovery factor (see ISA Standard 75.01, 1985)  $(P_1 - P_2/P_1 - P_0)^{0.5}$   
 $F_R$  = valve Reynolds number factor, (see ISA Standard 75.01, 1985)  
 $G_f$  = specific gravity of fluid,  $\rho/\rho_{\text{water}}$   
 $K$  = turbulent velocity head loss coefficient of valve trim and pipe,  $K_{vT} + K_{pT}$   
 $K_{vL}$  = velocity head loss coefficient of valve at Reynolds numbers below 10,000  
 $K_{vT}$  = velocity head loss coefficient of valve at turbulent flow, i.e.,  $Re_v \geq 10,000$   
 $K_{pL}$  = velocity head loss coefficient of pipe ( $8 \times L/D$ ) at same Reynolds numbers below 10,000  
 $K_{pT}$  = velocity head loss coefficient of 8 diameter length of pipe at turbulent flow ( $8 L/D = \text{Standard ISA Test Section for Measuring } C_{vT}$ ),  $Re_v \geq 10,000$ .  
 $L$  = length of pipe  
 $N_R = F_R/F_d$   
 $P_0$  = vena contracta pressure in kPa  
 $P_1$  = inlet pressure in kPa  
 $P_2$  = outlet pressure in kPa  
 $q$  = flow rate in m<sup>3</sup>/h  
 $Re_v$  = valve Reynolds number  
 $\nu$  = kinematic viscosity, cSt,  $10^{-6} \text{ m}^2/\text{s}$   
 $\rho$  = fluid density, Kg/m<sup>3</sup>

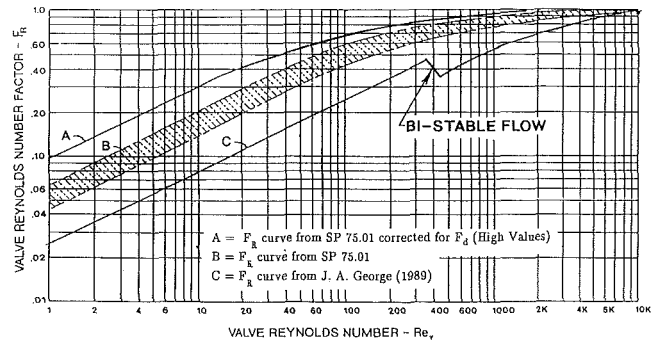


Fig. 1 Various correction curves for  $F_R$ . The ratio between turbulent valve flow coefficient and those measured at lower Reynolds numbers. Area above  $Re_v$  400 may exhibit unstable flow behavior.

## Introduction

During a study by Marcadet (1982) of flow phenomena in throttling valves having very small fluid conduits or orifices, it was found that the ratio between the flow rate under fully developed laminar conditions and the turbulent flow rate was significantly different for a given valve Reynolds number than guidelines established within the Instrument Society of America's (ISA) Standard 75.01 (1985) would have predicted. Similar discrepancies were found by George (1989) and Baumann (1991a).

Correction curves found in ISA Standard 75.01 (1985) are based on the pioneering work of Stiles (1967) who measured ratios between laminar, transitional, and turbulent flow on a number of control valves ranging from sizes  $1/2$  to  $1 1/2$  in. using fluids ranging from water to high viscosity oils. However, while his test curves were very consistent, there were significant disparities between different valve sizes and valve plug types. Stiles found no satisfactory explanation for these significant disparities, and the committee writing the ISA Standard 75.01 (1985) chose to integrate these into a broad tolerance spectrum shown as Curve B in Fig. 1. An example may serve to demonstrate the degree of error that could be caused using the current ISA sizing method:

- Using a ball valve having a  $C_{vT}$  of 10.4, it is desired to know the flowing quantity of Naphthalene having a kinematic viscosity  $\nu$  of 398 cSt at 20°C, an inlet pressure of 345 kPa, and an outlet pressure of 312 kPa. The pipe size is 15 mm. The  $F_L$  factor of the valve is 0.54, and the specific gravity  $G_f$  of the fluid is 1.15. The current Eqs. (9) and (11) and Fig. 1 in ISA Standard 75.01 (1985) can be solved simultaneously to yield the following:

$$q = 0.0865 \times F_R \times C_{vT} (P_1 - P_2)^{0.5} / (G_f)^{0.5} \quad (1)$$

$$q = 0.0865 \times 0.6 \times 10.4(33)^{0.5} / (1.15)^{0.5}$$

$$q = 2.9 \text{ m}^3/\text{h}$$

$F_R$  is determined from the valve Reynolds number given as:

$$Re_v = \frac{76000 \times F_d \times q}{\nu (C_{vT} \times F_L)^{0.5}} \left( \frac{F_L^2 C_{vT}^2}{0.00214 \times d^4} + 1 \right)^{0.25} \quad (2)$$

$$Re_v = \frac{76000 \times 1 \times 2.9}{398(10.4 \times 0.54)^{0.5}} \left( \frac{0.54^2 \times 10.4^2}{0.00214 \times 15^4} + 1 \right)^{0.25}$$

$Re_v = 249$ , yielding an  $F_R$  of 0.6 from Fig. 1 of the ISA Standard

Note, in the current standard, Table D-1 gives  $F_d$  as 1.0 for a ball valve; however,  $F_d$  should have been 0.9 for the chosen valve at the given opening. When  $F_d$  is changed and Eq. (11) of this paper is used to calculate  $F_R$ , a new simultaneous solution yields an  $F_R$  of 0.25, a valve Reynolds number of 92.7,

<sup>1</sup>H. D. Baumann Assoc., Ltd., Portsmouth, NH 03801.

Contributed by the Fluids Engineering Division of THE AMERICAN SOCIETY OF MECHANICAL ENGINEERS. Manuscript received by the Fluids Engineering Division October 11, 1991. Associate Technical Editor: F. T. Dodge.

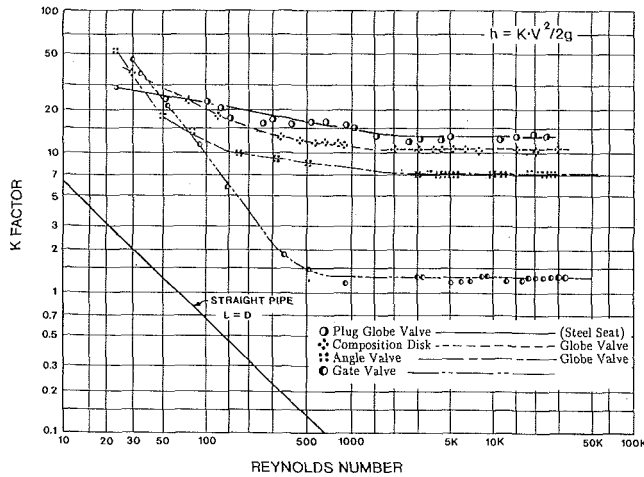


Fig. 2 Test data taken from Kittredge and Rowley (1957) on a number of 1/2 in. valves and a straight pipe with 15.94 mm inside diameter and using S.A.E. 10 oil as fluid.

and a flowing quantity of only 1.2 m<sup>3</sup>/h compared to the 2.9 m<sup>3</sup>/h flow rate given above. Even more significant errors appear in the sizing of small flow valves as shown by test data from Baumann (1991a) in his Figs. 5 and 6 when the current ISA method is used as a prediction method. This paper proposes a method that improves the sizing accuracy for not only small flow valves and globe valves, but also covers other valve styles such as butterfly valves and ball valves for which no current sizing method exists.

### Investigation of Prior Research Data

Independent verification of the data by Stiles (1967) was obtained from test results published by Kittredge and Rowley (1957) on a number of 1/2 in. valves and fittings. While the scattering of valve test data seemed at first discouraging (see Fig. 2), it was found that after converting the data into terms of  $C_v$  and  $F_R$  sizing coefficients, now in worldwide use by the valve industry (see ISA Standard 75.01, (1985) and the equivalent International IEC Standard publication 534-2-1) and converting the pipe Reynolds number into the ISA defined valve Reynolds  $Re_v$  (see Eq. (2)), the data did show good conformity to those of Stiles (see Fig. 3). In order to establish the  $C_v$  of a given test valve from Kittredge and Rowley (1957) data, an equation derived from the Darcy formula was used:

$$C_{vT} = \frac{5.98 \times 10^4 A}{\sqrt{K_{vT} + K_{pT}}} \quad (3)$$

Note, that the area of the pipe is used here since the  $K$  factors from the above reference are based on the fluid velocity in the pipe.

According to ISA Standard 75.01 (1985),  $F_R$  was established by dividing  $C_{vL}$  (or laminar flow coefficient) by  $C_{vT}$  or:

$$F_R = \frac{5.98 \times 10^4 A}{\sqrt{K_{vL} + K_{pL}}} \bigg/ \frac{5.98 \times 10^4 A}{\sqrt{K_{vT} + K_{pT}}} \quad (4)$$

or

$$F_R = \sqrt{K_{vT} + K_{pT}} / \sqrt{K_{vL} + K_{pL}} \quad (5)$$

Data for the fully developed laminar regime ( $Re_v \leq 100$ ) only showed very good correlation when the pipe Reynolds number was converted to a corresponding valve Reynolds number  $Re_v$ , as defined in ISA Standard 75.01 (1985), by accounting for  $C_{vT}$  and by multiplying  $N_R$  by  $F_d$  (see Fig. 3). The latter is the valve style modifier defined by Baumann (1991b) as the ratio of the hydraulic diameter of a given valve passage to the equiv-

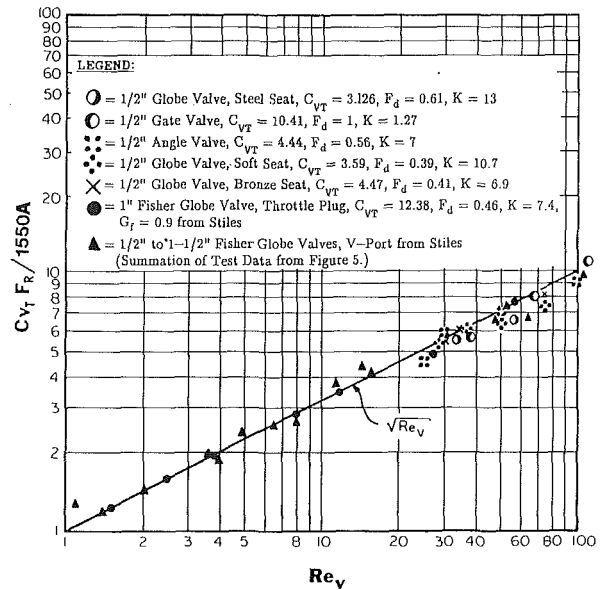


Fig. 3 Unifying relationship for all valves from Kittredge and Rowley's (1957) and Stiles' (1967) test data.

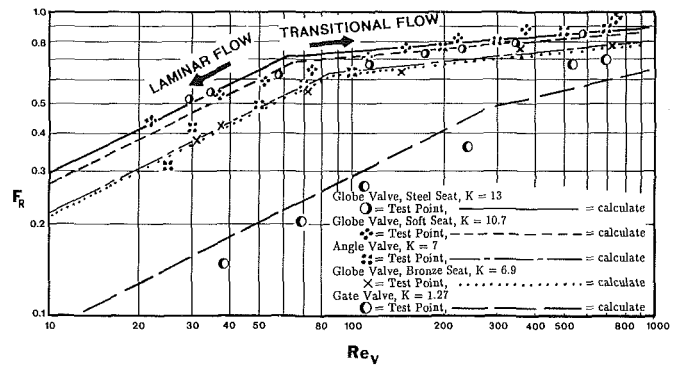


Fig. 4 Test data from Fig. 2 converted into  $F_R$  and plotted as a function of  $Re_v$  for different  $K$  values.

alent circular diameter of the corresponding flow area. For more discussion on the empirical determination of  $F_d$ , see below. Using regression analyses and plotting test data from Kittredge and Rowley (1957) against the valve Reynolds number  $Re_v$ , in the fully developed laminar flow regime all "pseudo  $C_v$ " numbers, i.e.,  $(1/1550) C_{vT} \times F_R$  divided by the pipe area fall on, or close to, a line given by  $(Re_v)^{0.5}$ . As indicated in Fig. 3, the data given by Stiles conforms to this finding. The results can be expressed by the relationship:

$$C_{vT} F_R = 1550 A (Re_v)^{0.5} \quad (6)$$

$$\text{or } C_{vT} F_R = A (Re_v)^{0.5} \text{ if } A \text{ is expressed in in}^2.$$

$$\text{Since } A = C_{vT} (K)^{0.5} / 5.89 \times 10^4 \text{ (m}^2\text{)} \quad (7)$$

from Eq. (3),

combining Eqs. (6) and (7) yields:

$$F_R = 0.026 (Re_v K)^{0.5} \quad (8)$$

This equation<sup>2</sup> shows that the ratio of laminar to turbulent flow is not dependent on valve size, as some data from Stiles (1967) might indicate, but rather on the half power of the velocity head loss coefficient  $K$ . The results for a  $K$  of 1.0 closely matches the line given by George (1989). Figure 4, which shows partial test data from Kittredge and Rowley (1957),

<sup>2</sup>NOTE:  $1 C_{vT} = 0.026 \text{ in}^2$ .



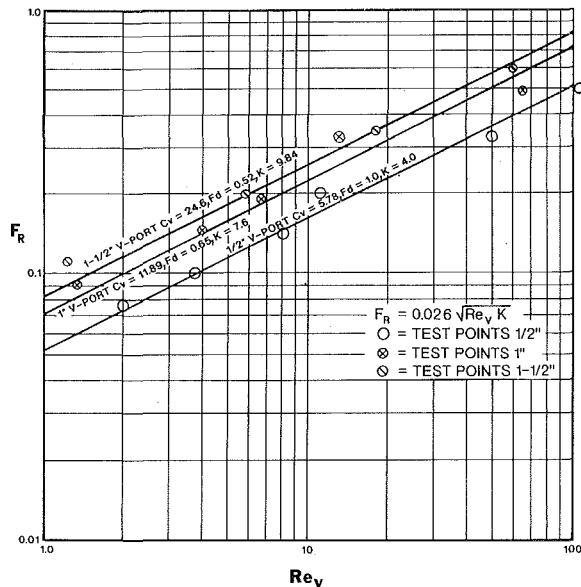


Fig. 5 Test data from Stiles (1967) for various V-port style valve sizes are plotted as a function of  $Re_v$  for valves having different  $K$  values.

seems to confirm the validity of Eq. (8). This finding explains the data in Stiles' (1967) Fig. 5, for example, showing an equivalent  $F_R$  at a  $N_R = 10$  of about 0.15 for a  $1/2$  in. valve, yet 0.22 for a  $1\frac{1}{2}$  in. valve. In view of the data from Fig. 2, it appears that this difference is solely due to the fact that the  $K$  factors varied proportionally to the valve size as shown in Fig. 5.

It, therefore, appears that in the truly laminar flow regime,  $C_{vT} \times F_R$  is constant for a given pipe area and valve Reynolds number.

This means that for any given valve the mass flow of a given fluid in the fully developed laminar regime is the same for a given pipe area, regardless of how torturous the flow path within the valve body or valve trim is, as long as the orificial discharge area is about equal to the pipe area. In other words, the valve simply becomes an extension in length to the adjacent piping. Note, that the above relationship applies only where the valve orifice diameter is approximately equal to the pipe inside diameter, i.e., where the fluid velocity in the pipe is not significantly different from that in the valve orifice and where there is no significant difference in the length of adjacent piping from those of the test section given in ISA Standard 72.02 (1988).

### Establishment and Application of a Sizing Method for Transitional and Laminar Flow

Having thus found a unifying relationship expressed by Eq. (6), it is possible to develop sizing equations which should give reasonably correct results, at least in the purely laminar flow regime. First, one has to calculate the valve Reynolds number from Eq. (2). The required turbulent flow coefficient  $C_{vT}$  for a valve, which is sufficient to pass a given quantity of viscous liquids or liquids flowing at low velocities, is also given in Eq. (9) of the ISA standard as:

$$C_{vT} = q(G_f)^{0.5} / 0.0865 F_R (P_1 - P_2)^{0.5} \quad (9)$$

The unknown factor here is  $F_R$  which is given for the laminar flow regime by Eq. (8) as:  $F_R = 0.026(Re_v K)^{0.5}$ . However,  $K$ , the velocity head loss coefficient of the valve and adjacent piping ( $K$ ) is usually not stated in the manufacturer's literature. It seems, therefore, more convenient to substitute  $C_{vT}/d^2$  for  $K$  in the calculation of  $F_R$ , thus again from the Darcy Equation,

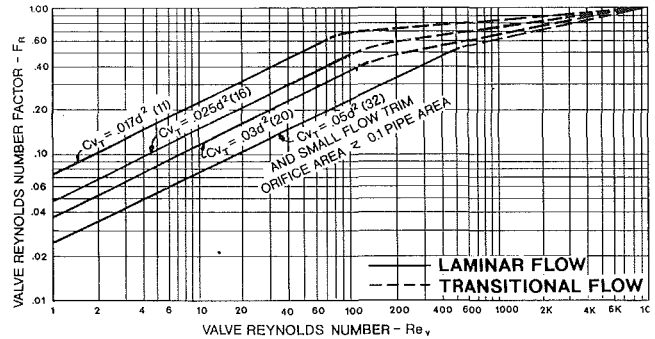


Fig. 6 Proposed correction factors  $F_R$  for valve Reynolds numbers  $Re_v$  below 10,000 based on flow coefficient per pipe diameter squared. NOTE: Numbers in parentheses apply when " $d$ " is expressed in inches.

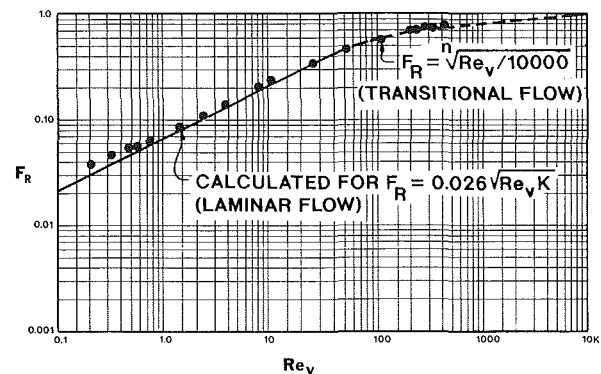


Fig. 7 Test data from Stiles (1967) on 1 in. throttle plug valve taken with "Mobil Compound DD," viscosity 451-589 cSt,  $C_{vT} = 12.38$ ,  $F_L = 0.91$ ,  $K = 7.03$ ,  $F_d = 0.46$ .

$$K = 0.00214 d^4 / C_{vT}^2 \quad (10)$$

$$\text{making } F_R = 1.2 \times 10^{-3} (Re_v)^{0.5} / (C_{vT} / d^2) \quad (11)$$

when Eqs. (8) and (10) are combined.

A problem arises in how to define the transitional flow regimes between  $Re_v$  100 and 10,000, where there is no established relationship and where we may encounter bistable flow phenomena. Here we suggest the use of the following curve fitting equation:

$$F'_R = (Re_v / 10000)^{1/n}, \quad (12)$$

where  $n = 1 + K + \log(Re_v)$ , an exponent that seems to best fit the available test data.  $F'_R$  establishes the correction factor for the transitional Reynolds number while  $F_R$  from Eq. (11) is applicable strictly for purely laminar flow. The inflection points between the laminar (steep slopes) and transitional (less sloped) lines indicating  $F_R$  in Fig. 6, clearly show that the effect of a torturous flow path in a valve is to delay the onset of laminar flow until the flow velocity is low enough (hence a lower Reynolds number) to prevent flow disturbances from being generated and thereby disturb streamlines. A less torturous valve, such as a fully open ball valve having a low velocity head loss coefficient  $K$ , or a high  $C_v/d^2$  value, will produce fewer eddies capable of disrupting the formation of downstream streamlines. Hence, fully developed laminar flow occurs at much higher fluid velocities, i.e.,  $Re_v$  numbers.

A set of curves generated from Eqs. (11) and (12) are illustrated in Fig. 6, while Fig. 7 shows a comparison of calculated  $F_R$  values for a 1 in. globe valve,  $F_d = 0.46$  with a  $C_{vT}/d^2$  of 0.017,<sup>3</sup> with data taken using Mobil Compound DD,  $\nu \cong 580$  cSt, as test fluid from Stiles (1967) (abstracted from original

<sup>3</sup> $C_{vT}/d^2 = 11$  when  $d$  is expressed in inches.

tabulated data). Fortunately, practically all valves sized for viscous fluids have full size trim, and therefore can be sized by the above method. The only exceptions are valves handling minute flowing quantities of either gas or liquid in which the flow passages are so small as to produce frictional pressure drop under low Reynolds numbers. Here, a velocity head loss coefficient of  $K$  of 1 can be assumed in most cases at least where  $C_{vT}$  is established by means of choked air flow, since there is virtually no hydraulic resistance in any part of the valve housing (the fluid velocity through the pipe and housing is insignificant), which normally accounts for the major portion of the  $K$  factors in full size valves. This is confirmed by data from George (1989).

### Establishing the $F_d$ Factor

The  $F_d$  factor, i.e., the ratio of the hydraulic diameter to the equivalent circular orifice diameter of the total flow area for a given valve trim has to be stated in the manufacturer's literature in order to allow the valve user the means to calculate  $Re_v$ . This factor can be calculated in most cases from drawing dimensions and from equations given by Baumann (1991b). The results agree reasonably with most of the test data in this paper. Fortunately, the above unifying method does allow for the development of an equation that can derive a value for  $F_d$  from test data under fully laminar conditions (i.e.,  $F_R \propto Re_v^{0.5}$ ).

Since, from Eq. (2),  $Re_v = 76000 q F_d / v (C_{vT} F_L)^{0.5}$ , neglecting the "velocity of approach" factor (the terms in parentheses to the 0.25 power), and  $F_R = 0.026 (Re_v K)^{0.5}$ ,

$$F_d = 0.019 (C_{vT} F_L)^{0.5} v F_R^2 / q K \quad (13)$$

In order to get correct results, sufficient test points have to be taken to ensure that  $F_R$  is proportional to  $(Re_v)^{0.5}$ . Finally, Eq. (13) should be employed for at least three consistent, separate laminar flow rates from which an average  $F_d$  value may then be taken. Any experimental determination of  $F_R$  or  $F_d$  should only be done with sufficient length of upstream and downstream pipe so that pressure measurements upstream and downstream are free of any flow disturbances caused by the valve to be tested. According to Beck (1944), such disturbances can propagate downstream up to 50 pipe diameters of pipe length for a pipe tee; for example, when Reynolds numbers are significantly above 380, but tend to reduce to only 10 diameters at this number. The length of the measuring section given by ISA Standard 75.02 of  $8 L/D$  should therefore only be used to measure  $F_R$  and  $F_d$  at valve Reynolds numbers below 100.

### Conclusion

Present sizing methods published by the Instrument Society of America for the prediction of valve flow rates at Reynolds numbers below 5000 have been shown to be incomplete and error prone. Besides the lack of a precise definition for the valve style modifier  $F_d$  there has to be a more detailed method to calculate the  $F_R$  factor for other than simple, single-seated globe valves with  $K$  factors around 12 and  $F_d = 1$  on which the present method is based. From prior test data, it was found that for valves having orifice sizes close to the pipe diameter, the flow coefficient  $C_v$  under laminar conditions ( $C_{vT} \times F_R$ ) is the same for a given valve Reynolds number and pipe area regardless of valve size or valve type. This finding leads to the derivation of equations for the estimation of  $F_R$  and for the verification of  $F_d$  from test data. The available test data shows good agreement with the estimated values of both terms. Finally, empirical equations are proposed to cover the transitional flow regime between truly laminar and fully turbulent

flow based on a valve's specific resistance coefficient  $K$  and the corresponding  $C_{vT}/d^2$  value.

### Acknowledgment

I would like to express my thanks and appreciation to Mr. Marc L. Riveland of Fisher Controls International for his support of my investigation and for giving me access to the original Stiles' test data.

### References

- Baumann, H. D., 1991a, "Viscosity Flow Correction For Small Control Valve Trim," *ASME JOURNAL OF FLUIDS ENGINEERING*, Vol. 113, pp. 86-89.
- Baumann, H. D., 1991b, "Determination of Peak Internal Sound Frequency Generated by Throttling Valves for the Calculation of Pipe Transmission Losses," *Noise Control Engineering Journal*, Vol. 36, No. 2, pp. 75-83.
- Beck, C., 1944, "Laminar Flow Friction Losses Through Fittings, Bends, and Valves," *Journal of the American Society of Naval Engineers*, Vol. 56, pp. 235-271.
- George, J. A., 1989, "Sizing and Selection of Low Flow Control Valves," *INTECH*, Vol. 36, No. 11, pp. 46-48.
- Instrument Society of America (ISA) Standard 75.01, 1985, *Flow Equations for Sizing Control Valves*, Instrument Society of America, Research Triangle Park, NC.
- Instrument Society of America (ISA) Standard 75.02, 1988, *Control Valve Capacity Test Procedure*, Instrument Society of America, Research Triangle Park, NC.
- Kittredge, C. P., and Rowley, D. S., 1957, "Resistance Coefficients for Laminar and Turbulent Flow Through One-Half-Inch Valves and Fittings," *Trans. ASME*, Vol. 79, pp. 1759-1766.
- Marcadet, L., 1982, *Low Flow Valve Sizing and Selection*, Maseonelan-Dresser, 107 Avenue Charles de Gaulle, Neuilly-s/Seine, France.
- Stiles, G. F., 1967, "Liquid Viscosity Effects on Control Valve Sizing," *Technical Manual TM17*, Fisher Controls International, Marshalltown, IA.

## Incompressible Fluid Flow Through Pipes Packed With Spheres at Low Dimension Ratios

R. M. Fand,<sup>1</sup> M. Sundaram,<sup>1</sup> and M. Varahasamy<sup>1</sup>

*This technical note reports the results of the last of a series of three studies of the flow of incompressible fluids through pipes packed with spheres. In the first of these studies, published in the Journal of Fluids Engineering in 1987, it was shown that certain experimentally determined parameters which govern incompressible fluid flow through such packings are substantially independent of the dimension ratio,  $D/d$ , for  $D/d \geq 40$ , where  $D$  and  $d$  represent the pipe and sphere characteristic dimensions (diameters), respectively. The second of the aforementioned studies, published in the Journal of Fluids Engineering in 1990, focused on the range  $1.40 \leq D/d < 40$ . In this range the flow parameters are functionally dependent upon  $D/d$  due to the so-called "wall effect." The present investigation deals with the range  $1.08 \leq D/d \leq 1.40$ , for which it is shown that the results are quite different from those obtained for higher  $D/d$ . Correlation equations are presented here by means of which the flow is characterized in the range  $1.08 \leq D/d \leq 1.40$ . It is anticipated that this information will have*

<sup>1</sup>Department of Mechanical Engineering, University of Hawaii at Manoa, Honolulu, Hawaii 96822.

Contributed by the Fluids Engineering Division of THE AMERICAN SOCIETY OF MECHANICAL ENGINEERS. Manuscript received by the Fluids Engineering Division April 21, 1992. Associate Technical Editor: F. T. Dodge.

<sup>4</sup>NOTE: The constant in Eq. (13) becomes 0.086 when  $q$  is given in U.S. Gallons per Minute.

tabulated data). Fortunately, practically all valves sized for viscous fluids have full size trim, and therefore can be sized by the above method. The only exceptions are valves handling minute flowing quantities of either gas or liquid in which the flow passages are so small as to produce frictional pressure drop under low Reynolds numbers. Here, a velocity head loss coefficient of  $K$  of 1 can be assumed in most cases at least where  $C_{vT}$  is established by means of choked air flow, since there is virtually no hydraulic resistance in any part of the valve housing (the fluid velocity through the pipe and housing is insignificant), which normally accounts for the major portion of the  $K$  factors in full size valves. This is confirmed by data from George (1989).

### Establishing the $F_d$ Factor

The  $F_d$  factor, i.e., the ratio of the hydraulic diameter to the equivalent circular orifice diameter of the total flow area for a given valve trim has to be stated in the manufacturer's literature in order to allow the valve user the means to calculate  $Re_v$ . This factor can be calculated in most cases from drawing dimensions and from equations given by Baumann (1991b). The results agree reasonably with most of the test data in this paper. Fortunately, the above unifying method does allow for the development of an equation that can derive a value for  $F_d$  from test data under fully laminar conditions (i.e.,  $F_R \propto Re_v^{0.5}$ ).

Since, from Eq. (2),  $Re_v = 76000 q F_d / v (C_{vT} F_L)^{0.5}$ , neglecting the "velocity of approach" factor (the terms in parentheses to the 0.25 power), and  $F_R = 0.026 (Re_v K)^{0.5}$ ,

$$F_d = 0.019 (C_{vT} F_L)^{0.5} v F_R^2 / q K \quad (13)$$

In order to get correct results, sufficient test points have to be taken to ensure that  $F_R$  is proportional to  $(Re_v)^{0.5}$ . Finally, Eq. (13) should be employed for at least three consistent, separate laminar flow rates from which an average  $F_d$  value may then be taken. Any experimental determination of  $F_R$  or  $F_d$  should only be done with sufficient length of upstream and downstream pipe so that pressure measurements upstream and downstream are free of any flow disturbances caused by the valve to be tested. According to Beck (1944), such disturbances can propagate downstream up to 50 pipe diameters of pipe length for a pipe tee; for example, when Reynolds numbers are significantly above 380, but tend to reduce to only 10 diameters at this number. The length of the measuring section given by ISA Standard 75.02 of  $8 L/D$  should therefore only be used to measure  $F_R$  and  $F_d$  at valve Reynolds numbers below 100.

### Conclusion

Present sizing methods published by the Instrument Society of America for the prediction of valve flow rates at Reynolds numbers below 5000 have been shown to be incomplete and error prone. Besides the lack of a precise definition for the valve style modifier  $F_d$  there has to be a more detailed method to calculate the  $F_R$  factor for other than simple, single-seated globe valves with  $K$  factors around 12 and  $F_d = 1$  on which the present method is based. From prior test data, it was found that for valves having orifice sizes close to the pipe diameter, the flow coefficient  $C_v$  under laminar conditions ( $C_{vT} \times F_R$ ) is the same for a given valve Reynolds number and pipe area regardless of valve size or valve type. This finding leads to the derivation of equations for the estimation of  $F_R$  and for the verification of  $F_d$  from test data. The available test data shows good agreement with the estimated values of both terms. Finally, empirical equations are proposed to cover the transitional flow regime between truly laminar and fully turbulent

flow based on a valve's specific resistance coefficient  $K$  and the corresponding  $C_{vT}/d^2$  value.

### Acknowledgment

I would like to express my thanks and appreciation to Mr. Marc L. Riveland of Fisher Controls International for his support of my investigation and for giving me access to the original Stiles' test data.

### References

- Baumann, H. D., 1991a, "Viscosity Flow Correction For Small Control Valve Trim," *ASME JOURNAL OF FLUIDS ENGINEERING*, Vol. 113, pp. 86-89.
- Baumann, H. D., 1991b, "Determination of Peak Internal Sound Frequency Generated by Throttling Valves for the Calculation of Pipe Transmission Losses," *Noise Control Engineering Journal*, Vol. 36, No. 2, pp. 75-83.
- Beck, C., 1944, "Laminar Flow Friction Losses Through Fittings, Bends, and Valves," *Journal of the American Society of Naval Engineers*, Vol. 56, pp. 235-271.
- George, J. A., 1989, "Sizing and Selection of Low Flow Control Valves," *INTECH*, Vol. 36, No. 11, pp. 46-48.
- Instrument Society of America (ISA) Standard 75.01, 1985, *Flow Equations for Sizing Control Valves*, Instrument Society of America, Research Triangle Park, NC.
- Instrument Society of America (ISA) Standard 75.02, 1988, *Control Valve Capacity Test Procedure*, Instrument Society of America, Research Triangle Park, NC.
- Kittredge, C. P., and Rowley, D. S., 1957, "Resistance Coefficients for Laminar and Turbulent Flow Through One-Half-Inch Valves and Fittings," *Trans. ASME*, Vol. 79, pp. 1759-1766.
- Marcadet, L., 1982, *Low Flow Valve Sizing and Selection*, Maseonelan-Dresser, 107 Avenue Charles de Gaulle, Neuilly-s/Seine, France.
- Stiles, G. F., 1967, "Liquid Viscosity Effects on Control Valve Sizing," *Technical Manual TM17*, Fisher Controls International, Marshalltown, IA.

## Incompressible Fluid Flow Through Pipes Packed With Spheres at Low Dimension Ratios

R. M. Fand,<sup>1</sup> M. Sundaram,<sup>1</sup> and M. Varahasamy<sup>1</sup>

*This technical note reports the results of the last of a series of three studies of the flow of incompressible fluids through pipes packed with spheres. In the first of these studies, published in the Journal of Fluids Engineering in 1987, it was shown that certain experimentally determined parameters which govern incompressible fluid flow through such packings are substantially independent of the dimension ratio,  $D/d$ , for  $D/d \geq 40$ , where  $D$  and  $d$  represent the pipe and sphere characteristic dimensions (diameters), respectively. The second of the aforementioned studies, published in the Journal of Fluids Engineering in 1990, focused on the range  $1.40 \leq D/d < 40$ . In this range the flow parameters are functionally dependent upon  $D/d$  due to the so-called "wall effect." The present investigation deals with the range  $1.08 \leq D/d \leq 1.40$ , for which it is shown that the results are quite different from those obtained for higher  $D/d$ . Correlation equations are presented here by means of which the flow is characterized in the range  $1.08 \leq D/d \leq 1.40$ . It is anticipated that this information will have*

<sup>1</sup>Department of Mechanical Engineering, University of Hawaii at Manoa, Honolulu, Hawaii 96822.

Contributed by the Fluids Engineering Division of THE AMERICAN SOCIETY OF MECHANICAL ENGINEERS. Manuscript received by the Fluids Engineering Division April 21, 1992. Associate Technical Editor: F. T. Dodge.

<sup>4</sup>NOTE: The constant in Eq. (13) becomes 0.086 when  $q$  is given in U.S. Gallons per Minute.

practical applications, such as, for example, calculating the “cost,” in terms of pressure drop, of enhancing the rate of convection heat transfer in heat exchangers by packing the tubes of the heat exchangers with spheres.

## Introduction and Statement of Objective

Circular cylinders packed with solid spheres represent a class of porous media. It was shown by Fand et al. (1987) that certain numerical parameters which govern incompressible fluid flow through such porous media are substantially independent of the dimension ratio,  $D/d$ , for  $D/d \geq 40$ , where  $D$  and  $d$  represent the pipe and sphere characteristic dimensions (diameters), respectively. Since these numerical values pertain only for sufficiently large values of  $D/d$ , they are referred to as “asymptotic values” of the parameters and are designated by the subscript  $\infty$ .

Fand and Thinakaran (1990) have shown that in the range  $1.40 \leq D/d < 40$  the flow parameters are functionally dependent upon  $D/d$ . The cause of this dependency is the so-called “wall-effect.” Within the annular “zone of the wall” the average porosity (void fraction) is greater than it is without, and hence the average velocity of flow is higher within the zone than without—this effect is commonly referred to as “channelling.” Fand and Thinakaran (1990) quantified the influence that the wall, via channelling, exerts upon the flow parameters for  $D/d \geq 1.40$  by means of empirically determined correlation equations that contain functions of  $D/d$ . These correlation equations express the relationship between the pressure gradient and the velocity for incompressible fluids whose density ( $\rho$ ) and dynamic viscosity ( $\mu$ ) are known.

The objective of the present study was to extend the range of predictability of incompressible flow through pipes packed with spheres by obtaining and correlating experimental data for values of  $D/d$  between 1.40 and the smallest value of  $D/d$  that was conveniently achievable in the laboratory<sup>2</sup>; more specifically, the present study deals with the range  $1.08 \leq D/d < 1.40$ .

## Background and Review of the Literature

There exists a range of the Reynolds number,  $Re$ , associated with flow through a porous medium that is sufficiently low as to render inertial forces negligible in comparison with viscous forces, and to which the following relationship, called Darcy’s law, is applicable:

$$P' = \frac{\mu}{K} v, \quad (1)$$

where  $P'$  represents the negative of the pressure gradient in the direction of flow,  $v$  is the volume rate of flow per unit area (called the superficial speed or Darcian speed or simply speed<sup>3</sup>),  $\mu$  is the dynamic viscosity of the fluid, and  $K$  is a constant of proportionality called the permeability. The Reynolds numbers corresponding to the lower and upper bounds of the Darcy regime will be designated by  $Re_{DL}$  and  $Re_{DH}$ , respectively. No precise information is available concerning the magnitude of  $Re_{DL}$ , but published data on Darcy flow indicate that  $Re_{DL} < 10^{-5}$ . Since  $Re_{DL}$  is so low as to be undetectable under ordinary circumstances, the range of the Darcy regime will hereafter be indicated by  $Re \leq Re_{DH}$ .

<sup>2</sup>The lowest possible value of  $D/d$  is unity, which corresponds to packing a pipe with spheres having the same diameter as the pipe. No flow is possible in this limiting case.

<sup>3</sup>The term “velocity” is used when the context makes the intended meaning clear ( $Re$  is based on  $v$  and  $d$ ).

The following equation accurately represents the value of  $K$  for porous media whose matrices are composed of spheres:

$$K = \frac{d^2}{36\kappa\alpha}; \quad \alpha = \frac{(1-\epsilon)^2}{\epsilon^3}, \quad (2)$$

where  $\epsilon$  is the porosity and  $\kappa$  is an experimentally determined dimensionless constant called the Kozeny-Carman constant. Substitution for  $K$  per Eq. (2) in Eq. (1) yields

$$P' = 36\kappa\alpha \left( \frac{\mu v}{d^2} \right); \quad Re \leq Re_{DH}. \quad (3)$$

Equation (3) can be recast as follows:

$$f' = \frac{36\kappa}{Re}; \quad Re \leq Re_{DH}, \quad (4)$$

where  $f'$ , called the  $\alpha$ -modified friction factor, is defined by  $f' = dP'/\alpha\rho v^2$ . Darcy flow is completely characterized<sup>4</sup> by Eq. (4) if  $\kappa$  is known for a given fluid ( $\rho$ ,  $\mu$ ) and packing ( $d$ ,  $\epsilon$ ).

Forchheimer (1901) was first to suggest a nonlinear relationship between the pressure gradient and fluid velocity for cases when the Reynolds number is so high that inertia forces are no longer negligible (as they are for Darcy flow). In 1901 he proposed a second order equation to fit experimental data as follows:

$$P' = av + bv^2, \quad (5)$$

where  $a$  and  $b$  are empirical constants.

Ergun (1952) generalized Eq. (5) and concluded that  $P'$  can be equated to the sum of two terms as follows:

$$P' = \left( \frac{A\alpha\mu}{d^2} \right) v + \left( \frac{B\beta\rho}{d} \right) v^2; \quad \alpha = \frac{(1-\epsilon)^2}{\epsilon^3}, \quad \beta = \frac{(1-\epsilon)}{\epsilon^3}, \quad (6)$$

where  $A$  and  $B$  are dimensionless constants which are referred to hereinafter as the first and second Ergun constants for Forchheimer flow. Equation (6) can be cast in the following useful form:

$$f'' = A/Re' + B \quad (7)$$

where  $f'' = dP'/\beta\rho v^2$  and  $Re' = Re/(1-\epsilon)$  are called the  $\beta$ -modified friction factor and modified Reynolds number, respectively.

It has been found that Eq. (6) represents turbulent flow, provided that the Ergun constants are properly evaluated. The Ergun constants for turbulent flow are denoted by  $A'$  and  $B'$  (instead of  $A$  and  $B$ ).

Forchheimer flow occurs in a region defined by  $Re_{FL} \leq Re \leq Re_{FH}$  and turbulent flow occurs in a region defined by  $Re \geq Re_{TL}$ . It has been shown in two prior studies that  $Re_{DH} = 2.3$ ,  $Re_{FL} = 5$ ,  $Re_{FH} = 80$  and  $Re_{TL} = 120$  for  $D/d \geq 1.40$  for pipes packed with spheres. In order to facilitate the mathematical characterization of the transition regions that lie between Darcy and Forchheimer and between Forchheimer and turbulent flow, Fand et al. (1987) replaced these regions by fictitious “points of transition,”  $Re_{DF}$  ( $= 3.0$ ) and  $Re_{FT}$  ( $= 100$ ), at which the flow is imagined to change abruptly from one kind to another. With this fiction the flow can be characterized within the transition regions by Eqs. (1) and (6) without incurring excessive error.

In order to account for the effect of a confining wall, Riechelt (1972) defined the following “wall-modified” parameters:

$$f_w = f''/M \quad \text{and} \quad Re_w = Re'/M, \quad \text{where} \quad M = 1 + \frac{2}{3} \left[ \frac{d}{D(1-\epsilon)} \right].$$

<sup>4</sup>In the present context, to “characterize” a flow means to provide an equation or equations that functionally relate  $P'$  and  $v$  for that flow.

Equation (4) can be rewritten in terms of the  $f_w$  and  $Re_w$  as follows:

$$f_w = \frac{36\kappa}{M^2 Re_w}; \quad (8)$$

and Eq. (7) can be rewritten as follows:

$$f_w = \frac{A_w}{Re_w} + B_w \text{ or } f_w Re_w = A_w + B_w Re_w. \quad (9)$$

$A_w$  and  $B_w$  are called the first and second Ergun-Riechelt parameters for Forchheimer flow. It has been shown that Eq. (9) holds for  $D/d \geq 1.40$  for turbulent flow if the Ergun-Riechelt parameters therein, now denoted by  $A'_w$  and  $B'_w$  (instead of  $A_w$  and  $B_w$ ), are properly evaluated.

It has been concluded on the basis of experimental data that each of the five flow parameters ( $\kappa$ ,  $A_w$ ,  $B_w$ ,  $A'_w$  and  $B'_w$ ) in Eqs. (8) and (9) can be represented, for  $D/d \geq 1.40$ , by correlations having the following common form:

$$Y = Y_\infty - ae^{-f(D/d)}, \quad (10)$$

where  $f(D/d) = p(D/d)^3 + q(D/d)^2 + r(D/d)$  and  $Y_\infty$ ,  $a$ ,  $p$ ,  $q$ ,  $r$  are numerical constants listed in the publication by Fand and Thinakaran (1990). The results of the present study show that Eq. (10) must be replaced by a different function of  $D/d$  for  $D/d < 1.40$ .

### Experimental Apparatus and Procedure

The experimental apparatus employed in the present study consisted of a precision-built stainless steel water tunnel into which were incorporated a series of interchangeable circular cylindrical test sections that were packed with glass spheres. The apparatus and general procedures were identical with those employed by Fand et al. (1987), except for a change (increase) in the lengths of the packed test sections and variations in  $D/d$ . The length-to-diameter ratios,  $L/D$ , of the test sections exceeded 150 in all cases, thereby, it is believed, rendering entrance effects negligible. Table 1 lists the experimental values of all geometric parameters. (The data for  $D/d = 1.40$  were taken from Fand and Thinakaran (1990).)

A test consisted of a set of simultaneous steady-state measurements of water temperature and velocity, plus the pressure drop across the entire test section, for which the porosity was determined by weighing and computing the volume of the glass spheres comprising the packing. A total of 266 tests were performed in the range  $0.3 \leq Re \leq 705$ . The uncertainties in the experimentally measured variables at 20:1 odds do not exceed 2 percent while those for the derived variables  $f_w$ ,  $\kappa$ ,  $A_w$ ,  $A'_w$ ,  $B_w$ , and  $B'_w$  lie between 3 and 5 percent.

### Results

The values of all five flow parameters were obtained by a computerized linear regression analysis of the experimental data based upon Eqs. (8) and (9) for each of the four test series ( $D/d = 1.40, 1.29, 1.17, 1.08$ ). It was then found that each of the five flow parameters could be represented by the following polynomial form:

$$Y = a + b(D/d) + c(D/d)^2; \quad 1.08 \leq D/d \leq 1.40, \quad (11)$$

where  $Y$  stands for any one of the parameters, and  $a$ ,  $b$ , and  $c$  are constants listed in Table 2. As is clear from a perusal of Table 2, Eq. (11) contains linear and quadratic branches. A comparison of Eqs. 10 and 11 reveals that the behavior of the

**Table 1 Experimental values of geometrical parameters**

Test series	$D$ (m)	$d$ (m)	$L$ (m)	$D/d$	$\epsilon$
A	0.0064516	0.0059901	1.0696	1.0770	0.4125
B	0.0070104	0.0059901	1.0696	1.1703	0.4974
C	0.0064516	0.0049997	1.0696	1.2904	0.5687
D	0.0055880	0.0039940	1.0696	1.3991	0.6168

**Table 2 Correlation constants to be used in conjunction with Eq. (11)**

$Y$	$1.08 < D/d < 1.17$			$1.17 < D/d < 1.40$		
	$a$	$b$	$c$	$a$	$b$	$c$
$\kappa$	2604.4	-4277.0	1776.4	171.3	-119.0	0
$A_w$	40536	-68761	29274	440.3	-240.4	0
$B_w$	143.82	-239.55	100.82	5.728	-3.558	0
$A'_w$	35852	-60094	25370	1103.3	-711.5	0
$B'_w$	153.67	-258.55	109.51	3.671	-2.219	0

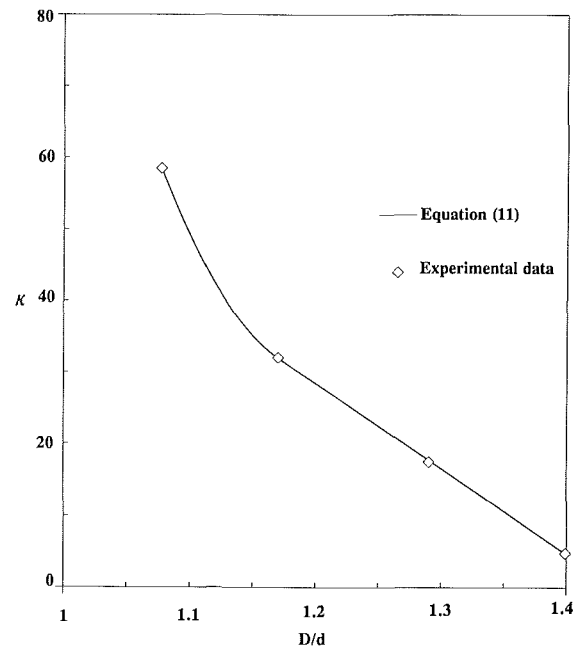


**Fig. 1 Kozeny-Carman constant as a function of the dimension ratio**

flow parameters is radically different below  $D/d = 1.40$  (where they are monotonically decreasing with  $D/d$ ) from what it is above  $D/d = 1.40$  (where they are monotonically increasing with  $D/d$ ). Equation (11) was forced to yield the same values of the flow parameters as does Eq. (10) for the particular value of  $D/d = 1.40$ ; further, the linear (determined by regression analysis) and quadratic branches of Eq. (11) were forced to have common points and equal slopes at  $D/d = 1.17$ , which insured that the graphs of the parameters would be "smooth." The common point was chosen to be at  $D/d = 1.17$  because it resulted in the minimum discrepancy (error) between the predictions of Eqs. (8) and (9) and the experimental results that these equations are purported to represent. To illustrate the behavior of the flow parameters for  $D/d \leq 1.40$ , a graph of  $\kappa$  per Eq. (11) is shown in Fig. 1 together with experimentally determined values.

Fand and Thinakaran (1990) found that the upper and lower bounds of all three basic types of flow were the same ( $Re_{DH} = 2.3$ ,  $Re_{FL} = 5$ ,  $Re_{FH} = 80$ ,  $Re_{TL} = 120$ ) for all values of

# A Numerical Study on the Generation Mechanism of Turbulence-Driven Secondary Flow in a Square Duct

Hyon Kook Myong<sup>1</sup>

The generation mechanism of turbulence-driven secondary flows in a square duct is numerically investigated in the present study by using an anisotropic low-Reynolds-number  $k-\epsilon$  turbulence model. Special attention is directed to the distributions of turbulence quantities, which are responsible for the secondary flow generation, such as the anisotropy of normal Reynolds stresses and the secondary Reynolds shear stress acting on the cross-sectional plane. The vorticity transport process is also discussed in detail, based on the numerical evaluation of the individual terms which appear in the streamwise vorticity transport equation

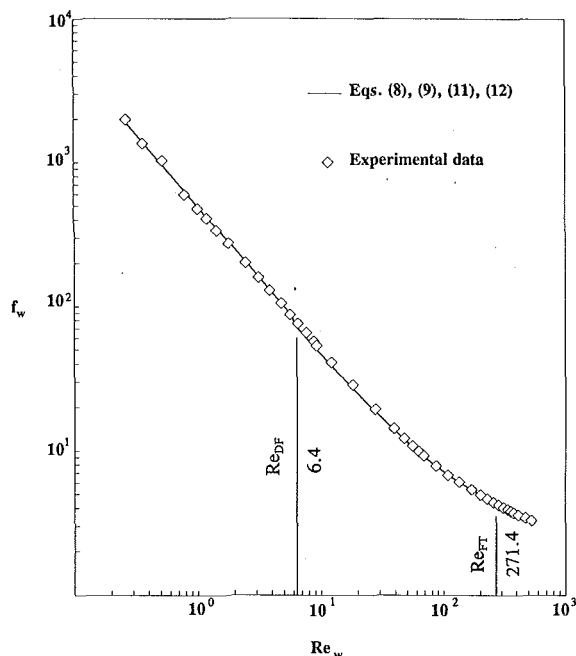


Fig. 2  $f_w$  as a function of  $Re_w$  for  $D/d = 1.077$

$D/d \geq 1.40$ . However, here it was found that these bounds are not invariant for  $D/d < 1.40$ . In the present study, the bounds were found by determining those experimental values of  $Re$  for which the data deviated from the linearity predicted by Eqs. (8) and (9). This procedure led to the finding that the bounds in question can be represented by the following linear equations for  $D/d < 1.40$ :

$$Re_{DH} = 10.6 - 5.90(D/d), \quad (12a)$$

$$Re_{FL} = 376.5 - 265.6(D/d), \quad (12b)$$

$$Re_{FH} = 707.0 - 448.2(D/d), \quad (12c)$$

$$Re_{TL} = 982.1 - 616.2(D/d), \quad (12d)$$

These equations reveal that the spans of the transitions increase as  $D/d$  decreases monotonically from  $D/d = 1.40$ . Also, it was found that the hypothetical points of transition mentioned in the review of the literature could be represented by the following linear equations for  $D/d < 1.40$ :

$$Re_{DF} = 17.8 - 10.6(D/d), \quad (12e)$$

$$Re_{FT} = 844.6 - 532.2(D/d). \quad (12f)$$

A graph of  $f_w$  obtained by utilizing Eqs. (8), (9), (11), and (12) is shown, by way of example, in Fig. 2 for  $D/d = 1.077$ . Figure 2 also contains relevant representative experimental data for visual comparison purposes. The mean deviation of the errors incurred by Eq. (11) relative to the experimentally determined values of each of the five flow parameters is less than 6 percent. This level of agreement is deemed sufficient to render the correlation acceptable.

## References

- Ergun, S., 1952, "Fluid Flow Through Packed Column," *Chemical Engineering Progress*, Vol. 48, No. 2, pp. 89-94.
- Fand, R. M., Kim, B. Y. K., Lam, A. C. C., and Phan, R. T., 1987, "Resistance to the Flow of Fluids Through Simple and Complex Porous Media Whose Matrices Are Composed of Randomly Packed Spheres," *ASME JOURNAL OF FLUIDS ENGINEERING*, Vol. 109, pp. 268-274.
- Fand, R. M., and Thinakaran, R., 1990, "The Influence of the Wall on Flow Through Pipes Packed with Spheres," *ASME JOURNAL OF FLUIDS ENGINEERING*, Vol. 112, pp. 84-88.
- Forchheimer, P., 1901, "Wasserbewegung durch Boden," *Zeitschrift Verein Deutscher Ingenieure*, Vol. 45, pp. 1782-1788.
- Reichelt, W., 1972, "Zur Berechnung des Druckverlustes eigphasig durchstromter kugel und zylinderchuttungen," *Chemie Ingenieur Technik*, Vol. 44, Nr. 18.

## Nomenclature

- $a, D$  = duct half width and hydraulic diameter, respectively
- $k$  = turbulent kinetic energy
- $\frac{Re}{v^2}, \frac{w^2}{v^2}$  = Reynolds number ( $Re \equiv U_b D / \nu$ )
- $\frac{Re}{v^2}, \frac{w^2}{v^2}$  = normal Reynolds stresses acting on the cross-sectional plane
- $\overline{w}$  = secondary Reynolds shear stress
- $U_b, U_c$  = streamwise bulk-mean and central mean velocities
- $V, W$  = mean secondary velocities
- $x, y, z$  = Cartesian coordinates
- $\nu$  = kinematic viscosity
- $\nu_t$  = eddy diffusivity of momentum
- $\epsilon$  = dissipation rate of  $k$
- $\Omega_x$  = streamwise vorticity

## 1 Introduction

The turbulent flow in straight noncircular ducts is characterized by the occurrence of turbulence-driven secondary flow. Since Brundrett and Baines (1964) and Perkins (1970) have shown from their experimental investigations that this turbulence-driven secondary flow results from the anisotropy of each Reynolds stress in the cross-sectional plane, a considerable number of investigations have been carried out, experimentally and numerically, to clarify the characteristics of this flow during past two decades (see e.g., Melling and Whitelaw, 1976; Gessner et al., 1979; Launder and Ying, 1973; Demuren and Rodi, 1984; and Myong and Kobayashi, 1991). These investigations, however, have focused mostly on the global features of turbulent flow quantities such as distributions of mean velocity and Reynolds stress components.

It is well-known that the secondary flow generation in a noncircular duct is directly associated with the streamwise vorticity and thus the vorticity transport equation shows the mechanism of the secondary flow generation. In particular, since the turbulence quantities of both the anisotropy of normal

<sup>1</sup>Thermal/Fluids Engineering Laboratory, Korea Institute of Science and Technology, Seoul 130-650, Korea.

Contributed by the Fluids Engineering Division of THE AMERICAN SOCIETY OF MECHANICAL ENGINEERS. Manuscript received by the Fluids Engineering Division February 5, 1992. Associate Technical Editor: J. Humphrey.

# A Numerical Study on the Generation Mechanism of Turbulence-Driven Secondary Flow in a Square Duct

Hyon Kook Myong<sup>1</sup>

The generation mechanism of turbulence-driven secondary flows in a square duct is numerically investigated in the present study by using an anisotropic low-Reynolds-number  $k-\epsilon$  turbulence model. Special attention is directed to the distributions of turbulence quantities, which are responsible for the secondary flow generation, such as the anisotropy of normal Reynolds stresses and the secondary Reynolds shear stress acting on the cross-sectional plane. The vorticity transport process is also discussed in detail, based on the numerical evaluation of the individual terms which appear in the streamwise vorticity transport equation

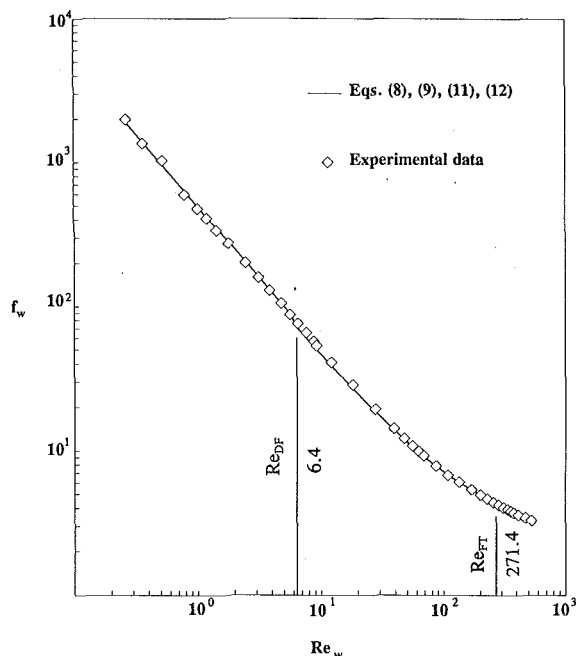


Fig. 2  $f_w$  as a function of  $Re_w$  for  $D/d = 1.077$

$D/d \geq 1.40$ . However, here it was found that these bounds are not invariant for  $D/d < 1.40$ . In the present study, the bounds were found by determining those experimental values of  $Re$  for which the data deviated from the linearity predicted by Eqs. (8) and (9). This procedure led to the finding that the bounds in question can be represented by the following linear equations for  $D/d < 1.40$ :

$$Re_{DH} = 10.6 - 5.90(D/d), \quad (12a)$$

$$Re_{FL} = 376.5 - 265.6(D/d), \quad (12b)$$

$$Re_{FH} = 707.0 - 448.2(D/d), \quad (12c)$$

$$Re_{TL} = 982.1 - 616.2(D/d), \quad (12d)$$

These equations reveal that the spans of the transitions increase as  $D/d$  decreases monotonically from  $D/d = 1.40$ . Also, it was found that the hypothetical points of transition mentioned in the review of the literature could be represented by the following linear equations for  $D/d < 1.40$ :

$$Re_{DF} = 17.8 - 10.6(D/d), \quad (12e)$$

$$Re_{FT} = 844.6 - 532.2(D/d). \quad (12f)$$

A graph of  $f_w$  obtained by utilizing Eqs. (8), (9), (11), and (12) is shown, by way of example, in Fig. 2 for  $D/d = 1.077$ . Figure 2 also contains relevant representative experimental data for visual comparison purposes. The mean deviation of the errors incurred by Eq. (11) relative to the experimentally determined values of each of the five flow parameters is less than 6 percent. This level of agreement is deemed sufficient to render the correlation acceptable.

## References

- Ergun, S., 1952, "Fluid Flow Through Packed Column," *Chemical Engineering Progress*, Vol. 48, No. 2, pp. 89-94.
- Fand, R. M., Kim, B. Y. K., Lam, A. C. C., and Phan, R. T., 1987, "Resistance to the Flow of Fluids Through Simple and Complex Porous Media Whose Matrices Are Composed of Randomly Packed Spheres," *ASME JOURNAL OF FLUIDS ENGINEERING*, Vol. 109, pp. 268-274.
- Fand, R. M., and Thinakaran, R., 1990, "The Influence of the Wall on Flow Through Pipes Packed with Spheres," *ASME JOURNAL OF FLUIDS ENGINEERING*, Vol. 112, pp. 84-88.
- Forchheimer, P., 1901, "Wasserbewegung durch Boden," *Zeitschrift Verein Deutscher Ingenieure*, Vol. 45, pp. 1782-1788.
- Reichelt, W., 1972, "Zur Berechnung des Druckverlustes eigphasig durchstromter kugel und zylinderchuttungen," *Chemie Ingenieur Technik*, Vol. 44, Nr. 18.

## Nomenclature

- $a, D$  = duct half width and hydraulic diameter, respectively
- $k$  = turbulent kinetic energy
- $\frac{Re}{v^2}, w^2$  = Reynolds number ( $Re \equiv U_b D / \nu$ )
- $\overline{v^2}, \overline{w^2}$  = normal Reynolds stresses acting on the cross-sectional plane
- $\overline{vw}$  = secondary Reynolds shear stress
- $U_b, U_c$  = streamwise bulk-mean and central mean velocities
- $V, W$  = mean secondary velocities
- $x, y, z$  = Cartesian coordinates
- $\nu$  = kinematic viscosity
- $\nu_t$  = eddy diffusivity of momentum
- $\epsilon$  = dissipation rate of  $k$
- $\Omega_x$  = streamwise vorticity

## 1 Introduction

The turbulent flow in straight noncircular ducts is characterized by the occurrence of turbulence-driven secondary flow. Since Brundrett and Baines (1964) and Perkins (1970) have shown from their experimental investigations that this turbulence-driven secondary flow results from the anisotropy of each Reynolds stress in the cross-sectional plane, a considerable number of investigations have been carried out, experimentally and numerically, to clarify the characteristics of this flow during past two decades (see e.g., Melling and Whitelaw, 1976; Gessner et al., 1979; Launder and Ying, 1973; Demuren and Rodi, 1984; and Myong and Kobayashi, 1991). These investigations, however, have focused mostly on the global features of turbulent flow quantities such as distributions of mean velocity and Reynolds stress components.

It is well-known that the secondary flow generation in a noncircular duct is directly associated with the streamwise vorticity and thus the vorticity transport equation shows the mechanism of the secondary flow generation. In particular, since the turbulence quantities of both the anisotropy of normal

<sup>1</sup>Thermal/Fluids Engineering Laboratory, Korea Institute of Science and Technology, Seoul 130-650, Korea.

Contributed by the Fluids Engineering Division of THE AMERICAN SOCIETY OF MECHANICAL ENGINEERS. Manuscript received by the Fluids Engineering Division February 5, 1992. Associate Technical Editor: J. Humphrey.



Reynolds stresses and the secondary Reynolds shear stress on the cross-sectional plane appear prominently in this equation, they do play an important role in the vorticity generation. However, due to the difficulty of experimental measurement, very little data on these quantities are available. Moreover, no systematic investigation on the contours of individual terms of the vorticity transport equation seems to have been reported elsewhere. The present study is thus motivated by the lack of a detailed numerical and experimental analysis for the generation mechanism of turbulence-driven secondary flow.

In the present paper, the generation mechanism of turbulence-driven secondary flow is investigated based on the numerical analysis for the three-dimensional fully developed turbulent flows in a straight square duct, with the anisotropic low-Reynolds-number  $k-\epsilon$  model. Special attention is directed to the distributions of turbulence quantities, which are responsible for the secondary flow generation, such as anisotropy of normal Reynolds stresses and the secondary Reynolds shear stress acting in the cross-sectional plane. The details of the vorticity transport process are also investigated through the numerical evaluation of the individual terms which appear in the streamwise vorticity transport equation.

## 2 Mathematical and Numerical Models

Since the mathematical and numerical models employed in the present study are the same as those in the previous works by the authors (Myong and Kobayashi, 1991; Myong, 1991), brief characteristic facts are only mentioned here. Contrary to the higher-order modes such as Reynolds (or algebraic) stress models, the anisotropic low-Reynolds-number  $k-\epsilon$  turbulence model used in the present study is derived from the standard (isotropic)  $k-\epsilon$  turbulence model and directly applicable to the wall region (Myong and Kasagi, 1990). In addition, the performance of this model for developing and fully developed three-dimensional turbulent flows in a square duct has already been found to be by no means inferior to that of the previous higher-order models (Myong and Kobayashi, 1991).

In the present study, the no-slip boundary condition is directly used in the wall, in place of the common wall function approach, since the turbulence structure in both regions close to the wall and close to the corner is conjectured to govern the secondary flow generation mechanism. In addition, the resulting set of equations are simplified only by the boundary-layer assumptions and then solved with a forward marching numerical procedure for three-dimensional shear layers until fully developed flow is attained. Detailed information on the constitutive set of momentum and model equations, solution procedure, and the grid configuration as well as the validation of numerical procedure is found elsewhere (Myong and Kobayashi, 1991).

## 3 Results and Discussion

The turbulence quantities of both the anisotropy of normal Reynolds stresses  $\overline{w^2 - v^2}$  and the secondary Reynolds shear stress  $\overline{vw}$  are known to play an important role in the vorticity (or secondary flow) generation, since the cross-sectional gradients of these quantities are primarily responsible for the secondary flow generation, as may be observed in the vorticity transport equation (see Eq. (3)). In the present model these two turbulence quantities are expressed as follows:

$$\overline{w^2 - v^2} = 2\nu_t \left( \frac{\partial V}{\partial y} - \frac{\partial W}{\partial z} \right) - C_3 \nu_t \frac{k}{\epsilon} \left[ \left( \frac{\partial U^2}{\partial y} \right) - \left( \frac{\partial U^2}{\partial z} \right) \right] + \frac{2}{3} \nu_t \frac{k}{\epsilon} \left[ \left( \frac{\partial \sqrt{k}}{\partial y} \right)^2 - \left( \frac{\partial \sqrt{k}}{\partial z} \right)^2 \right] \quad (1)$$

ISO ANISO

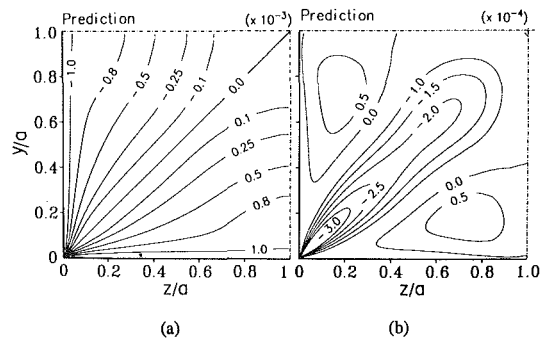


Fig. 1 Predicted contours of (a) the anisotropy of normal Reynolds stresses  $(\overline{w^2 - v^2})/U_c^2$  and (b) the secondary Reynolds shear stress  $\overline{vw}/U_c^2$

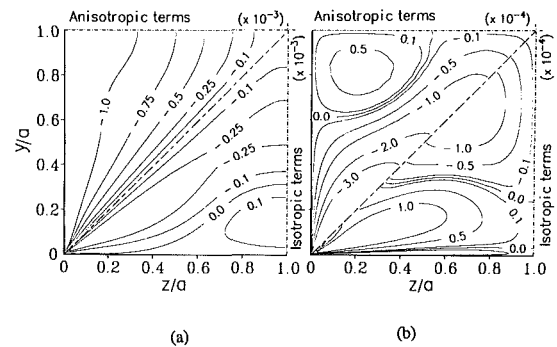


Fig. 2 Relative magnitudes of the secondary to the primary velocity gradient terms in the algebraic relations for (a)  $(\overline{w^2 - v^2})/U_c^2$  and (b)  $\overline{vw}/U_c^2$

$$\overline{vw} = -\nu_t \left( \frac{\partial W}{\partial y} + \frac{\partial V}{\partial z} \right) + C_3 \nu_t \frac{k}{\epsilon} \left( \frac{\partial U}{\partial y} \right) \left( \frac{\partial U}{\partial z} \right) \quad (2)$$

ISO ANISO

where ISO and ANISO represent the isotropic and anisotropic terms, respectively, and the value of model constant  $C_3$  is  $-0.15$  (Myong and Kobayashi, 1991).

The predicted contours of the anisotropy of normal Reynolds stresses  $\overline{w^2 - v^2}$  and the secondary Reynolds shear stress  $\overline{vw}$  are shown in Fig. 1. Compared with the experimental data of Brundrett and Bains (1964) and Fujita et al. (1986), it can be seen that the correct trends are predicted and qualitative agreement is reasonably good. Note here that, in contrast to the available experimental data of Brundrett and Bains, the prediction for secondary Reynolds shear stress shows the existence of the region where the shear stress has the positive sign, although relatively small in magnitude. At present, it is not clear whether such a region really exists.

The relative magnitudes of the secondary to the primary velocity-gradient terms (or the isotropic to the anisotropic terms) in the algebraic relations for  $\overline{w^2 - v^2}$  of Eq. (1) and  $\overline{vw}$  of Eq. (2) are compared for the present model in Fig. 2. It is shown from the figure that the magnitudes of the secondary velocity-gradient terms in the algebraic relations for  $\overline{w^2 - v^2}$



are much smaller than those of the primary ones, although both terms have nearly equal magnitudes around the corner bisector. For the secondary Reynolds stress  $\overline{v\overline{w}}$ , Perkins (1970) argued that two different mechanisms contribute to its generation. The first mechanism is associated with the gradients of the secondary velocities, and its contributions to  $\overline{v\overline{w}}$  can be represented in terms of an isotropic eddy diffusivity of momentum, while the second mechanism is associated with the distortion of the primary velocity gradients. Although the individual contributions to the generation of  $\overline{v\overline{w}}$  could not be determined from the experiment itself, he considered them to be of equal magnitude. The present predictions demonstrate clearly the above argument of Perkins, showing that the secondary velocity gradients contribute significantly to the generation of the secondary shear stress  $\overline{v\overline{w}}$  over most of flow domain. Note that these facts are also pointed out by Demuren and Rodi (1984).

For steady, incompressible, fully developed turbulent flow with constant properties the mean streamwise vorticity transport equation is written as follows:

$$\underbrace{V \frac{\partial \Omega_x}{\partial y} + W \frac{\partial \Omega_x}{\partial z}}_C = \underbrace{\frac{\partial^2}{\partial y \partial z} (\overline{v^2} - \overline{w^2})}_{P_1} + \underbrace{\left( \frac{\partial^2}{\partial z^2} - \frac{\partial^2}{\partial y^2} \right) \overline{v\overline{w}} + \nu \nabla^2 \Omega_x}_{P_2 + D} \quad (3)$$

where  $\Omega_x$  is the mean streamwise vorticity defined as follows:

$$\Omega_x = \frac{\partial W}{\partial y} - \frac{\partial V}{\partial z} \quad (4)$$

In Eq. (3), the term  $C$  represents the convection of streamwise vorticity by the mean motion of the secondary flows. The terms  $P_1$  and  $P_2$ , which are present only in the turbulent flow, express the influence of the turbulent stresses on the production or destruction of streamwise vorticity. Whereas the viscous damping is represented by the diffusion term  $D$ .

The predicted contours of the streamwise vorticity of Eq. (4) are shown in Fig. 3, which are normalized by  $U_c/D$ . The predictions show that the maximum values of the streamwise vorticity occur in the near-corner and the vorticity of opposite sign appears near the walls. Compared with the available experimental results of Brundrett and Bains, it seems likely to be that the correct trend is predicted and the qualitative agreement is also reasonably good.

Figure 4 shows the contours of magnitude of each term in the streamwise vorticity transport equation, which are normalized by  $U_c^2/D$ . It should be noted that the individual terms shown in the figure have all antisymmetric characteristics with respect to the corner bisector. On the generation mechanism of secondary flow in noncircular straight ducts, two different arguments have been reported. Brundrett and Bains (1964) reported that, of the two turbulent stress terms in Eq. (3), only the  $P_1$  term was significant and was balanced by the convection and viscous damping terms  $C$  and  $D$ . On the contrary, Perkins (1970) reported that the turbulent normal and shear stress terms came out to be of the same order of magnitude and of opposite sign, in agreement with the experimental findings of Gessner and Jones (1965). Recently, Demuren and Rodi (1984) asserted these facts. The present prediction shows that both production terms by the normal and shear stress terms are dominant, being of the same order of magnitude and of opposite sign, with much larger magnitude than the convection terms, while the diffusion term  $D$  is only significant in both regions close to the corner and close to the wall. It can be also seen that, although two production terms are dominant, the difference between these terms is the same order of magnitude as the convection term. Thus, the present prediction demonstrates clearly the above experimental findings of Perkins (1970) and Gessner and Jones (1965), showing numerically that the

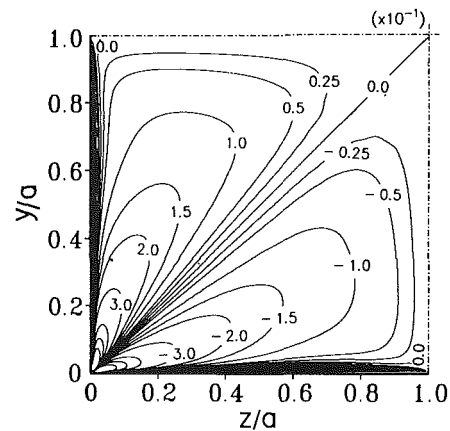


Fig. 3 Contours of the streamwise vorticity  $\Omega_x$  ( $Re = 65,000$ )

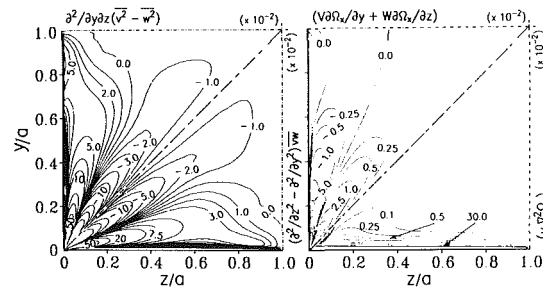


Fig. 4 Streamwise vorticity budget ( $Re = 65,000$ )

streamwise vorticity (or secondary flow) is generated by the difference between relatively large production terms and then convected to regions where the vorticity decays by the viscous damping.

#### 4 Concluding Remarks

In the present study, the generation mechanism of turbulence-driven secondary flows in a square duct is numerically investigated by using an anisotropic low-Reynolds-number  $k-\epsilon$  turbulence model. Special attention is directed to the distribution of the anisotropy of normal Reynolds stresses and the secondary Reynolds shear stress acting on the cross-sectional plane, which are responsible for the secondary flow generation. The vorticity transport process is also discussed in detail.

It should be noted here that the present paper has been directed to the qualitative understanding of generation mechanism of turbulence-driven secondary flow. The quantitative comparison with experimental data is difficult in the present stage, since there are little experimental results for comparison. Thus, further experimental work is necessary to complete the quantitative confirmation of the present numerical solution. And, the present predicted results can provide a body of material which future modelers and/or experimenters may wish to compare with their own results.

#### Acknowledgments

The present work was mainly undertaken at the Research Center for Advanced Science and Technology (RCAST) of the University of Tokyo. The author gratefully acknowledges the support of RCAST. The author is also grateful to Prof. N. Kasagi and Prof. T. Kobayashi at the University of Tokyo for many helpful discussions.

## References

- Brundrett, E., and Baines, W. D., 1964, "The Production and Diffusion of Vorticity in Duct Flow," *Journal of Fluid Mechanics*, Vol. 19, pp. 375-394.
- Demuren, A. O., and Rodi, W., 1984, "Calculation of Turbulence-Driven Secondary Motion in Non-Circular Ducts," *Journal of Fluid Mechanics*, Vol. 140, pp. 189-222.
- Fujita, H., Yokosawa, H., Iwata, S., and Takahama, H., 1986, "Turbulent Flow in a Square Duct with Roughened Walls on Two Opposite Sides (1st Report, Measurement of Flow Velocities and Turbulent Stresses)," *Transaction Japan Society of Mechanical Engineers*, (in Japanese), Vol. 52B, pp. 3491-3497.
- Gessner, F. B., Po, J. K., and Emery, A. F., 1979, "Measurements of Developing Turbulent Flow in a Square Duct," *Turbulent Shear Flows I*, ed. Durst, et al., Springer-Verlag, New York, pp. 119-136.
- Gessner, F. B., and Jones, J. B., 1965, "On Some Aspects of Fully Developed Turbulent Flow in a Rectangular Channel," *Journal of Fluid Mechanics*, Vol. 23, pp. 689-713.
- Lauder, B. E., and Ying, W. M., 1973, "Prediction of Flow and Heat Transfer in Ducts of Square Cross-Section," *Proceedings of the Institute of Mechanical Engineers*, Vol. 187, pp. 455-461.
- Melling, A., and Whitelaw, J. H., 1976, "Turbulent Flow in a Rectangular Duct," *Journal of Fluid Mechanics*, Vol. 78, pp. 289-315.
- Myong, H. K., 1991, "Numerical Investigation on Turbulent Fluid Flow and Heat Transfer in a Square Duct," *International Journal of Heat and Fluid Flow*, Vol. 12, No. 4, pp. 344-352.
- Myong, H. K., and Kasagi, N., 1990, "Prediction of Anisotropy of the Near-Wall Turbulence with an Anisotropic Low-Reynolds-Number  $k-\epsilon$  Turbulence Model," *ASME JOURNAL OF FLUIDS ENGINEERING*, Vol. 112, pp. 521-524.
- Myong, H. K., and Kobayashi, T., 1991, "Prediction of Three-Dimensional Developing Turbulent Flow in a Square Duct with an Anisotropic Low-Reynolds-Number  $k-\epsilon$  Model," *ASME JOURNAL OF FLUIDS ENGINEERING*, Vol. 113, pp. 608-615.
- Perkins, H. J., 1970, "The Formation of Streamwise Vorticity in Turbulent Flow," *Journal of Fluid Mechanics*, Vol. 44, pp. 721-740.

## Flow Behavior in Thin-Gapped Diamond-Shaped Channels With Pins

N. Ashgriz,<sup>1</sup> J. P. Seet,<sup>1</sup> and J. D. Felske<sup>1</sup>

### 1 Introduction

The present experimental study investigates the nature of the fluid flow in various modified version of a high heat-flux, multi-cell, very compact heat exchanger. The basic transport concept has previously been applied to the cooling of high power laser mirrors, for which it has been shown to achieve extremely high rates of heat transfer in single-phase liquid flow. The original device was patented by Schmidt (1975). It is composed of multiple square cells machined in a honeycomb arrangement into the backside of a silicon mirror blank. Each cell contains a circular pin at its center which spans the narrow gap between the mirror substrate on one side of the flow channel and the coolant header plate on the other. A schematic diagram of one of the cells with one pin at the center of the cell is shown in Fig. 1. The header design for delivering and returning the liquid flow is quite novel. Four diamond-shaped cells receive coolant from a single inlet and four cells exhaust coolant into a single outlet. The flow enters a cell at a corner and exits at the opposite corner. Hence, in each of the small cells in the honeycomb array, the coolant flows across the pin in the diamond direction.

Geometric and Reynolds number scaling were employed to design test cells which were about an order of magnitude larger

<sup>1</sup>Department of Mechanical and Aerospace Engineering, State University of New York at Buffalo, Buffalo, N.Y. 14260.

Contributed by the Fluids Engineering Division of THE AMERICAN SOCIETY OF MECHANICAL ENGINEERS. Manuscript received by the Fluids Engineering Division March 30, 1992. Associate Technical Editor: J. Humphrey.

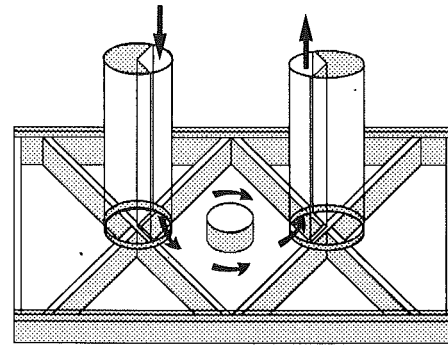


Fig. 1 Test section cover and base plates for the one pin array

than those presently employed for cooling mirrors. This allowed visualization of the fine details of these complex flows and enabled qualitative data to be readily obtained. One of several novel aspects of this type of cell is that just before the incoming liquid jet turns ninety-degrees and enters the narrow gapped, diamond shaped section, it encounters a forward-facing step produced by the tops of the cell walls which meet at the corner of the diamond. Because of this combination of flow modifiers, the velocity distribution in the cell is highly nonuniform. Corkscrew-like vortices are created near the cell inlet—somewhat like the vortices seen in the studies by Schofield and Logan (1988), and Sparrow and Berman (1984). Although some flow features are similar, overall the flow is radically different from those previously considered by others.

### 2 Experimental Setup

Figure 1 shows the test section which is comprised of a  $33.5 \times 13.7 \text{ cm}^2$  rectangular cover and base, fabricated from 1.27 cm (1/2 in.) and 2.22 cm (7/8 in.) thick transparent plexiglas, respectively. The narrow-gapped, diamond-shaped cell is located at the center of this section. The diamond is  $7.62 \times 7.62 \text{ cm}^2$  ( $3 \times 3 \text{ in.}$ ) and is formed by plexiglas parallelepipeds ( $1.07 \text{ cm} \times 8.7 \text{ cm} \times 1.14 \text{ cm}$ ) which are fixed to the base of the test section. The gap between the cover and the base is 1.14 cm. Into the base of the test section, two large holes were drilled and threaded (5.08 cm (2 in.) pipe thread) for connecting the inlet and outlet tubes. At these holes, the parallelepipeds meet, forming right-angled wedges through which the fluid enters and exits the test section. A 30 cm long, 270-degree ("pac-man" shaped) section of solid plexiglas rod was placed in both the inlet and outlet tubes so as to plug 3/4 of the cross-sectional area of each tube. As a result, all of the fluid flowing through the partially-plugged inlet pipe was directed into the test section. Only half of the 1.07 cm width of the parallelepipeds is exposed to the flow at the inlet and outlet holes. Hence, the inlet flow encounters a step on each leg of the wedge just prior to turning ninety-degrees and entering the cell. In order to achieve controlled entrance flows, plastic drinking straws, formed into a honeycomb-like matrix, were packed in the inlet tube prior to the plexiglas plug. In order to allow long test runs, a closed-loop flow system was designed. Water was employed as the test fluid for all experiments.

Four different pin arrays (0, 1, 9, and 47-pins) were constructed by mounting plexiglas pins to four different cover plates for the test section. In order to investigate the flow pattern for a different number of pins and a variety of pin sizes and arrangements, only the cover plate needed to be changed.

Particle streakline visualization was used to observe the flows. Two light sources (650W Type 4711 Molequartz projector bulbs) were positioned so as to minimize the shadows produced by the light passing through and around the pins. The water

## References

- Brundrett, E., and Baines, W. D., 1964, "The Production and Diffusion of Vorticity in Duct Flow," *Journal of Fluid Mechanics*, Vol. 19, pp. 375-394.
- Demuren, A. O., and Rodi, W., 1984, "Calculation of Turbulence-Driven Secondary Motion in Non-Circular Ducts," *Journal of Fluid Mechanics*, Vol. 140, pp. 189-222.
- Fujita, H., Yokosawa, H., Iwata, S., and Takahama, H., 1986, "Turbulent Flow in a Square Duct with Roughened Walls on Two Opposite Sides (1st Report, Measurement of Flow Velocities and Turbulent Stresses)," *Transaction Japan Society of Mechanical Engineers*, (in Japanese), Vol. 52B, pp. 3491-3497.
- Gessner, F. B., Po, J. K., and Emery, A. F., 1979, "Measurements of Developing Turbulent Flow in a Square Duct," *Turbulent Shear Flows I*, ed. Durst, et al., Springer-Verlag, New York, pp. 119-136.
- Gessner, F. B., and Jones, J. B., 1965, "On Some Aspects of Fully Developed Turbulent Flow in a Rectangular Channel," *Journal of Fluid Mechanics*, Vol. 23, pp. 689-713.
- Lauder, B. E., and Ying, W. M., 1973, "Prediction of Flow and Heat Transfer in Ducts of Square Cross-Section," *Proceedings of the Institute of Mechanical Engineers*, Vol. 187, pp. 455-461.
- Melling, A., and Whitelaw, J. H., 1976, "Turbulent Flow in a Rectangular Duct," *Journal of Fluid Mechanics*, Vol. 78, pp. 289-315.
- Myong, H. K., 1991, "Numerical Investigation on Turbulent Fluid Flow and Heat Transfer in a Square Duct," *International Journal of Heat and Fluid Flow*, Vol. 12, No. 4, pp. 344-352.
- Myong, H. K., and Kasagi, N., 1990, "Prediction of Anisotropy of the Near-Wall Turbulence with an Anisotropic Low-Reynolds-Number  $k-\epsilon$  Turbulence Model," *ASME JOURNAL OF FLUIDS ENGINEERING*, Vol. 112, pp. 521-524.
- Myong, H. K., and Kobayashi, T., 1991, "Prediction of Three-Dimensional Developing Turbulent Flow in a Square Duct with an Anisotropic Low-Reynolds-Number  $k-\epsilon$  Model," *ASME JOURNAL OF FLUIDS ENGINEERING*, Vol. 113, pp. 608-615.
- Perkins, H. J., 1970, "The Formation of Streamwise Vorticity in Turbulent Flow," *Journal of Fluid Mechanics*, Vol. 44, pp. 721-740.

## Flow Behavior in Thin-Gapped Diamond-Shaped Channels With Pins

N. Ashgriz,<sup>1</sup> J. P. Seet,<sup>1</sup> and J. D. Felske<sup>1</sup>

### 1 Introduction

The present experimental study investigates the nature of the fluid flow in various modified version of a high heat-flux, multi-cell, very compact heat exchanger. The basic transport concept has previously been applied to the cooling of high power laser mirrors, for which it has been shown to achieve extremely high rates of heat transfer in single-phase liquid flow. The original device was patented by Schmidt (1975). It is composed of multiple square cells machined in a honeycomb arrangement into the backside of a silicon mirror blank. Each cell contains a circular pin at its center which spans the narrow gap between the mirror substrate on one side of the flow channel and the coolant header plate on the other. A schematic diagram of one of the cells with one pin at the center of the cell is shown in Fig. 1. The header design for delivering and returning the liquid flow is quite novel. Four diamond-shaped cells receive coolant from a single inlet and four cells exhaust coolant into a single outlet. The flow enters a cell at a corner and exits at the opposite corner. Hence, in each of the small cells in the honeycomb array, the coolant flows across the pin in the diamond direction.

Geometric and Reynolds number scaling were employed to design test cells which were about an order of magnitude larger

<sup>1</sup>Department of Mechanical and Aerospace Engineering, State University of New York at Buffalo, Buffalo, N.Y. 14260.

Contributed by the Fluids Engineering Division of THE AMERICAN SOCIETY OF MECHANICAL ENGINEERS. Manuscript received by the Fluids Engineering Division March 30, 1992. Associate Technical Editor: J. Humphrey.

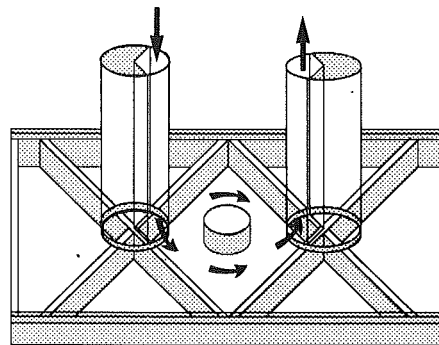


Fig. 1 Test section cover and base plates for the one pin array

than those presently employed for cooling mirrors. This allowed visualization of the fine details of these complex flows and enabled qualitative data to be readily obtained. One of several novel aspects of this type of cell is that just before the incoming liquid jet turns ninety-degrees and enters the narrow gapped, diamond shaped section, it encounters a forward-facing step produced by the tops of the cell walls which meet at the corner of the diamond. Because of this combination of flow modifiers, the velocity distribution in the cell is highly nonuniform. Corkscrew-like vortices are created near the cell inlet—somewhat like the vortices seen in the studies by Schofield and Logan (1988), and Sparrow and Berman (1984). Although some flow features are similar, overall the flow is radically different from those previously considered by others.

### 2 Experimental Setup

Figure 1 shows the test section which is comprised of a  $33.5 \times 13.7 \text{ cm}^2$  rectangular cover and base, fabricated from 1.27 cm (1/2 in.) and 2.22 cm (7/8 in.) thick transparent plexiglas, respectively. The narrow-gapped, diamond-shaped cell is located at the center of this section. The diamond is  $7.62 \times 7.62 \text{ cm}^2$  ( $3 \times 3 \text{ in.}$ ) and is formed by plexiglas parallelepipeds ( $1.07 \text{ cm} \times 8.7 \text{ cm} \times 1.14 \text{ cm}$ ) which are fixed to the base of the test section. The gap between the cover and the base is 1.14 cm. Into the base of the test section, two large holes were drilled and threaded (5.08 cm (2 in.) pipe thread) for connecting the inlet and outlet tubes. At these holes, the parallelepipeds meet, forming right-angled wedges through which the fluid enters and exits the test section. A 30 cm long, 270-degree ("pac-man" shaped) section of solid plexiglas rod was placed in both the inlet and outlet tubes so as to plug 3/4 of the cross-sectional area of each tube. As a result, all of the fluid flowing through the partially-plugged inlet pipe was directed into the test section. Only half of the 1.07 cm width of the parallelepipeds is exposed to the flow at the inlet and outlet holes. Hence, the inlet flow encounters a step on each leg of the wedge just prior to turning ninety-degrees and entering the cell. In order to achieve controlled entrance flows, plastic drinking straws, formed into a honeycomb-like matrix, were packed in the inlet tube prior to the plexiglas plug. In order to allow long test runs, a closed-loop flow system was designed. Water was employed as the test fluid for all experiments.

Four different pin arrays (0, 1, 9, and 47-pins) were constructed by mounting plexiglas pins to four different cover plates for the test section. In order to investigate the flow pattern for a different number of pins and a variety of pin sizes and arrangements, only the cover plate needed to be changed.

Particle streakline visualization was used to observe the flows. Two light sources (650W Type 4711 Molequartz projector bulbs) were positioned so as to minimize the shadows produced by the light passing through and around the pins. The water

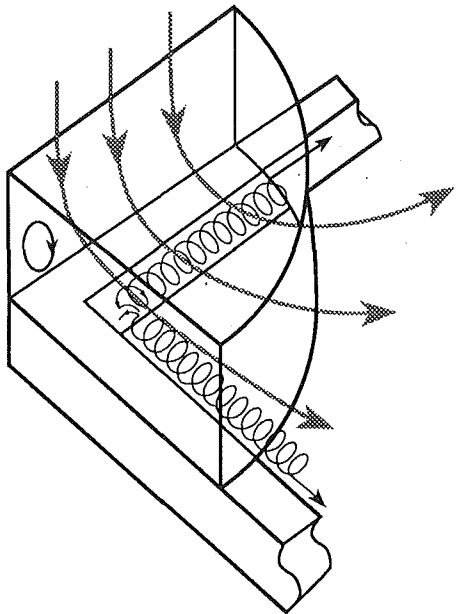


Fig. 2 Schematic diagram of flow patterns at the inlet for all pin arrays

was seeded with a small concentration of Pliolite particles (10 to 20 microns in diameter) which scattered the light from the two sources towards the camera. The concentration of the particles was small and their specific gravity sufficiently close to 1.0 so that they did not disturb the unseeded fluid flow by their presence. The central piece of the visualization system was a high speed video camera (EKtaPro 1000 manufactured by Kodak). Through the use of a new scanning system it can record up to 6000 images per second. The flow patterns were recorded by using this system and also by conventional still photography.

### 3 Flow Visualization Results

The flow behavior in the four different pin arrays (0, 1, 9, and 47-pins) was studied for Reynolds numbers up to 5000. Common to all of the arrays were the entrance and exit conditions. An enlarged schematic of the entrance section is shown in Fig. 2. As shown in this figure and in Fig. 1, water in the supply tube flows over a forward-facing wedge-shaped step, turns ninety-degrees, enters the diamond-shaped test section, flows from corner to corner of the diamond and leaves through another ninety-degree bend at the outlet of the test section where it then flows past a rearward-facing wedge-shaped step. Generally, flow past a step engenders a complex three-dimensional flow in which many streamwise vortices are created within the shear layer (Schofield and Logan, 1988). These vortices are shed at the edges of the step into the downstream flow. The right-angle bend also introduces nonuniformities into the velocity distribution, with the region of higher speed moving to the outside of the bend (Sparrow and Berman, 1984). Furthermore, bends generally create secondary flows in the form of helical vortices which become superimposed on the main flow. In the present geometry, these vortices are sometimes rather "tightly-wound" (corkscrew-like) and appear along the edges of the wedge-shaped entrance (see Fig. 2). Outside this edge region, the flow at the entrance and exit are essentially radially directed and of relatively high speed.

Next, a description of the flow behavior in the 9-pin test section is presented. The detailed description of the other test sections are presented by Seet (1990). Consider the staggered, "diamond-shaped" array of nine pins shown in Fig 3 for  $Re = 200$ . The pins are labeled from 1 to 9; frequent reference will be made to them by number. There are three different pin

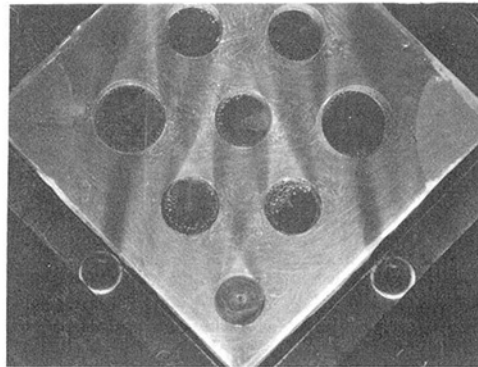


Fig. 3(a)

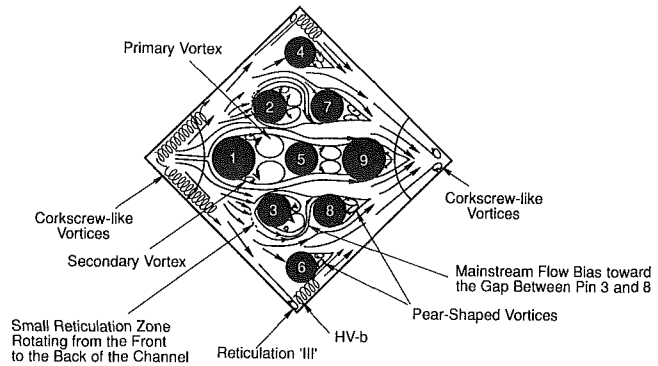


Fig. 3(b)

Fig. 3 Flow behavior in 9-pin cell at  $Re = 200$  (a) typical photograph, (b) the schematic of the flow pattern

diameters in the array: 1.524 cm (pins 1, 9); 1.22 cm (pins 2, 3, 5, 7, 8); and 1.07 cm (pins 4, 6). This configuration was designed to minimize the pressure induced deformations in the top surface to which the pins attached—the mirror surface of the actual device. The array may be considered to be composed of 'short pins' (length/diameter ranging from 0.75 to 1.07) having moderate spanwise and streamwise spacings (pitch/diameter ranging from 1.45 to 2.0).

Unlike the flow behavior in the 0-pin and 1-pin cases, for the 9-pin array the flow passes smoothly and uniformly around pin 1 without producing the large recirculation regions or helical vortices. The flow splits just ahead of pin 1 into two streams which then pass the three in-line pins (1, 5, 9) located on the centerline of the channel. Two small corkscrew-like vortices are observed at the entrance. Furthermore, at low Reynolds numbers (100–300) a small recirculation region exists just ahead of pins 2 and 3 in which the flow rotates from the top face to the bottom face of the channel. For  $Re > 400$ , this region progressively breaks down into a disturbed state due to its interaction with the nearby mainstream flow.

The most striking flow patterns for this array are the vortices which form along the centerline of the channel between the three in-line pins (1, 5, 9). This occurs as shown in Fig. 3(b) for Reynolds numbers ranging from about 200 to 300. The vortices are quite symmetric about the centerline. The primary vortices formed between pins 1 and 5 are relatively large and three-dimensional. In addition, secondary vortices are observed adjacent to the points of separation on pin 1. They are continuously convected into the primary vortices. On the other hand, no secondary vortices are identified near the separation points on pin 5; and the principal vortices formed in the gap between pins 5 and 9 are relatively small and two-dimensional. This difference in vortical structure is due to the relative sizes of the pins. Pin 5, being smaller, is not as effective as pin 9

in suppressing upstream vortical motions. Similar observations were made by Novak (1975). In addition, the spacing ratios of the three pins (1, 5, 9) are below the critical values identified by Ishigai et al. (1972) and King and Johns (1976). Consequently, vortex-shedding is expected to be suppressed by the downstream pin. This suppression is mainly due to the shear-layers separating from the upstream pin and reattaching to the downstream pin—thereby inhibiting the vortices behind the upstream pin from shedding downstream. When the Reynolds number is increased, the wake behind pin 1 becomes larger and unstable, causing the flow in the gap to move up and down intermittantly. Pin 9 inhibits the lateral expansion of the separated shear-layers of pin 5, holding them in the gap and thereby inducing a complex interaction between the shear-layers and the wake. Eventually the wake becomes so distorted that its structure breaks down—resulting in a region of disturbed flow.

For  $Re = 200$ , two vortices reside in each of the following wakes: between pins 3 and 8 (2 and 7), and behind pins 6 and 8 (4 and 7). The stagnation points on pins 3 and 6 (2 and 4) are approximately thirty-degrees clockwise (counter-clockwise) from a left-pointing horizontal axis. Hence, to the approaching bulk flow, pins 3, 6, 8 (2, 4, 7) appear to have a staggered arrangement. The vortices formed between pins 3 and 8 (2 and 7) are unsymmetric—the vortex on the side towards the wall of the test cell being both larger and accompanied by a secondary vortex. This asymmetry results from the bulk stream above pin 3 (below pin 2) being of higher momentum than the bulk stream below (above) it. Two pear-shaped, stationary vortices reside behind pins 6 and 8 (4 and 7). They do not shed because they are completely contained within the shear-layers on the rear sides of the pins. Near the wall beyond the closed corner of the diamond, two relatively small regions exist—recirculation zone 'III' and the region of helical vortices HV-b. Their sizes are much smaller than the corresponding sizes in the 0-pin and 1-pin cases due to the presence of the corner pins. For  $Re = 300$ , the mainstream flow between pins 3 and 6 (2 and 4) is entrained into the region between pins 3 and 8 (2 and 7)—contributing to the distortion of the vortices behind pin 3 (2). As the Reynolds number is increased from 300 to 500, the interaction between the vortices and the mainstream flow increases, leading eventually to a highly disturbed flow behind pin 3 (2).

For  $Re = 300$ , recirculation zone 'III' is hardly detectable while HV-b fills the region between pin 6 and the wall of the test cell, and exhibits some oscillatory behavior. This results in oscillations in the wake of pin 8. Increasing the Reynolds number to 400 causes instabilities in the vortices behind pin 6, causing the edge of this region to become less well-defined. For  $Re = 500$ , the two shear-layers behind pin 8 impinge upon one another with significant relative momentum, causing the position of the wake to fluctuate.

Two symmetrical vortices and two corkscrew-like vortices form behind pin 9 and in the exit, respectively. Due to the diamond-shape of the cross-section, the two converging shear layers behind pin 9 suppress the formation of secondary vortices near the points of separation. In addition, the vortices which are present remain stationary as the Reynolds number

is increased since the rapidly converging shear layers behind pin 9 suppress the tendency of these vortices to shed. For Reynolds numbers about 400, the wake behind pin 9 becomes wider, shorter and unstable, and the interaction between the shear-layers and the corkscrew-like vortices creates a disorderly flow between pin 9 and the exit.

#### 4 Conclusions

The results of the experiments reveal that: (1) The right-angle bend which follows the forward facing wedge-shaped step at the inlet to the flow cell creates: (a) secondary flow in the form of corkscrew-like vortices and (b) introduces non-uniformities in the velocity distribution in all pin arrays investigated. (2) The general flow patterns in the cell for all the pin arrays are characterized by a high velocity, three-dimensional flow near the entrance, a low velocity flow at the center of the cell, and a smooth, high velocity, two-dimensional flow near the exit. (3) Careful study of flow visualization photographs and films showed that as the Reynolds number increases from less than 100 to greater than 500, three basic types of flow are observed: (a) for  $Re < 100$ , a smooth flow fills the cell; (b) for  $200 < Re < 400$ , helical vortices and regions of recirculation are established; and (c) for  $Re > 500$ , a complex, disorderly flow exists throughout the cell. (4) Flow patterns such as corkscrew-like vortices and larger helical vortices exist for all pin arrays when  $Re > 200$ . The vigorous mixing which occurs in such small flow cells is an essential characteristic of this flow passage concept. It enables the attainment of significant enhancement of heat transfer at the cost of modest additional pressure loss. Among four different cells (0, 1, 9, and 47 pins) tested, the 9-pin cell showed the best characteristics for a high heat-flux, multi-cell, compact heat exchanger, since it distributed the flow more uniformly with moderate pressure loss.

#### Acknowledgment

The support of Bell Aerospace/Textron (Wheatfield, NY) and the encouragement of Dr. Frank Anthony, their program monitor, are gratefully acknowledged.

#### References

- Ishigai, S., Nishikawa, E., Nishimura, K., and Cho, K., 1972, "Experimental Study on Structure of Gas Flow in Tube Banks with Tube Axes Normal to Flow (Part I, Karman Vortex Flow Around Two Tubes at Various Spacings)," *Bulletin of the Japan Society Mechanical Engineers*, Vol. 15, No. 86, pp. 949-956.
- King, R., and Johns, D. J., "Wake Interaction Experiments with Two Flexible Circular Cylinders in Flowing Water," *Journal of Sound and Vibration*, Vol. 45, No. 2, Mar. 1976, pp. 259-283.
- Novak, J., 1975, "Strouhal Number for Two Cylinders of Different Diameters Arranged in Tandem," *Acta Technica, Czechoslovak Academy of Sciences*, No. 3, pp. 366-374.
- Schmidt, A. E., 1975, "Fluid Cooled Mirror," United States Patent 3,909,118.
- Schofield, W. H., and Logan, E., 1988, "Viscous Flow Around Two and Three Dimensional Wall Mounted Obstacles," AIAA Paper No. 88-3719-CP.
- Seet, J. P., 1990, "Flow Behavior in Compact Cooled Structures," M.S. thesis, Department of Mechanical and Aerospace Engineering, State University of New York, Buffalo.
- Sparrow, E. M., and Berman, Y. S., 1984, "Heat Exchanger Situated Downstream of a Right-Angle Bend," *Journal of Heat Mass Transfer*, Vol. 27, No. 9, 1984, pp. 1649-1657.